The Application of Colloidal Nanofabrication to the Study of Biological Systems

VOLUME I

Mairead Anne Wood

For the Degree of PhD

Centre for Cell Engineering,
Division of Infection and Immunity,
University of Glasgow

September 2003

Abstract

Topography plays a vital role in cell and tissue structure and function *in situ*. Furthermore, investigations into the effects of microtopography on cell behaviour *in vitro* indicate the ability to manipulate cellular activities according to topographical features and dimensions. The development of high-resolution microscopy techniques indicates nanotopography occurs *in vivo*, for example in the basement membrane of the corneal epithelia, suggesting its involvement in fundamental cell and tissue processes. By manipulating topographical components and ultimately controlling cell and tissue behaviour, micro- and nanotopography offer potential applications in implant surface modifications and ultimately implant success and also in tissue engineering.

Developments in the electronics industry have resulted in the ability to fabricate nanotopography using a variety of methods. The general protocols for nanomanufacturing lie in the high resolution and low cost of fabricating devices. With respect to biological investigations of nanotopography, surfaces patterned with the desired nanofeatures must occur across a large area (cm^2 rather than mm^2), be reproducible (allowing for consistency in experiments), and accessible (limiting the requirement for specialist equipment). Colloidal particles with nanometric dimensions fit this criteria and can be utilised with a functionalised substrate to produce nanometric spherical features.

Colloidal-based nanofabrication techniques were utilised, producing colloidal, nanopillared and grating patterns containing both planar and nanopillared surface topographies. Colloidal-based topographies were characterised using scanning electron microscopy (SEM), atomic force microscopy (AFM), laser profilometry and interference reflection microscopy (IRM). Surface area coverage and interparticle spacing of colloids adhered to a base substrate were calculated from SEM images. Charge screening and mobility restoration of colloids was used to alter area coverage and interparticle spacing. Colloidal surfaces were utilised as a mask for use with reactive ion etching, resulting in nanopillared patterning of substrates. Similarly, conventional photolithography and colloidal lithography were utilised to fabricate grating patterns of planar and nanopillared topographies lying collaterally on the same device. 20nm- and 50nm-diameter colloidal gold particles were used in these

investigations, and pillars were fabricated to either 80nm or 200nm in height in fused silica.

Epitenon, endothelial and fibroblast cells were investigated for behavioural alterations in relation to colloidal-based nanopatterned topography. Adhesion assays, time-lapse video microscopy and morphological examination utilising immunohistochemistry techniques in combination with fluorescence microscopy and scanning electron microscopy were applied to investigate behavioural alterations.

With respect to colloidal topographies, where colloids were adhered to a silica base substrate, utilising analysis of variance tests (ANOVA), the number of fibroblasts adhering to planar, 20nm- and 50nm-diameter colloidal substrates were significantly different, where $P=0.01$. ANOVA also indicated fibroblast adhesion was significantly different on planar control and colloidal topographies investigated at each time interval studied, namely 20 minutes, 1 hour and 3 hours, where $P=0.01$. Furthermore, ANOVA revealed that an interactive effect between topography and time acts to influence fibroblast adhesion. Cell-cell contacts were prevalent on colloidal topographies in comparison to controls in epitenon cells and fibroblasts as observed using time-lapse video microscopy, SEM and fluorescent imaging of cell cytoskeletons. However, cell-cell contacts occurring on 20nm-diameter colloids resulted in cellular aggregate formations, yet on 50nm-diameter colloids, regardless of cell type, resulted in alignment of cells with their neighbours. Furthermore, temporal alterations in fibroblast behaviour monitored using time-lapse video microscopy was noted and differed between topographies with different diameter colloids. Fibroblasts were observed to catapult across 20nm-diameter colloidal substrates, yet this phenomenon was absent in fibroblasts seeded on 50nm-diameter colloids. Similar differences were noted in relation to fibroblast cytoskeletal composition on 20nm- and 50nm-diameter colloidal topographies, where stress fibres were prevalent in cells on 50nm-diameter colloids, while highly developed microtubule networks were characteristic of cells in contact with 20nm-diameter colloidal substrates. SEM investigations of cell morphology indicated that cells expressed elongated protrusions on the colloidal topographies, absent in cells on planar control surfaces.

Nanopillared topography fabricated utilising a colloidal mask and reactive ion etching altered cell behaviour. Furthermore, nanopillar height and diameter was found to elicit

different cell responses. Specifically, fibroblasts seeded on 20nm-diameter pillars, regardless of height, formed cellular aggregates that appeared highly polarised with respect to internal and external environments. Furthermore, fibroblasts seeded on 200nm high pillars, regardless of diameter, exhibited extremely elongated rear detachment sites, containing both actin and tubulin. Statistical analysis of fibroblast adhesion on planar, planar etched and nanopillared topography at 20 minutes, 1 hour and 3 hours, using the Kruskal-Wallis test, indicates significant differences when all surfaces were compared at each time point.

Fibroblasts seeded on planar-nanopillared grating patterned topographies preferentially adhered to the nanopillared areas of the substrate. Furthermore, as cells on the 200nm high nanopillars spread across the grating pattern, recruitment of neighbouring fibroblasts to the nanopillared areas via cell-cell adhesions was observed.

A number of applications may benefit from the observations made with respect to cell behaviour on colloidal-based nanotopographies. Increased cell adhesion may be beneficial for implant integration. As fibroblast adhesion is significantly increased on colloidal substrates, patterning of an implant may improve successful integration. Many of the temporal observations made with respect to fibroblast motility and catapulting have been reported in developmental areas, for example the development of the avian cornea. Thus, colloidal nanofabrication when applied to the study of biological systems may help in the generation of a useful medical device or in the further understanding of fundamental processes.

Acknowledgements

To Alfred, Kathleen, Isabella and Alexander. Thank you for raising such wonderful children. To mum and dad for their continual support both emotionally and financially. I am indebted to you once again. To Kyrine, without whom, life would have been less interesting and much less fun. I think of you all, always.

This work would not have been possible without Adam Curtis and Chris Wilkinson. Thank you. Without the support and guidance, kindness and wisdom you have provided over the years, this thesis would remain unwritten.

To all within the Centre for Cell Engineering, especially Matt Dalby, Mathis Riehle, Cath Berry, Lucia Csaderova, Allison Beattie and Gregor Aitchison for help and advice, all of who played a part in the production of this thesis. Also to John Gallagher, Nikolaj Gadegaard, Graham Tobasnick, Andy Hart, George Marshall and Bob Hartley. Many thanks must also go to Margaret Mullin, for her patience and continual help in preparing biological samples for EM investigations and Lawrence Tetley, Integrated Microscopy Unit, Division of Infection and Immunity, University of Glasgow.

Thanks to all those within Electronics and Electrical Engineering, especially Mary Robertson, Linda Pollock, Eve Aitkenhead, Colin Roberts and friends, Dave Gourlay, Fraser Williamson and Douglas MacIntyre, for help, advice and training with respect to fabrication, dry etching and SEM use.

With respect to work conducted within the AO Research Institute, I would like to thank Geoff Richards, Gethin Owen, Osian Meredith, Mauro Alini and Robbi Peters for their help and for allowing me the opportunity to work in Davos during my PhD.

Many thanks to others working in similar areas, including Duncan Sutherland, Chalmers University of Technology, Gothenburg, Sweden, and those whose research paths have crossed, especially Jan A. van Mourik, CLB, Amsterdam, The Netherlands and Rose Johnstone, McGill University, Montreal, Quebec, Canada for donated publications regarding their research. Also to Mary Jones, Senior Lecturer in Medical Statistics, Keele University, for her advice regarding statistical analysis of cell adhesion data.

Thanks to all those whose company I enjoyed during my seven year stay in Glasgow, especially Laurie, Mark, Charlie Clark, The D-Karts and all those associated with these fellowships. Most of all, I cannot overlook the kindness and support of Iona and Dave. The Cava evenings are legendary.

For continual moral and financial support and much required help in deducing the finer points of biochemistry, I must thank Osian Meredith. Also for your patience and understanding of all things.

Finally I would like to apologise and thank those who feel they may have been overlooked in these acknowledgements...

Table of Contents

Wood, M. A., Meredith, D. O., Owen, G. Rh., "Steps Towards a Model Nanotopography" IEEE Transactions on Nanobioscience, 1, 4, pp133-140, 2002

Wood, M. A., Riehle, M. O., Wilkinson, C. D. W., "Patterning Colloidal Nanotopographies", Nanotechnology, 13, pp605-609, 2002

Wilkinson, C. D. W., Riehle, M. O., Wood, M. A., Gallagher, J. O., Curtis, A. S. G., "The use of materials patterned on a nano- and micro-metric scale in cellular engineering", Materials Science and Technology C, 19, pp263-269, 2002

Riehle, M. O., Dalby, M. J., Johnstone, H., Gallagher, J. O., Wood, M. A., Casey, B., McGhee, K., "Nanometric surface patterns for tissue engineering: Fabrication and biocompatibility in vitro", Materials Research Society Symposium Proc, 705, ppY5.1.1-Y5.1.11, 2002

Curtis, A. S. G., Casey, B., Gallagher, J. O., Pasqui, D., Wood, M. A., Wilkinson, C. D. W., "Substratum nanotechnology and the adhesion of biological cells. Are symmetry or regularity of nanotopography important?", Biophysical Chemistry, 94, pp275-283, 2001

List of Abstracts

The Effects of Irregular Nanotopography on Mammalian Cell Adhesion and Behaviour, M. A. Wood, A. S. G. Curtis and C. D. W. Wilkinson. Accepted as Oral Presentation. ***European Materials Research Society (E-MRS) Spring Meeting***, Strasbourg, France, *2002*

The Effects of Irregular Nanotopography on Mammalian Cell Adhesion and Behaviour, M. A. Wood, A. S. G. Curtis and C. D. W. Wilkinson. Accepted as Poster Presentation. ***European Materials Research Society (E-MRS) Spring Meeting***, Strasbourg, France, *2002*

The Effects of Random Nanotopography on Cell Adhesion and Behaviour, M. A. Wood, A. S. G. Curtis and C. D. W. Wilkinson. Accepted as Oral Presentation, ***Material-Cell interactions for the development of biocompatible medical devices, Summer School and Workshop in Biomaterials***, Ellös, Sweden, *2001*

The Effects of Random Nanotopography on Cell Adhesion and Behaviour, M. A. Wood, A. S. G. Curtis and C. D. W. Wilkinson Accepted as Oral Presentation. ***Society for Experimental Biology (SEB) Annual Meeting***, University of Kent, Canterbury, *2001*

The Effects of Random Nanotopography on Cell Adhesion and Behaviour, M. A. Wood, A. S. G. Curtis and C. D. W. Wilkinson. Accepted as Oral Presentation. ***3rd EuroConference, "Nanoscience for Nanotechnology"***, Somerville College, Oxford, *2000*

Accompanying Material

An accompanying Compact Disk entitled "The Application of Colloidal Nanofabrication to the Study of Biological Systems", Mairead Anne Wood, 2003 is located at the backboard of the thesis. Digital time-lapse video microscopy footage, and one image are included on the CD, and are arranged as follows:

Chapter 3:	Figure33311VideoA.tif	hTERT fibroblasts on 20nm-diameter colloidal topography
	Figure33311VideoB.tif	hTERT fibroblasts on 20nm-diameter colloidal topography (continued)
	Figure33312.tif	hTERT fibroblasts on 50nm-diameter colloidal topography
Chapter 4:	Figure4223IRM.bmp	Interference Reflection Microscopy image of 50nm-diameter, 200nm high pillared topography
	Figure432.tif	HGTFN endothelial cells on 50nm-diameter, 200nm high pillared topography
Chapter 5:	Figure531VideoA	hTERT fibroblasts on 50μm grating planar-nanopillared (20nm-diameter, 200nm high) pillared topography
	Figure531VideoB	hTERT fibroblasts on 50μm grating planar-nanopillared (20nm-diameter, 200nm high) pillared topography (continued)

All tif images should be viewed using Object-Image or ImageJ applications. Videos in Chapter 5 should be viewed using QuickTime.

List of Tables

List of Graphs

List of Equations

List of Figures

Chapter 1: Introduction

As life expectancy increases and mortality rates decrease in the Developed World, implants are frequently required to replace defective tissues as a result of biological wear and tear associated with ageing (Tuljapurkar et al, 2000, Kirkwood, 1996). Injuries, for instance fractures, occurring as a result of accidents are similarly treated through the application of implants and tissue reconstruction. The utilisation of medical implants in the treatment of disease and defect has commanded a greater understanding of the tissue-implant interface. As a result, implant surfaces can be optimised, encouraging integration and successful outcomes with respect to implanted material *in vivo*. For example, when considering periodontal disease, bone tissue is observed to be in close contact, 100 to 900μm, but not in direct conjunction with the implant surface of replacement teeth and edentulous areas. The establishment of this zone, and ultimately implant-tissue integration, is critical to the success of the implant (O'Neal et al, 1992). As a result, modified surfaces have been developed with, for example, hydroxyapatite (Dalby et al, 2001) and bioactive coatings (Gil et al, 2002), for use in orthopaedic and dental implants.

Adhesive interactions are important to many physiological and pathological events and are modulated through a variety of cellular activities (MacSween and Whaley, 2002). Furthermore, the local environment and implant materials are central to cellular response. Complement activation and phagocyte adhesion occurring at the biofluid-implant interface *in vivo* can cause problems and are believed to be responsible for the initiation of unwanted, chronic inflammatory response in many circumstances (Tang et al, 1998), which can result in rejection of the implant. Complement activation is associated with the structural degradation of bovine bioprosthetic heart valves, ultimately resulting in the reduction of implant success (Moczar et al, 1996). Chronic inflammatory response is similarly costly with respect to hip replacements, where macrophages attack titanium implant surfaces, producing material degradation that necessitates secondary, replacement operations. Thus, with respect to optimal biological interfaces used in medical and surgical applications, the key to successful interface reactions lies in an understanding and management or manipulation of host response to implanted materials.

When considering biological-substrate interfaces, three main classifications exist with respect to implant material characteristics. These are the physical architecture of the surface, or topography, chemical and viscoelastic properties (Kasemo and Gold, 1999). It is unlikely that any one of these factors is responsible for observed cell reactions *in vitro* and *in vivo* suggesting synergistic effects occurring between these elements, discussed by Britland and co-workers with respect to BHK fibroblast response to surfaces expressing both chemical and topographical modifications (Britland et al, 1996). By controlling and altering material properties, investigation into the importance of each can be conducted with respect to their effects on cell and tissue behaviour, offering methods of biological manipulation for use in implant integration and increased understanding of fundamental cell behaviour.

Fabrication techniques employed in our understanding of cell and tissue response to materials have arisen from the microelectronics industry, specifically from methods utilised in the production of integrated circuits (Wilkinson et al, 2002, Flemming et al, 1999, Voldman et al, 1999). For example, microcontact printing has been applied in chemical (James et al, 1998), topographical (Hidber et al, 1996) and viscoelastic (Balaban et al, 2001) investigations of cell behaviour. Furthermore, developments within this industry have led to the production of topography with in-plane nanometric features (Xia et al, 1999). As a result, biological investigations of cell and tissue response to nanotopography are now emerging (Andersson et al, 2003, Dalby et al, 2003[a-b], Dalby et al, 2002[a-e], Wood et al, 2002[a], Riehle et al, 2002, Wilkinson et al, 2002, Curtis et al, 2001, Hanarp et al, 1999, Wilkinson et al, 1998, Turner et al, 1997, Wojciak-Stodhard et al, 1996, Wilkinson, 1995, Clark et al, 1991).

1.1 The cell-substrate interface

The cell-substrate interface requires specific attention when considering cell reactions to topography. Initial contact between the cell and its environment is established at this interface, and is the first step in a series of intracellular and molecular events that are to occur in relation to the substrate (Katz et al, 2000, Galbraith and Sheetz, 1998). Furthermore, a solid-liquid interface occurs at the instant cells are seeded on an experimental surface, where, for example, thermodynamic and kinetic reactions, alter the properties of a surface (Zhdanov and Kasemo, 2000).

1.1.2 Interface processes

Kasemo et al (1988, 1994 and 1999) propose that a number of events occur when a substrate surface is contacted by a biofluid, whether it be blood *in vivo* or media containing cells *in vitro*. These events are believed to act by modifying the device surface in a manner resulting in "a casual connection between the detailed properties of a native implant surface and the ultimate tissue response" (Kasemo and Gold 1999). This results in the previously characterised surface adopting a further modified state, which, in turn, determines the final interaction between cells and the substrate.

Immediately upon the production of the device in question, contamination in the form of hydrocarbons and both inorganic and organic sulphur and nitrogen compounds from the ambient environment, is thought to occur (Kasemo and Gold, 1999). This is likely to be due to the increased surface energy at the interface occurring at the atomic scale via unterminated bonds (Kasemo and Lausmaa, 1994). Contamination can be controlled through the utilisation of cleaning and "passivation" techniques, where the reactive bonds of the outer atomic layer are saturated. Upon immersion in a bioliquid, the substrate surface is hydrated with water molecules. The interaction of the water with the material determines the following events as a result of a hydrophobic or hydrophilic layer being presented to ions, proteins and cells that subsequently reach this interface. The concepts of hydrophobicity and hydrophilicity are directly related to the binding strength of water to the surface at a molecular scale, which, in turn, is related to the contact angle for water droplets.

Hydrated ions are incorporated into the surface water layer, where these interactions are governed by the surface forces of the electrostatic double layer present at the material interface. Biomolecules, for example proteins, are next to contact this modified surface, where they adsorb. Proteins may experience conformational alterations (Zhou et al, 1997), dependent upon the immediate contacts established at the substrate interface, and possible replacement, where smaller proteins are superseded by larger proteins in the fluid, may occur via the "Vroman effect" (Kasemo and Gold, 1999). To minimise their free energy, proteins may denature (Kasemo and Gold 1999). Proteins continue to adsorb to the surface. Thus, upon reaching the surface, cells are presented with an ionically screened and protein-coated substrate, which, in turn, has been influenced by the features, for example chemical, topographical or mechanical, present at the surface of the material. The effects of surface characteristics whether chemical or topographical,

on the proteins interacting at this boundary will determine the effectiveness of cell interactions. It is probable that the protein layer is never totally static, but subject to slow, dynamic changes (Kasemo and Gold, 1999), reflective of the cellular-substrate processes as a whole.

The highly dynamic nature of conditions initially occurring at the cell-substrate interface are thought to reduce with time as the system stabilises and the material is further masked reducing topographical, chemical and viscoelastic cues. Thus the time-space domain of the interface and its evolution must be considered (Kasemo and Gold, 1999), as the surface undergoes continuous remodelling (Kasemo and Lausmaa, 1994).

Although surface modification occurs as a result of contact between the substrate and biofluid, the dynamic hydration and protein layer is surface specific, as different surfaces will develop altered biomolecular coatings under the same conditions (Kasemo and Lausmaa, 1994). Thus, topographical factors contribute to the identity of the biomolecular layer established following the introduction of cells to a substrate. Protein, ion and other substances can be exchanged between the biomolecule-coated cell membrane and the material surface, due to the dynamics of these factors, resulting in a complex and dynamic interface (Kasemo and Lausmaa, 1994). Interactions can occur via penetration of the cell membrane by released ions or molecules (Fromherz, 1997), or via activation of cell membrane receptors (Kasemo and Gold, 1999, Kreiss and Vale, 1999, Alberts et al, 1995). Cells interact with the protein-coated experimental substrate by extending processes, and contact the surface via membrane-bound proteins and receptors. Thus, there is no requirement of direct cell-surface contact for a surface-specific cell interaction to be elicited.

1.1.3 Cell interactions in relation to a substrate

Cell-substrate adhesion establishment and composition is paramount to the effects of a surface on cell behaviour and, ultimately, cell fate (Galbraith and Sheetz, 1998). Focal adhesion complexes (FACs) are generally accepted as the anchorage points of the plasma membrane of cells to the substratum with which it is in contact. Hydrophobicity, protein expression, rigidity and topography occurring at the substrate surface can influence the location, structure and function of these anchorage sites within their external capacity (Schwarz et al, 2002, Balaban et al, 2001, Katz et al, 2000, Lo et al, 2000). With respect to transmembrane and internal cellular environments, focal adhesions are mediated by transmembrane receptors associated with actin

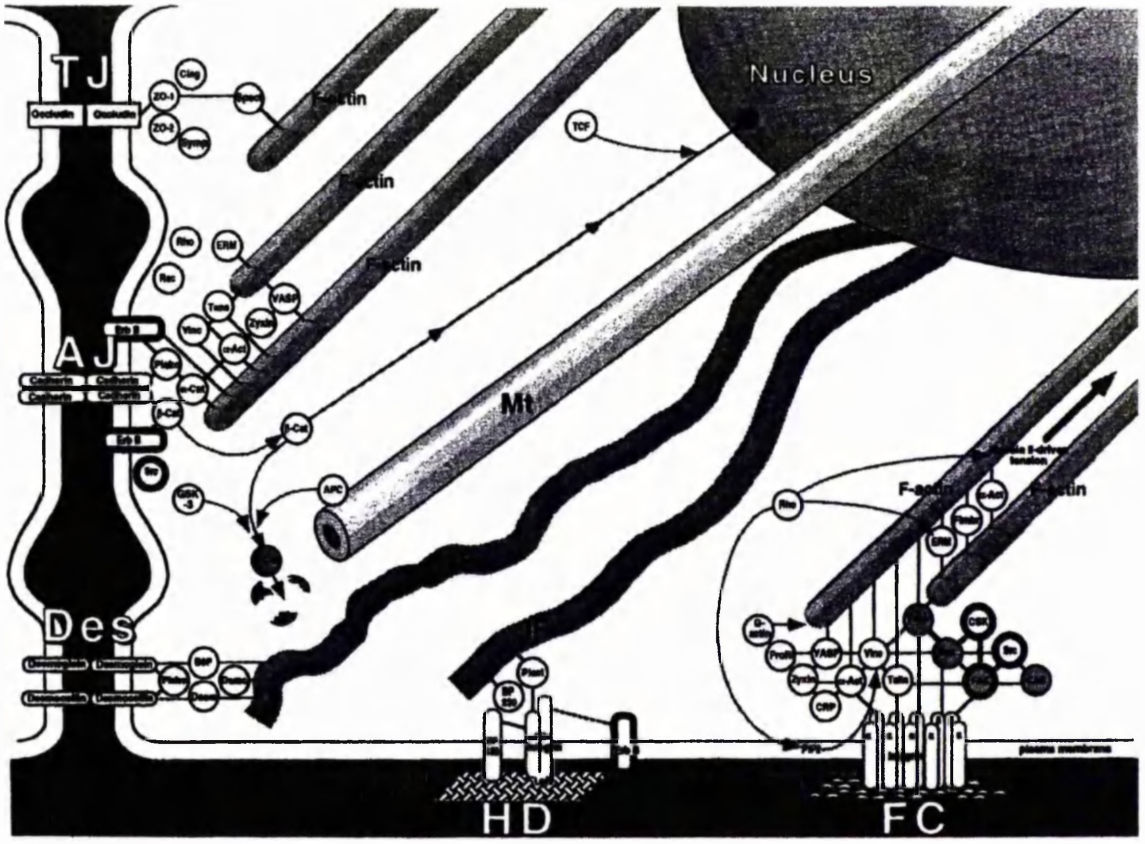

Figure 1.1: Molecular interactions between cell junctions and the cytoskeleton. Focal contacts (FC) form adhesions between the cell and underlying substrate. Signalling events occur via molecular interactions between integrins and the actin cytoskeleton, determine cell behaviour and fate. Proteins (contained within circles) believed to be capable of direct interactions are connected by a solid line. Indirect molecular interactions are denoted by lighter, grey lines. Tyrosine kinases are contained within circles with heavy dark shells. Proteins contained within shaded circles undergo tyrosine phosphorylation in response to cell-substrate adhesions (FC). (Image from Kreiss and Vale, 1999, pp5).

microfilaments located within the cell, Figure 1.1. A variety of cytoskeleton-associated anchor proteins are involved in the assembly, disassembly and stabilisation of FACs. For example, talin and α-actinin interact with the cytoplasmic domain of the β1 chain of integrin, and with actin, respectively, Figure 1.1, resulting in the association of integrin transmembrane receptors and the actin cytoskeleton, (Kreiss and Vale, 1999). Bidirectional signalling and interaction between the cell cytoskeleton and integrins is crucial in the reactions of cells to a substrate or topography (Schoenwaelder and Burridge, 1999), Figure 1.2.

Immediately upon seeding of cells on a substrate, focal adhesion contacts emerge. Maturation of these adhesion sites occurs over time, seen in the "dot-to-dash" morphological sequence of vinculin, with "dots" of vinculin indicating immature, nascent contacts and "dashes" indicative of more stable, mature adhesions (Berdshadsky et al, 1985). Mature "dash" FAC morphology is indicative of cells entering or in S-phase (Meredith et al, 2003), highlighting the importance of FACs with respect to cell-

cycle progression, ultimately resulting in proliferation. Furthermore, the dynamic nature of focal contacts and their pivotal role in microfilament regulation and resultant contractile forces occurring within cells (Schwarz et al, 2002, Choquet et al, 1997, Crowley and Horwitz, 1995), suggest FACs act as a mechanosensory mechanism, relaying information between internal and external environments (Geiger and Bershadsky, 2001, Schoenwaelder and Burridge, 1999).

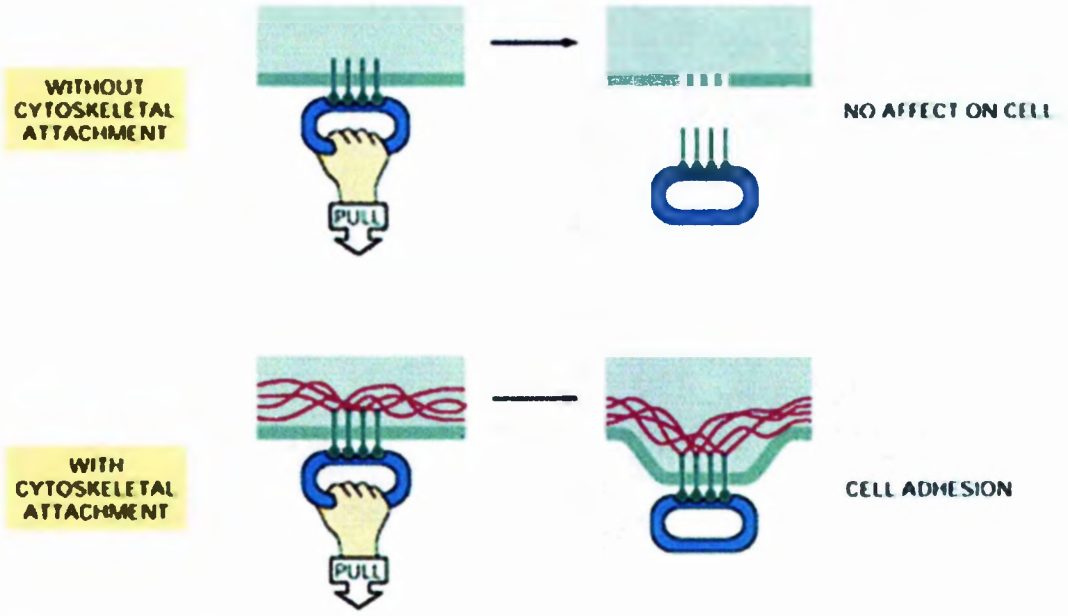

Figure 1.2: The importance of the cytoskeleton in cell adhesion. Without the cytoskeleton attachment at adhesion sites, the cell would be unable to establish interactions at the cell-substrate interface. When adhesion complexes are expressed by cells information is transmitted across the membrane via membrane proteins to the cytoskeleton, triggering a cellular response. The same principle described for adhesive interactions can be applied to cell-surface molecules. (Courtesy of Alberts et al, 1995, pp970).

The effects of cell-substrate adhesions are directly linked to fundamental cell behaviours, for example cell polarisation, movement and motility and spreading (Horwitz and Parsons, 1999, Huttenlocher et al, 1996) required prior to proliferation, ultimately determining progression through the cell-cycle. These processes of the cell-cycle are reliant on the nature of adhesions established by the cell, their interactions with the cell cytoskeleton via FAC-associated proteins, Figure 1.1, and ultimately signal transduction and gene regulation (Alpin et al, 1999, Cooper, 1999, Schoenwaelder and Burridge, 1999). Anchorage-dependency, the process where adhesions are established prior to progressing to signal transduction, must occur if cells are to progress through the cell-cycle, and cells must be able to sense and communicate with their surrounding environment through focal adhesion contacts (Geiger and Berdshadsky, 2001). Cell-shape mediated growth follows, where cells spread across the substrate. This stage is indicated by the presence of actin stress fibres within the cell cytoplasm. Cells

progressing through these cycles are then capable of division and proliferation, resulting in completion of the cell-cycle (Murray and Hunt, 1993).

The development and morphology of the cell cytoskeleton is indicative of many of the processes observed in the advancement of a cell population reflecting the occurrence of adhesions required in cell-cycle progression. Ultimately, it is the alterations of cell-cycle that are investigated when researching cell response to alternative environments. Actin microfilaments and microtubules perform various functions within the cell (Salmon and Way, 1999, Preston et al, 1990). The cytoskeleton acts as a scaffold resulting in structural determination and morphology of the cell, and also acts as a communication network transporting membrane-bounded organelles and various proteins throughout the cell. Motility and cell movement in relation to a substrate, cell contractility and rigidity occur as a direct result of actin and tubulin dynamics in relation to focal adhesion structure (Beningo et al, 2001, Lo et al, 2000, Horwitz and Parsons, 1999, Choquet et al, 1997, Huttenlocher et al, 1996). Positioning and anchoring of cell-surface receptors appears to be related to the cytoskeleton, with transmembrane proteins linking cell-surface receptors, which, in turn, attach to cytoskeletal elements, via attachment protein (Kreiss and Vale, 1999), Figure 1.1. Phagocytosis and endocytosis also involve steps where microtubules in particular are observed to play a fundamental role in vesicle formation. Microtubules and actin microfilaments both contribute towards cell polarisation and spatial organisation of the cell cytoplasm, perhaps the most fundamental function in which they are both involved (Alberts et al, 1995).

In summary, cell behaviour is dependent upon adhesive interactions with a substrate (Geiger and Bershadsky, 2001, Schoenwaelder and Burridge, 1999, Galbraith and Sheetz, 1998). The structure and function of adhesions influences actin and tubulin cytoskeletal behaviour, Figure 1.1 (Beningo et al, 2001, Lo et al, 2000, Horwitz and Parsons, 1999, Choquet et al, 1997, Huttenlocher et al, 1996), which, in turn alters cell shape, morphology, spreading, motility and ultimately, proliferation. These processes are involved in cell-cycle progression and, ultimately, cell fate (Murray and Hunt, 1993) in both a physiological and pathological context (MacSween and Whaley, 1992).

1.2 Cellular Behaviour in Relation to Microtopography

The effects of surface topography on cell behaviour were observed as early as the 15th century by Merstide and also by Loebe and Fleisder. In 1911, Harrison noted cell alignment to individual fibres of spider's webs (Harrison, 1911). It was not until 1934 that the term "contact guidance", the "directed locomotory response of cells to an anisotropy of the environment" (Lackie and Dow, 1999) was coined by Weiss (Weiss, 1934). Within the past three decades, advances in the microelectronics industry, aimed towards integrated circuit fabrication, has resulted in the ability to produce patterned topography with accurate dimensions in the x-, y- and z-planes. This has led to the development of microtopography for use in experimental biology, where cell response to various types of patterned substrates have been recorded, (Flemming et al, 1999, Curtis and Clark, 1990).

An array of fabrication techniques have been developed over the past decade for use in biological investigations of cell response to both chemical and topographical patterning of substrate surfaces (Craighead et al, 2001, Ito, 1999). Furthermore, the synergistic and hierarchical effects of surface chemistry and topography have been investigated, where BHK cells were observed to align preferentially to superimposed orthogonal chemically adhesive tracks rather than grooved topography (Britland et al, 1996). However, the proportion of cells aligning to grooved topography, with superimposed aminosilane patterns present, was found to increase with increasing groove depth, particularly at 3 and 6μm on 5 and 12μm pitch patterns. In these instances, actin stress fibres in cells traversing the topographical groove in line with the chemical pattern were aligned to both the chemical and topographical tracks in an opposing manner. Further investigation utilising confocal microscopy indicated that the opposing stress fibres were at different heights within the cell, separated by approximately 1.5μm. These results indicate the ability of BHK cells to sense and respond to both chemical and topographical guidance cues simultaneously under certain conditions.

The importance of topographical cues in relation to cell adhesion, morphology, behaviour and protein regulation and expression have emerged in relation to a variety of patterns (Flemming et al, 1999). These include V-shaped grooves (Chou et al, 1995, Oakley and Brunette 1993), cylindrical substratum (Rovensky and Samoilov, 1994),

steps (Clark et al, 1987), microspheres (Miyaki et al, 1999) and grooves (Wojciak-Stodhard, 1995[a-c], Clark et al, 1990).

Oakley and Brunette (1993) examined the sequence in which microtubules, focal contacts and microfilament bundles in human gingival fibroblasts align to Titanium-coated V-shaped, 3μm-deep, 30μm-pitch grooves. Microtubules were first to align parallel to the bottom of grooves, as early as 20 minutes, and preceded orientation of the cell as a whole. Between 40 and 60 minutes, actin microfilaments aligned to the wall or ridge edge of the topography. However, fibroblasts were aligned prior to microfilament alignment. Focal adhesions were distributed radially at early times, and, following 3 hours, the majority of FACs aligned either perpendicular, or parallel to the micrometric grooves. Cell area was reduced on grooves in comparison to planar controls, and an increase in height of fibroblasts was also recorded on the experimental substrate. Oakley and Brunette suggested these observations could be attributed to the exposure of shear-sensitive elements in the fibroblasts being exposed to anisotropic strain. As a result, cells may respond by aligning to the shear-free plane, defined as the plane perpendicular to the direction of the largest principal stress. Furthermore, microtubules, which, in this instance, appear to determine cell orientation, could become more stabilised in the strain-free environment.

Similar work was conducted, where gingival fibroblasts, seeded on 3μm deep V-shaped micromachined grooves coated with 50nm Titanium with 6 to 10μm repeat spacing, appear significantly elongated and orientated compared to cells on planar controls (Chou et al, 1995). Furthermore, fibroblast height was recorded as 1.5-fold greater than controls. On a per cell basis, fibronectin mRNA was significantly increased as was secreted fibronectin on the grooves, with a 2-fold increase recorded, in comparison to control cells. Fibronectin mRNA stability was also altered in relation to the V-shaped groove topography, and a 2-fold increase in the amount of fibronectin assembled in the ECM at all time points was observed. Chou and colleagues thus proposed that V-shaped groove substrata directly influence cell shape and fibronectin at transcriptional and post-transcriptional levels, and, in addition, the amount of fibronectin assembled in the ECM. A possible shape and function relationship for cells was suggested, as was the relationship between mRNA and the cytoskeleton with respect to fibronectin stability as a result of topography-dependent and time dependent divergence. Furthermore, Chou

discloses that preliminary results indicate enzymes associated with ECM remodelling were also affected by V-shaped groove topography.

Cylindrical substrata with a high degree of curvature (12-13 or 25μm radii) alters cell size, shape and alignment, yet is less optimal for cell adhesion in comparison to control, planar surfaces (Rovensky and Samoilov, 1994). Cells exhibiting defined, elongated microfilaments were observed to orientate along cylinders rather than around their circumference. Where actin formed circular bundles or was unpolymerised, cells were observed to follow the cylindrical contours of the surface. These observations suggest alignment of cells to the sheer-free plane (Oakley and Brunnette, 1993), or relative inflexibility of microfilament bundles results in limited bending of actin-rich features (Dunn and Heath, 1976). Furthermore, a variety of different cell types, ranging from mouse embryo fibroblasts to fully transformed epithelial cells at different stages of the cell-cycle were investigated, and different responses, dependent upon these factors, to the cylindrical substrate were recorded. These observations indicate that microtopographical effects on cell behaviour occur as a result of genetic predisposition, cell-cycle stage, topographical dimensions and cylindrical curvature.

Polystyrene microspheres have been spin coated in the presence of sodium chloride to fabricate hexagonally packed monolayer colloidal topography (Miyaki et al, 1999). Water contact angle was calculated to decrease with increasing pitch of the microspheres. Neutrophil-like cells were observed to adhere to this microtopography, and active oxygen release altered according to diameter of the spheres, where a maximum release was recorded for approximately 1μm diameters in comparison to topographies composed of 0.6 to 1.2μm diameter spheres. Thus, Miyaki and colleagues proposed that microsphere pitch was an important factor in cell reactions to this surface.

Similar observations were made in relation to the effects of single-step topography measuring between 1.5 and 10μm on cell types ranging from BHK fibroblasts to rabbit neutrophils (Clark et al, 1987). Neutrophils did not respond to steps in any manner. However, BHK fibroblasts and chick embryonic neural cells traversing steps was gradually inhibited as step height increased and as a result, cell alignment also increased. Where BHK cells approached step heights of 10 to 18μm, almost all cells aligned. Prevention of crossing the topographical step occurred irrespective of their direction of cell approach. Furthermore, all steps significantly increased the degree of

cell alignment regardless of whether cells were ascending or descending the feature. Neural cell processes fail to cross steps with a height of 4μm, yet processes follow the step edge. The degree to which a cell is impeded in its movement is dependent upon the size of the step feature, where alterations in the cells ability to cross and align to increasing step height is a gradual one (Clark et al, 1987).

Following investigation of cell reactions to a single step feature, Clark and colleagues examined the effects of multiple-grooved substrata on cell behaviour (Clark et al, 1990). Grooves of various dimensions, with 2-24μm repeats and 0.2 to 1.9μm depths, were fabricated, and BHK, MDCK and chick embryo cerebral neurons were seeded on the experimental microtopographies. Repeat spacing has little effect on cell behaviour. However, groove depth was pivotal in determining cell alignment, where increased depth resulted in increased alignment. Clark suggested that the cell alignment observed occurs in an attempt to minimise cytoskeletal distortion. Interestingly, multiple-grooved substrata results in greater cell alignment when compared to individual step features, suggesting multiple patterning confronts cells where little or no free area exists to escape the effects of the topography. Multiple grooves thus elicit a much stronger response in comparison to individual topographical features. This in turn appears to be amplified by population density for contact-inhibited cells, as BHK cell alignment was observed to increase proportionally with population density (Clark et al, 1990).

Similar observations have been reported regarding cell behaviour on microgrooved topography. Investigations by Wojciak-Stodhard and colleagues (1995[a]) indicate that microtubules in BHK fibroblast align to grooves at 20 minutes following initial plating. Actin microfilaments, located at the wall-ridge edges, are observed in these cells after 40 to 60 minutes of contact with grooved substrata. As a result, Wojciak-Stodhard and colleagues propose that microtubule, rather than microfilament alignment, determine cell orientation on microgrooved topographies (Wojciak-Stodhard et al, 1995[a]). Furthermore, microfilaments are believed to be central in the initiation of BHK cell response to these substrates, where microtubules are also involved at later times. Actin condensations were observed at groove/ridge boundaries as early as 5 minutes post-seeding. Furthermore, disruption of actin filaments with Cytochalsin D (Carter, 1967) resulted in reduced cell orientation on grooves, while depolymerisation of microtubules resulted in cell spreading across many grooves. Furthermore, macrophages in contact with grooved substratum display increased spreading and F-actin content. In addition to

this, macrophage speed and persistence of movement is upregulated (Wojciak-Stodhard et al, 1995[b]). The observed alignment of cells to microgrooved topography has resulted in the proposal of grooved substrata with a depth of 5μm depth as a means to facilitate healing of severed flexor tendons *in vitro* (Wojciak-Stodhard et al, 1995[c]). These findings indicate research into the effects of micropatterned topography not only serve to enlighten our understanding of fundamental cell behaviour, but can also be applied to *in vivo* defects through the production of microfabricated medical devices (Voldman et al, 1999).

In summary, microtopography is capable of altering fundamental cell behaviour, both *in situ* and when utilising artificial substrata *in vitro* (Curtis and Clark, 1990). Focal adhesion contacts, cytoskeletal morphology, cell alignment, motility and protein expression are altered in accordance to a variety of microtopographies in comparison to planar controls (Miyaki et al, 1999, Wojciak-Stodhard et al, 1995[a-b], Chou et al, 1995, Rovensky and Samioilov, 1994, Oakley and Brunette, 1993, Clark et al, 1990). Cell and cytoskeletal alignment are observed most distinctly on grooved topographies (Wojciak-Stodhard et al, 1995[a-c], Chou et al, 1995, Oakley and Brunette, 1993, Clark et al, 1990). Topographic feature dimensions elicit different behavioural responses in cells. Furthermore, cell response to microtopography is cell-type specific, and cells from the same population, but at different stages of the cell-cycle effect alternate responses.

1.3 Fabrication techniques producing nanopatterned surfaces

Nanostructured devices used in biological research are ultimately dictated by trends occurring within the electronics industry. As a result, features with dimensions of less than 100nm, more similar to the dimensions of entities found within cellular environments (Kasemo and Gold, 1999), are now emerging in topographical studies with respect to cell behaviour and interactions at the nanometric level due to the accessibility of these techniques.

The general protocols for nanomanufacturing lie in the high resolution and low cost of fabricating devices (Xia et al, 1999). This may include the high cost fabrication of a master, with structures replicated in great quantity in an inexpensive process, resulting in the initial outlay of the master being an insignificant part of the overall cost of structures. The definition of a deliberate pattern is by its very nature a serial process, where every picture element has to be defined one by one. If utilised in the production of replicas, the structures, having undergone the writing process, are referred to as master die. The economical and convenient route to multiple copies of a master is termed replication, where information is transferred to a functional material, usually of a polymeric nature, from the master, rapidly, in a single step and with high precision. Thus, nanopatterning can be separated into three main categories: primary pattern definition or writing, pattern transfer and mechanical transfer techniques, Figure 1.3.

As the required structures and functions of nanopatterned materials differ between electronic engineering and biology, focus has been placed on the fabrication of in-plane nanostructures, in use and development, believed to be important in the future investigations and understanding of cell reactions to a variety of nanotopographies. A summary of nanofabrication techniques, limits and qualities is provided in Table 1.1. Furthermore, in practice, more than one fabrication process is often implemented to achieve the final design of a device (Wood et al, 2002[b], Ilic and Craighead, 2000, Casey et al, 1997, Chen and Ahmed, 1993).

Overview of Nanolithography techniques and processes

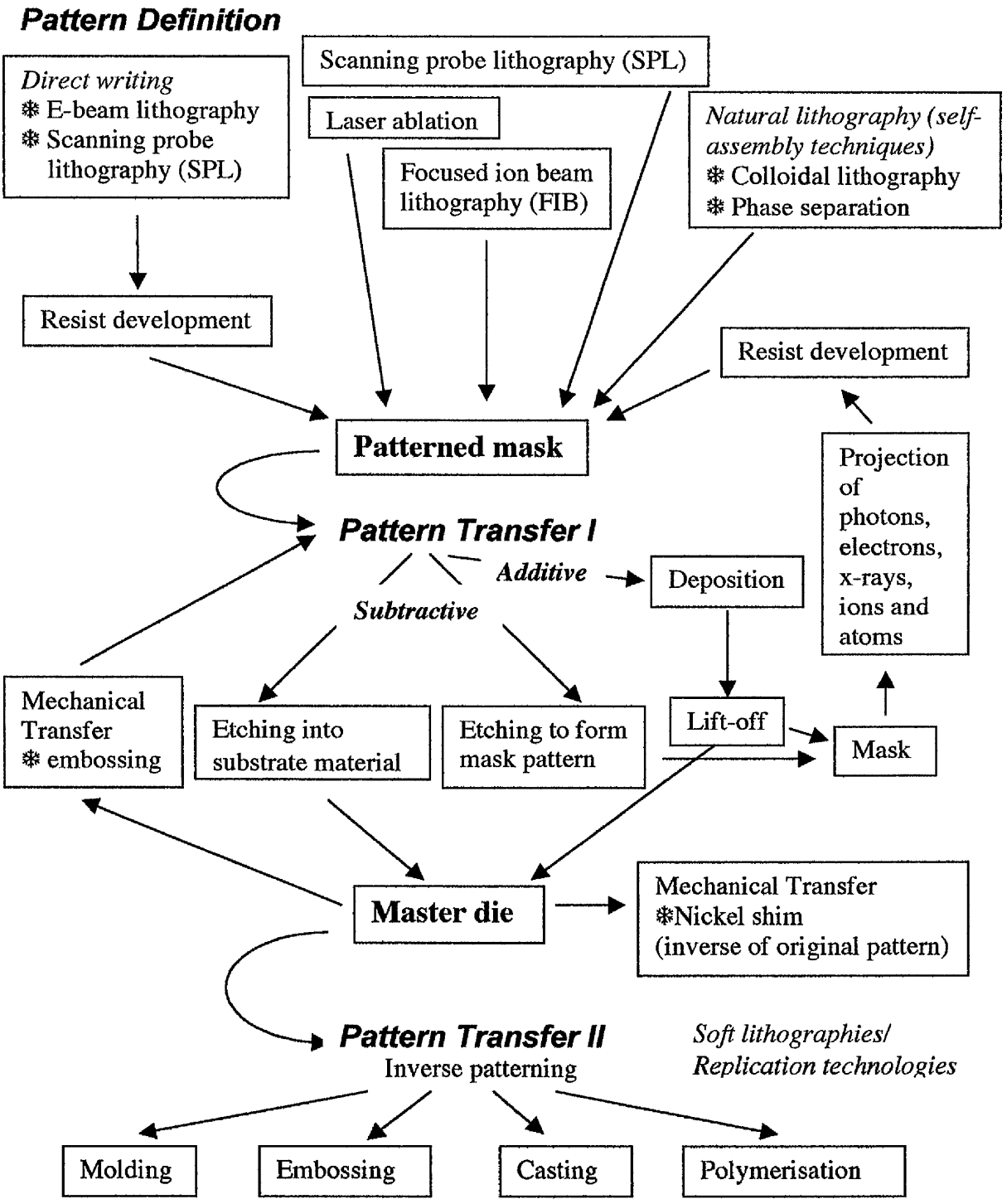

Figure 1.3: Pattern definition or pattern writing is the first stage in nanofabrication, resulting in patterning of a resist, masking of a base substrate utilising self-assembly techniques or direct writing on a base substrate via laser ablation, FIB or SPL methods. Following mask fabrication, patterns can be transferred in a step where pattern definition is utilised either in the form of a patterned resist or mask, termed in this diagram "Pattern Transfer I". Patterns are transferred to the desired substrate material either by subtractive etching or additive lift-off techniques. Pattern transfer results in the fabrication of a master die. A subsequent pattern transfer step, termed here "Pattern Transfer II", can be performed where a master die is utilised to transfer an inverse representation of the original pattern to a deformable polymer. The processes described in this second stage of pattern transfer are often referred to as soft lithography techniques or replication technologies.

Fabrication technique	Methods of achievement	Advantages	Disadvantages	Notes
Conventional Lithography (using Photons, Particles and Scanning Probes to alter properties of resists)	Contact Mode Photolithography	Large areas can be patterned in a single step inexpensively High-throughput Resolution is 0.5-0.8μm with UV light and 0.1μm with DUV light	Minimum feature size determined by diffraction occurring as light passes through gap between mask and resist Mechanical contact can damage fragile structures on mask and substrate Lateral motion problems aligning mask to existing features Theoretical resolution is limited by Rayleigh diffraction, thus wavelength can be reduced to increase feature resolution	Most highly developed and widely used of technologies now practised Mask required
	Projection Printing Photolithography	Large areas can be patterned in a single step inexpensively High-throughput Significantly smaller features on resist than on mask No contact or alignment problems	Theoretical resolution is limited by Rayleigh diffraction, thus wavelength can be reduced to increase feature resolution Lack of transparent materials suitable for wavelengths below 193nm	Integrated Circuits are manufactured using Projection Printing Photolithography Mask required
	E-beam Lithography	Depth of mask is accurate and reproducible Extremely high resolution capability (due to resolution of electron optical lenses which are limited by spherical and chromatic (voltage control) abberations Practically, 4nm beam diameters of high current are now available By using thin membranes (10-100nm) as substrates, 7nm features are possible	Resolution mainly determined by scattering of primary and secondary electrons in resist film and substrate Impractical for mass production due to lengthy writing time/serial process, although methods are emerging in an attempt to resolve this issue (ie. Gadegaard et al, 2003)	Often used where other methods simply fail Mainly used to produce photomasks, master die or for fabricating small structures for research Projection techniques (ie. SCALPEL) being developed may allow for mass production of nanopatterned structures Can be maskless Used to make masks
	X-ray Lithography (XRL)	Possible route to reducing wavelength limitations seen in photon-based lithography	Lack of commercially feasible means of producing masks	XLR requires further development, especially when considering the associated optics of this system, if it is

		Soft X-ray (EUV) methods using reflective optics has resulted in successful nanopatterning Proximity XRL using wavelengths <1nm, results in the production of routine structures with dimensions of 30nm	Lack of suitable optics to reduce image of mask Placing mask in close proximity of sample (10mm) is challenging	to play a serious role in nanopatterning of substrates
	Focused Ion Beam Lithography (FIB)	Approx 15nm features have been fabricated using 50keV Ga^+ 2-lens systems Higher resist exposure sensitivity (approx 2X) compared to e-beam Negligible ion scattering in reist with very low backscattering from surface	Serial technique, thus slow Sample damage by high-energy ions Source brightness is not as good as e-beam Chromatic abberation is worse from ion thermal noise	Development of FIB is believed to result in success of system in nano-patterning of implants, repair of photo and x-ray mask defects, inspection in IC processes, failure analysis and surface characterisation
	Scanning Probe Lithography (for example AFM, STM, NSOM, SECM)	SPL techniques can be applied to image and modify surfaces with atomic resolution (smallest features are a few tenths of a nanometer) Approximately 30nm patterns of alkanethiol have been written on gold substrates Can induce/enhance oxidation of silicon substrates, expose thin resist films(AFM), induce phase transition in solid materials and manipulate atoms or molecules(STM) and deposit metals (SECM)	Serial technique therefore time-consuming and low throughput Only extremely small areas can be patterned in this manner Poor alignment	Possible to build arrays of probe tips which will increase throughput, but introduce cost and complexity to method
	Electrically Neutral Metastable Atoms	50nm features fabricated in single step over large area with stencil mask 70nm features produced with directed deposition with light force lens	Atom neutrality requires development of new types of optics based on light forces if used with projection systems	Further development is required with respect to the fabrication of nanopatterned topography As a holographic system, parallel line patterns can only be made

Soft Lithography (Replication Technologies)	Replica Moulding (REM)	Small, fragile structures are preserved due to elastomer mould Low surface energy allows easy seperation of mould replica Mechanical/thermal deformation can be applied to mould resulting in new pattern High accuracey/reproducible Single master can be used repeatedly Multiple copies of indistinguishable nanostructures from single master can be produced rapidly and economically (Xia et al, 1999)	Possible distortion of pattern dimensions occurring in polymeric materials during casting and curing Requires development of registration for multilevel fabrication	REM has been readily applied wrt nanopatterning in biological investigations. A standard of analysing materials produced in this manner must evolve, possibly in-line with microscopy techniques, allowing for all properties of the final device to be determined and thus comparable with similar work.
	Microcontact Printing (μCP)	SAMs can be formed over large areas in one single impression μCP can be applied to curved substrates suggesting possible 3D fabrication applications, and can also be used on inner surfaces not accessible to projection lithography techniques SAMs patterned using μCP can be used as resist in selective wet etching or as templates in selective deposition (metal grain size and etching process may affect nanostructure edge resolution) Edge roughness of <50nm recorded, with capability of producing lateral dimensions <100nm (Xia et al, 1999)	Success relies on conformational contact between stamp and substrate on rapid formation of highly ordered monolayers as a result of self-assembly Success also relies upon the autophobicity of the printed SAM In-plane dimensions of 500nm, with difficulties occurring in handling dimensions <100nm	Mechanical properties of stamp, ink and substrate will be useful for optimisation of μCP wrt <100nm features Primarily used in relation to chemical modification of surfaces. However, subsequent lithography processes can transfer chemical patterns into substrate as a nanotopography
	Solvent-assisted Micromoulding (SAMIM), and Casting	Many polymeric materials (ie. PS, PMMA) can be used to create relief structures reflecting PDMS mould Materials can be added to solvent and thus incorporated in final relief structure	Requires volatile solvent that dissolves substrate and wets (but not alter/damage) PDMS mould Wetting and damage to surface of mould by polymer has yet to be determined	Polymer casting applies the same principles as SAMIM, but is a single-step process, where the master is used to pattern the polymer directly rather than using the transitional mould step.

		Can produce complex 3D structures over large areas in single step "Self-cleaning" - dust and contaminant particles remain in moulded polymer, thus each cycle of use cleans mould	Shrinkage is often a problem	Casting shares all the advantages of SAMIM, however the disadvantages associated with the polymeric mould in SAMIM is removed resulting in a more accurate method of nanopattern fabrication
	Embossing with Rigid Master	Simple, reliable, cost-effective, high through-put method Si/SiO_2 master has been used to generate 25nm lateral features in silicon over large areas ($\leq 3cm^2$) (Chou et al, 1996) "Self-cleaning"	Release of polymer being embossed can be problematic. Mould release agents may be unsuitable for biological purposes Possible damage to master under pressure Distortion in embossed structures due to thermal cycling during moulding	Standard method of fabricating holograms, diffraction gratings and compact discs Embossing results suggest possible re-examination of existing microfabrication techniques for use in nanofabrication Hot embossing lithography (HEL) has yielded promising nanopatterning results, with sub-100nm lateral resolution (Schift, 2001)
	Near-field Phase-shift Photolithography (NSOM), using an Elastomeric Mask	Spontaneous, non-destructive conformal, atomic-level contact of soft mask with photo-resist over large areas ($\geq$100's of cm^2) without external force Elimination of mask-resist gap, thus exposure of resist in near-field of mask Mask insensitive to modest bowing/warping of substrate, thus can be applied to curved surfaces Significantly exceeds diffraction limit of wavelength of light in air Features of <50nm possible using UV due to exposure of top surface of resist occurring directly in near-field of mask (Xia et al, 1999)	Dust/contaminants may locally frustrate contact Patterns other than line patterns with fixed width are difficult Distortion of elastomer mask due to lateral deformation when contacting resist Vertical deformations may cause sagging of recessed regions of mask	Reducing wavelength of light, resist thickness, thickness of modulating component of mask and surface sensitive resists may improve resolution of this technique

Self-assembly Techniques	Aggregated Surfactant Molecules/ Phase separated Block Copolymers/ Crystalised Proteins/Aggregated Meso-scale objects/ Colloidal Particles	Final self-assembled monolayers are close to, or at thermodynamic equilibrium, thus generally reject defects Self-assembly techniques are capable of producing nanopattered structures	Development of these methods are required if they are to be utilised in nanofabrication due to defects and distortion of patterns, dimensional stability and registration problems, which are often not fully understood or controlled	The concept of self-assembly originates from biological processes Self-assembly techniques are based on noncovalent interactions
Size Reduction	Isotropic Deformation	Cost-effective strategy, which does not require access to high resolution lithography techniques Reversible if used with an elastomeric material	Limited nanopatterns Size reduction in one (or 2) directions is obtained at the expense of an increase in the other two (or 1) dimensions Success depends on uniform distortion of the material which may be difficult to achieve sub-100nm	Routine size reduction of features is conducted using conventional microlithographic techniques
	Anisotropic Etching	Lateral dimensions are reduced in a controlled manner	Limited to simple patterns, for example grooves Must be combined with other techniques	

Table 1.1: Fabrication techniques in use and development producing in-plane nanopatterned surfaces for possible biological investigations. This table outlines the nanofabrication procedures, limits and qualities involved in pattern definition, transfer and mechanical transfer methods (Xia et al, 1999) and is discussed in more detail in Appendix I.

Techniques utilised in device fabrication for use in biological investigations must be inexpensive, high-throughput, reproducible, accessible and capable of patterning large areas due to the nature of these experiments. Soft lithography or mechanical transfer and self-assembly techniques fit these criteria most readily, and, as a result, are utilised most frequently when investigating the effects of nanotopography on cell behaviour. However, problems associated with the reproducibility of replication technologies with regard to pattern distortion, conformational contact and applied solvents, Table 1.1, indicates this method may not be appropriate for investigations into cell reactions as a result of nanopatterns containing individual features with dimensions of less than 100nm.

Self-assembly techniques, for example phase-separated block copolymer and colloidal lithography, offer inexpensive, high-throughput, simple methods of sub-100nm resolution pattern definition in comparison to conventional lithography, for example photo- and e-beam lithography, Table 1.1. Periodic arrays have been fabricated using block copolymer lithography, where 20nm holes with 40nm pitch have been constructed using polystyrene-b-polyisoprene (PS-b-PI) and a trilayer resist technique (Park et al, 1997 and 2001). However, when considering regularity and symmetry of substratum nanotopography may greatly influence elicited cell response (Curtis et al, 2001), block copolymers do not offer the accuracy required in these types of biological experiments. For example, the specification for the deviation from the true position is 10nm in a 0.5 x 0.5mm area when an electron beam is used to produce similar nanometric dots at this pitch. Furthermore, the deviation from perfect positioning between each 0.5 x 0.5mm area is 80nm at mean plus 2 sigma (personal communication with Prof C. Wilkinson). In the case of block copolymers, misplacement by an amount of 1 dot in good small arrays will result in marked deviation on a larger scale where one square area will differ in orientation by a few degrees from its neighbour. Moreover, as observed in replication technologies, Table 1.1, surface contamination, regardless of how minimal, will disturb the arrangement locally and cause such a twinning of the pattern. Polystyrene-poly(bromostyrene) blends have been fabricated for use in biological investigations, where composite films are annealed resulting in the mobilisation of PS to the surface producing nanometric islands with dimensions ranging between 13 to 95nm in the z-plane (Dalby et al, 2002[a-e] and 2003[a]). Colloids utilised during nanopattern definition have similarly emerged in biological investigations (Andersson et al, 2003, Dalby et al, 2003[b], Wood et al, 2002[a], Hanarp et al, 1999).

Nanoparticles offer suitably sized, functional components for developing in-plane patterns (Willner et al, 2000). Natural lithography (Deckman and Dunsmuir, 1982 and 1983) is an extremely convenient route to developing nanofeatures over large areas for biological investigations. Colloidal gold particles, previously utilised in the development of single-electron devices (Sato et al, 1996), have emerged as a versatile method of producing nanometric features (Burnmeister et al, 1997). Every aspect of nanopatterning can be altered with respect to colloidal fabrication techniques, for example colloidal and substrate materials, colloidal shape, size and monolayer distribution which is reflected in feature pitch (Willner et al, 2000). Furthermore, electrostatic repulsion occurring between individual colloids results in irregular monolayer patterning in the absence of charge shielding materials. Irregular patterning of substrates utilising alternative nanofabrication techniques, for example e-beam lithography, is time consuming and difficult, thus colloidal lithography is greatly advantageous for irregular in-plane nanopattern production.

Colloids are generally spherical or quasi-spherical in shape (Xia et al, 1999), although controllable colloidal shapes have been reported (Ahmadi, 1996), and can be favoured for dimensions within the nanometric range. For instance, monodispersed colloidal gold particle dimensions can be selected by changing the molar ratio of trisodium citrate to $HAuCl_4$ during suspension preparation (He et al, 2000), while nanoparticles composed of different materials can be similarly synthesised using other reducing agents (Willner et al, 2000). Furthermore, colloidal suspensions are inexpensive and readily available in a number of sizes to purchase (British Biocell International, Cardiff, UK) further simplifying the fabrication process.

Colloids can be fabricated in a number of materials (Willner et al, 2000), including polymers (Ng et al, 2002, Hanarp et al, 2001, Fitch and Clark, 1999, Seeger et al, 1999[a], Burnmeister et al, 1997, Johnson and Lenhoff, 1996, Hulteen and Van Duyne, 1994, Adamczyk et al, 1990). Noble metals, for example gold (Eastham et al, 2002, Chen, 2000, He et al, 2000, Schmidt et al, 2000, Fink et al, 1997), titanium-coated gold (Mayya et al, 2001) and palladium (Reetz et al, 1997) have also been utilised as colloidal materials. Magnetic (Zhong et al, 2000) and semiconductor nanoparticles, termed "Q particles" due to their quantum properties (Alivisatos, 1996) have also been produced.

Colloidal nanoparticles can be assembled as monolayers. When nanometric colloidal dimensions are selected, adsorption techniques are required where nanoscale control over morphology of packing is available (Pohl et al, 1999, Aizenberg et al, 1998). Many methods exist to produce surface functionality at this level (Willner et al, 2000, Cass and Ligler, 1998, Hunter, 1987). Amino-functional silanes are frequently utilised as adhesion agents for colloidal gold particles on hydroxy-group terminated substrates (Wood et al, 2002[a], Sato et al, 1996, Lewis et al, 1999). The aminosilanes couple with the hydroxyl group sites forming siloxane bonds with the substrate following immersion in water. Molecules are oriented with the free amino groups directed away from the substrate surface. The affinity of the amino groups to gold results in the immobilisation of Au colloids on the silane-treated surface (Sato et al, 1996). Other methods of functionalised surface production for colloid immobilisation are practised, including avidin-biotin systems (Cass and Ligler, 1998), spin-coating (Hulteen and Van Duyne, 1994) and tilting of silicon (100) substrates (Ng et al, 2002), chemically grown hydrophilic oxide layers (Seeger and Palmer, 1999), electrophoretic deposition of colloids (Giersig and Mulvaney, 1993), poly(ethylenimine)- (Peschel and Schmid, 1995) and poly-L-lysine-coating (Wood et al, 2002[b]), triple layer positively charged precursor films (Hanarp et al, 2003 and 1999) and DNA-directed colloidal immobilisation (Niemeyer et al, 2001).

Colloidal density on functionalised surfaces is also controllable (Willner et al, 2000, Hunter et al, 1987). However, it should be noted that nanoparticle lattices fabricated in this manner have a configurational disorder and can never be identically reproduced (Remacle et al, 1998). When a functionalised substrate is immersed in a colloidal sol, surface assembly is under kinetic control at early time. Following colloidal immobilisation at later time, colloidal coverage is limited by interparticle repulsion (Grabar et al, 1996). These factors and the citrate ions adsorbed on particle surfaces, limiting colloidal coverage, can be modified, resulting in nanoparticle packing of surfaces.

Salt-stabilisation is one approach to counteracting interparticle repulsion (Hanarp et al, 1999, Reetz et al, 1997, Grabar et al, 1996), whereby sodium acts as a counter ion in relation to the negative citrate coating of colloids, decreasing the electrostatic repulsion decay length, termed the Debye length. The polyelectrolyte coating of metal colloids

can also be modified, where colloidal charge is immobilised, limiting ionic and hydrophobic polyanion and polycation interactions (Gittin and Caruso, 2001). Furthermore, synthesis of ligand-stabilised transition metal nanoparticles results in uniform particle size, colloidal stabilisation by inert ligand shells, equidistant particle arrangements due to defined ligand shells and the ability to vary feature pitch via chemical modification of ligand shells (Peschel and Schmid, 1995). Substrates coated with poly-L-lysine (Wood et al, 2002[b]) and bifunctional aminosilanes (Sato et al, 1997) have been utilised to increase colloidal density during monolayer surface patterning. With respect to bifunctional aminosilanes, treated surfaces are immersed in a colloidal sol and subsequently subjected to an alkanethiol solution. This treatment replaces citrate adsorbates with the alkanethiol molecules due to the strong affinity of sulphur to gold. Furthermore, this bonding is capable of displacing the amino group, present on the substrate, and gold bonds, resulting in the mobilisation of colloids on the surface. The occurrence of colloidal mobility results in grain formation, and repeated treatments allow for high-density packing of the nanoparticles (Sato et al, 1997). Temperature-controlled self-assembly techniques have also emerged in relation to high-density colloidal monolayer patterning, resulting in very accurate, periodic in-plane topographies (Ng et al, 2002).

Following fabrication of a colloidal monolayer with selected dimensions, density and materials, substrates can be used as masks with respect to pattern transfer, Figure 1.3. Colloidal patterned substrates can be exposed to dry etching resulting in nanopillar patterning of the base substrate (Wood et al, 2002[b], Lewis et al, 1998 and 1999). Pillar diameter reflects colloidal dimensions present in the original etch mask, and pillar profile is determined by etch time (Tsutsui et al, 1993). Furthermore, metals, for example nickel or silver, can be evaporated onto the colloidal monolayer following which, nanoparticles can be removed using lift-off techniques, resulting in metal masks reflecting areas of the surface originally devoid of colloids (Ng et al, 2002). Samples fabricated in this manner can be exposed to dry etching techniques resulting in nanopillar patterning of the base substrate, where pillar diameter correlates with gaps between the original colloids composing the mask (Seeger and Palmer, 1999, Hulteen and Van Duyne, 1998). Pillar height is once again determined by etching time and the integrity of the mask (Tsutsui et al, 1993). Pillar diameter and pillar pitch can be altered via selection of appropriate colloidal diameter. It should be noted that in comparison to etching colloids, where cylindrical pillars evolve, etching of metals initially evaporated

onto colloidal patterned substrates followed by colloidal lift-off results in prism-shaped pillars. Nanopillared topographies fabricated in a base substrate, for example fused silica, can be utilised during mechanical transfer, resulting in inverse patterning of deformable polymers, for example polystyrene (Wood et al, 2002[b]).

The versatility and simplicity of colloidal fabrication has resulted in its application in in-plane nanopatterning for biological research (Andersson et al, 2003, Dalby et al, 2003[b], Wood et al, 2002[a], Hanarp et al, 1999). Furthermore, colloidal deposition can be controlled, resulting in patterning of specific areas of a substrate (He et al, 2000, Sato et al, 1996, Laibinis et al, 1992). As a result, cells on a control, planar and experimental nanotopography may be viewed simultaneously under constant culture conditions and their preferences and interactions at planar-nanopillared boundaries can be observed (Wood et al, 2002[b]).

1.4 Cellular Behaviour in Relation to Nanotopography

Microtopographies of various designs and dimensions elicit a multitude of cellular reactions ranging from cell and cytoskeletal alignment on grooved surfaces to alterations in protein and gene regulation, Section 1.2. These observations indicate surface topography affects cell behaviour. The possibility that nanotopography may alter cell response in relation to a substrate was first proposed by Rosenberg in the 1960s (Rosenberg, 1962 and 1963). Furthermore, nanoscale topography has been observed *in situ*. For example, pores and fibres with dimensions ranging from 30 to 400nm have been recorded in the basement membrane underlying the corneal epithelium in Rhesus macaque monkeys (Abrams et al, 2002).

Development of nanofabrication techniques has enabled the production of a variety of nanotopographies for biological research allowing for investigations into the effects and functions of topography at the nanometric scale on cell behaviour (Riehle et al, 2002, Wilkinson et al, 2002, Curtis and Wilkinson, 2001, Flemming et al, 1999, Wilkinson et al, 1998, Wilkinson, 1995). As previously discussed, Section 1.3, investigations into cell response to nanotopographies require surfaces patterned over large areas in batch which are highly reproducible, high throughput, preferably inexpensive and fabricated in biocompatible materials, preferably in recognised biodegradable or bioresorbable polymers (Dalby et al, 2002, Riehle et al, 2002). As a result, in-plane nanopatterning of substrates applied to-date in biological investigations have utilised a number of fabrication techniques fitting this criteria, including conventional photolithography techniques (Wojciak-Stodhard et al, 1996, Clark et al, 1991) and reactive ion etching (RIE) (Turner et al, 1997), colloidal-based lithography (Andersson et al, 2003, Dalby et al, 2003[b], Wood et al, 2002[a], Hanarp et al, 1999), replication technologies (Gallagher et al, 2002) and polymer demixing techniques (Dalby et al, 2002[a-e] and 2003[a]).

The observed responses of cells to micrometric grooved substrata, Section 1.2, in combination with the further development of conventional photolithography techniques and the possible role of nanotopography in cell behaviour *in situ* has led to the development of nanometric grooves for biological investigations (Wojciak-Stodhard et al, 1996, Clark et al, 1991). For instance, square grooves with 260nm period, comprising 30nm-wide grooves

with 130nm separation and depths ranging from 100 to 400nm, were used to investigate epithelial, fibroblast and neuronal cell behaviour in relation to nanometric topography (Clark et al, 1991). BHK fibroblast alignment was dependent on groove depth, where more cells were observed to align on deeper, 400nm, grooves in comparison to shallower, 100 and 200nm, grooves. MDCK epithelial cells were observed to align to grooves equally, regardless of nanometric depth, and displayed fibroblast morphology where a leading lamella and trailing edge were evident. Furthermore, individual MDCK cell reactions to nanometric grooves differed in comparison to epithelial cell-islands which did not align to the topography. When these cells became confluent, little difference in orientation was observed in comparison to epithelium on control, flat substrates. Neural outgrowths from chick embryo cerebral neurons were unaffected by the nanometric grooves, regardless of the depths examined. Clark and colleagues proposed that cell-cell contacts largely over-ride the effects of substratum topography and close spacing of topographical cues increase cell response to features of a given depth.

Grooved substrata, ranging from 30 to 282nm in depth, have been used to assess the effects of nanotopography on macrophage behaviour (Wojciak-Stodhard et al, 1996). Macrophage adhesion and spreading was activated more quickly, by 20 to 30 minutes, on the nano-grooves in comparison to cells on the planar controls. Gratings increased adhesion in P388D1 macrophage, the effects of which was dependent on groove depth. However, adhesion of macrophage from rat peritoneum increased on grooved substrata regardless of the nanometric dimensions. Membrane protrusions in the form of microspikes were also more frequent on the grooved substrata, oriented perpendicular to the grooves. P388D1 macrophage area exhibited a 2-fold increase on the experimental substrates, regardless of their dimensions, in comparison to cells on control surfaces, where a groove depth of 71nm was required for a significant increase in spread area and orientation of peritoneum macrophage in comparison to controls. Furthermore, at 15 minutes, cell morphology on the nanogrooves was typical of activated macrophage, where cells were strongly adhered and produced numerous microspikes. As a result, P388D1 cells phagocytosed more fluorescent beads on the grooves, and this phenomenon was dependent on groove depth. Cell orientation increased with increasing groove depth and decreasing groove width, suggesting dimensions in each plane of the structure had a significant impact on elicited macrophage response. F-actin content increased in cells on the grooved topographies with twice the

amount calculated at 15 minutes in comparison to controls, accumulated at groove-ridge boundaries and was dependent on groove depth, but not groove width. For patterns with less than 30 or 40nm depth, F-actin alignment was absent, and a lack of cell orientation resulted. Focal adhesion formation was observed along discontinuities and was accompanied by phosphorylation of tyrosine co-localised with F-actin, vinculin and vitronectin receptor $\alpha V\beta 1$, but not fibronectin receptor $\alpha 5\beta 1$, I-CAM-1 or $\alpha 3\beta 1$ integrins. Phosphotyrosine did not co-localise with F-actin in cells on planar controls. Increased tyrosine phosphorylation was accompanied by increased F-actin on the grooved substrata, substantiating previous observations that changes in actin dynamics depends on changes in actin-binding proteins associated with microfilaments at the leading edge of cells, which is dependent upon the phosphorylation of tyrosine. Wojciak-Stodhard and colleagues proposed that increased phagocytosis may occur as a result of clustering of specific membrane receptors, for example $\alpha 5$ integrins and clustering of $\beta 1$ integrins may induce tyrosine phosphorylation, consistent with the observations made during this work.

Silicon has been textured using reactive ion etching (RIE) and wet, chemical etching, producing nanopattened substrates for biological investigations (Turner et al, 1997). Silicon grass, a product of the RIE step, is composed of columnar structures with approximately 57nm diameter and 270nm height. Following wet etching of this surface, a smoother structure is obtained, with peak-to-valley troughs of 115nm and depressions of 100 to 250nm. These topographies were fabricated on the same surface in a grating arrangement. LRM55 astroglial cells were observed to attach almost exclusively to wet-etched areas, displaying well spread, epithelial-like morphology and were closely adhered to the substrate. When in contact with the silicon grass, cells were rounded or spindle-shaped, and less closely adhered to the surface. The apical surface of cells on the silicon grass displayed complex projections and ruffles, in comparison to the smooth appearance of astroglial cells on the smoother, chemical etched topography, displaying fewer projections. LRM55 cells subjected to a surface where a wet etched gradient had been produced, silicon grass being at one extreme of the pattern and smoother etched surfaces subjected to wet etching for increased periods at the other, indicated cells preferred wet etched surfaces in comparison to silicon grass. The degree of cell preference and spreading increased with increasing wet etching, where nanopatterning deviated less from planar surfaces. However, primary

astrocytes preferred silicon grass and failed to spread on the wet etched surface. Furthermore, processes extended by the primary cells were confined, to a degree, to the silicon grass patterns. Turner and co-workers suggest that LRM55 cells may have inadvertently been selected to grow on flat surfaces, however, previous investigations indicating cell response to topographical patterning is cell-type dependent, Section 1.2, suggests this occurrence may be due to the different requirements of each individual cell type.

Polymer-demixing of, for example, polystyrene and poly(4-bromostyrene), can be utilised to produce island topography in the nanometric range (Dalby et al, 2002[a,b,d&e] and 2003[a]), where the ratio of polymers can be altered to control topographical shapes and polymer concentration in the casting solution can be adjusted to allow features of different dimensions to be produced (Dalby et al, 2002[e]). A variety of island nanotopographies have been fabricated in this manner for use in biological investigations, where the height of islands range from 13nm (Dalby et al, 2002[d]) to 95nm (Dalby et al, 2002[a]). Islands with 13nm height have a diameter of approximately 263nm and 527nm centre-to-centre spacing (Dalby et al, 2002[d]), while islands with a height of 95nm have a diameter of 1μm and 1.67μm centre-to-centre spacing (Dalby et al, 2003[a]). This technique results in a uniform chemistry at the substrate surface with which cells are confronted.

Fibroblasts respond to 13nm high islands through increased spreading and proliferation, where filopodia projections are frequent and contain F-actin, and tubulin is better developed with defined individual microtubules observed. Furthermore, vinculin is increased in fibroblasts on these islands indicating the surface is highly adhesive. Microarray results show upregulation of cell signalling genes including FAC-associated genes, for example integrin subunits, G-protein receptor elements and tyrosine kinases, and Rho, Rac and Ras genes which are primarily involved in cell morphology and motility events. Similarly, ion channels, growth hormones, collagen precursors (II, IV and V), ECM and ECM-remodelling proteins, cytoskeletal and receptor genes were upregulated in fibroblasts as a result of contact with the 13nm high polymer islands (Dalby et al, 2002[a & d]). Dalby and colleagues propose that 13nm-islands have a stimulatory effect on fibroblasts in comparison to planar polystyrene and poly(4-bromostyrene) controls, resulting in

increased ECM and ECM remodelling proteins indicating cells are more differentiated on the 13nm islands (Dalby et al, 2002[a]). Changes in transcriptional and translational factors denote signalling of cells to the nucleus when seeded on the 13nm islands (Dalby et al, 2002[d]). Furthermore, increased cell attachment and spreading is required for up-regulation of genes, which, in turn, is required for cell differentiation, verified by these microarray results.

In contrast, fibroblasts seeded on the 95nm islands exhibit reverse behaviour, where spreading and proliferation is significantly reduced in comparison to cells on the 13nm high islands and planar controls (Dalby et al, 2002[e]). Fibroblasts were more rounded with unorganised cytoskeletons consisting of diffuse actin and lack of stress fibres (Dalby et al, 2002[a]). Furthermore, fibroblast response to 35nm high islands was similar to cells on planar controls, with little or no change effected by topography exhibiting this vertical dimension (Dalby et al, 2002[e]).

HGTFN endothelial response to 13nm, 35nm and 95nm high islands was similarly examined (Dalby et al, 2002[b]). Cell area was greatest on 13nm and poly(bromostyrene) planar controls in comparison to 35nm and 95nm islands and polystyrene planar controls. Furthermore, cell area was significantly greater on 35nm and 95nm islands in comparison to planar polystyrene substrates. Cell thickness was increased on all samples in comparison to the polystyrene control, and flat poly(bromostyrene) and 13nm islands accommodated longer and wider endothelial cells. Furthermore, cells formed a multilayer following 1 week of contact with the 13nm high island topography, absent on all other experimental substrates. Endothelial cells cultured on the 13nm high islands contained many distinct stress fibres and developed microtubule networks which radiated from the nucleus towards the membrane periphery (Dalby et al, 2002[b]). In relation to the 95nm high islands, cell spreading was stimulated, resulting in large lamella, increased stress fibre formation and anchoring of the cells to the islands at their peripheral membranes (Dalby et al, 2002[a]).

No significant difference was found when comparing mononuclear cell reactions to planar controls and 95nm high islands during *in vitro* biocompatibility testing of these surfaces (Dalby et al, 2002[a]). Furthermore, platelet reactions to these control and experimental surfaces were also compared, and no significant difference was detected. These

observations are highly desirable *in vivo*, as negligible blood cell response to material should increase integration of implants by preventing formation of fibrous capsule formation and localisation of immune cells to the defect site. In summary, nanoislands were observed to elicit specific, cell type-dependent morphology and cytoskeletal responses, ultimately accumulating in altered proliferation and gene expression, the regulation of which are observed in cytoskeletal, morphological and FAC imaging.

Colloidal-based fabrication techniques have proposed roles in nanostructured model biomaterial surfaces (Hanarp et al, 1999) and model nanotopographies (Wood et al, 2002[a]) due to their alterable and definable characteristics, Section 1.3. Colloidal-patterned substrates have been utilised in investigations of cell reactions to nanotopographies (Andersson et al, 2003, Dalby et al, 2003[b]). Colloidal gold particles with 50nm-diameter, adhered to a base substrate via an aminosilane, were presented to epitenon cells as a static topography, where it was noted that cells were capable of direct interactions with the nanofeatures at their peripheral membranes (Wood et al, 2002[a]). An alternative lithography technique, where 110nm negatively-charged polystyrene colloids are adhered to a substrate via a triple layer of polyions with net positive-charge and subsequently coated with titanium, has also been utilised in biological investigations (Andersson et al, 2003). In this instance, uroepithelial cells were less well spread, less round with more stellate morphology and increased membrane protrusions. Furthermore, a reduction in pro-inflammatory cytokine IL-6 and chemokine IL-8 was recorded on the colloidal substrates, implying this colloidal topography would be beneficial to implant coating due to suppressed immune response activators.

Colloidal monolayers produced in a similar manner utilising multilayer polyelectrolytes and 110nm-diameter polystyrene colloids have subsequently acted as an etch mask to form 160nm high cylindrical pillars in PMMA (Dalby et al, 2003[b]). Fibroblasts seeded on the nanocolumns were significantly less spread, with approximately half the area of cells on control planar PMMA surfaces. Large difference in cytoskeletal organisation between these two groups were also noted, where stress fibres were less evident on the nanotopography and vimentin remained in close proximity to the nucleus with less defined filaments in comparison to weaving networks radiating from the nuclear region of fibroblasts on controls. Tubulin appeared highly organised on the nanocolumns where clear tubules were

absent in controls. However, at higher magnification microtubules appeared less dense on the experimental nanotopography. Small vinculin accumulations were observed on the nanocolumns, indicating reduced adhesion on this surface in comparison to fibroblasts on planar PMMA, possibly due to a reduced surface area presented by the columnar features. Nuclear area calculated using the largest measured diameter of a single nucleus in the z-plane, was significantly reduced on the patterned substrate. However, average intensity measurements of DAPI used to stain the nucleus, indicated nuclei were thicker on the nanocolumns, and, thus, more compact. Furthermore, the distance between chromosome 3 centromeres on the nanotopography was shorter for interphase cells in comparison to fibroblasts on the control, planar substrate. A number of shifts in gene expressions, predominantly repression of genes were also recorded on the colloidal-based topography. Dalby and co-workers suggested these observations were a result of "self-induced" mechanotransduction, where nanocolumnar topography altered nuclear morphology and chromosome positioning leading to alterations in the probability of gene transcription (Dalby et al, 2003[b]).

Cell reactions to numerous nanotopographies investigated to-date often consider a single set of parameters, where cell type, feature dimensions and materials remain constant. Although interesting, and often insightful, a more systematic approach offers greater understanding of cell reactions to nanotopographies. For example, Dalby et al (2002[a,b,d&e]and 2003[b]) indicate that nanoisland features elicit different responses in fibroblasts and endothelial cells, and, although cell-specific, different island heights act to alter these responses within the cell types. An alternative approach taken by Curtis et al (2001), where a direct comparison is made between opposing nanopatterns, similarly increases our perception of cell reactions to nanotopography. In this instance, endothelial and epitenal fibroblast adhesion was markedly reduced on regular nanopits in comparison to irregular nanopillars with similar dimensions. Furthermore, cell adhesion on regular nanopits was reduced in comparison to planar controls, while cell adhesion on irregular nanopillars was increased in comparison to planar controls. Curtis et al proposed that observed cell reactions may occur as a result of van der Waals' attractions, a phenomena where non-linear effects are only observed within the 100nm range, between water "fingers" preventing full wetting of nanopatterned surfaces occurring when forces were symmetrically balanced. Furthermore, as regularly arranged pillar arrays decrease in pitch,

van der Waals' interactions increase, enhancing surface non-wettability. This hypothesis corresponds to markedly reduced cell adhesion on regular nanopillar arrays in comparison to irregular nanopillar patterns and planar controls. Moreover, centre-to-centre spacing of regular orthogonal close-packed nanopillars ranging from 100 to 300nm resulted in reduced cell adhesion on more 100nm pitch, where the number of cells adhering to these surfaces gradually increased with increasing pitch (Curtis et al, 2001).

The studies discussed within this section indicate nanotopography can be utilised to manage or manipulate cellular response. As previously observed in relation to microtopography, Section 1.2, different cell types often exhibit altered behaviour in relation to the same nanotopography. Furthermore, feature dimensions are paramount to elicited cellular response, where adjustments in a single plane can often have a dramatic effect on cell behaviour. The nature of physics shaping self-assembled nanopatterns, specifically colloidal monolayers, gives insight into the occurrence of forces, for example van der Waals' interactions, at the nanoscale. As a result, forces appearing at a nanometric level in relation to natural lithography techniques offer alternative perceptions with respect to mechanisms underlying the effects of nanotopography on cell behaviour.

1.5 Justification of experimental approach

An inexpensive, high-throughput, reproducible method of fabrication was devised through the utilisation of colloids which allowed for nano-featured topography to be produced across greater areas (cm^2 rather than mm^2) required when investigating cell reactions to topography, Section 1.3. Nanotopographies were produced using a natural lithography technique (Deckman and Dunsmuir, 1982 and 1983). A base substrate of either silicon, quartz or borosilicate glass (all with silica (SiO_2 surface oxide) layer) was treated with a functional aminosilane and subsequently coated with gold colloidal particles (Sato et al, 1997) measuring either 20nm- or 50nm-diameter, Section 3.2. Irregularly patterned colloidal monolayers were characterised and imaged using a combination of Scanning Electron Microscopy (SEM), Section 3.2.1.1, and Atomic Force Microscopy (AFM), Section 3.2.1.2. Percentage area coverage and interparticle spacing for irregular nanopatterns fabricated using 20nm- or 50nm-diameter colloids were calculated, Section 3.2.1.1.1. Attempts were made to alter colloidal densities on substrates by exploiting particle properties, Section 3.2.2, for example the Debye length (Hanarp et al, 1999) and electrostatic repulsion (Sato et al, 1997, Grabar et al, 1996). Increasing colloidal monolayer distribution results in increased regularity of colloidal patterning, Section 1.3. Fabrication of nanopatterns with irregular and regular characteristics in the same materials allows for comparable surfaces when investigating cell behaviour in relation to these topographies. Furthermore, regularity and symmetry of nanofeatures have been implicated in elicited cell response to a surface, Section 1.4 (Curtis et al, 2001).

Selected on availability, both rat epitenon and HGTFN endothelial cells were seeded on colloidal topographies and morphological examinations were conducted using scanning electron microscopy techniques, Sections 3.3.1 and 3.3.2, respectively, allowing for high resolution imagining of both cells and the nanotopography to be conducted simultaneously. SEM investigations allowed for the determination of the stability of nanotopographies fabricated in this manner following cellular interactions. Secondary electron (SE), backscattered electron (BSE) and X-ray microanalysis were employed to determine the stability of colloids following cell adhesion to the nanotopography, Section 3.3.1 (Wood et al, 2002[a]). Cell morphology, also determined using SEM techniques, in relation to the epitenon and endothelial cells on the colloidal surfaces acted to identify early indications of cell reactions and circumstance in relation to the

experimental substrates. Furthermore, high-resolution SEM imaging allows for interactions of cells with individual nanofeatures to be identified. hTERT fibroblast adhesion, morphology and behaviour was investigated in relation to the colloidal topographies using a variety of methods including time-lapse video microscopy, Section 3.3.3.1, basic adhesion assays, Section 3.3.3.2, scanning electron microscopy, Section 3.3.3.3, immunohistochemical staining of the cell actin and tubulin cytoskeleton and fluorescent microscopy, Section 3.3.3.4. Time-lapse video microscopy has been used continuously throughout this work as a means of reference in relation to fixed sample analysis, and is believed to give insight into cell reactions in a temporal manner. Adhesion assays, conducted within the first minutes and hours of cells contacting the experimental nanotopographies were employed to indicate an increase or decrease in cells adhering to colloidal substrates in relation to a planar control. As one of the first interactions occurring at the cell-substrate interface, Section 1.1, adhesion assays also suggest the portent of cells in relation to the colloidal substrates. Similarly, morphological studies, employing fluorescent antibody staining of the actin and tubulin cytoskeleton, indicate a number of cellular characteristics in relation to a substrate, Sections 1.2 and 1.4. Furthermore, as new molecular techniques emerge and are implemented in experimental studies of cell reactions to various situations, morphological states, especially with respect to the microfilament and microtubule arrangements, are being attributed to the specific occurrence of intracellular molecular signalling events. Interfacing between the cytoskeleton and adhesion sites is also enlightening as to the types and strengths of adhesions occurring between the cell and its substrate.

A continual area of contention when considering surface topographies for use in biological investigations is the possible role of chemistry inadvertently presented on the substrate. As the fabricated nanotopographies are composed of gold colloidal particles adhered to a base substrate with SiO_2 surface, the influence of the colloidal chemistry in relation to cellular reactions had to be determined. As a result, a second nanotopography was developed through the utilisation of the original colloidal lithography as an etch mask, Section 4.2 (Lewis et al, 1998 and 1999). Samples were dry etched, resulting in a relief pattern of nanopillars, the height of which was determined by the exposure time of the sample to the reactive ions during etching (Tustsui et al, 1993). Both 20nm- and 50nm-diameter colloids were used as an etch mask, with heights in both instances of either 80nm or 200nm. Following etching, colloids were removed from the pillar tops

using a gold etch. This resulted in nanopillared topography presented in the silica oxide of either a silicon or fused silica substrate. For biological investigations, an optically transparent medium, for example fused silica, is generally required allowing for optical microscopy techniques to be utilised. Pillars with a height of 80nm were used to emulate the previous dimensions of the colloidal particles. Pillars were also etched to 200nm, to investigate the possible affects of nano-feature height in relation to cell behaviour. Nanopillared topographies were characterised using a combination of SEM, Section 4.2.2.1, AFM, Section 4.2.2.2 and IRM (Interference Reflection Microscopy), Section 4.2.2.3, techniques.

Preliminary investigations where epitenal fibroblasts seeded on 20nm-diameter, 200nm high pillars and HGTFN endothelial cells on 50nm-diameter, 200nm high pillars were conducted. Epitenon cells were seeded on the experimental substrate and examined at 1 hour using SEM, indicating early responses of these cells to the nanotopography, Section 4.3.1. Time-lapse video microscopy of endothelial cells on nanopillared topography offered insight into the temporal behaviour of these cells in relation to their environment, Section 4.3.2. hTERT fibroblast adhesion on 20nm-diameter, 200nm high, 200nm planar etched and planar control surfaces was examined at periods previously stipulated when examining fibroblast adhesion to the colloidal topographies, allowing for comparisons to be drawn between these results, Section 4.4.1. The inclusion of a planar etched substrate allowed for the possible involvement of the etching process in cell reactions to nanopillared topographies to be investigated. Planar etched substrates were etched to the same depth, using the same plasma during the same RIE run as the nanopillars under investigation thus acting as directly comparable control substrates. Fibroblast cytoskeletal morphology was investigated on the nanopillared surfaces, again at periods previously stipulated when examining actin and tubulin morphology in fibroblasts on the colloidal topographies, Section 4.4.2.

A substrate was devised where planar and nanopillared topographies lie collaterally on the same device, Section 5.2 (Wood et al, 2003[b]). As a result, cell reactions to the experimental, nanopatterned and control, planar surface could be monitored simultaneously, allowing for constant culture conditions. Furthermore, cells can also be examined for their interactions along a boundary and their preference for either surface. hTERT fibroblasts were monitored in relation to a 50μm grating pattern accommodating repetitive planar and 20nm-diameter, 200nm high pillar sequences

using time-lapse video microscopy, Section 5.3.1. Fluorescent staining of the actin and tubulin cytoskeleton on both planar and nanopillared surfaces allowed for comparisons to be drawn between the cytoskeletal morphology of cells in relation to both surfaces, Section 5.3.2. 3T3 fibroblasts were also investigated on planar-nanopillared substrate patterns using SEM, where cell interactions at groove boundaries and with individual nanofeatures were examined, Section 5.4.1.

In summary, irregular nanotopographies were fabricated using colloidal lithography techniques and their effect on cell behaviour was monitored. 20nm- and 50nm-diameter colloidal particles were utilised in separate instances, allowing for the effects of colloidal diameter on observed cell behaviour to be investigated. Attempts to fabricate comparable regular patterns were made permitting the importance of nanotopography symmetry in relation to elicited cell response to be studied. Nanopillared surfaces were also fabricated utilising colloidal monolayers as an etch mask, where cells were confronted with a uniform surface chemistry. Nanopillar heights of 80nm and 200nm were fabricated for 20nm- and 50nm-diameter pillars to study the importance of these parameters in elicited cellular response. A device where planar and nanopillared topographies lie collaterally across the substrate was deigned, where cell behaviour could be monitored simultaneously on control and experimental surfaces.

High-resolution microscopy techniques, namely SEM, AFM and IRM, were used to characterise nanotopographies. SEM was also employed to image cell interactions with individual nanofeatures. SE, BSE and X-ray microanalysis were performed to distinguish the stability of colloids following cell seeding. Time-lapse video microscopy was utilised, indicating temporal alterations in cell behaviour on nanopatterned substrates and acted as a reference for fixed sample analysis. Adhesion assays were performed to indicate fibroblast response to colloidal-based nanotopographies. Cell morphology was investigated using SEM and fluorescent staining of the actin and tubulin cytoskeleton. Constant time intervals were selected for these studies, regardless of the surface topography under investigation, allowing for comparable results. Furthermore, these techniques were chosen to allow comparisons to be drawn between these investigations and similar work conducted by other groups. Epitenon, endothelial and fibroblast cells were examined to indicate whether observations of cell behaviour in relation to colloidal-based nanotopographies were a result of cell-specific or universal cell response.

Chapter 2: Cell Types, Origins, Materials and Methods

2.1 Introduction

Rat epitenon and HGFTN endothelial cells, 3T3 Swiss mouse fibroblasts (European Collection of Cell Cultures) and Infinity™ Telomerase-Immortalized h-TERT-BJ1 fibroblasts (Clontech Laboratories, Inc., USA) were used to investigate cell behaviour in relation to nanotopography. Cell materials and methods outlined within this chapter are constant regardless of the experimental surface being investigated.

Initially, rat epitenon and HGTFN endothelial cell reactions to the colloidal topographies were examined. These cell types were selected due to their availability within the lab. However the history and phenotypes of these cells were not certain, with little or no publications existing to detail their origins or viability. As constituents of very specific tissue types, epitenon cells of tendon regions and endothelial cells of vascular areas, any notable alterations in cell behaviour as a result of nanotopography would appear only to have intrinsic value with respect to the tissues from which cells were isolated. This is, of course, not necessarily invalid if a solution to disease or defect specific to these areas is being sought. However, as a preliminary investigation of cell reactions to irregular nanotopography has been undertaken, a broader approach to the subject in hand would appear of greater worth. The vital role of endothelial cells *in vivo* cannot be underestimated when considering, with the exception of cartilage, all cells in the body lie within a few microns of a capillary composed mainly of endothelium and a fine layer of adjacent material termed the basal lamina.

Following the purchase of an Infinity™ Telomerase-Immortalised human fibroblast cell line (Clontech Laboratories, Inc., USA), all subsequent experimental work was conducted using these h-TERT BJ-1 fibroblasts. Not only was there literature to support the history of this cell type (Clonetech Website), but fibroblasts having undergone life-span extension via Telomerase introduction have been shown to preserve their original phenotype (Jiang et al, 1999). Fibroblasts are known for their extensive occupancy throughout the body, not only found in skin and all cavity linings, but also as a first point of contact between an implant surface and the host. Thus, fibroblasts were selected due to their universal appeal when dealing with implant materials and more widespread disease and defects. 3T3 Swiss mouse fibroblasts (purchased from the

European Collection of Cell Cultures, ECACC) were used briefly in conjunction with planar-nanopillared topography. 3T3 cells were selected as, in keeping with the cell type being investigated on these surfaces in Glasgow, they were the only fibroblasts available when working at the AO Research Institute, Davos. Although originally selected under conditions favouring contact inhibition, this phenomena has now been lost and should not be overlooked when interpreting the electron microscopy images captured and discussed in Section 5.4.1.

Epitena, endothelia and hTERT fibroblasts were viewed in relation to all colloidal topographies discussed in Chapter 3. However, due to the lack of background knowledge of both the epitenon and endothelial cells, and also due to time constraints, hTERT fibroblasts alone were monitored on experimental nanopillared surfaces, dealt with in Chapter 4, and the planar-nanopillared surfaces outlined in Chapter 5. 3T3 Swiss Albino mouse fibroblasts were also used to examine cell behavioural alterations in relation to patterned planar-nanopillared topography due to their availability while investigating colloidal uptake by epitenon cells at the AO Research Institute, Davos, Switzerland.

This chapter outlines the use of basic reagents in relation to the cell types under investigation, the advantages and the disadvantages of all cell types used throughout this project, cell culture constituents and the methods employed to investigate cell reactions to the experimental nanotopographies. Concerns regarding use of cell lines capable of indefinite proliferation are also raised and discussed. All work with regard to cell culturing was performed under sterile conditions, practising aseptic techniques, in a laminar flow hood.

2.2 Basic Reagents

A variety of reagents are referred to throughout the materials and methods section for cell culture media and fixing and staining techniques. These reagents are detailed in this section, and should be referred to when listed in the materials and methods text.

2.2.1 Hepes Saline

Hepes saline, heated to 37°C in a water bath, was used to wash cells prior to sub-culturing or seeding on experimental surfaces and was also used to wash all surfaces under investigation prior to the addition of cells. By washing surfaces prior to cell

seeding, any debris will be rinsed from the surface, the structure will be wetted and also brought into line with the 37°C temperature at which cells have been incubated.

All constituents of the Hepes saline, 140mM Sodium chloride (NaCl, 8g/L), 5mM Potassium chloride (KCl, 0.4g/L), 5mM d-Glucose (1g/L), 10mM HEPES (2.38g/L) and 0.001mM Phenol red Sodium-salt (0.1g/L), are added to 1 litre of Reverse Osmosis water. The inclusion of Phenol red Na-salt allows the pH of the resulting solution to be monitored visually, with red solution indicating more acidic conditions and orange solution denoting alkaline pH. Prior to application, whether to cells or substrates, the Hepes saline is always warmed in a water bath to 37°C.

2.2.2 Antibody mix

The antibody mix is used in all cell culture media to limit the occurrence of infections, and is composed of the following; 150mls L-Glutamine, concentration of 114mM is mixed with 12.5mls Fungizone (11.9μg concentration), 100mls Penicillin/Streptomycin (1950U/ml) and 7mls of 7.5% Bicarbonate. The resulting antibiotic mixture is applied to cell culture media's in the amounts stated for each different media outlined in Section 2.4.

2.2.3 7.5% Bicarbonate ($NaHCO_3$)

7.5% bicarbonate is used in the antibiotic mix and is also added to ECT media and HO-based ECT media, both for epitenon cell cultures, and HAMS F10 media used to culture endothelial cells. 7.5% bicarbonate is made by adding 7.5g Sodium bicarbonate to 100mls of RO water. The bicarbonate solution is then sterilised to remove any contaminants, either by autoclaving or by passing the mixture through a 0.2μm dosing filter.

2.2.4 Versene (ethylenediaminetetraacetic acid, EDTA) Buffer

Versene buffer, containing the chelating agent EDTA, an active constituent of the trypsin-versene mix used to detach cells from culture flasks during sub-culturing, or prior to seeding cells on surfaces being investigated. The chelator acts to buffer the ion in question, by strongly, and reversibly binding to calcium in this instance. The trypsin-versene mix is a standard solution used universally when cell culturing to detach cells from a surface, although with few exceptions for example macrophages do not trypsinise well from surfaces. Trypsin-versene acts as a calcium-magnesium chelator,

resulting in detachment of cells from a substrate via buffering of the free concentration of these ions.

The versene buffer is composed of 140mM Sodium chloride (8g/L NaCl), 5mM Potassium chloride (0.4g/L KCl), 5mM d-Glucose (1g/L), 10mM Hepes powder (2.38g/L), 0.5mM EDTA (0.2g/L) and 0.001mM Phenolred Na-salt (0.1g/L) all of which are added to 1 Litre RO water.

2.2.5 Phosphate Buffered Saline (PBS)

PBS is used to wash cells, thus removing protein debris from the surface, prior to fixing and staining either when investigating cell adhesion and viability, or preparing cells for use with fluorescent microscopy or Scanning Electron Microscopy (SEM).

A 10* concentrate bulk solution is made as outlined below, and this is converted to a 1* PBS solution by diluting the 10* concentrate 1:9 with RO water. If PBS is to contact cells immediately prior to fixing, where cells are being taken from 37°C temperature conditions, the saline is heated in a water bath to this temperature. This is believed to prevent alterations in cell adhesion and morphology as a result of heat shock, although very little exists in the literature to support this.

The 10* stock solution contains the following which are added to 1 Litre RO water; 73.7mM Na_2HPO_4 (11.5g/L), 14.7mM KH_2PO_4 (2g/L), 1368.9mM Sodium chloride (80g/L NaCl), and 26.8mM Potassium chloride (2g/L KCl). Once all reagents are suspended in 1 Litre RO water, the pH must be adjusted to 7.4.

2.2.6 4% Formaldehyde

This reagent is used in fixing protocols, especially with respect to Fluorescent staining, adhesion studies and also Electron Microscopy sample preparation. 1 part 38% Formaldehyde is added to 9 parts Phosphate Buffered Saline. If a permeabilising buffer is to be subsequently applied to samples, 2g sucrose is added to the formaldehyde solution. This is mixed and heated in a water bath to 37°C prior to applying to cultured cells, to prevent heat shock of cells.

2.2.7 0.5% Tween 20 in PBS

A wash containing 0.5ml Tween 20 added to 99.5mls PBS is used when conducting the Fluorescent staining protocol, Section 2.7.3.1. The Tween wash acts to remove excess

antibodies that have been previously added to the cells being investigated. Removing excess antibodies prevents non-specific binding resulting in cleaner, more specific images that represent a truer picture of tubulin and actin (being stained for) within the cells.

2.2.8 1% Bovine Serum Albumin (BSA)/PBS

1g of Bovine Serum Albumin is suspended in 100mls of PBS and is used to prevent non-specific antibody binding when fluorescently staining tubulin and f-actin in relation to experimental topographies. The protocol for fluorescent staining is outlined in Section 2.7.3.1.

2.2.9 Permeabilising Buffer

10.3g sucrose, 0.292g NaCl, 0.06g $MgCl_2$ (hexahydrate) and 0.476g Hepes powder are added to 100mls of PBS. The pH is then adjusted to 7.2, following which, 0.5ml Triton X is added. The permeabilising buffer is used to remove cell membranes' which allows for specific chemicals, in the instances of this project, antibodies and molecular dyes, to contact the underlying cytoskeleton, for instance microtubules and actin filaments.

2.3 Cell Types and Origins

Four different cell types were used in relation to the experimental nanopatterned topographies. These were epitenon cells extracted from rat tendon, endothelial cells obtained from a vascularised human tendon granuloma, 3T3 Swiss Mouse fibroblasts and hTERT BJ-1 human fibroblasts. As all these cells are capable of indefinite proliferation, they carry the advantage of uniformity across cultures. The main disadvantage however is the differences in genotype and phenotype in comparison to their *in situ* counterparts. hTERT fibroblasts have the distinct advantage with regard to this as cells are not strictly "immortalised", but proliferate indefinitely due to a known cause. This occurs by preventing cells from undergoing replicative senescence due to their active expression of telomerase which maintains telomeres from entering a threshold state associated with proliferative arrest.

When culturing cells *in vitro*, it is of utmost importance to preserve cell phenotype and genotype. This allows comparisons to be drawn between *in vitro* experimentation and *in situ* conditions. The origins and cell types are outlined below, with concerns regarding expression in comparisons to their *in situ* counterparts discussed.

2.3.1 Rat Epitenon Cells

An explant of flexor tendon was extracted from neonatal rat and grown in culture using ECT media, Section 2.4.1, by Mr Graham Tobasnick. Once epitenon cells had migrated from the explant and a primary culture was established, the epitena were trypsinised from the culture plate surface with macrophages remaining attached to the culture surface. Clonal purification was conducted with respect to the eptitenon cells to ensure that they were in fact epitena and a viable stock had been obtained. This resulted in the establishment of an indisputable homozygous cell line.

A fine connective tissue sheath surrounding the entire complex hierarchical scheme known as tendon, epitenon, is contiguous with paratenon on its outer surface and underlying endotenon. Epitenon comprises a relatively dense fibrillar network of 8 to 10nm thick collagen strands with cells, and there is little variation in density or fibril orientation across the tissue. Epitenon fibrils are occasionally fused with the superficially located tendon fibrils (Kannus, 2000).

Possible problems arising when extracting cells in this manner occur mainly in cells from different areas of the tendon being unintentionally selected in the explant, which results in their presence in the final culture. This is due to the position of epitena and its presence in the overall structure of tendon. Heterozygous cell populations resulting in this manner distract from the positive discrimination of the cell type being investigated. As clonal purification of the epitenon cells was conducted, identification that these cells were in fact epitena from rat tendon was made.

Phenotypic (and also genotypic) transformation arising from continual passages of the primary culture is a constant issue surrounding *in vitro* cell culturing. These cells, as with many rodent lines, are capable of indefinite proliferation due to their selection from foetal cells that actively proliferate *in situ*, and their subsequent continual culture *in vitro*. The number of passages the epitenon had undergone prior to plating on the experimental topographical surfaces was uncertain, thus the behaviour of cells in relation to their original phenotype and genotype is debatable. However, epitenon cells are known to be very stable and non-immortalising (personal communication with A. Curtis). Yet, in view of the uncertainty of the number of passages of cells in this culture, epitenon extracted from rat flexor tendon were used only in preliminary experiments.

2.3.2 HGTFN Endothelial Cells

Endothelium tissue lines all blood vessels and lymphatics within the body and posses an array of functional and adaptive properties. This tissue is composed of extremely flat, 1 to 2 microns thick, endothelial cells measuring approximately 10 to 20 microns in diameter and containing a central nucleus. Endothelial cells are composed of relatively simple cytoplasm, with only a few organelles that are concentrated in the perinuclear zone.

Endothelial cells act as selective filters, regulating the passage of gases, fluid and various molecules from blood to underlying tissues, across their membrane. Different organs have different types of endothelium, and are determined by whether cells form a tightly or loosely bound tissue. Such tissue is distinguished by the overlapping regions at the intercellular junctions and is crucial with regard to the integrity, and helps to seal, the vessels. Loosely bound endothelium is also termed "leaky" due to its ability of transporting larger molecules from the circulation to underlying tissue. Pinocytotic vesicles are concentrated adjacent to the cell membrane, and are involved in the passing of materials, especially fluids, from the blood stream into the underlying tissues. Gases rapidly diffuse through the endothelium, and this is observed particularly in lung capillaries. Cell surface molecules act as receptors and interaction sites for a whole host of molecules, especially those concerned with leucocyte attraction or repulsion. Under healthy conditions, leucocytes are repelled by endothelium allowing for the free flow of blood within vessels. During inflammatory response, E-selectin is expressed by the endothelial cell surfaces', and binds leucocytes circulating within the blood. Leucocytes attach to the endothelium surface and then pass from the blood, through the endothelial cells and into the underlying tissues through the process known as diapedesis. Leucocytes pass through endothelial cells as part of their lifecycle, especially capillaries, as they monitor antigens in tissues. Macrophages also pass from blood through endothelial cells to gain access to various tissues within the body (Blue Histology Website).

Endothelial cells secrete numerous regulatory molecules, which act in coagulation, vasoconstriction, fibrinolysis and platelet activation and inhibition processes (MacSween and Whaley, 1992). Haemostasis, the arrest of bleeding through blood clotting and blood vessel contraction, is deemed the most important function of

endothelial cells, with von Willibrand's Factor, also known as Factor VIII, the vitally important molecule produced by cells during this process.

An endothelial cell line originating from human granuloma tissue (HGT) surgically removed from tendon was established by extracting cells from the granuloma explant using an immuno-magnetic separation technique, as performed by Professor Adam Curtis. Following extraction of cells from the vascular area of granuloma, a number of endothelial-specific traits were explored in the isolated culture to ensure the cells originated from genuine endothelium.

Granuloma tissue occurs within the body as a direct result of evasion by a persistent microorganism or foreign body, of the unmodified chronic inflammatory response. Thus, the granuloma acts as a specialised form of chronic inflammation to deal with pathogens evading the generally successful inflammatory response initiated by the body in response to pathogen contact.

In its purest form, concentric layers of various cell types especially associated with immune reactions comprise the granuloma lesion, with little or no vascularisation occurring, Figure 2.1. Caseous necrosis often exists at the core of the lesion, however this is not always the case, especially when considering a heavily vascularised granuloma, as was the case in the tissue from which the HGTFN cells were extracted. As blood flow through the area occurs in vascularised tissue, lack of nutrients representative of tissue undergoing necrosis should be limited.

Epithelioid cells and multinucleated giant cells are contained within the layer surrounding the centre of the granuloma, and act as specialised macrophages with respect to the pathogens causing the existence of the inflamed area. The giant cells arise due to cytokine stimulation, which results in the cytoplasmic fusion of macrophages within this layer. Lymphocytes encapsulate these layers, which are, in turn, included within the final outer layer containing fibroblasts.

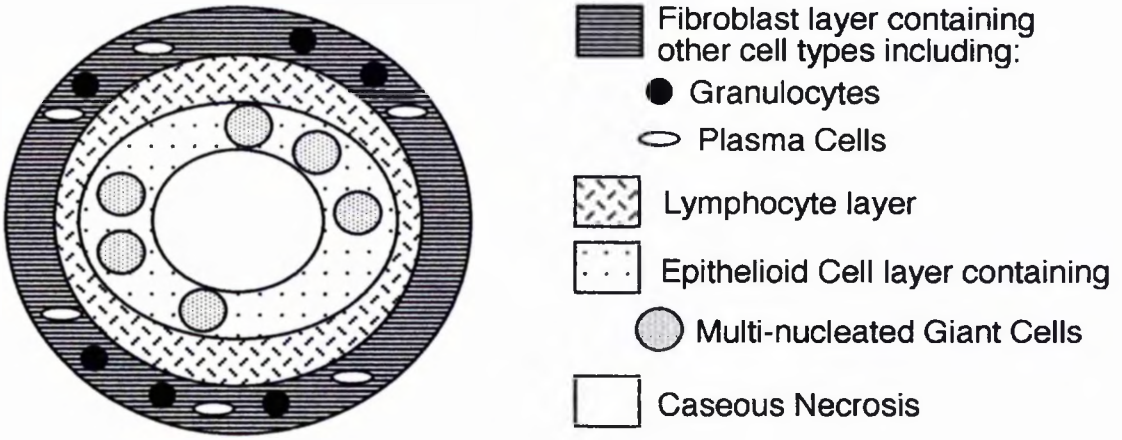

Figure 2.1: Transverse section of Caseating granuloma. A direct result of chronic granulomatous inflammation, the presence of epithelioid cells is essential for a histological diagnosis. All granulomas acquiesce a distinctive histological appearance; an epithelioid macrophage accumulation engulfed by a lymphocyte cuff. Giant-cell, Necrotizing and Caseating granulomas are the most common. If vascularisation has occurred, in the absence of tuberculosis, a Giant-cell granuloma is probable.

The presence of fibroblasts in the outer layer is believed to occur as an attempt is made by the body to enclose the inciting stimulus utilising fibrous connective tissue. It should be noted this is an extremely common reaction seen in foreign body response and is almost always found when implanted materials are introduced to a defective site. Capsule formation is believed to prevent complete biointegration of an entity within the body. However, fibrous encapsulation of such materials is poorly understood, and may be linked to the mechanical properties of the materials under investigation. As fibrous tissue, in these instances, co-exists with foreign body response, chemotaxis, either via immune cell signalling, cytokinesis or alterations in pH at such areas will have a pivotal role in the establishment of the connective tissue. When considering the great occurrence and problems caused by the fibrous tissue, especially with regard to implant surfaces, the understanding of the mechanisms involved in its establishment are poor. This suggests that many elements may play a role.

Little in depth work surrounds proliferation rates of cell lines and their likeness to cancerous cell types. Alterations in regulated proliferation of both cancerous cells and related cell lines could be drawn, resulting in a better understanding of the similarities between these cells and thus indicating the viability of cell lines as representative of their original phenotype and genotype. This could be conducted using microarray or similar gene analysis studies, with specific markers used to highlight proliferation genes, with similarities being drawn between the gene expression in both cancer cells and cell lines from similar tissues. A more direct result could be ascertained by

implanting cell lines into an animal model and monitoring the behaviour of the implanted material, with comparisons between tumour behaviour made. Incidentally, this approach has been taken with regard to the hTERT fibroblasts used during this project (Jiang et al, 1999).

As the endothelial cells extracted from the human granuloma tissue arose within this area due to vascularisation of the site, they are less likely to exhibit abnormal behaviour in comparison to cells extracted from the actual granuloma. The vascularisation would occur due to influx of endothelial and basal lamina into the granuloma from healthy vascular tissue referred to as angiogenesis.

Angiotensin converting enzyme (ACE), Weibel-Palade bodies, collagen type III and high expression of low-density lipoprotein (LDL) receptors were all investigated to indicate whether cells were in fact from endothelium. All these attributes would indicate human endothelial cells had been isolated. If cells expressed Ulex europaeus, also known as common gorse, lectin, a characteristic trait of human endothelium, a positive identification, when considering the expression of all the outlined factors associated with this cell type, could be made. The presence of cytokeratins would indicate epithelia (from the tendon where the granuloma was removed) were present and a heterozygous culture had been established. Cytokeratins were not found to be present, with a positive identification of all other factors being made. The extracted cells were thus identified as originating from endothelium.

As has been discussed with regard to the epitenon cells used in preliminary experiments, uncertain and high passage numbers appear to detract from the original phenotype of cells under investigation. HGTFN endothelial phenotype has recently been reviewed and documented (Dalby et al, 2002[b]) to ensure that de-differentiation had not occurred following the initial characterisation of the HGTFN cells. Dalby et al investigated the presence of P-Selectin found in the Weibel Palade bodies of endothelial cells (van Mourik et al, 2002), using LDL binding and cd62P detection, resulting in a positive response being recorded in comparison to fibroblast controls which exhibited negative results. cd62P mediates rolling of neutrophils, platelets and some T-cell subsets along the luminal surface of blood vessels. It can therefore be concluded that the HGTFN cells exhibit specific traits, for example high expression of LDL receptors, attributed to endothelial cells.

2.3.3 hTERT BJ-1 Infinity™ Telomerase-Immortalised Human Fibroblasts

hTERT BJ-1 cells have the advantages associated with permanent cell lines, namely availability, better cross-culture uniformity and easier genetic manipulation, and also the genotypic and phenotypic stability normally associated with primary cultures. This is due to the active expression of human telomerase reverse transcriptase subunit (hTERT) in BJ-1 fibroblasts extracted from primary neonatal male foreskin. Active hTERT expression occurs due to the transfection of cells with a hygromycin-resistant retrovirus expressing hTERT. hTERT expression results in the indefinite proliferation of transfected cells, yet cells are believed to maintain a stable, normal genotype, primary cell morphology and function, are contact inhibited and actively express telomerase (Clontech Laboratories, Inc., USA).

As many stem cells and germline populations are telomerase positive *in situ*, with infinite division capabilities, active telomerase expression is not believed to be a sign of oncogenic properties (although cancerous cell behaviour requires high telomerase expression, allowing for alterations in, and less regulated proliferation).

Further research has shown that telomorase expression in normal cells, namely BJ-1 fibroblasts, does not appear to induce changes associated with malignant phenotype (Jiang et al, 1999). This was based on the evidence that transformed cells do not require anchorage-dependence to proliferate and may form tumours *in vivo*. Parent hTERT BJ-1 fibroblast clones did not form colonies in soft agar, and did not form tumours in nude mice after a 5-month period. These results indicate that hTERT fibroblasts maintain anchorage-dependent growth, as seen in negative controls, and are not oncogenic.

hTERT BJ-1 fibroblasts have the advantage of greatly extended or infinite life span in the absence of mutations in cell-cycle checkpoint genes and resultant genetic stability due to their capability of evading senescence due to telomerase activity. These fibroblasts do not express the general disadvantages linked to phenotypes and genotypes exhibited in immortalised cell lines, instead reflecting features found in young normal cells, for instance diploid status, growth characteristics and gene expression. As hTERT BJ-1 fibroblasts have been modified to exhibit indefinite proliferation via expression of hygromycin-resistant retrovirus transfection, the ability of cells to proliferate is understood and documented.

Ideally, in cell culture, cell types under investigation should exhibit phenotype and genotype characterised by their counterparts *in situ*. This would appear to be the case with hTERT BJ-1 fibroblasts, with genetic stability and growth characteristics mimicking those found *in situ*.

2.3.4 3T3 Swiss Albino Mouse Embryo Fibroblasts

3T3 mouse Swiss Albino embryo fibroblasts were used to investigate fibroblast reactions to planar-nanopillared topography, Section 5.4, when visiting the AO Research Institute, Davos. These had previously been purchased from the European Collection of Cell Cultures (ECACC). Isolated in the 1960's, this cell line was evolved under conditions favouring the retention of contact inhibition. However, due to the longevity and subsequent transformation of the cell line, these cells no longer exhibit contact inhibition of cell proliferation. Furthermore, 3T3 fibroblasts are immortalised and are not stable.

3T3 fibroblasts were used due to their availability in Davos, and were believed comparable to previous work using hTERT fibroblasts. However, due to the loss of contact inhibition in the 3T3 cells and its presence in hTERT, comparisons can only be drawn with regard to the cells contact inhibition status.

When considering 3T3 mouse fibroblasts were initially isolated under conditions favouring the retention of contact inhibition, and, in more recent years the trait selected for has been lost, the problems associated with de-differentiation of cell phenotype and genotype is highlighted. Through continuous culture and increased passages, alterations in cell behaviour are often demonstrated due to de-differentiation.

2.4 Cell Culture Media

All media can be stored for up to one month at 4°C following which antibiotics should be replenished. All media can also be frozen at -20°C, and following thawing can be used for up to one month. Media should not be refrozen.

All live cells require to be kept at body temperature, 37°C, constantly, either in a hot room or incubator. All cell work was conducted under sterile conditions in a lamina flow hood.

2.4.1 ECT Media for Rat Epitenon Cultures

Epitenon cells were extracted from rat tendon as discussed in Section 2.3.1. Once isolated and a viable culture was established, cells were incubated in ECT media. This consists of 67% Eagles Water (dH_2O), 8% 10* concentrate BHK (Baby Hamster Kidney) 21 Media, 10% Tryptose Phosphate, 10% Calf Serum, 2.5% antibiotic mix and approximately 2.5% bicarbonate to adjust the ECT media pH to around 7.2%. This media is CO_2 buffered.

2.4.2 H-ECT Media for Rat Epitenon Cultures

This media was used in conjunction with epitenon cells both in Glasgow and Davos. An incubation oven was used at the AO Research Institute, Davos with CO_2 being circulated throughout. Thus, flasks containing cells required to be left open, allowing for CO_2 buffering, which resulted in an increased contamination risk. Due to the trip being limited to one month, any possibility of cell infections had to be eliminated therefore an HO-buffered media was preferred as flasks could be closed preventing any possible infection problems.

The H-ECT media incorporates 73% 22mM Hepes water, 8% Tryptose Phosphate, 8% Calf Serum, 2% antibiotic mix containing L-Glutamine and 0.4-1% Bicarbonate ($NaHCO_3$). Due to the presence of the Hepes, this media does not require CO_2 buffering, and therefore, when contained within an incubation chamber supplied with circulating CO_2 as was the case in Davos, the lid of flasks can be closed to prevent contamination of cells.

2.4.3 Complete Hams F10 Media for HGTFN Endothelial Cultures

The HGTFN endothelial cell line was established from a vascularised human granuloma tissue explant. The method of explant extraction and cell line establishment is discussed in Section 2.3.2. Endothelial cells were cultured in complete Hams F10 which consists of 84% 22mM Hepes, 9% 10* concentrate Hams F10, 3% Foetal Calf Serum, 2% antibiotics, 1% ITS and approximately 1% bicarbonate to adjust pH. Due to the presence of Hepes in this media, cells do not require CO_2 buffering.

2.4.4 Complete DMEM Media for hTERT-BJ1 Fibroblast Cultures

hTERT-BJ1 fibroblasts were purchased from Clontech Laboratories, Inc., USA. Cells were cultured in complete DMEM which incorporates 70% DMEM, 18% Medium 199, 9% Foetal Bovine Serum, 2% antibiotics and 1% 100mM sodium pyruvate. Cells grown

in this medium require CO_2 buffering; approximately 13mls CO_2 in a 75cm^2 flask culture flask.

2.4.5 Complete H-DMEM for hTERT-BJ1 Fibroblast and 3T3 Swiss Albino Mouse Fibroblast Cultures

H-DMEM was used for fibroblast cultures that could not be CO_2 buffered. This was the case while working in at the AO Research Institute, Davos. In this instance, hTERT and 3T3 fibroblasts were cultured in H-DMEM, allowing for flasks to be sealed, as CO_2 was not required from the circulation supplied by the incubator, minimising contamination risks. Due to the limited time available to work in this lab, this risk of contamination had to be eliminated, and was done so by using HO-based DMEM media.

9% Tryptose phosphate, 9% Foetal Bovine Serum, 9% 10* concentrate DMEM and 3% antibiotic mix were added to 70% HO water. The pH was adjusted by adding a few drops of filter-sterilised 1M NaOH to allow successful cell culture (with pH reflecting *in situ* conditions, approximately 7.2). The resulting media had a more orange appearance in comparison to pink, acidic appearance. Colour monitoring in this manner occurs due to the Phenol red contained within the media. Due to the HO water, this media does not require CO_2 buffering.

2.5 Cell Culturing Procedures and Methods

General culture techniques were applied to all cell types throughout this work, and are discussed within the following sub-sections.

2.5.1 Cell seeding or Sub-culturing using Trypsin-versene

When cells are being prepared for investigation on an experimental surface, or require sub-culturing when reaching approximately 70% confluencey, they must be detached from the culture flask in which they are being grown. This method, using a trypsin-versene mix, is applied when using all three cell types; namely epitenon, endothelial and fibroblast cells.

Firstly cells are washed twice in the culture flasks with Hepes saline (approximately 10mls of Hepes for a 75cm^2 flask). A trypsin-versene mix (0.5mls trypsin in 20mls versene as described in Section 2.2.4) is then added to the flask to cover the cell monolayer (around 3mls for a 75cm^2 flask). Cells are then placed in either a hot room or similar incubation conditions for around 5 to 10 minutes. Incubating at this stage

encourages cell-cell and cell-substrate detachment due to 37°C being the optimum temperature for trypsin function. Following this, the media appropriate for the cell type being used is added to the mixture to stop the detachment process (10mls for 75cm^2 flasks). The cell-containing solution is pipetted into a universal, and this is placed in a centrifuge for around 4 minutes at 1500 rpm, 20°C. Following centrifugation, the supernatant is collected and disposed of and cells are re-suspended in the appropriate medium. Due to fibroblasts generally reaching confluence in a shorter time period and tending to form a sheet on the culture flask surface, h-TERT undergo a second re-suspension process where they are collected in a syringe via a 21 gauge needle and are gently passed through this needle, completing the process.

It should be noted that all experimental substrates are immersed in Hepes saline heated to 37°C for approximately 10 minutes prior to cell applications. This ensures that surfaces are biocompatible by removing any residual ethanol or similar chemicals. Due to the temperature of the Hepes saline, surfaces should be less likely to induce heat (or cold) shock response to seeded cells.

2.5.2 Freezing Cell Stocks

It is desirable to freeze cells as this allows for access to stocks at all times regardless of any contamination or infection problems that may be encountered. It also allows for cells from the same passage to be investigated.

Freeze mix for cells consists of 70% Foetal Bovine Serum, 20% Media (chosen in relation to the cell type being frozen) and 10% DMSO. Cells undergo the trypsin-versene process as outlined above, however following centrifugation and removal of the supernatant, cells are resuspended in approximately 3mls freeze mix. This is placed in a sterile ampoule and placed immediately in either a -70°C freezer, or immersed and stored in liquid nitrogen. Frozen cells can be stored indefinitely providing they are not thawed at any point during this period.

2.5.3 Seeding cell cultures from frozen stocks

Cells are taken from the -70°C freezer or liquid nitrogen and rapidly thawed at 37°C with constant agitation. Cells can either be thawed in the hand, or by immersion (making sure the seal of the lid is not covered by water in case of contamination) in a water bath. Immediately upon thawing, cells are transferred to a 75ml culture flask

containing 10mls of media, the choice of which is dependent on the cells being cultured. If the media requires CO_2 buffering, approximately 13mls of filtered CO_2 should be added to this size of flask. Cells should then be incubated at 37°C until almost reaching monolayer conditions. Upon reaching this state, culture media should be extracted, cells should be washed with Hepes saline solution and sub-cultured as previously described, Section 2.5.1.

2.6 Time-Lapse Video Microscopy

When examining cell reactions to a nanotopography using time-lapse video microscopy, cells are seeded onto the surface under investigation and placed in a "sandwich box" and gassed (if required). The box is then sealed with insulation tape and placed, in this instance, under a Zeiss Axiovert 25 Phase-contrast microscope. Cells on the surface are brought into focus using the microscope eyepiece. The light path is then switched to allow CCTV video monitoring. The CCD CV-M50 video camera is fitted into the microscope underneath the stage, and connected to a Panasonic Time-lapse VHS videocassette recorder (model number AG-6730). The video recorder is, in turn, connected to a JVC TM-1700PN monitor. The image on the monitor must then be brought into focus once more before recording can begin.

All video recordings were conducted using time mode 000hours, resulting in a frame being captured approximately every 10 minutes. One exception was made when monitoring HGTFN endothelial cells on nanopillars, where 4 frames were captured per second, Section 4.3.2.

2.7 Cell Fixing and Staining Techniques

A number of techniques were used to fix and often stain cells, either for general adhesion counts, Section 2.7.1, immunohistochemistry resulting in fluorescent labelling of the cell cytoskeleton, Section 2.7.2, preparation of Electron Microscopy samples, Section 2.7.3, or for X-ray microanalysis, Section 2.7.4.

2.7.1 Formalin Fixing and Coomasie Blue Staining of Cells

Coomasie Blue is used as a non-specific protein stain and, thus, non-specifically stains proteins on a cell highlighting the cell area, overall morphology and nucleus. By counting the number of nuclei in a sample, where one nucleus equals one cell, comparisons between cells adhering to different topographies can be made.

Coomasie Blue is composed as follows; 225ml RO water is combined with 225ml methanol and 50ml glacial Acetic acid, following which, 1.25g Coomasie Brilliant Blue R-250 is added. This solution is stirred for 30 minutes, and then filtered through Whatmans number 1 filter paper.

Cells are firstly seeded on the surfaces of interest and incubated for the required time. Upon reaching this period, the media is extracted from the structures and PBS, heated to 37°C, is used to wash the samples twice. This removes excess proteins that would otherwise mask the underlying cells, detracting from their true state.

Following the PBS rinses, cells are fixed in 4% Formal saline (also referred to as Formalin, or as 4% Formaldehyde/PBS, Section 2.7.2) at 37°C for approximately 10 minutes. The fixative is then removed from the samples and coomasie blue is added to the surfaces for 3 to 5 minutes (depending upon the amount of staining required). The coomasie blue is then removed and samples are washed in tap water. Samples are then stored in water and viewed using a light microscope.

2.7.2 Immunohistochemistry and Fluorescent Staining of F-Actin and Tubulin

The compositions of all reagents mentioned within this section are outlined elsewhere, Section 2.2. PBS and formaldehyde are warmed to 37°C prior to use in an attempt to prevent heat shock of cells, which may result in adhesion and morphological alterations. Cells cultured on the experimental or control surfaces are firstly washed in PBS at 37°C for approximately 5 minutes. The PBS is removed, and cells are fixed in 4% Formaldehyde/PBS (with 2% sucrose) for 15 minutes at 37°C. Permeabilising buffer is then added at room temperature to the structures housing cells and the topography under investigation and incubated for 5 minutes at 4°C. The permeabilising buffer is then removed, and cells are incubated in 1% BSA/PBS (heated to room temperature, approximately 20°C) for 5 minutes at 37°C. Cells on the experimental structure are now premeabilised and any excess staining has been accounted for due to BSA incubation, thus antibody application can be made. The primary antibody, β-tubulin raised in mouse against human, binds to tubulin within cells, while an F-actin probe, rhodamine Phalloidin, is used to bind F-actin and will fluoresce due to the inclusion of Rhodamine within the structure. The phalloidin, a bicyclic heptapeptide produced by the deadly mushroom *Amanita phalloides*, binds specifically and tightly to the actin filaments.

However, fluorescently stained phalloidin is not a universal probe for actin and will not bind to G-actin (Preston et al, 1990). Both of these binding molecules, the β-tubulin and Phalloidin are diluted 1:50 with 1% BSA/PBS. Cells and structures are then incubated in the primary antibody and Rhodamine Phalloidin for 1 hour at 37°C. Due to the presence of the fluorescent Rhodamine, cells must be protected from light as prolonged excitation of the Fluorophores present in Fluorescent molecules results in photobleaching.

Three 5 minute washes in 0.5% Tween 20/PBS at room temperature follow the antibody incubation, and are applied to remove excess antibodies. The secondary antibody for tubulin raised in horse against mouse, and will therefore bind to the primary antibody raised in mouse against human, 1:50 with 1%BSA/PBS is added for 1 hour at 37°C.

Following the incubation in the secondary antibody, the cells adhered to the experimental structures are once again washed 3 times for 5 minutes each in 0.5% Tween20/PBS at room temperature. Again, this is to remove excess antibodies, in this instance biotinylated horse against mouse antibody.

Fluorescein-streptavidin, 1:50 with 1%BSA/PBS, which binds Biotin (which is contained in the secondary antibody, which is bound to the primary antibody, bound to the tubulin under investigation) is added to the samples for 30 minutes at 4°C. Three 5 minute washes at room temperature in 0.5% Tween20/PBS follows to remove excess Streptavidin.

Samples, if not created on a standard glass microscope slide, are mounted on such, and a drop of Vectashield containing Dapi is added to stain the nucleus (via Dapi) and mount the sample (via Vectashiled), upon which a glass coverslip is subsequently placed. Samples were then viewed using a Vickers M17 microscope in oil immersion mode with a 50x objective.

2.7.3 Scanning Electron Microscopy Preparation - Hitachi S-900

All samples to be used in conjunction with the Hitachi S-900 Field-Emission Electron Microscope (FESEM), Electronics and Electrical Engineering, Glasgow had firstly to undergo processing by Critical Point Drying (CPD). Water must be removed at the critical point in this manner to avoid the disruptive passage of the gas-liquid phase

boundary as occurs when using an electron microscope. CPD offers a fast and generally reliable and artefact-free means of achieving this (Bozzola and Russell, 1990), and is discussed in more detail later in this section.

Cells are firstly seeded on the experimental surface and incubated for their specific time. PBS is then warmed to 37°C in a water bath, and used to replace the media in sample containers. This wash is repeated. 2.5% Gluteraldehyde suspended in a Phosphate buffer (PO_4) is added to the samples, also at 37°C, and left for 30 minutes (if cells are in a monolayer only) to 1 hour (if cells may have occasion to break the monolayer or be densely packed). Cells and samples can then be stored in 0.1M Phosphate buffer.

Three changes of 0.1 PO_4 buffer at 10-minute intervals follows to ensure complete removal of excess Gluteraldehyde. A 1% Osmium Tetroxide (OSO_4) solution is added to the samples for 30 minutes following removal of the last phosphate buffer rinse. The addition of the Osmium Tetroxide allows for contrast between the cell and the surrounding surface when viewed using the EM due to the difference in densities of these materials. The osmium is extracted and 3 rinses using distilled water is applied to the surfaces at 10-minute intervals.

Alcohol dehydration using increasing concentrations of ethanol follows, with each step lasting for 10 minutes. Samples containing cells were put through an ethanol series of 30%, 40%, 50% 60%, 70%, 80%, 90% and 96%. Two rinses in absolute alcohol (100% ethanol) for 10 minutes each followed, with samples then being placed in Dried Absolute alcohol for a further 10 minutes. Samples were placed in porous sample holder and Critically Point Dried for approximately 1 hour 40 minutes.

Following the final steps of dehydration, the sample immersed in dehydrant, in this instance 100% ethanol, is placed in the CPD chamber, also known as a bomb. During CPD, the ethanol is displaced with liquid CO_2, a transitional fluid. The temperature of the transitional fluid is gradually increased, and in response to this, fluid pressure increases. As a result, the transitional fluid eventually reaches a critical point; a particular temperature-pressure combination specific for the transitional fluid. The critical point when using ethanol as a dehydrant, and liquid carbon dioxide as a transitional fluid is 31.1°C and 1,073PSI (Bozzola and Russell, 1990). At this point,

transition occurs, and the density of the liquid phase equals that of the vapour phase. The success of CPD is dependent upon total immersion of the specimen in a dense vapour phase, preventing the damaging liquid-air interface, which occurs during air-drying and often results in collapse or shrinkage of biological samples.

Prior to viewing in the Hitachi S-900 FESEM, samples were sputter coated with 10nm Gold-palladium (Au/Pd, 80/20) using an Emscope SC 500 (Emtech Ltd, Kent, UK) sputter coater. This ensures conductance of the sample materials and prevents sample charging by the electron beam.

2.7.4 Scanning Electron Microscopy Preparation - Hitachi S-4100 and S-4700

A general overview of the materials and techniques used at the AO Research Institute, Davos, Switzerland are documented elsewhere (Wood et al, 2003), but are outlined in brief for reference as follows. All imagining at the AO Research Institute was conducted using either a Hitachi S-4100 or S-4700. A standard chemical fixation for cell monolayer cultures based on a fixation technique previously described (Richards et al, 1995) was conducted. All solutions were used at room temperature, approximately 20°C. H-ECT media was pipetted from the sample, following which, a 2 minute rinse in 0.1M PIPES (Piperazine-1, 4-bis-2-ethane sulfonic acid, Fluka), pH 7.4 was applied. A primary fixation was exercised using 2.5% Glutaraldehyde in 0.1M PIPES, pH 7.4 for 5 minutes. A 60 minute rinse in 0.5% Osmium Tetroxide suspended in 0.1M PIPES, pH6.8 was carried out. Three 2-minute rinses in double distilled water followed. The cells fixed on the substrate under investigation were then taken through a complete ethanol series, 50%, 60%, 70%, 80%, 90% and 96% for 5 minutes each. 3 immersions in 100% ethanol for 5 minutes was then applied, followed by 3 rinses in 100% Fluorosil for 5 minutes each. Following dehydration, samples were critically point dried in a POLARON E3000 critical point drier.

2.7.5 Preparing Cells for X-ray Microanalysis using an Hitachi S-4100 FESEM

Epitenon cells were cultured on the experimental colloidal surface as described in Section 3.3.1. Experiments were stopped at 48 hours, the theory being that the longer the cells were left to react with the colloidal topography, the more time there was to dislodge, or ingest the colloids. Epitena seeded on the colloidal surface were trypsinised from the surface at 48 hours, by adding a trypsin-versene mix (0.5ml trypsin added to 20ml versene). Having been left to react for approximately 5 minutes, this reaction was stopped by adding H-ECT media. The cell suspension was pipetted from the structure,

and the solution was placed in a universal and centrifuged at 1000 rpm for 5 minutes. The supernatant was extracted, and cells were resuspended in H-ECT media. These resuspended cells were plated onto a control, Thermanox (Polyethylene tetraphthalate, Nunc. Brand Products) surface for 1 hour at 37°C. Cells were plated on a control surface where no colloidal gold particles were attached to allow any colloids present within the cell to be distinguished from the surrounding topography. Following the one-hour incubation period on the control surface, cells and the Thermanox substrate underwent chemical fixation and dehydration as previously described, with the Osmium treatment omitted from the procedure. This was to ensure maximum contrast between any gold colloids present within the cells, and the cellular material encapsulating the colloids. Samples were carbon coated by evaporation of C rods to 10nm thickness, as measured with a quartz film monitor, positioned at a fixed place relative to the specimen, in a Bal-tec MED020 unit (Balzers, Liechtenstein). Carbon coating allowed for the detection of gold to be attributed to cell containment and not the coating material. These samples were viewed using a Hitachi S-4100 FESEM, and X-ray microanalysis (ISIS 300, Oxford Instruments) was performed using an Isis 300 (Oxford Instruments, Whitney, UK) detector in conjunction with this Electron Microscope.

2.8 Discussion

When culturing cells *in vitro* it is of the utmost importance to preserve phenotype and genotype as exhibited by the cell type *in situ.* This allows for findings conducted *in vitro* to reflect plausible alterations in behaviour if implants containing the experimental topography and chemistry were introduced to the tissues from which the cells have been isolated. Ultimately, research concerned with nano-featured patterning of substrates will be utilised in implant modification if the elicited response of cells to the surface is advantageous to recovery of defect tissue, the host and biointegration of the final implant.

The epitenon and endothelial cells (discussed in Sections 2.3.1 and 2.3.2, respectively) carry the common problems associated with indefinite proliferation of cells resulting in high passage numbers, namely the possibility of de-differentiation in genotype and phenotype. Due to their availability at the beginning of this project, epitenon and the HGTFN endothelial cell lines were used in preliminary examination of nanotopographical effects on cell behaviour. Following the purchase of the hTERT BJ-1 fibroblasts, immortalised by transfection resulting in the active expression of telomerase

allowing for maintenance of telomerase above the threshold found in senescent cells, all subsequent experiments were conducted using these. Due to the nature by which this fibroblast cell line was selected, cells exhibited the advantageous aspects associated with both permanent and primary cell lines; namely good cross-culture uniformity, accessibility, ease of genetic manipulation and a phenotype and genotype reflective of young "normal" fibroblasts.

Chapter 3: The effects of colloidal topography on cell behaviour

3.1 Introduction

Colloidal nanotopographies were fabricated by adhering 20nm- or 50nm-diameter colloidal gold particles to a silica base substrate functionalised with an aminosilane. These irregular nanopatterns were assembled across surfaces measuring a minimum of 5x5mm^2 and a maximum of 76x26mm^2, resulting in topography being presented to cells over large areas. These colloidal structures were characterised using scanning electron microscopy (SEM), Section 3.2.1.1, from which percentage area coverage and nearest neighbour analysis were calculated, Section 3.2.1.1.1, and also atomic force microscopy (AFM) operated in tapping mode, Section 3.2.1.2. backscattered electron microscopy (BSE) was also employed to investigate colloidal accumulation in relation to surface defects or scratches, Section 3.2.1.1. Sub-monolayer colloidal densities were investigated and altered by charge screening of colloids with Sodium chloride and Sodium citrate and also alkanethiol mobility restoration methods, Section 3.2.2.

Alterations in cell behaviour as a result of unmodified irregular 20nm- and 50nm-diameter colloidal topographies were investigated using three different cell types and a variety of techniques. Rat epitenon cells were imaged at 1 hour using SEM, where results revealed the possible uptake of colloids by the cells, Section 3.3.1.1, and also at 24 hours, where morphology observations were recorded, Section 3.3.1.2. This was investigated further using a combination of secondary electron (SE), backscattered electron (BSE) detection and X-ray microanalysis, Section 3.3.1.1. The results obtained from this work indicated that the colloidal substrates were presented to cells as a static, stable nanotopography (Wood et al, 2002[a]). The effects of colloidal topography on HGTFN endothelial cell morphology were also investigated at 2 and 4 hours using SEM, Section 3.3.2.

Time-lapse video microscopy of hTERT fibroblasts on both 20nm- and 50nm-diameter colloidal topographies was performed, Section 3.3.3.1, as were adhesion assays at 20 minutes, 1 hour and 3 hours, Section 3.3.3.2. Morphological examination of fibroblasts on these surfaces at 20 minutes, 1 hour, 3 hours, 8 hours and 24 hours was conducted using SEM, Section 3.3.3.3, and also fluorescence microscopy, where actin and tubulin were labelled, Section 3.3.3.4.

3.2 Nanotopography fabrication utilising colloidal gold particles

Many different methods of attaching colloidal particles to a base substrate, usually silicon, with SiO_2 surface oxide, have been documented in the literature. The first to publish such a natural lithography technique with respect to polystyrene colloids were Deckman and Dunsmuir (1982 and 1983). Other pioneers to follow in their footsteps were Sato, Lewis and Ahmed (Sato et al, 1996, Lewis et al, 1998, Lewis et al, 1999). The technique used within this chapter is based on their methods.

When referring to silicon or fused silica as a base substrate in this research, silicon dioxide (also referred to as silica) was always present at the surface. As cells and chemicals added to the silicon contact SiO_2 any mention of either silicon or fused silica surfaces refers to the silica (silicon dioxide) oxide layer. Base substrates of 22 x 22cm^2 borosilicate glass coverslips underwent a Caro's Acid wash (1 part (<30%) Hydrogen peroxide: 3 parts (95%) Sulphuric Acid (v/v) at 80°C). Following this, substrates were immersed in Reverse Osmosis (RO) water, and then reacted with Sodium hydroxide, 0.5M for 20 minutes. The NaOH treatment acts to connect the SiO_2 base surface oxide to the silanol. A further rinse with RO water under sonication was necessary to ensure cleanliness of structures. Substrates were then blown dry with nitrogen, before being oven dried at 70°C (±15°C) for 1 hours.

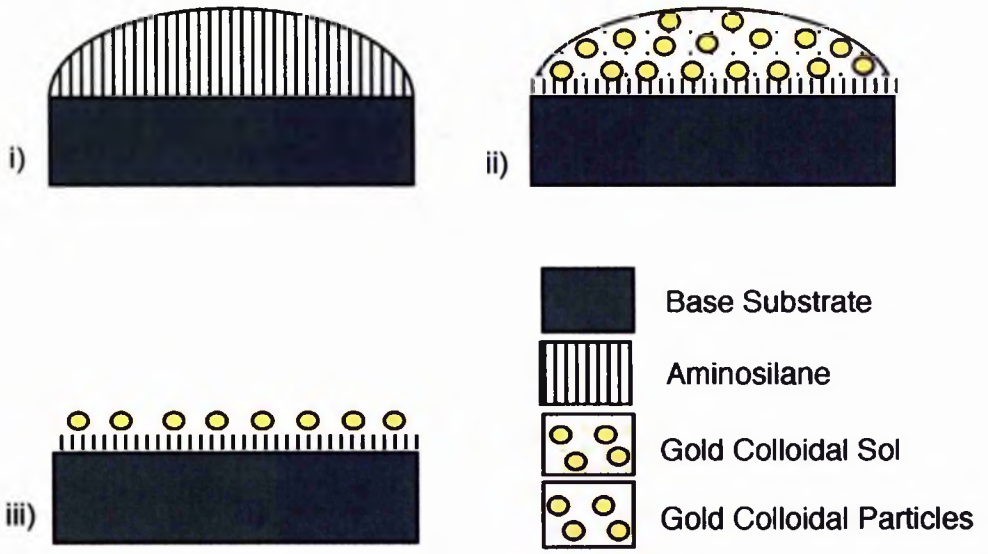

Figure 3.1: Schematic overview of the colloidal topography fabrication process. Base substrates, having been acid cleaned, dried and immersed in Sodium hydroxide are reacted with an aminosilane, i). A colloidal sol is added to the functionalised surface, ii), where gold colloids bind with the NH-groups of the aminosilane present on the substrate surface. The sol is dried from the surface, resulting in the final colloidal nanotopography, iii).

To create an active silanol, 200µl of 0.1% N-(β-Aminoethyl)-Ψ-amino-propyltrimethoxysilane (AAPS) (Pierce, UK, product number: 80379), was dissolved in 9.8ml of acetic ethanol (1ml of Glacial Acetic Acid per 100mls Ethanol, pH 5), and stirred for 5 minutes. The resultant solution was added to the surface using a syringe and 0.2µm dosing filter, and left to react for 20 minutes, Figure 3.1(i). The solution was then removed and the substrate washed in 100% ethanol to remove excess material. A further rinse with RO water under sonication was required to ensure cleanliness of the surfaces following this process.

Gold Colloid Size (nm)	Particle Size Distribution (%CV)	Particles per ml	Product description
20	<15%	7.0×10^{11}	EM.GC20
50	<20%	4.5×10^{10}	EM.GC50

Table 3.1: Catalogue description of 20nm- and 50nm-diameter colloids suspended in an aqueous sol used during this research (information from British Biocell International Ltd, Cardiff, UK). Particle distribution and the number of colloids per ml of sol are highlighted.

Subsequently substrates were immersed in either a 20nm-diameter colloidal sol, or 50nm-diameter colloidal sol, Table 3.1, (Product Numbers EM.GC20 and EM.GC50 respectively, British Biocell International Ltd, Golden Gate, Ty Glas Avenue, Cardiff, UK. CF14 5DX), depending upon the dimensions of the nanofeatures being sought. Substrates were immersed in the sol for 24 hours, Figure 3.1(ii). The 24 hour immersion of base substrates in the colloidal sol was believed to result in maximum coverage of colloids on the surface without the addition of organic adsorbates, discussed in Section 3.2.1.1.1. The immersion period was based on a number of factors. Firstly, when a surface is immersed in a sol, colloidal assembly at early time (t) is under kinetic control, where particle coverage is established by $t^{1/2}$ dependence. However, at later times, as the colloidal layer covers the functional silane, colloids attempting to reach the surface are repelled due to interparticle repulsion (Grabar et al, 1996). As sub-monolayer colloidal patterning approaches a coverage limit, where interparticle repulsion prevents additional colloidal adhesion to the substrate surface, coverage stabilises (Hanarp et al 1999). These factors were further explored through a series of experiments determining percentage area coverage of colloids in relation to their base substrates, the results of which support the 24 hour immersion period, and are discussed in Section 3.2.1.1.1.

Structures were removed from the sol following the 24 hour period and left to dry naturally, with the remaining solution evaporating from the surface over time. The final structure, Figure 3.1(iii), was then characterised using scanning electron microscopy (SEM) and atomic force microscopy (AFM).

3.2.1 Surface Characterisation of colloidal topographies

Due to the nanometric dimensions of colloidal surface features, characterisation was restricted to high resolution scanning electron microscopy (SEM), backscattered electron microscopy (BSE) and atomic force microscopy (AFM).

From the SEM images captured, percentage surface area coverage of colloids in relation to the base substrate were calculated and is discussed in Section 3.2.1.1.1. Nearest neighbour analysis was also conducted, indicating interparticle spacing between colloids on the substrate, Section 3.2.1.1.1.

3.2.1.1 Scanning Electron Microscopy

All original SEM imaging of colloidal surfaces were conducted using a Hitachi S-900 field emission scanning electron microscope (FESEM). Images were captured and processed using Quartz PCI imaging programme. Sample sizes when using the S-900 were limited to a maximum of $5mm^2$ due to the size of the holder used with this microscope. As colloids were adsorbed on a base substrate of non-conductive silicon and the gold composition of the nanoparticles is conductive, samples did not require coating.

It should be noted that Figures 3.2 and 3.3 were not taken at the same magnification and thus the scale bar should be referred to in each instance. This is due to the difference in detection of the 20nm-diameter and 50nm-diameter colloids at equal magnification. Different methods were utilised in an attempt to control colloidal patterning on the functionalised surface. 20nm-diameter colloids were either applied at 15-minute intervals six times, Figure 3.2a), or were immersed in the sol for 24 hours, Figure 3.2b). 50nm-diameter colloids were applied to the silanised surface either using 4, Figure 3.3a), or 6 applications of the sol, Figure 3.3b). These micrographs were used to calculate colloidal area coverage for each size of particle and mean interparticle spacing found in each instance, Section 3.2.1.1.1, as it is difficult to deduce any alteration in density of the 20nm- and 50nm-diameter following different sol applications.

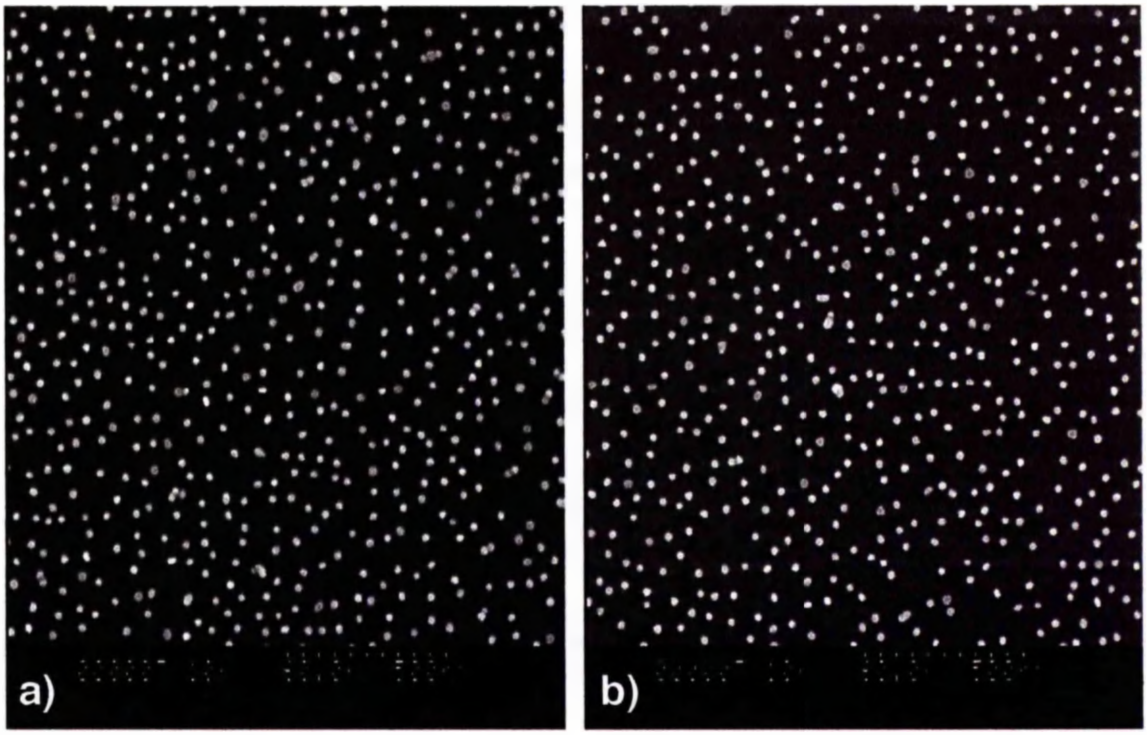

Figure 3.2: Scanning electron micrograph, using an Hitachi S-900, of 20nm-diameter colloids adhered to silica following a) 6 applications of sol, where 1 application was approximately 15 minutes and b) 24 hour immersion in the sol.

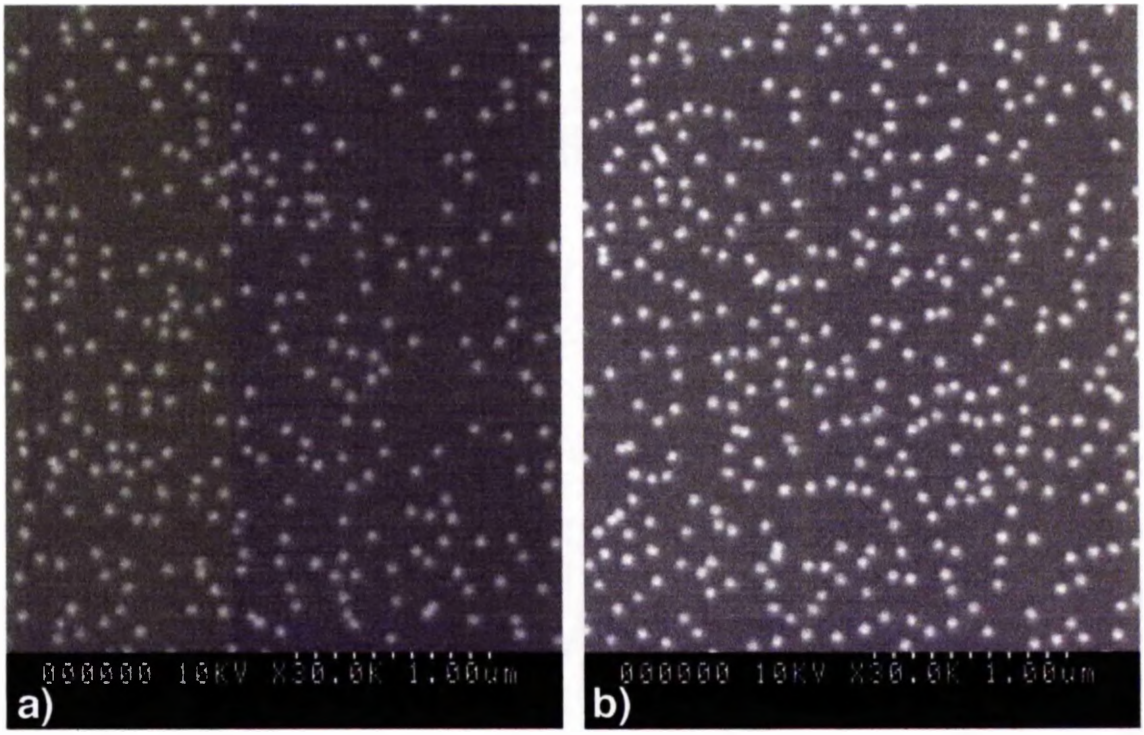

Figure 3.3: Scanning electron micrograph, using an Hitachi S-900, of 50nm-diameter colloids adhered to a silica surface following a) 4 applications of sol or b) 6 applications of sol. All applications lasted approximately 15 minutes.

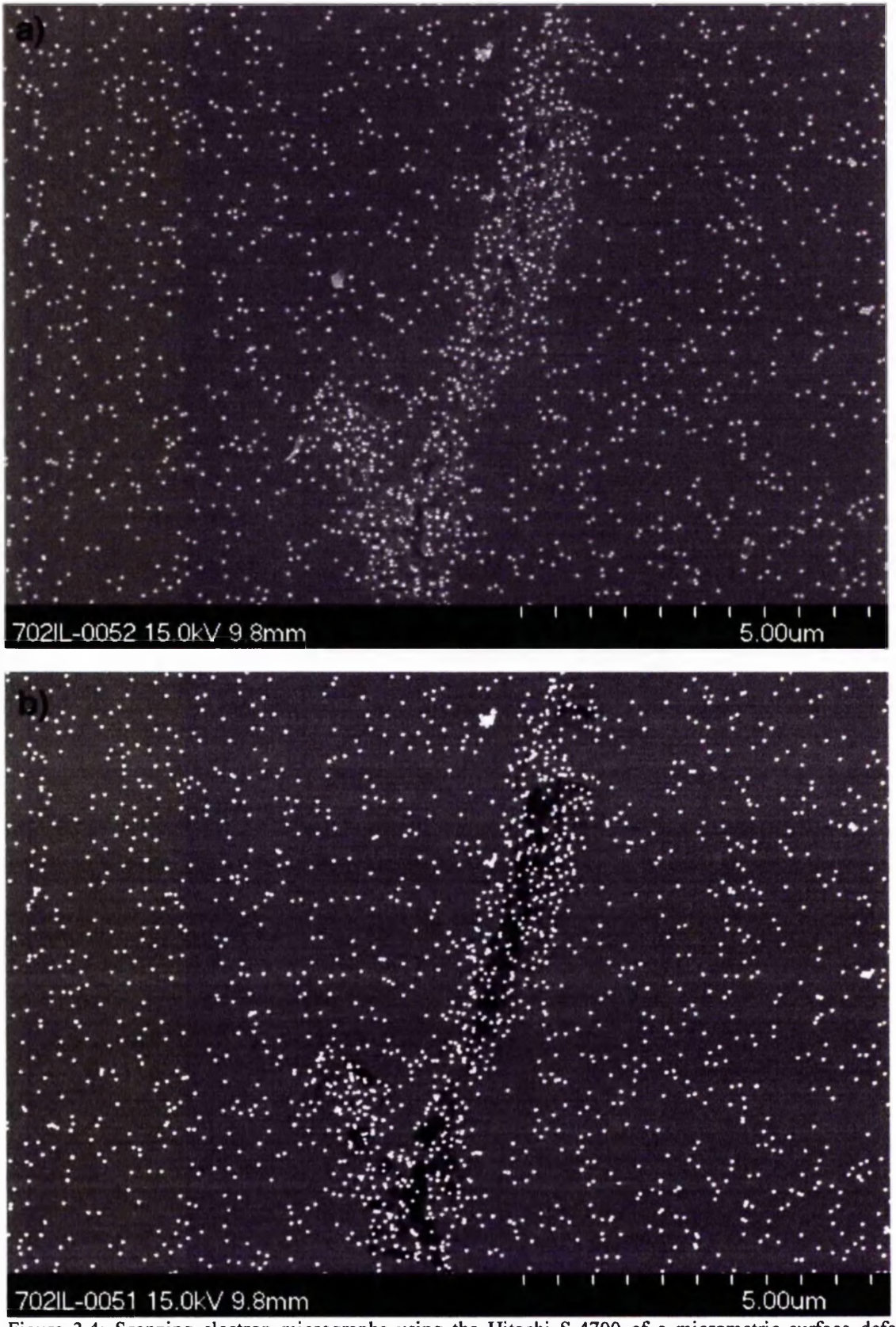

Figure 3.4: Scanning electron micrographs using the Hitachi S-4700 of a micrometric surface defect surrounded by densely packed colloids. Initially observed by secondary electron detection, a), backscattered electron detection of the area, b), indicated colloidal aggregation occurred as a result of a scratch on the surface of the base substrate.

When investigating the possibility of colloidal uptake by epitenon cells at the AO Research Institute, Davos, a region of one substrate exhibited altered colloidal density in relation to its surroundings, Figure 3.4a). The cause of this was uncertain. However Backscattered electron detection using a Hitachi S-4700 indicated colloidal aggregation in this area was the result of a micrometric scratch or defect, Figure 3.4b). Colloidal aggregation occurring as a result of micrometric flaws on planar surface appears to alter nanopatterning of colloids, most probably due to altered surface energy and resultant capillary forces, although an increase in the surface area of this defect may also account for the observed colloidal clustering. This is discussed in greater detail in Section 4.2.1.

3.2.1.1.1 Surface area coverage of colloids in relation to the base substrate and interparticle spacing

Using the scale bar in each image, 1 micron in relation to the 50nm-diameter colloids and 500nm when discussing the 20nm-diameter colloids, Figures 3.3 and 3.2 respectively, a square with sides equal to the scale bar was measured onto an acetate and placed over the photomicrograph in question. The image was printed at A4-size, allowing for more accurate measurements to be obtained. The width and height proportions for all images used were constrained using this option available in Adobe Photoshop. This prevents corruption of the original dimensions.

Twelve areas were selected in a non-specific manner using this method, and the number of colloids within the measured acetate grid (either $1\mu m^2$ or $500nm^2$, 50nm- and 20nm-diameter colloidal topography photomicrographs respectively) were counted. The percentage surface area covered by the colloids in relation to the base substrate was calculated by firstly multiplying the number of beads counted within the given area by πr^2, where r is the radius of the colloid in question. This calculation was then divided by the square-area of the base substrate, across which the number of colloids had been calculated, with the final sum transferred to a percentage, Equation 3.1.

$$\% \text{ Area Coverage} = \frac{\pi r^2 (n)}{A^2} \times 100$$

Equation 3.1: Equation used to calculate percentage area coverage of colloids in relation to a given substrate surface area. The number of colloids adhering to the specific area of the base substrate in question ($1\mu m^2$ and $500nm^2$ for 50nm- and 20nm-diameter colloids respectively) was firstly counted, and the sum, n, was then multiplied by πr^2. This sum was divided by the surface area of the base substrate over which the colloids were counted, A^2, ($1\mu m^2$ and $500nm^2$ for 50nm- and 20nm-diameter colloids respectively). Percentage area coverage was then calculated by multiplying the total by one hundred.

Twelve different areas of each SEM micrograph, Figures 3.2 and 3.3, were used to calculate the percentage area coverage of colloids in each experiment, namely 6 applications and 24 hour submersion in the 20nm-diameter colloidal sol, and 4 and 6 applications in the 50nm-diameter colloidal sol. Twelve percentages, Appendix II, were then used to calculate mean values for the percentage area coverage of colloids on each surface with respect to each condition outlined, Table 3.2. Due to the scale bars in each image and their use in the percentage calculations, all measurements are relative and therefore comparable.

Percentage area coverage of 20nm colloids on silica	6 applications of sol	24 hour submersion in sol
	5.13%	5.07%
Percentage area coverage of 50nm colloids on silica	4 applications of sol	6 applications of sol
	6.09%	7.13%

Table 3.2: Percentage area coverage of 20nm- and 50nm-diameter colloidal particles. 20nm-diameter colloids were subjected to 6 applications of the colloidal sol and also 24-hour submersion in the sol, resulting in 5.13% and 5.07% surface area coverage respectively. 50nm-diameter colloidal particles were added to the aminosilanised silica substrate using either 4 or 6 applications as described previously, resulting in 6.09% and 7.13% surface area coverage, respectively.

The 50nm-diameter colloids were firstly employed to investigate the effects of multiple sol applications to aminosilanised base substrates. Surfaces and colloids were left to react for a minimum of 15 minutes following each fresh application of sol. The solution was then removed via a pipette so as not to completely remove all solution from the surface and thus prevent capillary forces from acting. Further applications of the sol were then reapplied in this manner. Following 4 repeats of sol application, mean percentage area coverage in relation to the base substrate was calculated as 6.09%. Following 6 applications of 50nm-diameter colloidal sol in this manner, a mean surface coverage of 7.13% was calculated, Table 3.2. The results suggest that by increasing the number of sol applications, surface area coverage of colloids also increases. However, as each immersion lasts 15 minutes, the substrate undergoing 6 sol applications in comparison to 4 will have been subjected to the colloidal sol for 30 minutes longer than the substrate immersed only 4 times. This suggests that the amount of time functionalised substrates are immersed in the colloidal sol may account for the increase in surface area coverage of immobilised colloids. This possibility is further supported by colloidal kinetics (Grabar et al, 1996), which is discussed in further detail in Section 3.2.2. Furthermore, the 2 additional immersions undergone by samples in the instance

of the 6-times application experiment only resulted in an approximately one percent increase in colloidal area coverage.

As time has been implicated in the coverage of a functionalised surface by colloids (Grabar et al, 1996), when monitoring 20nm-diameter colloidal adhesion, one substrate underwent 6 applications as described previously, while another was immersed in the 20nm-diameter colloidal sol once, for 24 hours. This comparison allowed the effects of the number of sol applications and colloidal sol immersion time in relation to area coverage to be monitored. It would appear that the determining factor with respect to colloidal area coverage on an amino-functionalised substrate is, indeed, time. Percentage area coverage following 6 sol immersions was calculated as 5.13%, while area coverage following immersion of aminosilanised substrates in the 20nm-diameter colloidal sol for 24 hours was calculated as 5.07%, Table 3.2. The area coverage using either of these methods appears to result in a surface coverage of approximately 5.1%. These results support the work previously described by Grabar et al (1996), where colloidal adhesion is under kinetic control at early times. Similarly, work conducted by Hanarp and colleagues (1999), also suggests that immersion time of substrates in a sol is the main determinant of colloidal distribution with respect to functionalised surfaces (personal communication with D. Sutherland). Thus, unless otherwise stated, all colloidal substrates were prepared by immersion in sol for 24 hours.

The three nearest neighbour distances for each particle were calculated using the same acetate-overlay method. The three nearest neighbouring colloids to each single, individual colloid within the acetate square were measured centre-to-centre using the appropriate acetate scale bar. This insured that the nearest neighbouring colloid was contained within the three results. Once all nearest neighbours were calculated in this manner, the smallest distance between each individual colloid and its nearest neighbour was entered into Microsoft Excel. The mean, standard deviation, standard error, minimum and maximum distance between nearest neighbours in the population and the count (n), indicating the number of colloids used to calculate the smallest distance to their nearest neighbour, were determined.

Once again the SEM photomicrographs, Figure 3.2 and 3.3, previously used to calculate the percentage area coverage of colloids were utilised to calculate the nearest neighbour data. As a result, nearest neighbour statistics were determined for 20nm-diameter

immobilised colloids, adhered to the base substrate, having undergone 6 repeated sol applications and 24 hour immersion in the sol, Table 3.3, and 50nm-diameter colloidal topographies subjected to either 4 or 6 repeated sol applications, Table 3.4.

	6* Applications of Sol	24 hour immersion in Sol
Mean	56.80	61.25
Standard Deviation	11.35	13.62
Standard Error	0.87	1.06
Count (n)	172	164
Minimum	20.00	40.00
Maximum	90.00	125.00

Table 3.3: Nearest neighbour descriptive statistics of 20nm-diameter colloids adhered to a silica base substrate. Following six 15-minute applications of the sol, mean nearest neighbour distance was calculated as 56.80nm compared to 61.25nm for 24-hour immersion of substrates in the sol. Minimum distance between nearest neighbours were greater, 40nm, on the 24-hour immersed samples compared to 6 applications (20nm). This suggests 24-hour immersion of substrates in the sol results in more regular patterning of surfaces, with limited colloidal clumping or aggregates occurring.

Following 6 immersions in the colloidal sol, the mean nearest neighbour distance, calculated for 20nm-colloids in this instance, was 56.8nm, where n=172. The minimum distance between neighbours was 20nm, and occurred when two colloids contacted each other at their circumference. The maximum distance between neighbouring 20nm-diameter colloids was 90nm. Standard deviation and standard error were calculated as 11.35nm and 0.87nm respectively. Less dense colloidal coverage was calculated for aminosilanised substrates immersed in 20nm-diameter colloidal sol for 24 hours. Mean distance between nearest neighbouring colloids was 61.25nm, where n=164, 4.45nm greater than the mean spacing calculated for colloids on the base substrate following 6 immersions in the sol. Minimum distance between neighbouring colloids was 40nm suggesting that contact between particles was limited, Debye length was not compromised and nanopatterning was more regular. This coincides with the self-assembly of colloids at early time being under kinetic control. As a result, colloidal coverage is limited by interparticle repulsion (Grabar et al, 1996). Maximum spacing between nearest neighbours was 125nm, suggesting lower density coverage in comparison to the substrate immersed 6 times in the sol, where maximum interparticle spacing is increased by 35nm. Standard deviation and standard error were calculated as 13.62 and 1.06 respectively.

When considering the data collected for both area coverage and interparticle spacing of substrates immersed in the 20nm-diameter colloidal sol, either 6 times at approximately 15-minute intervals, or for 24 hours, little difference exists with respect to area coverage. However, the data suggests colloids immersed for 24 hours in comparison to 6 applications resulted in a more regular sub-monolayer distribution with individual colloids occurring rather than regions where two or more colloids may be in contact, distracting from individual nanofeatures. As a result, substrates were immersed in the 20nm colloidal sol for 24 hours when preparing experimental colloidal topography.

	4* Applications of Sol	6* Applications of Sol
Mean	111.05	113.78
Standard Deviation	36.71	41.93
Standard Error	3.17	3.61
Count (n)	134	135
Minimum	50.00	50.00
Maximum	210.00	290.00

Table 3.4: Nearest neighbour descriptive statistics of 50nm-diameter colloids adhered to a silicon base substrate. Nearest neighbours were counted following both 4* applications and 6* applications of the 50nm-diameter containing colloidal sol. Mean interparticle spacing between colloids following both treatments are remarkably similar, with 111.05nm distance measured for 4 applications and 113.78nm for 6 applications. Minimum distances were recorded in both conditions as 50nm suggesting aggregation establishment occurring in 50nm-diameter colloids following repetitive applications. Surprisingly, a maximum distance of 290nm was calculated following 6 applications compared to 210nm following only 4 applications.

With respect to substrates coated with the 50nm-diameter colloids, the same calculations were made. However, as discussed in relation to the surface area coverage, base substrates were immersed either 4 or 6 times in the 50nm colloidal gold sol. The mean distance between neighbouring 50nm-diameter colloids following 4 immersions was 111.05nm, where n=134. The minimum distance between these colloids was 50nm, indicating colloids in contact at their circumference, and a maximum of 210nm distance between neighbours was recorded. Standard deviation of 36.72 suggests a less regular colloidal population occurring following 4 immersions in the 50nm-diameter colloidal sol in comparison to the more regularly patterned 20nm-diameter colloids. Standard error was 3.17. Similarly, the mean distance between 50nm-diameter colloids following 6 immersions in the sol was 113.78nm, where n=135. Once again, the minimum distance between neighbouring colloids, 50nm, indicates that in some instances neighbouring colloids were in contact with one another. A maximum distance of 290nm

was calculated between neighbours. A standard error of 41.93 suggests less regular patterning of the 50nm-diameter colloids in relation to their 20nm-diameter counterparts. Standard error occurring in the 135 colloids investigated was calculated as 3.61.

Differences found between the distribution of 20nm-diameter colloids on substrates immersed either 6 times or for 24 hours in the sol, indicated more regular patterning of the substrate following 24-hour immersion. Furthermore, colloidal contacts were infrequent, resulting in a pattern reflecting individual nanofeatures with more constant dimensions. Experiments involving the 50nm-diameter colloidal sol suggested repetitive application resulted in less regular patterns, with colloidal contacts occurring throughout the population, regardless of application numbers. As a result of these findings, all colloidal structures, whether employing 20nm- or 50nm-diameter gold colloids, were fabricated by immersing an aminosilanised base substrate in the desired sol for 24 hours.

3.2.1.2 Atomic Force Microscopy

A Nanoscope atomic force microscope (AFM) was used in tapping mode to characterise colloidal distribution and dimensions. Contact mode was originally attempted, but this resulted in a flat surface being imaged, as the colloids appeared to be dislodged from the base substrate by the AFM tip. This brought into question the stability of the colloidal structures, as did initial investigations of epitenon cell morphology using scanning electron microscopy, Section 3.3.1.

Unfortunately, following revision of this thesis, a lack of substrates and time constraints prevented high resolution AFM imaging of 20nm-diameter colloidal topography. Colloidal substrates with 50nm-diameter particles were imaged at high resolution, Figure 3.5, where scans were produced across 2.5μm x 2.5μm areas of the surface. This scan size resulted in each pixel composing the image measuring 4.88nm, allowing for highly accurate measurements of colloids to be made during section analysis, Figure 3.6. Section analysis of the 50nm-diameter colloidal substrate allowed a number of characteristics, including colloid height, interparticle spacing and colloid diameter to be measured. Colloid height (red arrows and text in Figure 3.6) was measured as 64nm. Although a greater diameter value of the 50nm-diameter colloids was measured, this recording is consistent with the stated particle size distribution outlined by the colloidal

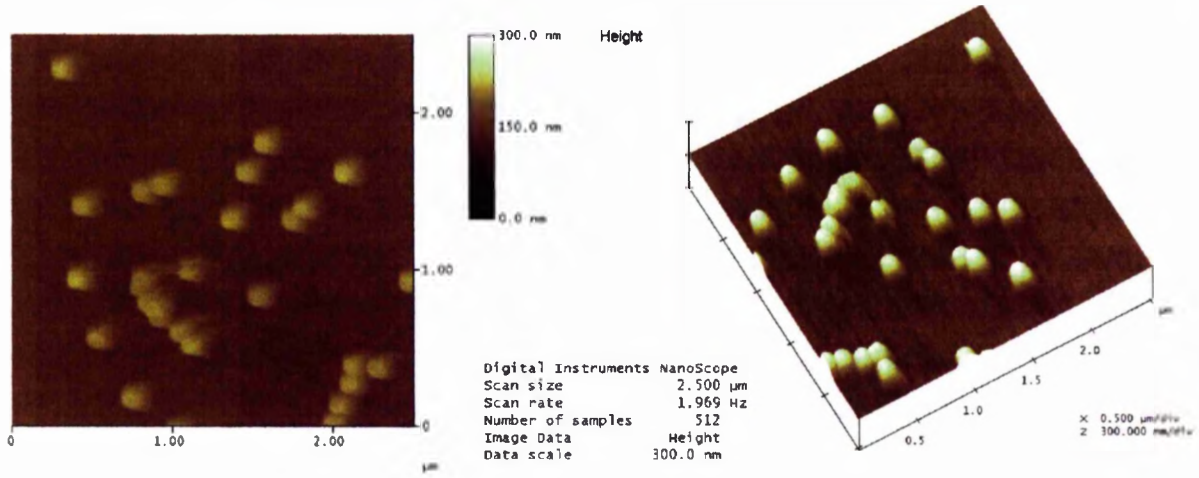

Figure 3.5: Atomic force microscopy image of 50nm-diameter colloidal particles on a silicon substrate with SiO_2 surface. Tapping mode was employed in relation to Nanoscope imaging of the topography to prevent colloids being dislodged by the cantilever. The original scan (left of figure) was firstly captured at high magnification across a 2.5µm x 2.5µm area, resulting in a measurement of 4.88nm per pixel composing the image, allowing for accurate measurements of the surface, Figure 3.6. The original scan was then produced as a 3D image (right of figure), indicating colloid height in the z-plane. Colour scale indicating height of the colloids refers to the original image (left).

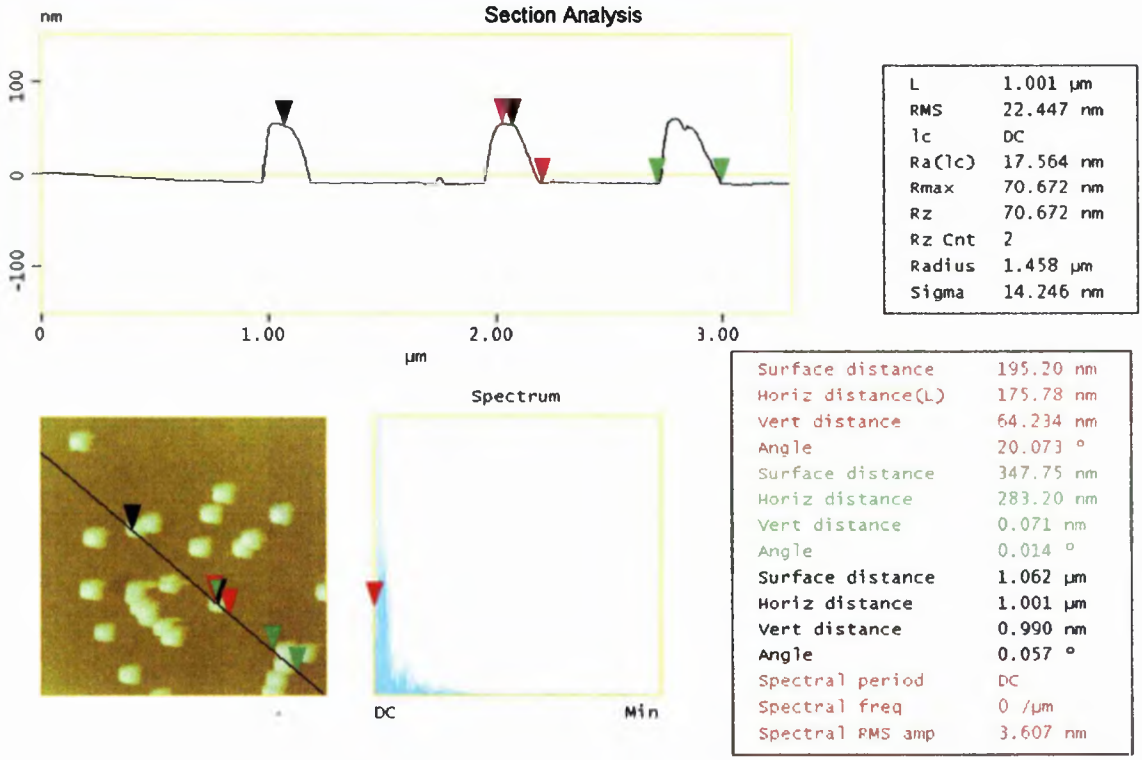

Figure 3.6: Section analysis of 50nm-diameter colloidal surfaces AFM image captured in Figure 3.5. Colloid height (red arrows) is recorded as 64nm. Although slightly greater than the claimed 50nm-diameter of the particles, this recording is consistent with the <20% particle size distribution maintained by colloidal manufacturer British Biocell International Ltd (Table 3.1).

manufacturer (British Biocell International Ltd) as less than 20%, Table 3.1. Centre-to-centre analysis of colloids was also investigated (black arrows and text, Figure 3.6), although nearest neighbours were not selected in this instance and the horizontal distance is thus not comparable to previous nearest neighbour analysis, Table 3.4. However, vertical distance measured between the two colloids selected was recorded as 0.99nm, indicating good homogeneity of the 50nm-diameter colloids within the sol. The base of two colloids in contact with one another was also measured as 283nm (green arrows and text, Figure 3.6). It is generally believed that the greatest horizontal distance between the circumferences of two colloids in contact would measure twice the diameter of the colloids in question, for example 100nm for two 50nm-diameter colloids. However, the horizontal distance measured using the AFM in this instance, suggests this may not be the case. One possible explanation lies in the initial colloidal diameter being greater than the measurement stated by the manufacturer due to particle size distribution. However, this measurement is more likely an AFM artefact due to the inability of the cantilever to follow the curvature of the nanometric spherical colloids.

3.2.1.3 Laser Profilometry

A UBM Laser Profilometer (UBM Messtechinik, Ettlingen, Germany) was used in an attempt to image surfaces. However, the capibilites of the machine did not extend as far as the nanometric scale required, Figure 3.7. This highlighted a growing concern with respect to nano-featured surfaces. When investigating the finer features of a surface, the overall topography, on the micrometric and macrometric scales, is often overlooked. For example, what was originally described as possible capillary actions with respect to colloidal patterning of a substrate (Wood et al, 2002[a]) may actually be underlying micrometric surface topography, in this case a gentle hill upon which, repulsive interparticle forces are altered resulting in what appears to be more densely patterned colloids. This possibility is further validated by two factors. Firstly, it is stated that capillary forces should not act on particles with dimensions less than 50nm-diameter (personal communication with Dr D. Sutherland), and the colloids used in this instance were 20nm-diameter. Secondly, during the course of this work, colloidal aggregations have been found in areas of surface damage, Figure 3.4, indicating micrometric surface features may often act to shield the repulsive forces of colloids.

As an ongoing issue, it is often impossible to truly image a surface at both micrometric and nanometric scales. When considering the addition of cells, this problem is further

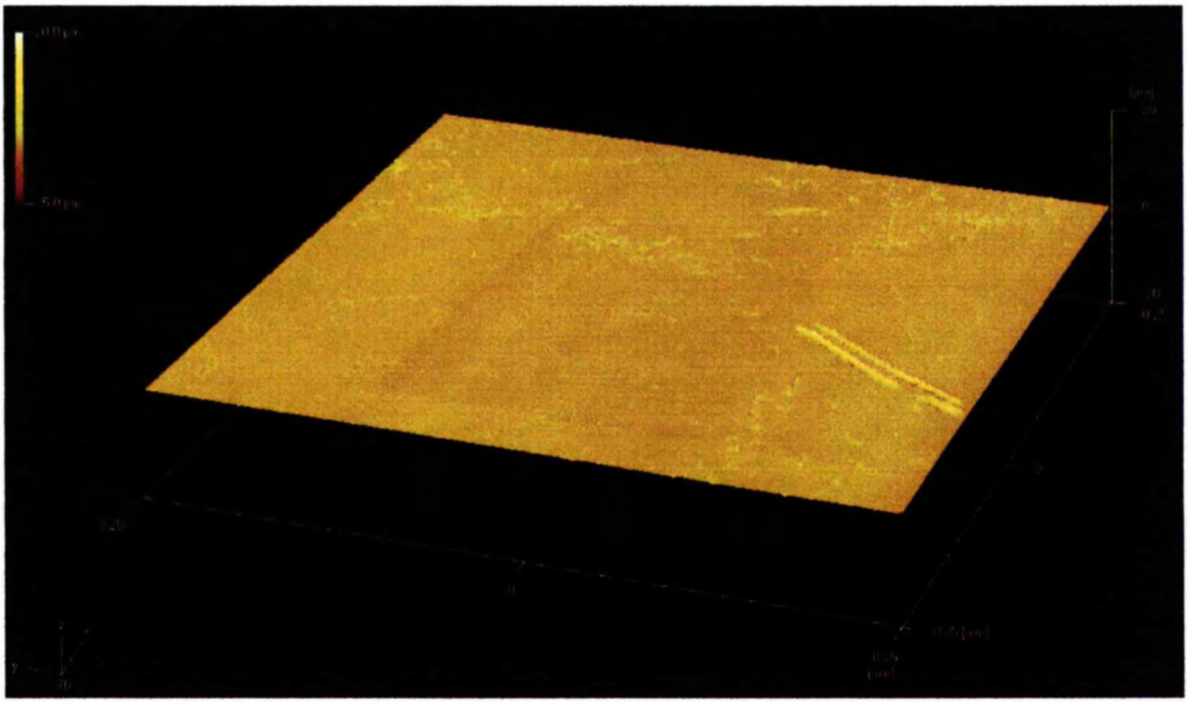

Figure 3.7: UBM laser profilometry image of a 50nm-diameter colloidal topography on a glass (borosilicate) base substrate. A 0.5mm x 0.5mm^2 area was scanned at the lowest possible settings. The colour scale (top left) indicates the tallest (20μm) and shortest (5μm) surface features (in the z-plane) sensed by the profilometer. An array of features approaching the 20μm scale are visible in this image. This highlights the requirement for nanometric surface designs to be further investigated at the micrometric level.

heightened, as cells obscure the view of the topography underlying them. Transmission electron microscopy (TEM) is emerging as a real key to understanding cell reactions in relation to various scales. This is particularly true if the substrate upon which cells have been seeded is capable of being sectioned as the biological sample is being transversely sectioned. This allows for cell interactions with the substrate to be viewed directly, with both external and internal cellular features to be related to the topography on which cells have been cultured. One problem, however, with this method is that the nanometric feature dimensions and micrometric cells are fixed and therefore do not provided real-time information. Furthermore, only a very thin section of sample can be viewed of the cell in relation to its substrate.

3.2.2 Colloidal Kinetics and Altering Sub-monolayer Densities

Both 20nm- and 50nm-diameter gold colloidal particles used to create the nanotopographies described have citrate ions adsorbed on their surface, resulting in each individual colloid possessing an overall negative charge resulting in particle dispersion in an aqueous solution. Colloidal gold particles are derived from $[AuCl_4]^-$, which has an intrinsic fixed negative charge as a result of strongly adsorbed Cl^- and/or coating of $[AuCl_4]^-$ as a result of incomplete $[AuCl_4]^-$ reduction (Grabar et al, 1996).

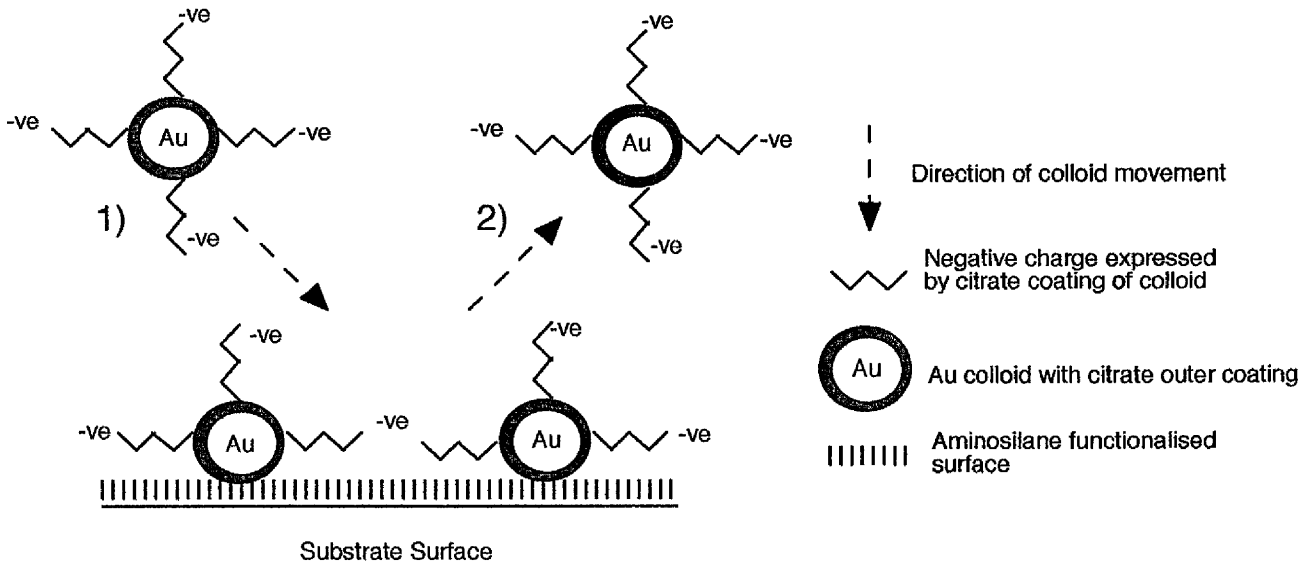

Figure 3.8: Transition from kinetic adsorption to electrostatic repulsion of the colloids. The simple $t^{1/2}$ no longer applies to the colloidal system. As the functionalised surface is covered with gold colloids, subsequent colloidal attachment is prevented. In 1), a colloid approaches the surface. However, due to the adhesion of particles that have undergone kinetic adsorption, no free NH_2 groups are available to bind to. Any amino groups that are not directly attached to a colloid are unable to attach subsequent colloids due to the negative citrate charge of previously adhered colloids. Thus, 2), colloids are prevented from attaching to the surface or other colloids.

When a surface (in this case an AAPS functionalised surface) is immersed in a sol, surface assembly at early time (t) is under kinetic control where particle coverage conforms to a simple $t^{1/2}$ dependence (Grabar et al, 1996). At later times, where particles are bound to the surface via the aminosilane under these conditions, colloidal coverage is limited due to interparticle repulsion, Figure 3.8.

When colloidal adsorption reaches this state, approximately 5.1% with respect to 20nm-diameter colloids and 6 to 7% for 50nm-diameter colloids, Section 3.2.1.1.1, inter-particle repulsion prevents additional particle immobilisation. This is due to the functionalised surface being either in contact with a colloid, reducing the available immobilising area, or being shielded by the negative charge of the citrate-coated immobilised colloid. This self-limiting nature of colloids in relation to a surface is key to altering colloidal density and packing at a substrate surface. The most common approach to creating close-packed arrays of colloids at a surface employs organic adsorbates as a means to charge screening, Sections 3.2.2.1 to 3.2.2.3. It is based on this understanding of colloidal kinetics that the following experiments were utilised.

3.2.2.1 Charge screening of colloids using Sodium Chloride (NaCl)

A now standard method of altering colloidal coverage of a surface exploits the Debye length of individual particles outlined in the DLVO theory through the use of a salt (Hanarp et al, 1999, Hunter, 1987). By decreasing electrostatic repulsion decay length or Debye length, electrostatic repulsion of colloids can be screened. This allows colloids to be distributed at an increased density on a given surface in comparison to non-salt-treated sols.

Quartz Crystal Microbalance (QCM) has indicated that by increasing NaCl concentration in particle solution to 10mM, 110nm negatively charged polystyrene colloids result in an increased surface coverage, calculated as 38% (Hanarp et al, 1999). However, at this high salt concentration, aggregates of up to 10 particles are observed thus detracting from the evenly spaced, individual colloidal topography being sought to investigate cell reactions to nanofeatures. Such a surface is difficult to quantify, as colloids are either in densely packed grains or sparsely spaced. Furthermore, the irregular patterning suggests problems when reproducing this topography.

The gold colloidal particles used in these experiments carry an overall negative charge due to the citrate coating of their outer shell. One approach favoured for altering colloidal density is to add Sodium chloride to the colloidal sol prior to its application on a surface. When applied as a solution, the Na^+ acts as a counter ion in relation to the citrate-coated colloids by reducing repulsion. As a result, colloids may become more closely packed, as the charge which was originally present and kept them apart, Figure 3.8, has now been masked.

In preliminary experiments utilising 50nm-diameter colloidal gold particles, a low salt concentration of approximately 0.1mM was chosen in an attempt to reduce the occurrence of aggregates on the surface as previously observed by Hanarp and colleagues (1999). NaCl (Sigma, UK) was prepared as a stock solution with RO water, and stirred. Base substrates of silicon (with silica surface layer) underwent cleaning and aminosilanisation as previously described, Section 3.2. Immediately prior to immersing structures in the colloidal sol, 0.1mM NaCl was added to the sol and vortexed to ensure the salt solution was evenly distributed within the colloidal sol. Silicon structures with an active aminosilane surface were then immersed in the composite solution. Samples were left to react for 24 hours, as QCM investigations indicated that diffusion rate and the increased number of colloidal particles adsorbing at saturation following NaCl addition to the colloidal sol must result in an increase in time required for saturation (Hanarp et al, 1999).

Surface coverage of colloids was found to be either one of two extremes; little or no coverage, or extremely dense aggregates, Figure 3.9. Dispersed coverage of 50nm-diameter colloids, Figure 3.9a), resulted in less evenly distributed surface area coverage of the nanoparticles in comparison to untreated surfaces, Figure 3.3. Where colloidal density did increase, the gold particles were in direct contact with their neighbours, resulting in colloidal grain formations across the substrate, Figures 3.9b)-d). However, large areas of the surface in this instance were completely devoid of colloids. It later emerged when developing planar-nanopillared structures that problems existed within the drying technique being used on surfaces; namely different pressures of nitrogen in different guns. It would appear that these problems were also present when attempting to increase colloidal density using Sodium chloride due to the lack of colloids on the surface and also the presence of crystals on the colloidal topography, Figure 3.9. Furthermore, when fabricating nanopillared topography through the implementation of

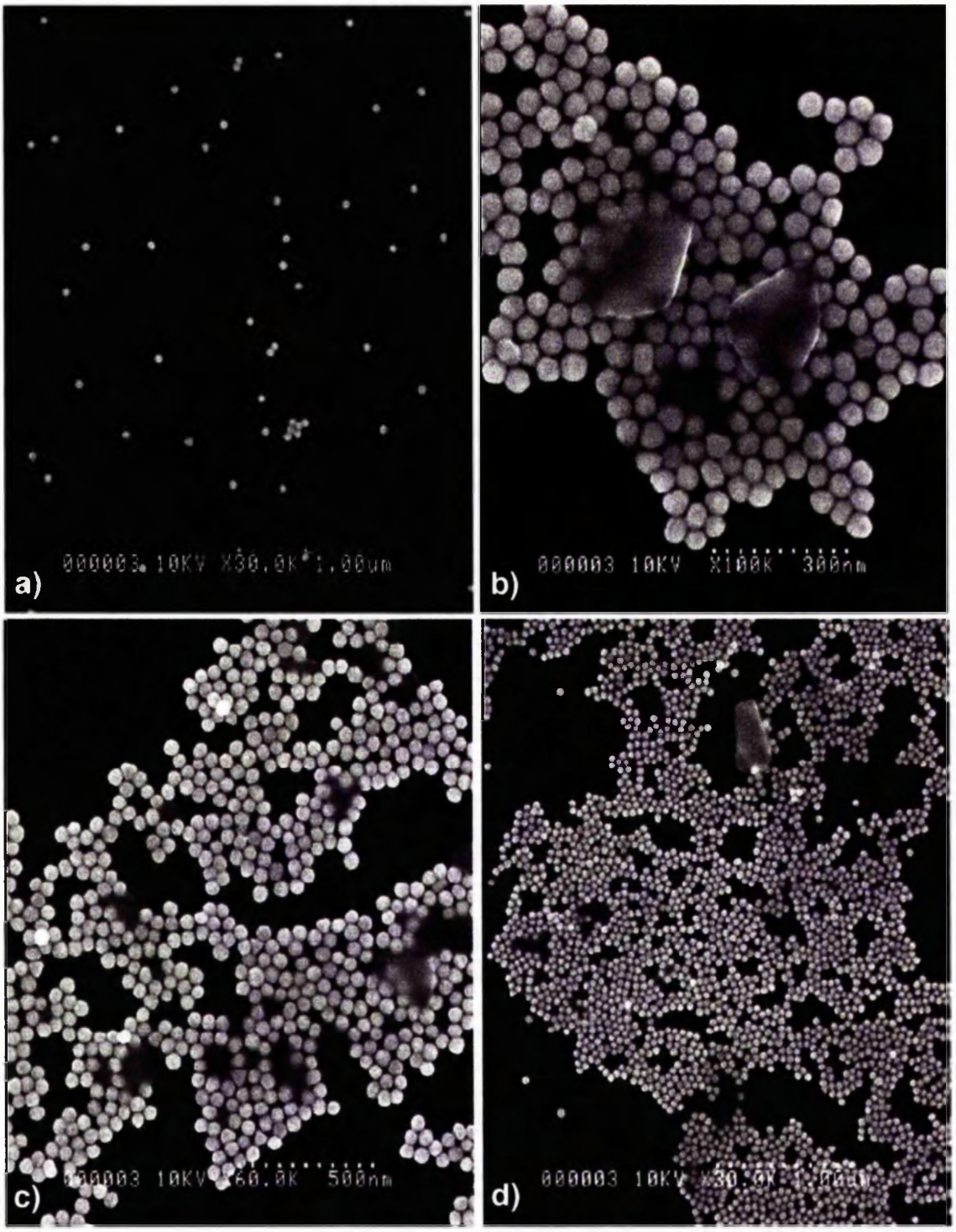

Figure 3.9: Scanning electron micrograph, using the Hitachi S-900, of aminosilanised base substrates following immersion in 50nm, 0.1mM Sodium chloride-treated colloidal sol showed colloidal surface distribution to be lower a), or more densely packed b)-d), in comparison to untreated surfaces. Distribution of colloids across the surface was inconsistent regardless of the number of times substrates were re-immersed in the salt-treated sol, resulting in densely packed colloids surrounded by denuded areas, b)-d), or low distribution, a). This was later believed to be a direct result of drying techniques used. Surface drying problems would account for the crystals observed, obscuring the underlying tightly-packed colloids, b)-d).

a colloidal etch mask, colloids in contact with one another etched as a "nanomountain" rather than individual pillars. Thus, Sodium chloride treated colloidal substrates were not used as topography to investigating cell behaviour in relation to nanometric features.

3.2.2.2 Charge screening of colloids with Sodium citrate

There are two specific time periods that govern colloidal distribution on a surface, Section 3.2.2. At early times surface assembly is under kinetic control described by a simple $t^{1/2}$dependence. At later times, colloidal gold coverage is limited by interparticle repulsion, effectively inhibiting additional particle immobilisation. The decrease in colloidal adhesion can be attributed to one of two factors when considering equations describing the diffusion of spherical particles to a planar surface. These are either a decrease in the particle concentration of a sol or a reduction in the sticking probability, Equation 3.2. Partial screening of these repulsive interactions can be achieved via the addition of strong organic adsorbates to colloids attached to a surface prior to a subsequent sol immersion (Grabar et al, 1996).

$$q=0.163\, pnyt^{1/2}$$

Equation 3.2: where q= number of particles reaching $1cm^2$ per unit time, p= sticking probability, n= particle concentration in number per cm^3, y= constant (incorporating particle radius, viscosity, and temperature), t= time in seconds. Kinetic information with respect to the substrate-colloid interaction is conveyed by the sticking probability, where the ratio between the number of particles bound and the number reaching the surface is found (Park et al, 1987 and 1989).

Four different adsorbates, poly(vinylpyrrolidone) (PVA), trans-1, 2-bis(4-pyridyl)ethylene (BPE), $HOCH_2CH_2SH$ and trisodium citrate dihydrate and their effects on screening the repulsive forces between gold colloids are described by Grabar et al (1996). In an attempt to create a densely packed colloidal monolayer, the trisodium citrate dihydrate was selected. The citrate adsorbate method was selected in comparison to the others documented within Grabars' work due to the compromise the other adsorbates elicited when considering monolayer or sub-monolayer colloidal topography, where colloidal aggregates resulted in multi-layer configurations.

Caro's Acid, NaOH and aminosilane-treated, Section 3.2, borosilicate glass coverslips were immersed in 50nm-diameter colloidal sol for 5 minutes and then placed in a beaker of RO water. Following this, samples were immersed in 4mM Sodium citrate

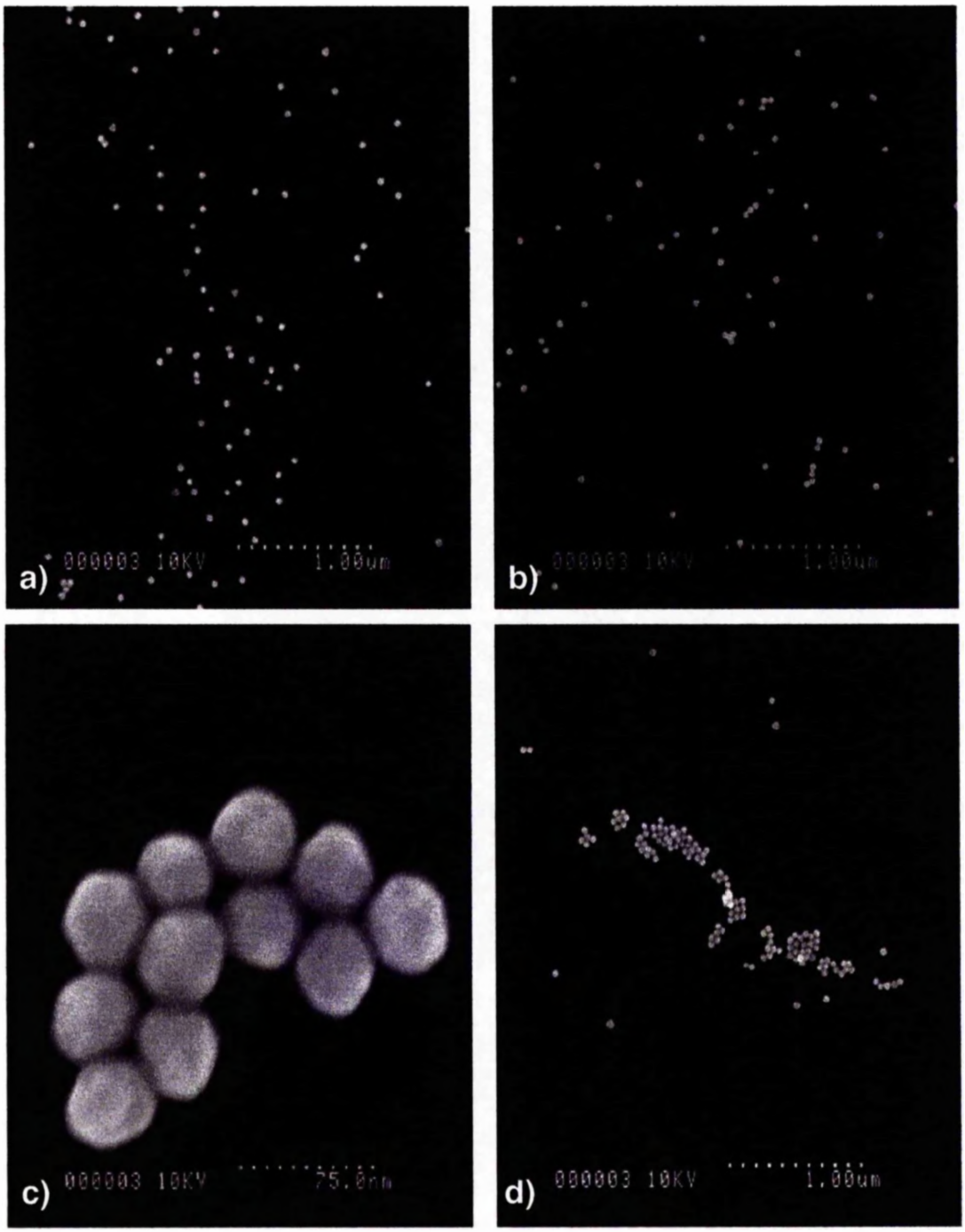

Figure 3.10: Scanning electron micrographs (Hitachi S-900) of 50nm-diameter colloids treated with sodium citrate. Similar problems associated with previous attempts to alter monolayer surface density of colloids using Sodium chloride are observed. Inconsistent distribution occurs across the surface. In some areas very low-density distribution is observed, a) and b), while in others, close-packed colloidal grains indicate the presence of charge-shielding via the sodium citrate, c) and d). However, in all images, a)-d), exposed areas of the surface are observed, devoid of colloids. This indicates possible faults in the drying technique, as does the trail of colloids, a), appearing to be patterned by a directed, external force or directed nitrogen gas.

(Sigma, UK) for 8 minutes and rinsed in RO water once again. This cycle was repeated, with increasing colloidal immersion times. These were 5, 10, 20, 30, 60, 90, 120, 150, 180, 210 and 240 minutes. Each substrate immersion in the adsorbate lasted for 8 minutes at each time point. Adsorbance of the colloids to the functionalsied substrate should be proportional to their repeated sol immersion concentration and the electromagnetic properties of the particles due to continual adsorbate immersion, as stated by Beer's Law (Grabar et al, 1996, Chemical Education website).

Scanning Electron photomicrographs were captured using an Hitachi S-900 of substrates subjected to this process, Figure 3.10. As similarly observed in relation to the Sodium chloride-treated structures, Section 3.2.2.1, gross discrepancies occurred throughout the sample. Colloids were observed adsorbed to the substrate at either low densities, Figures 3.10a) and b), or at high density, where colloids were in contact with one another forming a grain, Figures 3.10c) and d). Large areas of the substrate surface were devoid of colloids in all instances, Figures 3.10a)-d). As previously suggested, Section 3.2.2.1, the lack of success of colloidal patterning using screening techniques may occur as a result of ill-defined nitrogen drying methods. This is further suggested in the patterning of dispersed colloids, Figure 3.10a), where the particles appear to be distributed across a specific axis (top-to-bottom), suggestive of additional factors contributing to this distribution pattern.

3.2.2.3 Alkanethiol mobility-restoration of colloids results in lattice formation

A method developed by Sato, Brown and Johnson (1997) was employed in an attempt to create a highly ordered, and thus dense, colloidal lattice, which would not distract from the monolayers being sought. An organic surfactant treatment of both the substrate and the colloids was performed using an alkanethiol.

Silicon surfaces were prepared as previously described, Section 3.2, and functionalised using an aminosilane. Immersion in a 50nm-diameter colloidal sol for 24 hours resulted in the submonolayer patterning as previously seen, Figure 3.3, and is described in Section 3.2.1.1.1. Following this process, the surface housing the submonolayer colloidal lattice was immersed in 5mM ethanol and dodecane-1-thiol [$Me(CH_2)_{11}SH$] composite solution for 24 hours. Samples were then immersed in ethanol briefly and dried with a sterile flow of nitrogen gas. Four repetitive applications of alternating colloidal and alkanethiol immersion were conducted resulting in the final colloidal

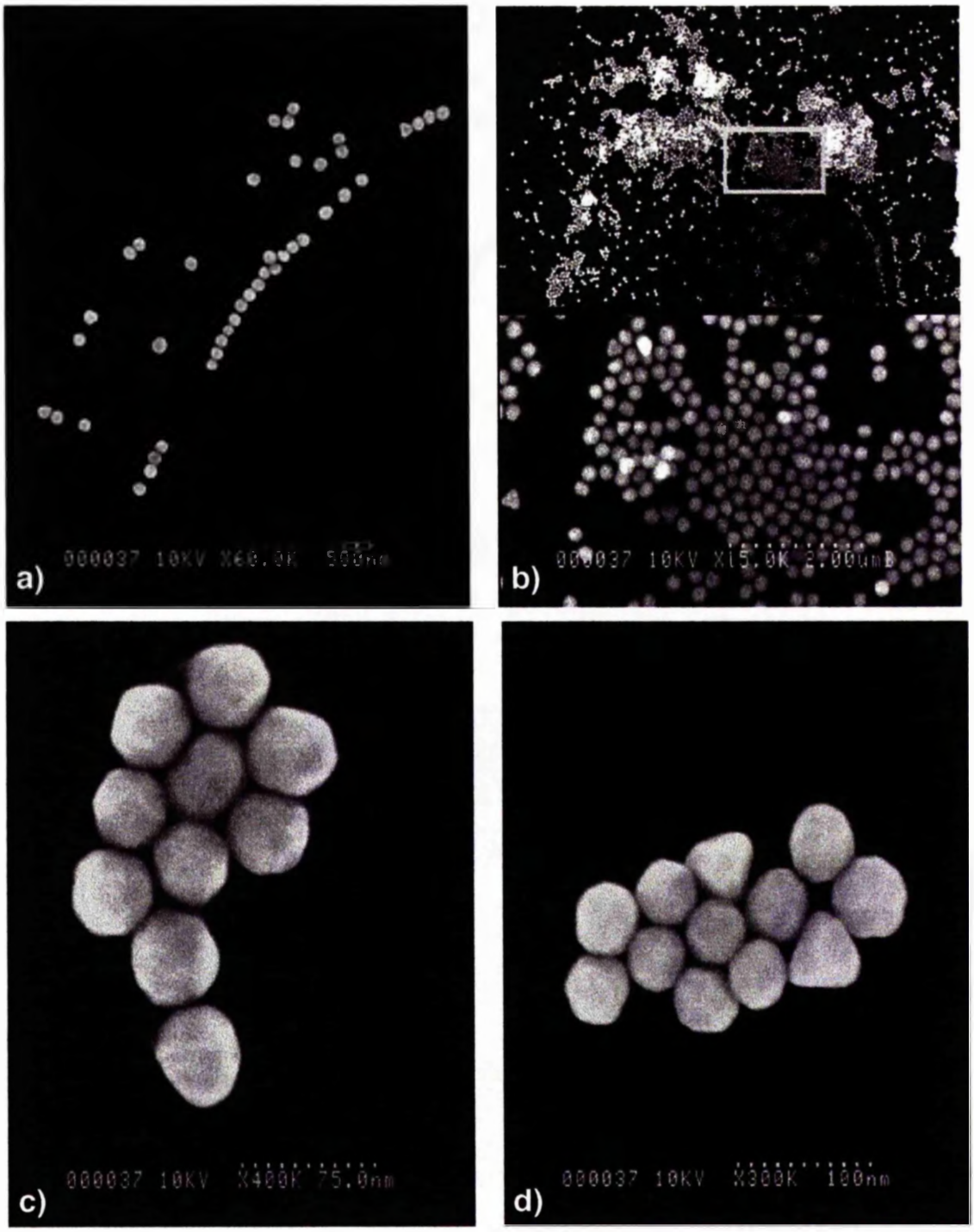

Figure 3.11: Scanning electron (Hitachi S-900) micrographs of 50nm-diameter colloids treated with an alkanethiol. Inconsistencies are observed with regard to colloidal distribution, a) and b), across the substrate surface. The "line" of colloids, a), indicate possible drying technique problems, as, in theory, these particles would gather into a larger grain, c) and d), rather than be aligned as a necklace, especially considering the high density grain formations, b), following the immersion treatments. The successful patterning of small grains, c) and d), indicate the potential of this application when attempting to increase colloidal density.

patterning viewed in Figure 3.11.

This treatment replaces the citrate adsorbates present on colloidal surfaces with alkanethiol molecules due to the strong affinity of the sulphur present in the alkanethiol molecule to gold. In addition, the new sulphur-gold bond can displace bonding between the amino group (NH_2) and the gold. This results in the complete ligation of the colloids with the alkanethiol molecules (Sato et al, 1997). As the molecular binder of bifunctional aminosilanes is detached from the colloids, the gold particles are released and acquire limited mobility with respect to the surface. Colloids can thus move and collide with additional particles on the surface resulting in grain formation, the size of which is dependent upon the amount of available migrating colloids. Where colloids have detached from the surface, the NH_2 groups are now free to bind colloidal gold particles through subsequent sol immersions. The alkanethiol treatment is then repeated, and colloidal grain size on the surface increases. Four repetitions of the alternating colloidal, alkanethiol immersions were applied to the experimental substrates to prevent disruption of the 2D film or monolayer, which would result in the emergence of 3D surface structures (as described by Sato et al, 1997). As can be seen in Figure 3.11, this method was less successful than described by Sato and colleagues. It was not until later in the project that problems associated with the drying of the surfaces were truly realised. However, the success in areas of the samples suggest, with refinement, this method could result in densely packed colloidal topography, although possibly only across small regions, for example $1\mu m^2$.

In summary, the sodium citrate and alkanethiol treatments appear most promising with respect to the development of well-organised colloidal monolayers. However, as described throughout this thesis, problems associated with drying the sol from sample surfaces have resulted in limited success of these techniques. However, approaches to drying techniques with respect to colloidal patterning of substrates appear to result in very accurate monolayer topographies (Ng et al, 2002). With respect to densely packed colloidal surfaces as an etch mask for nanopillar fabrication, only areas completely unmasked by the colloids are etched, resulting in larger surface features, resembling mountainous topography in comparison to individual nanofeatures, Section 4.2.2.

3.3 Investigating cell behavioural alterations in relation to colloidal topographies

Having investigated many aspects of the colloidal topographies using both the 20nm- and 50nm-diameter gold colloidal particles, and the limited success of the density alterations, the technique outlined in Section 3.2 was used to fabricate surfaces for cell investigations. Preliminary experiments were conducted using both the HGTFN endothelial and rat epitenon cells, Section 2.3, where scanning electron microscopy of cells on substrates at a given period was used, as was time-lapse video microscopy. A more in-depth approach using very specific time periods to investigate cells with an array of techniques including the SEM, immunocytochemistry techniques and fluorescence imaging, time-lapse video microscopy, light and phase-contrast microscopy were used to investigate hTERT fibroblast response to colloidal topographies.

3.3.1 Rat Epitenon Cell Reactions to Colloidal Topographies

The first cell type to be investigated following the establishment of the colloidal topographies under investigation were rat epitenon cells. Morphological investigations of the cells in relation to both the 20nm- and 50nm-diameter experimental colloidal topographies were conducted. Cells were seeded at a density of 10,000 per ml in 3mls ECT media. Cells were fixed on the colloidal topography at 24 hours and taken through a dehydration series and were critically point dried, Section 2.7.3, allowing samples to be imaged using SEM.

Initial images captured using the Hitachi S-900 gave cause for concern as the epitenon cells appeared to be manipulating their environment either by moving or removing the colloids either via physical means or phagocytosis, Figure 3.12. Previous publications by Albrecht-Buehler (1976, 1977[a] and 1977[b]), where 3T3 fibroblasts seeded on a heterozygous colloidal population (colloids with non-uniform diameter), move the particles across their bodies, thus confirming the possible occurrence of this phenomenon. More recently, the uptake of polymer nanoparticles containing bovine serum albumin (BSA), in the range of 270 to 370nm in diameter, by endothelial cells has been characterised (Davda and Labhasetwar, 2002). This study indicated that cellular uptake of nanoparticles was dependent on both incubation period, where complete growth medium containing a suspension of polymeric nanoparticles was

added to cells *in vitro*, and the concentration of nanoparticles in the media. Ingested nanoparticles appeared mainly localised within the cell cytoplasm in this instance.

As 3T3 fibroblasts have previously demonstrated manipulation of colloids present on a base substrate through sol evaporation and electrostatic interactions, (Albrecht-Buehler, 1976), and endothelial colloidal uptake has recently been characterised, (Davda and Labhasetwar, 2002), the possibility of epitenon manipulation and uptake of gold colloidal particles was brought into question. When considering the possibility of manipulation of colloidal topography by epitenon cells, evident in Figure 3.12, subsequent investigation using backscattered electron microscopy and conventional secondary electron detection in conjunction with X-ray Microanalysis was undertaken.

The results of this approach indicated that the cells were in fact confronted with a static nanotopography, with the lack of colloids in preliminary images, Figure 3.12b), likely to occur due to physical stress at the surface via cell breakage during dehydration and CPD. As a result, the colloidal topography developed as outlined in Section 3.2 has been proposed as a method of creating a model nanotopography for use in biological investigations (Wood et al, 2002[a]).

3.3.1.1 Possible colloidal uptake by epitenon cells

This work has been documented, to which the reader is also referred (Wood et al, 2002[a]), and is discussed as follows. Colloidal topographies were fabricated, Section 3.2, and submerged in Hepes prior to the application of cells. Epitenon cells were added to the experimental surfaces at a concentration of 10,000 per ml, and were buffered in 3mls H-ECT media, Section 2.4.2. Cells were incubated at 37°C for 24 hours, as this time was felt sufficient for cells to adhere to the substrate, spread and move across the colloidal topography, and this period exceeds that of 4 hours where cells exhibited the possibility of colloidal manipulation or uptake, Figure 3.12. This increased time period is sufficient for epitenon cells to fully interact with their underlying experimental topography when considering cell adhesion and motility.

Following the 24-hour incubation period, cells were fixed and processed for electron microscopy as outlined in Section 2.7.4. Secondary electron imaging at low magnification and low keV (to prevent damage to cells) was used to firstly locate cells, Figure 3.13. Once detected, a peripheral area of the cell was selected for investigation

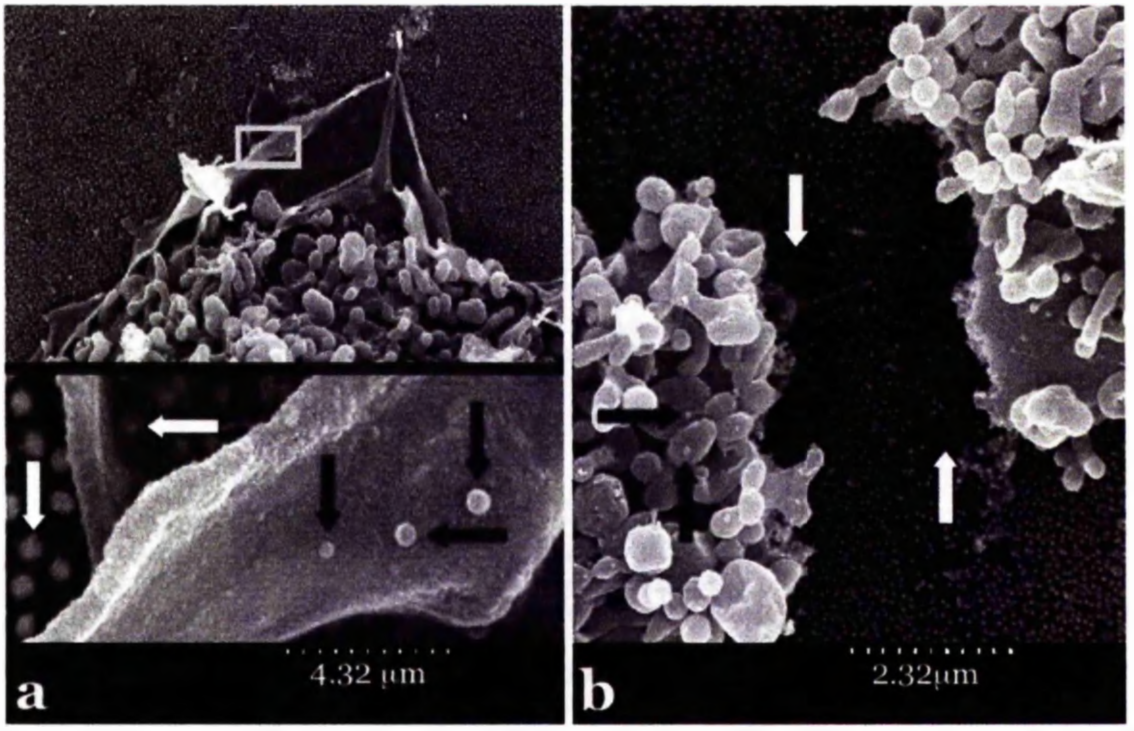

Figure 3.12: Scanning electron micrograph (Hitachi S-900) of possible colloidal uptake by epitenon cells at 4 hours. Black arrows in both images indicate entities within the epitenon cells sharing similar characteristics with colloids on the base substrate (indicated by white arrows in both images). The boxed area in the upper portion of image a) is observed at higher magnification in the lower portion of the photomicrograph. Breakage of a cell, b), is most likely to have occurred during dehydration of the sample prior to viewing using the S-900.

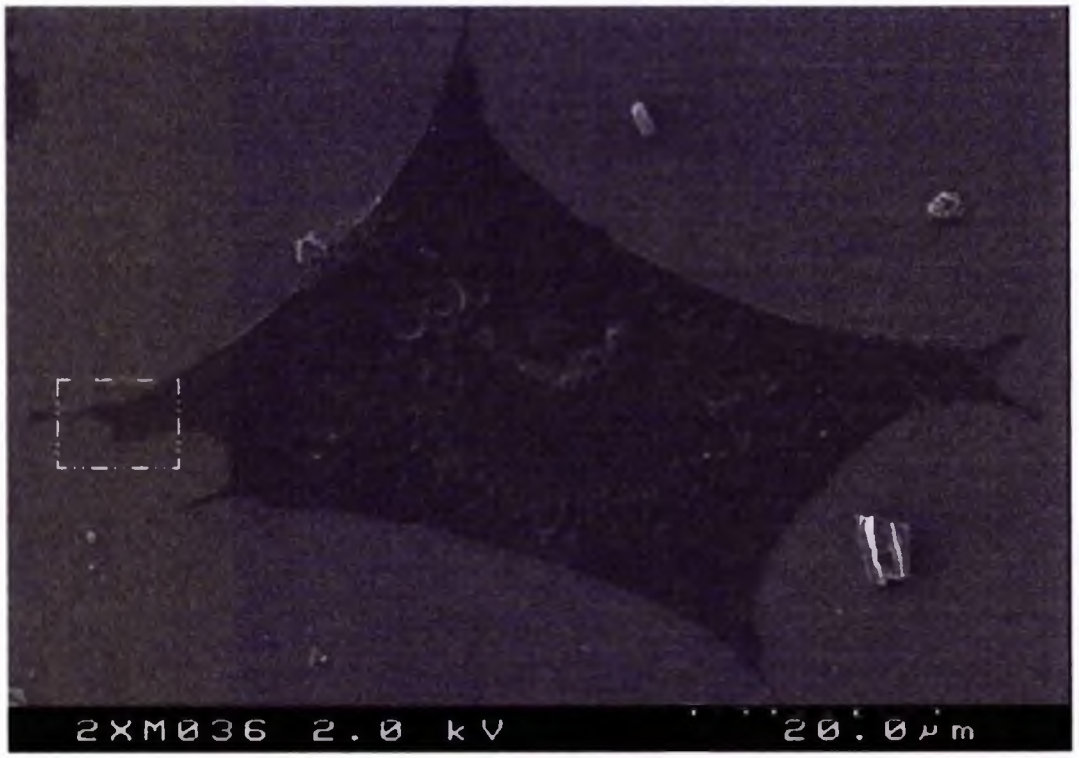

Figure 3.13: Low magnification secondary electron (SE) Image, at 2keV, of a rat epitenon cell on 50nm colloidal topography. The area of cell within the white box is observed at higher magnification in Figures 3.14-3.16, using both SE and BSE modes with increasing keV to determine colloidal distribution of the topography underlying the epienon cell.

using secondary electron (SE) and backscattered (BSE) detection. This method has been discussed in the publication previously referred to (Wood et al, 2002[a]), and is covered within this section using similar images of an alternative cell investigated at 48 hours. Images were taken at the peripheral membranes, as cells were thinnest at these areas, and traction forces occurring during movement are located at these sites (Dembo and Wang, 1999). This suggests mechanical forces, with strong propulsive forces established via nascent focal adhesions are located mainly at the anterior leading edge (Beningo et al, 2001), As a result, colloidal manipulation from their original position by cells would occur at these areas. Albrecht-Buehlers' work (1976) also indicated colloidal movement by fibroblasts occurrs directly at the peripheral membrane, with particles being moved across the apical surface towards the nuclear (central) area of the cell.

The area selected in the instance discussed, highlighted by the white boundary in Figure 3.13, was investigated at higher magnification to allow for imaging of the 50nm-diameter colloids. A low accelerating voltage of 2 keV was utilised to allow imaging of the specimen surface detail, both cellular and colloidal, using secondary electron (SE) detection, Figure 3.13. The membrane of the epitenon cell in question appears well spread, with thinner regions, with respect to nanofeature elevation, observed in the furthest extended areas, boxed area of Figure 3.13, resulting in imagining of colloids underlying this area. Increasing the accelerating voltage to 4keV using the SE detector results in more information being retrieved with regard to the colloidal topography due to increased Backscattered electrons hitting the SE detector, Figure 3.14a). Greater contrast between the colloids and overlying cell results due to the SE and BSE coefficients of the gold colloids increasing proportionally with keV at a higher rate than the low density epitenon cell. The colloids underlying the thinly spread epitenon cell membrane appear at similar, irregular density as those present on the cell-free surface, Figure 3.15a). Detecting backscattered electrons, collected by a yttrium aluminum garnet (YAG) single crystal scintillation detector positioned between the objective lens and specimen, results in greater colloidal topography detail underlying the cell, Figure 3.15b). Backscattered electrons are emitted from the specimen with energies ranging from 50keV to the energy of the primary beam used. The extent of depth from which backscattered electrons emerge is dependent upon the accelerating voltage, and can be emitted from a depth of up to 6μm below the sample surface (Abrahams and DeNee, 1973). This emergence depth allows information to be gathered from within the

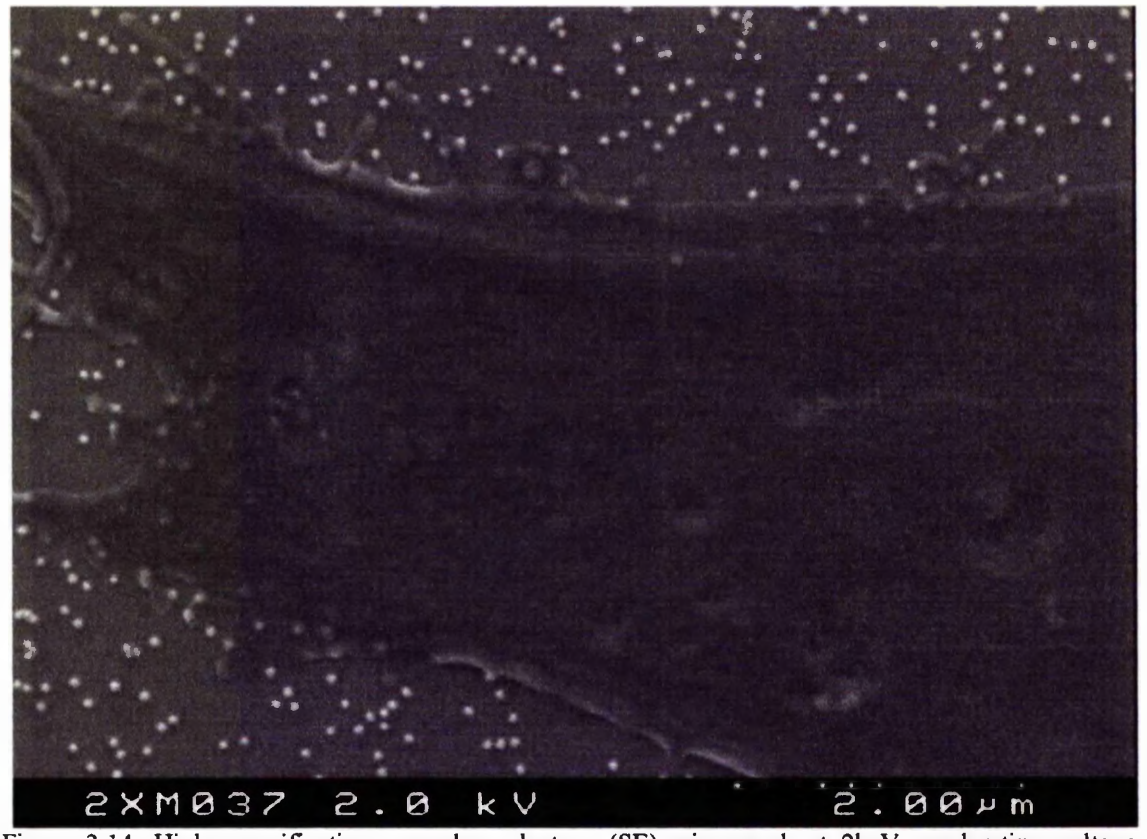

Figure 3.14: High magnification secondary electron (SE) micrograph at 2keV accelerating voltage, previously highlighted, white box in Figure 3.13, of peripheral epitenon membrane on 50nm-diameter colloidal topography. Surface morphology of the cell is observed due to the depth at which SE emerge from the sample. White "beads" represent the 50nm-diameter colloids on the silicon base substrate. Colloids underlying the cell are not visible, as the electrons being detected are secondary electrons (SE).

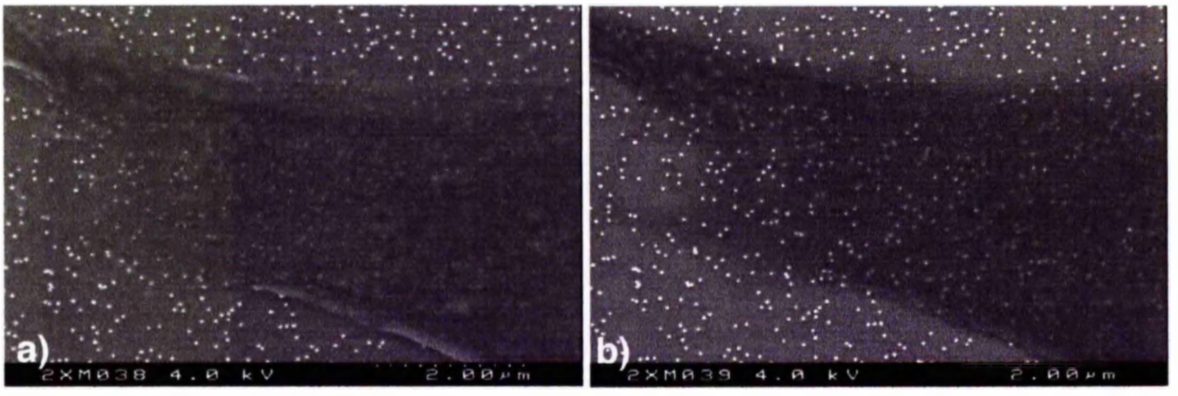

Figure 3.15: SE, a), and BSE, b), photomicrographs at 4keV of epitenon area under investigation. Underlying colloids are observed in both the SE, a), and BSE, b), images. This is due to the increase in accelerating voltage resulting in increased BSE hitting the SE detector. Thicker regions of the epitenon cell obscure the underlying colloidal topography when detecting secondary electrons, a). Greater information is gathered with respect to the substrate underlying the cell when detecting backscattered electrons (BSE), b). This is due to the emergence depth of BSE. The distribution of colloids underlying the peripheral membrane appears similar to the cell-free areas of the surface, b), although thicker areas of the cell obscure underlying topography to the right, b).

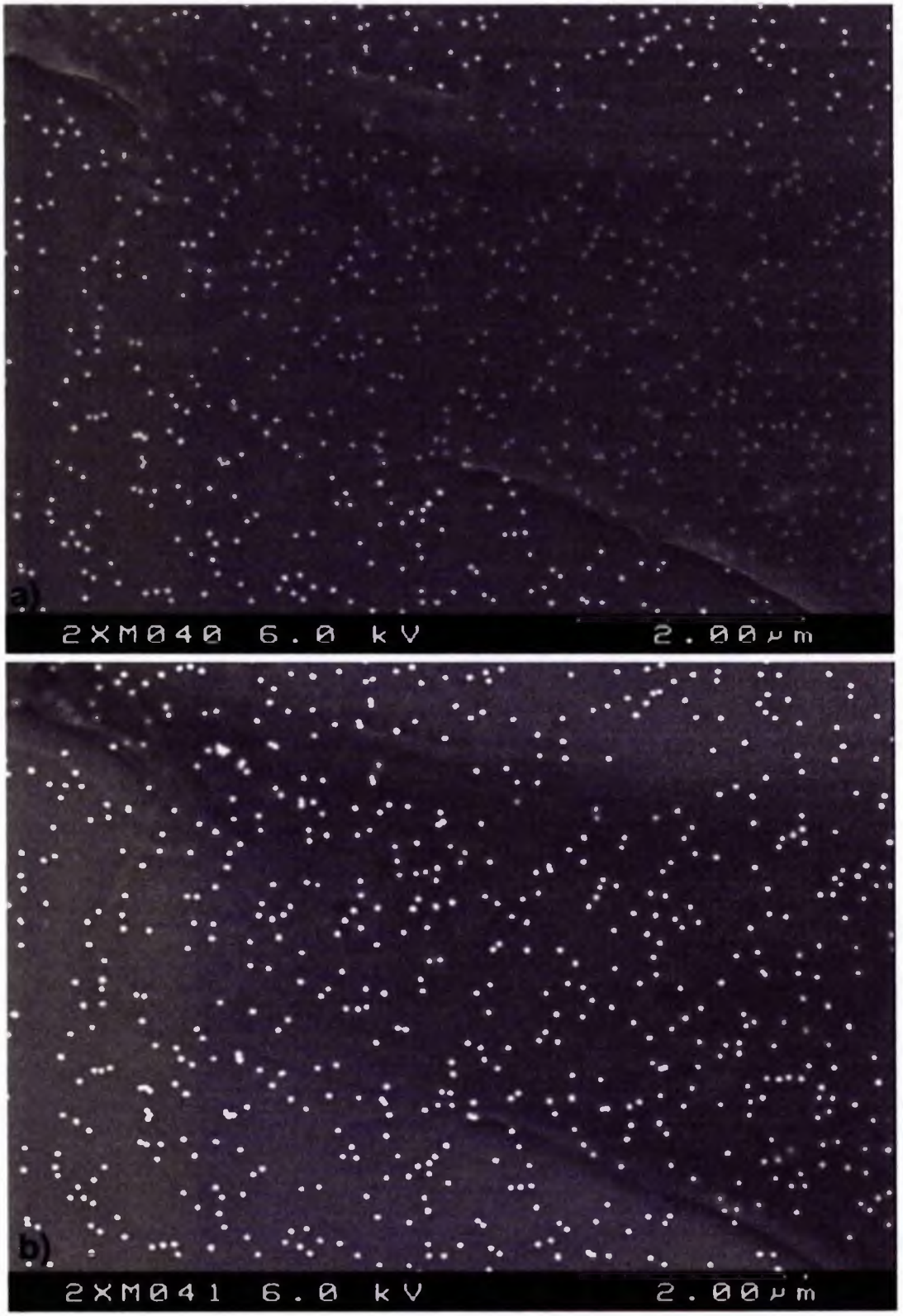

Figure 3.16: SE, a), and BSE, b), photomicrographs at 6keV of the epitenon peripheral membrane on 50nm-diameter colloidal topography previously highlighted in Figures 3.13-3.15. By increasing the accelerating voltage, emerging backscattered electrons hitting the SE detector, a) and also the BSE detector, b), results in less obscured imaging of the colloids due to the increased emergence depth of the BSE.

specimen, or in this instance, the underlying colloidal topography. By increasing keV when using a BSE detector, electrons of higher energy can emerge from deeper within the sample. The underlying colloidal topography imaged using the BSE detector, with an accelerating voltage of 4keV, indicates similar distribution of colloids both under the cell and in cell-free areas, Figure 3.15b). However, thicker areas of the epitenon membrane obscure the underlying topography at 4keV. By increasing the accelerating voltage, more information can be acquired with respect to colloids underlying these thicker cellular regions.

At an accelerating voltage of 6keV, Figure 3.16, the colloidal topography previously obscured by the overlying epitenon cell is more clearly observed. When detecting secondary electrons (SE), Figure 3.16a), the increase in the number of colloids visible is, once again, due to increased backscattered electrons (BSE) hitting the SE detector. When detecting emerging BSE from the specimen at 6keV, Figure 3.16b), all colloids underlying the epitenon cell can be seen. This is due to the relationship between the accelerating voltage and extent of depth from which BSE emerge. BSE detection at 6keV, Figure 3.16b), results in more visible colloids in comparison to SE detection at 6keV, Figure 3.16a), due to the difference in emergence depths of SE and BSE at the same accelerating voltage. As colloids are present under the epitenon cell and appear similarly distributed in comparison to those on the surrounding cell-free substrate, manipulation and uptake of the topography is unlikely to occur. Subsequently, in an effort to verify these results, X-ray microanalysis was performed on epitenon cells initially seeded on the 50nm-diameter colloidal topography for 48 hours, trypsinised from the surface, and plated on a control, Thermanox (Poly-ethylene tetraphtalate, Nunc, Rochester, NY) surface. BSE was used to locate features, for instance, size, shape and density, similar to the gold colloids, Figure 3.17a). These entities were located and magnified and X-ray microanalysis using ISIS 300, Oxford Instruments installed on the S-4100 FESEM was used to detect the presence of gold. BSE was utilised in contrast to SE, as Backscattered electrons emerging from within the sample would indicate the presence of phagocytosed colloids, rather than, as is the case when considering SE, the presence of colloids on the outer membrane of the cell. Gold would be detected at 12.7275keV using X-ray microanalysis, and, as is observed in the graph, Figure 3.17b), no gold was detected. As X-ray microanalysis is extremely sensitive, detecting 0.01% of an element present within a specified area (private communication with Professor C. Wilkinson), and no gold was detected using this method, supporting the previous results

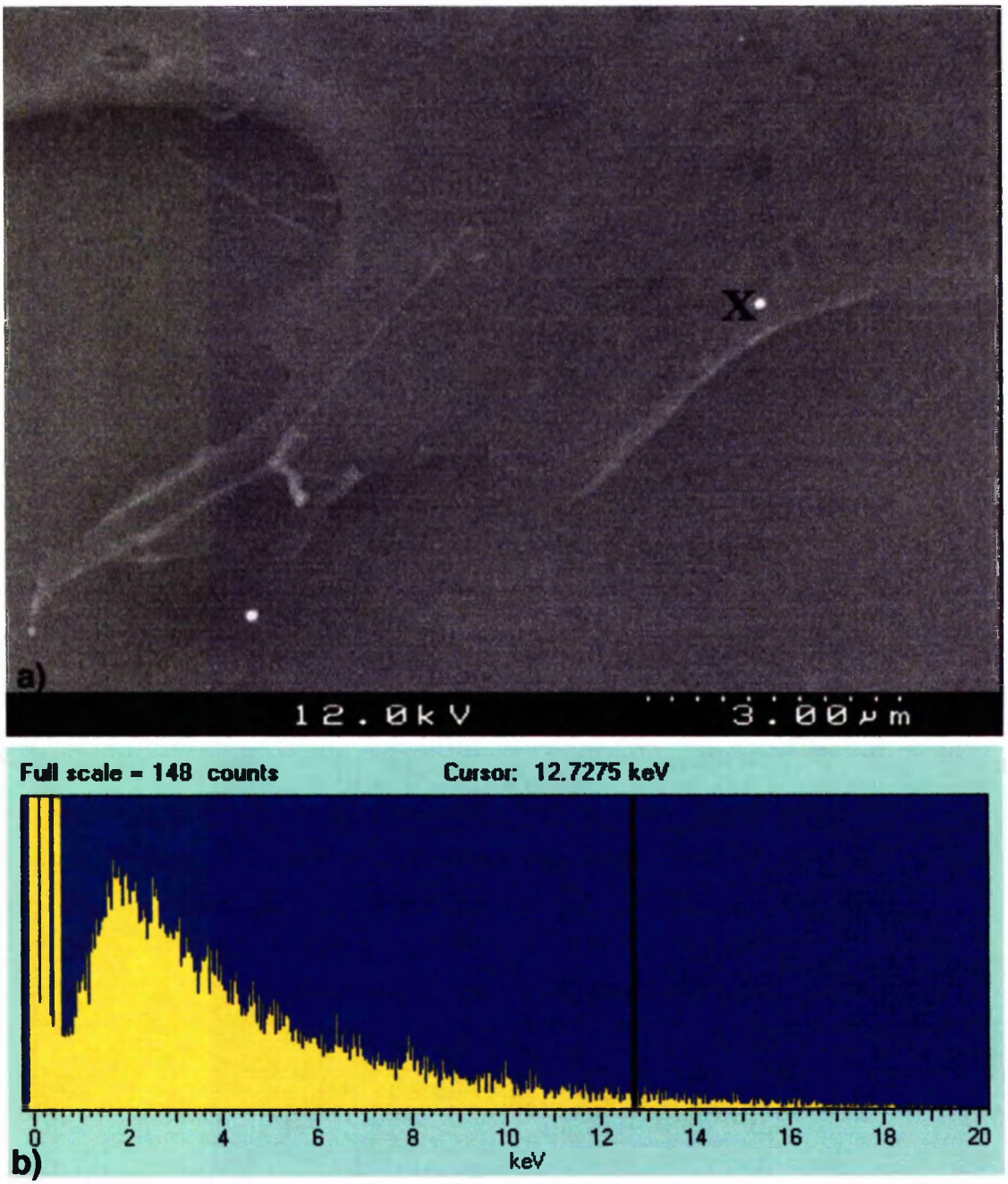

Figure 3.17: BSE photomicrograph, a), taken with the Hitachi S-4700 of an epitenon cell which has been trypsinised from the 50nm-diameter colloidal surface and plated on a control, Thermanox surface. "X" indicates the area that appears to contain a feature similar in size, shape and density to previously BSE imaging of colloids. This area was investigated at higher magnification and X-ray microanalysis was performed. The cursor in the resulting graph, b), at 12.7275keV marks the keV where gold would be detected. As can be seen in this graph, no gold was detected confirming both the SE and BSE findings that the epitenon cells are confronted with a static nanotopography.

of both the SE and BSE images. Thus, uptake of 50nm-diameter colloidal gold particles by epitenon cells had not occurred, and the cells were being confronted with a static, stable nanotopography.

3.3.1.2 Scanning Electron Microscopy of Epitenon Cell Morphology

During the investigation of possible colloidal uptake by epitenon cells at the AO Research Institute, epitena morphology was also observed on samples at 24 hours, Section 3.3.1.1. Epitenon cells were cultured on the experimental 50nm-diameter colloidal topography for 24 hours, with seeding density of 10,000 cells per ml in 3mls H-ECT media, Section 2.4.2. Unfortunately, due to time constraints, epitenon cell reactions in relation to a planar control were not viewed, and only a small number of images were captured with respect to morphological alterations in epitena on 20nm-diameter colloidal topographies, discussed later in this section. An Hitachi S-4700 was used with an SE detector, unless otherwise stated in figure legends, to investigate cell morphology.

Epitenon cells appear capable of direct interactions with the surrounding colloidal topography, Figure 3.18. The membrane contacts established with the colloids on the substrate in this instance do not appear to exhibit typical filopodia morphology. This suggests either transient, passive adhesions between the peripheral membrane and the colloids, or the beginnings of lamellipodia or filopodia formation.

Similar features observed in relation to hTERT fibroblasts in contact with both 20nm- and 50nm-diameter colloidal topography using time-lapse video microscopy, Section 3.3.3.1, SEM, Section 3.3.3.3 and fluorescence microscopy, Section 3.3.3.4, are also exhibited by the epitenon cells on the colloidal topographies imaged using SEM. A low magnification image, Figure 3.19, indicates that at 24 hours, epitenon cells are well spread with established cell-cell contacts. Epitenon cells appear aligned with neighbouring cells in this image, indicating the possible biomechanical role cells may perform in relation to their neighbours. Elongated detachment sites, or protrusions are also observed, linking individuals remote from one another.

When considering the time-lapse footage and stills of hTERT fibroblasts seeded on colloidal topography, Section 3.3.3.1, cell divisions often appear to occur at the periphery of multi-cellular aggregates. This is observed in Figure 3.20, where an

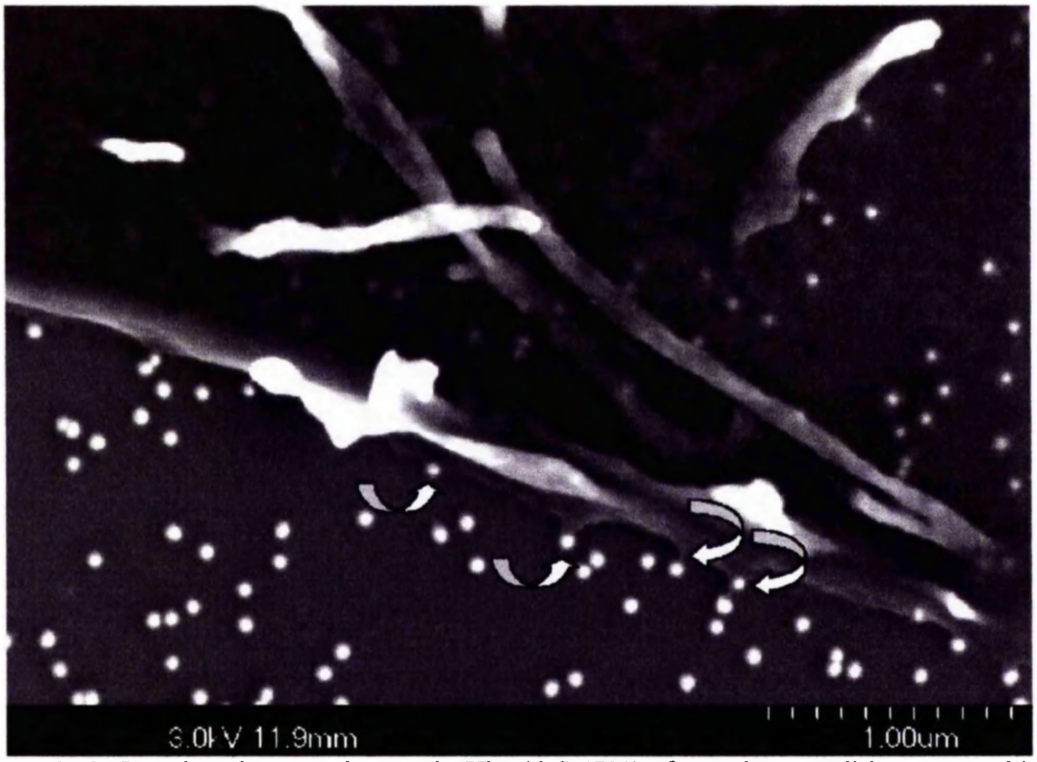

Figure 3.18: Scanning electron micrograph (Hitachi S-4700) of an epitenon cell in contact with 50nm-diameter colloidal topography. Epitenon cells are capable of direct interactions with nanofeatures at the peripheral membrane. Arrows highlight areas of membrane in contact with the 50nm-diameter colloidal gold particles.

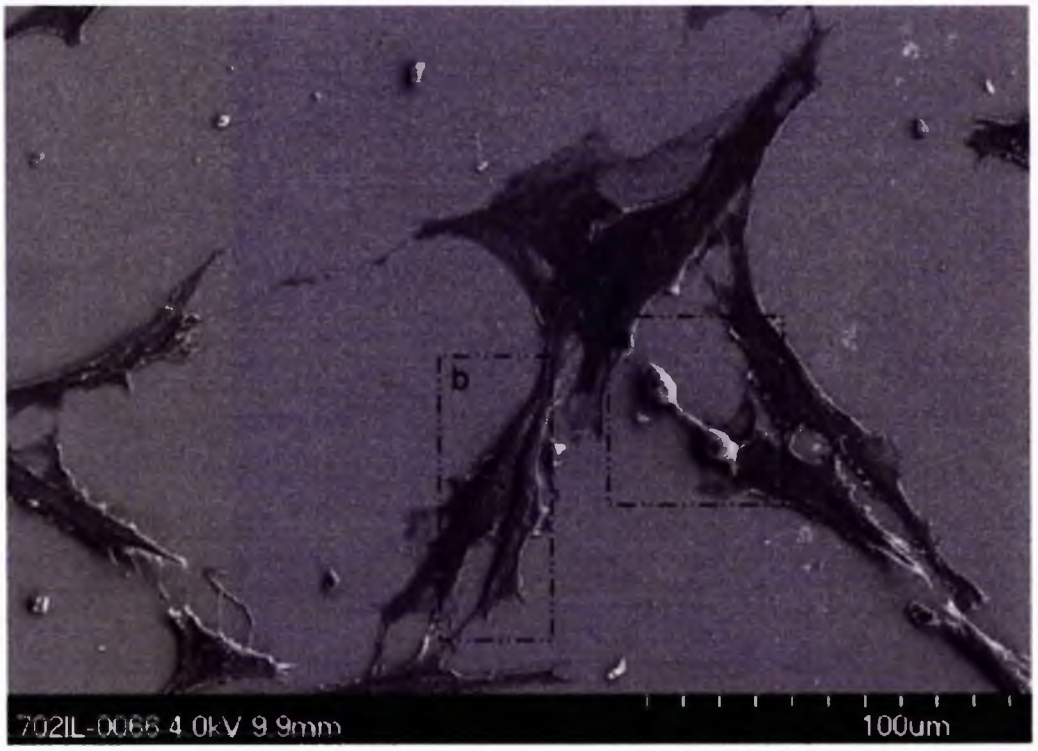

Figure 3.19: Low magnification scanning electron micrograph of epitenon cells on 50nm-diameter colloidal topography captured using the Hitachi S-4700. Cell-cell contacts are established between cells across this area of experimental substrate. Cells in the process of division, outlined area a), are examined at higher magnification in Figures 3.20 and 3.21. Intercellular alignment also appears as a feature of epitena behaviour, highlighted in enclosed area b), which is viewed at higher magnification in Figures 3.22 and 3.23.

epitenon cell appears to have undergone cytokinesis following mitosis at the periphery of an established cellular aggregate on the 50nm-diameter colloidal surface. The daughter cell to the right of this image has anchored to the underlying apical membrane of a neighbouring cell. The adhesions between the opposing daughter cell and the experimental colloidal topography appear to lack distal anchorage sites, with adhesions only apparent at either side of the cell, established via very fine filopodia-like protrusions. Final separation of daughter cells is reliant not only upon the establishment of the cleavage furrow, but also migration of both cells resulting in severing of the intercellular connection (Mullins and Biesele, 1977). Due to the involvement of motility in the final separation process of cytokinesis, investigations of cell-substrate forces have indicated compression of the substratum increases between daughter cells until the intercellular bridge ruptures (Burton and Taylor, 1997). When considering Figure 3.20, epitenon daughter cells undergoing the final stages of cytokinesis appear highly elevated with regard to the colloidal topography. As there is a lack of contact with the experimental surface, it is unlikely that traction force will result in compression of the substrate. Following rupture of the intercellular bridge, recoil of the daughter cells results in their directed movement along an established migration axes suggesting compression of substratum in that direction (Burton and Taylor, 1997). The lack of adhesions and possible routes to establish traction observed in the daughter cell on the 50nm-diameter colloidal topography, Figure 3.21, may account for the elongated membranous extensions occurring between cells on the colloidal nanotopography, and also the catapulting of cells along migration axes, Section 3.3.3.1.1. Furthermore, cells with a broad area of contact were also documented to generate large traction forces for longer periods of time suggesting an increased role of motility in this instance in final cleavage. This, in turn would suggest a more pivotal role of the cleavage furrow with respect to final rupture of the intercellular of the daughter cells observed in Figure 3.20, due to a lack of spreading in each cell.

Scanning Electron Microscopy allows for the physical attributes of cell-cell contacts to be visualised, Figure 3.22. Extremely thin, elongated protrusions appear to act as a means of anchorage between neighbouring epitenon cells. The term "anchorage" is used, as at the distal areas of these cellular "strings", appendages appear to end either as a pad in contact with the cell being attached to, or have a two or three thinly-pronged formation, Figure 3.22. Similar string-like extensions occur between epitenon cells, with no discernible distal sites attached to the neighbouring cell. These protrusions

appear to occur when cells are some distance apart, with more robust, thicker extensions linking epitena in very close contact, Figure 3.22, suggesting their contractile function.

A further feature of the epitenon cells seeded on the 50nm-diameter colloidal nanotopography, Figure 3.22, is the high degree of alignment between cells seen at the upper membrane surfaces, suggesting the presence of a highly stressed and organised cytoskeleton. Overlapping of two epitenon cells in the left of the image can be viewed in greater detail in the lower magnification image, Figure 3.19, area b). The elongated stress marks along the length of the cell on the right, Figure 3.22, and the contacts between all cells seen in this image suggests the possibility of contact guidance occurring via cell-cell interactions. This furthers the possibility of problems occurring during the establishment of cell-substrate adhesions, and, as a result, cell-cell contacts are increased. Contacts between epitena on the experimental nanotopography where cells are encountering a certain degree of overlap, Figure 3.23, appear shorter and thicker in comparison to the appendages previously seen to bridge wide gaps between neighbouring cells. This suggests a contractile function of these membrane elongations, where appendages may be used to close gaps between neighbouring cells. Thinly spread membrane overlying the experimental nanotopography appears as a passive feature in relation to the possible contractile behaviour of the appendages, with no indication of focal adhesion sites or stress. Furthermore, the "anchorage" sites at the distal region of the appendages in contact with the neighbouring cell in close cell-cell contacts, exhibit similar morphology with respect to the string-like anchorage sites occurring between epitenon cells separated over a greater distance, Figure 3.22. These similarities between the connecting protrusions suggest they may either originate in the same manner, or are presented in different stages of their function.

A cell within this population, with no established cell-cell contacts, appears very well spread on the surface, denoted by "X" in Figure 3.24. Spreading does not appear to be limited in individual cells as appears in cells forming multi-cellular aggregates, also observed in Figure 3.24. Thinly spread areas of membrane on either side of the cell, similar to the wings of a flying squirrel, should also be noted. These regions are unlikely to contain any significant proportion of the cytoplasm, organelles or cytoskeleton, or a significant number of adhesion sites or cell surface receptors in comparison to the bulk of the cell.

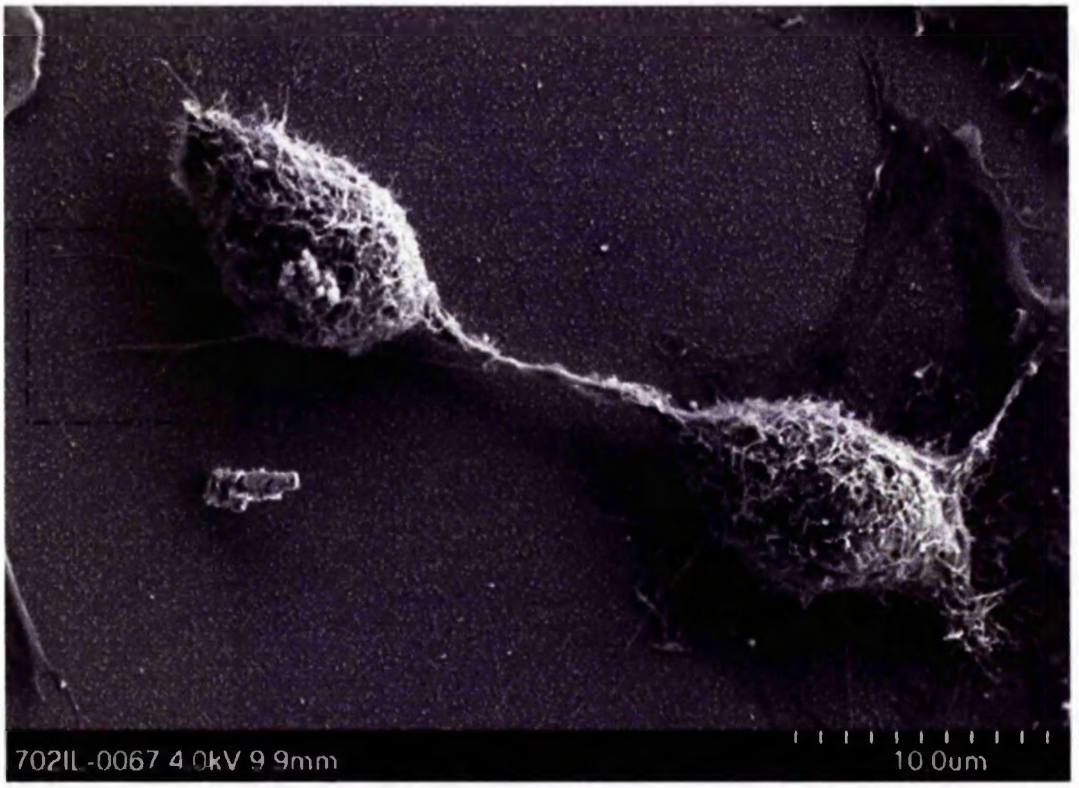

Figure 3.20: Higher magnification of area a) in Figure 3.17, where epitenon cells undergoing division are presented. The cell on the right of the picture has established adhesions with the underlying spread cell, while the opposing cell on the left is tilted towards its partner due to a lack of adhesions with the colloidal substrate. The area contained in the box is seen at higher magnification in Figure 3.21.

Figure 3.21: High magnification micrograph of the area enclosed within the box in Figure 3.20, again using the Hitachi S-4700 highlighting cell-substrate adhesions between the dividing cell and the 50nm-diameter colloidal topography. Processes protruding from the epitenon cell are extremely thin resulting in limited contact with the substrate, which may affect both cell adhesion in relation to the surface and also motility required during breakage of the intercellular connection.

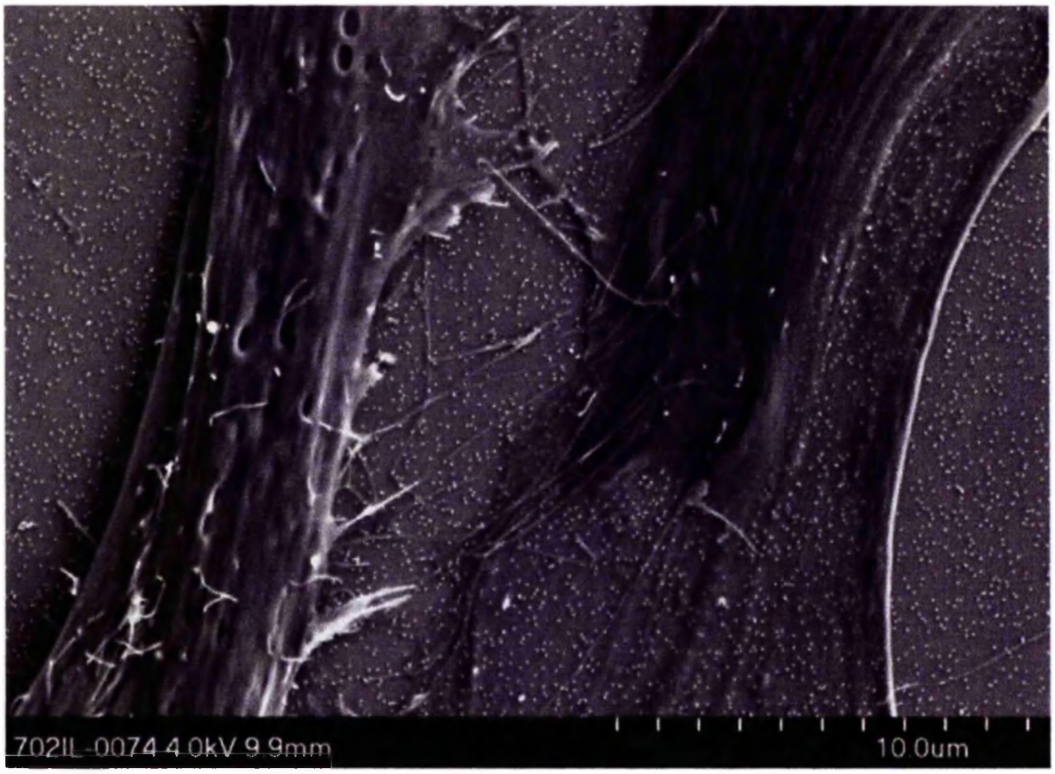

Figure 3.22: High magnification micrograph of cell-cell contacts highlighted in box b) seen in low magnification Figure 3.19. Thin string-like extensions appear to anchor one epitenon cell to another, with morphology of connections occurring as a pad, closed arrow, or two or three pronged finger-like protrusions, open arrow. Note the alignment of stress features seen in the cell membranes.

Figure 3.23: High magnification micrograph (highlighted in area b) of Figure 3.17), where epitenon cell-cell contact has resulted in overlapping of thinly spread peripheral regions of membrane. The membrane is so thinly spread that underlying 50nm-diameter gold colloidal particles are visible as previously seen when investigating possible uptake of colloids by the cells, Section 3.3.1.1. Note that connecting string-like fibres are shortened in this image, where cells are in direct contact, and not as long compared to those visualised in cells further apart, Figrue 3.22.

String-like protrusions are not only observed between immediately neighbouring epitenon cells, but also between cells within an aggregate separated by a number of other cells (closed arrow in Figure 3.24). This type of anchoring appendage, due to the continuity of the feature, suggests these two cells are in fact pulling apart. This is further seen when considering the morphology of the cell on the right of this pairing, Figure 3.24, and the possible presence of a leading lamella in the opposing direction of the connected cell. As motility is believed to play an important role in severing the intercellular connection (Mullins and Biesele, 1977), and cells in this image appear to have undergone movement along an established migration axes, problems may exist within the motility contributing to final dissociation. Possible accounts may include alterations in a specific migratory axis (applying to either cell involved), traction force required between the cell and substrate during migration, or the establishment of secure adhesions between the cell and substrate resulting in a reduction of traction force required to complete cell division. A further possibility is the alteration of an intracellular molecular release factor required in separating cells upon movement in opposing directions. One epitenon cell also appears to exhibit these elongated structures both at the anterior and posterior of the cell body, suggesting both trailing rear detachment sites and frontal protrusions (open arrows in Figure 3.24).

The existence of string-like anchoring elongations is observed in greater detail in Figure 3.25 and 3.26. Areas of epitenon cells in direct contact, or recently in direct contact, are seen as rugged accumulations of spiky membrane, closed arrows in Figure 3.25. An instance where cells are bridging a gap across the membrane and expressing these features highlights connections from this region in the form of filopodia attaching to the colloidal topography, open arrow, Figure 3.25. This elongation appears to being ripped apart, with material primarily establishing cell-cell contacts being redistributed to form a cell-substrate adhesive function. The high amount of stress occurring across the rope-like structure is indicated by the breakage of a parallel arrangement, indicated by "X" in Figure 3.25.

Many of the cellular extensions appear in contact with the substrate surface, open arrows, Figure 3.26, occurring close to the cell body. The epitenon cell in the top left of the image has many protrusions spreading across the colloidal substrate, attached to the surface, and no cell-cell contacts occur via these extensions. This suggests the possibility that these elongations are a result of initial cell-substrate interaction.

Verifying this theory, a further two elongations appear to be in contact with the colloidal substrate (open arrow), protruding from the main cell seen in the right of the image. These extensions converge at a fork, and the continuous united extension appears to anchor the cell it establishes contact with back to the forked region in contact with the surface. As time progresses, the stress between the "captured" cell and the elongations connected to the cell-substrate fork may cause the cell-substrate adhesion to break, resulting in a cell-cell bridge previously observed, Figure 3.20.

The anchorage sites between epitenon cells connecting the cells on the right of the image to the elevated cell on the left, closed arrows in Figure 3.26, exhibit a morphology previously described as two or three finger-like extensions, suggesting cells have established the contacts and the elongations may perform a contractile function resulting in alignment of cells. The possibility that the cell in the left of this image has previously been in contact with its neighbouring cells and is attempting to relocate to a cell-free region of the substrate cannot be overlooked. Regardless, this morphology and cell behaviour appears to occur as a direct result of epitenon cells reacting to the colloidal topography.

Thinly spread peripheral membranes are further observed in well spread cells (arrows in Figure 3.27). Highlighted area a) appears to indicate two cells separated by an area of colloidal topography, with no cell-cell contact occurring. However, upon closer examination of this area, Figure 3.28, appendages are observed to bridge this gap. Three cells also appear to be involved in this substrate bridging process, with the thin, elongated epitenon cell visible in the lower section of the image overlapping a more thinly spread cell positioned perpendicularly to its motility axis. To further elaborate upon the previous possibility of these extensions occurring as a result of cell interactions with the substrate, an elongation (arrows in Figure 3.28) in contact with two linked cells is seen to be thicker at regions protruding from either cell. Thickening in these regions suggests, firstly, an establishment between both cells has been made in the form of the elongated filopodia-like structure. Both cells appear to be in a similar stage with respect to this elongation, with either contraction or increased stress occurring at areas nearest each individual cell, resulting in elevation of the structure from the surface nearest cell contact. Another possibility is that, following cell-cell contact via this protrusion, each cell is attempting to infiltrate the structure, perhaps through the establishment of (further) cytoskeletal networks.

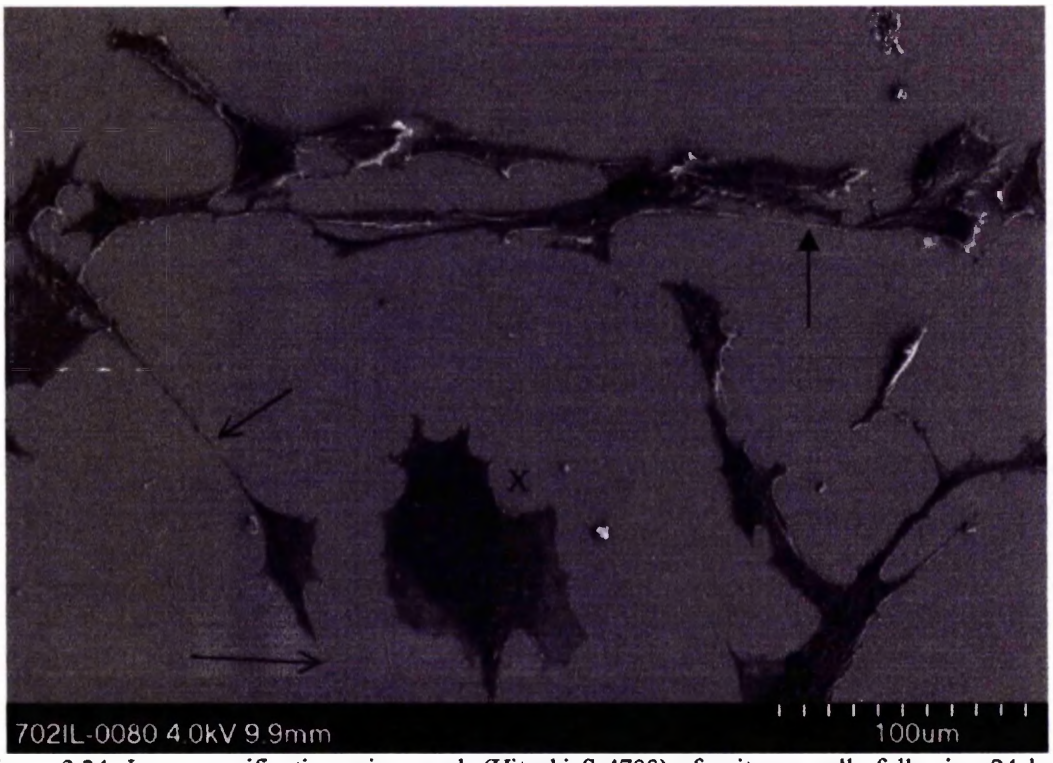

Figure 3.24: Low magnification micrograph (Hitachi S-4700) of epitenon cells following 24 hours of contact with 50nm-diameter colloidal topography. An individual epitenon cell, lower centre, is seen to be flat and well spread in comparison to epitena in cell-cell contact situations. Arrows indicate protrusions linking cells not in immediate contact, where a gap across the substrate is bridged. This may be due to cells pulling apart (closed arrow), or possible contractile elongation's (open arrows). The region enclosed within the white box is investigated at higher magnification in Figures 3.25 and 3.26.

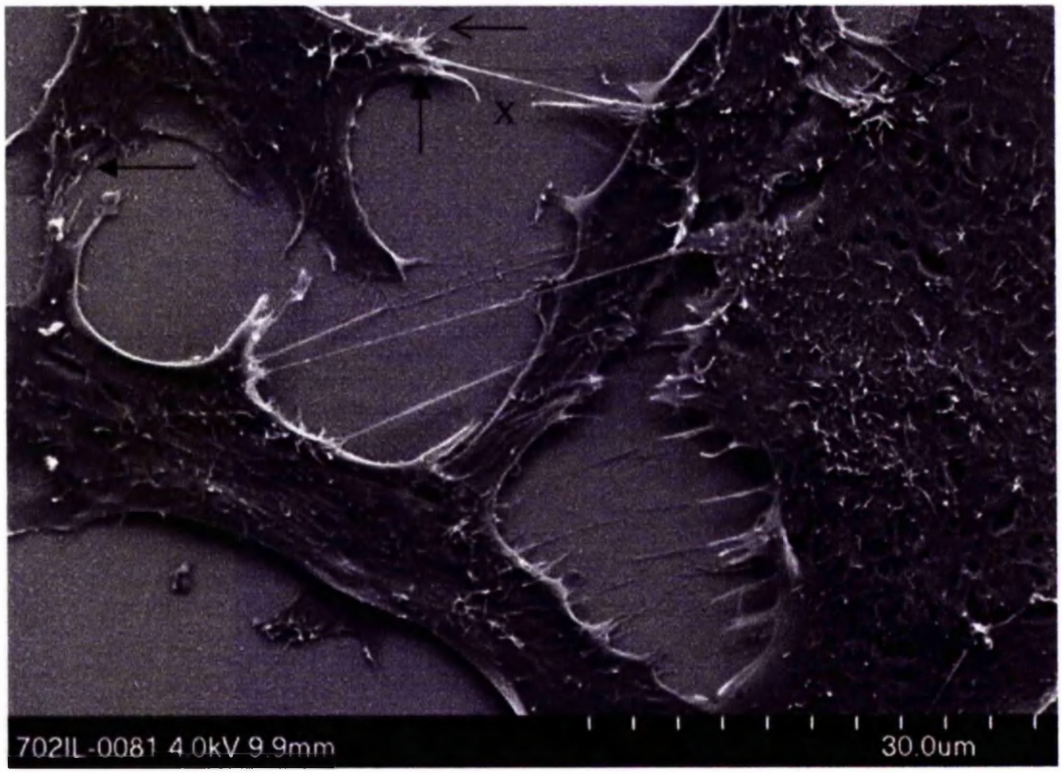

Figure 3.25: High magnification micrograph of white-boxed area in Figure 3.24. Rugged adhesions occur between cells where close contact is established at thicker membrane areas (arrows). String-like elongation's link cells across greater separations, viewed at higher magnification in Figure 3.26. "X" highlights a broken elongation suggesting a large amount of stress occurring within these structures.

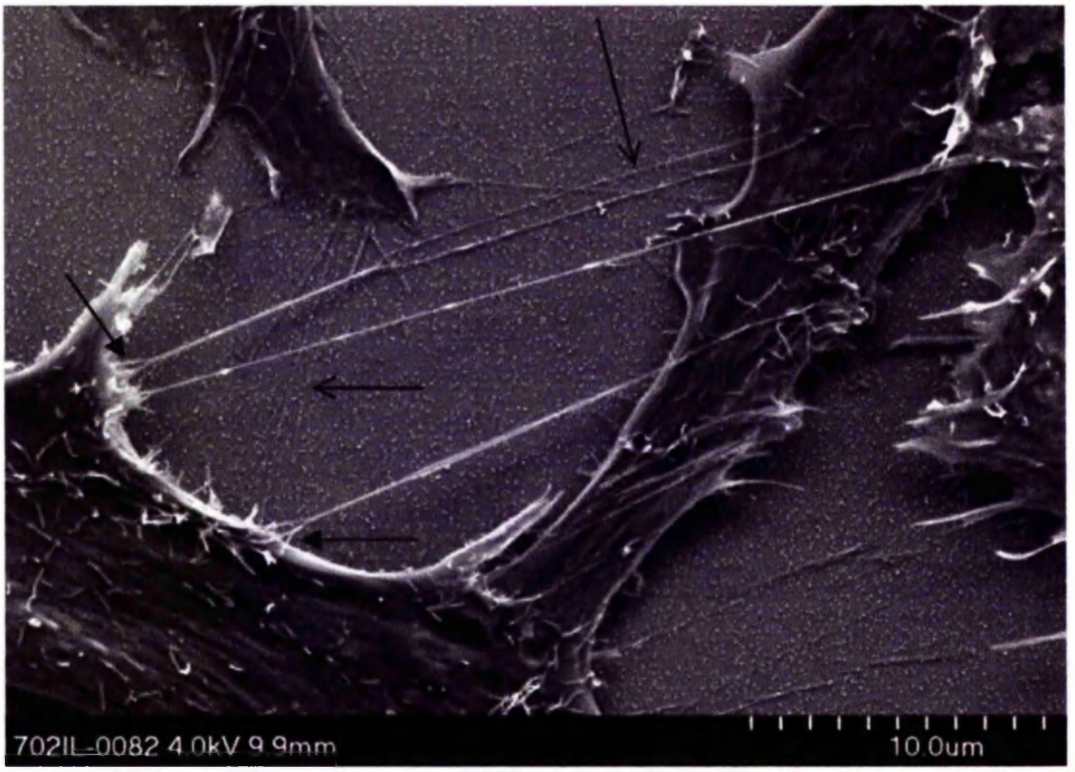

Figure 3.26: High magnification micrograph of Figure 3.25 of string-like elongation's connecting cells to neighbouring individuals. Cell protrusions terminate in pronged finger-like projections (closed arrows). The eptienon cell in the top left of this image has similar projections emanating from its peripheral membrane along the colloidal substrate (horizontal open arrow). Similar contact between cell projections terminating in the contact with the cell on the left (closed arrows), is seen to contact the surface in elongated areas close to the cell body (vertical open arrow).

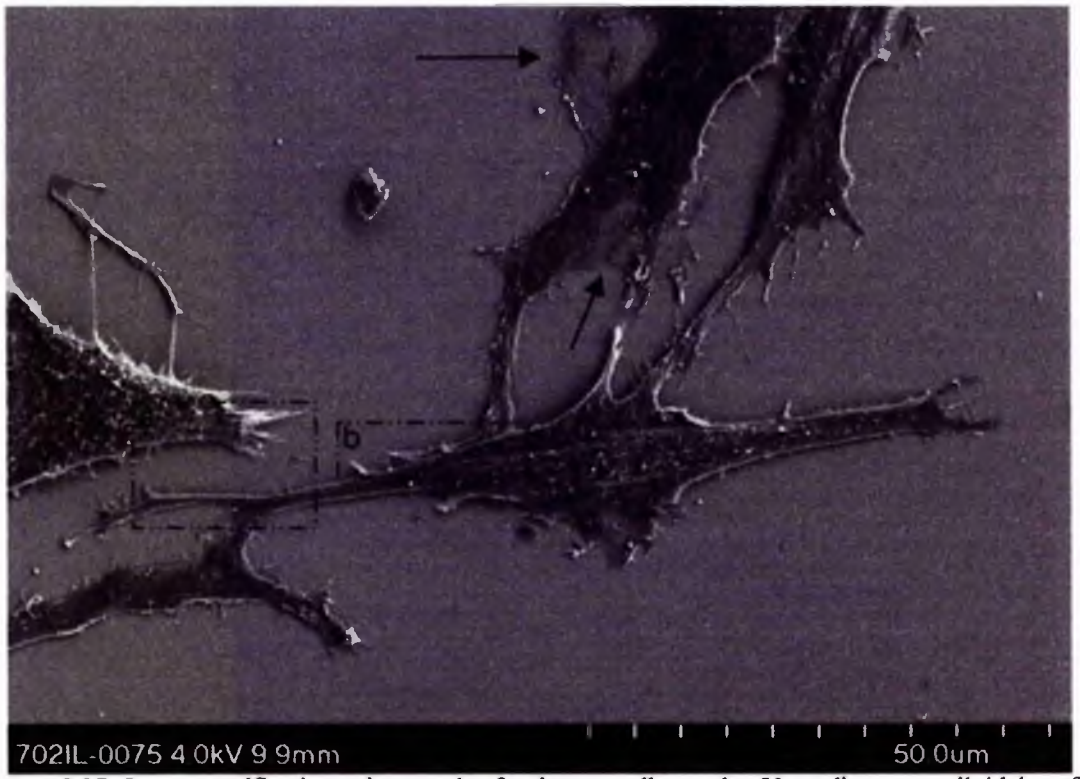

Figure 3.27: Low magnification micrograph of epitenon cells on the 50nm-diameter colloidal surface. Areas a) and b) are seen at higher magnification in Figures 3.28 and 3.29 respectively. Alignment appears in cells in contact with neighbours. Very thin peripheral membranes are also observed in spread cells (arrows).

Area b) highlighted in Figure 3.27 was investigated at higher magnification to elaborate upon the structure and morphology of the more obvious cell-cell contacts viewed in the lower magnification image. In an attempt to visualise the interaction more successfully, the sample underwent rasta rotation (approximately 180° from the original position), Figure 3.29. The linkages established between these two cells, alters considerably from those previously documented. Firstly, what appears to be the protruding, frontal region of the cell in the lower half of the image, appears in the process of establishing alignment with the epitenon cell in the upper portion of the image. Intertwining between the frontal extension of the cell in the process of aligning, and the area of the neighbouring cell nearest to the colloidal substrate is observed. A threading mechanism in relation to the protrusion and the "eye" of membrane underlying the cell in the upper half of the image is also seen (closed arrow in Figure 3.29). Interactions occurring in this manner would appear to act in the alignment of cells via cell-cell interactions, and may account for single cell progressions into tissue formation and sheet movements seen, for example, during embryogenesis. It should be noted that the triangular formation of a colloidal aggregate (indicated by open arrow, Figure 3.29) appears to have resulted in the established direction of a membrane protrusion having encountered this artefact.

Extensions elongating from individual cells in denuded areas of the substrate oftendisplay little directional alignment and the string-like entities exhibit a more coil-like morphology, possibly due to the lack of adhesions resulting in their otherwise linear state (arrows in Figure 3.30a)). Lack of stress in these features suggests that the rigidity of features observed in cell-cell contacts may be directly induced via cell-cell attachments. Backscattered electron detection was used to image these features, Figure 3.30b), and indicate density of the material in relation to the surface and the cell. No BSE information is retrieved from the sites of interest, Figure 3.30b), suggesting very low-density structures. This may account for a lack of cytoskeletal features within these cellular regions. The presence of fibrils closer to the cell body protruding towards the distal region of the elongated features (arrow, in Figure 3.30b)), substantiate the previous proposal that the cytoskeleton invades these elongated areas following their initial production. Membrane elongations, lacking developed cytoskeleton features, may serve as the primary instigating factor of cell-cell and cell-substrate contacts. Following cellular production of these string-like membrane protrusions on the colloidal topography, an area now accessible to the developing cytoskeleton is established. These

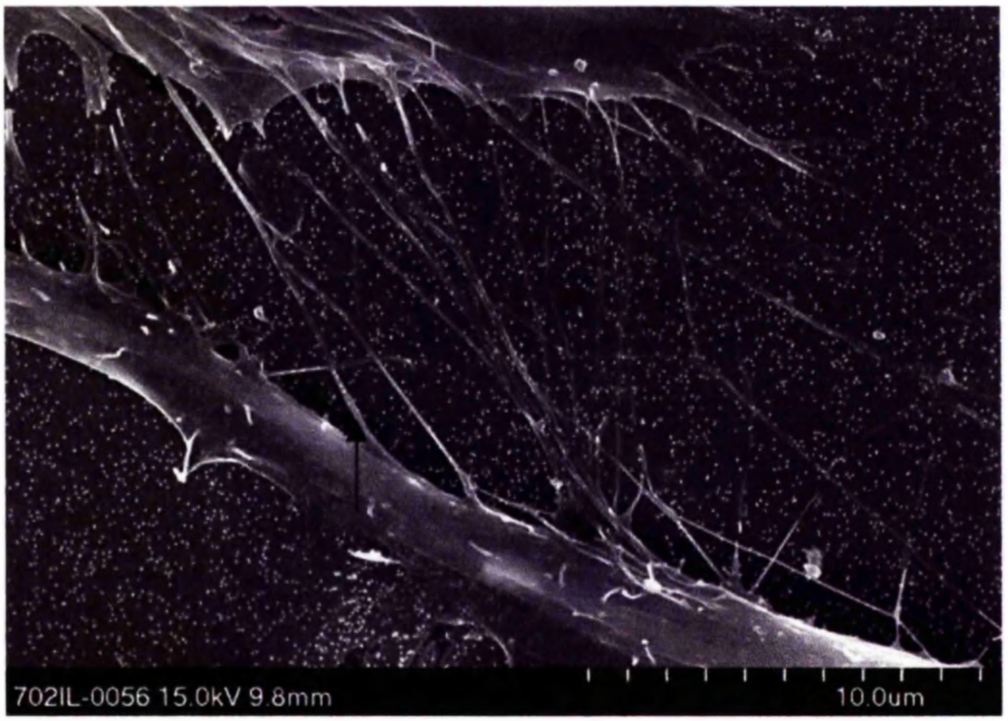

Figure 3.28: High magnification micrograph of highlighted area a) in low magnification image, Figure 3.27. Once again, string-like connections are seen to contact both the experimental colloidal topography and in other instances, appear elevated above the substrate. Arrows highlight thicker areas of one such protrusion, with possible elevation from the substrate in these areas. Note that the areas of three cells are observed within this image.

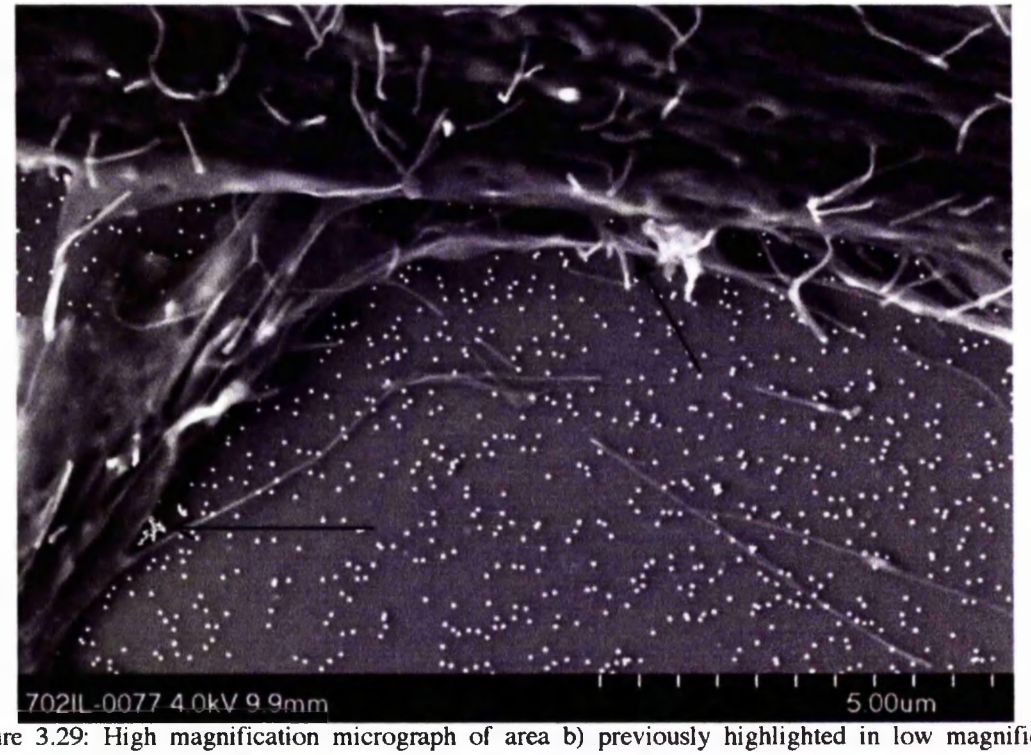

Figure 3.29: High magnification micrograph of area b) previously highlighted in low magnification Figure 3.27, of a cell-cell contact interface. This cell-cell adhesion alters in comparison to previous images where string-like structures are seen to bridge gaps across the colloidal substrate. Established cell-cell contact in this instance is seen to result in alignment of one cell (lower portion of image) to the other (upper area). Intertwining between elongations is observed, with possible threading of features also noted (closed arrow). Note the triangular colloidal aggregate at the fork of the membrane extension (open arrow). This suggests protrusion of the extension from the cell body has met resistance resulting in its directional appearance towards the neighbouring cell.

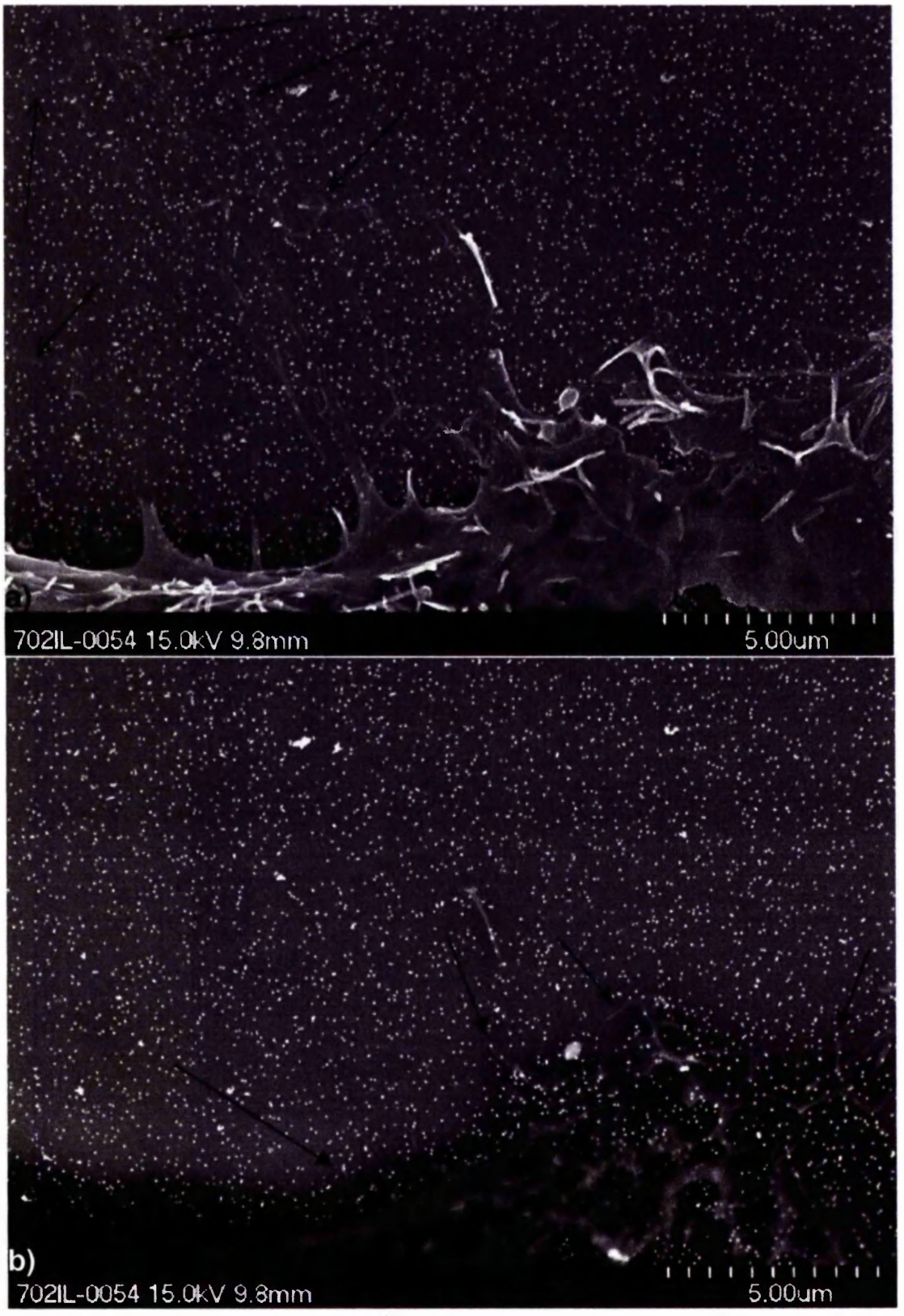

Figure 3.30: Membrane protrusions occurring at the periphery of an epitenon cell on the 50nm-diameter colloidal topography, after 48 hours. SE detection, a), suggests a lack of stress occurring across the protrusions, resulting in coil morphology in areas of the elongated membrane structures (arrows in a)). BSE detection, b), suggests the density of the material composing the protrusions is very different from that of the cell body. Cytoskeleton filaments appear to be extending from the cell body along the paths created by the membrane extensions (arrows). This suggests the protrusions are not a result of the cytoskeleton, but rather peripheral cytoskeletal features result by invading the established path.

features may act as a path along which microtubules and actin filaments can become established, resulting in the more rigid features, apparently under greater stress, acting as a direct link between neighbouring cells and also between the cell and the surrounding nanotopography. This, in turn, suggests cell-surface receptor expression, either in a transient form seen in focal adhesion complexes, or in cell-cell adhesions, occurring along the length of these protrusions. Although the effect of chemotaxis has previously been discussed and is believed not to play an important role in the reaction of cells to nanotopography investigated within this work, the possible role of chemokines in the initial production of these protrusions can not be underestimated. In many instances, cells appear extremely elongated on the nanotopography and this may result in slight increases in molecules, for instance calcium, via stress-receptor induced phenomena. This type of transient molecular gradient may account for tensile protrusions occurring in the approximate direction of the chemical source.

3.3.2 HGTFN Endothelial Cell Reactions to Colloidal Topographies

HGTFN endothelial cells were plated on 50nm-diameter colloidal patterned substrates, with a silicon (silicon dioxide surface layer) base, at a density of 10,000 cells per ml suspended in 3mls complete HAMS F10, Section 2.4.3. Cells were left to attach to the 50nm-diameter colloidal experimental surfaces and a planar silicon control in a hot room at 37°C. Endothelial cells were fixed on the experimental structure at 2 hours and 4 hours, prior to undergoing dehydration and Critical Point Drying (CPD), Section 2.7.3. These two time periods were selected to determine any initial reactions, for instance morphological changes of endothelial cells in relation to the colloidal topography. Endothelial cells attached to the experimental surfaces were then examined using the Hitachi S-900 FESEM, Figures 3.31-3.34.

At 2 hours, cells would be in the process of developing adhesions established upon contacting the surface, with the possibility of cell spreading occurring. The control cells seeded on the planar, silicon substrate exhibited a morphology characteristic of endothelium namely cells were spherical in shape with a central nucleus, Figure 3.31a). Peripheral membrane areas appeared smooth, with little sign of developed sensory mechanisms for example filopodia, Figure 3.31b). Membrane ruffles appear to be developing in these images suggesting the cells are establishing, or have established adhesive contacts with the surface, are polarised and are in the process of spreading on the control planar substrate.

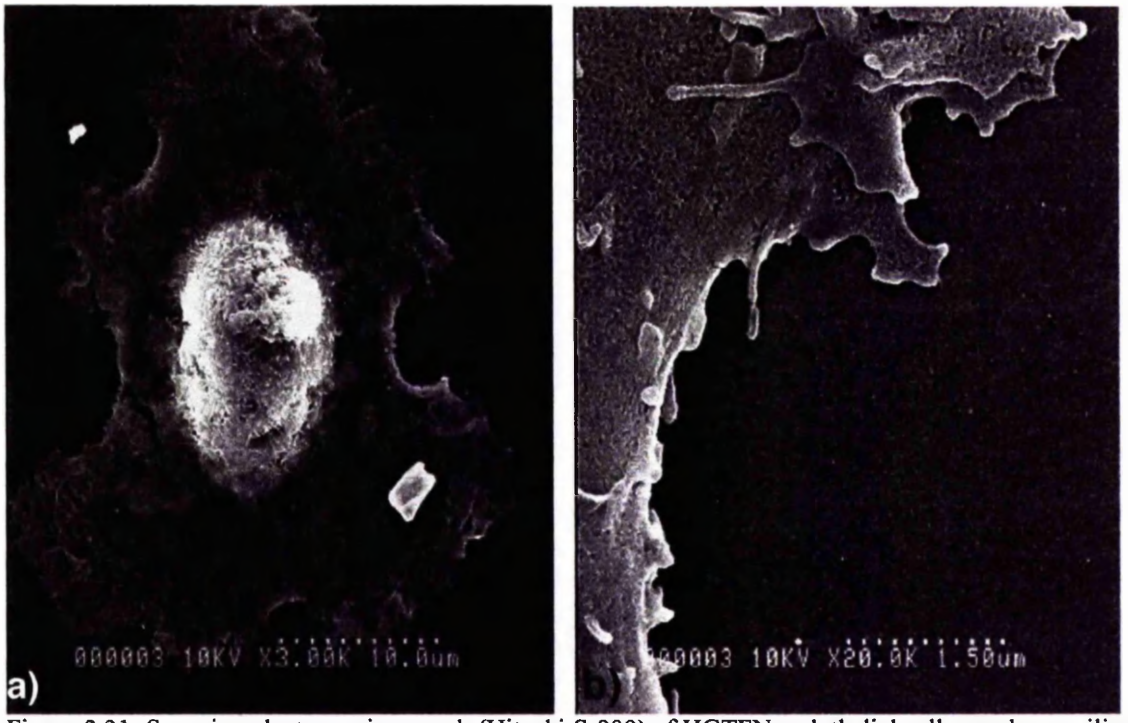

Figure 3.31: Scanning electron micrograph (Hitachi S-900) of HGTFN endothelial cells on planar, silicon control at 2 hours. Note the typical "squamous" morphology of cells as seen in endothelium linings in the vascular system a) and lack of membrane extensions, for example filopodia b).

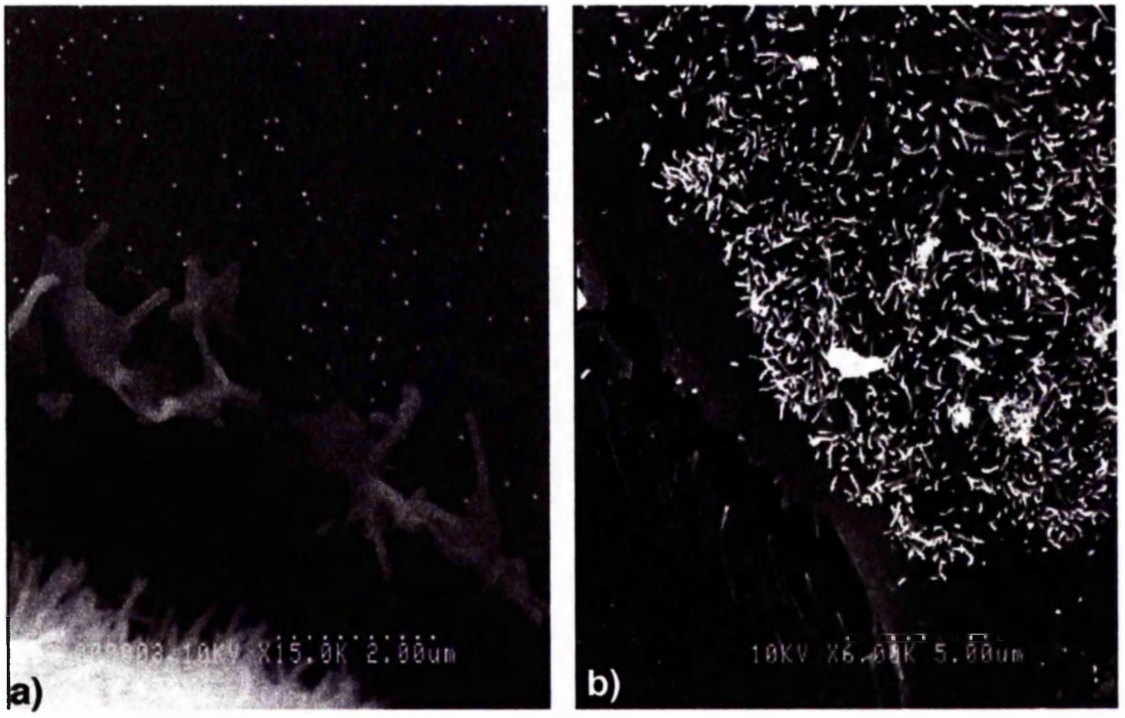

Figure 3.32: Scanning electron micrograph of HGTFN endothelial cells on 50nm-diameter colloidal topographies at 2 hours. The membranes of endothelial cells grown on the colloidal surface appear to be developing lamellipodia, even at this early time, a). Thin membranous extensions, or filopodia (as seen in more depth at 4 hours, Figure 3.34) are already present at this time, b). Breakage of the thin protrusions is likely to be a direct result of their thickness and the dehydration and critical point drying processes.

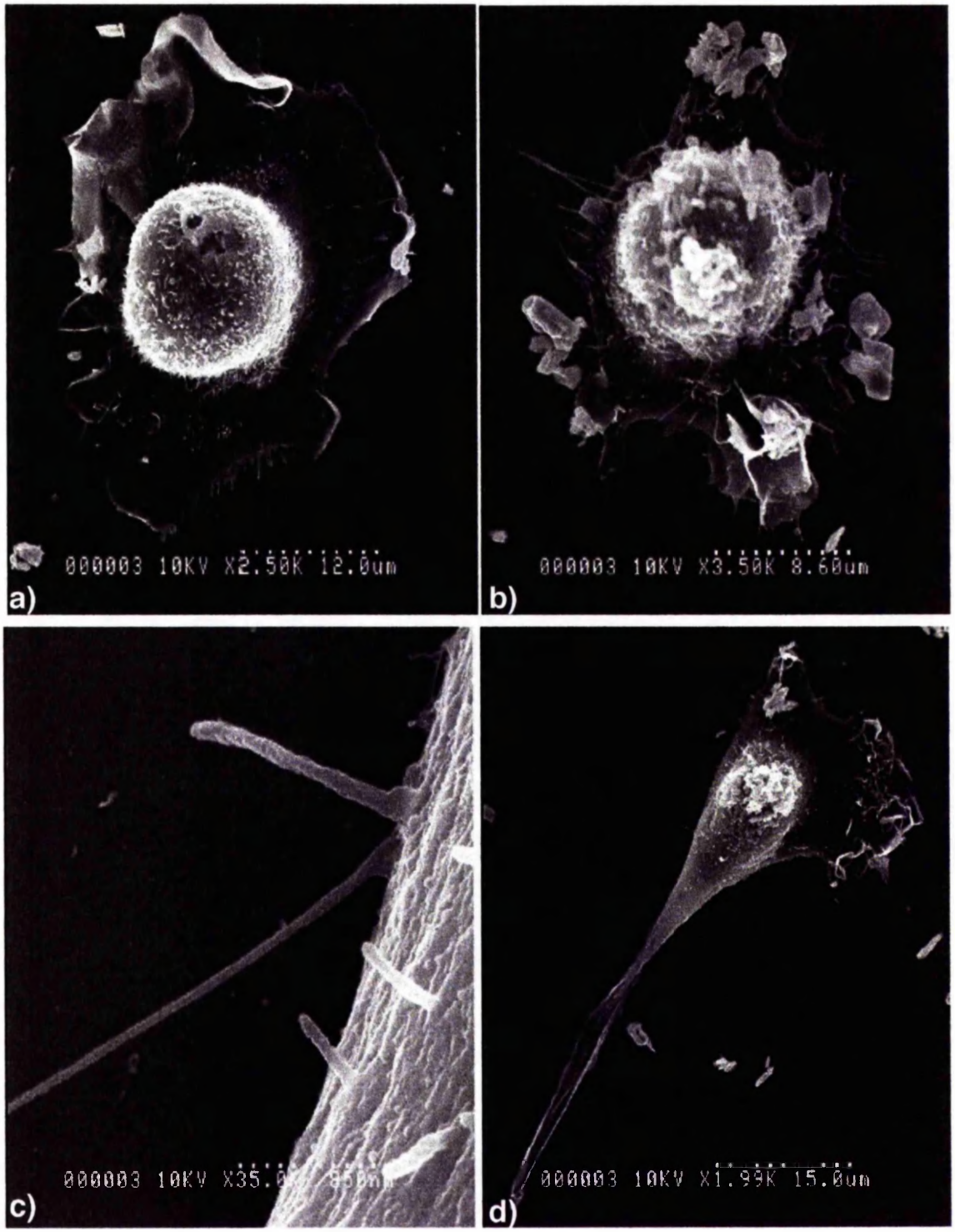

Figure 3.33: Scanning electron micrographs (Hitachi S-900) of HGTFN Endothelial cells on a planar control (silicon) at 4 hours. Cells indicate a more typical morphology as seen in endothelium *in situ*. Cells have adhered to the planar surface and are showing signs of spreading, indicated via membrane ruffling at peripheral sites, a), b) and d). Endothelial cells show signs of moving across the surface, due to the development of a leading edge with membrane ruffling, d). A high magnification image of a peripheral site of the cells is observed, c). These areas show little or no development of filopodia extension, especially not to the extent seen on the experimental counterparts.

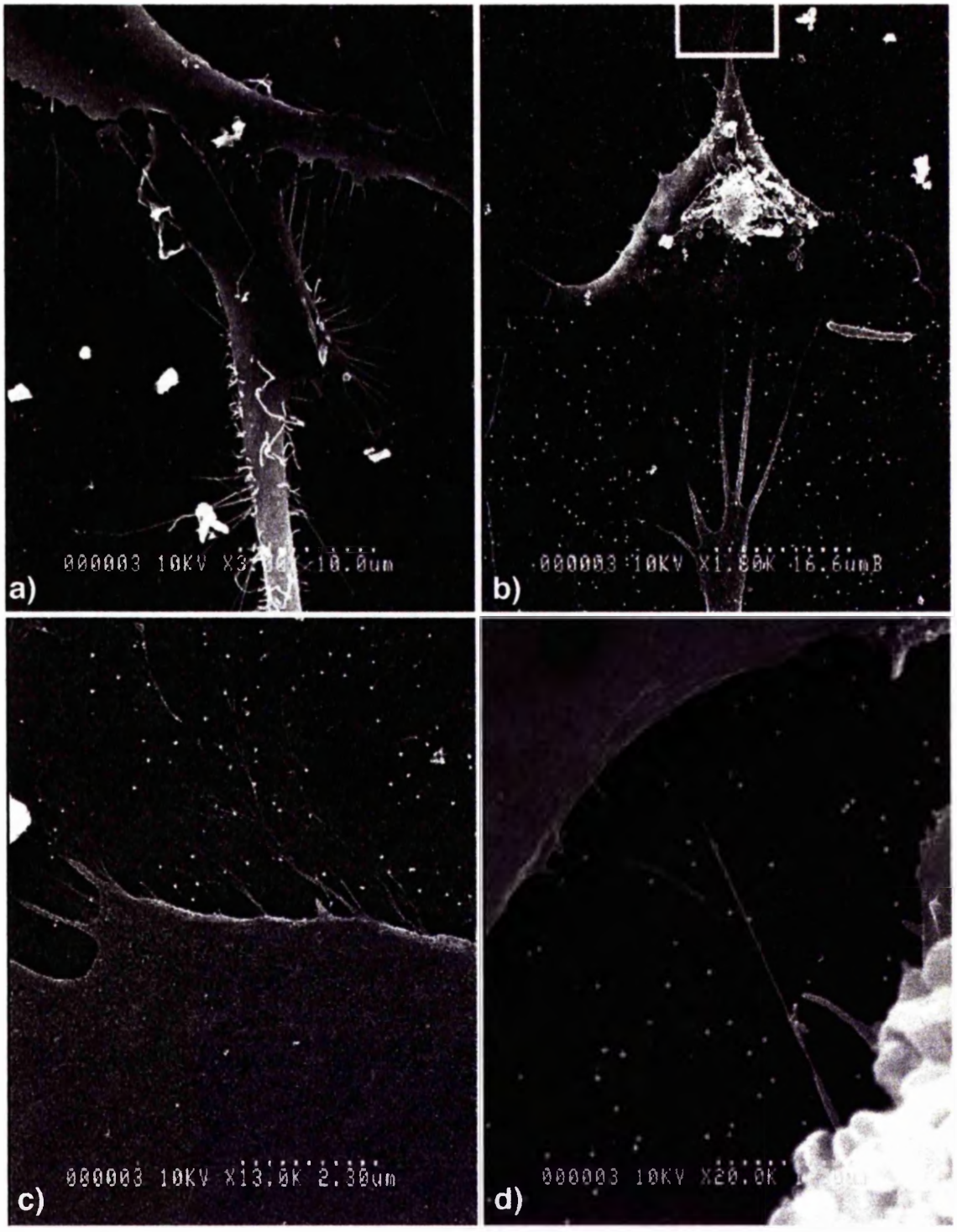

Figure 3.34: Scanning electron micrographs (Hitachi S-900) of HGTFN endothelial cells on 50nm-diameter colloidal topography at 4 hours. Filopodia extensions were seen throughout the cell population on the colloidal surfaces. Cell morphology is altered from the normal squamous appearance observed in controls, Figure 3.33. Filopodia are more generally seen at the leading edge of cells b), but their appearance along the entire periphery, a), is also observed. Fine, thin protrusions are also observed at cell peripheries, c) and d).

HGTFN endothelial cells on the 50nm-diameter colloidal topography appear similar morphologically to those discussed for the control cells. However, very thin filopodia extensions were present in many of the cells at the peripheral regions, Figure 3.32, and appear attached to the surface. Cells appear more compact and less well spread in comparison to controls. Unfortunately in this image, the processes involved in the preparation of samples for the electron microscope (dehydration and CPD), appear to have broken the filopodia from the main body of the cell.

At 4 hours, endothelial cells on the control planar surface have generally not progressed morphologically compared to the 2-hour samples. Cells still appear to be rounded with central nuclei. Membrane activity appears increased, with more ruffling occurring and lamella and filopodia extensions attaching to the surrounding flat surface, Figures 3.33a)-c). In some instances, polarity development is observed, with cells developing a leading edge and rear detachment site indicating movement across the surface, Figure 3.33d).

On the 50nm-diameter colloidal topography at 4 hours, endothelial cells have formed a morphology distinct from those cells monitored on the control, Figure 3.34. Cells appear either elongated, Figure 3.34a), or extremely flattened with signs of possible elongation via an elongated front membranous edge, Figure 3.34b). Both states show spiky lamellapodia and filopodia extensions developing at peripheral sites, reaching and adhering to the surrounding surface, although not necessarily to the colloids. These features depict the occurrence of cell sensing in relation to the surrounding environment. A further morphological alteration in endothelial cells on the experimental topography in comparison to cells on the control surface is the occurrence of very fine fibrils. These appear to be cast from the peripheral membranes, Figure 3.34c) and d). These do not appear to be filopodia, as they do not exhibit the rigidity generally observed in this sensing feature. These fine extensions appear more in accordance with cellular matter being trailed by the cell. What may have began life as filopodia, are now a shell of their original feature, similar to lug worm casts found in sand. This observation is further strengthened when examining Figures 3.34c) and d). Firstly, all the very delicate features described appear to be "trailing" at the cell periphery, Figure 3.34c), and being left behind, or detaching from the main cell body. Secondly, the fine extension seen in Figure 3.34d) appears much thicker towards the cell body in comparison to the point attached to the surface which, incidentally, appears to be in

contact with a colloid. The cytoskeletal elements composing this feature appear to be retracting into the cell rather than protruding into the already established extension.

Unfortunately, prior to subsequent investigation of HGTFN endothelial cells on the colloidal topographies, the cell stock was lost due to a power loss resulting in defrosting of endothelial stocks. HGTFN endothelial cells do reappear briefly in Section 4.3.2 in relation to 20nm-diameter, 200nm high pillared topography.

3.3.3 hTERT Fibroblast Cell Reactions to Colloidal Topographies

Investigation of hTERT fibroblast reactions to both 20nm- and 50nm-diameter gold colloidal topography follows. As the mechanism of indefinite proliferation of this cell-type is understood, Section 2.3.3, a clearer understanding of the origins and cause of this behaviour are known with available publications to support the various arguments associated with *in vitro* cell culture.

All surfaces were fabricated in the manner described in Section 3.2. Following sample fabrication, and prior to seeding cells on the substrate, the structures were soaked in Hepes, warmed to 37°C for a minimum of ten minutes. hTERT adhesion, morphology and behaviour were explored using a variety of techniques including time-lapse video microscopy, Section 3.3.3.1, adhesion assays, Section 3.3.3.2, Scanning Electron Microscopy, Section 3.3.3.3 and fluorescence staining of the actin and tubulin cytoskeleton, Section 3.3.3.4. Cells were monitored on planar glass, or fused silica for use with SEM, substrates acting as a control surface, 20nm-diameter colloidal topographies and 50nm-diameter colloidal topographies.

3.3.3.1 Video Microscopy analysis of hTERT fibroblasts on Colloidal Topographies

Fibroblasts were seeded on various occasions at 10,000 cells per ml in 3mls media on the experimental substrates and recorded using time-lapse video microscopy, Section 2.6. These video recordings can be viewed in full on the accompanying CD, with video stills being included and described within this section.

As a technique to viewing the life cycle of cells in relation to a given condition, time-lapse video microscopy is often overlooked. Understandably, many materials are not light transmitting, and therefore cannot be viewed easily in this manner. However it would be more beneficial to fabricate experimental surfaces in adequate materials, allowing for temporal observations to be made in relation to imaging of cells fixed at specific time points. Only in doing so can results in the form, for example, of SEM or fluorescent microscopy images disclose any relevant information with regard to temporal cell reactions.

3.3.3.1.1 Video stills of hTERT fibroblasts on 20nm colloidal topography

The first video stills collection, Figure 3.35, documents the initial behaviour of hTERT fibroblasts in relation to 20nm-diameter colloidal topography over the first 12 hours following initial seeding of cells. It should be noted that the black marks in all of images composing Figures 3.35-3.37 are due to dirt on the camera lens, and thus are consistent throughout images. Video stills are labelled i) to vi) in ascending time, but it should be noted that the time intervals between each image are not equal. The video stills were selected on the grounds of indicating the progression of four main areas of cells of interest best, marked A, B, C, and D in the images. Individual cells in these groups are labelled 1 or 2 so as to differentiate between a single cell and what appears to be a single cell. Figure 3.35i) was captured approximately 2 hours following cell seeding on the experimental surface. During this time (as can be viewed in Figure3.35Video on the accompanying CD), fibroblasts appear to be actively sensing their surrounding environment indicated by transient lamellapodia development, membrane ruffling and in some instances, filopodia extensions. The transient nature of these membrane activities is reflected in Figure 3.35i), where cells appear well rounded with no signs of spreading. Although fibroblasts are interacting with their 20nm-diameter colloidal environment through lamella and filopodia development, the situation, even following contact with the substrate for upwards of 2 hours, is not inductive to cell spreading required for progression in the cell cycle. As is observed in the video, but not portrayed in the included still images, each cell is constantly trying to establish adhesive interactions with the surface with limited success. This results in the lack of spread cells in Figure 3.35i). Lack of spreading cells may be a result of the lack of excreted extra cellular matrix (ECM) or problems associated with ECM attaching to the surface and protein confirmation issues in relation to the nanotopography. Four areas of interest are depicted in the first frame included in this set. It should be noted that "B", even at this early time, appears to contain two cells. There is nothing dramatically unusual in this until we move approximately 5 hours 30 minutes into the investigation and see that cell "B" now appears to be only a single cell (on the right of "B", Figure 3.35ii)).

At this time point, approximately 6 hours post-seeding, Figure 3.35ii), cells appear to have gained some directional movement in comparison to the lack of central displacement observed in the video footage at earlier times, and also the relative position of cells in comparison to their original location in the first video still, i). As mentioned earlier, cell B appears as a normal single cell. However, following close

analysis of the video footage, this "single" cell is, in fact, two cells (B1 and 2) together. A similar story appears in relation to both C and D cells, although these fibroblasts are still distinguishable as individual cells, their behaviour evolves through these stills as two cells acting as if they were a united entity. At this period, Figure 3.35ii), cells have established contact with the relevant cell outlined in these images; C1 and C2 are in contact, and D1 and D2 are also in contact. Cell A appears extremely elongated, and the direction of movement of the cell is indicated by the arrow in this image.

One hour 30 minutes later, Figure 3.35iii), cell A has continued in its established direction of movement, indicated by arrows. The long "tail" of the fibroblast should be noted as similar features appear in many of the fluorescence images of these cells in relation to colloidal topographies, Section 3.3.3.4. Cell B, previously appearing as a single entity, has now emerged as 2 cells following limited movement across the substrate surface. Initially spread, the membrane appears to have detached from the surface, and cells appear in their initial two-cell configuration. Cell C1 and 2, although distinguishable as two separate fibroblasts are behaving as a single unit. Direction of movement is indicated with an arrow in Figure 3.35iii). One fibroblast appears to be leading the other, with a large amount of membrane ruffling indicated at its leading edge. Cells appear to be "stuck" together, and do not appear to dramatically limit the others motile abilities. Cells D1 and 2, having made contact with one another in Figure 3.35ii), appear to spring backwards towards the top left area of the image. In the video, this appear as a result of both contact between cells, and the possible strength of the adhesion of the contractile tail of D1 in association with a possible decrease in adhesion of the other areas of both fibroblasts resulting from the cell-cell contact. This would account for the area where both cells end up as a "ball" of 2 cells, at the point where the "tail" of D1 was attached.

Ten minutes later, Figure 3.35iv), both D cells appear in the same state as previously observed, although are once again emerging as separate individuals. Both C1 and C2 are continuing their journey as one unit, in the direction established some 2 hours 30 minutes previously, Figure 3.35ii). B1 and B2 fibroblasts are in a similar state of 2 individual cells as compared to Figure 3.35iii), but once again the boundaries between these cells are beginning to lessen, with one cell, B2, overlapping part of its neighbour, B1. The main reason for inclusion of this video still, a mere 10 minutes after the

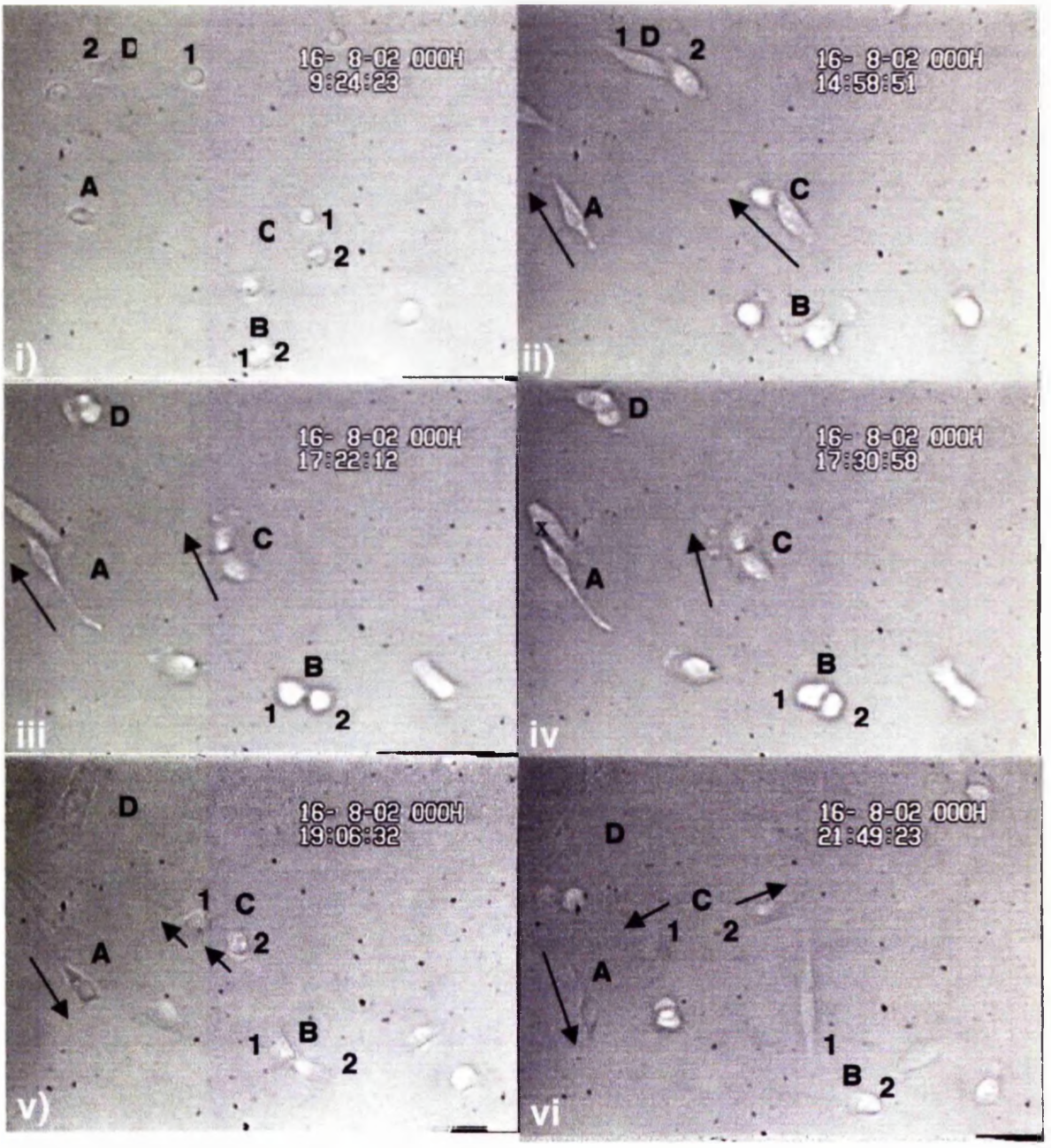

Figure 3.35: Time-lapse video microscopy stills of hTERT fibroblasts on 20nm-diameter colloidal topography at early times, over a 12 hour 30 minute period. It should be noted that i)-vi) are not separated by equal time points. Images were captured using a Ziess microscope with 30X objective lens. Fibroblast A)'s behaviour is unusual. Firstly, the cell traverses the substrate with directional motility, ii)-iii). Following contact with a neighbouring cell, A) alters its direction of movement and the bulk of the cell moves across the previously established detachment site. Cell C)'s behaviour is also unusual, where C1) and 2) traverse the substrate in a follow-my-leader fashion, where membrane connections appear paramount to this behaviour, ii)-iv). Furthermore, cellular aggregates are also observed, B) and D), i)-iv).

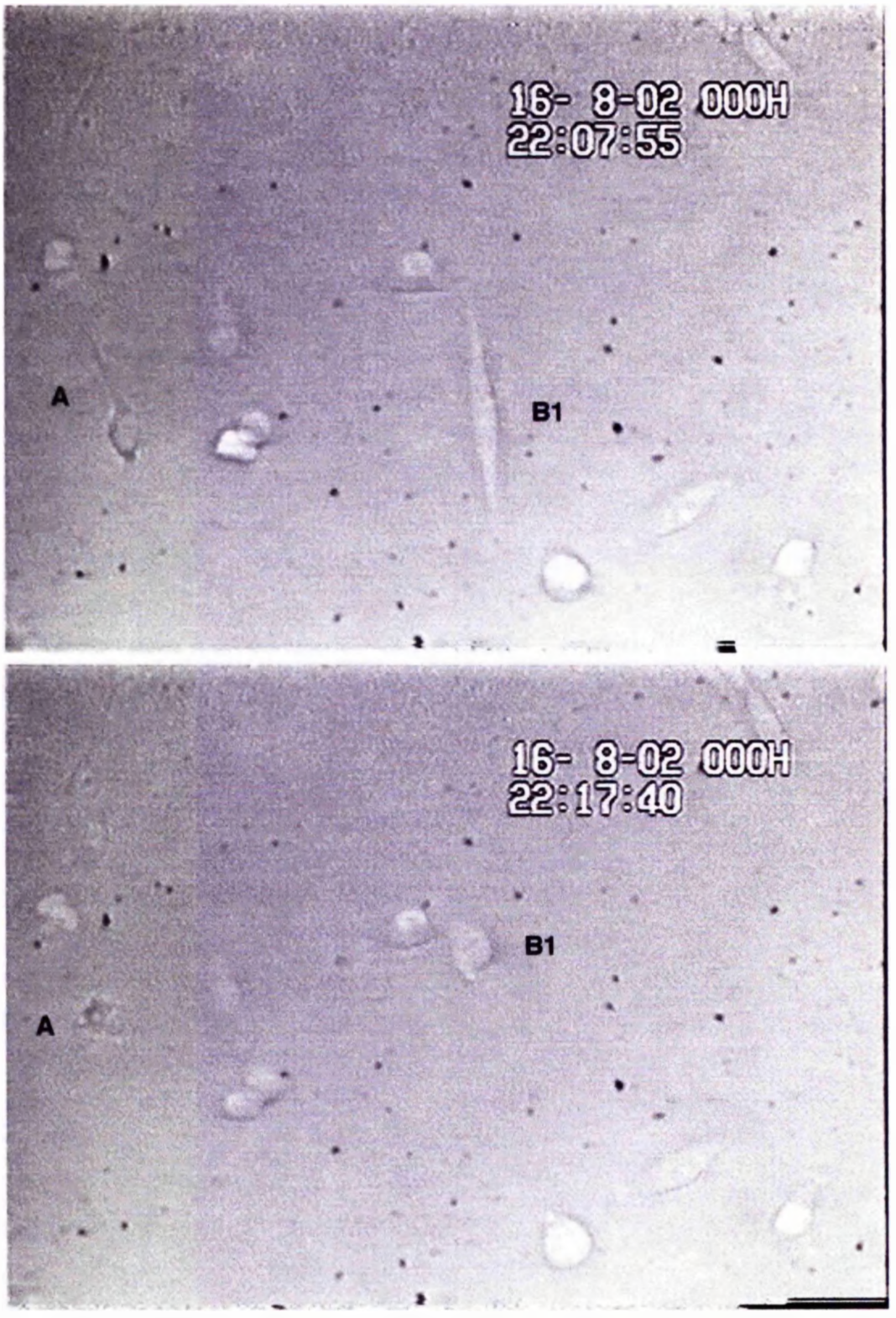

Figure 3.36: Still images from time-lapse video microscopy analysis using a Zeiss microscope with 30X objective. Elongated hTERT fibroblasts (A and B1) appear to display no conclusive directional movement, and catapult from the surface into a ball shape via their distal detachment site. This footage is continued from Figure 3.35.

previous still (Figure 3.35iii)), is the apparent contact established between cell A and its neighbour, "x" in Figure 3.35iv). This contact results in the reversal of movement initially established by cell A observed in Figure 3.35v), with arrows indicating movement of cells. Not only is this behaviour unusual, but the cell appears to move backwards across its extended rear detachment site. Cell B1 and 2 are emerging as separate cells, but appear to continue contact at a very fine shared point of membrane as they spread across the substrate, with the movement of each cell in alternative directions. Cells C1 and 2 appear to separate, though cells continue to move in the same direction, indicated by the presence of arrows in Figure 3.35v). Cell D, where previously D1 and 2 were observed as very separate cells although sticking together, have formed what appears to be a large cell from both individual cells. This is similar to the early stages of B1 and 2 which appeared briefly as 2 individual cells prior to appearing as one large "united" cell.

Approaching 3 hours later, Figure 3.35vi), cell B1 and B2 have separated completely, with B2 forming a rounded state and B1 appearing extremely elongated. Cells C1 and C2 having separated previously, Figure 3.35v) continuing movement in the same direction are now observed to move in opposite directions. Cell D appears as one large cell, although it is still suspected that this unit contains a minimum of 2 cells as observed previously in the video footage, Figure3.35Video. Cell A continues to move across its rear detachment site, and by this point, 12 hours from the first image, appears to have moved completely across its original contractile tail.

All the images in Figure 3.35 show a number of individual fibroblast reactions to the 20nm-diameter colloidal topography, even if these individual reactions occur via cell-cell contact with neighbouring cells. As fibroblasts in these images do not appear to move directly towards each other, where contacts are made following membrane contacts, the phenomena of chemotaxis is unlikely to contribute to these observations. The fact cells appear to become stuck on one another arises via membrane extensions, especially filopodia. This could be due to cell sensing of the 20nm-diameter colloidal topography resulting in very fine cytoskeletal arrangements at these sites. Thus, when two cells make contact via filopodia, differentiation between the protrusion and the colloidal topography are not sufficient for cells to deduce as is generally observed. The ability of cells to separate as seen in both cells B1, B2, C1 and C2 may occur due to lack of definition between cellular and topographical substrates following contact of

protrusions or detachment sites. Cellular aggregates containing more than one cell and thus multiple nuclei are particularly prevalent in fluorescent images, Section 3.3.3.4, suggesting similar behaviour is observed in these instances. When reviewing the video footage, especially as the cell population increases in the following documented stills, Figure 3.36, it appears that contact inhibition is somehow altered. However, it is difficult to determine whether contact promotion occurs, or cell-cell contacts are established unreservedly, with no bias established between the experimental substrate and cells, thus it is suggested that cells appear to have problems distinguishing between surrounding cells and the 20nm-diameter colloidal substrates.

Many of the cells appear to elongate on this topography, catapult from the surface towards either the leading or trailing adhesion sites. This is demonstrated in cell D1, Figure 3.36ii)-iii), and also in cells A and B1 in subsequent Figure 3.36 This action would suggest that adhesions at the sites cells catapult towards are greater than opposing cell-substrate interactions, Figure 3.35i), and may account for cell A's behaviour. Having moved in one direction and contacted another cell, the rear detachment site appears to be so strongly adhered, that the cell is capable of crawling back across it's previous trail. In fluorescence images and some video footage, cells appear to leave very fine detachment sites, many of which are present across the surface and show in fluorescence images as very fine threads of actin filaments and microtubules. These observations indicate possible problems of rear detachment arising in fibroblasts on these nanotopographies.

Another possibility of this catapult behaviour may be due to cells forming attachments with contacting cells which, in turn, displaces the adhesions cells have established with the substrate. Contact inhibition or contact repulsion may also have a role in this response. All fibroblasts exhibiting this behaviour have recently contacted other cells. Also, where fibroblasts which are not elongated, but travelling as a unit containing more than one cell, a single cell is often observed to spontaneously detach in the afore mentioned catapult motion. The sudden occurrence of this motion suggests complete spontaneous detachment from the surface, not dissimilar to a person pulling on a rope which snaps resulting in their falling in the direction of pulling. If one fibroblast within a cellular aggregate detaches from the surface in this movement, the adjoined cell appears to follows suit if not immediately, very soon afterwards. This suggests either the force with which the first cell detaches from the surface is great enough to displace

the neighbouring cells substrate adhesions, or that the cells are connected, and therefore acting as one "united" cell in this situation also. The localised nature of adhesion sites in the elongated cell with respect to the surface would account for the force required for the spontaneous movement towards either of the furthest extended adhesions. If displacement of the cell-substrate adhesions occurred in relation to the establishment of cell-cell adhesions, instigation of such a movement may result.

Two further possibilities for this behaviour exist. Firstly, as the cell polarises upon contact with the substrate, the colloidal topography may have a disorientating effect and polarity as is observed in cells on a flat substrate, where distinctions drawn between the basal lamina and apical surface are not established in the conventional form. This could be due to cells sensing nano-features on the substrate representative of tissues, where polarised circumstances may be altered, suggesting the expression of non-apical surface molecules appearing on the apical surface of cells. Secondly, the rigidity of substrates is believed to have a direct effect on cell behaviour and movement (Dembo and Wang, 1999). The progressive movement of cells across the substrate may be limited, with cells tending not to stray from their original positions. If cell-cell contacts are an important factor of this behaviour, where cells are adhering together possibly due to non-bias assessment of the substrate and extending neighbouring cells, the rigidity and permanence of cells as a substrate for other fibroblasts to form contacts with is poor. This would account for cell catapulting even when elongated where adhesions should be firmly established. The main route that should be taken to test these possibilities would be to stain for vinculin, Section 1.1.3, indicating its distribution with respect to cell-cell and cell-substrate contacts. Another possibility is to mark known baso-lateral and apical proteins and draw comparisons between their arrangement on a control planar surface and the experimental 20nm-diameter colloidal topography. Confocal microscopy could be utilised to determine the distribution of the markers across the cell, or a comparative study using fluorescence or weight of the acquired markers from controls and experimental digested cells could be employed.

It may be energy efficient for fibroblasts to traverse the topography as a unit rather than as individual cells as observed in cardiac precursor cells during embryonic development. When doubling (or even greater in some cases where upwards of three cells are seen to form a unit) the volume of a single cell, the amount of area coverage would directly influence the possible amount of cell-substrate adhesions. Similarly, the

amount of energy required by the cells to move across the surface may be reduced, and the possibilities with regard to cell spreading to enable proliferation bettered when fibroblasts are in contact due to tensile strength which is possibly absent with respect to cell-substrate adhesions.

The footage documented in Figure 3.37 expands upon the previous video stills, where cells, through division, are increasing in number. Thus, the occurrence of cell-cell contacts as observed at early times is increased. These images are taken at a later stage of the same video experiment, 15 hours after fibroblasts were first seeded on the 20nm-diameter colloidal topography.

By this period, the occurrence of extended membrane extensions is notable throughout the fibroblast population, indicated in Figure 3.37 by a line with a circle on either end of it parallel to the feature of interest. These extensions occur at the rear of cells, suggesting they are associated with cell traction forces and rear detachment. Protrusions appear to be established primarily between cell-cell contacts on the 20nm-diameter colloidal topography, and result in one of three scenarios. Firstly, the catapult effect as described previously occurs, where two cells connected by an elongation (and it is often difficult to see where one cells protrusion ends and another's begins) pull in an opposing direction, resulting in elongation breakdown and resultant "ping". The second scenario occurs as the cell moves forwards and the resulting detachment at the distal position becomes ever longer and thinner with time. The fibroblast leaves a path of cellular material almost certainly consisting of actin and tubulin, as indicated by fluorescence imaging, Section 3.3.3.4, that either remains attached to the cell or is detached and remains on the substrate. In this situation, the thread appears extremely thin, more so than those observed at earlier times, Figures 3.35 and 3.36. The third possible outcome of these membranous features is that they are once again attached to another fibroblast in a cell-cell fashion. The fibroblasts, for reasons uncertain and appearing likely as a factor of force exerted by neighbouring cells, close the gap via established interactions of protrusions, and form a cellular unit. This situation appears most evident in Figure 3.37, where cells appear to overcome their social inhibitions by increasing the amount of contact established with fellow fibroblasts *in vitro*.

The first two images in Figure 3.37, i) and ii), indicate the occurrence of behaviour previously described for fibroblasts on 20nm-diameter colloidal topography at early

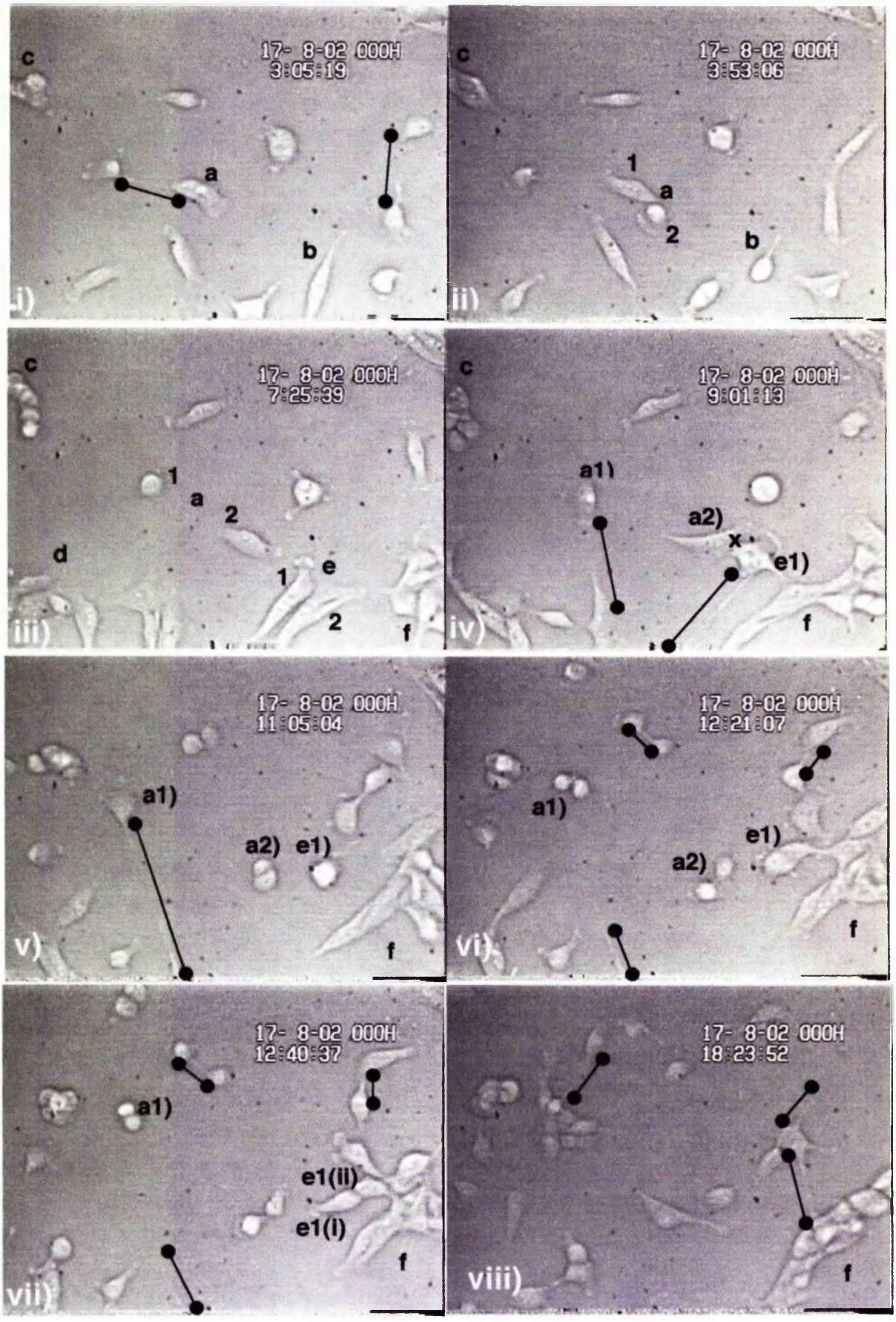
17- 8-02 000H
3:05:19
c
a
b
i)
17- 8-02 000H
3:53:06
c
1
a
2
b
ii)
17- 8-02 000H
7:25:39
c
1
a
2
d
1
e
2
f
iii)
17- 8-02 000H
9:01:13
c
a1)
a2)
x
e1)
f
iv)
17- 8-02 000H
11:05:04
a1)
a2)
e1)
f
v)
17- 8-02 000H
12:21:07
a1)
e1)
a2)
f
vi)
17- 8-02 000H
12:40:37
a1)
e1(II)
e1(I)
f
vii)
17- 8-02 000H
18:23:52
f
viii)

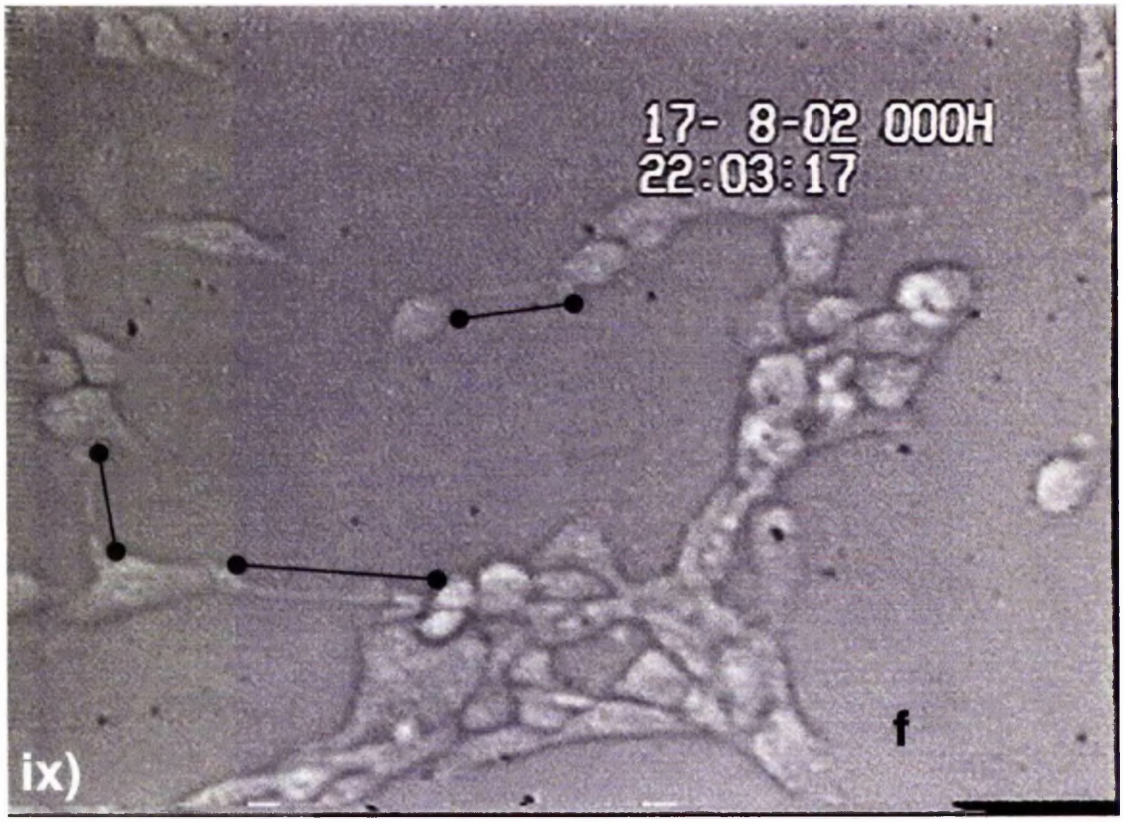

Figure 3.37: Time-lapse video microscopy using a Zeiss microscope with 30X objective of hTERT fibroblasts on 20nm-diameter colloidal topography, i)-ix). 18 hours, i) following initial seeding on the topography, and protrusions acting as cell-cell contacts are apparent throughout the population, indicated by a line with circles at either end. These occur through to the final image, ix) taken 33 hours following seeding. Fibroblasts are observed to catapult across the colloidal substrate, seen previously at earlier times, Figures 3.35 and 3.36. Furthermore, cell-cell aggregates appear to recruit more cells via membrane protrusions. When considering the vast amount of uninhabited surface free from cells, fibroblasts appear to preferentially interact as part of an aggregate. What often appear as individual cells, e1), iv), emerge as a number of fibroblasts migrating as a unified cellular entity, vi) and vii).

times, Figure 3.35 and 3.36. Cell a) appears in the first still as a single cell, however, in Figure 3.37ii), taken approximately 50 minutes later, cell a) has split to reveal it was composed of two cells. Close inspection of the video indicates this is not merely a result of cell division, as they originate from a three cell-situation formed in conjunction with the fibroblast appearing on the left of the line highlighting the extension in image i). Fibroblasts appear almost to wander out of each other, with no strain apparent in each individual as they continue to meander across the nanotopography. Three and a half-hours later (Figure 3.37iii)), and these cells which were once unified, have completely separated and departed company moving in opposite directions across the experimental topography.

Similar behaviour is observed in Figure 3.37i) - iv). In image i), cell c) appears as an entity containing more than one cell, although the apparent number is not obvious. In ii), 50 minutes later, the area denoted by c) appears as if a single cell, although boundaries within the mass indicate there may be more than one cell when considering previous evidence of this type of behaviour occurring. In Figure 3.37iii), 3 hours 30 minutes later, what originally appeared as a single cell has taken the form of approximately 4 or 5 non-spread, rounded fibroblasts. From further examination of the video footage, some of the cells in this group c) may arise as a result of cell division, however this does not account for all the cells present within the aggregate. A further hour and a half later, Figure3.3.7iv) and the cells, still appearing extremely rounded, are more spread and cell boundaries can be clearly defined indicating a number of cells within the group. Further examples of this behaviour can be observed with respect to cell e) in Figures 3.37i)-vii), which initially catapults across the nanotopography, rounds-up and emerges as two individual cells, which then establish contact with a neighbouring aggregate.

Cell b), Figure 3.37i) and ii), serves to highlight the previously described "ping" effect. Figure 3.37i), cell b) is extremely elongated, stretching across the colloidal topography. Within 50 minutes, Figure 3.37ii), the cell has violently retracted in the discussed catapult motion in what appears to be the overall direction of original motion.

At this point, approximately 24 hours after seeding on the experimental topography, a number of cell aggregates are emerging across the surface, highlighted in regions c), d) and f) in Figure 3.37iii). Cell-cell contacts appear numerous, and cells are reluctant to

move into less densely populated regions of the substrate as previously described by Abercrombie and Heaysman (1952) in relation to contact inhibition of fibroblasts following emergence from tissue explants *in vitro*. It would appear that the greater the number of cells populating aggregates, the more cells are attracted and attach to these groups. When cells contact an aggregate via intercellular contacts, a cell(s) from the group appear to greet the new member along the membranous extension connecting the two or more cells. In this manner, the new group member appears to be swallowed into the communal cytoplasm, and, thus, no catapult is observed. This is demonstrated by cell e)2 joining group f). As the bulk of these accumulation increases, if cell-cell adhesions do displace cell-substrate adhesions, the tensile strength of the cells within the group may be great enough to anchor the new member.

A further example of cell-cell contact resulting in catapulting of the fibroblasts involved is observed in cell e1) and a2), Figures 3.37iv)-vi). What emerges from these rounded fibroblasts are not two single cells, but two separate cellular bundles containing what appears to be two cells each. One hour and 30 minutes later, and these bundles appear to re-establish contact with the experimental surface housing the 20nm colloidal topography. Cell e1) now moves towards the assemblage f), Figure 3.37vi), and contact with members of the group is established via a membranous connection. Twenty minutes later, Figure 3.37, viii), and the cellular entity of e1) emerges as two individual cells, although no evidence, following close inspection of the video, exists to support normal cell division as a cause of this increase in cell number. Many cell factions appear across the 20nm-diameter colloidal topography with increasing time, and very few single cells are observed on the surface although cell-free space exists. Contact inhibition appears altered, as cell-cell contacts increase, yet little attempt is made by the fibroblasts to move into unoccupied areas.

Adhesion between cells would appear to be very strong, as the cell can move across the surface with little difficulty in the rearrangement of focal contacts, but cannot detach its tail from a cell-cell contact, cell a1), Figure 3.37iv). When this adhesion does break (as detachment would be a more gentle process), the cell is projected forward by its established directional movement of the cell and the direction of movement of the pinging tail, overbalancing and losing contact with the experimental substrate. As the cell rounds up following this event, it is believed that the cell-substrate contacts are

overpowered and lost or reduced by this action, as the cell is no longer capable of exhibiting a spread morphology.

The final image in these sequence of video stills, Figure 3.37ix), shows the results of the general behaviour described throughout this section after 33 hours following initial seeding on the 20nm-diameter colloidal topography. The focus here surrounds the group of cells f), highlighted throughout Figure 3.37. Cells in this accumulation appear relatively contracted in shape and size, with little sign of spreading on the surface. Only one cell in this image appears as an individual, with all others assuming a cellular mass via cell-cell contacts. Fibroblasts that appear less involved with group f) appear to have shared connections with the mass via long extensions. These filopodia-like structures are highlighted in image ix) by lines parallel to the feature. This image highlights alterations in contact inhibition, as cell-cell contact appears to be actively sought and cells do not move into unoccupied substrate surface regions, instead preferring cell contact establishment to substrate adhesions. This is further elucidated in Chapter 5, where a planar-nanopillared structure was developed, and cell reactions exhibited in this section were observed on the nanopillared areas only, and not the planar areas.

Summary of time-lapse video microscopy analysis

It is important to establish the behaviour of the cells as observed in the time-lapse video images. This allows for experimental analysis with regard to adhesion, morphology and cytoskeletal arrangements fixed at specific time points to be referred back to the overall reactions of cells at these given periods. Many of the imaging methods indicated cells were multi-nucleated. Initial beliefs were that cells had dedifferentiated to form either muscle myocytes, or were mutated which would directly alter results rendering them void. However, due to the use of time-lapse video microscopy, the understanding that cell social inhibitions were somehow altered resulting in many cells forming a cellular unit and thus expressing many nuclei within a large cellular body allowed for the interpretation of the results. The possibility that this phenomenon is a result of continual culture and loss of contact inhibition in the hTERT cells is examined but appears unlikely. This is due to the results of cells grown on a planar control and the reactions of cells seeded on an alternating planar-nanopillared surface, where increased cell-cell contact only appears as a result of contacting the nano-featured topography.

The most notable behaviour observed in the time-lapse video microscopy images of fibroblasts on the 20nm-diameter colloidal topography include catapulting of cells across the substrate, increased cell-cell contacts resulting in aggregate formation, and very long elongated protrusions, Figures 3.35 to 3.37. Catapulting of fibroblasts is often observed immediately following contact with another member of the population, and may arise due to an imbalance in proximal and distal adhesions occurring at the cell-substrate interface. Increased cell-cell contacts, where aggregates form, regardless of the uninhabited free surface suggests alterations in contact inhibition. Elongated protrusions appear to function as a means of connection between neighbouring fibroblasts on the nanotopography. The absence of cell movement into unoccupied areas of the substrate suggests cell-cell contacts are preferred in comparison to cell-substrate interactions. This is most obvious when considering the occurrence of cell clusters on the 20nm-diameter colloidal topography at later times, for example Figure 3.37ix), with little evidence of individual cells on the substrate surface.

3.3.3.1.2 Video stills of hTERT fibroblasts on 50nm-diameter colloidal topography

In comparison to fibroblasts seeded on the 20nm-diameter colloidal topography, Section 3.3.3.1.1, cells on the 50nm-diameter colloidal substrate do not exhibit the catapult motion or cell-cell contacts resulting in indefinable boundaries between fibroblasts with an aggregate. However, elongated, globular protrusions, as observed on the 20nm-diameter colloids, are present in cells on the 50nm-diameter colloidal substrate. Furthermore, cell-cell contacts are observed on the 50nm-diameter colloids, but result in cell alignment with neighbours rather than aggregate formation.

Immediately upon seeding fibroblasts on the 50nm-diameter colloidal topography settle and spread on the surface, Figure 3.38a). The majority of cells in this image demonstrate radial membrane ruffling, although an instance of proximal-distal polarised ruffling is also observed, "P" in Figure 3.38a). Upon 30 minutes of contact with the substrate, Figure 3.38b), peripheral extensions appear to interact with the nanopattern (dashed arrows), resulting in the expression of stressed protrusions culminating in localised globular membrane sites (solid arrows).

Following attachment and membrane protrusion activity, cells are observed to begin spreading, Figure 3.38c), prior to elongation and movement. The fibroblast displaying polarised membrane ruffles has already begun to stretch at this time in comparison to

those displaying radial membrane ruffling. Cell-substrate interactions result in spiky, star-shaped morphology (open arrowheads), suggestive of rigid cytoskeletal morphology as a result of specific, localised adhesive interactions at the substrate interface. These adhesive interactions appear prior to the occurrence of migrational axis establishment, which results in cell stretching, elongation and motility in the direction of the protruding extensions, Figure 3.38d)-f).

The fibroblast initially exhibiting polarised membrane behaviour, Figure 3.38a), is observed to elongate across the colloidal topography following approximately 1 and a half hours of contact with the substrate, closed arrowhead with diamond tail in Figure 3.38c). Over the next hour, Figure 3.38d), the cell stretches from right to left in this image. Further stretching, resulting in a highly-stressed morphology, is observed three and a half hours post-seeding, Figure 3.38e). At this time, neighbouring fibroblasts are also exhibiting similar elongated and stretching behaviour. However, a further 30 minutes in contact with the 50nm-diameter colloidal topography and the elongated fibroblast (closed arrowhead in Figure 3.38f)), is observed to traverse its previously established rear detachment site, resulting in the central displacement of its body in the opposing direction, indicated by arrow direction, previously established. It should be noted that similar behaviour was observed at early times in fibroblasts on the 20nm-diameter colloidal topography, Figure 3.35iii)-v).

Cell-cell contacts also emerge within the fibroblast population as cells begin to move across the substrate. One example, 18 hours post-seeding is highlighted, Figure 3.39. Two neighbouring fibroblasts form contact via a shared membrane region, "x" in Figure 3.39a). Following 1 hour of this contact, the shared membrane area of the cells is increased, Figure 3.39b). Rather than catapult into an aggregate as previously observed in relation to the 20nm-diameter colloidal substrate, Section 3.3.3.1.1, fibroblasts follow their original direction of movement, direction of arrows in Figure 3.39c). Furthermore, this direction appears to be associated with other cell-cell contacts previously established, and resultant arc-like morphology at the peripheral edges of these fibroblasts is observed. Two and a half hours after initial connection was made, and these fibroblasts continue to move in opposing directions, resulting in their alignment to one another in a proximal-distal continuous manner, Figure 3.39d). Where initial contact was made, x" in Figures 3.39a)-d), a very thin, well-spread area of membranous material emerges, highlighted area surrounding "x" in Figure 3.39d). The emergence of

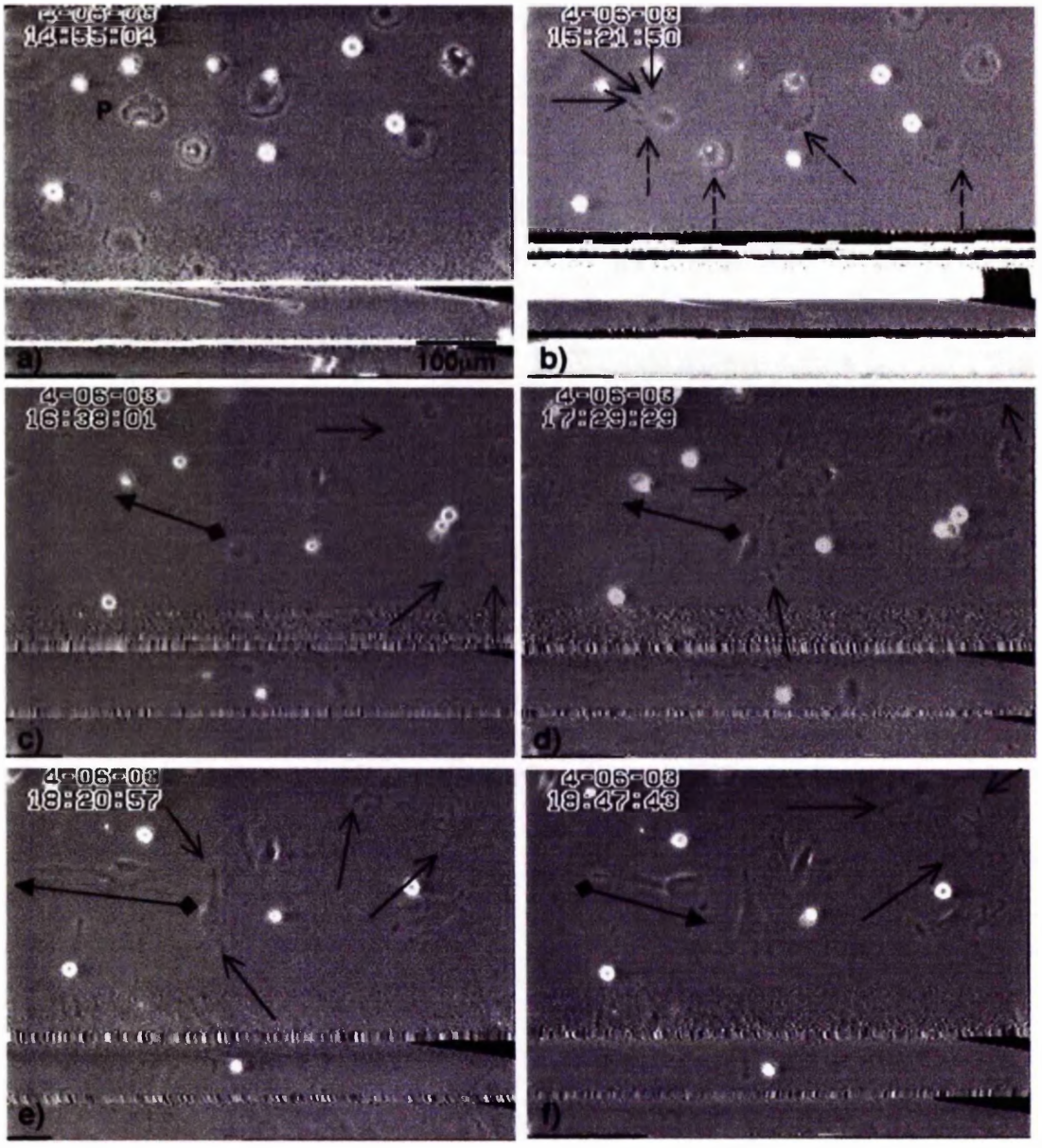

Figure 3.38: Time-lapse video microscopy of hTERT fibroblasts on 50nm-diameter colloidal topography. Imaging was conducted using a Zeiss microscope with 30X objective. Immediately upon seeding, a), most cells are observed to spread their membrane in a radiating manner as they settle on the substrate, although an instance of polarised membrane behaviour is observed (P). Thirty-minutes following seeding, b), and globules are observed to form in membrane ruffles, or lamella (broken arrows). More developed protrusions (solid-line arrows) with globular or spiky appearance are also seen at this early time in the cell originally displaying polarised mambrane ruffling. This cell proceeds to elongate (closed arrow with diamond tail) across the colloidal substrate one hour later, c), while its neighbours begin to exhibit globule-containing protrusiosn (solid-line arrows). Over the next hour, d), the elongated fibroblast stretches across the surface (closed arrow-head with diamond tail), and other cells in the population continue to develop spiky protrusions and exhibit more spread morphology compared to previous images. 3 and a half hours following seeding, and the elongated cell continues to stretch (closed arrow-head), resulting in a highly-stressed appearance, e). Neighbouring cells also appear to stretch across the nanotopography via their spiky protrusions (open arrow-heads). Thirty minutes later, f), and the elongated fibroblast appears to have traversed its established detachment site, resulting in central displacement of its body in the opposing direction previously established.

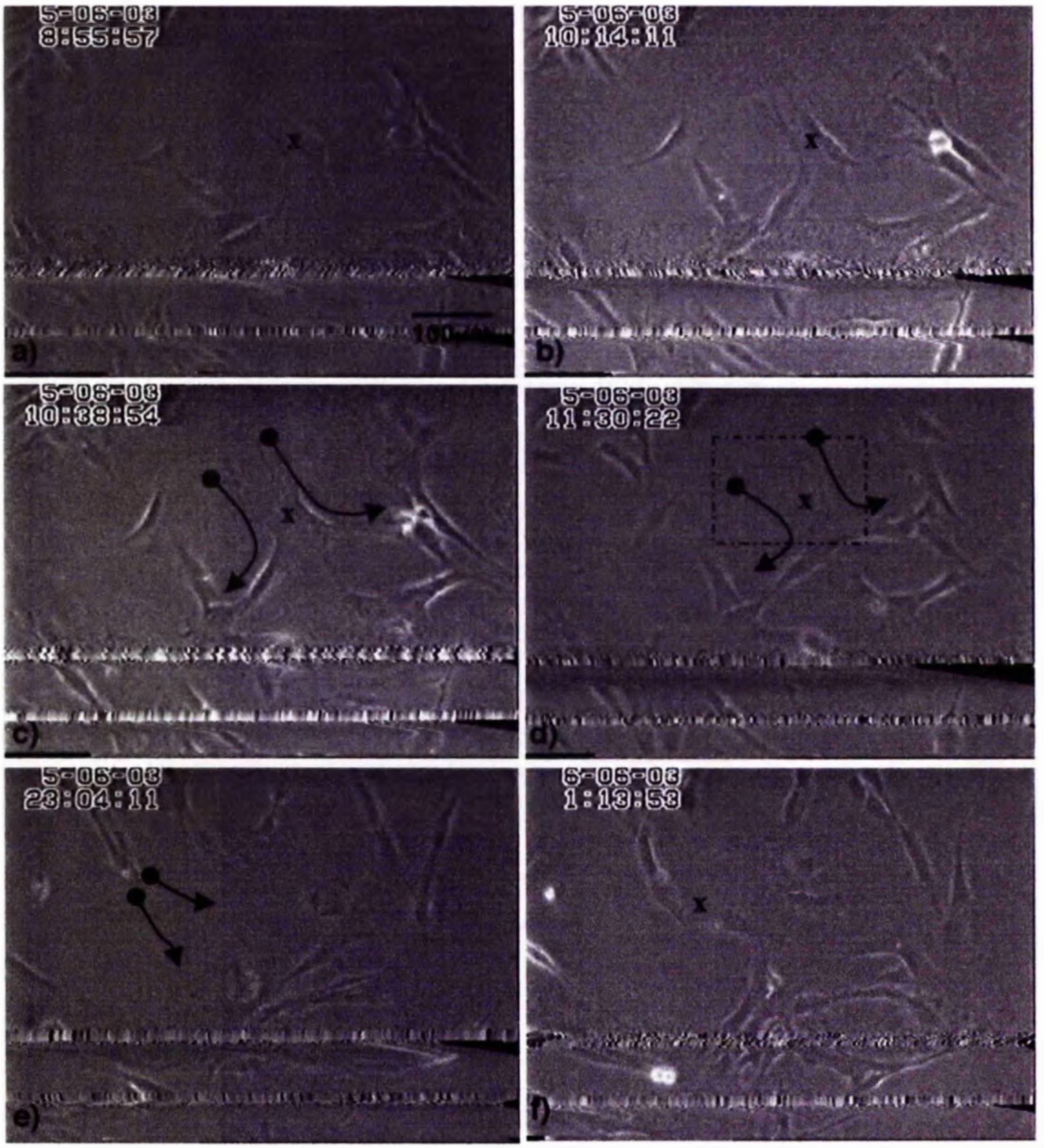

Figure 3.39: Time-lapse video microscopy of hTERT fibroblasts on 50nm-diameter colloidal topography (continued from Figure 3.38). Two individual fibroblasts are observed to contact one another ("x"), a). Approximately one hour following this intial contact, b), cells appear to align with one another via a common pivotal membrane contact ("x"). The two fibroblasts are then observed to move in opposing directions, c), indicated by arrows, although some areas of the cells still remain in contact ("x"). As the fibroblasts move away from one another and their initial point of contact, a very thin, well-spread area of membrane emerges, boxed area in d), surrounding the initial cell-cell contact. The boundaries of each cell at this site is difficult to distinguish. Further cell-cell contacts are also observed at later times, e) and f), continuing overleaf. Initiation of cell-cell interaction in this instance appears to occur via extremely thin, globular elongations protruding from one of the fibroblasts, arrows in e). As a neighbouring cell traverses one of these protrusions, f), cell-cell contact is initated ("x").

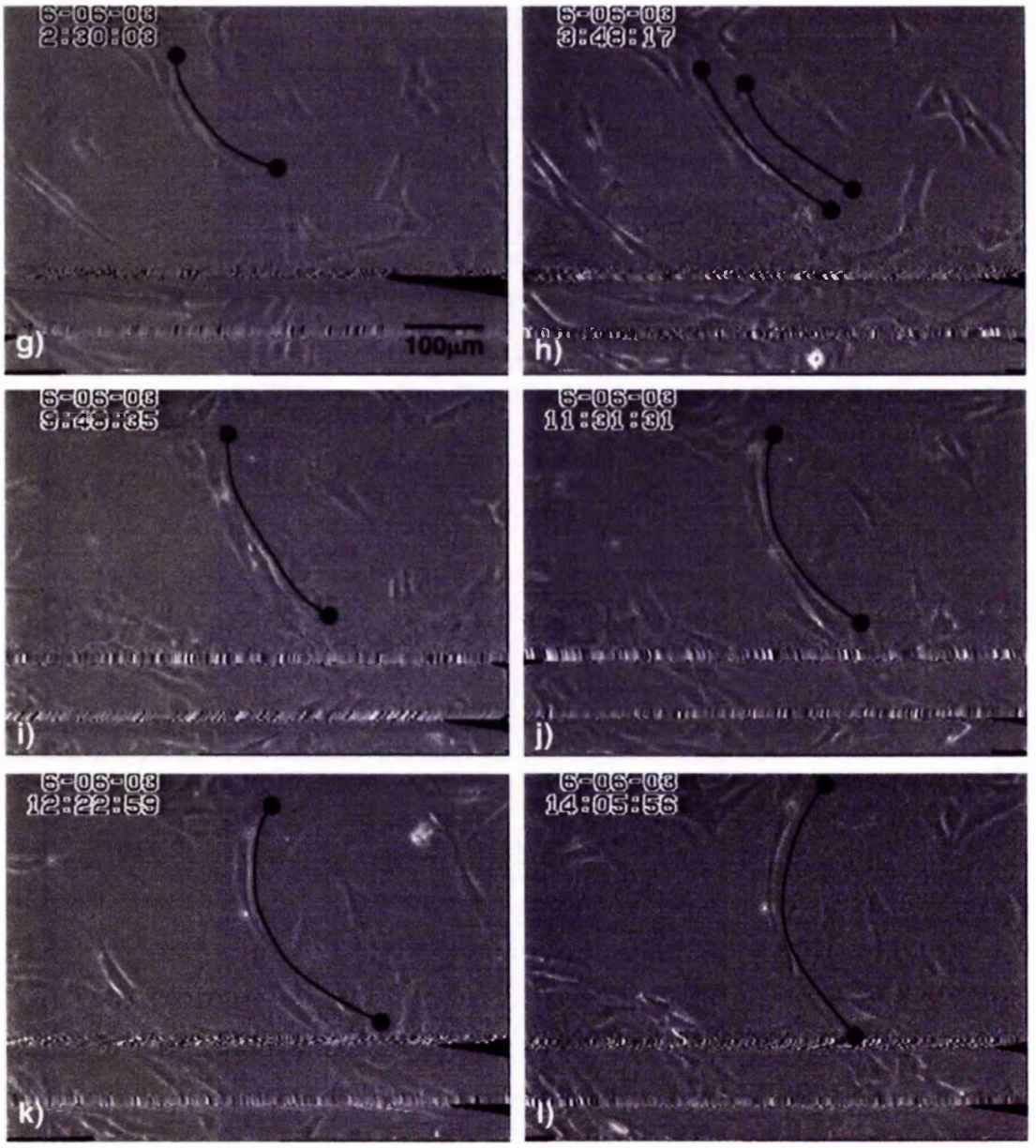

Figure 3.39 (continued): Time-lapse video microscopy stills (using Zeiss with 30X objective), of cell behaviour following cell-cell contact via an elongated protrusion (e) and f) previously). Following initial cell-cell contact, f), fibrobasts on the 50nm-diameter colloidal topography elongate in-line with one another, while still in contact, line in g). One hour following this observation, h), and a further cell appears to align parallel to the cell-cell elongation. Over the following 10 hours, i)-l), the elongated fibroblasts appear to shorten their right side as we look at the images, resulting in a greater arched appearance in this regions. This behaviour suggests the possibile occurrence of acto-myosin contractility.

this shared membrane region suggests continual interaction between the cells involved, and also cell-substrate adhesive interaction.

As previously observed in relation to fibroblasts on the 20nm-diameter colloidal topography, Section 3.3.3.1.1, very fine, elongated protrusions extending from the main body are observed in cells on the 50nm-diameter colloidal substrate, arrows in Figure 3.39e). In comparison to the protrusions observed on the 20nm-diameter colloids, elongated membrane extensions contain globular regions along their length on the 50nm-diameter colloids, Figure 3.39e). These elongations are also implicated in cell-cell contact establishment, Figure 3.39f), where a denuded region of the surface is traversed by the protrusion, which contacts a neighbouring cell. Following cell-cell contact, fibroblasts appear to exert tension across one another, resulting in elongations and stretching of contacting cells in a continuous manner, Figure 3.39g), as previously described in Figure 3.39a)-d). Another neighbouring fibroblasts is observed to align in a parallel fashion to these elongated connected cells, Figure 3.39h). Continuous contact over 12 hours following initial cell-cell contact, Figures 3.39g)-l), results in contraction of the aligned cells at the right side of their bodies (highlighted with line terminating in circles). This observation suggests actomyosin contractile behaviour occurring within the fibroblasts. This type of function is discussed in further detail in Section 5.3.1, where contractile "purse-string" mechanisms, occurring via actomyosin cables, associated with epithelial wound healing is discussed.

In summary, fibroblasts on the 50nm-diameter colloidal topography interact with one another, resulting in cell alignment to their neighbour. Aggregate formation previously described in relation to the 20nm-diameter colloids, where rounded cells form islands via cell-cell contacts, with lack of definition between individual cell boundaries, is absent on the 50nm-diameter colloidal topography. However, cell-cell contact is observed throughout the population, but individual boundaries, where peripheral membranes define contacting cells, are present. Tension occurring between cells in contact often results in the curved appearance of peripheral membranes at one edge of the cell. Actomyosin has been implicated in this type of contractile behaviour, and during epithelial wound healing, occurs between cells with established adherens junctions, and cells drag their basal lamina underneath them as a results (Jacinto et al, 2001). Furthermore, elongated filopodia-like protrusions are observed, where localised globular beading occurs across their length, absent in similar features observed on the

20nm-diameter colloidal topography. The composition of these features is elucidated in Section 3.3.3.4, where fluorescent staining of the actin and tubulin cytoskeleton indicates these globules are cytoskeletal-containing islands.

3.3.3.2 hTERT Cell Adhesion on Colloidal Topographies

hTERT fibroblast adhesion to both the 20nm- and 50nm-diameter colloidal topographies, and a control planar topography with a hydroxylised surface, all with borosilicate glass coverslip base substrates was examined. Cells were cultured at a concentration of 10,000 per ml in 3mls media on the experimental surfaces and cells were fixed with Formalin and stained with Coomassie Blue, Section 2.7.1, at 20 minutes, 1 hour and 3 hours.

Fibroblast adhesion on each experimental surface was calculated by firstly counting 30 non-specifically chosen fields of view using a Vickers light microscope with 10x Phaco 1 objective lens (170/-, 10/0.25). Cells lying within an area of the experimental surface contained within the 10 x 10 square graticule present in the eyepiece of the microscope were counted. One nucleus was considered to equate to one cell. A square graticule, placed in the eyepiece, was used to highlight an area of the surfaces at this magnification measuring 0.93mm^2. This was calculated by placing a 1mm-graticule scale on the microscope stage, and measuring the length of the square graticule observed through the eyepiece. The data accumulated in this manner, Appendix III, was then entered into Statview, a statistical application, and descriptive statistics and distribution histograms were obtained for each surface at each time point, Appendix IV.

A degree of statistical knowledge is required if a correct statistical test is to be applied and understood in relation to experimental results. Furthermore, the test statistic, a single number produced by a statistical test, has no relevance unless the user or the reader understands that the probability distribution of a test statistic is known, generally calculated and tabulated by a statistician. The basis of a statistical test is the presumption there is no difference between sample means, generally termed a Null Hypothesis (H_0). Thus, a statistical test produces a value for its test statistic, and it must be determined whether that value exceeds some probability threshold that suggests rejection of a Null Hypothesis. An alternative to a Null Hypothesis, where a difference between samples does exist, is termed H_1.

The variables under investigation must firstly be determined if an appropriate statistical test is to be selected. For example, the number of fibroblasts adhering to three different surface topographies at three different intervals was recorded when investigating the effects of nanotopography on fibroblast adhesion. Thus, the effects of topography and time, both independent variables, required to be estimated in relation to fibroblast adhesion, a dependent variable. As a result, two-way analysis of variance (ANOVA) was selected to analyse the influence of two variables, topography and time, upon a sample mean. ANOVA allows comparisons to be made between any number of sample means in a single test, overcoming the risks of committing Type 1 or Type 2 errors during data analysis. Type 1 errors, where H_0 is rejected when it should be accepted, arise if a level of significance, for example P=0.05, is consistently accepted when examining a large number of samples, where, in this instance, a wrong conclusion will be drawn on average once in every 20 tests performed. By setting the acceptable significance level to the more stringent P=0.01, type 1 errors can be reduced. However, as the probability of making a type 1 error is reduced, the probability of making a type 2 error, namely failing to reject H_0 when it should be rejected, is increased. In most statistical analysis, the aim is usually to limit the probability of committing type 1 errors by erring on the side of caution, thus H_0 is generally accepted at $P<0.01$.

A residual plot, Graph 3.1, where the mean number of fibroblasts adhering on each individual topography namely planar, 20nm- and 50nm-diameter colloidal surfaces, at each time point (20 minutes, 1 hour and 3 hours) was firstly constructed. Residual plots allow interactive effects between variables to be easily observed. If interaction is observed, then a biological explanation may be sought. In brief, if there are more than two categories of each variable, as observed in this adhesion experiment where three time points and three topographies are being compared, the sample mean for each situation is connected as a line. Roughly parallel lines indicate that the effects of the two variables, for example time and topography, are additive, where transition from variable A, in this instance time, has added an equal amount to the mean fibroblasts adhering to each topography. Similarly, it may be that the transition from each experimental surface has added an equal amount to the mean number of fibroblasts adhering at each time point. However, if the lines connecting the mean values in the residual plot are not parallel, there may be an interaction. An interaction is observed between the mean number of fibroblasts adhering to each experimental substrate over the three time intervals investigated, Graph 3.1.

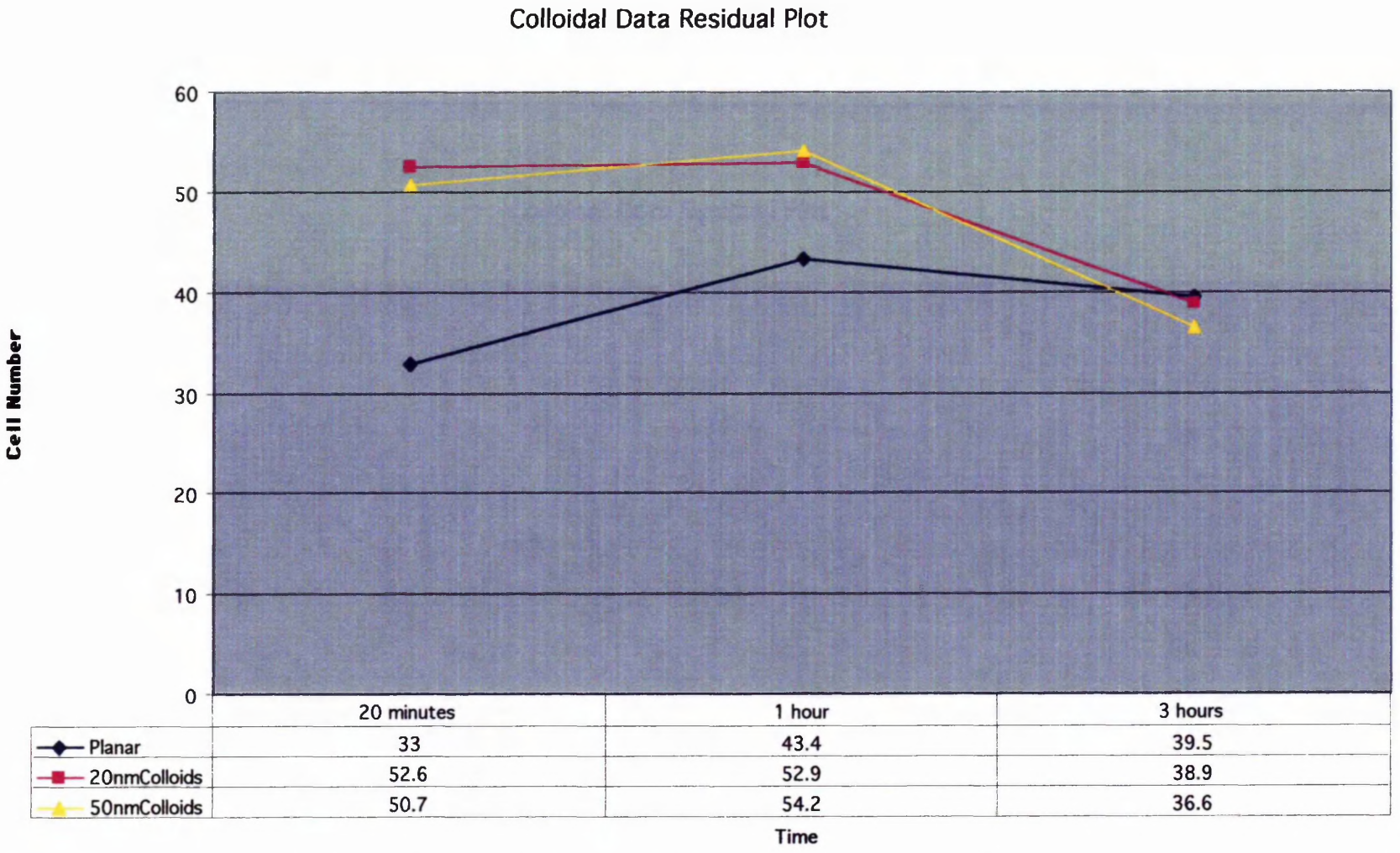

Graph 3.1: Residual plot of mean fibroblast adhesion on planar, 20nm- and 50nm-diameter colloidal topographies at 20 minutes, 1 hour and 3 hours. Lines connecting the mean values, written in the table at the base of the graph, are not consistently parallel between the number of cells adhering on each substrate at each time interval, indicating possible interaction between the variables. Interaction is further supported at 3 hours where lines connecting the means cross-over one another, or interact.

Variable B: Surface Topography					
Variable A Time		*Planar* Situation 1 Column 1	*20nm colloids* Situation 2 Column 2	*50nm colloids* Situation 3 Column 3	**Total for Row**
	20 minutes Row 1	n = 30 X= 33 s = 35.97 s^2= 1293.66 Σx= 990 $(\Sigma x)^2$= 980100 Σx^2= 37516	n = 30 X= 52.6 s = 59.19 s^2= 3504 Σx= 1578 $(\Sigma x)^2$=2490084 Σx^2= 101616	n = 30 X= 50.7 s = 56.45 s^2= 3186.79 Σx=1521 $(\Sigma x)^2$=2313441 Σx^2=92417	**n_t = 90** **Σx_t= 4089** **Σx^2_t= 231549**
	1 hour Row 2	n = 30 X= 43.4 s =46.49 s^2= 2160.86 Σx=1303 $(\Sigma x)^2$=1697809 Σx^2=62665	n = 30 X=52.9 s = 56.46 s^2=3187.86 Σx=1586 $(\Sigma x)^2$=2515396 Σx^2=92448	n = 30 X=54.2 s = 62.4 s^2=3893.48 Σx=1627 $(\Sigma x)^2$=2647129 Σx^2=112911	**n_t = 90** **Σx_t= 4516** **Σx^2_t= 268024**
	3 hours Row 3	n = 30 X=39.5 s = 40.85 s^2=1668.41 Σx=1186 $(\Sigma x)^2$=1406596 Σx^2=48384	n = 30 X=38.9 s =41.2 s^2=1697.28 Σx=1167 $(\Sigma x)^2$=1361889 Σx^2=49221	n = 30 X=36.6 s =37.85 s^2=1433 Σx=1097 $(\Sigma x)^2$=1203409 Σx^2=41557	**n_t = 90** **Σx_t=3450** **Σx^2_t= 139162**
	Total for Column	**n_t = 90** **Σx_t= 3479** **Σx^2_t= 148565**	**n_t = 90** **Σx_t= 4331** **Σx^2_t= 243285**	**n_t = 90** **Σx_t= 4245** **Σx^2_t= 246885**	***n_T = 270*** ***Σx_T= 12055*** ***Σx^2_T= 638735***

Table 3.5: Contingency table outlining the number observations per sample, n, mean, X, standard deviation, s, sample variance, s^2, sum of observations, Σx, the square of the sum, $(\Sigma x)^2$ and the sum of squares of the deviations (termed "sum of squares"), Σx^2. The subtotal of number of observations, $\mathbf{n_t}$, subtotal of sum of observations, $\mathbf{\Sigma x_t}$ and subtotal of the sum of squares, $\mathbf{\Sigma x^2_t}$ for each row representing each time interval, and for each column representing each topography was then calculated. The total of these items for all rows which is also equal to the total of all columns was then calculated (bottom right cell). The contingency table contains the information required to calculate ANOVA. The highest value of s^2 is highlighted by a red box and the lowest value by a blue box. The highest value is divided by the lowest value to obtain F_{max}, the homogeneity of variance, which is then compared to a tabulated critical value prior to proceeding with ANOVA.

The residual plot of the means indicates that cell adhesion increases on all 3 substrates between 20 minutes and 1 hour, and decreases between 1 hour and 3 hours. However, the rates of increase and decrease at these periods are not equal, indicating a possible interaction between the variables, namely time and topography, on fibroblast adhesion.

A contingency table was composed as outlined by Fowler et al in "Practical statistics for field biology", pp190-194 (1998). Initially, descriptive statistics calculated in Statview were entered into the contingency table for the mean and standard deviation. Sample standard deviation is calculated as:

$$s = \sqrt{\frac{\Sigma(x-X)^2}{n-1}}$$

where X is the sample means and n is the number of observations in the sample.

However, *an alternative standard deviation is calculated for descriptive statistics where n is used as the denominator rather than the degrees of freedom (n-1).* This is extremely important to note, as the reduction of the number of the observations in the sample has the effect of increasing the standard deviation, *greatly affecting further calculations.* This discrepancy in the standard deviation for descriptive statistics and sample standard deviation can be seen when comparing the values of s in Appendix IV and Table 3.5 respectively.

Parametric statistical tests are based on a number of assumptions, the two most important being that data is distributed normally and variance between samples is homogenous. A homogeneity of variance (F_{max}) check is calculated prior to proceeding with ANOVA, and is obtained by dividing the largest sample variance (s^2 max) by the smallest sample variance (s^2 min), highlighted by a red and blue box respectively in the contingency table, Table 3.5. It was during the homogeneity of variance check that the discrepancies between the standard deviation calculation were noted. For example, when calculated using the standard deviation presented in the descriptive statistics produced in Statview, Appendix IV, F_{max} was calculated as 17.09, where the denominator used in this equation was n, as described above. However, when F_{max} was calculated by hand using the degrees of freedom ($n-1$=29 in this instance), F_{max} was calculated as 3.01, Table 3.5. These values were then compared to the critical value of F_{max} (Fowler et al, 1998, Appendix 9), 3.21 for a=9 (number of samples being compared) and v=30 (degrees of freedom nearest to those in use,

namely 29). Thus, the values calculated for descriptive statistics of the data, 17.09, suggest that the variance within the data is too great to proceed with a parametric test. However, *this is not correct,* as ***the actual sample standard deviation, 3.01, calculated using the degrees of freedom is less than the tabulated F_{max} critical value of 3.21, indicating we may proceed with ANOVA.***

Following the calculations required for ANOVA (Fowler et al, 1998, pp190-194), data was summarised in an ANOVA table, Table 3.6.

Source of variation	Sum of squares	df (degrees of freedom)	Variance	F
(between samples)	(15628.34)	(8)		
Variable A Time	*6396.31*	*2*	*3198.16*	*9.84***
Variable B Topography	*4889.09*	*2*	*2444.55*	*7.52***
Interaction	4342.94	4	1085.74	3.34
Within samples	84873.23	261	325.18	

Table 3.6: ANOVA table of summarised data. F-values exceed the critical value at P=0.01 for the appropriate numbers of degrees of freedom when referred a table of distribution of F (Fowler et al, 1998, Appendix 10). **indicates significance at $p<0.01$.

The first Null Hypothesis states there are no significant differences between the number of fibroblasts adhering to planar, 20nm- and 50nm-diameter colloidal substrates (Variable B). However, the value of F=7.52 for Variable B, Table 3.6, exceeds the tabulated value at P=0.01 where F-distribution is recorded as 4.6052 at df 2, 261. H_0 is thus rejected indicating that surface topography affects fibroblast adhesion.

Similarly, the second Null Hypothesis states that there are no significant differences between time and the number of fibroblasts adhering to each individual substrate. The F-value, 9.84, calculated using the original data for Variable A, Table 3.6, exceeds the tabulated value at P=0.01 of 4.6052 for df 2, 261. The Null Hypothesis is thus rejected, concluding that the number of fibroblasts adhering to each individual substrate at the time intervals investigated are significantly different, thus following initial cell seeding, fibroblast adhesion is significantly different at 20 minutes, 1 hour and 3 hours on all the topographies investigated.

The third Null Hypothesis employed is that there is no interaction between the substrate topography and time, which influences the mean number of fibroblasts adhering to a

surface. The F-value calculated for the interaction between Variable A and B, 3.34, exceeds the tabulated value of P=0.01, of approximately 3.3192 for df 4, 261, resulting in rejection of the Null Hypothesis. Thus, it can be concluded that an interactive effect between topography and time acts to influence fibroblast adhesion.

The results of the analysis of variance indicate there are statistically significant differences between the means of the samples, however further analysis is required to identify the specific means that are statistically different. The Tukey Test allows for sensitive identification of differences between the means, and was calculated by constructing a Tukey trelis for two-way ANOVA, Table 3.7 (as outlined by Fowler et al, 1998, pp194-195). The test statistic T was calculated as follows:

$$T = (q)\sqrt{\frac{\text{within variance}}{n}}$$

$$= (4.39)\sqrt{\frac{325.18}{30}}$$

$$= \boldsymbol{14.45}$$

where q is obtained from the Tukey Table (Fowler et al, 1998, Appendix 11) and has a value of 4.39 for a=9 (total number of means being compared), and v=261 (degrees of freedom of $\text{Variance}_{\text{within}}$). n=30 (number of data used to calculate mean) and within variance=325.18 (calculated during ANOVA).

Comparisons were drawn between all sample means, by subtracting each mean and comparing it to the test statistic T, where negative signs are ignored, Table 3.7.

There are 9 out of a possible 36 pairs of means whose differences are statistically significant, bold italic values in Table 3.7. The mean number of fibroblasts adhering to planar and 20nm-diameter colloidal substrates at 20 minutes and planar and 50nm-diameter colloidal substrates at 20 minutes are statistically significant, indicating fibroblast adhesion is altered on the colloidal substrates in comparison to planar controls at 20 minutes. This could occur as a result of protein conformation alterations on the nanotopographies in comparison to controls at early times, or possibly due to physical effects occurring at the solid liquid interface, for example van der Waal's interactions. When referring to the residual plot, Graph 3.1, fibroblast adhesion is increased on the colloidal substrates at 20 minutes in comparison to planar substrates, suggesting adhesion is greater on the nanotopographies. With respect to focal adhesion contacts, cells may be stimulated by the nanofeatures, resulting in increased interactions with their surrounding via, for example

filopodia, as observed in SEM and fluorescent microscopy images, Sections 3.3.3.3 and 3.3.3.4, respectively.

Sample	2	3	4	5	6	7	8	9
Sample 1 X=33	(X_1-X_2) ***19.6***	(X_1-X_3) ***17.7***	(X_1-X_4) ***10.4***	(X_1-X_5) ***19.9***	(X_1-X_6) ***21.2***	(X_1-X_7) *6.5*	(X_1-X_8) *5.9*	(X_1-X_9) *3.6*
Sample 2 X=52.6		(X_2-X_3) *1.9*	(X_2-X_4) *9.2*	(X_2-X_5) *0.3*	(X_2-X_6) *1.6*	(X_2-X_7) *13.1*	(X_2-X_8) *13.7*	(X_2-X_9) ***16***
Sample 3 X=50.7			(X_3-X_4) *7.3*	(X_3-X_5) *2.2*	(X_3-X_6) *3.5*	(X_3-X_7) *11.2*	(X_3-X_8) *11.8*	(X_3-X_9) *14.1*
Sample 4 X=43.4				(X_4-X_5) *9.5*	(X_4-X_6) *10.8*	(X_4-X_7) *3.9*	(X_4-X_8) *4.5*	(X_4-X_9) *6.8*
Sample 5 X=52.9					(X_5-X_6) *1.3*	(X_5-X_7) *13.4*	(X_5-X_8) *14*	(X_5-X_9) ***16.3***
Sample 6 X=54.2						(X_6-X_7) ***14.7***	(X_6-X_8) ***15.3***	(X_6-X_9) ***17.6***
Sample 7 X=39.5							(X_7-X_8) *0.6*	(X_7-X_9) *2.9*
Sample 8 X=38.9								(X_8-X_9) *2.3*
Sample 9 X=36.6								

Table 3.7: Tukey trelis for 2-way ANOVA. Samples correspond to those used in the Contingency table, Table 3.5. Test statistic T=14.45. There are 9 out of a possible 36 pairs of means whose differences exceed this value and whose differences are statistically significant at P=0.05 (highlighted in bold italic).

Significant differences were also calculated between the number of cells adhering to the planar at 20 minutes and 20nm-diameter colloids at 1 hour and planar at 20 minutes and 50nm-diameter colloids at 1 hour, once again indicating alterations in cell response to colloidal nanotopographies at 1 hour in comparison to the planar control at 20 minutes. A further significant difference is recorded between cells adhering to 50nm-diameter colloids at 1 hour and planar at 3 hours, again highlighting differences in fibroblast adhesion between experimental and control substrates at different time intervals. Furthermore, significant differences were calculated between fibroblast adhesion on the 20nm- and 50nm-diameter colloidal substrates at different time (20nm-diameter colloids at 20 minutes and 50nm-diameter colloids at 3 hours, 20nm-dimaeter colloids at 1 hour and 50nm-diameter colloids at 3 hours, 50nm-diameter colloids at 1 hour and 20nm-diameter colloids

at 3 hours). These results indicate that different cell-substrate interactions are occurring between the different nanotopographies at different time points. Interestingly, cell adhesion on the 50nm-diameter colloids at 1 hour and 50nm-diameter colloids at 3 hours are significantly different, suggesting temporal alterations may occur between the fibroblasts and the 50nm-diameter colloidal topography, possibly via alterations in FAC assembly and disassembly. With reference to the residual plot of fibroblast adhesion means, Graph 3.1, a reduction in cell adhesion is observed on the 50nm-diameter colloids at 3 hours in comparison to 1 hour. This may occur as a result of reduced cell-substrate interactions during cell motility, where cells have been observed to catapult across the colloidal substrate at this time, Section 3.3.3.1.2.

3.3.3.3 hTERT Cell Morphology on Colloidal Topographies - Scanning Electron Microscopy

hTERT fibroblasts were seeded at a density of 10,000 per ml in 3mls media on planar, 20nm- and 50nm-diameter colloidal topographies, fixed and critically point dried, Section 2.7.3, at 20 minutes, 1 hour, 3, 8, 24 and 48 hours. Samples were then imaged using a Hitachi S-900 field emission scanning electron microscope (FESEM).

Fibroblasts fixed and treated for use with the SEM at 24 and 48 hours were confluent, resulting in loss of cells on some of the substrates. Thus, only fibroblasts seeded on planar and 20nm-diameter colloidal substrates were imaged at 24 hours, as cells on the 50nm-diameter colloidal topography were washed from the sample as a sheet. Similarly, all samples at 48 hours were devoid of cells, washing from the surface as a sheet during dehydration suggesting over-confluent growth, possibly due to initial high seeding densities on the experimental substrates.

3.3.3.3.1 Fibroblast morphology at 20 minutes

At 20 minutes, fibroblasts on the planar substrate appear to have adhered, and are in the process of settling on the surface, with some early signs of spreading, Figure 3.40a)-b). The apical membrane exhibits protrusions similar to lamellapodia, where the cells are sensing their surrounding environment and distinguishing between basolateral and apical regions. Lamella ruffling is observed, Figure 3.40a), suggesting cells are beginning to spread and

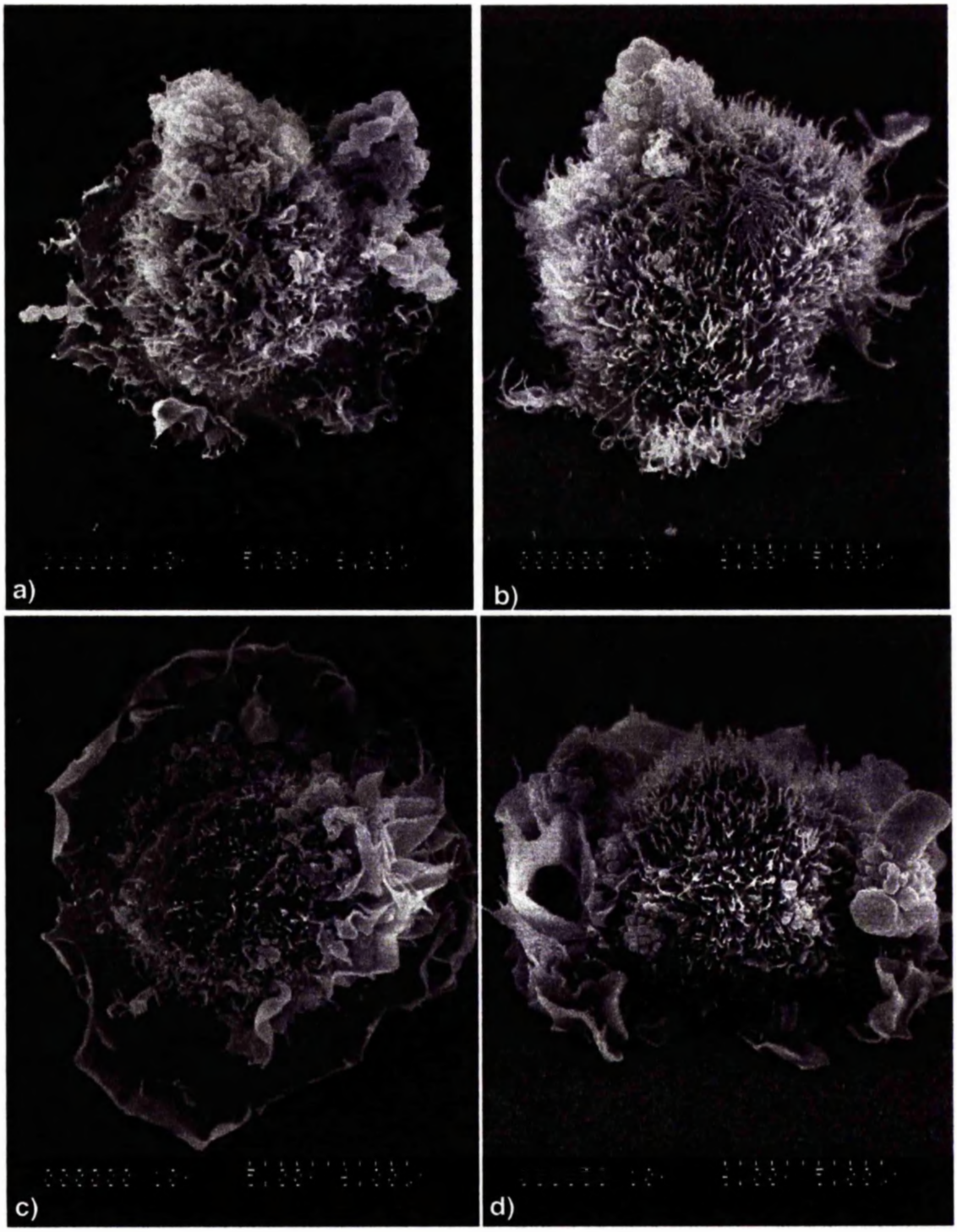

Figure 3.40: Scanning electron micrographs, captured using the Hitachi S-900, of hTERT fibroblasts on control, planar substrates, a) and b), and 20nm-diameter colloidal topographies, c)-f) at 20 minutes (continued overleaf). Cells on the planar topography display spread, a) or spreading, b), morphology, with many membrane protrusions occurring on their apical surface at 20 minutes. On the 20nm-diameter colloidal topography, fibroblasts were observed to either be well spread, c) and d), or rounded, with a basolateral layer of filopodial features supporting the cell on the nanotopography, e)-f). Spread cells on the 20nm-diameter colloidal structures displayed smoother lamella extensions in comparison to their control counterparts.

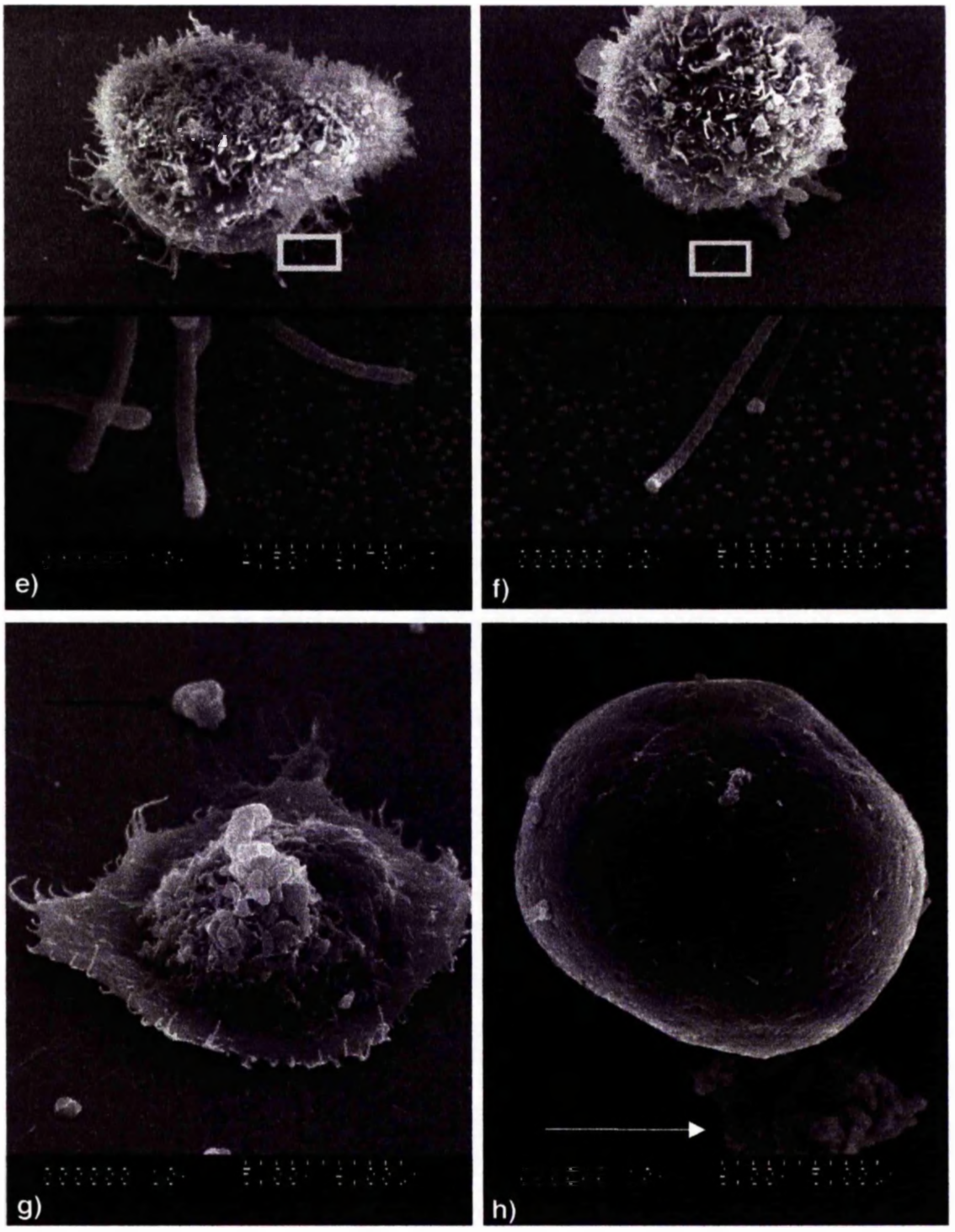

Figure 3.40 continued: Scanning electron micrograph, captured using the Hitachi S-900, of hTERT fibroblasts on 20nm-diameter colloidal topography, e) and f), and 50nm-diameter colloidal topography, g) and h) at 20 minutes. Fibroblasts on the 20nm-diameter colloidal structures were spread, c) and d), or elevated from the nanotopography by filopodia-like features, e) and f). Protrusions close to the cell body, e), appear thicker than those which extend further from the main bulk of the fibroblast, f). Fibroblasts on 50nm-diameter colloidal topographies were spread, g), similar to those on the 20nm-diameter colloids, or very rounded, h), with few characteristic cellular features. Arrows in g) and h) indicate the presence of cellular debris.

traverse the underlying planar surface. Immediately behind these regions, the cell membrane appears smooth, Figure 3.40a), again suggestive of cell spreading. Other hTERT fibroblasts within this population exhibit elongated protrusions at 20 minutes, indicating anchoring and adhesion development on the planar substrate, Figure 3.40b). These extensions appear to extend from the cell perpendicular to its peripheral membrane.

Fibroblasts on the 20nm-diameter colloidal substrate are also observed to have adhered to the surface at 20 minutes, Figure 3.40c)-d). However, in comparison to their counterpart controls, greater membrane ruffling is observed, Figure 3.40d), and cells appear more spread, Figure 3.40c), at this early time. The membrane immediately behind the ruffling periphery also appears smoother than previously observed with respect to fibroblasts on the planar control, resulting in fibroblasts with a smoother appearance, Figure 3.40c) and d). Fibroblasts on the 20nm-diameter colloidal topography are also observed to exhibit very rounded forms, with membrane protrusions occurring both on the apical and basolateral surfaces, Figure 3.40e) and f). Lamellapodia and filopodia extending towards the colloidal topography often appear to support the cell above the substrate, Figure 3.40e). As an early reaction to the nanotopography, these features are likely to be involved in initial adhesion of the cell to the substrate surface, acting as individual anchor points as opposed to the expression of adhesion sites by the majority of the underlying membrane. These protrusions appear thicker when closer to the cell body compared to their more extended state. Filopodia may sense more remote regions of the nano-patterned environment as these features are often observed to extend some distance from the main cell body, Figure 3.40f). Furthermore, the most elongated protrusion in Figure 3.40f) appears to be stationed at approximately the same height as the colloids in the z-plane, suggesting that upon contacting the colloids, the cell extension cannot interact with the immediately surrounding planar regions. Regardless of their function, these elongated membrane protrusions must be capable of adhering to the surrounding substrate due to the observed interactions with the underlying topography, Figure 3.40f).

hTERT fibroblasts on the 50nm-diameter colloidal topography at 20 minutes similarly displayed one of two forms. Firstly, cells can be spread on the 50nm-diameter colloids, Figure 3.40g), as observed in fibroblasts on the 20nm-diameter colloidal topography. Once again, the membrane immediately behind the periphery of the cell appears

smooth, and fibroblasts appear more spread than their control counterparts on the planar substrate, Figure 3.40a) and b). Cellular debris or possibly protein globules are also observed, indicated by arrows, Figure 3.40g) and h). In many instances throughout this fibroblast population on the 50nm-diameter colloids at 20 minutes, cells appear very rounded and display few features associated with more active counterparts, Figure 3.40h). Initially these globular cells were difficult to identify due to their lack of membrane features. However, their occurrence across the 50nm-diameter colloidal topography was so great that, regardless if they were cells, their occurrence was noted. Upon further inspection, very slight protrusions, seen in more detail in spread cells, were observed and the size of these entities corresponded with more developed rounded fibroblasts. In these instances, fibroblasts would appear to be highly polarised with respect to internal and external environments. However, there appears to be a lack of distinction between apical and basolateral polarity. Yet cells must have formed some type of adhesion with the nanopatterned substrate if they are still present on the surface following EM processing, Section 2.7.3.

3.3.3.3.2 Fibroblast morphology at 1 hour

hTERT fibroblasts on the control planar substrate appear rounded, with little indication of spreading on the surface at 1 hour, Figure 3.41a) and b). This is unusual when considering more spread cells were observed on the planar structures following 20 minutes of contact, suggesting that these cells were settling on the surface rather than spreading, Figure 3.40a) and b). Elongated protrusions are observed to radiate from rounded cells at 1 hour, Figure 3.41a) and b), suggesting cells are in the process of anchoring and adhering to the substrate. When viewed at a 40° tilt in the positive direction, fibroblast height appears great, again highlighting the lack of spreading in the control cells. The apical membrane is also observed to be littered with protrusions, Figure 3.41a) and b), suggesting discrimination between apical and basolateral regions.

Fibroblasts on the 20nm-diameter colloidal topography exhibit a range of morphologies at 1 hour, Figure 3.41c)-h). Some fibroblasts appear similar in shape to those observed on the control substrate, Figure 3.41c). However, only fine extensions were observed in the control-cell population, whereas, in instances on the 20nm-diameter colloidal topography, thin filopodia are permeated by thicker membrane, indicating cell spreading. The most notable difference at 1 hour between fibroblasts cultured on the planar substrate and 20nm-diameter colloids is the presence of well spread cells on the

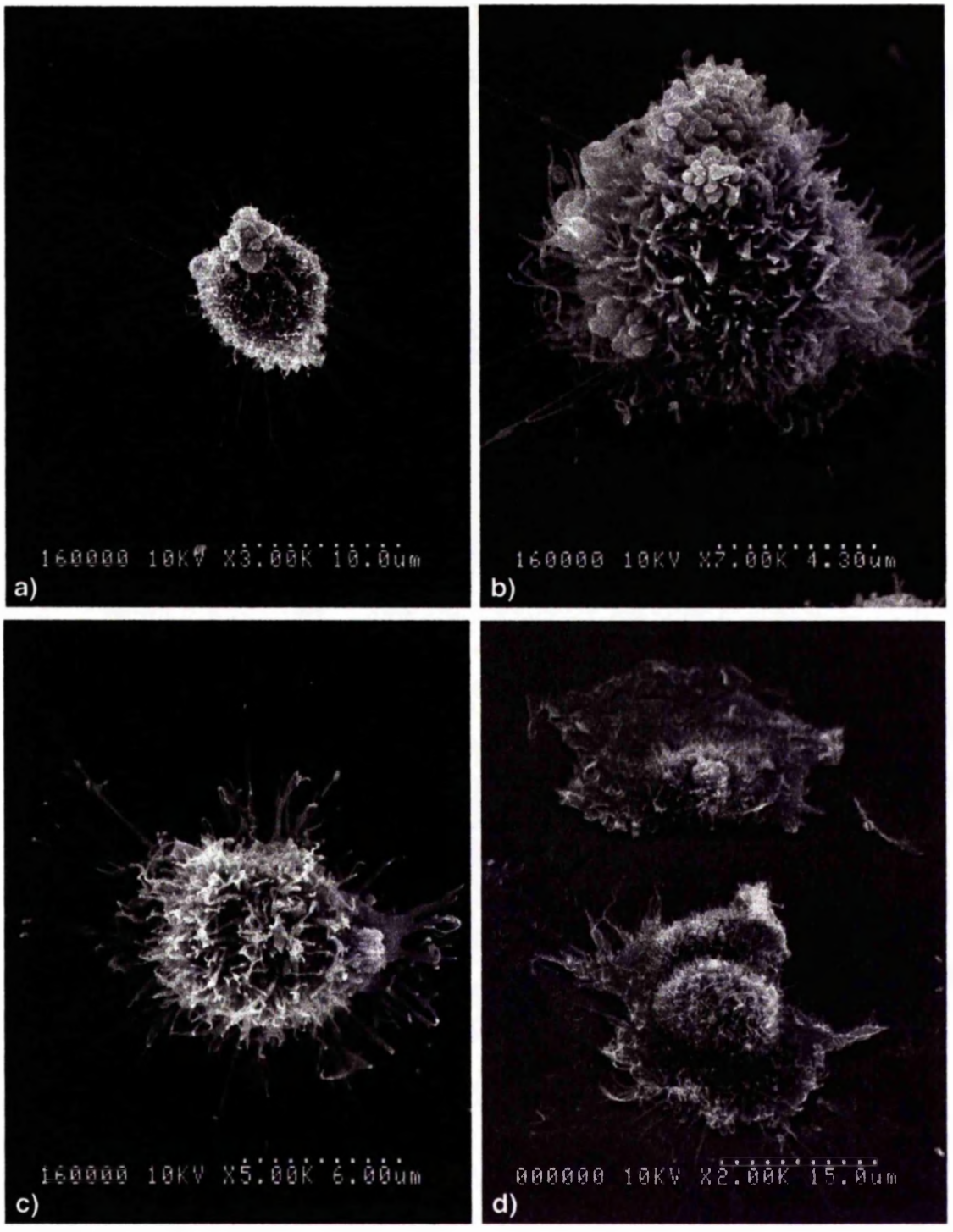

Figure 3.41: Scanning electron micrograph (Hitachi S-900) of hTERT fibroblasts on planar control, a)-b) and 20nm-diameter colloidal topography, c)-h), at 1 hour. Cells on the planar substrates appear to anchor themselves via elongated filopodia protrusions, a) and b). The majority of the fibroblast population appear in this stage of adhesion, with few cells exhibiting spread morphology. When viewed at a 40° tilt in the positive direction, b), cell height appears greater than if cells were more spread and flattened, again suggesting this process is lacking. Fibroblasts on the 20nm-diameter colloidal topography also display similar anchorage morphology, c), however, the thin filopodia appear to act as guide lines for further membrane development. Possibly as a result, many of the fibroblasts on the nanotopography appear flattened and well spread, d).

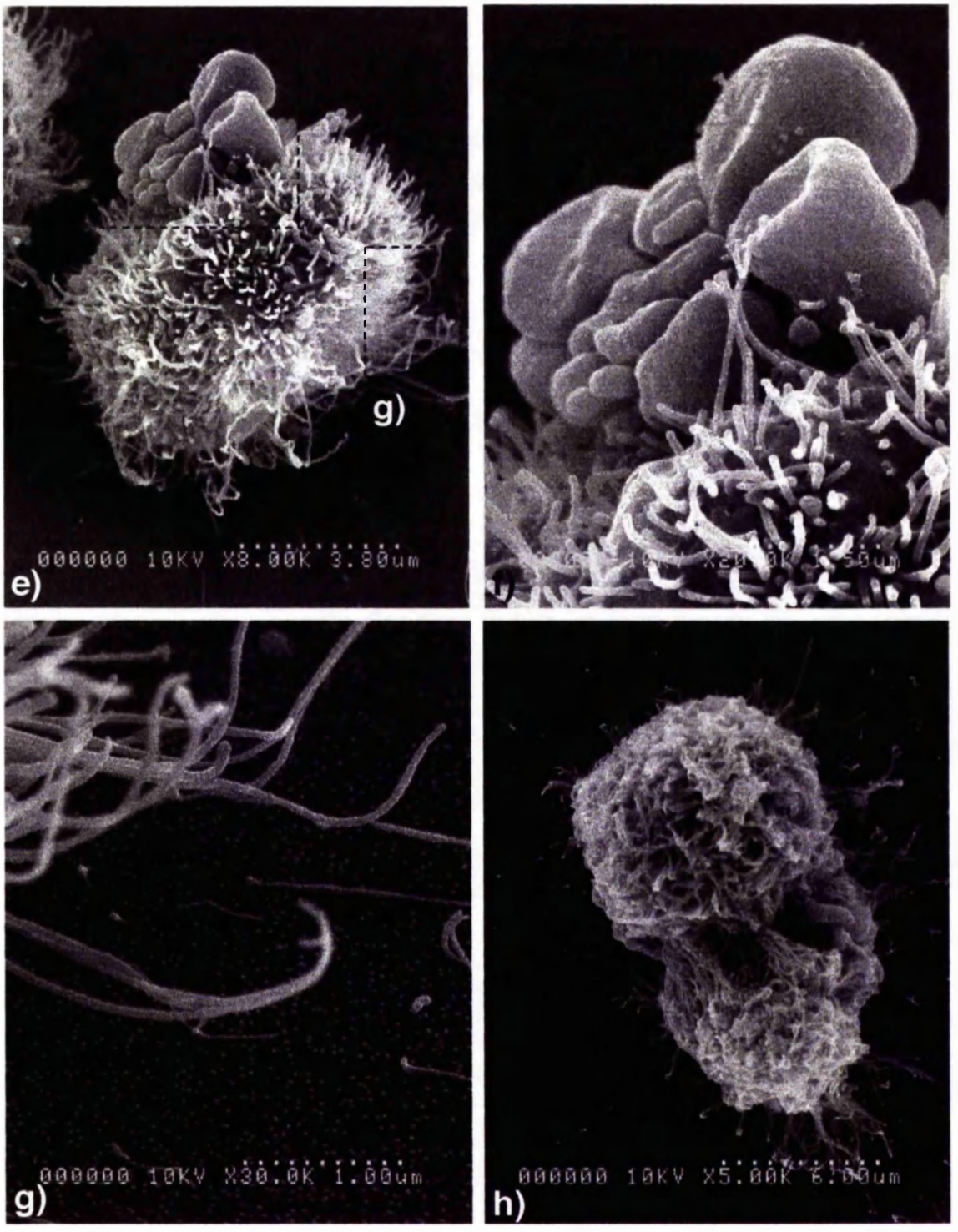

Figure 3.41 continued: Scanning electron micrographs of hTERT on 20nm-diameter colloidal substrates at 1 hour. Cells are observed to be in a spread state, d), or rounded, e), with many membrane protrusions, f) and g). The boxed areas in e) represent higher magnification of specific features, where f) and g) are displayed in more detail. Clustered membrane features are observed at this time, f), although they have not been positively identified. Protrusions, similar to filopodia are also seen to occur between the cell and its surrounding topography, g). Filopodia-like extensions were observed in abundance when cells were in contact with one another, possibly in the process of dividing, h).

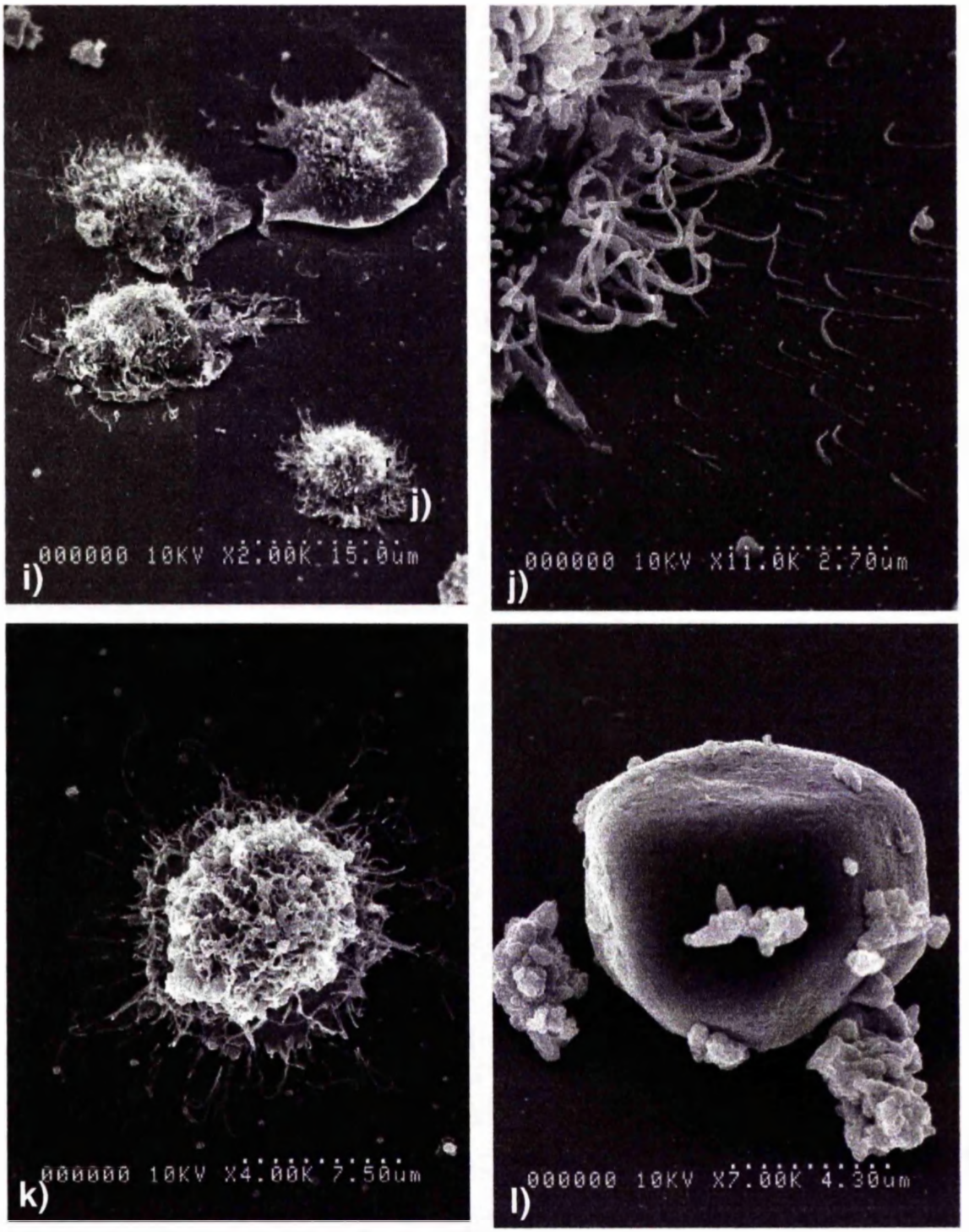

Figure 3.41 continued: Scanning electron micrographs of hTERT fibroblasts on 50nm-diameter colloidal substrates at 1 hour. Cells are observed to be spread, i), spreading, k), or very rounded with little distinguishable external cellular features, l). Rounded fibroblasts, l), display shape and morphology similar to rounded cells observed on 50nm-diameter colloids at 20 minutes. Spread or spreading cells, i) and k) respectively, exhibit a generally smooth peripheral lamella, with spiky nuclear regions. Filopodia extensions, j), appear to act as anchor sites between the fibroblasts and the nanotopography, and appear to act as an intermediate step between cell adhesion and spreading.

nanotopography, Figure 3.41d). Again, as observed at 20 minutes, the extent of spreading suggests possible stimulation of the cells by the colloidal topography in comparison to control fibroblasts. Spread cells are generally highly polarised in an apical and distolateral manner, resulting in differentiation between the underlying substrate and surrounding environment required for this type of behaviour. The uneven appearance of the apical membrane and presence of localised protrusions extending away from the cell body in distal and lateral areas also suggests cell polarisation in this axis more readily associated with cell movement and translocation.

Rounded fibroblasts are also observed on the 20nm-diameter colloidal topography at this time, Figure 3.41e) and h), appearing similar to the rounded fibroblasts observed on the colloidal topography at 20 minutes, Figure 3.40. Once again, rounded fibroblasts appear to be elevated from the nanotopography, Figure 3.41e), and exhibit a number of fine membrane protrusions extending away from the main body towards the colloidal substrate, Figure 3.41g). These extensions appear to act as anchorage points, the remains of which are observed on the nanopatterned surface, Figure 3.41g). This possibility is further compounded when examining the distribution of filopodia in fibroblasts dividing at 1 hour on the 20nm-diameter colloidal substrate, Figure 3.41h). The migrational axis required during cell division must originate from cell-substrate adhesions. In this image, cell alignment indicates the development of such an axis running diagonally, from top left to bottom right. Positioning of filopodia also appear to align parallel to the cells, suggesting the implications of the protrusions in both cell-substrate adhesion and cell directionality. Colloids appear to underlie these anchors, depicted by arrows in Figure 3.41g). It may be deduced that these protrusion remnants are robust in comparison to connecting areas where they have broken during EM processing. Furthermore, this observation indicates the occurrence of adhesive interactions between areas of the protrusions and the surrounding substrate, in particular between the basolateral membrane of the extensions and underlying colloids.

An, as yet, unidentified globular cluster is also observed on the rounded cell imaged in Figure 3.41e), viewed at greater magnification in Figure 3.41f). The possibility of this feature occurring whilst the sample underwent dehydration has been rejected, as membrane blebbing would be more frequent throughout the population of cells. As each individual section of the cluster appears similar to its neighbouring region, it is likely that this feature is composed of a number of similar or equal entities.

Fibroblast morphologies on the 50nm-diameter colloidal topography at 1 hour share similarities with cells seeded on the 20nm-diameter colloids at this time. In some instances, cells are observed to be spread, Figure 3.41i), or in the process of spreading, Figure 3.41i) and k). One of the spread cells also appears in the process of distal-lateral polarisation, top right in Figure 3.41i), suggestive of motile behaviour. Spreading cells, Figure 3.41k), display similar processes with respect to their counterparts on the 20nm-diameter colloidal topography, namely, elongated protrusions. These appear firstly to have anchored the cell in position and act as guides for larger areas of pervading membrane, Figure 3.41k), almost comparable to an umbrella and its associated spokes. Rounded cells, Figure 3.41i), display radiating protrusions, Figure 3.41j). This behaviour previously observed in fibroblasts on the 20nm colloids at this time, Figure 3.41e) and g). Membrane protrusions radiating from the rounded fibroblast on the 50nm-diameter colloids have adhered to the substrate, Figure 3.41j), once again suggesting their role in anchoring the cell to the surrounding substrate. As previously observed at 20 minutes, extremely rounded cells with little or no distinguishable surface features are present at 1 hour on the 50nm-diameter colloidal topography, Figure 3.41l), suggesting polarised behaviour with respect to internal and external environments. The fibroblast in this instance also appears to have cellular debris or proteins located at the membrane surface, Figure 3.41l).

3.3.3.3.3 Fibroblast morphology at 3 hours

Fibroblasts on the planar substrate at 3 hours exhibit spread, Figure 3.42a), rounded, Figure 3.42b) or elongated, Figure 3.42d), morphologies. Apical membrane surfaces appear spiky in all instances. Membrane protrusions are observed at the periphery closest to the planar substrate in spread fibroblasts, Figure 3.42a), and appear to act in both anchorage and contractile behaviour associated with this morphology. Rounded cells, Figure 3.42b), indicate the fibroblast population on the flat surface at 3 hours may be at different stages within the cell cycle. Protrusions occurring at the periphery of cells are shorter and thicker in rounded fibroblasts on the planar substrate, Figure 3.42b) and c), in comparison to their spread neighbours, Figure 3.42a). Furthermore, the peripheral protrusions observed at 3 hours on the control substrate, Figure 3.42b) and c), do not appear to interact directly with the surrounding surface, unlike those observed in cells at earlier times on the colloidal topography, Figure 3.40e)-f) and 3.41d), g) and h). Elongated cells in the control population at 3 hours suggest motile behaviour and

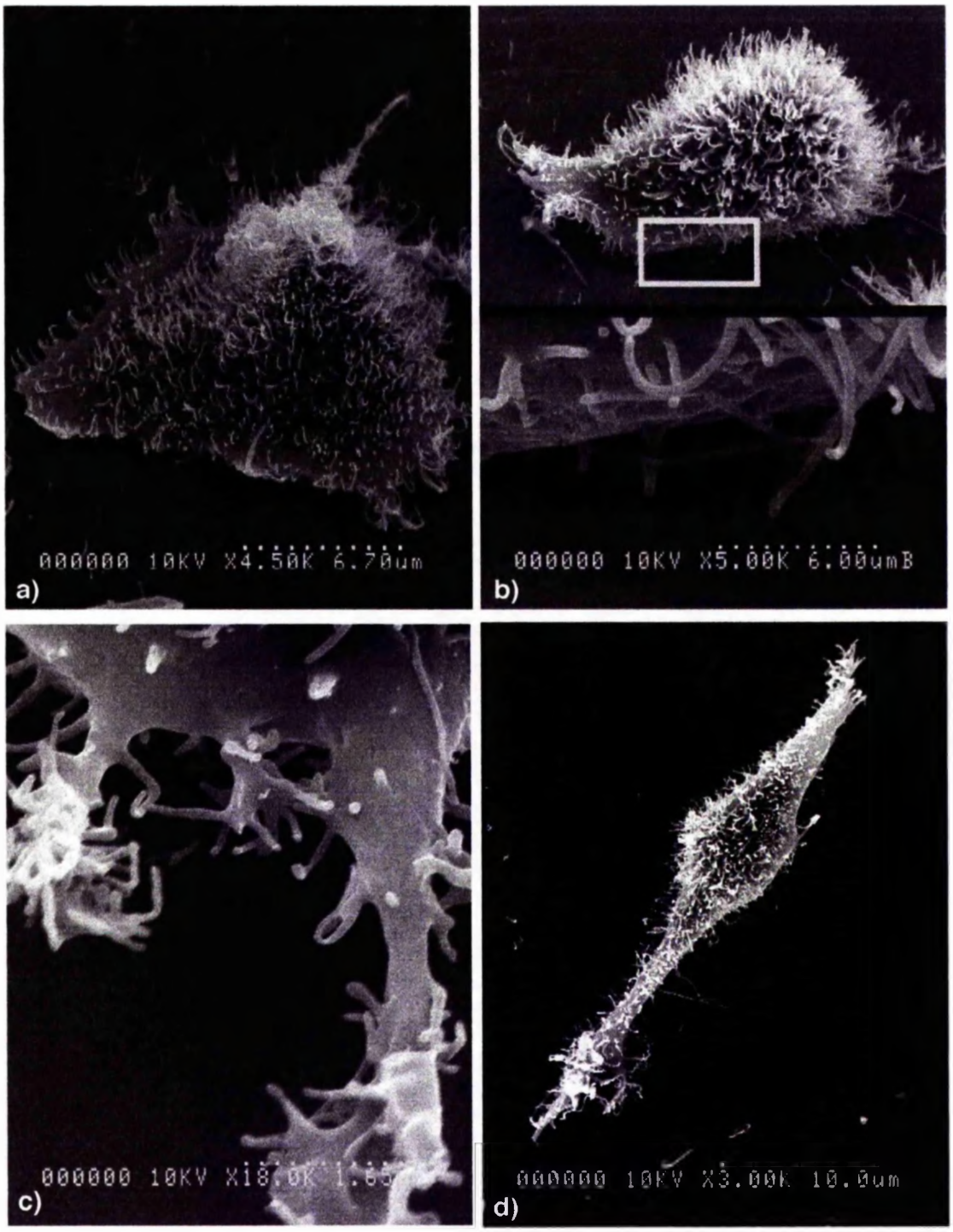

Figure 3.42: Scanning electron micrographs, using a Hitachi S-900, of hTERT fibroblasts on planar, control surfaces at 3 hours. Fibroblasts appear spread, a), with membrane protrusions radiating from the main body, rounded, b) with peripheral extensions, b) and c), or traversing the planar surface, d). Cells exhibit spikes of membrane on the apical surface and also at the periphery closest to the planar substrate. Peripheral extensions observed in fibroblasts on the planar substrate at 3 hours do not appear to interact directly with the underlying flat surface, b) and c).

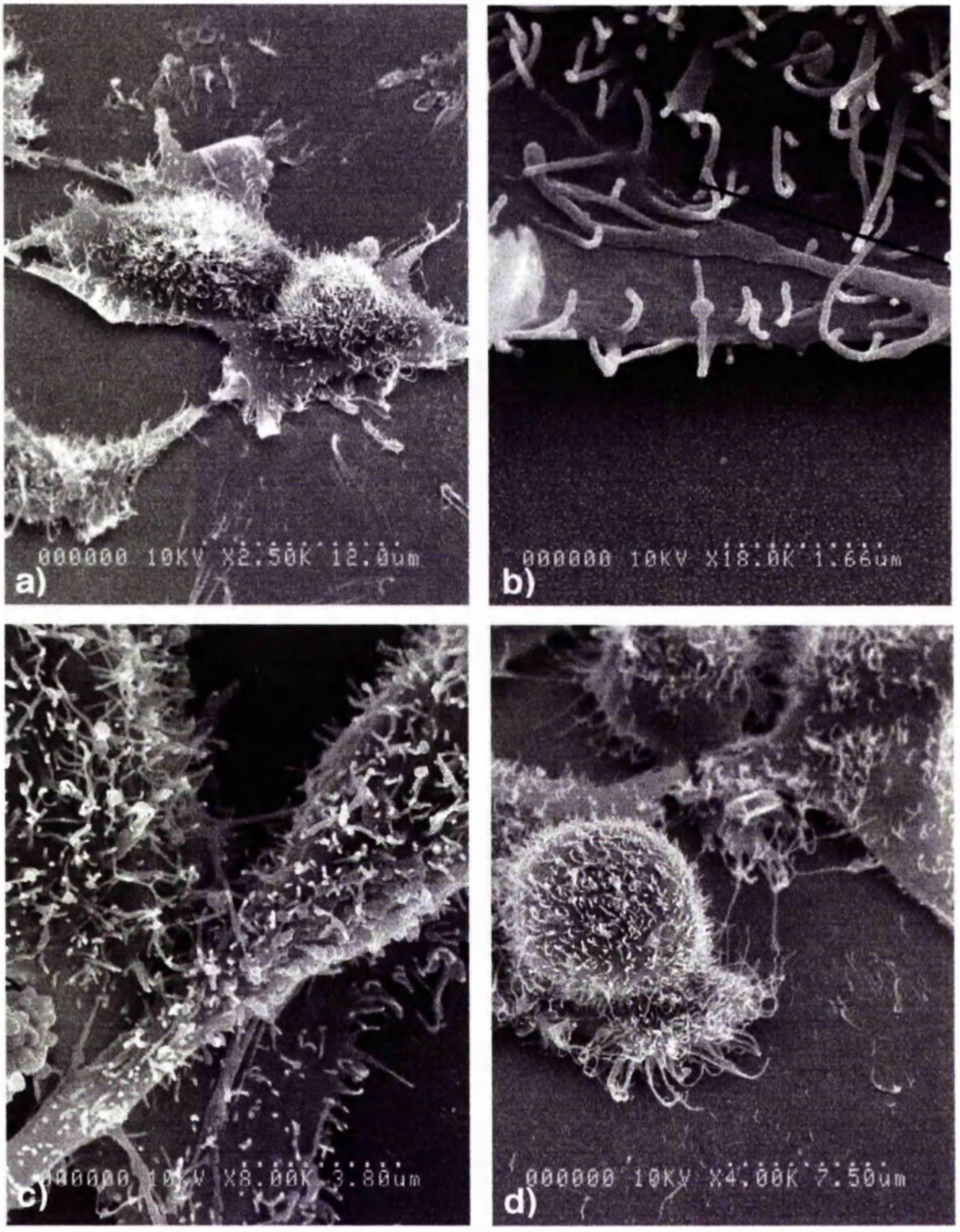

Figure 3.43: Scanning electron micrographs, using a Hitachi S-900, of hTERT fibroblasts on 20nm-diameter colloidal topography at 3 hours. Cell-cell contacts occur throughout the cell population at this time period on the nanotopography. Contacts between individual fibroblasts appear to occur via membrane protrusions, b) and c). Furthermore, cells are also observed poised upon one another, c) and d). Most cells appear well spread, a)-d), on the 20nm-diameter colloids at 3 hours.

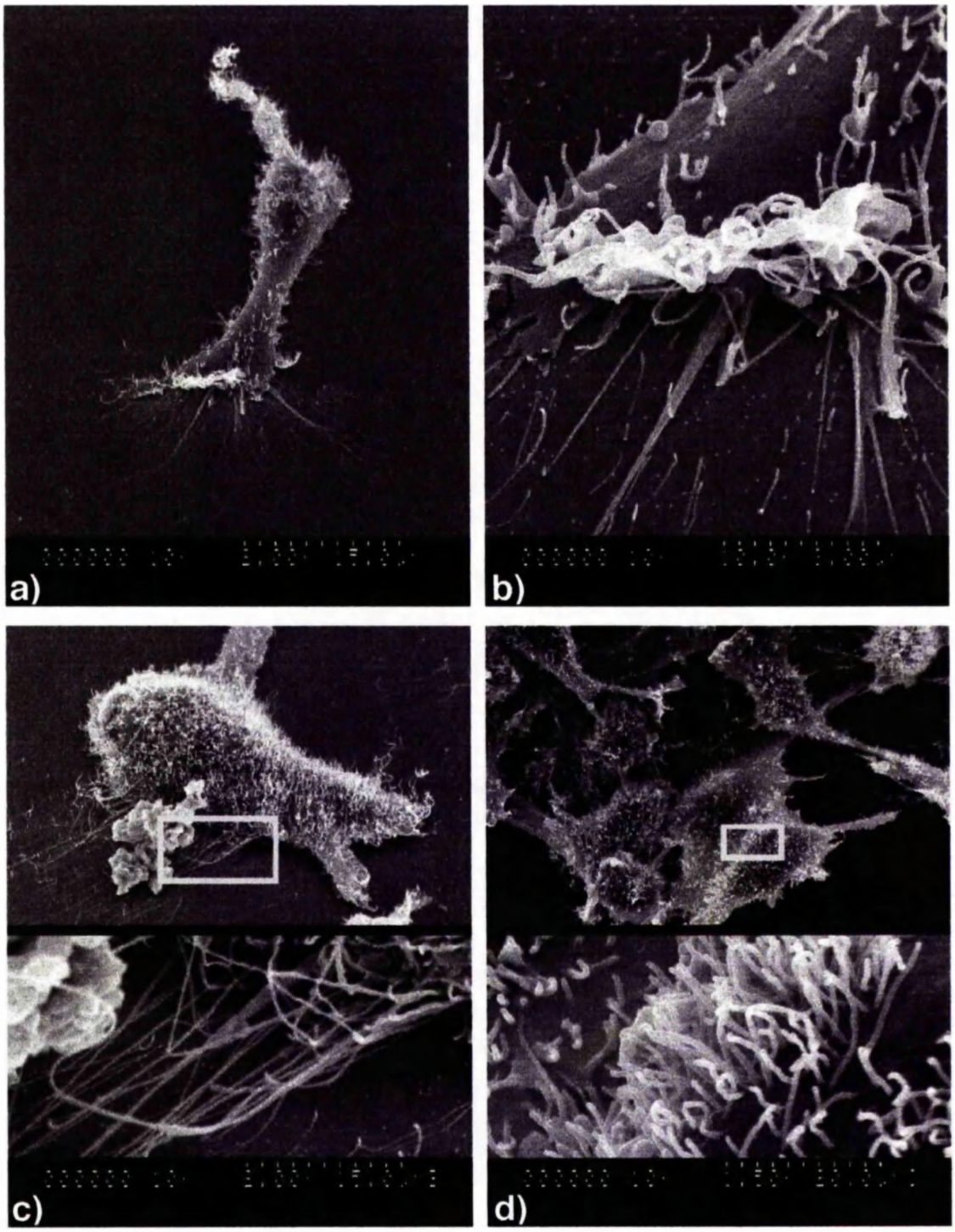

Figure 3.44 Scanning electron micrograph, captured using the Hitachi S-900, of hTERT fibroblasts on 50nm-diameter colloidal topography at 3 hours. Most cells appear to be in the process of moving across the colloidal topography, d), displaying many elongated membrane processes at their leading edge, b). A tangle of filopodia was also observed, c), at the periphery of cells, possibly during spreading. Fibroblasts in contact with one another were seen throughout the population, where membrane protrusions appeared to occur at areas of interaction, d). Fibroblasts in large cell aggregates also appeared to overlap, d).

translocation across the planar substrate, Figure 3.42d), at this time. Fibroblasts on the control, planar surface appear sparse, with the majority of cells occupying their own individual space.

In contrast, hTERT fibroblasts on the 20nm-diameter colloidal topography appear almost always within close proximity, if not in contact with or poised upon other cells at 3 hours, Figure 3.43a)-d). The majority of cells on the 20nm-diameter colloidal topography are observed to be well spread, Figure 3.43a) and c). Cell-cell contacts appear throughout the population, Figure 3.43a) and b), with overlapping occurring, Figure 3.43c) and in some instances, fibroblasts appear to sit directly upon other cells, rounded cell in Figure 3.43d). As with cells on the planar substrate at 3 hours, fibroblasts seeded on the 20nm-diameter colloids exhibit a spiky apical membrane, Figure 3.43a)-d). Thick, elongated protrusions extend from fibroblasts on towards neighbouring cells, Figure 3.43a), often resulting in the establishment of cell-cell contacts, Figure 3.43b). Rather than occurring via adherens junctions as previously surmised, cell-cell contacts appear to occur via physical protrusive interactions, highlighted by arrow in Figure 3.43b), where membrane elongations extend towards neighbouring cells, and, upon contact with the membrane of the neighbour, cohesion occurs.

A variety of possibilities exist to explain this observation. Firstly, fibroblasts on the 20nm-diameter colloidal substrate may not be able to distinguish between the substrate nanotopography and surfaces of fellow cells, resulting in problems differentiating between the base substrate and cell substrate. Secondly, due to the extension of very long and thin protrusions at early times, it is possible that, upon encountering the periphery of neighbouring cells these protrusions become entangled, similar to joining two stickle bricks together. This is a possible mechanism to explain some of the cell-cell contacts observed. However, the three-pronged membrane protrusion visible in Figure 3.43b) appears well formed and decisively placed when considering a chance entanglement. The final and most probable explanation is concerned with the comparable rigidity of the 20nm-diameter colloidal topography and neighbouring fibroblasts as adhesive substrates for cells. The nanopatterned substrate may not be beneficial for the establishment of contractile forces within the cell required during adhesion, spreading, motility and proliferation. However, when investigating video footage, Section 3.3.3.1, and also when considering that cells are capable of motile

behaviour resulting in contact with neighbouring fibroblasts, it would appear that the base substrate is highly efficient during these phenomena. It may be possible that the substrate is too rigid, resulting in too great a force between the cell and the surface, and, as a consequence, stress occurring throughout the cytoskeleton and across the fibroblasts may be greater than is beneficial. This may be disadvantageous, resulting in increased cell-cell contacts as a mechanism of escape by the cell from the surface, or more likely a balance between a highly rigid surface and less rigid cellular substrate. Regardless of the factors causing cell-cell contacts, it may be concluded that membrane protrusions are involved in their establishment, Figure 3.43b) and c).

hTERT fibroblasts on the 50nm-diameter colloidal topography are also observed to extend fine, elongated membrane protrusion, Figure 3.44a)-c), and establish cell-cell contacts at 3 hours, Figure 3.44d). Cells often appear elongated, Figure 3.44a), suggestive of movement across the substrate surface. Upon closer investigation, Figure 3.44b), the colloids appear sparsely patterned across the base substrate, where protrusions radiate from the membrane periphery in close contact with the surface. Once again, fine, thin elongations appear to have an anchorage function with respect to the cell body and underlying substrate, Figure 3.44c). This image suggests the main cell body is slightly elevated from the underlying substrate. Filopodia-like extensions appear roughly parallel to one another, indicating the direction of stress occurring at the cell periphery in this instance. These elongated membrane extensions also appear very tangled, Figure 3.44c), and project some 5 to 10μm across the colloidal patterned substrate. Fibroblasts composing aggregates, Figure 3.44d), as previously observed on the 20nm-diameter colloidal topography at 3 hours, appear to attach to one another via membrane interactions. These cells often appear elevated from the surface, frequently traversing neighbouring fibroblasts. This type of behaviour was previously noted in hTERT fibroblasts cultured on the 20nm-diameter colloidal substrates at 20 minutes, Figure 3.40e) and f).

3.3.3.3.4 Fibroblast morphology at 8 hours

Fibroblasts seeded on the planar control at 8 hours are beginning to display morphologies similar to these observed in cells on the nanotopographies at earlier times, Figure 3.45a)-d). For example, more elongated filopodia structures project from the peripheral membrane, Figures 3.45b) and d). Lamellapodia are also observed between the cell and underlying planar substrate, Figure 3.45a), however, these projections

appear thicker and less elongated in comparison to protrusions observed on the nanotopography, resulting in non-specific cell-substrate interactions. Globular repeats are also recorded in the control cells at 24 hours, Figures 3.45b)-d), suggestive of extracellular matrix production at this time on the planar control. Although unidentified, the repetitive nature of this globular string, and the nanometric dimensions suggest the possibility of collagen production. Cell-cell contacts between neighbouring fibroblasts are also observed on the planar substrate at this time, Figures 3.45b) and d), occurring via thick, rope-like structures across large areas, rather than specific, individual membrane protrusions observed between fibroblasts on the 20nm-diameter colloidal topography at 3 hours, Figure 3.43b)-d). This observation suggests that cell-cell contacts, although seen at earlier times on the nanotopographies, are a naturally occurring feature of hTERT fibroblast behaviour.

The most notable difference between cells seeded on the planar substrate and those on the 20nm-diameter colloidal topography at 8 hours is the presence of globular entities occurring on fibroblast membranes and the surrounding substrate, Figure 3.46a)-d). Globules are attached to the apical membrane of cells, Figure 3.46a) and c), suggesting that the unidentified entities are either produced by cells, or possibly washed upon their surface during EM processing. However, as in some cases, arrows in Figure 3.46a), these globules are observed only at the membrane periphery, rather than across the entire surface. In other instances, globules appear to be encapsulated within string-like filopodia extensions, Figure 3.46b), and also at areas of the peripheral membrane. These locations suggest globules are produced by, rather than being washed onto, cells. Smaller, less rounded masses sharing similar characteristics are also observed on the apical surface of fibroblasts on the 20nm-diameter colloidal substrate at 8 hours, Figure 3.46c).

Elongated filopodia strings are present in cell-cell contact establishment, Figure 3.46b). At high magnification, what originally appeared to be a filopdia extension is observed to be string-like membrane elongations with intermittent globules running across its length, Figure 3.46d). Once again, this may be associated with extracellular matrix production due to its repetitive nature and spacing. In all instances, fibroblasts appear well spread on the 20nm-diameter colloidal substrate, especially in comparison to control counterparts at 8 hours.

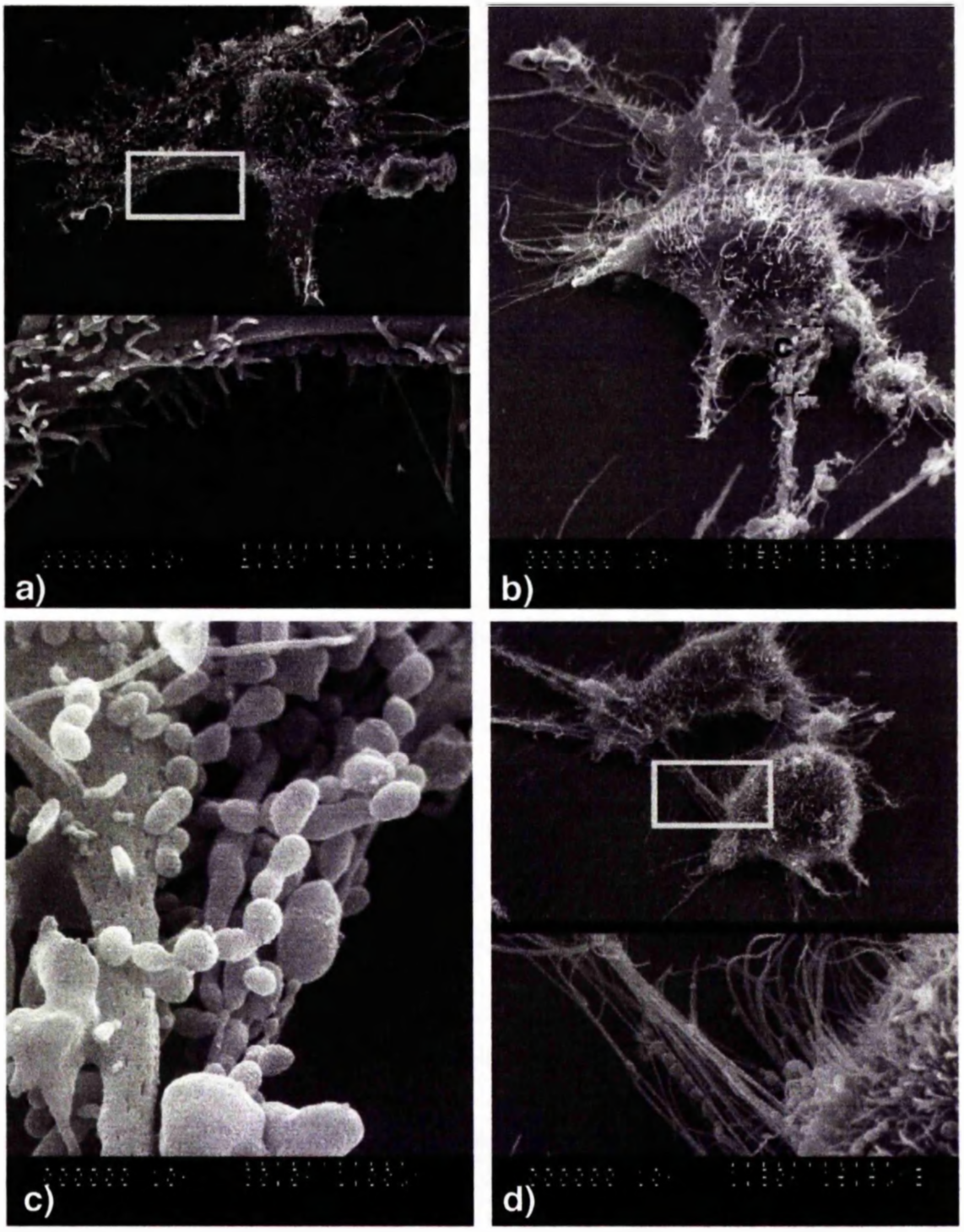

Figure 3.45: Scanning electron micrograph, captured using an Hitachi S-900, of hTERT fibroblasts on planar topography at 8 hours. Most cells appear spread at this time period, a) and b). Short membrane extensions, or lamellapodia, are seen extending towards the planar silica surface. Longer protrusions, or filopoida-like structures are also observed radiating from cells, b) and d). At 8 hours, signs of extracellular matrix production are also observed, c) and d). The boxed area in b) can be viewed at higher magnification in c). Enclosed areas in a) and d) are viewed at higher magnification in the lower portion of these images.

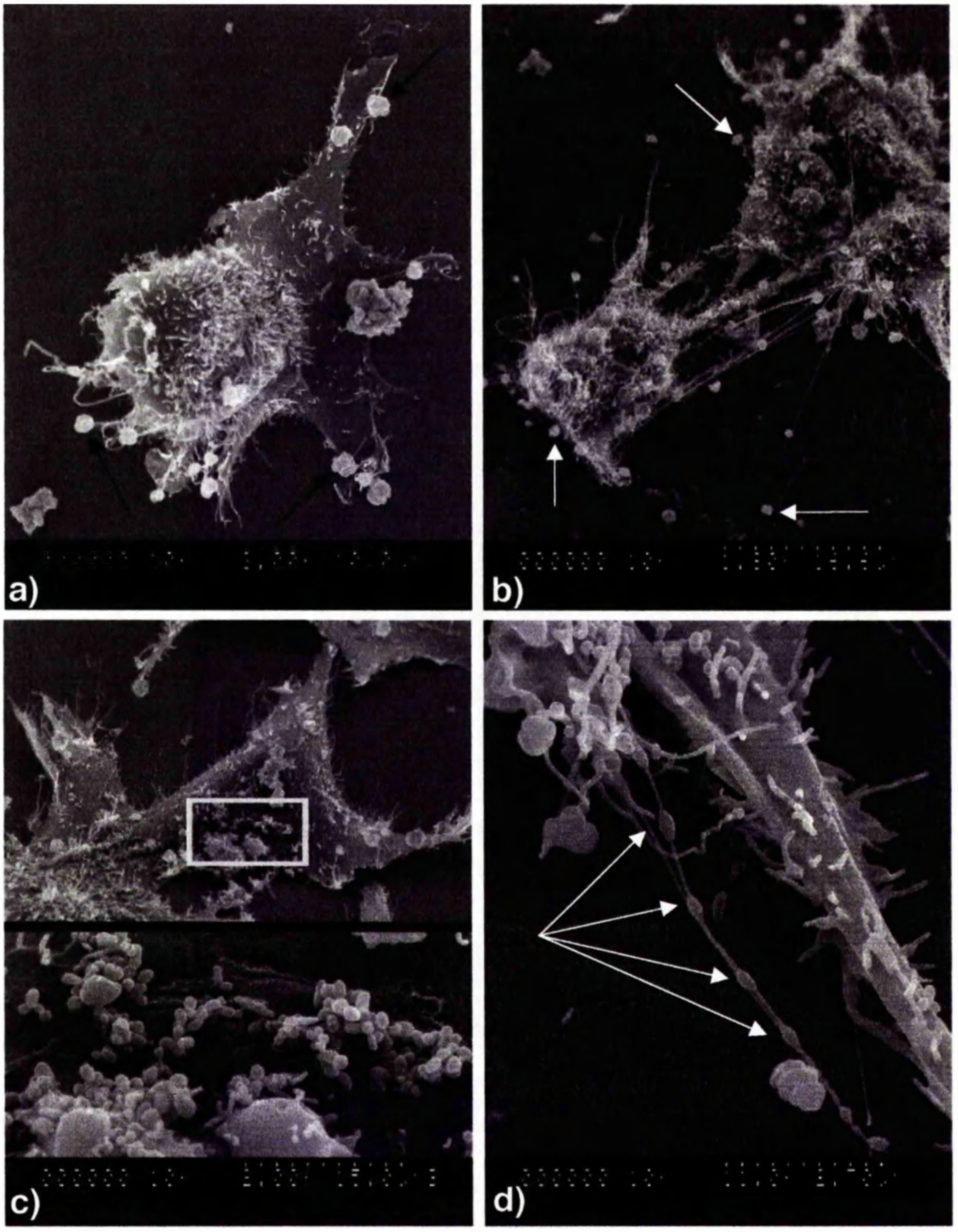

Figure 3.46: Scanning electron micrograph (Hitachi S-900) of hTERT fibroblasts on 20nm-diameter colloidal topography at 8 hours. Most cells within the population appear well spread, a)-c). In comparison to fibroblasts cultured on the planar substrates, Figure 3.45, an abundance of spherical cellular products, measuring approximately 2μm diameter are observed, arrows in a) and b). Other cellular products, similar to those observed in the control but less regular, are also seen, c) and d). The extended string of globular repeats produced by a fibroblast on the 20nm-diameter colloids, d), may share similar characteristics as elongations observed in fluorescent images, Section 3.3.3.4. Membrane protrusions similar to filopodia appear as the main linking factor during cell-cell contacts, b).

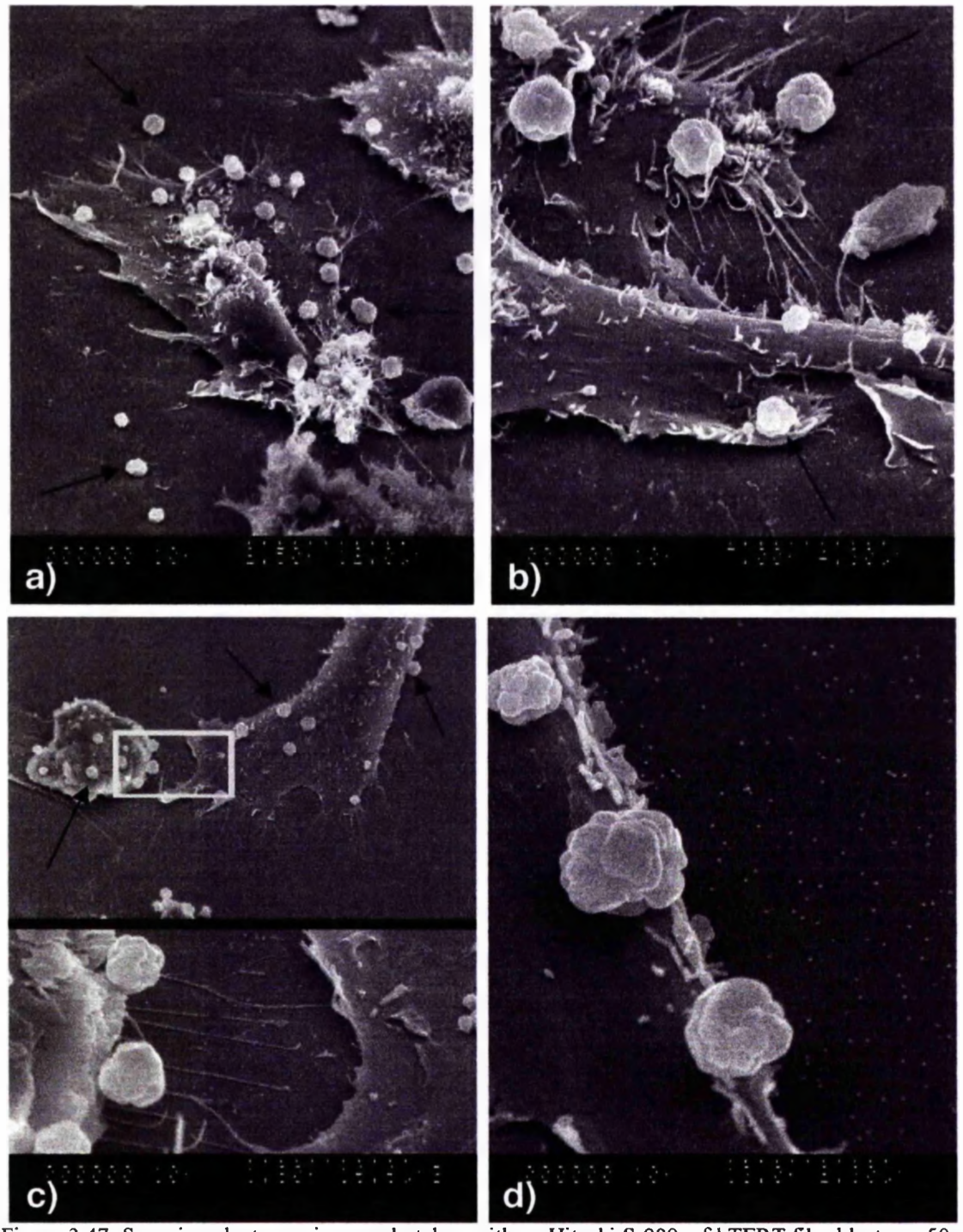

Figure 3.47: Scanning electron micrograph, taken with an Hitachi S-900, of hTERT fibroblasts on 50nm-diameter colloidal topography at 8 hours. Most cells exhibit a spread morphology, a) and c). Globular products appear both on cell membranes, and also on the surrounding colloidal surface, specifically denoted by arrows in a)-d), similar to those observed in the fibroblast population at 8 hours in contact with the 20nm-diameter colloids, Figure 3.46a)-d), both in morphology and dimensions. A comparison between the 50nm-diameter colloid dimensions and the cellular products can be seen in d). Filopodia-like extensions are also prevalent at cell peripheries at this time on the 50nm-diameter colloidal substrates, b) and c), and tend to run across the colloidal surface rather than link directly to neighbouring fibroblasts.

On the 50nm-diameter colloids at 8 hours, all fibroblasts display a greater amount of globular entities at their peripheral membrane, indicated by arrows in Figures 3.47a)-d). Cells are also observed to be more spread and flatter than on the 20nm-diameter colloidal topography at this time. Once again, elongated membrane protrusions radiate from cell peripheries, Figures 3.47a)-c). These areas often correspond to the positioning of the globules, although globules can occur at the periphery if filopodia protrusions are absent, Figure 3.47d). Although thin, elongated protrusions often appear elevated from the substrate surface when connecting neighbouring cells, Figure 3.47b), finer features are also observed to radiate across, or in very close contact with the underlying colloidal topography, Figure 3.47c).

3.3.3.3.5 Fibroblast morphology at 24 hours

Cell-cell contacts are observed, Figure 3.48a), between hTERT fibroblasts on the planar control at 24 hours although individual cells can still be found, Figure 3.48b). This occurs as a result of increased proliferation, resulting in a reduction of available surface space. Globular entities, previously observed in images of cells on the nanotopogrphies at 8 hours, are also present, both on the apical surface of fibroblasts, open arrows in Figure 3.48b), and also on the surrounding planar substrate, closed arrow in Figures 3.48b) and d). Cell-cell contacts appear to occur via thick, fibrous projections emitted from the extremities of the peripheral membrane, Figure 3.48a). Well-spread fibroblasts display filopodia from their most peripheral sites, Figure 3.48b), again implicating the function of these features in the role of anchorage and adhesion. Thin, elongated protrusions are also observed to be in close contact with the substrate surface, Figure 3.48d). Thicker, finger-like projections are present at the basolateral-substrate interface, Figure 3.48c), suggestive of motile behaviour and their role in this function. The reduced clarity of globules in cells on the planar substrate at 24 hours may be due to their different origin in comparison to those observed on the nanotopographies at earlier times.

hTERT fibroblasts on the 20nm-diameter colloidal topography exhibit distinctly different morphologies compared to their control counterparts at 24 hours, Figures 3.49a)-d). Cell-cell contacts are rife, Figures 3.49a) and b), although denuded areas of the substrate are observed, Figures 3.49a)-d). Furthermore, fibroblasts in contact with their neighbours appear to elevate their main bulk from the 20nm-diameter colloidal topography, Figure 3.49a). This observation may serve to further enhance the previous

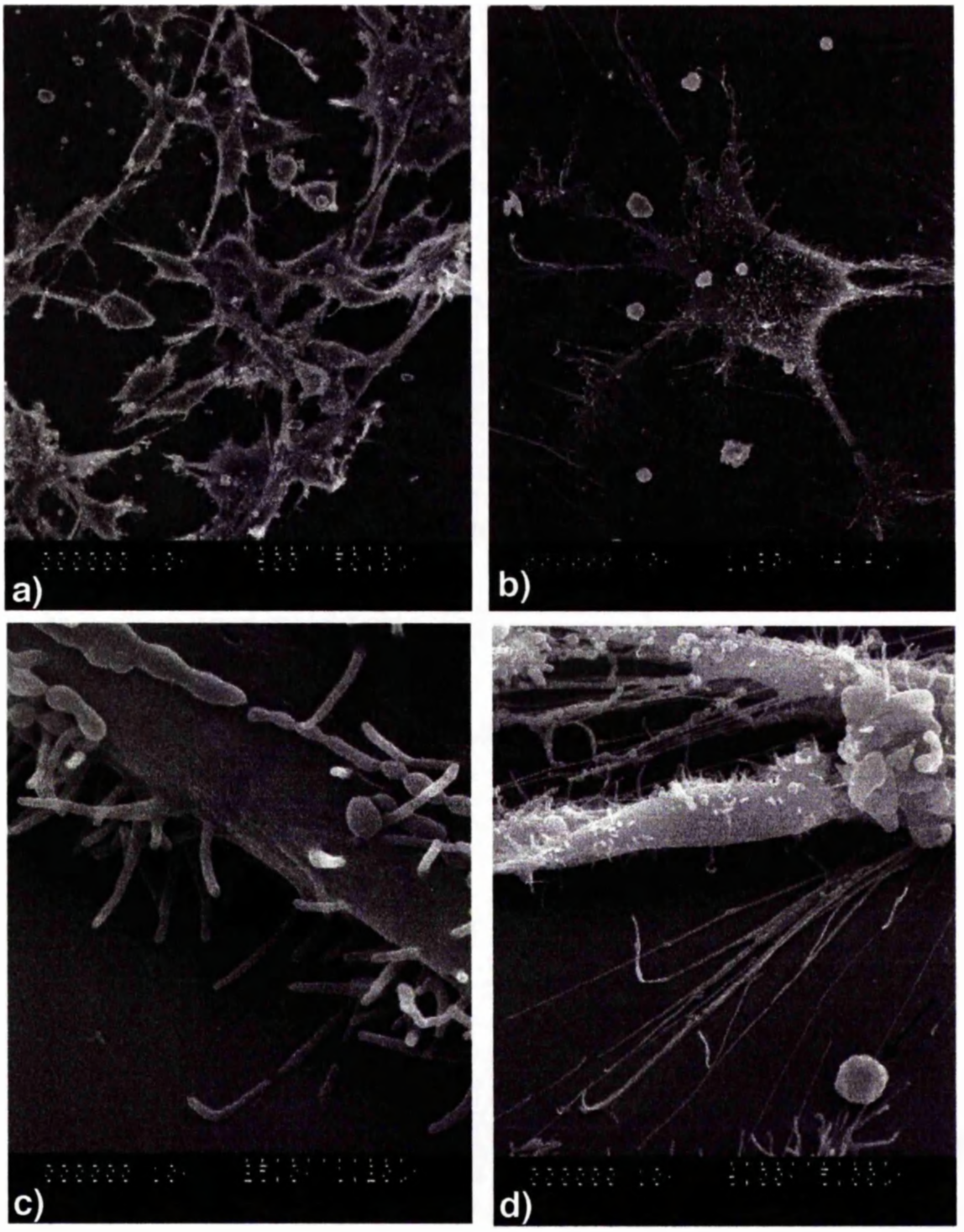

Figure 3.48: Scanning electron micrograph, imaged using the Hitachi S-900, of hTERT fibroblasts on planar control silica at 24 hours. Cell-cell contacts are observed at this time, a), unseen at earlier times suggesting increased proliferation resulting in a reduction of surface area available to fibroblasts. Individual fibroblasts can still be imaged however, b), and appear well spread on the planar substrate. Filopodia-like extensions can be seen to protrude from the membrane periphery, b) and d), and appear at the edges of flattened cells. Globular debris is also observed within this fibroblast population following 24 hours of contact with the flat surface, both surrounding cells, closed arrows in b) and d), and on the apical surface of membranes, open arrows in b). Extensions occurring at the under edge of cell peripheries, c), appear relatively short in comparison to those observed in fibroblasts on the colloidal topographies, and also the thin elongations occurring at the extremities of spread cells, b) and d).

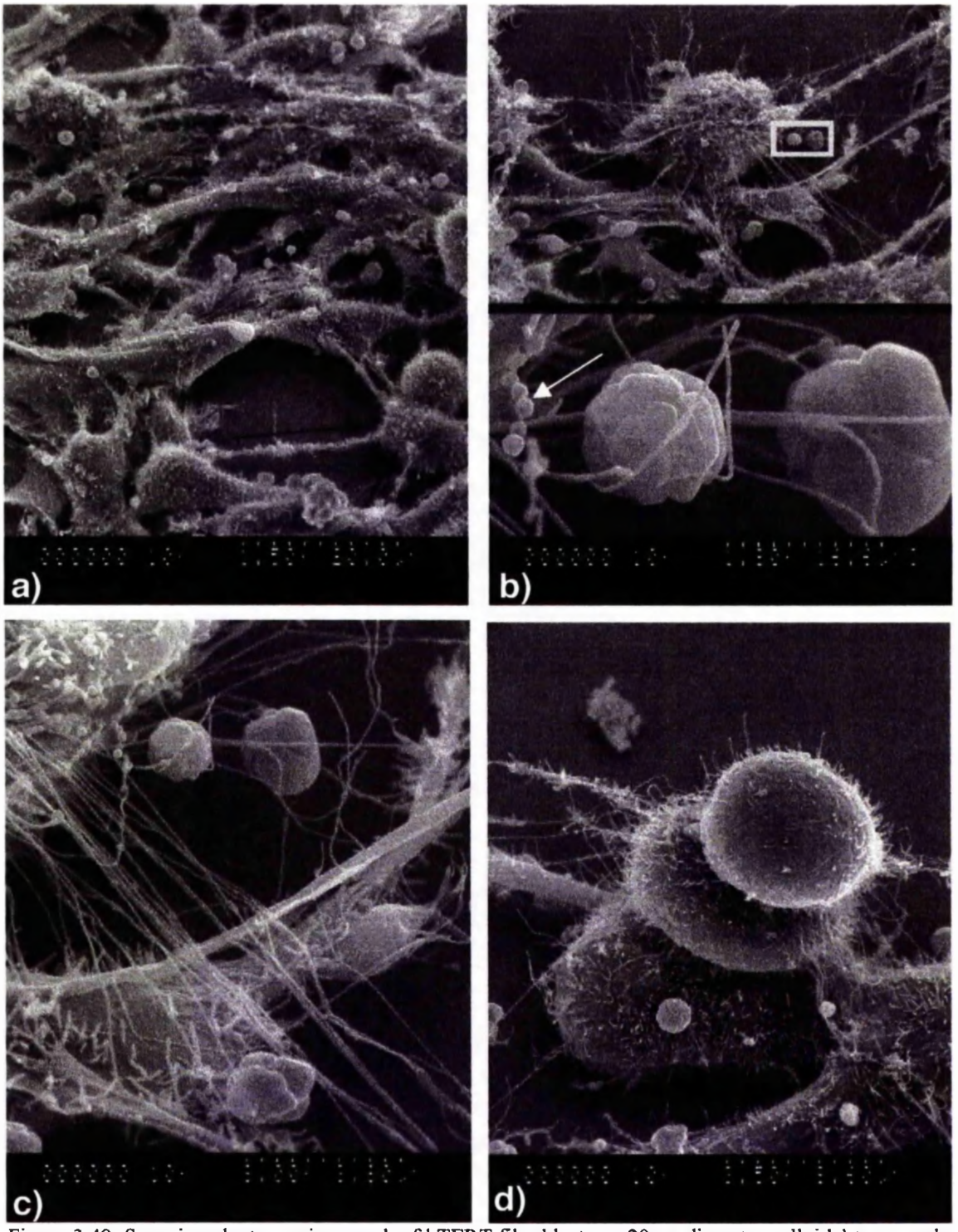

Figure 3.49: Scanning electron micrograph of hTERT fibroblasts on 20nm-diameter colloidal topography at 24 hours. Cell-cell contacts are apparent at this time between fibroblasts cultured on the 20nm-diameter colloidal topography, a). In comparison to the cell-cell contacts observed on the planar substrate at 24 hours, Figure 3.48, fibroblasts on the nanotopography appear almost to elevate their bulk above the substrate via these intracellular interactions (highlighted by arrows in a)). Many fine, string-like elongations are observed to protrude from fibroblasts on the nanotopography, b) and c). The boxed area in the upper portion of b) is seen at higher magnification in the lower portion of the image. Further detail of this area is observed in c). Globules, previously observed at earlier times in fibroblast populations on the nanotopographies, and also in control populations at 24 hours, are entangled within these extensions. Protrusions from cells on the nanotopography appear elevated from the substrate. Fibroblasts are also observed not only to overlap, but actually pile upon one another, d).

hypothesis that cell-cell contacts are required to balance tensile strength occurring throughout the cytoskeleton as a result of contact with the colloidal nanotopographies. Cells elevated from the substrate via cell-cell contacts exhibit more fibrous connections than previously observed, indicated by arrows in Figure 3.49a). These thick protrusions may act as contractile arms, bridging cells and closing gaps within the aggregates, similar to the purse string effect discussed in Section 5.3. Not only are cell-cell contacts observed, cells piled upon one another are also noted, Figure 3.49d). Fibroblasts in this image are rounded, suggesting a lack of tensile strength required during spreading. However, the polarity experienced by cells on the 20nm-diameter colloidal topography at 24 hours with respect to internal and external environments and also their capabilities with regard to distinguishing between the patterned substrate and surrounding cells is brought into question.

Globular entities previously observed in samples at 8 hours are also observed on the 20nm-diameter colloids at 24 hours, Figures 3.49a)-d). In one instance, Figures 3.49b) and c), globules appear to be incorporated into protruding filopodia extensions, suggesting cell awareness of these entities. Further indications of extracellular matrix production are also observed, white arrow in Figure 3.49b), where elongated protrusions appear entangled thus raising the possibility of cell snagging or stickle bricking. This would account for the increased cell-cell contact and possibly also the elevated appearance of fibroblasts in relation to their substrate, where tension occurring via filopodia connections cause elevation of the cell mass.

Unfortunately, due to hTERT fibroblast proliferation on the planar, 20nm- and 50nm-diameter colloidal substrates, cells sheets forming on these surfaces were washed from the samples during electron microscopy preparation. As a result, no images are included with regards to cell morphology on the 50nm-diameter colloidal topography at 24 hours, and all samples at 48 hours were lost.

In summary, at 20 minutes, hTERT fibroblasts appear more spread on the 20nm-, Figure 3.40c) and d), and 50nm-diameter, Figure 3.40g), colloidal topographies in comparison to cells on the planar control, Figure 3.40a) and b). Cell membranes appear smooth and flat directly behind the lamella on the colloidal substrates, with more ruffling observed in comparison to controls. Fibroblasts exhibiting a more rounded morphology on the 20nm-diameter colloidal topography also appear to elevate their

main body above the patterned substrate via small finger-like projections occurring around the basolateral regions, Figure 3.40e) and f). In some instances on the 50nm-diameter colloids at these times, fibroblasts are very rounded, and display no obvious membrane features, Figure 3.40h), suggesting polarity establishment between internal and external environments.

At 1 hour, fibroblasts on the planar controls appear more rounded, with filopodia extensions appearing to act as an anchorage system, Figure 3.41a) and b). In contrast, fibroblasts on the 20nm- and 50nm-diameter colloidal topographies appear more spread, Figures 3.41c), d), and 3.41i) respectively. Furthermore, cells on the colloidal topographies exhibit increased filopodia protrusions, Figure 3.41c), d), g) and j) and k), rather than the symmetrical extensions observed on the planar control, Figure 3.41a). Globular features are observed on apical membranes of cells on the 20nm-diameter colloidal topography, Figure 3.41e) and f), suggestive of polarity development and protein secretion. As previously observed at 20 minutes, fibroblasts on the 50nm-diameter colloidal substrate often appear very rounded, with no definitive membrane features, Figure 3.41l).

At 3 hours, fibroblasts on the planar substrate are spread or spreading, Figure 3.42a), and also appear elongated, Figure 3.42b), suggesting motile behaviour. Although lamellapodia are observed, Figures 3.42b) and c), they do not appear as elongated as exhibited by cells on the nanotopography. Furthermore, extensions protruding from the control cells appear short, and do not appear to adhere directly with the substrate surface. Cell-cell contacts occur across the 20nm-diameter colloidal topography at 3 hours, Figures 3.43a)-d), and appear to arise as a result of direct membrane interactions via filopodia protrusions, Figures 3.43b) and c). Cells can also be seen upon the apical surface of neighbours, Figure 3.43d). Filopodia, when not extending to neighbouring cells, appear to adhere and traverse the underlying nanotopography on both the 20nm- and 50nm-diameter colloids, Figures 3.43a) and Figure 3.44a)-c) respectively. Fibroblasts on the 50nm-diameter colloidal topography also exhibit more tangled protrusions, Figure 3.44c), in comparison to those on the planar and 20nm-diameter colloids. Cell-cell contacts via membrane protrusion interactions are also observed in the cell population seeded on the 50nm-diameter colloidal topography, similarly seen at 3 hours on the 20nm-diameter colloids. Fibroblasts also appear elongated in some

instances, suggesting motile behaviour, Figure 3.44a) and b), similarly observed on the planar substrate at this time.

hTERT fibroblasts on the planar substrate at 8 hours, once again exhibit small lamellipodia extensions, Figure 3.45a), which do not appear to interact directly with the underlying substrate, previously noted at 3 hours. Cells exhibit spread morphology, Figures 3.45a), b) and d), and extend elongated protrusions from their periphery across the substrate, Figures 3.45b) and d). These extensions once more appear to function as anchorage points, providing tensile strength during cell spreading. Chains of repetitive globular material, Figures 3.45b)-d), suggest matrix synthesis by fibroblasts on the planar substrate at 8 hours. Previously absent cell-cell contacts are also observed at this time, Figure 3.45d). On the 20nm-diameter colloidal topography, elongated filopodia appear as a pivotal feature of cell-cell contacts, Figures 3.46b) and c). Furthermore, the globular entities previously observed at earlier times are more frequent, located at cell peripheries, Figures 3.46a) and b), and also on the nanopatterned substrate, Figure 3.46b). Other repetitive chains are observed on the apical membrane of fibroblasts at 8 hours, Figure 3.46c), and also in protrusions occurring within the vicinity of the main cell body, Figure 3.46d), indicating possible ECM production, previously observed on the planar substrate at this time. Patterning of protrusions may be associated with the actin and tubulin islands observed using fluorescence microscopy of fibroblasts on colloidal topography, Section 3.3.3.4. Fibroblasts on the 20nm-diameter colliodal topography appear well spread at 8 hours, Figures 3.46a)-c). Globular entities are also frequent in cells imaged on the 50nm-diameter colloidal topography at 8 hours, Figures 3.47a)-d). Furthermore, these globules appear at cell peripheries and also on the nanopatterned substrate, Figures 3.47a)-d), similarly observed on the 20nm-diameter colloids at this time. Cell-cell contacts appear in areas where filopodia elongations are also present, Figures 3.47a)-c). Furthermore, elongated membrane protrusions are often seen to contact the substrate surface directly, Figure 3.47c), previously unseen on the planar controls.

By 24 hours, cell-cell contacts are also observed on the planar control substrate, Figure 3.48a), where cells appear relatively flat on the surface. Globular entities are also observed both on the apical surface of cells, open arrows in Figure 3.48b), and on the substrate surface, closed arrows in Figure 3.48b). Lamellapodia protruding from the basolateral layer of cells are short, with no obvious adhesive interaction with the flat

surface, Figure 3.48c), previously observed at earlier times in control samples. However, more elongated filopodia-like structures are observed to traverse the base substrate, forming very close, if not direct contacts with the surface, Figure 3.48d), previously observed at earlier times on the nanotopographies. Cell-cell contacts are consistent throughout the fibroblast population on the 20nm-diameter colloidal topography at 24 hours, Figures 3.49a)-d). Cells in contact with neighbours in this manner appear to raise their main bulk above the nanopatterned surface via fibrous protrusions, indicated with black arrows in Figure 3.49a). Furthermore, cells are also observed to pile upon one another, Figure 3.49d). Globular entities previously observed to occur across 20nm- and 50nm-diameter samples at earlier times, and also on the planar substrate at 24 hours, appear to be entangled within very thin membrane protrusions, Figure 3.49b) and c).

3.3.3.4 hTERT Cell Morphology in relation to Colloidal Topographies - Fluorescence Microscopy and the Actin and Tubulin Cytoskeleton

hTERT fibroblasts, 10,000 cells per ml in 3mls media, seeded on 20nm- and 50nm-diameter colloidal nanotopographies and a control, planar surface were fluorescently stained using an immunohistochemistry technique, Section 2.7.2. A double stain for both actin and tubulin was implemented, and cells were fixed and treated at a number of time intervals believed to be important in the general scheme of fibroblast behaviour observed in the time-lapse video microscopy results, Section 3.3.3.1 and adhesion studies, Section 3.3.3.2. At one and three hours, processes involved in cell attachment should be visible, and alterations in cytoskeletal arrangement should indicate cell polarisation and possibly the initiation of motility and movement of cells across the experimental substrata. By eight, twenty-four and forty-eight hours, alterations of cytoskeletal composition should reflect further polarity development, cell movement and proliferation. It should be noted that all cells were prepared and seeded from the same batch at equal time periods (give or take a few seconds).

3.3.3.4.1 Microfilament and Microtubule dynamics at 20 minutes

hTERT fibroblasts on both the 20nm- and 50nm-diameter colloidal topographies and a planar control surface were fixed and stained for actin and tubulin at 20 minutes, Figure 3.50. Cells on the planar control appear rounded, with indications of actin polymerisation at the peripheral sites, suggesting cells are settling on the substrate, adhering to the surface and beginning to spread, Figure 3.50ai) at 20 minutes. Many

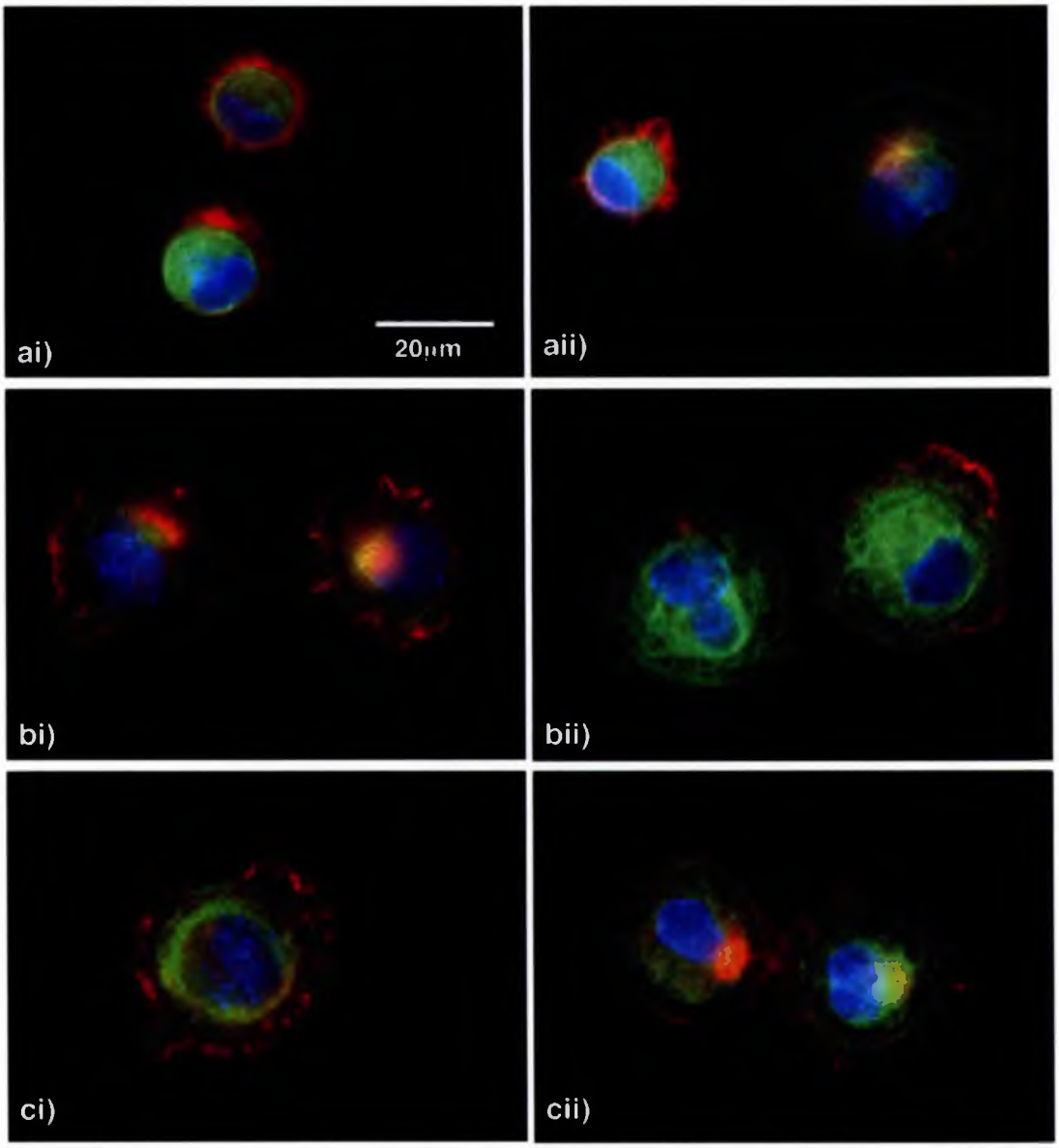

Figure 3.50: Fluorescent imaging of hTERT fibroblasts at 20 minutes on planar control substrate, a), 20nm-diameter colloidal topography, b), and 50nm-diameter colloidal topography, c). 50X oil immersion objective was used with the Vickers microscope to image cells using fluorescence. Fibroblasts on the planar control surface appear rounded, with little spreading occurring due to the limited time cells have been in contact with the substrate, ai). Early signs of spreading can bee seen in some cells, which express actin-rich, ruffling lamella, aii). Tubulin does not appear to be significantly polymerised in fibroblasts at this time period on planar surfaces. In contrast, microtubule networks can be seen throughout some cells on the 20nm-diameter colloidal topography, bii), where cells are well spread, appearing larger than those cells on the control, at 20 minutes. Active ruffling at peripheral membranes is observed, bi) and ii), and possible polarised behaviour (in a proximal-distal manner) is indicated by non-radial ruffling of lamella, bi). hTERT fibroblasts on the 50nm-diameter colloids appear most similar to cells seen on the control planar surface than those on the 20nm-diameter colloidal topography at 20 minutes. Fibroblasts on the 50nm-diameter colloidal substrate appear to be spreading, slightly more so than control cells, with radial or cicumferential actin-rich lamellas, ci). Tubulin polymerisation is observed in these cells also, cii), but not to the extent seen in cells on the 20nm-diameter colloidal topography.

cells are observed to be more spread in comparison to their more rounded neighbours, Figure 3.50aii), with peripheral actin ruffling, and microtubule networks developing. In contrast, fibroblasts on the 20nm-diameter colloidal substrates appear much more spread, with microtubules, as a result of tubulin polymerisation, appearing to constitute a larger area of the cells, Figure 3.50bii). Microtubule development at this early time allows for relocation of intracellular organelles, which, in turn, contributes to cell polarisation due to spatial allocation of internal components. This suggests that cells have more adhesive contacts with the substrate, required during cell spreading, and are more active with regard to polymerisation of cytoskeletal components. Less well spread cells on the 20nm-diameter colloidal substrate at 20 minutes, Figure 3.50ai), differ from fibroblasts on the control planar substrate at this time due to the highly defined actin-rich membrane ruffling occurring at cell peripheries. Constant remodelling of actin is required in membrane ruffling, suggesting cells are more metabolically active in comparison to their control counterparts. Furthermore, the more advanced state of fibroblast morphological development on the 20nm-diameter colloidal structure in comparison to cells on the planar substrate suggests possible up-regulation of proteins and molecules required to support this behaviour.

Similarly, hTERT fibroblasts on the 50nm-diameter colloidal substrate appear well spread in comparison to cells on the control planar surface, Figure 3.50ci) and cii), although not to the same extent as observed on the 20nm-diameter colloidal substrate. The spread appearance of cells on the 50nm-diameter colloidal structures suggests an increase in cell-substrate adhesion areas in comparison to the control cells, due to the increased surface area of cells in contact with the experimental topography. Active, developed membrane ruffling is once again defined by the presence of actin aggregates occurring at cell peripheries, Figure 3.50ci). Microtubule network establishment, Figure 3.50cii), highlights the capabilities of the cell with regard to repositioning of internal features, and may act in the proximal-distal polarised state of fibroblasts.

3.3.3.4.2 Microfilament and Microtubule dynamics at 1 hour

In Figure 3.51ai), fibroblasts on the control planar surface at one hour appear rounded indicating lack of polarisation and spreading. No leading edge appears, indicating lack of motile behaviour. Actin in an immature lamellipodia is seen to radiate from the nuclear area, suggesting cell-substrate contacts are present, and the cell is beginning to spread across the surface. Tubulin appears unpolymerised, seen here as a bulk of

individual heterodimers with no microtubule assembly present. This suggests the cells are metabolically repressed on the planar surface, establishing surface contacts and in the early stages of polarisation and spreading. hTERT fibroblasts also exhibit a more advanced state with respect to cytoskeleton organisation on the planar substrate, left in Figure 3.51aii). Membrane ruffling indicated via the actin staining (in red) appears active, suggesting this cell is polarised, sensing the surrounding environment and attempting to spread on the planar surface. Some microtubule (in green) assembly can also be seen, again suggesting the establishment of cell polarity and communicative pathways throughout the cell. The microtubule assembly observed also suggests that the cell is becoming more rigid and stable structurally.

Fibroblasts seeded on the 20nm-diameter gold colloidal topography, in contrast to planar controls, exhibit a slightly more advanced cytoskeletal arrangement, with polymerisation of actin resulting in microfilament production and development of microtubule networks. Figure 3.51bi) highlights two cells at different stages of development with respect to the arrangement of actin and tubulin within the cytoplasm. The cell in the left of this image shares similar cytoskeletal characteristics as described for one of the cells grown on the planar surface, Figure 3.51aii). Actin polymerisation resulting in membrane ruffling is present as the cell sends micro-filaments to peripheral regions in an attempt to sense the surrounding environment. Little polymerisation of tubulin can be seen, and therefore a deficiency in the number of established microtubules is indicated. It should be noted that the peripheral ruffling observed here appears spiky in comparison to the smooth appearance of the developing lamellipodia of the fibroblast on the planar surface. The microfilaments in the fibroblasts on the 20nm-diameter colloidal surface appear more rigid, linear and thicker than those on the control surface. This suggests that the microfilaments on the experimental surface may be stabilised by a single or number of actin-binding proteins, for example tropomyosin, myosin II and/or α-actinin. The function of tropomyosin is to strengthen filaments, myosin II occurs between parallel micro-filaments encouraging contractile activity of the individual actin bundles believed necessary in cell motility, while α-actinin may link actin filaments with opposite polarity end-to-end resulting in filamentous actin bundles (Preston et al, 1990). This type of actin filament arrangement may be an unsophisticated protrusion required in the migration of the fibroblast. This cell would also have adhesive contacts of some sort at the substrate interface.

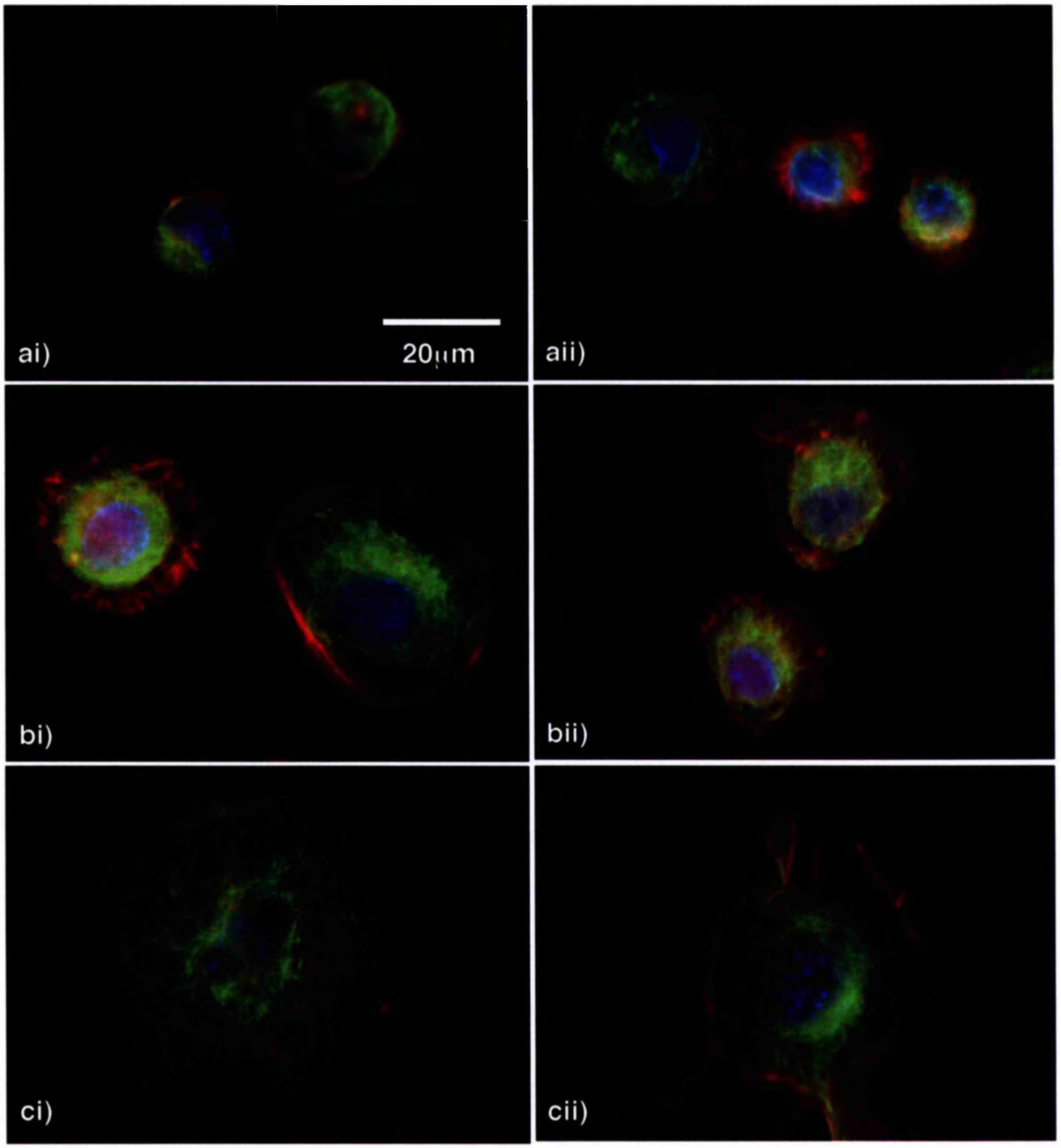

Figure 3.51: hTERT fibroblasts on planar control, a), 20nm-diameter colloidal topography, b), and 50nm-diameter colloidal topography at 1 hour. Fluorescent imaging highlights actin (red) and tubulin (green) distribution throughout the cell. Nuclei are blue. Images captured using Vickers microscope with 50X oil immersion objective. Fibroblasts on the planar control, appear to have just reached the surface, with little spreading in some instances, ai). Spreading in some cells is observed, aii), where actin lamella radiate at the peripheral membrane. Tubulin appears to lack polymerisation in cells on the control surface at 1 hour. Fibroblasts on the 20nm-diameter colloidal substrate appear well spread, bi) at one hour, where actin ruffling is observed, as are actin belts encapsulating the main bulk of the cell. Microtubule formation also appears to be occurring. In some instances cells appear to be in the process of locomotion, bii), where actin aggregations occur as a leading edge (upper portion of cells), with more tapered areas reflective of a detachment site. Cells on the 50nm-diameter colloidal topography also appear well spread, ci), with a well developed microtubule network, reflective of cells during telemorase. Cell motility is also suggested in the polymerised appearance of the cytoskeleton, bii).

The fibroblast in the right of Figure 3.51bi) shows very organised tubulin and actin cytoskeletons, especially when considering this early time period. The cell appears well spread with polarised actin filaments resulting in the emergence of stress fibres, which are abundant in the nuclear region. At the peripheral membrane, protrusions, although structurally immature due to the lack of filament bundles, are observed. These features suggest the early stages of cell migration. The ring of actin encircling the microtubule network and nuclear area should be noted in this fibroblast, and appears very similar to an adherens belt, also known as a zona adherens. A contractile bundle of actin filaments, the zona adherens is a specialised intercellular junction, where microfilaments are often inserted from cells sharing the junction (Alberts et al, 1993). Although this definition of the intercellular junction would not apply in the instance of the actin circle seen within the fibroblast seeded on the 20nm-diameter colloidal topography, the similarities should be noted. The tubulin observed within this area appears to be forming a microtubule network, although the microtubules are not very well defined, appearing as non-polymerised tubulin. The tubulin appears to be encapsulated within the circle of actin, and is not present towards the peripheral membrane, but surrounds the nuclear region.

Figure 3.51bii) shows two fibroblasts on the 20nm-diameter colloidal surface at one hour also. Cells appear polarised, with the emergence of a leading edge suggested in both cells due to the high concentration of polymerised actin filaments at the top edge in the triangular shape of the cell. A very localised area of actin towards the bottom of the cells in the image indicates the development of a detachment site required in locomotory behaviour. Microtubule network development appears to extend to the peripheral regions of the fibroblasts to the same degree and extent of the actin filaments present.

hTERT fibroblasts on the 50nm-diameter colloidal topography at one hour exhibit a great deal of organisation in both the actin and tubulin cytoskeleton, compared to cells seeded on both the planar control and 20nm-diameter colloidal topography. The fibroblast in Figure 3.51ci) exhibits a highly developed and organised microtubule network, which extends to the peripheral limits of the cell. In comparison to the microtubules, the actin within this cell appears much less organised, composed mainly of what appears to be cross-linked filaments composing a gel-like network. Some areas of the microfilament network appear to contain a number of contractile bundles

suggesting the local presence of actin-binding proteins, for example fimbrin and α-actinin in these regions. The cell is extremely well spread, displaying a spherical morphology, suggesting a number of adhesive contacts between the cell and the colloidal surface have been established, as required in signal transduction and cell-shape mediated growth, Section 1.1.3.

Figure 3.51cii) highlights a fibroblast seeded on 50nm-diameter colloidal topography with a highly developed cytoskeleton at 1 hour. hTERT fibroblasts display most organised cytoskeletal arrangements on the 50nm-diameter colloidal surfaces, with least micro-filament and microtubule organisation on the control planar surfaces. It should be noted that the cell in this figure appears to have an attachment with a neighbouring cell in the lower part of the image, with tubulin and actin extensions appearing impossible to separate between the two cells. When considering the video-microscopy images of hTERT fibroblasts on the 50nm-diameter colloidal surfaces, cell-cell contacts appear to occur throughout the cell population seeded on colloidal nanotopographies. The lack of distinction between microtubules and microfilaments between neighbouring cells is observed in greater detail at later time periods of 8 hours, 24 hours and 48 hours.

The actin cytoskeleton of the fibroblast in Figure 3.51cii) appears to be very well developed, with both contractile bundles, appearing in the nuclear region, and tight parallel bundles, at the peripheral membrane forming lamellipodia and filopodia, both motile structures, seen. The presence of filopodia indicates sensing and direct interaction between this cellular feature and the surrounding topography and environment. The presence of stress fibres indicates the establishment of FAC's, as established adhesions are required at one or both ends (or an actin mesh network) of a stress fibre. Stress fibres are believed to occur due to the generation of tensions throughout the cell, suggesting cell rigidity and possible contractility in this fibroblast, and disappear rapidly when attachments between the cell and the substrate dissociate. This is of particular interest when considering the "ping" effect observed in Section 3.3.3.1.1 where fibroblasts are seeded on a 20nm-diameter colloidal topography. Stress fibres are also seen to occur as cells spread during cell-shape mediated growth during the cell-cycle. Stress fibres occur often as temporary contractile bundles of actin microfilaments and myosin II (although more established bundles are known to exist). The microtubule network appears well organised, with polymerised tubulin filaments in many places reaching as far as the microfilaments at the cell periphery. This indicates

an active network is present for membrane-bounded organelles, resulting in the spatial organisation of organelles within the cytosol. As in Figure 3.51ci), the cytoskeleton in this polarised and organised state, forms a basis for the establishment of adhesive contacts and cell-surface signalling pathways, and is capable of supporting these connections with the extracellular environment.

3.3.3.4.3 Microfilament and Microtubule dynamics at 3 hours

At 3 hours, hTERT fibroblasts on the planar control surface appear to be either well spread, Figure 3.52ai), or are arranged in such a manner as to suggest early stages of motility, Figure 3.52aii). Spread cells appear surrounded by a peripheral band of actin, with some actin-rich alignments occurring throughout the cell, suggestive of stress fibres. The appearance of stress fibres is also observed in cell attempting to traverse the planar surface, Figure 3.52aii). Stress fibre formation is generally attributed to the development of mature focal contacts, suggesting that cells on the planar substrate have developed cell-substrate adhesive contacts at 3 hours. Microtubule distribution in spread cells, Figure 3.52ai), at 3 hours indicates the ability of cells to position internal organelles, allowing for spatial distribution of the cytoplasm. Furthermore, cells with developed microfilaments and microtubules are capable of communicating information spatially. This would allow for the development of motile behaviour as observed in some cells on the planar substrate at 3 hours, Figure 3.52aii). During movement, cells must be capable of assembling and disassembling focal contacts and expressing a cytoskeleton capable of supporting its bulk properties while continually remodelling. Actin stress fibres present in the direction of stress of the cell, Figure 3.52aii), suggests the direction of cell movement, with polarised microfilaments and microtubules occupying a larger area, the leading edge, in comparison to the rear detachment site. The polymerised state of the cytoskeletal elements acts to support organelle movement, and also act as a scaffold for the cell. The membrane ruffling occurring at the leading edge indicates the continual sensing of a cell in relation to its underlying substrate.

In comparison to fibroblasts on the control planar substrate, hTERT cells on the 20nm-diameter colloidal topography display less typical fibroblast morphology, Figure 3.52bi) and bii). Cells on the 20nm-diameter colloids appear spread, Figure 3.52bi), with longer, more defined actin stress fibres suggesting more mature focal contacts, greater cell-substrate adhesive interactions and thus a more stabilised state in relation to the colloidal topography. Microtubule networks in spread cells on the 20nm-diameter

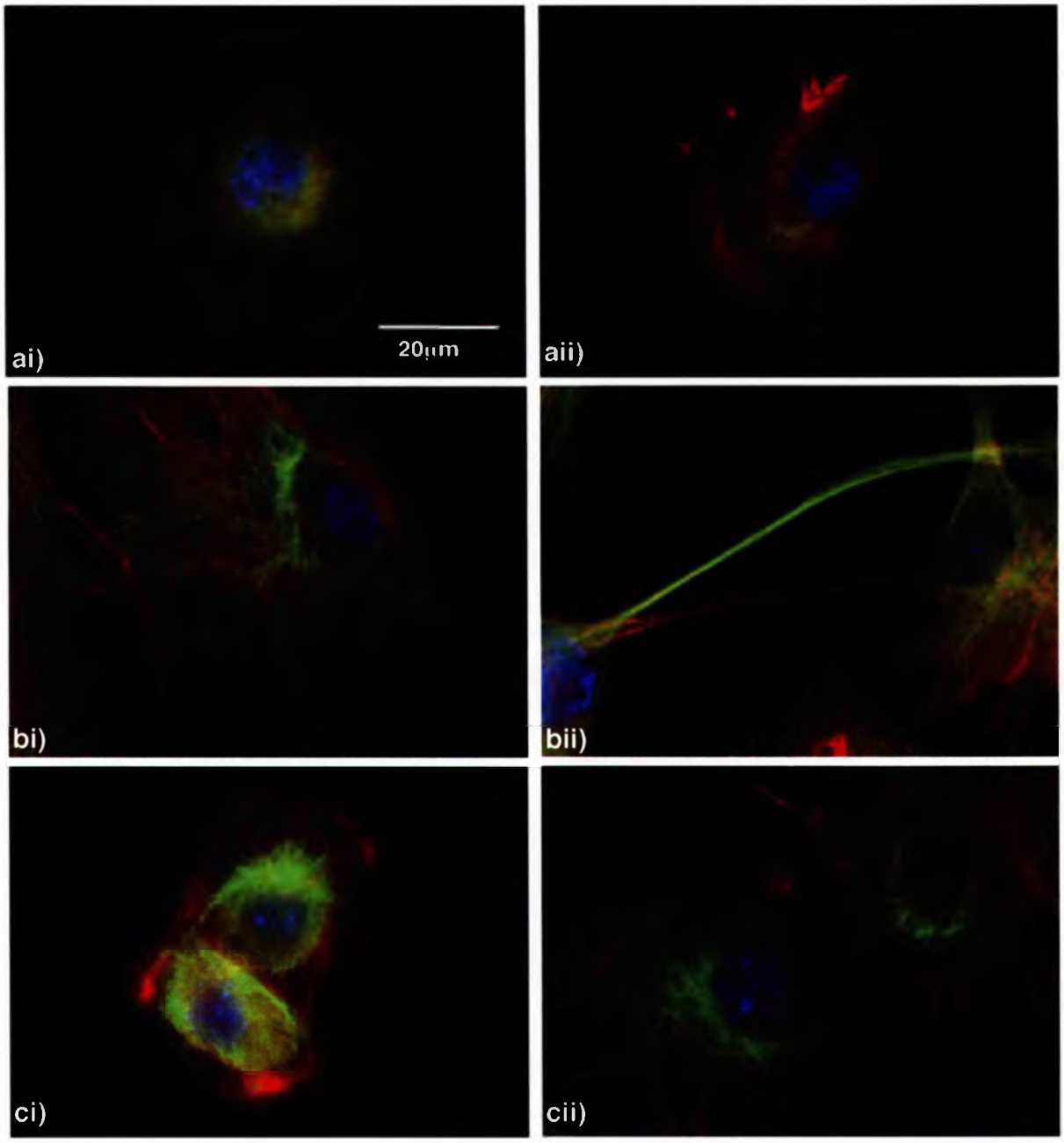

Figure 3.52: Fluorescent imaging, captured using the Vickers microscope with 50X oil immersion objective, of the actin and tubulin cytoskeleton of hTERT fibroblasts on a) planar control, b) 20nm-diameter colloidal topography and c) 50nm-diameter colloidal topography at 3 hours. Fibroblasts on the control planar surface display radial actin distribution in the form of membrane ruffles, ai), indicative of cell spreading, and in some instances signs of movement, seen here as a leading edge and detachment site aii). Fibroblasts on the 20nm-diameter colloidal topography appear very spread, with many long actin stress-fibres suggesting stable cell-substrate adhesions exist, and developed microtubule networks, bi). Fibroblasts on the 20nm-diameter colloidal substrate also exhibit actin and microtubule-containing elongations at their distal regions, bii), and are seen to form aggregates. hTERT fibroblasts on the 50nm-diameter colloidal topography have spiky, actin-rich peripheral protrusions at 3 hours, ci), suggesting filopodial extensions are actively sensing the surrounding substrate. Difficulty in distinguishing between the fibroblasts boundaries is observed in this instance. Similarly, cell-cell contacts, or overlaps appear in spread cells, cii). Actin stress-fibres are observed in these cells, again suggesting stable focal adhesions, as viewed in relation to cells on the 20nm-diameter colloidal topography at 3 hours, bi).

colloids appear primarily to be located around the nucleus, with tubules extending to the peripheral membrane again suggesting stability of the cell and also spatial arrangements of intracellular organelles. Cell-cell contacts with possible cross-talk occurring via cytoskeletal processes are also observed, Figure 3.52bi), as differentiation between cell cytoskeletons of these cells is difficult. Cell-cell contacts also occur in the form of extensions and elongations bridging cell-free areas of the substrate, where processes contain both actin and tubulin, Figure 3.52bii). As overlaps of cell processes occur in this instance, it is possible that fibroblasts in contact with the 20nm-diameter colloidal substrate are incapable of discriminating between the experimental substrate and cell surfaces.

Fibroblasts on the 50nm-diameter colloidal topography also appear spread in some instances, Figure 3.52cii), again displaying stress fibre formations which are more elongated and distinct in comparison to those observed on the planar control, suggesting more stable cell-substrate adhesions. Similarly, as seen in relation to the 20nm-diameter colloidal surface, the bulk of the microtubule network appears central to cells, surrounding nuclei and extending towards the membrane periphery. Cell-cell contacts between fibroblasts on the 50nm-diameter colloids are also observed, and it is once again difficult to discriminate between the cytoskeletons of individual cells, Figure 3.52bii). Less spread, more rounded fibroblasts, Figure 3.52ci), exhibit a spiky periphery, where actin-rich lamellapodia or filopodia suggest localised sensing of, and interaction with, the 50nm-diameter colloidal topography at 3 hours.

3.3.3.4.4 Microfilament and Microtubule dynamics at 8 hours

Actin and tubulin within cells seeded on both the experimental colloidal topographies appear polarised at 8 hours, with stress fibres occurring across the cells and microtubules appearing to radiate from nuclear areas towards the membrane periphery in these cell populations. In comparison, hTERT fibroblasts on the planar control have less well defined stress fibres, suggesting less stress across cells on the flat surface, with unpolymerised tubulin observed throughout cells.

Fibroblasts on the planar substrate at 8 hours appear to be either spread, Figure 3.53ai), or exhibit actin localisation at both distal and proximal regions suggesting motile behaviour, Figure 3.53aii). Microfilaments are observed to be mainly located at peripheral regions in spread cells, Figure 3.53ai), suggesting cell-substrate adhesions are

present, allowing for the development of this morphology. Microtubules are also observed in spread cells, suggesting spatial positioning of intracellular components. Microtubules, in fibroblasts displaying motile morphology appear to be mainly situated within the nuclear region, extending primarily towards the detachment site, but also observed to be infiltrating the leading lamella.

In contrast, fibroblasts on the 20nm-diameter colloidal topography display highly spread morphology, with very definite, defined actin stress fibres, Figure 3.53bi). Stress fibres in fibroblasts on the 20nm colloids appear not only at the membrane periphery, but also within the nuclear region. This suggests possible stress occurring across the cell nucleus, which in turn, may alter gene expression (Dalby et al, 2003°). Furthermore, the presence of cell-substrate adhesions occurring under the nucleus is also suggested, thus microfilaments may act to buffer nuclear-substrate interactions. Microtubules appear well developed throughout cells, with many localised tubulin points occurring, Figure 3.53bi). The arrangement of these tubulin dots suggests possible tubulin-substrate interactions, as the localised tubulin occurs in very small, spherical groups, similar to the underlying colloidal topography. Furthermore, a microtuble tail appears at the rear of this cell, Figure 3.53bi), where actin is also present, reflecting the detachment sites previously observed in the video microscopy images, Section 3.3.3.1.

Fibroblasts on the 20nm-diameter colloidal topography also display cell-cell interactive behaviour, Figure 3.53bii). Again, these cells have highly developed stress fibres in comparison to cells on the control planar substrate, which are located both at cell peripheries and nuclear regions. Overlapping of cell peripheral regions is observed between two cells, and no definite boundary between cytoskeletal elements can be deduced. Tubulin appears polymerised, with microtubules interwoven in many instances. The most distinctive features of fibroblasts on the 20nm-diameter colloidal topography in comparion to those on the control surface is the abundance of thick actin stress fibres, especially underlying the cell nucleus, and the presence of microtubules radiating from the nuclear region towards the membrane periphery. Although the cytoskeleton is dynamic, these cells display stable morphology at this period, highly suggestive of strong cell-substrate adhesions. Furthermore, the stress occurring across the cell appears to be spatially regulated, where the cytoskeletal features are distributed throughout the cell rather than

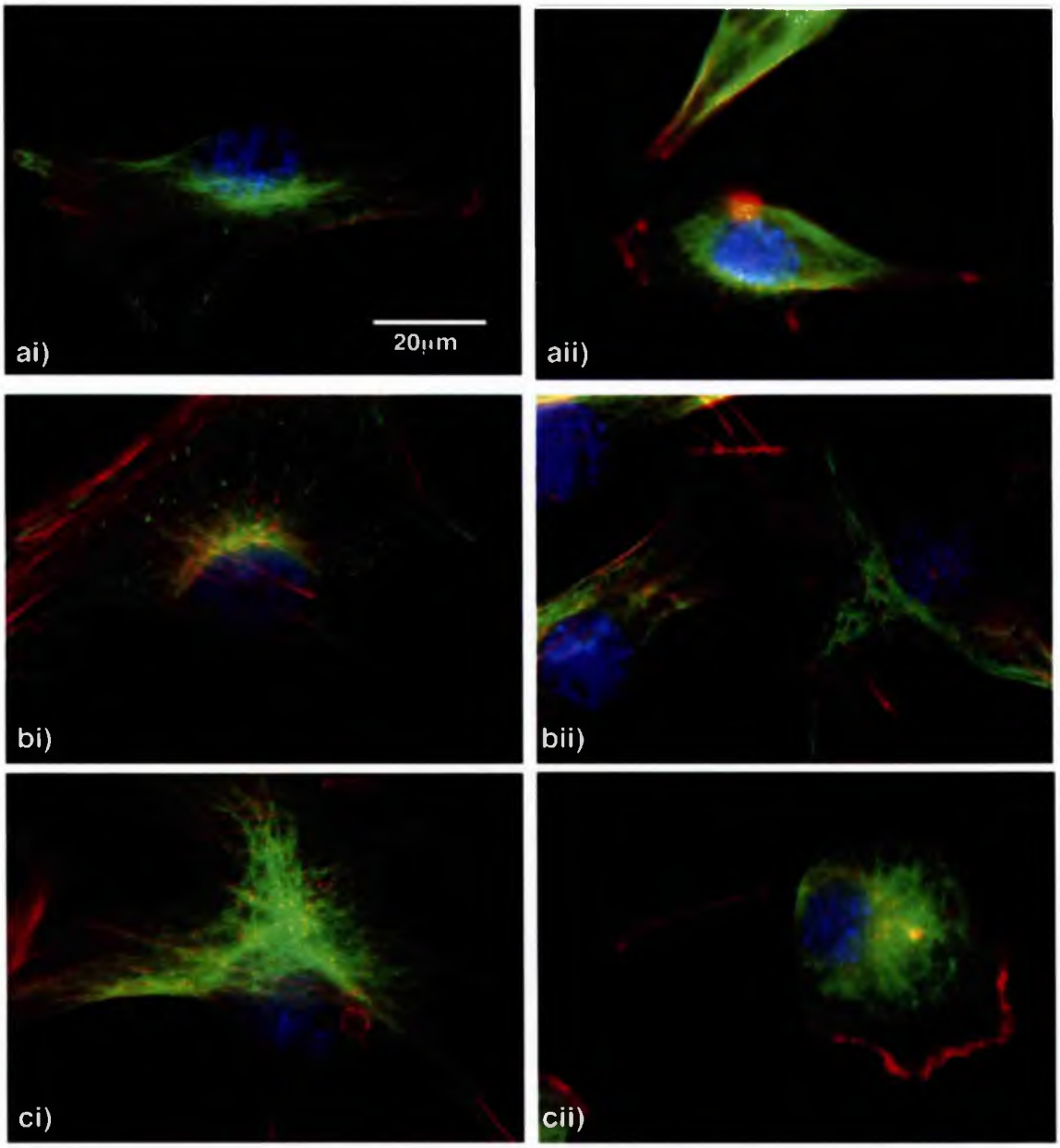

Figure 3.53: hTERT fibroblasts on a) planar control, b) 20nm-diameter colloidal topography and c) 50nm-diameter colloidal topography at 8 hours. Fluorescent imaging was obtained using a 50X oil immersion objective in conjunction with the Vickers Microscope. Actin is depicted in red, tubulin in green and nuclei are blue. Fibroblasts on the planar control surface appear motile, and appear to be in the process of elongation, ai) and aii), where an actin-rich leading edge is beginning to develop (to the left), with actin accumulation locating at the detachment site (right). Microtubule networks appear throughout the cell as it spreads. The most notable morphological difference between fibroblasts on the control planar substrate and the 20nm-diameter colloidal topography at 8 hours is the presence of highly defined actin stress-fibres occurring in cells on the experimental substrate, bi). This suggests the presence of stable focal adhesion complexes. Furthermore, the direction of stress-fibres would appear to be related to cell-cell stress established when neighbouring cells contact, bii). Cells appear spread, with nuclei located at peripheral regions. Similarly, hTERT fibroblasts on the 50nm-diameter colloidal topography at 8 hours also display a centrally displaced nuclei, ci and ii). Cells appear well spread, with trailing cytoskeletal elongations, ci). Stress-fibres do not appear as prominently in fibroblasts on the 50nm-diameter colloids in comparison to cells on the 20nm-diameter colloidal topography. Fibroblasts often display a more rounded shape at 8 hours when in contact with the 50nm-diameter colloidal substrate, cii), and trailing spiky tails are seen, patterned with nodules of actin and tubulin.

being located in specific regions. The presence of the actin stress fibres in nuclear, central regions further supports this possibility. The observed cell-cell interactions indicate a possible lack of discriminate behaviour on the part of the cells, between neighbouring cells and the experimental substrate. Due to the stress features observed throughout cells, cell-cell interactions may occur as a means of stabilising cell-substrate interactions, via adhering to entities with similar rigidity.

hTERT fibroblasts on the 50nm-diameter colloidal topography display morphology similar to fibroblasts on both the planar control and 20nm-diameter colloidal substrate. Fibroblasts appear well spread, Figure 3.53ci), similar to those cells observed on the 20nm-diameter colloids. However, actin stress fibres appear longer and thinner in cells on the 50nm-diameter colloidal topography, and, although located in peripheral and nuclear areas, do not appear to underlie the nucleus as previously observed in cells on the 20nm-diameter colloids. As a result, cell nuclei appear less rounded, Figure 3.53ci), suggesting possible distortion of this organelle which may result in altered gene expression (Dalby et al, 2003°). Although associated with the lack of stress fibres underlying the nucleus, the presence of microfilament bundles distending from the nuclear region, Figure 3.53ci), is likely to contribute to the stress applied to the nucleus, as is the protrusion occurring away from the cell in a similar region.

Fibroblasts on the 50nm-diameter colloidal substrate are also observed to exhibit rounded morphology, with a leading edge indicated by actin-rich ruffles, and an elongated, globular detachment site, primarily composed of microfilaments, Figure 3.53cii). When considering the time-lapse video footage, Section 3.2.2.1, it is possible that this cell has previously undergone stretching, resulting in rounding behaviour and the emergence of an elongated detachment site. This possibility is further supported through the lack of stress fibres, suggesting a lack of mature focal adhesions. Beaded regions of the detachment feature indicate the possibility of direct cell-substrate interactions, as the morphology of these sites reflects the topography of the 50nm-diameter colloidal topography underlying the cell. The actin ruffling present at the proximal region of the cell periphery indicates movement and resultant spreading, Figure 3.53cii). Microtubules appear to radiate from the nuclear region towards the periphery, suggesting reorganisation of intracellular components, which, in turn, will result in cell polarisation.

3.3.3.4.5 Microfilament and Microtubule dynamics at 24 hours

hTERT fibroblasts on the control planar substrate appear spread, Figure 3.54a), and instances of motile cell behaviour are also observed, Figure 3.54b), at 24 hours. In spread fibroblasts, Figure 3.54a), actin microfilaments are located throughout the cell with stress fibres present at the periphery and within the nuclear region. Lamella ruffling appears to occur at one edge of the cell, suggesting polarisation, which may result in cell motility in the direction of the developing leading edge. Microtubule networks occurring throughout the fibroblast also suggests the fibroblast is polarised, and also indicates the ability of the cell to communicate throughout this network in a spatial manner. The spread morphology of the cell can also indicate the presence of cell-substrate adhesions through which tension can be produced allowing for this shape. Translocation and motility of cells within this fibroblast population at 24 hours is also suggested, Figure 3.54b). In this instance, the cell appears elongated, where actin distribution suggests the presence of both a leading edge (right) and a rear detachment site (left). Actin stress fibres underlying the cell nucleus appear to be aligned along this stress axis. Microtubules appear throughout the cytoplasm, once again suggesting mechanisms of communication and cell-substrate adhesions are present. The elongated shape of the cell suggests that a large amount of mechanical stress is occurring between the proximal and distal adhesion sites, and this is further supported by the presence of stress fibres occurring across this axis.

The most notable alteration in cell morphology occurring between fibroblasts on the both colloidal topographies in relation to control cells is the presence of very thin, elongated extensions occurring on the nanotopographies at 24 hours. In addition to this observation, fibroblasts on the colloidal topographies also appear to establish cell-cell contacts with neighbouring cells, either via these elongated extensions or their immediate peripheral regions.

At 24 hours, hTERT fibroblasts on 20nm-diameter colloidal topographies display elongated protrusions, apparently due to rear detachment alterations, often measuring upwards of approximately 100μm in length, Figure 3.55a) and 3.55d). Elongated cellular protrusions appear to be mainly composed of actin microfilaments, although tubulin globules are also present along the length of the actin rich structure. Elongated cytoplasmic extensions appear to contribute to the overall stress occurring across the

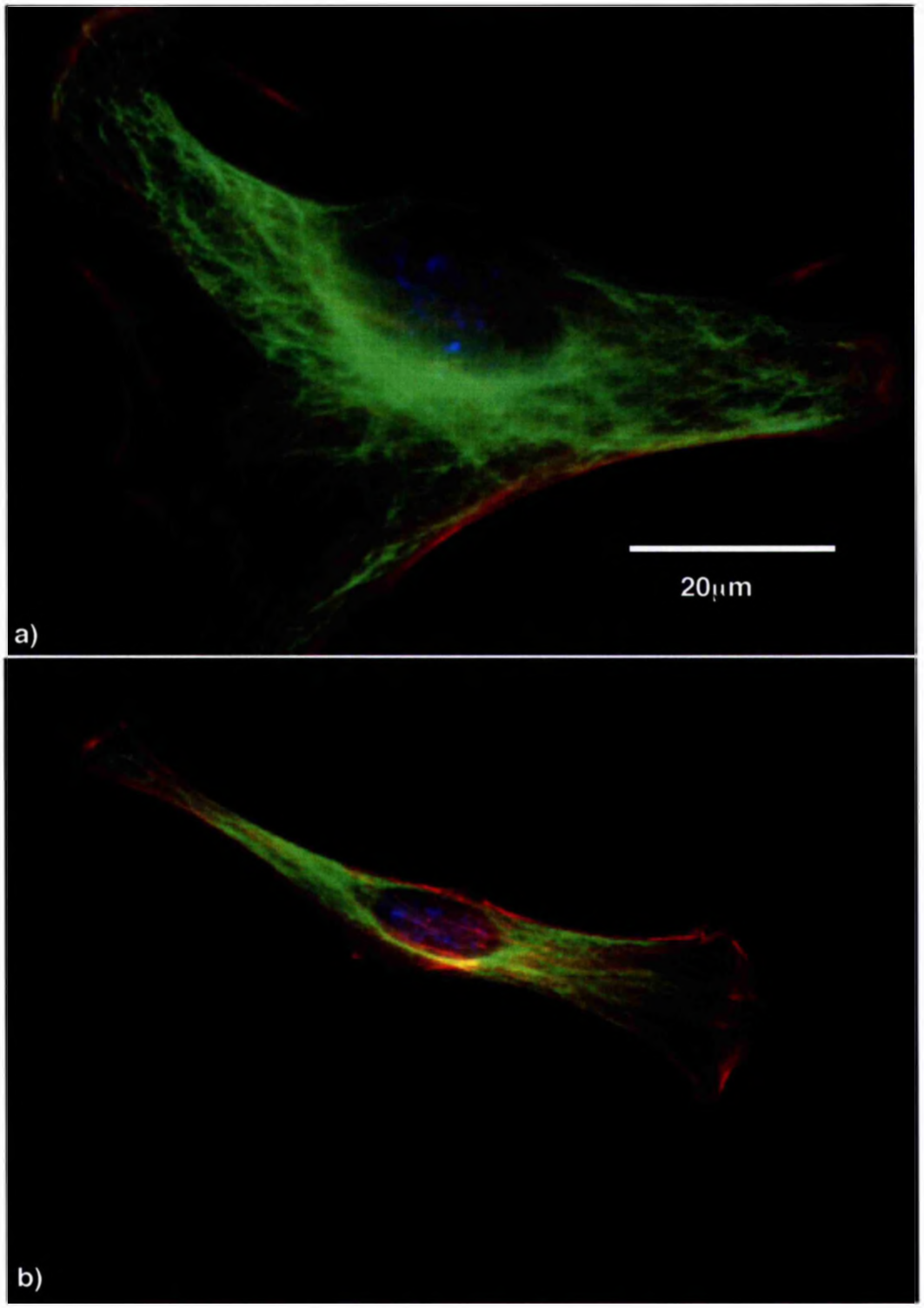

Figure 3.54: hTERT fibroblasts on control planar surface at 24 hours, imaged using the Vickers microscope with 50X oil immersion objective. Actin is depicted as red, tubulin green and nuclei blue. Fibroblasts appear either well spread, a), with actin ruffling at the cell periphery and polymerised tubulin networks surrounding the nuclear region, or are more elongated, b), with a leading edge appearing as actin-rich membrane ruffling in one direction (right side of cell), and a detachment site containing less actin in comparison (left side of cell).

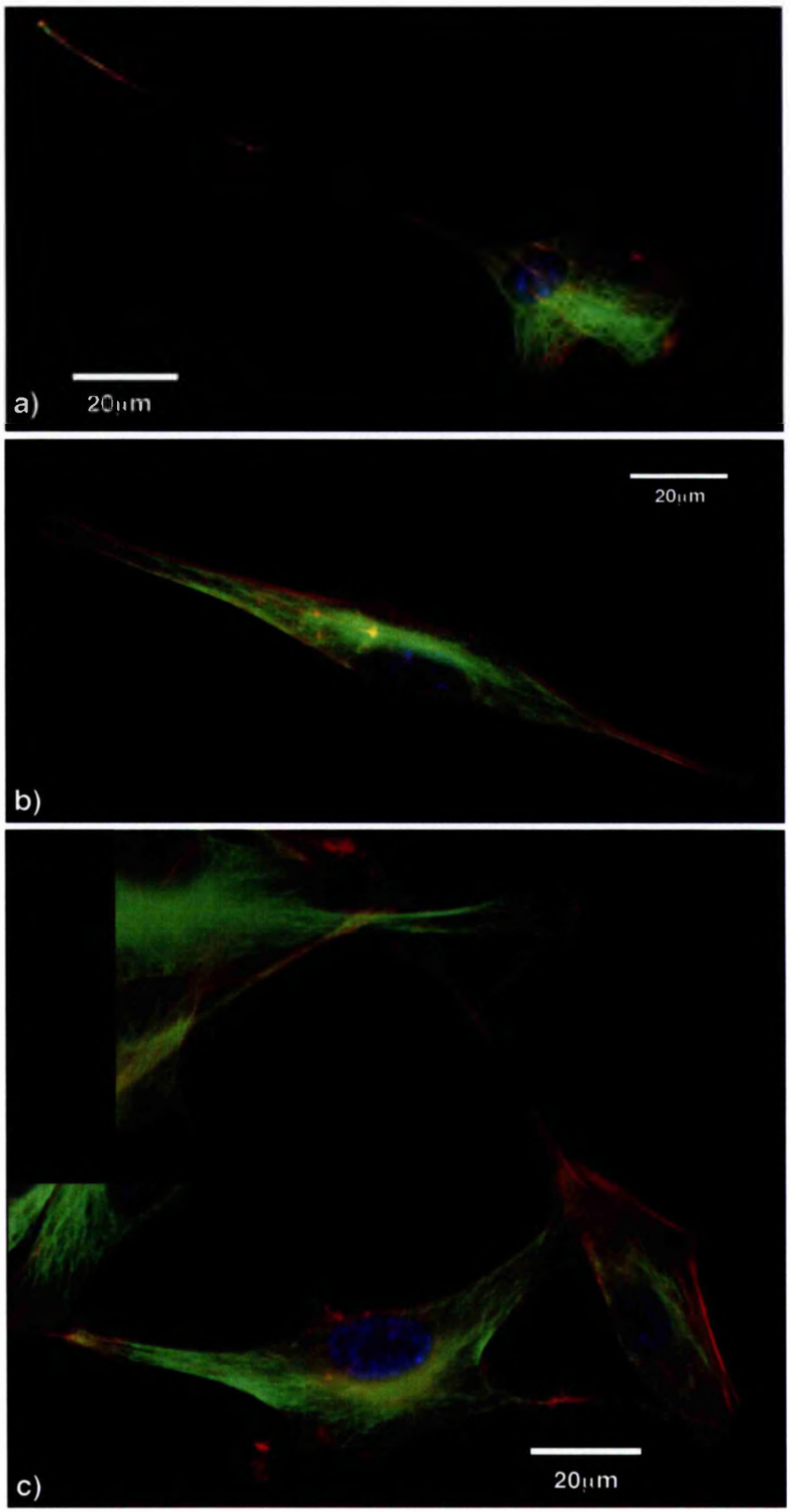

Figure 3.55: hTERT fibroblasts seeded on 20nm-diameter colloidal topography at 24 hours. A Vickers microscope using 50X oil immersion objective was used to image cells. Red highlights actin, green tubulin and nuclei are coloured blue. At 24 hours, fibroblasts exhibit an elongated tail, a), suggesting their previous movement across the substrate surface. Many cells also appear elongated, b), stretching across the colloidal topography. In cases where cell-cell contacts are observed, c), fibroblasts often appear stretched between neighbouring cells, suggesting limited cell-substrate interactions.

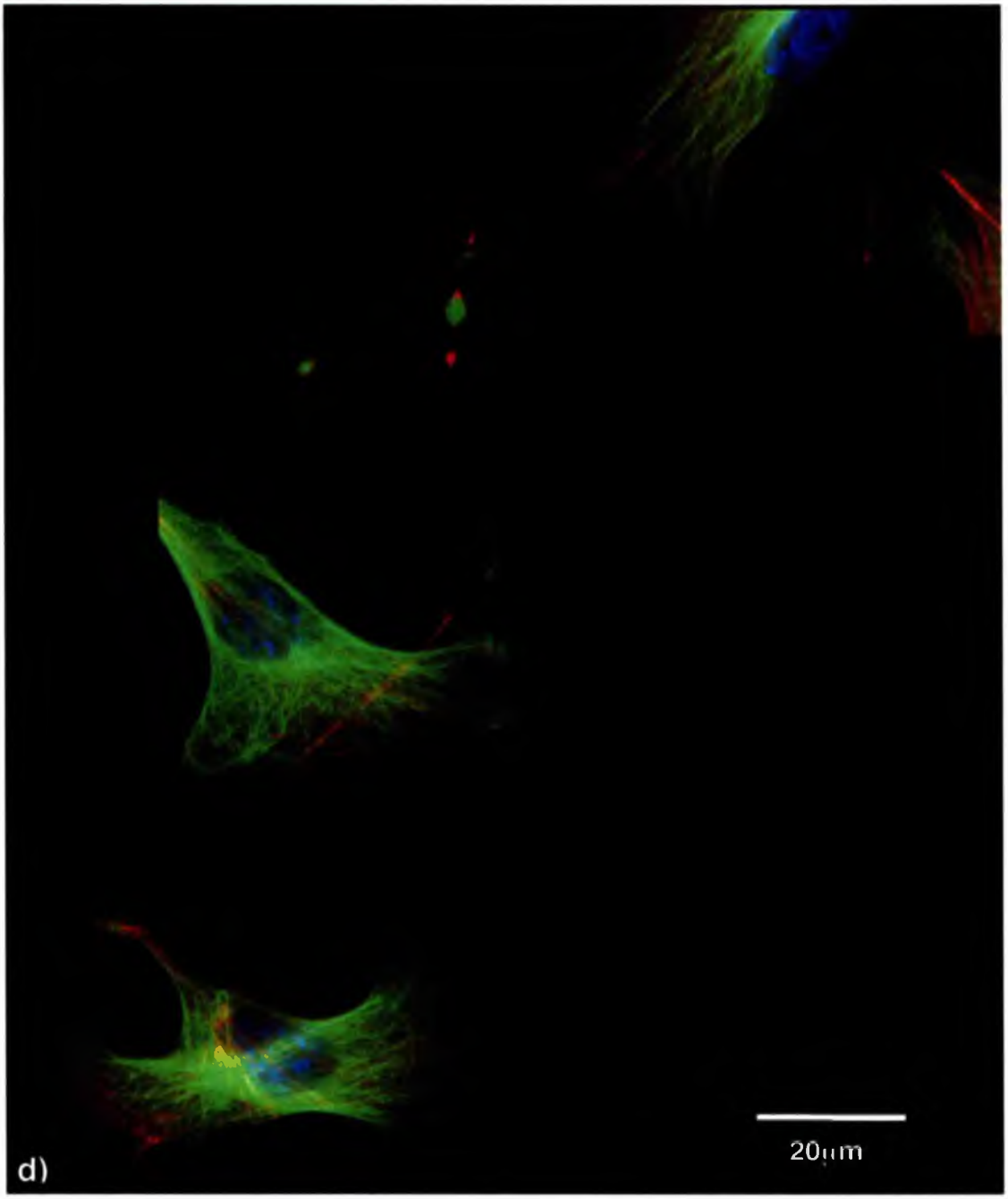

Figure 3.55 continued: hTERT fibroblasts on 20nm-diameter colloidal topography at 24 hours. A Vickers microscope with 50X oil immersion objective was used to view cells. Actin is depicted as red, tubulin green and nuclei blue in this image. Fibroblasts appear motile, with leading edges suggested by actin distribution spread at one periphery, and a rear detachment site established at the opposing side of cells. Thin, elongated structures containing both actin and tubulin appear to suggest a history of previous areas traversed by cells.

Figure 3.56: hTERT fibroblasts on 50nm-diameter colloidal topography at 24 hours. Imaging conducted using Vickers microscope with 50X oil immersion lens. Actin is coloured red, tubulin is green, while nuclei are blue. Cells appear elongated, with processes seen to measure between 60μm, a), to 100μm, b), in length. These ""tails" appear generally at the distal, detachment site areas, a), but are also observed to bridge cell-cell contacts, b). These elongations contain both microfilaments and microtubules.

cell body, resulting in the presence of actin-rich stress fibres, Figure 3.55a). Stress fibres appear more prominently in fibroblasts displaying thicker, straighter extensions, Figure 3.55a) in comparison to those exhibiting more meandering, less directed elongations, Figure 3.55a). Furthermore, actin- and tubulin-containing protrusions appear only to occur as a single entity per cell, indicating their occurrence as a result of rear detachment alterations rather than highly elongated filopodia. Fibroblasts on the 20nm-diameter colloidal substrates elongated and stretched, similar to those observed on the planar surfaces, Figure 3.55b). In comparison, cells on the nanotopography appear more elongated, where proximal and distal regions appear to mirror one another, with no distinct difference apparent between these regions. Cell-cell contacts are also observed on the 20nm-diameter colloidal topography, Figure 3.55c), where distinctions between the cells and their neighbours is difficult. The actin and tubulin cytoskeletons located at cell-cell contacts appear to merge resulting in a lack of defined boundaries between individuals. Furthermore, stress fibres occurring within nuclear regions appear almost to connect cell-cell adhesion sites, suggesting the establishment of a major axis of stress occurring between these two points, Figure 3.55c). Spiky peripheral actin accumulations occur at the cell-substrate periphery, suggesting incomplete polymerisation of microfilaments at these regions and sensing of the surrounding environment. These fine structures are also observed in other fibroblasts of the same population, Figure 3.55a) and b), at 24 hours, although in these instances, protrusions appear much more defined, resembling filopodia. Trailing extensions of actin, with globular beading containing tubulin islands are also observed, Figure 3.55d). These features are believed to occur due to distal dragging rather than proximal protrusion, as only one structure occurs per cell, in direct opposition to any membrane ruffling or leading lamellae. Globular islands containing tubulin may occur as remnants of otherwise healthy microtubule extensions, where distance between the extension and cell body increases, resulting in disconnection from the main microtubule network. A further possible explanation is the occurrence of microtubule capping via associated proteins preventing further development of these structures. This behaviour is suggested in the time-lapse video footage of endothelial cells displaying elongated detachment sites, Section 4.3.2. Furthermore, fibroblasts appear to traverse elongated actin- and tubulin-containing features, with undetectable alterations in cytoskeletal morphology. This suggests that elongated detachment sites may have problems in regulating integrin detachment (Munerva et al, 2001, Palecek et al, 1998). Cells exhibiting these very fine elongated structures appear otherwise well spread, with microtubule networks occurring

throughout the cell, with microfilaments located at peripheral sites, Figure 3.55d). Stress fibres are also observed throughout cells indicating the occurrence of cell-substrate interactions.

hTERT fibroblasts on the 50nm-diameter colloidal topographies also display similar elongated detachment sites at 24 hours and cell-cell contacts, Figure 3.56, in relation to observed fibroblast cytoskeletal morphology on the 20nm-diameter colloids at 24 hours. However, elongations tend to be wider in comparison to those observed on the 20nm-diameter colloidal topography, although very fine features are also observed, Figure 3.56b). This could possibly be due to the increased size of the colloids, or could be attributed to altered mechanical stress occurring across the cells as a result of cell adhesive interactions with the 50nm-diameter gold colloids.

Actin stress fibres are observed in one instance to occur perpendicular to a cell-cell contact site, with unbroken microfilament composition, Figure 3.56a). This suggests possible cell-cell interactions have a bearing on the direction and degree of stress occurring between neighbouring cells. Similar cell-cell peripheral contacts are also observed in Figure 3.56b), where actin stress fibres appear to occur approximately parallel to the cell-cell contact site, again suggesting cell-cell contact-induced stress. The extended elongation does not, as previously seen, terminate on the nanopatterned substrate in this instance, and, instead, appears to bridge an elongation protruding from a neighbouring fibroblast, Figure 3.56b). A further alteration in the morphology of this type of extension is that tubulin rather than actin is the main cytoskeletal component. Tubulin occurs throughout the length of protrusions, suggesting possible molecular cross-talk between inter-connected fibroblasts. Cells display spread morphology, where the periphery is composed of actin microfilaments, suggesting established cell-substrate interactions, further highlighted by the presence of stress fibres throughout fibroblasts on the 50nm-diameter colloidal topographies at 24 hours.

3.3.3.4.6 Microfilament and Microtubule dynamics at 48 hours

At 48 hours, fibroblast morphology appears similar on planar, 20nm- and 50nm-diameter colloidal substrates as observed in relation to their counterparts at 24 hours. Cells on the planar substrate appear spread on the substrate, with cytoskeletons reflecting the occurrence of motile behaviour, Figures 3.57a) and b). Microtubule networks compose the bulk of the cells, which display actin-rich peripheries indicating

lamella ruffling required during translocation. Rear detachment sites are also present, where localised actin grouping, smaller in size in comparison to the leading edge, appears at the distal cell site. Fibroblasts on the planar surface are also observed to group, Figure 3.47c), resulting in cell-cell contact establishment. As cell-cell contacts were absent at earlier times, this may occur due to cell proliferation, resulting in reduced free surface at 48 hours. Alternatively, as multi-cellular groups have been observed on the colloidal substrates at earlier times, cell aggregation may be a feature of the hTERT fibroblast population used. However, as the first observed occurrence of this behaviour on the planar topography is noted at 48 hours, and hTERT fibroblasts are contact inhibited, the former explanation appears most valid.

The elongated detachment sites, previously observed in fibroblasts on both colloidal topographies, are once again seen at 48 hours, Figures 3.58 and 3.59. However, the very fine extensions occurring on the 20nm-diameter colloidal topography at 24 hours are lacking in the fibroblasts at 48 hours. Instead, tubulin-rich, rather than actin-rich, thicker elongations are observed on the 20nm colloidal substrate. As there are no indications of cytoplasmic elongations occurring independently of cells, for example existing as an individual entity across the substrate, four possible scenarios exist to explain the evolution of the previously observed cellular extensions. Firstly, fibroblasts may retract the elongated detachments sites over time. Secondly, cells may "repopulate" elongations, resulting in the observed tubulin-rich structures at 48 hours, rather than the initial fine actin-rich feature observed on the 20nm-diameter colloidal topography at 24 hours. A third possibility is that motile cells, traversing the substrate, in this instance the 20nm-diameter colloidal topography, may incorporate the remains of the cytoplasmic extensions, detached from cells, into the bulk of their cytoplasm. The most probable explanation is that fibroblasts, following retraction of the extension, begin again to form an elongated detachment site. This may initially be composed mostly of tubulin, but with time, and elongation extension, tubulin may constitute the main bulk of the feature. It should be noted that finer extensions are observed in fibroblasts on the 20nm-diameter colloidal substrate, Figure 3.58a), where an elongated cell appear to be under a great amount of stress, associated with this type of stretching behaviour.

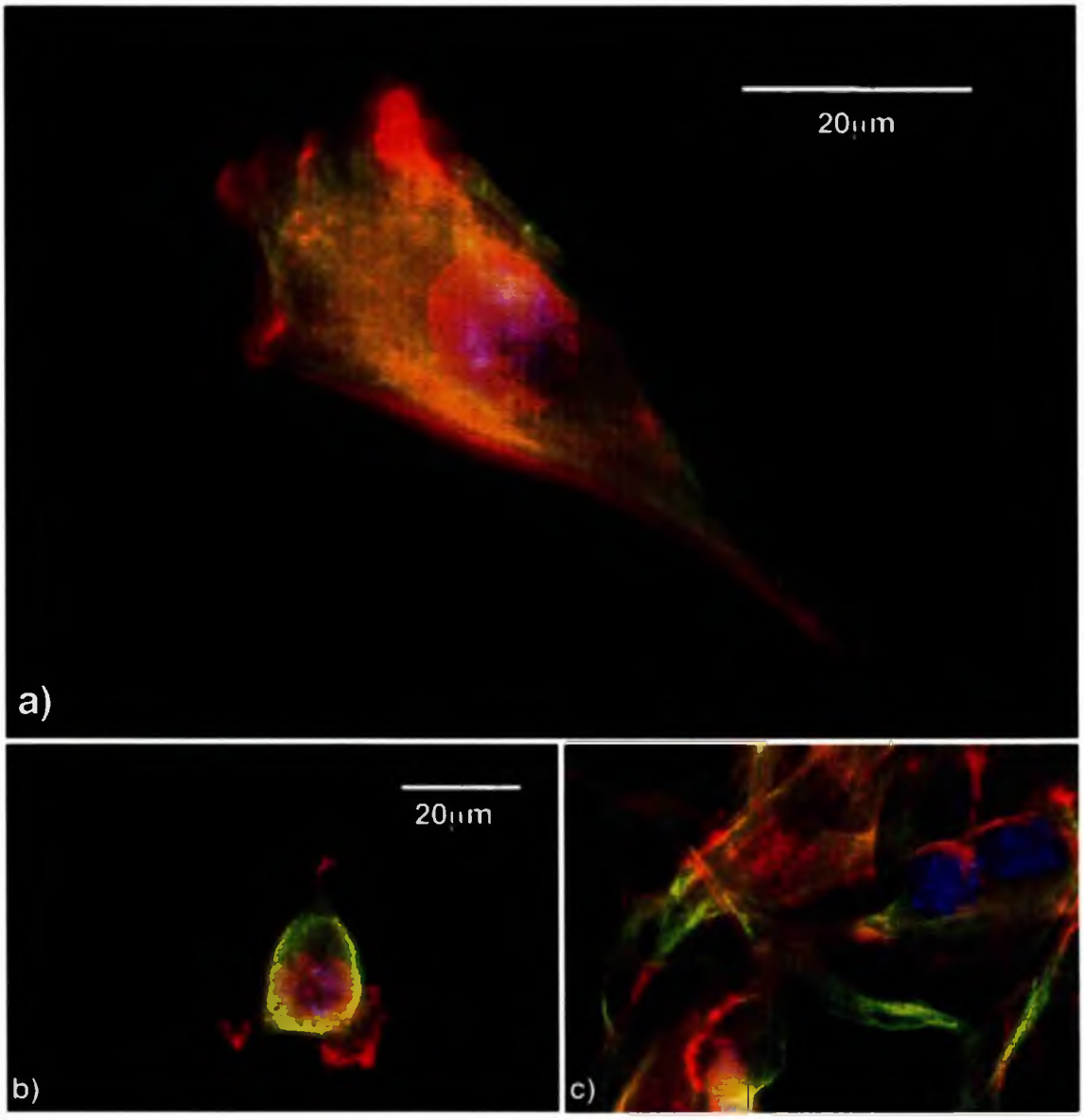

Figure 3.57: hTERT fibroblasts on control planar substrate at 48 hours. Vickers microscope was used with 50X oil immersion objective. Actin is red in these images, tubulin green and nuclei blue. Cells appear to be motile, with a leading edge seen as actin-rich membrane ruffling, a), and a thin elongated detachment site containing both actin and tubulin. The early stages of polarisation, required during motile behaviour, are also observed, b), where the cell differentiates between proximal and distal regions through actin development. Some instances of cell-cell contact are also seen at 24 hours when fibroblasts are in contact with the planar control substrate, c).

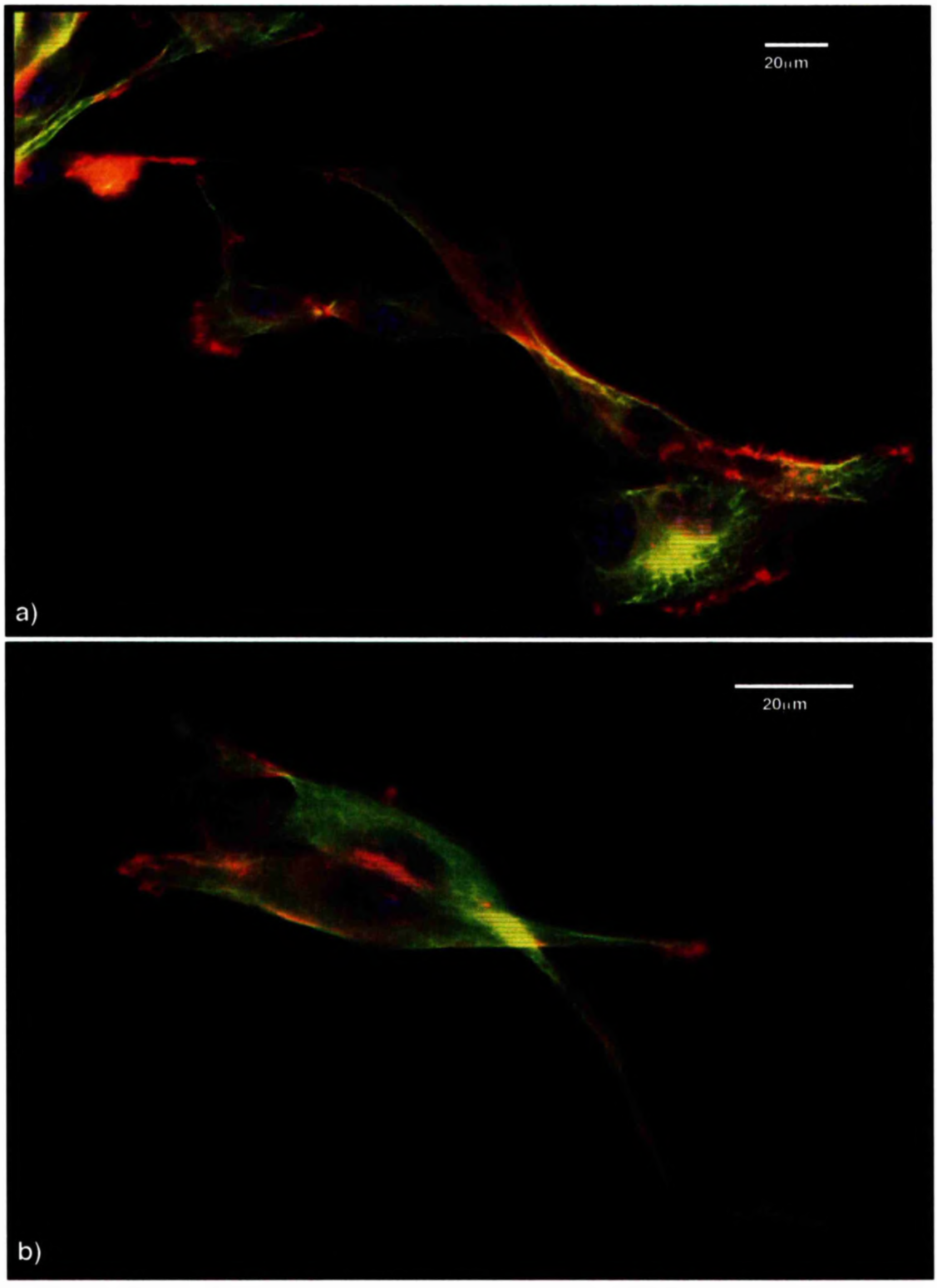

Figure 3.58: hTERT fibroblasts on 20nm-diameter colloidal topography at 48 hours. Imaging was conducted with 50X oil immersion objective of Vickers microscope. Fibroblasts do not tend to appear as individual entities at 48 hours on the 20nm-colloidal surface. Many appear as large aggregates containing upwards of ten cells, a), interconnected via microfilament and microtubule elongations. Cells in aggregates of 2 are also observed, b), with a lack of discrimination between the experimental surface and neighbouring cells resulting in overlapping of cell processes.

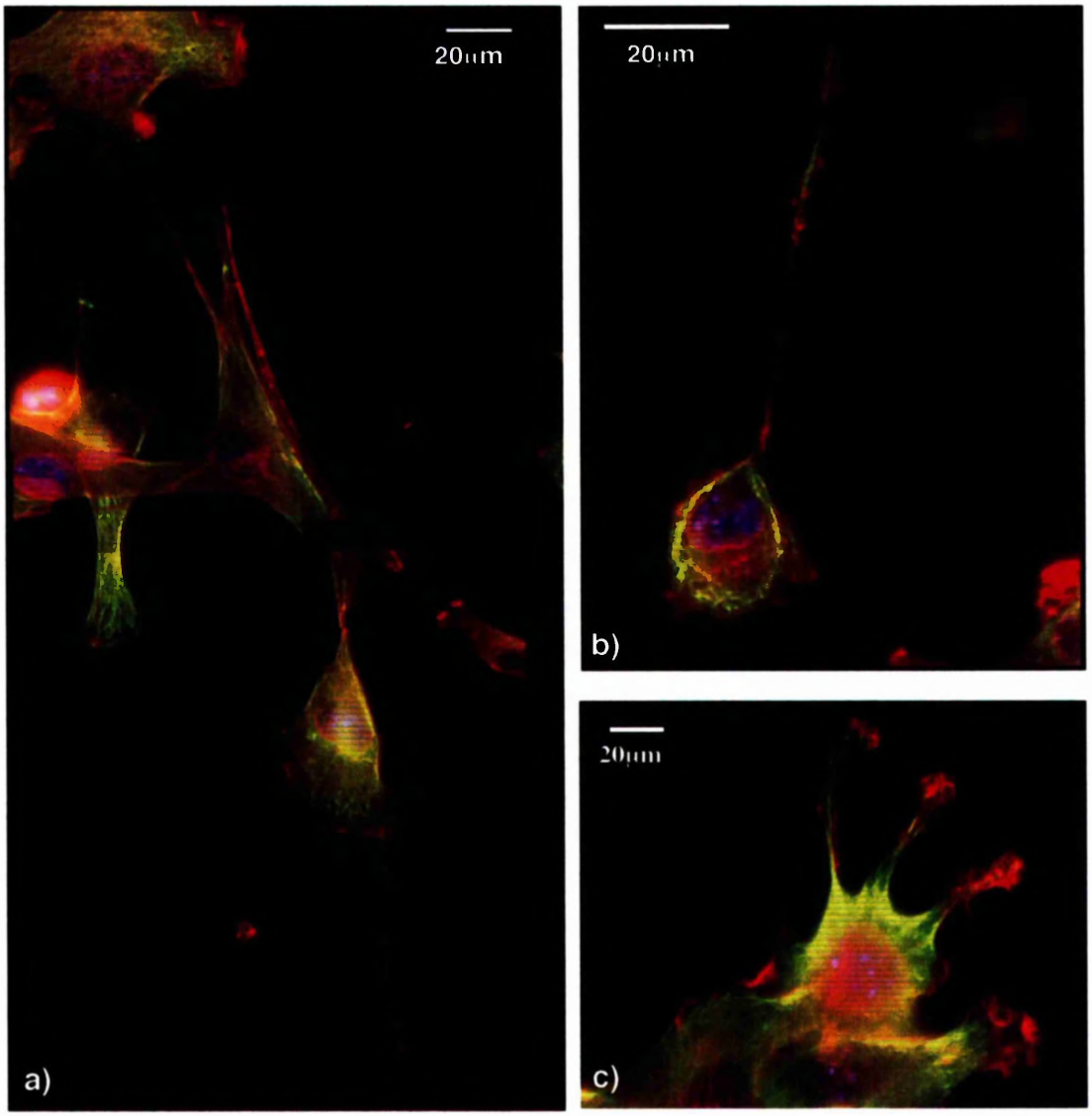

Figure 3.59: hTERT fibroblasts on 50nm-diameter colloidal topography at 48 hours, observed using a Vickers microscope with 50X oil immersion objective. Actin is depicted as red, tubulin green and nuclei blue. Fibroblasts often appear in aggregates, a), similar to those cells on the 20nm-diameter colloidal surfaces at 48 hours, with actin processes appearing to bridge gaps between neighbouring cells. Actin and tubulin containing elongations are also observed and suggest the previous movement of cells across the experimental 50nm-diameter colloids, b). Actin-rich protrusions are seen in cells attempting to emerge from an aggregate, c).

Cell-cell contacts are also a feature of fibroblasts on the 20nm-diameter colloidal topography at 48 hours, Figures 3.58a) and b). Although contact is often observed at a tubulin-composed peripheral site, or via a tubulin-rich elongation, overlapping of cells is also apparent. In some instances, fibroblasts appear to traverse one another, Figure 3.58b). In Figure 3.58a), cells appear to bridge denuded areas of the 20nm-diameter colloidal substrate via cell-cell adhesions, suggesting cell-cell contacts are more readily established as opposed to cell-substrate interactions. Actin ruffling at cell peripheries is also observed, suggesting cells are undergoing motile behaviour and are actively sensing their surrounding environment, Figure 3.58a).

In contrast to fibroblasts on the 20nm-diameter colloidal topography, cells on the 50nm-diameter colloids at 48 hours display very fine, elongated actin-rich detachments, Figures 3.59a)-c), in contrast to the thicker extensions observed in cells on this surface at 24 hours. Cell-cell contacts are also observed throughout the fibroblast population, Figure 3.59a), via fine actin-rich extensions. Cells in this image, and also in Figure 3.59c), appear to overlap one another. A further indication that these features occur as a result of incomplete rear detachment is observed in Figure 3.59b), where a rounded fibroblast with actin-rich ruffling, exhibits an elongated tail in opposition to the ruffling lamella. The beaded appearance of the elongation, appearing to mimic the underlying colloids, suggests incomplete actin polymerisation, possibly as a result of the underlying nanofeatures. Multiple protrusions occurring in fibroblasts associated at the periphery of a cellular aggregate, Figure 3.59c), suggests the established cell-cell contacts may be more influential than the cell-substrate adhesions. As a result, in an attempt to depart from the group, or in an attempt to spread on the colloidal substrate, three separate protrusions have developed, each displaying actin ruffling tips, Figure 3.59c). Similarly, a cell on the outer region of the group exhibits a single actin-rich protrusion. Microtubule networks occur within all cells on the 50nm-diameter colloidal topography, located within the main bulk of the cytoplasm and extending towards the peripheral membrane.

Summary

In summary, at 20 minutes, fibroblasts on the 20nm-diameter colloidal topography appear well spread in comparison to cells on the planar and 50nm-diameter colloidal substrates, with control cells displaying the least spread morphology. Furthermore, fibroblasts seeded on the 20nm-diameter colloids exhibit greater actin and tubulin polymerisation in comparison to other experimental samples at this early time.

At 1 hour, hTERT fibroblasts on the 50nm-diameter colloids have a more developed cytoskeleton in comparison to cells on the 20nm-diameter colloidal and planar structures. Observed cytoskeletal arrangements suggests the establishment of focal adhesion complexes (FACs), rigidity and structures required for cell locomotion, for example lamella ruffles, due to the presence of stress fibres in this instance.

By 3 hours, fibroblasts on the nanotopographies display spread morphology, especially in relation to the 20nm-diameter colloids, when compared to the planar control cells. Cell-cell contacts are also observed on the colloidal topographies, occurring at peripheral sites, or via elongated protrusions, both of which contain microfilaments and microtubules. These features are absent in controls. Stress fibres occur throughout fibroblasts on the nanotopographies and cells on the 50nm-diameter colloids exhibit lamellapodia and filopodia, which appear to interact directly with the substrate at specific, localised areas.

At 8 hours, hTERT fibroblasts on the 20nm-diameter colloidal topography express morphology which deviates greatly from cells on the control planar substrate and 50nm-diameter colloids, with highly developed stress fibres and microtubule networks, localised tubulin aggregates and also cell-cell overlapping observed. Cells on the 50nm-diameter colloids also appear well spread and localised beaded protrusions containing actin are present at rear detachment sites. In comparison to control fibroblasts, cells on the colloidal nanotopographies are more spread and have more polymerised cytoskeletons resulting in the presence of microtubules and microfilaments.

The most notable difference in cell morphology occurring between fibroblasts on the colloidal nanotopographies and planar control is the presence of very fine, elongated extensions, often measuring upwards of 100μm, occurring on the experimental surfaces at 24 hours. These elongated extensions appear to occur due to a lack of cell-substrate FAC disassembly within rear detachment sites. Cell-cell contacts are also prevalent in cells on the colloidal substrates, occurring via the observed membrane extensions or through contact at the peripheral membrane. In these instances, cells in contact with one another appear to exhibit stress across their connections, observed in the alignment of microfilaments and stress fibres. Actin stress fibres and developed microtubule networks are also observed in relation to the colloidal structures.

At 48 hours, cell morphology has varied little in comparison to that observed at 24 hours. Elongated detachment sites are still present at this time in cells on the colloidal topographies. However, rather than fine microfilament-containing structures, tubulin-rich thicker protrusions are observed on the 20nm-diameter colloidal topography. However, fibroblasts on the 50nm-diameter colloids continue to protrude actin-rich elongations at 48 hours. Cell-cell contacts are also observed throughout the fibroblast populations on both colloidal structures in comparison to cells seeded on the planar control, although in one instance, cell-cell contacts are also observed on the planar substrate.

3.4 Chapter Summary

Static topographies can be fabricated utilising colloidal lithography techniques, Section 3.2, to investigate cell reactions to nanometric surface patterns. Silica substrates with colloids adhered via an aminosilane can be characterised using scanning electron microscopy, Section 3.2.1.1, and atomic force microscopy in tapping mode, Section 3.2.1.2. AFM analysis allows for direct measurements of colloid dimensions, Section 3.2.1.2. Laser profilometry is not capable of detecting nanometric features, but highlights inadvertent micrometric patterning of surfaces, Section 3.2.1.3. Microtopography occurring on nanopatterned surfaces is further observed in relation to colloidal aggregation caused by micrometric surface faults, Figure 3.4.

Scanning electron micrographs of colloidal patterned surfaces provide images which allow for colloidal surface area coverage and interparticle spacing to be calculated, Section 3.2.1.1.1. Data obtained in this manner indicates area coverage and interparticle spacing is dependent on the time allowed for substrate immersion in a colloidal sol, Tables 3.2 - 3.4. These observations coincide with previous proposals that colloidal spacing on a surface is dependent on substrate immersion times, allowing for transition from kinetic adsorption to electrostatic repulsion of colloids (Grabar et al, 1999), Figure 3.8. Colloidal coverage obtained when using an aminosilane as an adhesive agent, Section 3.2, resulted in a surface coverage of approximately 5.1% for 20nm-diameter colloids following 24-hour immersion and 7% for 50nm-diameter particles following six applications lasting approximately 15 minutes each, Table 3.2. Furthermore, 24-hour immersion in the 20nm-diameter colloidal sol resulted in the reduction of colloidal aggregates, Table 3.3, resulting in more regular patterning of nanotopographies in this manner.

Patterning of surfaces with colloids is dependent upon mesophysic interactions, for example electrostatic repulsion, reduction in sticking probability and Debye length, thus charge screening of colloids can be employed as a means of increasing surface coverage, Section 3.2.2. Sodium chloride, Section 3.2.2.1 and Sodium citrate, Section 3.2.2.2, can be applied to either the sol or adhered colloids respectively to screen electrostatic repulsion of colloids. Based upon similar principles, an alkanethiol can also be applied to adhered colloids, Section 3.2.2.3. However, bonding of the alkanethiol to gold colloids also displaces bonds between the gold and aminosilane present at the

substrate surface resulting in mobility of the nanoparticles in relation to the base substrate. These methods of altering colloidal surface density were met with limited success, Figures 3.9 - 3.11, due to techniques associated with surface drying. Furthermore, when etching densely packed colloids, "nanomountains" arise, Section 4.2.2.1, detracting from the individual colloidal-based nanofeatures sought throughout the pattern. Thus studies of cell behaviour in relation to densely packed colloidal topographies were not practised, and colloidal topographies were produced for biological investigations following 24-hour immersion in sols in the absence of charge-shielding and mobilisation molecules.

When investigating epitenon cell behaviour in relation to the colloidal topographies, Section 3.3.1, the stability of the nanopatterned features was brought into question, Section 3.3.1.1, with entities resembling colloids appearing on the apical membrane and colloidal density reduced in some cell-inhabited areas, Figure 3.12. However, through the utilisation of secondary electron, Figure 3.13, 3.14, 3.15a) and 3.16a), and backscattered electron, Figures 3.15b), 3.16b) and 3.17b), detection and X-ray microanalysis, Figure 3.17b), the possibility of colloidal uptake was eliminated (Wood et al, 2002).

Epitenon cell morphology was subsequently investigated at 24 hours on the 50nm-diameter colloidal topographies, Figures 3.18-3.30. Epitenon cells were capable of direct interactions with individual colloids at their peripheral membrane, Figure 3.18. Cells were also observed to utilise neighbouring apical membranes of epitenon as a substrate during division, Figure 3.20, where dividing cells exhibited elongated intercellular connections suggesting altered migration qualities with respect to final separation of cells via traction occurring at the cell-substrate interface. This possibility was further highlighted in the very thin, elongated cell-substrate contacts occurring on the colloidal surface, Figure 3.21, where limited contact was observed. Cell-cell contacts were observed throughout the epitenon cell population, Figures 3.22-3.29. String-like membrane appendages terminating as pads appear to anchor cells to their neighbours, Figure 3.22. Overlapping cells were also observed, Figure 3.23, via thinly spread membranes, where thin protrusions appear to act as intercellular connections. More fibrous extensions were present in cell-cell aggregates, once again terminating in pad-like features on neighbouring apical membranes, Figure 3.25, 3.26 and 3.28, suggesting bridging of cells across denuded areas of the colloidal topography.

Epitenon cells on the 50nm-diameter colloids were also observed to align to neighbouring cells, Figure 3.29, via intertwining of protrusive extensions. In this instance, stress occurring across cells visualised in ridges occurring across their membranes, Figure 3.22 and 3.29, appear to influence their neighbours. Membrane protrusions occurring in the absence of neighbouring cells was investigated using secondary electron (SE) and backscattered electron (BSE) detection, Figure 3.30. Distinction between these fine elongations and the main cell body indicates differences in the density of these features, suggesting differences in composition. It is possible that very elongated protrusive extensions under low-stress, resulting in lack of rigidity, may act as precursors to the more fibrous features observed previously.

Cell-cell contacts occurring via elongated protrusions appears to be a result of contact promotion, or altered contact inhibition, as epitenon density across the substrate is low, thus contact is not established due to limited available substrate. Yet cells continue to be observed in groups or aggregates rather than individuals when seeded on the 50nm-diameter colloidal topography at 24 hours.

HGTFN endothelial cells display similar behaviour, Section 3.3.2, especially following 4 hours of contact with 50nm-diameter colloidal topography, Figure 3.34, deviating from cells on control planar substrates at this time. Very spiky peripheral membrane protrusions are observed, with endothelial cells appearing elongated and stretched. Cell-cell contacts are also present at this time in endothelial cells, Figure 3.34a).

Time-lapse video microscopy monitoring of hTERT fibroblasts, Section 3.3.3.1, indicates altered cell behaviour in response to colloidal topography. Fibroblast behaviour is further modified in response to different sized colloids when comparing cells on the 20nm-diameter, Section 3.3.3.1.1, and 50nm-diameter, Section 3.3.3.1.2 colloidal topographies.

Videos of fibroblasts on the 20nm-diameter colloids indicate cells catapult across the substrate during motile behaviour, Figure3.3.3.1.1Video on accompanying CD, suggesting an imbalance in proximal and distal cell-substrate adhesions and a great amount of stress occurring across the main cell axis. Cell-cell contacts resulting in cellular aggregate formation, where membrane boundaries between neighbours are

indistinguishable, suggests cell-cell adhesion preferences in comparison to cell-substrate focal adhesion complex establishment. Once again, as observed in epitenon cells, the presence of uninhabited, cell-free substrate and the occurrence of cell-cell contacts suggest possible contact promotion behaviour. Elongated peripheral membrane protrusions are also observed, as seen throughout this work, where cells are seeded on nanotopographies.

In relation to 50nm-diameter colloidal topography, time-lapse video microscopy of hTERT fibroblasts, Section 3.3.3.1.2, indicates similar elongated protrusions. However, the morphology of these extensions is altered in comparison to those observed on the 20nm-diameter colloids, expressing a beaded pattern along their length. Cell-cell contacts occurring on the 50nm-diameter colloidal substrate result in alignment of fibroblasts to their neighbours, with individual boundaries distinguishable, thus separating cells in a manner previously lacking on the 20nm-diameter colloids. Thus, time-lapse video microscopy observations of hTERT fibroblast behaviour in relation to both 20nm- and 50nm-diameter colloidal topographies indicate feature size and/or distribution of colloids is important in determining fibroblast reactions to nanotopography.

With respect to adhesion assay experiments, Section 3.3.3.2, analysis of variance (ANOVA) indicated that hTERT fibroblast adhesion is affected by surface topography when comparing planar, 20nm- and 50nm-diameter colloidal substrates, and that the mean number of cells adhering to each individual surface are also affected by time, Table 3.6. Furthermore, ANOVA revealed that an interactive effect between topography and time acts to influence fibroblast adhesion. A Tukey test was employed to identify the specific differences between the means within the data, Table 3.7. Specific differences were found between the mean number of fibroblasts adhering to planar and 20nm-diameter colloidal substrates at 20 minutes and planar and 50nm-diameter colloidal substrates at 20 minutes. Increased fibroblast adhesion on the nanotopographies at these early times was further supported by a residual plot of the data where all three substrates were compared at all three time intervals as a graph, Graph 3.1. Furthermore, cell adhesion on the 50nm-diameter colloids at 1 hour was significantly different when compared to the mean number of fibroblasts adhering to the same topography at 3 hours, indicating a temporal function with respect to cell adhesion on the 50nm-diameter colloids.

Scanning electron microscopy imaging of hTERT fibroblasts on colloidal and planar substrates elucidate previously observed behaviour, Section 3.3.3.3. At 20 minutes, cells appear more spread on the colloidal substrates in comparison to controls, Figure 3.40. Fibroblasts on the 20nm-diameter colloids also exhibit fine protrusions, which contact the substrate at localised sites, Figure 3.40e) and f). In some instances, fibroblasts on the 50nm-diameter colloids appear very rounded, with little membrane activity, suggesting highly polarised behaviour with respect to internal and external environments. Fibroblasts are still observed to be most spread on the colloidal substrates at 1 hour in comparison to controls, Figure 3.41. Numerous elongated peripheral protrusions are seen to extend across the colloidal topography. Furthermore, cells on the 20nm-diameter colloids exhibit clustered apical membrane features, Figures 3.41e) and f), suggesting distinction and polarisation with respect to apical and basolateral sites. Some instances of rounded cells with very smooth membranes are once again observed on the 50nm-diameter colloidal topography, Figure 3.41e).

At 3 hours, fibroblasts on the colloidal topographies exhibit very spiky peripheral membrane extensions, especially on the 50nm-diameter colloids, Figure 3.44. Cell-cell contacts, absent in controls, are also present, Figure 3.43 and 3.44, with overlapping of fibroblasts observed. Furthermore, peripheral extensions observed on the 20nm-diameter colloids appear to attach directly to the apical surface of neighbouring cells, Figure 3.43b), where rather than terminating in pads as observed in epitenon cells, protrusions appear to attach via a finger-like pronged terminus. Fibroblasts on the planar substrates display extra-cellular matrix production features at 8 hours, Figure 3.45, and are well spread. The most notable difference between these and cells on the colloidal substrates is the presence of globular entities occurring on membranes and the nanotopography, Figure 3.46. Cell-cell contacts via elongated protrusions are also observed at this time on the nanotopographies. In particular, extensions anchor neighbouring cells on the 20nm-diameter colloids, Figure 3.46, and appear to have some contractile function. This is also observed on the 50nm-diameter colloidal topography, however the amount and extent of protrusions are less frequent, Figure 3.47. Protein production is also observed on the colloidal substrates at 8 hours, Figures 3.46 and 3.47. Following 24 hours contact with the substrates, fibroblasts on the planar controls also exhibit cell-cell contact behaviour, elongated protrusions and further evidence of ECM production, Figure 3.48. In comparison, fibroblasts on the 20nm-diameter colloidal

topography appear intertwined and entangled with one another, where cell-cell contacts allow fibroblasts to elevate their main body from the nanopatterned surface, Figure 3.49. Furthermore, cells appear to assemble upon one another, suggesting alterations in contact inhibition. The globular entities previously observed at 8 hours appear intertwined with long, fine string-like elongations, indicating their possible cellular origin, Figure 3.49.

Immunohistochemistry coupled with fluorescence microscopy allows insight into cytoskeletal morphology, Section 3.3.3.4, with respect to previous behavioural alterations in fibroblasts on the colloidal topographies. Developed microtubule networks are observed as early as 20 minutes in fibroblasts seeded on the nanotopographies, Figure 3.50. Cells also appear well spread especially in relation to the 20nm-diameter colloids. By 1 hour, fibroblasts on the nanotopographies are more spread in comparison to controls, Figure 3.51. Microtubule networks appear more developed, and actin stress fibres are also observed, especially in cells on the 50nm-diameter colloidal topography, where cell morphology deviates greatly from the more generally observed circular spread form. Microtubule networks indicate polarisation and spatial arrangements occurring within cells, while well-defined stress fibres indicate FAC development with respect to cell-substrate adhesions.

Spread morphology on the colloidal topographies is greater in comparison to controls, especially in cells on the 20nm-diameter colloidal topography, by 3 hours. Cell-cell contacts are also observed on the nanotopographies, occurring at the peripheral sites or via protrusions where, in both instances, microfilaments and microtubule arrangements appear central to their establishment. Stress fibres are also observed in fibroblasts on the colloidal topographies, and lamellapodia and filopodia extensions appear to interact with the 50nm-diameter colloidal substrate. Cell shape and morphology on the 20nm-diameter colloids at 8 hours is greatly altered in comparison to fibroblasts on the other experimental structures, where cells express defined stress fibres, developed microtubule networks, localised tubulin aggregates and overlapping with neighbouring cells. On the 50nm-diameter colloids, spread cells display beaded rear detachment-located elongations composed mainly of actin.

Protrusions measuring upwards of 1mm are observed on the colloidal topographies at 24 hours, where cell-cell contacts are present throughout these populations, occurring

via peripheral or protruding membrane features. Stress, observed in microfilament alignment, appears continuous in relation to each fibroblast and its nearest neighbour contact. Similar fibroblast morphologies are present at 48 hours, where fibroblasts on the 50nm-diameter colloids continue to protrude actin-rich elongations. However, cells on the 20nm-diameter colloidal topography exhibit thicker, tubulin-containing protrusions. Cell-cell contacts continue across the colloidal substrates at this time, a feature absent on control, planar structures.

In conclusion, colloidal topographies are observed to alter epitenon, endothelial and fibroblast behaviour and morphology in relation to control, planar substrates, indicating their ubiquitous, rather than cell-specific, effects. 20nm- and 50nm-diameter colloidal topographies are observed to elicit different behavioural responses in hTERT fibroblasts. With respect to fibroblast adhesion, 20nm-diameter colloidal substrates are more adhesive at 20 minutes in comparison to 50nm-diameter colloidal and planar control surfaces. At 1 hour, 50nm-diameter colloidal substrates are most adhesive, while at 3 hours, adhesion is observed to be similar on all structures, including controls. Analysis of variance (ANOVA) identified an interactive effect between topography and time, influencing fibroblast adhesion. A Tukey test detected 9 pairs of means from a possible 36, whose differences were statistically significant, Table 3.7.

Time-lapse video microscopy observations indicate temporal alterations in fibroblast behaviour on colloidal topographies. At early times, cells spread on the 20nm-diameter colloids and become motile. In one instance, a fibroblast is observed to elongate and initially move in one direction where, upon contact with another cell, orientates the bulk of the cytoplasm in the opposite direction, traversing its still-adhered rear detachment. Fibroblasts are also seen to catapult across the substrate and establish cell-cell contacts via elongated protrusions or peripheral contacts resulting in aggregate formation. Individual fibroblasts within such a grouping on the 20nm-diameter colloids are indistinguishable from members of the aggregate. In comparison, fibroblasts seeded on the 50nm-diameter colloidal topography lack catapulting behaviour. However, cell-cell contacts are observed, also occurring via membrane peripheries or protrusions, but do not result in the aggregate formation. When cell-cell contacts are established on this substrate, fibroblasts are observed to influence one another's alignment. Scanning electron micrographs indicate cell-cell contacts via elongated membrane protrusions terminate in either pad-, as observed in epitenon cells, or pronged-, as in fibroblasts,

structures at the apical membrane of neighbours. Peripheral contacts appear to be established via entanglement of short membrane protrusions.

Both tubulin and actin cytoskeletal elements are observed to be involved in these observations. At early times of up to 3 hours, spread fibroblasts exhibit developed microtubule networks and defined stress fibres. Elongated protrusions are composed mainly of microfilaments in cells on both colloidal topographies. By 8 hours, fibroblasts on the 50nm-diameter colloids display beaded elongated detachment sites composed mainly of actin; absent in fibroblasts on the other surfaces. At later times, 48 hours, previously observed actin-rich elongations on the colloidal substrates are observed to be composed mainly of tubulin on the 20nm-diameter colloidal topography. Highly defined stress fibres, observed most frequently in fibroblasts on the 50nm-diameter colloidal topography at later times, 3 hours onwards, would account for the observed fibroblast alignment relative to cell-cell contacts in the time-lapse video work.

Contact inhibition appears altered in epitenon, endothelial and fibroblast cells on colloidal topographies, as cell-cell contacts are observed in the presence of uninhabited, cell-free surfaces. Elongated membrane protrusions are also observed in these cell types on both the 20nm- and 50nm-diameter colloidal topographies. The main distinction between fibroblasts as a result of different colloidal sizes is the catapulting behaviour observed on the 20nm-diameter colloids and altered cell-cell contact behaviour. Individual fibroblast boundaries are indistinguishable in cellular aggregates observed on the 20nm-diameter colloidal topography. In comparison, cell-cell contacts occurring on the 50nm-diameter colloids do not result in groupings, but rather in alignment of individual fibroblasts relative to their neighbours.

These results indicate cell behavioural alterations in response to colloidal nanotopographies are dependent on feature size. Colloidal diameter also controls feature distribution, indicating colloidal frequency or feature pitch within nanopatterned topographies may contribute to the different cell behaviours observed when comparing one cell types reaction to both the 20nm- and 50nm-diameter colloidal substrates.

Chapter 4: The Effects of Nanopillared Topography on Cell Behaviour

4.1 Introduction

When considering cell reactions to colloidal gold topography, previously discussed in Chapter 3, the role of colloidal chemistry involvement in cell reactions when in contact with the experimental substrates requires further attention. An approach, where feature dimensions parallel previous work involving the colloids but removing the presence of the gold particles, was taken, where colloidal surfaces were used as an etch mask in relation to the SiO_2 surface oxide of the base substrate. Colloidal lithography has previously been utilised as an etch mask with respect to the electronics industry (Lewis et al, 1998 and 1999). This method resulted in nanopillars etched in silicon (rather than silica as described within this chapter), with colloids remaining in the final structure on pillar peaks, their original position in the etch mask. Dry etching was selected in comparison to wet etching so that the structures would be approximately vertical. Wet etching also involves the introduction of chemicals, which may affect the SiO_2 chemistry previously present on the colloidal surfaces, or prove harmful to cell cultures. Following dry etching of the colloidal substrates, the colloidal gold particles were removed from the resultant nanopillared structure, allowing for alterations in surface chemistry across the experimental surface to be minimised.

The vertical dimensions of the pillars can be altered by simply altering the time the colloidal mask is exposed to the plasma during the dry etch. Pillar diameter is related to the colloid size acting as a mask during this process. Both 20nm-diameter and 50nm-diameter colloidal particles were used as etch masks, resulting in possible comparisons to be made with respect to the previous observations of cell behaviour in relation to the colloidal topographies, as discussed in Chapter 3. Comparisons made in this manner should indicate the possible role of the colloidal material and chemistry in relation to cellular reactions to the topographies, and the role of the nanometric feature dimensions in elicited cellular response, as a number of vertical dimensions were examined.

Preliminary experiments where cells were plated on the nanopillared surfaces were conducted using both epitenon cells and HGTFN endothelial cells. Epitenon cells were viewed following one hour in contact with the surface using scanning electron Microscopy, where morphological alterations are observed on 20nm-diameter, 200nm-

high pillars. HGTFN endothelial cells were recorded using time-lapse video microscopy, for a period of 36 hours, on 50nm-diameter, 200nm high pillars.

Later experiments were conducted using hTERT fibroblasts which were seeded on 20nm-diameter, 200nm high pillars, control planar substrate, and control etched surface and cell-substrate adhesion was monitored on all these surfaces at 20 minutes, 1 hour and 3 hours. Fluorescence microscopy imaging was also conducted to reveal actin and tubulin cytoskeleton arrangements in hTERT cells on nanopillars of various dimensions, at periods paralleling previous observations on the colloidal topography, Section 3.3.3.2 and 3.3.3.4.

4.2 Fabricating nanopillared topography

Silicon and fused silica, both with a surface oxide of silica, were used as base substrates when fabricating nanopillared topographies, Figure 4.1. Surfaces were treated as previously described in relation to colloidal topography fabrication in Section 3.2, Figure 4.1ii). This resulted in a colloidal mask with similar interparticle spacing as previously described for the colloidal topography, Section 3.2.1.1.1. Similarities in feature spacing allows for similar, comparable dimensions seen in both the colloidal structures and nanopillared topography.

Following the fabrication of a colloidal mask, a dry etch process was utilised to etch pillars with either 20nm- or 50nm-diameter, into fused silica or SiO_2 coated silicon substrates, Figure 4.1iii). Fused silica was etched in an Oxford Plasma Technology RIE-80 (referred to throughout as a BP80) dry etch machine using CHF_3. The silica substrates transmit light and so can be used in conjunction with phase-contrast, light and time-lapse video microscopy following the addition of cells. Silicon was etched in an Oxford Plasma Technology RIE-80 dry etch machine using $SiCl_4$ and was imaged using SEM, either when viewing the accuracy of the method or cell interactions with the nanopillars at high magnification following dehydration and critical point drying (CPD) of cells, Section 2.7.

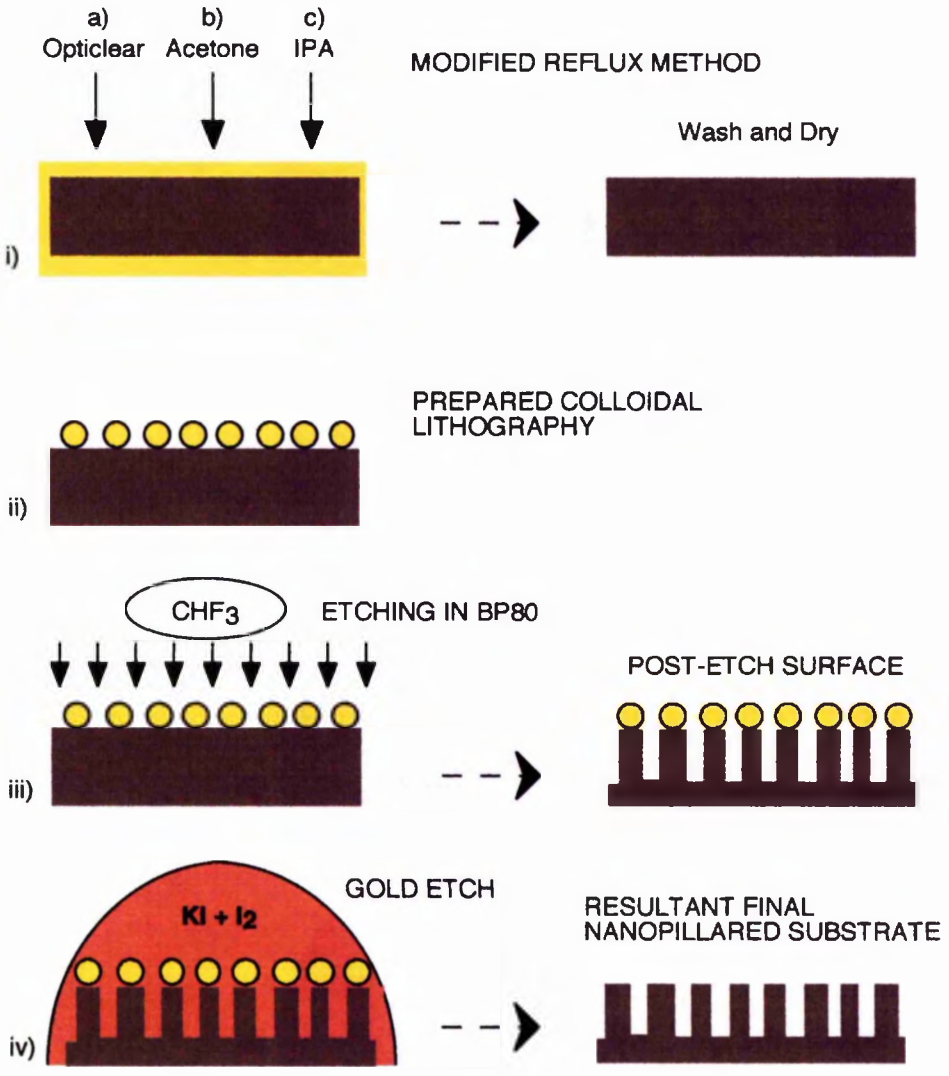

Figure 4.1: Schematic representation of nanopillar fabrication in SiO_2 with fused silica base substrate. It should be noted that final nanopillars are irregular, reflecting the original colloidal mask, rather than regular as may be interpreted from this schematic representation. The quartz cutting process results in the presence of wax on the quartz base substrate. This must be removed to allow for etching. A modified reflux cleaning method was employed, i), where samples are firstly immersed in Opticlear at 50°C for 1 hour, i(a), then, under the same conditions, Acetone, i(b), followed by immersion in IPA at the same temperature for 1 hour, i(c). Cleaned samples are then rinsed in RO water under sonication to remove remaining residue. Colloids are adhered to the cleaned base substrate, ii), using an aminosilane as previously described, Section 3.2. The colloids act as an etch mask during dry etching in the BP80 for quartz using CHF_3, iii), (RIE-80 etch machine is used for silicon with $SiCl_4$). Following dry etching, colloids remain on the structure, either in their original position or in a new position following sputtering from the surface, or undermining resulting in movement from their original position. The colloids are removed using a Potassium Iodide and iodine gold etch, iv). The final structure is then rinsed in RO water.

A problem emerged during the fabrication of nanopillars in fused silica base substrates, where pillar heights were reduced in relation to the predicted height. Obviously, this problem was occurring due to insufficient etching, although the cause of this was unclear. This problem appeared to arise following an alteration in the quartz fabrication

by the manufacturer (personal communication with M. Roberts). When making quartz coverslips or slides, bulk quartz is held, during cutting to the appropriate size, by either paraffin wax or bees wax. Previously, following this method, samples were subjected to trichloroethylene to remove residual wax from the final structures. However, use of this chemical is banned as a carcinogen resulting in residual wax remaining on the final quartz substrates. A method, based upon a reflux technique conducted in the Electronics and Electrical Engineering Department, University of Glasgow, was therefore required prior to colloidal application on treated quartz surfaces, described below, to remove residual wax.

The alternative reflux method, Figure 4.1i), involved firstly heating Opticlear, contained in a beaker, in a water bath to 50°C in the fume cupboard. Quartz samples were then introduced to the Opticlear at this temperature and left for approximately 1 hour. Opticlear is poured from the beaker containing the quartz, and Acetone is added to the substrates and placed in the pre-heated water bath in the fume cupboard for a further hour. The Acetone is disposed of, and a subsequent immersion in IPA for 1 hour at 50°C ensues. Structures are removed from the IPA and placed in a fresh beaker of RO water. The beaker containing the quartz and water is then sonicated for approximately 10 minutes, and the structures are then dried with a nitrogen gun followed by a 1hour bake at 70°C to complete the drying process. Only following residual wax removal can treatment of the quartz using the colloidal method, Section 3.2, occur if samples are to etch properly, Figure 4.1ii).

The machine selected for the dry etching process is solely dependent upon the base substrate being used, in this case either silicon or quartz, due to the gas required to etch the material. It is not regarded as good practice in dry etching to mix fluorine- and chloride-containing gases, thus different RIE machines are used (referred to as BP80 and RIE-80 machines) to etch SiO_2 and Si. By altering the etch time, etch depth can be controlled. The height of the pillars is dependent upon the durability of the mask and the degree of lateral (as distinct from vertical) etching. Etch rate is in the region of 40nm per minute. The gold is slowly sputtered from the surface by the physical action of the ions, and lateral etching slowly undermines the mask. Undermining of the colloidal mask is a particular concern when increasing the etch depth, and has been seen to occur in relation to the planar-nanopillared surfaces, Chapter 5. Gold aggregates occurring due to drying problems, form nanomountains in silica when etched, and are seen to be

surrounded by very small pillars occurring due to etching of the sputtered colloids from these aggregates. The conditions for each dry etch machine used, RIE-80 for silicon and BP-80 for quartz, for each pillar height produced, either 80nm or 200nm, are presented in Table 4.1. The diameter of the colloids used to create a mask has no bearing upon these settings.

Machine	Pillar height	Etch Time	Gas	Flow Rate	Power	Chamber Pressure
RIE-80	80nm	2 min	$SiCl_4$	9sccm	100W	9mTorr
(silicon)	200nm	5 min	$SiCl_4$	9sccm	50W	10mTorr
BP80	80nm	2 min	CHF_3	20sccm	100W	16mTorr
(quartz)	200nm	5 min	CHF_3	20sccm	100W	16mTorr

Table 4.1: RIE-80 and BP80 etch machine settings for etching nanopillars in SiO_2 surface of silicon and quartz respectively. Etch depth is controlled by altering the etch time.

Following etching of the nanopillars in the SiO_2 surface of either silicon or quartz utilising the colloidal etch mask, Figure 4.1iii), the colloidal gold particles were removed from the surface in an attempt to create an even surface chemistry across the structure. A potassium iodide and iodine solution (32g potassium iodide, 200ml water, 8g iodine, Merk, UK) was applied, post-etch, to the surface, Figure 4.1iv). Samples were immersed in the $KI + I_2$ for approximately 20 seconds as the gold etch etched at a rate of approximately 2nm per second (personal communication with L. Pollock). Substrates were immediately rinsed in a beaker of RO water to remove residual etchant, and then dried in blown nitrogen gas.

4.2.1 Acid cleaning etches micrometric surface imperfections

It was at this point in the project that the affect of Caro's Acid on surface structures was examined, Figure 4.2. The ability to clean structures with nanofeatured surfaces is important even though, during this project, following the addition and examination of cells in relation to the topography, substrates were discarded. However, structures often require subsequent cleaning prior to the application of biological material to remove residues, which may contaminate cell cultures.

A quartz slide was scored using a diamond-tipped scriber and examined using light microscopy, Figure 4.2a). Due to the dimensions of the scribe tip and the resolution of the light microscope, the scratch is examined at the micrometric scale. This should

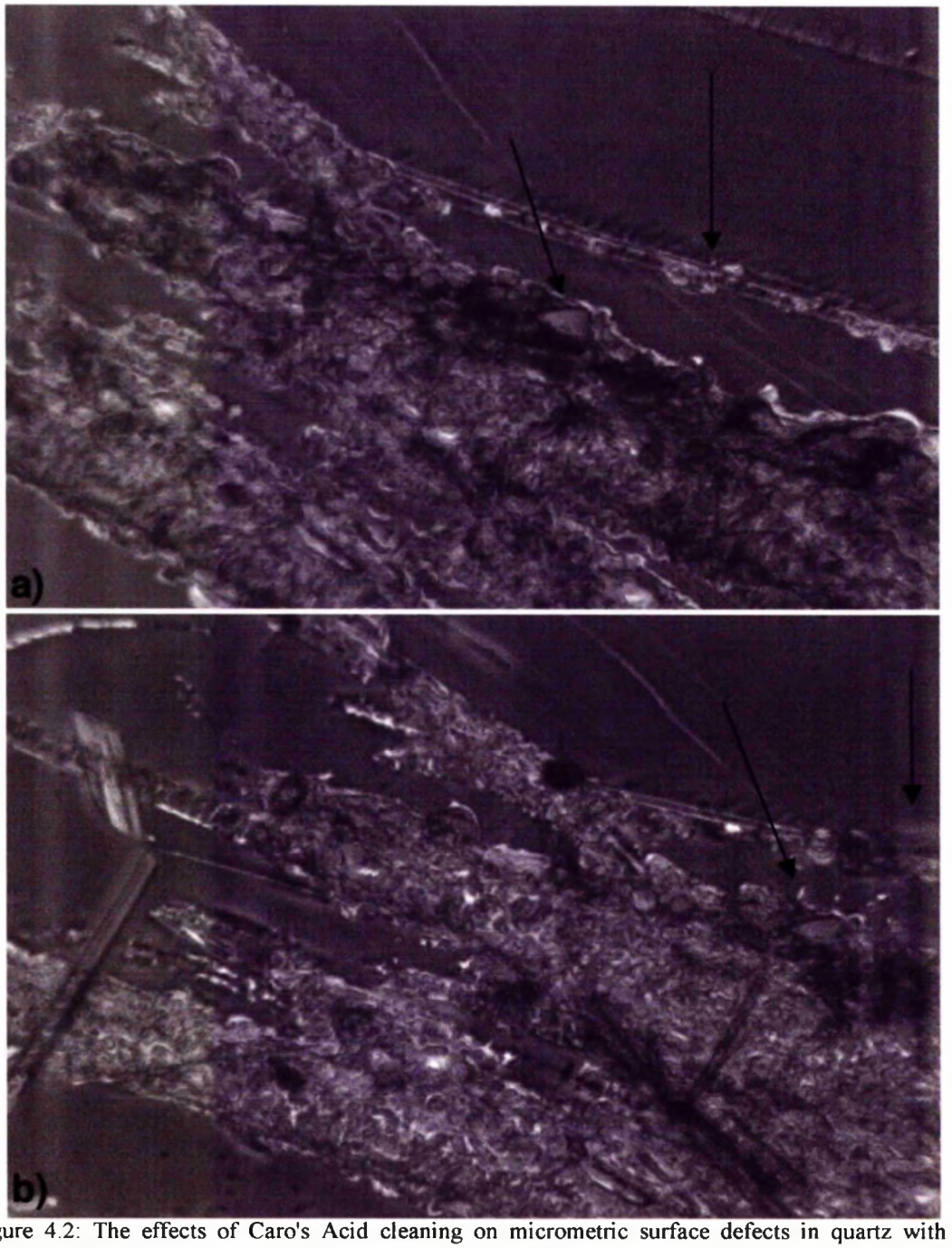

Figure 4.2: The effects of Caro's Acid cleaning on micrometric surface defects in quartz with silica surface oxide. A diamond-tipped scriber was used to mark the quartz and a light microscopy image was captured of the inflicted defect, a). The substrate was then cleaned for 20 minutes using a Caro's Acid wash (1 part (<30%) hydrogen peroxide: 3parts (95%) sulphuric acid (v/v)). The structure was then rinsed in RO water, dried, the defect area was located and a light microscopy image taken, b). Arrows are included as a reference between features on the pre- and post- acid wash surface. As regions of the marked surface appear altered following acid cleaning, b), it would appear that the Caro's wash has an etching effect on micrometric surface features.

indicate possible erosion of the base substrate, in this instance quartz with silica surface. The sample was then immersed in Caro's Acid (1 part (<30%) hydrogen peroxide: 3parts (95%) sulphuric acid (v/v)), for 20 minutes as is the time in the general application of this wash in previous experiments, Section 3.2. The sample was removed from the acid and rinsed in RO water under sonication, again adhering to the established protocol. The area previously examined using the Leiss Microscope was located, and an image captured of the scratch following the Caro's Acid treatment, Figure 4.2b). Areas in each of these images, denoted by arrows, suggest possible etching effects on micrometric flaws on the silica surface due to the increased defect area when using Caro's Acid. This suggests that a subsequent wash using this acid following etching of nanopillars in the surface oxide would deviate from the established nanotopography. This experiment also suggests that, unless surfaces are completely without flaws, surface defects occurring during manufacturing and handling of the base substrates will result in amplification of these features, detracting from the nanotopography. The implications of amplified micrometric surface defects have been discussed previously in relation to the laser profilometer image, Section 3.2.1.3, and indicates the need to investigate fabricated surfaces both at the nano- and micro-metric scales.

Caro's Acid appeared to etch micrometric surface features, and general concerns have been aired with regard to the effects of acid treatments on nanotopography (personal communication with Mary Robertson and Brendan Casey). Thus, as a precautionary measure, any cleaning of the nanofeatured surfaces, following dry and gold etching, was conducted utilising the modified reflux method as discussed previously within this section. All substrates, as previously explained, were rinsed in Hepes heated to 37°C immediately prior to seeding cells on the surface.

4.2.1 Characterising Nanopillared topography

Scanning Electron Microscopy using a Hitachi S-900 with Secondary Electron detector, Nanoscope Atomic Force Microscope and Vickers Interference Reflection Microscope (IRM) using oil immersion were used to image nanopillared structures. As discussed previously in relation to the colloidal topographies, imaging of surface features is limited to the resolution capabilities of available microscopes. The two main imaging techniques involved the use of high resolution FESEM and AFM as previously utilised in relation to the characterisation of colloidal surfaces. However, Interference Reflection Microscopy was also used in relation to 50nm-diameter, 200nm high pillars

in quartz, as the increased lateral dimensions of these pillars, imaged using both electron and atomic force microscopy, in comparison to the 50nm-diameter of the colloids, may, theoretically, be detected using this method.

4.2.1.1 Scanning Electron Microscopy Imaging of Nanopillars

An Hitachi S-900 FESEM was used to image nanopillars etched in the surface oxide (SiO_2) of silicon or quartz base substrates. All nanopillared structures must be sputter-coated with Gold-palladium acting as a conducting material in order to increase contrast of the features across the surface, the method of which is described in Section 2.7.3. All samples were viewed at a 40° tilt in the positive direction so that the vertical dimensions of the features could be viewed, Figure 4.3.

Low magnification SEM imaging of 50nm-diameter, 200nm high pillars, Figure 4.3a), indicates localised differences across the substrate surface. This again confirms previous observations that both nano- and micro-metric measurements of experimental surfaces should be performed. Low magnification imaging of nanotopographies gives insight into the type of surface the cells are exposed to upon plating on the substrate. Increasing the magnification gives insight into the more fundamental features of the nanopillared surface, Figure 4.3b). Areas where colloids appear to have been in contact in the original etch mask results in the occurrence of larger diameter features, detracting from individual nanopillars (closed arrows in Figure 4.3b)). Lateral etching, as distinct from vertical etching, also appears to have occurred, undermining the original colloids forming the mask (open arrows in Figure 4.3b)). This results in a non-uniform pillar diameter, with greater width occurring at the base of pillars, tapering to a diameter more in accordance with the original colloidal mask. This is better seen at increased magnification, Figure 4.3c).

As original colloids composing previous experimental topography, Chapter 3, have either a 20nm- or 50nm-diameter, etch depth, dictated by etch time, can be altered to reflect these dimensions, Figure 4.3d). 50nm-colloids were used in this instance as an etch mask, with vertical height of the pillars measuring 80nm. Pillars in this instance appear more spherical and rounded in comparison to the 200nm high pillars, resembling a more colloidal appearance.

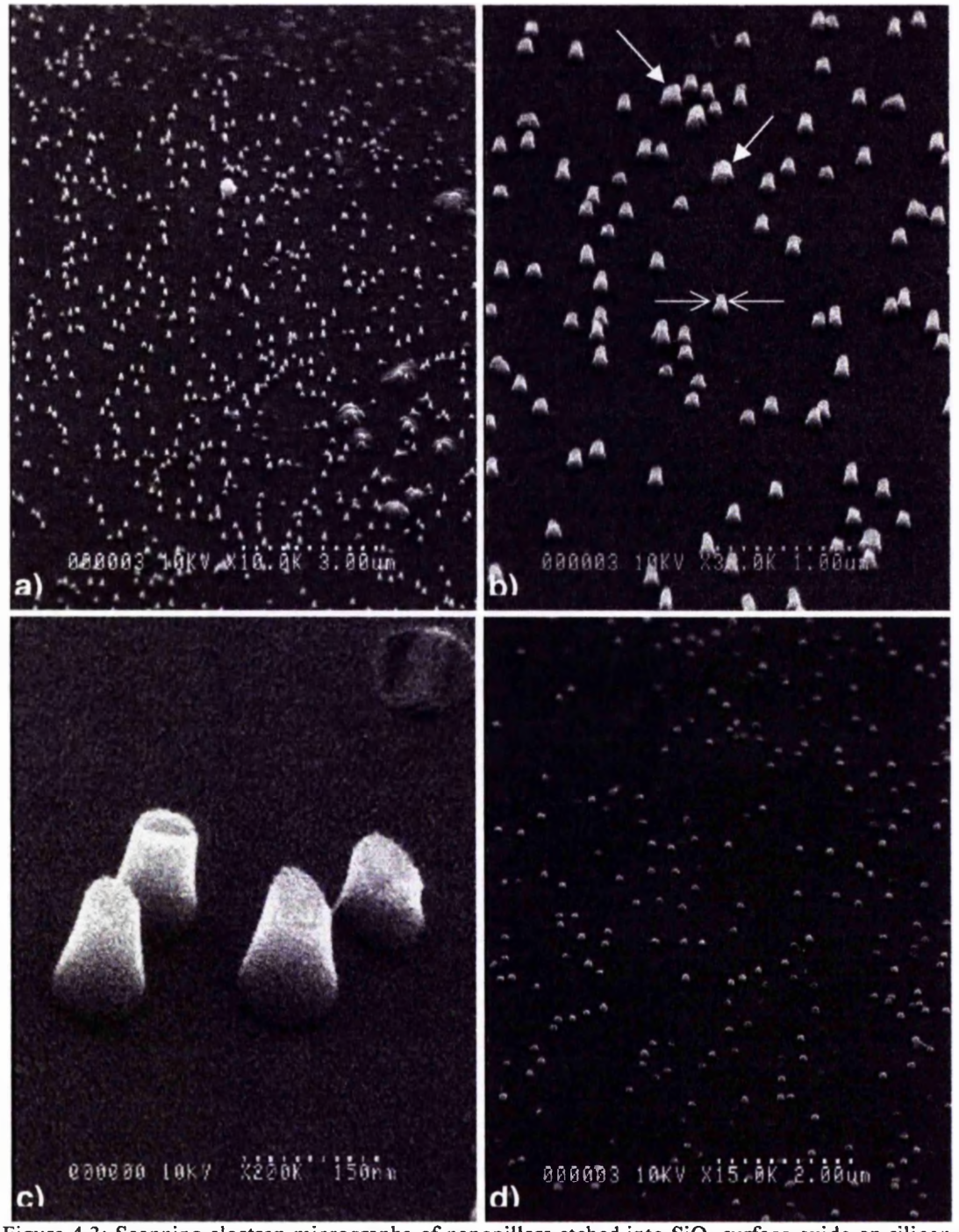

Figure 4.3: Scanning electron micrographs of nanopillars etched into SiO_2 surface oxide on silicon using a Hitachi S-900. Images a)-c) indicate pillars fabricated using a 50nm-diameter colloidal mask, with dry etching resulting in 200nm height. Low magnification image, with 40° tilt allowing vertical dimension viewing, of these pillars, a), indicates the type of surface underlying cells on the experimental substrate. At higher magnification, b), areas where colloids have been in direct contact with one another have etched as a mound (closed arrows) rather than individual pillars. Possible lateral etching in relation to the upper portion of pillars can also be seen, (open arrows). An increased magnification photomicrograph, c), indicates pillars are flat topped, where colloids were originally positioned as an etch mask, in relation to the planar base substrate. Pillar bases appear wider than pillar tops protected during etching by the 50nm-diameter gold colloids. By reducing etching times, pillars with similar morphology to the original colloidal dimensions, can be fabricated, d). Pillars in this instance were fabricated again using a 50nm-diameter colloidal mask, and reduced vertical height of 80nm.

4.2.1.2 Atomic Force Microscopy Imaging of Nanopillars

A Nanoscope Atomic Force Microscope in contact mode was used to image nanopillared topography. Both a 2.5μm x 2.5μm area, Figure 4.4, and 10μm x 10μm area of 50nm-diameter, 80nm high pillared topography, Figure 4.5, were imaged in this manner. The higher magnification image, Figure 4.4, gives a greater insight into the accuracy of the method employed in fabricating the nanotopography. Furthermore, the 2.5μm x 2.5μm scanned area is composed of pixels measuring 4.88nm, allowing nanometric details to be viewed in this image.

The distribution of pillars appears similar to previous images of the 50nm-diameter colloidal topography, Section 3.2.1, and also the Scanning Electron photomicrographs of the nanopillared structures, Section 4.2.1.1. Section analysis indicates that 50nm-diameter colloidal masks subjected to the 80nm etch have an approximate height of 60nm. Furthermore, at low magnification, Figure 4.5, nanopillars appear to have a sharp apex. When compared with the high magnification AFM image, Figure 4.4, and SEM imaging of the nanopillars, this would appear to be an artefact of AFM imaging at this magnification, where nanopillars are actually flat-topped. In comparison to AFM imaging of the colloidal mask, nanopillars appear less curved than the nanoparticles utilised in their fabrication.

At a lower magnification, Figure 4.5, nanopillar imaging is in greater accordance with the type of area a cell would cover following seeding on the experimental nanotopography, as the scan is conducted across a 10x10μm area. The topography imaged here appears similar with respect to lateral dimensions of features, to a previous experimental nanotopography termed "silicon grass", developed by Turner et al (1997). Conditions conducive to solids being deposited via sputtering from the chamber wall or precipitated from the plasma, onto a silicon base substrate during reactive ion etching were found to deposit a mask resulting in the formation of nanometric pillars during etching, producing "silicon grass". This surface pattern was further developed using conventional photolithography to mask grating patterns across the silicon grass, which was exposed to a hydrofluoric acid wet etch. The final surface resulted in a rough silicon grass area, and less rough, wet etch modified grass where feature diameters and heights were non-uniform (Turner et al, 1997).

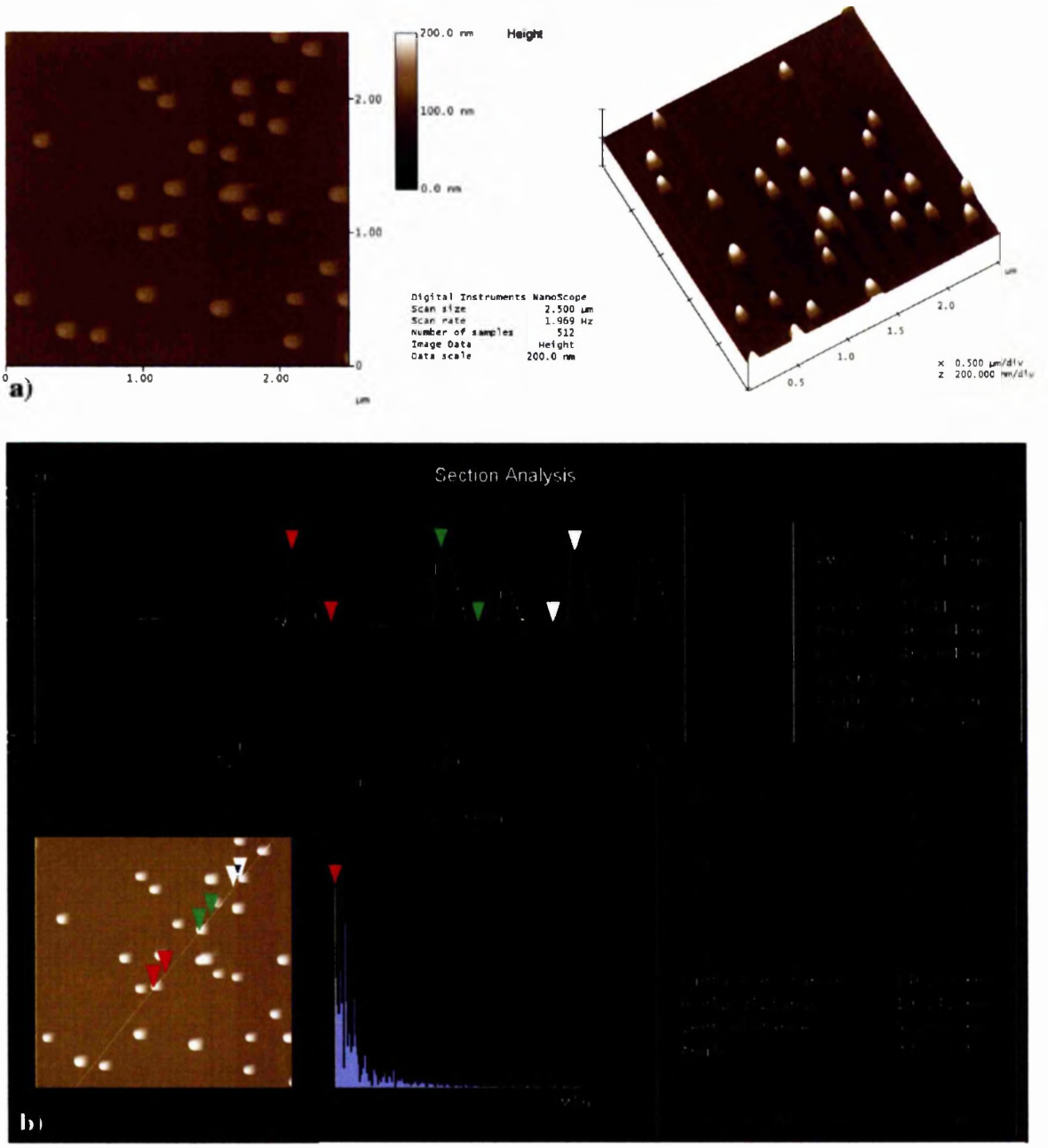

Figure 4.4: High resolution AFM imaging of a 2.5µm x 2.5µm area of 50nm-diameter, 80nm high nanopillared topography with silicon base substrate. Nanopillar distribution, a), appears similar to the original colloidal mask. Section analysis, b), of the topography indicates pillars have a vertical height of approximately 60nm (red, green and white text). In comparison to AFM images of the original colloidal mask, nanopillars appear less spherical.

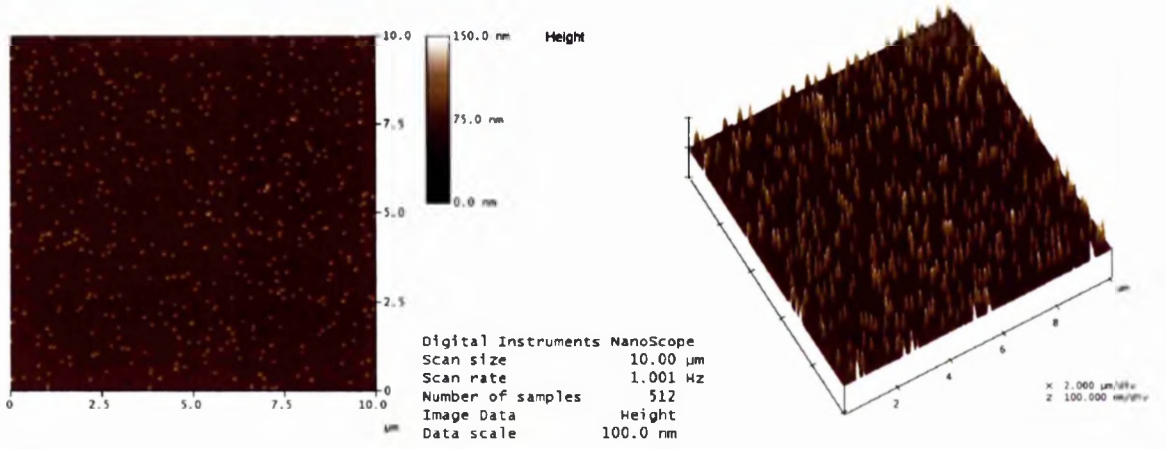

a)

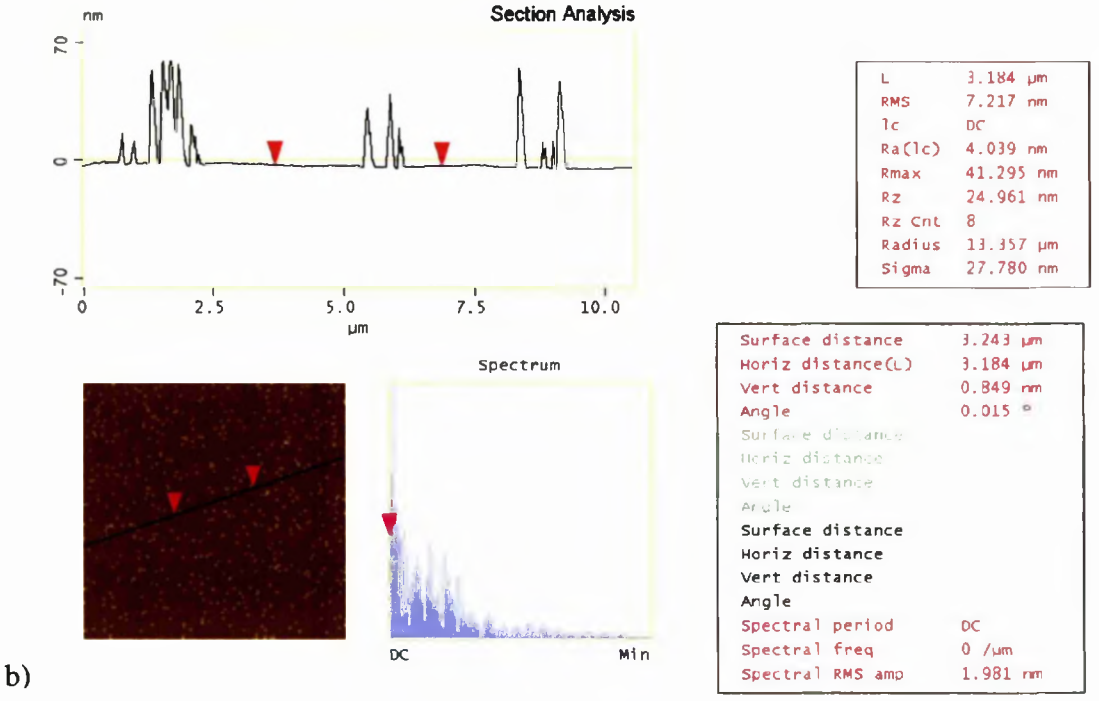

b)

Figure 4.5: Low magnification AFM of 50nm-diameter, 80nm high nanopillars captured using an Nanoscope AFM. The 10µm x 10µm area scanned is more in keeping with the type of substrate cells are confronted with, a). Section analysis, b), indicates the height of the nanopillars is approximately 60nm. Furthermore, nanopillars appear to have a peak at their apex, however, higher magnification AFM and SEM imaging indicates pillar tops are flat and this is an artefact of AFM imaging at this resolution.

The most obvious difference between silicon grass structures and the nanopillared topography described herein is the type and reproducibility of mask used, and also the surface chemistry present in the final substrate. A colloidal etch mask allows for some determination of the final diameter of pillared topography, whereas the mask produced to create silicon grass is reliant on the type and size of solids deposited in the etch machine chamber. The height of pillars fabricated using a colloidal mask is also easier to control, as the mask is theoretically static and presented in a sub-monolayer conformation. In contrast, the solids deposited as a mask in the fabrication process of silicon grass lithography, are less controlled, resulting in pillars of varying vertical dimensions. It is thus concluded that the nanometric features of silicon grass are less well controlled in comparison to the colloidal-based structures.

4.2.1.3 Interference Reflection Microscopy as a means of Nanopillar imaging

50nm-diameter, 200nm high pillars were imaged using interference reflection microscopy in relation to the Vickers IRM microscope. RO water was added to the surface immediately prior to being imaged. A glass coverslip was then placed on top of the water and structure, and immersion oil was placed on top of the coverslip for use with a 50X oil immersion objective lens. The lens was lowered onto the surface, and the topography was brought into focus.

Theoretically, it is possible to image, at best, 250-300nm lateral features using an interference reflection microscope with a filter to create a wavelength of 488nm. With respect to incoherent light, lateral resolution can be calculated as:

$$|Y| \approx 0.61 \frac{\lambda 0}{\mu \sin\theta}$$

where $|Y|$ is lateral resolution, $\lambda 0$ is the wavelength being used; in this case, the lowest wavelength possible being 448nm, $\mu \sin\theta$ is the numerical aperture of the objective lens; in this case, 0.95 for the 50x oil immersion objective (Born and Wolf, 1997). This simplified equation does not take into consideration the fact that that resolution is ultimately dependent on contrast (Bucklew and Saleh, 1985), however serves in this instance to approximate the possible lateral resolution achievable. While the normal resolution unit of this sum is approximately 250nm, the nanofeatures will

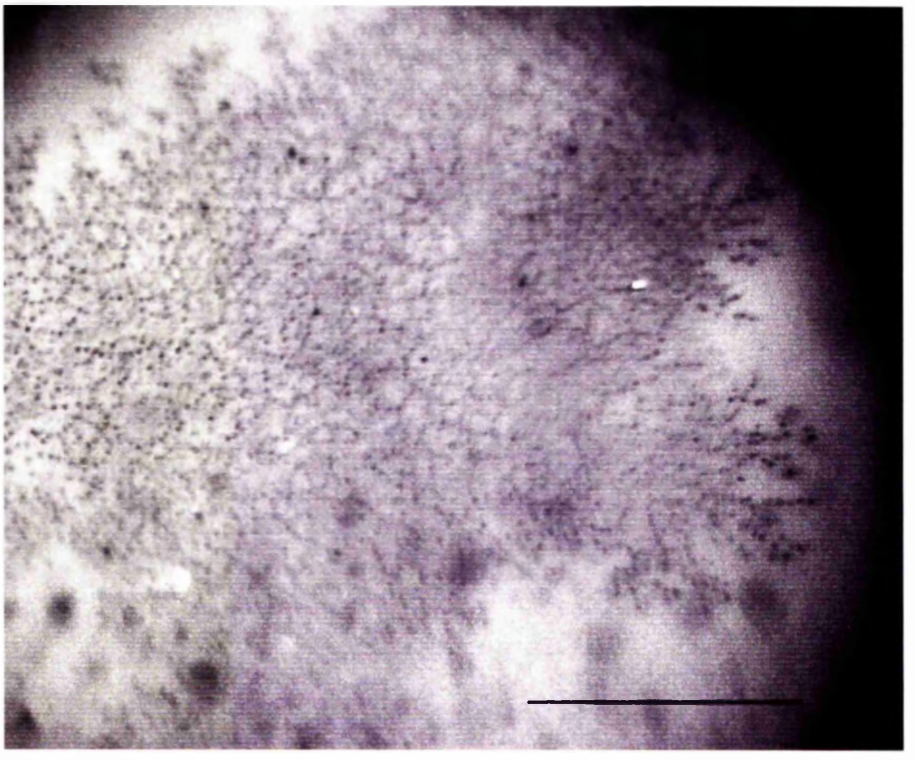

Figure 4.6: Interference reflection microscopy image of 50nm-diameter, 200nm high pillars etched in SiO_2 with quartz base substrate. Imaging conducted using Vicker microscope with 50x oil immersion objective. Although individual nanopillars cannot be distinguished, this method gives some insight into the distribution of individual etched features, and, thus the nano-texture of the modified substrate. (Scale bar: 20μm).

still scatter light. Something of this is observed in Figure 4.6, however, the reader is referred to the original digital image, Figure4.6 on the accompanying CD.

4.3 Preliminary investigations of cell reactions to nanopillared topography

Following fabrication of the nanopillared topography, Section 4.2, cells were seeded on the experimental surface and investigated for behavioural alterations in relation to the surface patterning. Epitenon cells were seeded on 20nm-diameter, 200nm high pillars in SiO_2 with a silicon base substrate, and were dehydrated and subjected to critical point drying, Section 2.7.3, prior to viewing using an Hitachi S-900 FESEM, Section 4.3.1. Scanning Electron microscopy imaging allows for both the experimental nanometric topography and cells in relation to this surface to be investigated. HGTFN endothelial cells were seeded on 50nm-diameter, 200nm high pillars formed in SiO_2 with a quartz base substrate allowing for light transmitting time-lapse video microscopy to be utilised, Section 4.3.2. Observations of endothelial cell reactions to nanopillared topography were thus investigated in a temporal manner.

These initial experiments using both epitenon and endothelial cells were conducted to allow an insight into the types of cell reactions to the fabricated pillared substrate. Upon procuring hTERT fibroblasts in the lab, where data existed describing their cause of uninhibited proliferation as previously explained, Section 2.3.3, focus was shifted from the epitenon and endothelial cells, with no further investigation of these cell type behavioural alterations in relation to the nanopillared topography. Investigating a number of cell types also suggests whether reactions are cell-specific or apply more universally across a number of different cell types and populations.

4.3.1 Epitenon cell morphology at 1 hour on 20nm diameter, 200nm high nanopillars - SEM

Rat epitenon cells were seeded on 20nm-diameter, 200nm high pillars in SiO_2, with a silicon base substrate, measuring $5mm^2$ and placed in a six well-plate at a concentration of 10,000 cells per ml in a 3ml media suspension. Cells were fixed following a one hour incubation, and dehydrated prior to undergoing critical point drying, Section 2.7.3. Samples were then sputter-coated with gold-palladium and imaged using the Hitachi S-900 Scanning Electron Microscope.

Cells fixed at one hour post-seeding appeared to have attached to the substrate, and had began to spread across the nanopillared surface, Figure 4.7. Lamellipodia extensions and protrusions were observed at cell peripheries, in particular at the leading edge of cells, indicated by closed arrows in Figure 4.7a). Longer extensions were also observed occurring perpendicular to the leading membrane, open arrow in Figure 4.7a).

The peripheral areas were examined for direct interactions between epitenon cells and the 20nm-diameter, 200nm high pillars. Debris appeared in very specific instances across the pillared substrate, either cellular or protein in origin, arrows in Figures 4.7b) and c). As epitenon cells have only been in contact with the surface for one hour, the origin of the debris is most likely to be cellular occurring due to breakage's of protrusions during dehydration and critical point drying of the samples. These could possibly be remnants of cell-substrate adhesions occurring via fine lamellipodia or filopodia, susceptible to breakage during processing. It is interesting to note that the debris appears located within areas enclosed by the nanopillars. In comparison to similar interactions observed between colloidal nanotopography and cells, Section 3.3.3.3, the protrusions and elongations of epitenon cells appear similar to lamellipodia in comparison to filopodia, although filopodia-like extensions are observed (arrows in Figure 4.7a)). This may be due to the limited time the cells have had to interact with the experimental substrate, where areas of the epitenon cells in direct contact with the pillars still appear relatively thick, Figure 4.7d). At a tilt of 40°, the height of pillars can be seen. The epitenon cell in this image, Figure 4.7d), does not appear to be in close contact with the substrate and is observed to be almost elevated from the substrate, suggesting cell-substrate interactions appear in the uppermost z-plane of the substrate, or pillar tops. Protrusions parallel to one another also appear to feature following one hour of contact with the nanopillared topography, Figures 4.7c) and d). Unfortunately, due to a lack of time and greater focus being allocated to the reactions of the hTERT fibroblasts in relation to the nanotopographies, no further investigation of epitenon cells in relation to the nanopillared topography was attempted.

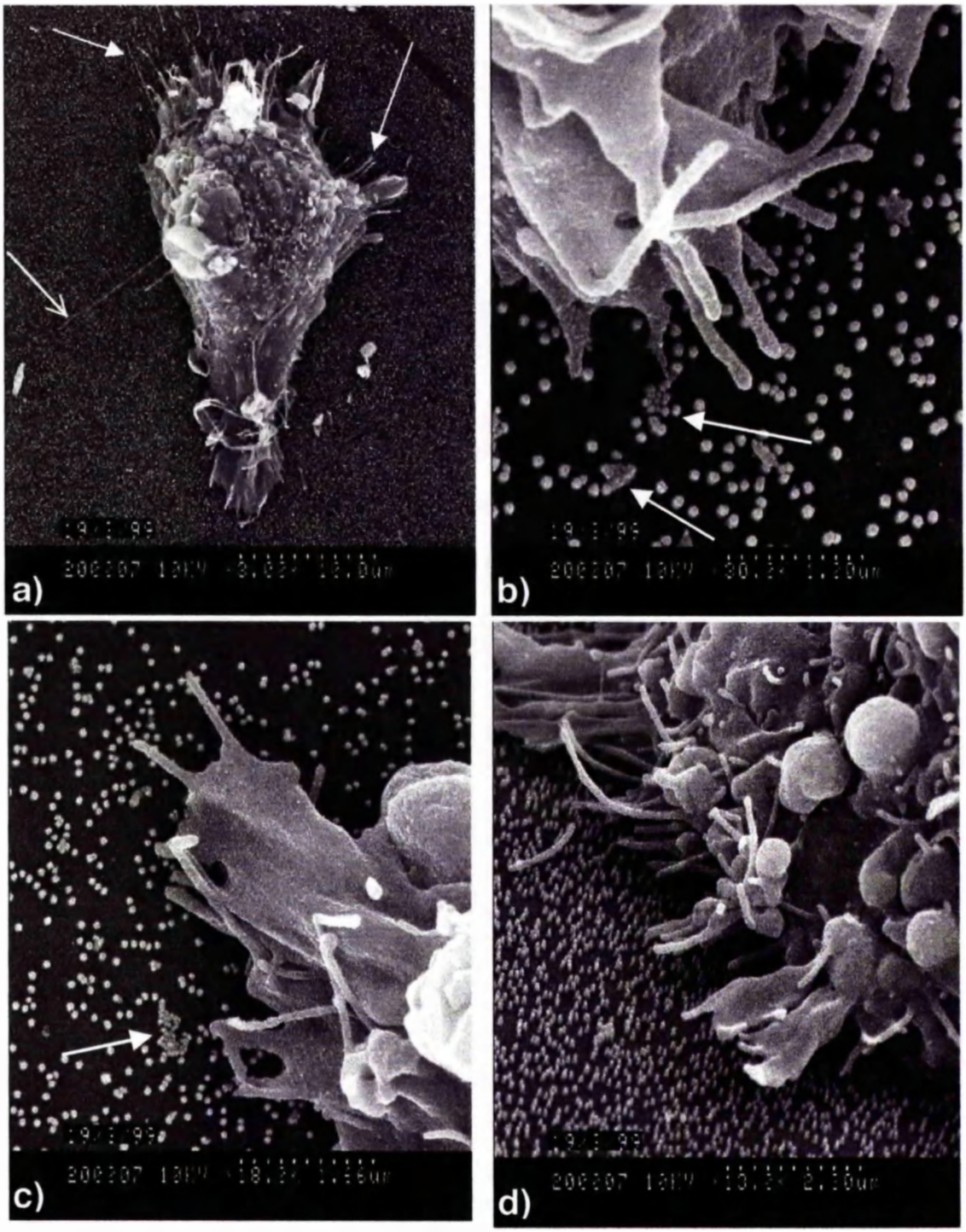

Figure 4.7: Scanning electron micrograph (Hitachi S-900) of rat epitenon cells on 20nm-diameter, 200nm high pillars etched in SiO_2 surface of silicon, following 1 hour of plating. Cells appear to spread on the nanopillared surface, even at this early time. Suggestions of movement through an observed leading edge, a), is also present at this early time, with many protrusions similar to filopodia (arrows in a)), observed, especially at the leading edge. Possible protein aggregates, (arrows in b) and c)), are seen contained within nanopillar aggregates. Thick lamellipodia extend away from the cell body and also upwards, away from the nanopillared topography, d). All marks in the left hand corner of the images are dates.

4.3.2 Temporal observations of HGTFN endothelial cell behaviour on 50nm-diameter, 200nm high nanopillars using time-lapse video microscopy

A preliminary investigation was performed using time-lapse video microscopy to analyse HGTFN endothelial cell reactions in relation to 50nm-diameter, 200nm high pillars. 150,000 endothelial cells suspended in 3 ml of media, were seeded on the experimental topography contained within a 36mm-diameter petri dish, and monitored using the phase contrast setting on the Leica DM IRB (Argus 20, C4505) Astrocam with 20X objective over a 36-hour period. Stills from the video have been selected to indicate endothelial cell reactions to the nanopillared topography at specific time-points, Figure 4.8. Once again, the reader is referred to the original video footage available on the accompanying CD named Figure4.8Video.

Immediately upon contact with the nanopillared surface, membrane ruffling is observed, Figure 4.8a). As ruffling occurs at one peripheral extreme, referred to as the proximal area, of cells, these observed features would appear to have become established as a leading edge. This is unusual when considering the more generally observed radial spreading of a smooth-edged circumferential lamella of cells seeded on planar surfaces at early times. Spreading of the leading edge is viewed within the first hour of plating, following the establishment of membrane ruffles in only one area of the cell, suggesting polarity development with respect to spatial and temporal organisation of intracellular bodies. Actin remodelling specific to these sites is likely to result in the developing leading edge observed. A ubiquitous calcium-activated protease, calpain, has been implicated in actin remodelling during cell spreading. The importance of calpain-dependent cytoskeleton remodelling during the polarised movement of crawling and the non-polarised movement of spreading (Potter et al, 1998), implicates modified calpain activity in the unidirectional lamella activity of HGTFN endothelial cells on the nanopillared surface may occur as a result of modified calpain activity. Modified calpain activity in the development of a leading lamella is likely to occur as a result of altered intracellular calcium transients in this area of the cell only, perhaps via stretch activation of calcium channels (Lee et al, 1999). Stretch activation of calcium channels may occur as the cell contacts the nanopillared topography forming nascent focal adhesions at pillar apices. This behaviour would have a direct effect on cytoskeletal form and function. It is thus proposed that regions of the cell exhibiting leading edge patterning were the first areas to contact the surface of pillars. This would account for

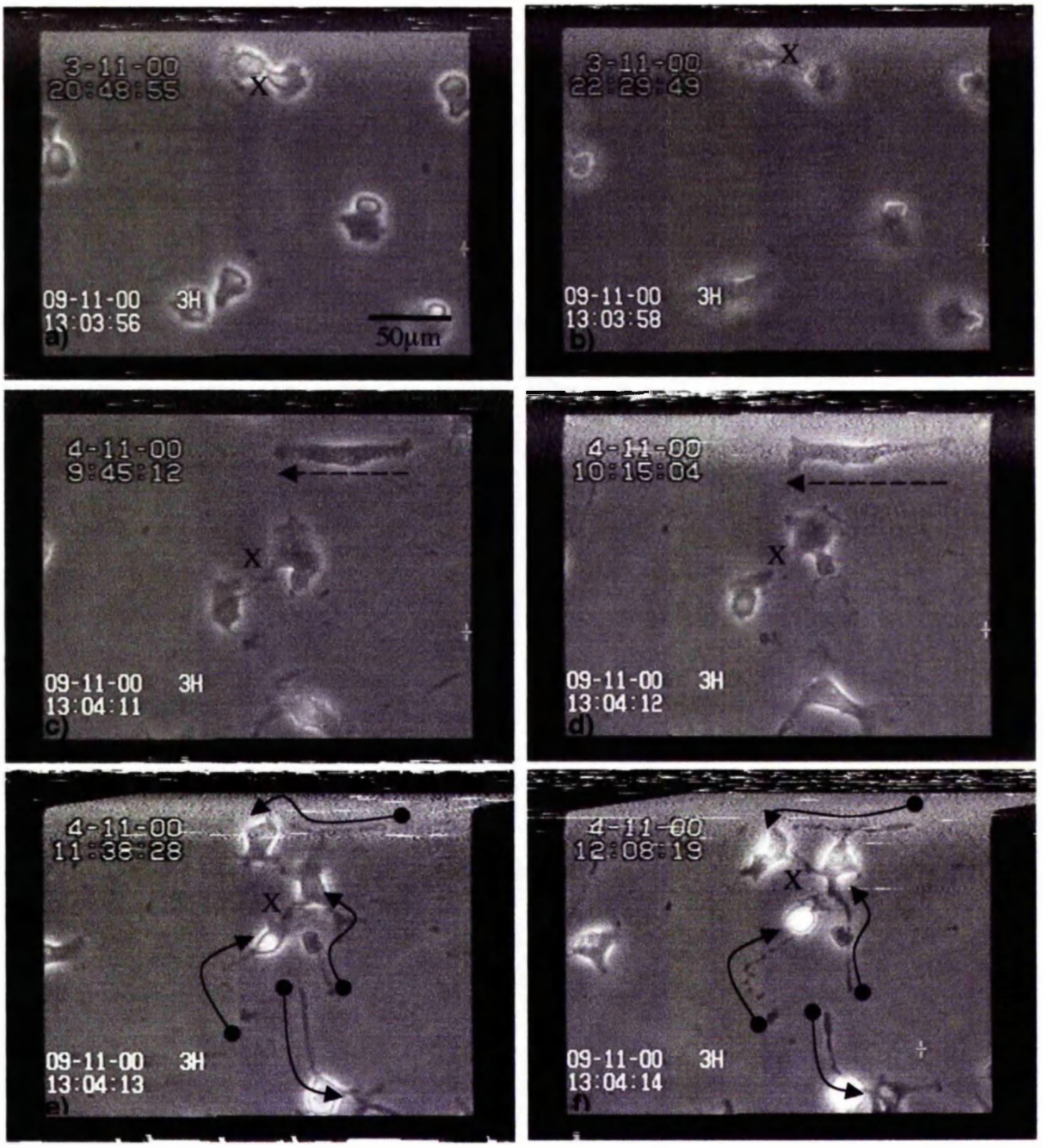

Figiure 4.8: Time-lapse video stills of HGTFN endothelial cells seeded on 20nm-diameter, 200nm high pillared topography viewed using the Astrocam with 20X Ph1 objective lens over 35 hours (video stills and descriptions continued overleaf). "X" depicts cell-cell contacts on the pillared surface. Dashed arrows indicate elongated stretching of endothelial cells. This behaviour appears prior to the occurrence of rear detachmnet problems. Black arrows with closed arrow head and circle on arrow tail highlights rear detachment elongation which appear to reduce over time. Open arrow head with diamond shape at the rear of the arrow indicates protrusions occurring at the advancing edge of cells. Immediately upon seeding on the 20nm-diameter, 200nm pillared topography, endothelial cells appear to establish a polarised leading edge in one direction only, a). Cells seeded in close proximity with one another connect via an intercellular bridge, "X" in b). One of the distinct morphologies displayed by cells is an enlongated stretching across the surface, broken arrow in c) and d). Following extension, problems appear to arise with respect to rear detachment, resulting in a trailing tail and motility inhibition, d) and e). As the detachment site does not appear to retract correctly, the endothelial cells become rounded and the detachment elongation becomes thinner and, eventually, shorter, e) - n). This suggests that following reduced motility, intracellular mechanisms act to dissociate detachment adhesions in an attempt to regain motility across the nanopillared topography. Extracellular factors would result in breakage of detachment elongations remaining adhered to the extracellualr surface. (continued overleaf, pp 218).

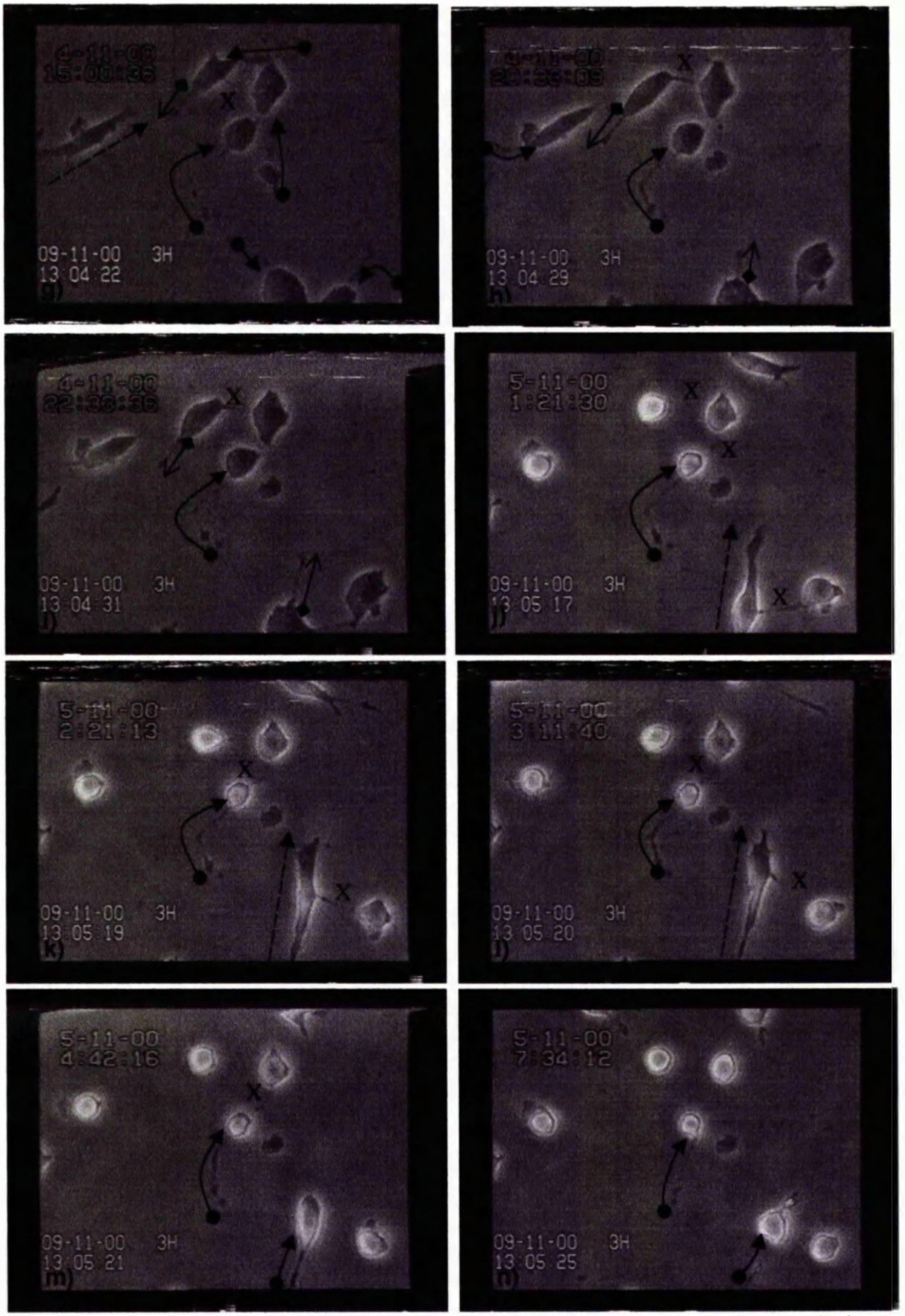

Figure 4.8 (continued): Following reduction of the detachment site, protrusions at the leading edge begin to emerge, open arrow heads with diamond-feature at rear of arrow, g) - i). Cells can extend along these elongations, broken arrows in i)-l). When rounded with restricted motility, cell-cell connections appear, "X" in i) - m). These defining features appear to occur in a cyclic fashion.

modified calpain activity via stretch activation of calcium channels, as cell-substrate interactions result in stresses occurring across the cell membrane, resulting in ruffle remodelling.

Two endothelial cells apparently seeded within close proximity of one another (indicated by "X", Figure 4.8a)), are seen to move in separate directions, as viewed in relation to both ruffling leading edges and monitored movement in the video footage, Figure 4.8Video on the accompanying CD. As these cells move in opposite directions, an intercellular bridge appears to grow in proportion to the distance traversed by the cells, "X" in Figure 4.8b). This appears consistent with previous observations, both in relation to epitenon and fibroblast cells seeded on the colloidal topography, Sections 3.3.1 and 3.3.3, respectively. The development of the intercellular bridge is suggested within the first hour of contact with the nanopillared surface, occurring as neighbouring endothelial cells establish contacts, and appears specifically following one hour. The cells do manage to break this bridge and proceed to move across the surface in opposite directions as previously discussed in relation to epitenon cell-cell contacts on 50nm-diameter colloidal substrates, Section 3.3.3.1.2. This again suggests the possibility of cells exhibiting these bridging features sharing functional roles, as seen in severing of intercellular bridges, occurring during cytokinesis. In this instance, the intercellular connection is severed via mechanisms associated with both the cleavage furrow and directed motility along an established migration axis (Mullins and Biesele, 1977). However, the endothelial cells seen to undergo this type of behaviour are not in fact dividing, suggesting intercellular connections occur as a result of increased cell-cell adhesion contacts, or possibly a lack of discrimination by the cell in relation to cell-cell and cell-substrate contacts. This instance of endothelial cell separation, Figure 4.8a) and b), suggests that cell-cell contacts are established on the nanopillared substrate in a nascent or transient manner as the intercellular connection was established following direct cell-cell contact rather than initiating it, as previously hypothesised, Chapter 3. Furthermore, as cells are motile, and directed motility along established migration axes is an important contributing factor in severing intercellular bridges during cytokinesis, it may be deduced that stress occurring across cells, which is reliant on the interaction of the cytoskeleton with focal adhesion contacts, is not sufficient to immediately break cell-cell contacts. This is further supported by the period of time elapsing between detection of the bridge and the breakage being greater than 2 and a half hours.

Following 12 hours of contact with the nanopillared substrate, endothelial cells appear to be either extremely elongated, or, more prominently within this observed population at this period, exhibit rounded morphologies, with the exception of many very fine beaded membranous protrusions, or rear detachment sites occurring at peripheral regions, Figure 4.8c). The morphology of the endothelial cells in this instance is extremely distorted in comparison to control cells, and suggests a great amount of stress occurring at cell-substrate adhesion sites, resulting in their spiky peripheral elongations radiating from the rounded cell body. The elongated cell in this image, indicated with broken arrow, Figure 4.8c), is later seen to adopt a similar morphology, Figure 4.8e)-g), following extreme elongation and stretching, Figure 4.8c) and d). Possible problems occurring in the detachment of the posterior tail site may account for this type of morphology. This appears even more likely, as, following further inspection of the video footage, Figure 4.8Video, these features are not seen to originate from cellular protrusions and only occur at rear detachment sites.

Endothelial cells exhibiting this type of morphology, where rear detachment is lacking resulting in extremely long, thin, elongated, spiky tails, appear to lack motility and movement, Figure 4.8e)-n). Reduction, resulting in cessation of directed movement, is suggested upon the emergence of rear detachment problems, when endothelial cells begin to reduce motility across the nanopillared topography. With time, movement is further reduced, observed as a lack of central displacement by cells, as the rear detachment area increases in a proximal-distal manner, suggesting release mechanism failure with respect to this feature, results in reduction and possibly inhibition of movement. This observation highlights the possible spatial and temporal organisation of endothelial cells with respect to focal adhesion assembly and disassembly, in relation to 50nm-diameter, 200nm high pillared topography, as lack of adhesion disassembly at the detachment site is presented in this instance, stalling cell motility, translocation and movement.

As cell motility becomes increasingly limited, cell-cell adhesions via thin membrane protrusions mirroring the elongated detachment structures, occur between neighbouring cells, denoted by "X" in Figures 4.8c)-m). Increasing peripheral spike protrusions directed towards neighbouring cells occur following reduction in movement and motility of cells across the substrate, Figure 4.8e)-f), appearing as linking factors bridging individual cells. This may occur due to the difference in rigidity between the

SiO_2 nanopillared surface and cell membranes. The nanopatterned SiO_2 appears to inhibit movement while the surface of neighbouring cells may function as a more receptive substrate. Following the occurrence of cell-cell contacts via peripheral elongations, cells become almost stationary, and exhibit a rounded morphology, Figure 4.8g), following the beginning of retraction of elongated detachment features. Thin detachment sites and cell-cell bridging are still observed in these rounded cells, however, cell processes involved in these features are limited to one extended area found either at the proximal, originally leading edge, or distal, detachment site, Figure 4.8h)-k). At this point, cells become stationary, with no central displacement, resulting in limited directed motility. The only movement occurring in cells at this period is observed at the peripheral extensions, and mainly at the rear detachment site, suggested in Figures 4.8f)-n), but can be observed most clearly in the video footage on the accompanying CD, Figure4.8Video.

There are three possible mechanisms contributing to cell-substrate attachment, all of which are associated with the cytoskeleton-integrin-ECM (or surface topography) interactions, thus are implicated in altered rear detachment of cells. The concentration and resulting adhesiveness of the extra cellular matrix (ECM), integrin expression by the cell, and/or integrin-ECM ligand affinity are possible contributing factors when considering increased adhesion of rear detachment sites of cells in relation to a surface (Palecek et al, 1998). As cell-surface adhesion increases via one or more of these means, two possible factors, related to these mechanisms resulting in intermediate or highly adhesive cell-substrate interactions, are believed to govern rear cell detachment. Firstly, physical mechanisms reliant upon cytoskeleton contraction in relation to the substrate adhesion is thought to result in detachment of the cell rear, with little or no integrins remaining on the substrate due to the weakest area of the connection occurring at the integrin-ECM domain. Alternatively, biochemical mechanisms may act to weaken integrin-associated adhesions intracellularly. This would result in fractures occurring at the integrin-cytoskeleton linkage, with integrin-containing adhesion receptors remaining attached to the ECM or substrate surface.

The calcium-dependent protease calpain, previously suggested as a contributory factor of actin remodelling during early stages of endothelial cell interactions with the pillared topography, has been implicated in the release of cytoskeletal linkages during rear retraction of cells at high cell-substrate adhesiveness (Palecek et al, 1998). Calpain has

also been associated with cell spreading (Potter et al, 1998), cell locomotion and motility (Glading et al, 2002), and may indirectly regulate integrin activation via cytoskeletal linkage (Calderwood et al, 1999). Furthermore, calpain inhibition results in reduced cell migration rates and inhibits cell invasiveness (Perrin and Huttenlocher, 2002). The two commonly accepted mechanisms by which calpain is associated (when considering cell motility) are its role as a signalling intermediate (Potter et al, 1998) and its effects on focal adhesion assembly and disassembly (Galding et al, 2002, Huttenlocher et al, 1997).

Upon reduction of motility, rear detachment elongations present at endothelial cell peripheries appear to be slowly reeled in, with a reduction in width of protrusions being observed followed by a reduction in length, Figures 4.8e)-n). As endothelial cells in these images do not break rear detachments, resulting in cellular material remaining on the nanopillared surface, factors influencing reduction of elongated detachments are highly likely to be related to cytoskeleton contraction events. As cellular breakage does not occur and reduction of detachment sites by the cell is slow, extracellular, integrin-ECM/substrate, and intracellular, integrin-cytoskeleton adhesion complexes would appear to be well balanced, with neither appearing stronger or weaker than the other, resulting in the preservation of elongated rear detachment sites. It may therefore be deduced that integrin complexes binding to the nanopillared topography, and possibly the extra cellular matrix is stronger than the traction forces required by the cell to break these adhesions to continue motility and migration across the surface. When considering the limited surface area represented by the pillar tops, integrin binding is likely to be localised with respect to these regions, upon initial and early contact with the nanopatterned substrate, Figure 4.9a). Furthermore, as focal contacts develop, integrins may contact pillar regions in the upper portion of the feature, surrounding the definitive pillar top, Figure 4.9b). If this is seen to be the case, traction force, generally seen to occur across one major axis established by the leading edge of a cell, is unlikely to be capable of dislodging an adhesion site in this instance. As the integrins have bound to both the planar top of the nanopillars, and the curved area immediately supporting this area, greater traction force will be required in some directions relative to others if adhesions are to be disassembled or broken, Figure 4.9b). Furthermore, as the nanopillars are relatively close to one another on the nanometric scale, establishment of traction force in one main axis is unlikely to dislodge all adhesions occurring across a micrometric area.

In this case, integrin-ECM/substrate detachment is difficult, resulting in the elongated trails left at the opposite end of cells in relation to the leading lamella. As the adhesions under these circumstances are likely to be localised, with tension occurring as a result of very specific cell-substrate integrin adhesion complexes, conformation of proteins associated with FACs (Bershadsky et al, 1985) may be altered, Figure 4.9b). This may result in altered binding site configuration of cytoplasmic proteins linking integrins and the cytoskeleton, or integrins themselves, which, in turn, will result in possible problems occurring via protease attachment resulting in unsuccessful cleavage of the integrin-cytoskeleton adhesion sites. However, the endothelial cells do appear capable of retracting these detachment elongations, albeit slowly. Therefore, confirmation alterations of molecular binding sites, although possible, are unlikely to be irreversible. As the elongated detachment area appears to occur immediately following cell elongation and stretching in relation to the nanopillared topography, this behaviour is more likely to be attributable to the down-regulation of stretch-activated calcium channels and resultant intracellular effects.

It has previously been demonstrated that following a number of stretch-induced calcium-channel activation's (approximately 3 induced stretches using an externally applied mechanical force transmitted via elastic substrata) results in the disruption of transient calcium levels within a cell (Lee et al, 1999). Having undergone an apparent increase in stress, Figure 4.8c)-e) and h)-n), the endothelial cells used in this experiment may adapt to the repeated stretch stimuli initiated through interactions with the pillared nanotopography. This would result in a reduction of intracellular calcium transients required by proteases, for instance calpain, resulting in reduced protease function, Figure 4.10d). The delayed retraction of detachment sites may occur as a result of delayed calcium release from intracellular calcium stores, which are generally activated following increased intracellular calcium transients occurring as a result of calcium influx via transmembrane calcium channels. Furthermore, observations by Lee et al suggest that movement of "tethered" cells is impeded following the inability to detach a small portion of the cell following induced mechanical stretching, and this is also seen in relation to the endothelial cells seeded on the 50nm-diameter, 200nm high pillared topography, Figure 4.8.

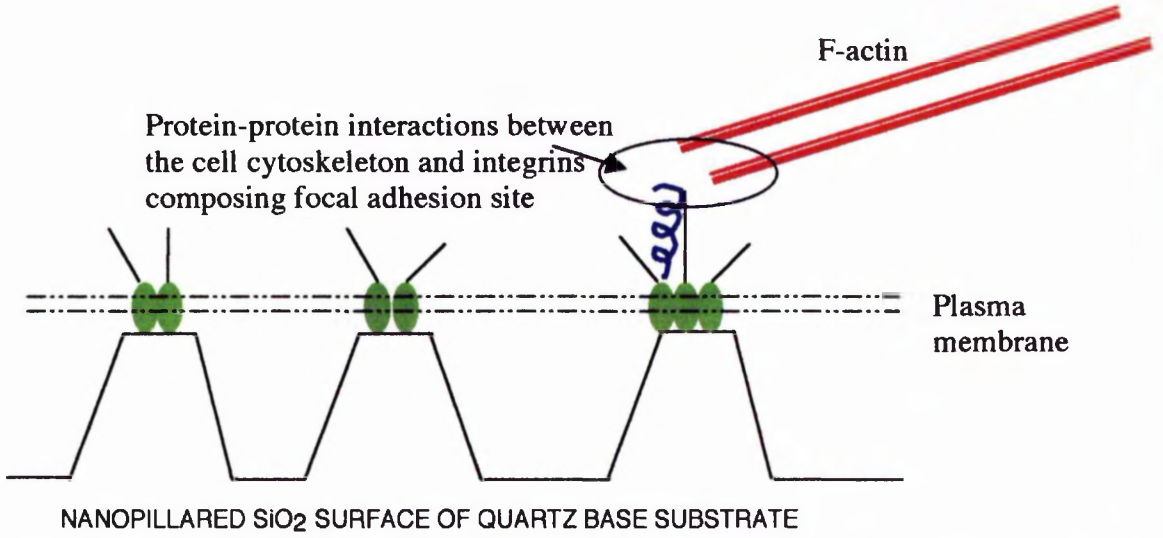

Figure 4.9a): At early times (immediately upon seeding, or shortly after), endothelial cells in contact with the nanopillared topography form nascent focal contacts with the flat tops of the pillars. Cytoplasmic proteins, for example talin (blue spiral) act to connect the cytoskeleton, in this instance f-actin, and the transmembrane integrins, which are in contact with the extracellular environment.

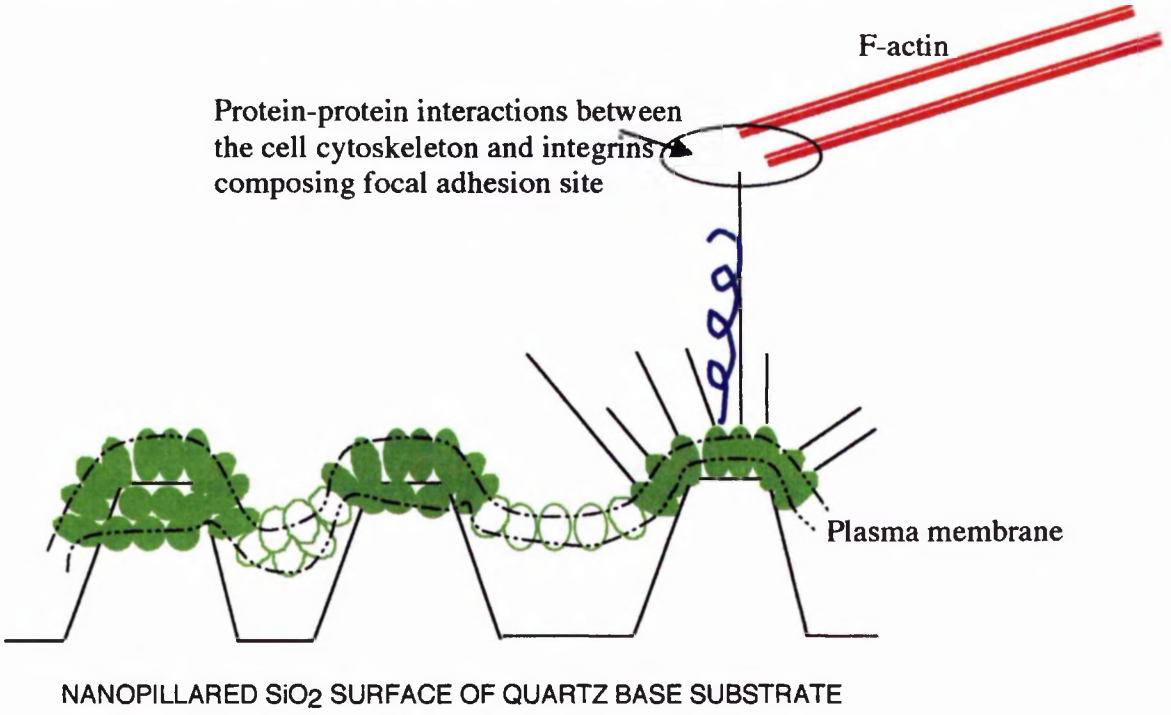

Figure 4.9b): Following the development of nascent cell-substrate adhesion sites, located at the flat top of the pillars (a), mature focal adhesion development occurs. Due to the physical topography the nanopillars present, the general "dot-to-dash" progression cannot occur, as the interparticle spacing of colloids composing the original etch mask results in contact sites being less than the 10μm required (Bershadsky et al, 1985). Integrins located at the plasma membrane are thus limited to the immediate areas surrounding the pillar apex as an interaction site. This results in integrins contained within focal adhesions patterned in a 360° radial manner surrounding the previously established integrin complex located at the flat pillar tops. As the stress required to physically detach the integrins from the substrate must be increased across one axis in relation to individual FACs, stress between the cytoskeleton, for example f-actin, and the integrins is increased. This may result in conformational alterations in associated proteins, for example talin (blue spiral), which would, in turn, present an altered proteolitic site for remodelling molecules, for example calpain.

Following 48 hours in contact with the nanopillared topography, one cell is seen to undergo the previously described behaviour of endothelial cells suggesting the possibility of cyclic events composing this behaviour, Figure 4.8h)-n). Firstly, a leading edge develops, in this case via a lamellipodia, Figure 4.8h)-k), followed by elongation and stretching of the cell across the experimental substrate, Figure 4.8j)-l). Furthermore, subsequent rounding of the cell body results in greater elongation of the detachment site, Figure 4.8m)-n), and eventually the slow process of rear detachment via this retractile mechanisms is observed, Figure 4.8m)-n). The majority of cells observed within this population do not undergo the subsequent cycle of events described in this instance, and remain rounded with continued lessening of the rear detachment sites. This may be due to the time-scale of the experiment, where more time is required if this observation is to be made, and also no subsequent supply of fresh media.

It is proposed that a four-step cycle exists in the events undertaken by HGTFN endothelial cells in contact with 50nm-diameter, 200nm high pillared topography, Figure 4.10. The first stage occurs immediately upon seeding endothelial cells and their initial contact with the nanopillared substrate. Cell processes, for example filopodia and lamellipodia extend towards the nano-patterned surface. The first processes to contact nanopillars result in polarity development across the cell, with an overall displacement resulting in a unidirectional leading periphery, Figure 4.10a). This is suspected to be due to the stress occurring at these adhesion sites where cells contact pillars, and, as a result, stretching of the membrane occurs. As the membrane is stretched, stretch-activated calcium channels are activated resulting in an influx of calcium. This influx, in turn, activates specific FAC-associated biochemicals, for example the calpain protease, previously associated with actin remodelling during cell spreading (Potter et al, 1998), in this case occurring at the leading lamella, Figure 4.10a).

Following adhesion of endothelial cells to the nanotopography, and stretching at one specific region of peripheral membrane, cells progress to an elongated morphology, Figure 4.10b). This has been previously described by the rate of lamella extension exceeding the rate of retraction, resulting in elongation with tension between the proximal and distal areas of the cell increasing (Potter et al, 1998). This action inhibits further lamella extension and overall cell speed is reduced. It is at this point that cytoskeletal tension exceeds a critical threshold resulting in the activation of stretch-activated calcium channels. The influx of extracellular calcium results in the release of

calcium from intracellular stores, and this transient increase in [Ca^{2+}] can then activate various detachment mechanisms leading to the retraction of the rear detachment (Lee et al, 1999). Three mechanisms have been proposed by Lee and colleagues, which lead to rear retraction of a cell, all of which are calcium-dependent. Actomyosin-based contractile force may act to pull the distal detachment area, calcium-dependent phosphotases, and/or proteases acting independently or in combination with cytoskeleton tension resulting in detachment retraction may disassemble cell-substratum adhesions. However, this rear detachment retraction is not observed in relation to the endothelial cells observed in contact with the 50nm-diameter, 200nm high pillared topography. This suggests failure in one or more of these calcium-mediated mechanisms.

As the cell undergoes further stretching, Figure 4.10c), this time across its entire length, it is possible that calcium channels throughout the cell membrane are stretch activated, resulting in an influx of intracellular calcium throughout the endothelial cell as previously described for keratocytes (Lee et al, 1999). The presence of the calcium transient may result in increased calcium-dependent phosphatase and/or protease activity, resulting in up-regulation of associated inhibitors throughout the cell (Perrin and Huttenlocher, 2002). Lee and colleagues described the adaptive response of stretch-activated calcium channels in relation to an externally applied force, were keratocytes failed to respond to the applied suction following a maximum of three repeated applications. Thus, when considering the stress occurring across endothelial cells, described herein, stretch-activated channels may express such an adaptive response. As a result, following up-regulation of the phosphatase and/or protease inhibitors and the inhibition of [Ca^{2+}] due to the adaptive response of the stretch-activated channels, FAC-associated biochemical activity may be reduced due to both the lack of calcium and also the increase in endogenous inhibitors. This results in lack of rear detachment, Figure 4.10d), suppressing cell motility and migration, and also lamella ruffling.

A reduced function in biochemical mechanisms associated with the weakening of integrin-associated adhesions intracellularly due to environmental circumstances, endogenous inhibitor levels may also decline due to their regulatory relationship. Cytoskeletal tension will also be reduced across cells, as the cell adopts a more rounded morphology following the disappearance of a leading edge. The rounded morphology of the endothelial cells in contact with the nanopillared topography following the previous

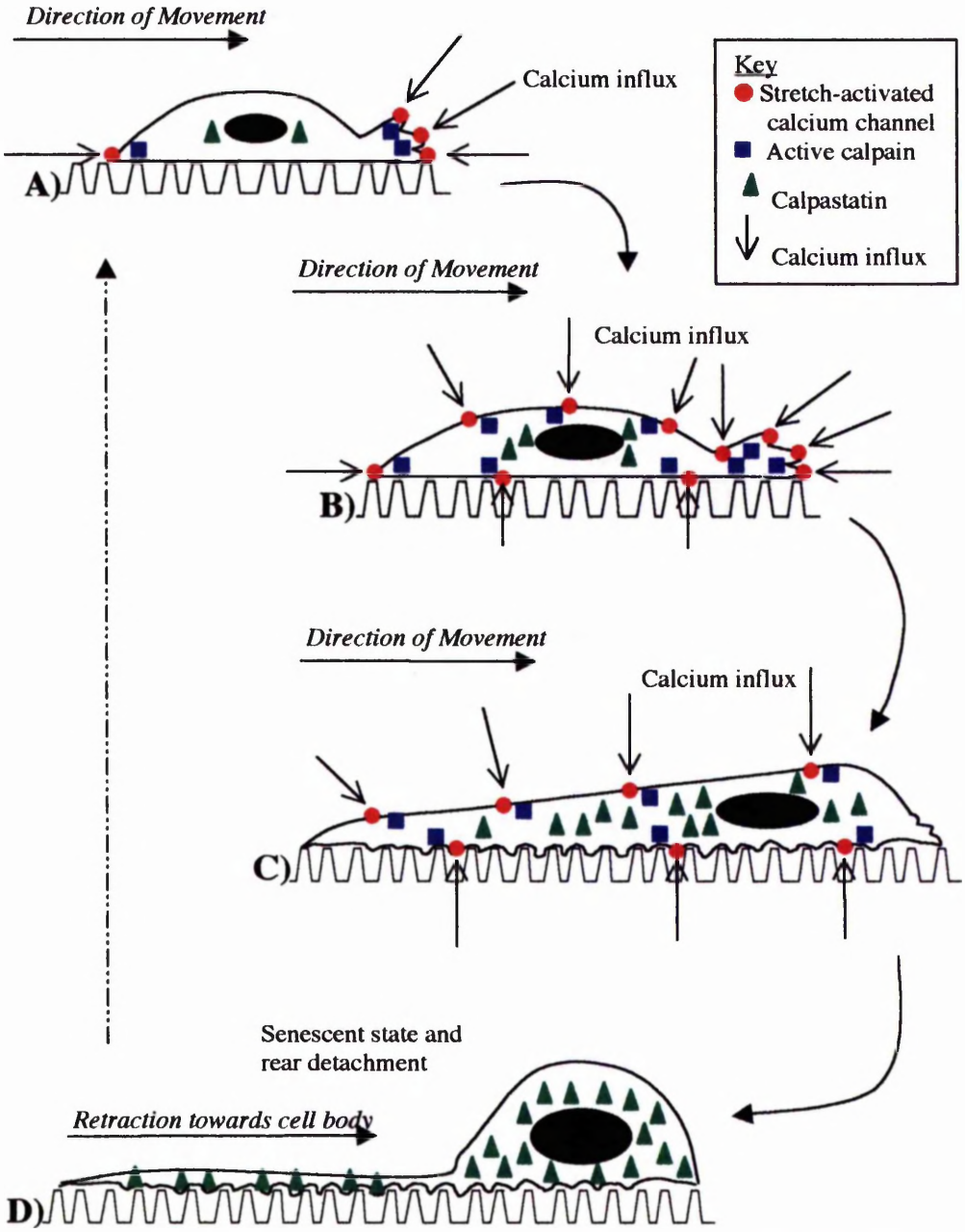

Figure 4.10: Schematic representation of stretch-activated calcium channel activation based on time-lapse video microscopy observations of endothelial cell behaviour in relation to 50nm-diameter, 200nm high pillared topography. When cells first contact the surface, A), a leading edge in one extreme region of the membrane develops, possibly due to the localised cell-substrate adhesion to the planar topped pillars. This results in activation of calcium channels, resulting in localisation and up-regulation of the calcium-dependent protease calpain. As the cell elongates, further stretching results in greater calcium channel activation, B), and increased calpain activation. Calpastain, the endogenous inhibitor of calpain, is also up-regulated as a direct result of increased calpain activity. Cells undergo further stretching, C), which results in adaptation of stretch-activated calcium channels which have been under constant stress following adhesion to the nanotopography. This results in a gradual reduction of calcium influx via active channels, with calpain reduction occurring as a direct result. Calpastain continues to be up-regulated due to the abundance of active calpain. The stress exerted by the cell on its membrane as it stretches eventually results in adaptation of stretch-activated calcium channels. Calcium influx ceases, with calpain activation theoretically prevented as a result, D). Calpastatin continues to be abundant in the cell cytoplasm, preventing further calpain activity also. The endothelial cells are then observed to enter a senescent state. Activation of membrane ruffling has been observed to occur in some circumstances following this senescent period, resulting in cell progression through this cycle being repeated (dashed arrow).

observed behaviour of cell motility and stretching further supports the proposed hypothesis that biochemical mechanisms associated with integrin weakening, in this instance, is initially up-regulated due to increased intracellular calcium transients. Subsequent down-regulation of phosphotase and/or protease activity results following calcium channel adaptation to repeated stretch stimuli at later times. Kulkarni and co-workers (1999) showed that cell spreading in endothelial cells was absent following calpain protease inhibition. However, endothelial cells on the nanopillared topography spread well in the first few hours of contact with the experimental surface described herein. It is only after spreading, elongation and stretching that cells round up detracting from their previous well-spread, elongated morphology. Thus, phosphatase and/or protease activity would appear to function in these early instances, as cells are capable of spreading. Only after elongation, where it is proposed that stretch-activated calcium channels are stimulated, resulting in an initial influx of calcium, following which, cells adapt to the stress resulting in reduced intracellular calcium, does reduced calpain activity appear to occur. It is at this point that cell morphology appears rounded, similar to the calpain-inhibited endothelial cells discussed by Kulkarni et al (1999).

The lack of a leading lamella following elongation and rounding of cells may also be related to phosphatase and protease activation, as these are required in actin remodelling during cell spreading and motility; the main component mechanism of lamella extension. As endogenous inhibitor reduction occurs proportionally to specific biochemical down-regulation, phosphatase and/or protease activity may once again begin. However, the lack of transient intracellular calcium results in a marked decrease of their activity, Figure 4.10d). The resultant reduction may account for the senescent appearance of endothelial cells on the nanopillared topography, where, little-by-little, the rear detachment sites are reduced. Intracellular calcium required during biochemical disassembly of integrin-associated adhesions in the trailing tail results in the detachment of cytoskeletal linkages (Palecek et al, 1998) via, for instance talin cleavage (Calderwood et al, 1999).

As no evidence exists of cellular debris remaining attached to the extracellular substrate, a lack of biomechanical mechanisms are possible, with a lack of fractures at the integrin-cytoskeletal noted. This suggests physical mechanisms reliant upon cytoskeleton contraction (for example actomyosin-based contractile forces) in relation to the substrate adhesion site may act, with little or no integrin-containing cellular

debris remaining on the surface. However, these mechanisms of rear detachment suggested by Palecek and colleagues describe rear detachment in relation to an adhesive surface, where adhesion strength is determined by ECM concentration. The observations that endothelial cells are apparently unable to detach or retract rear sites in this manner, indicates the cell-substrate adhesion plaques are altered in comparison to previous cell-substrate experiments.

When considering cell-substrate adhesions with respect to an extracellular matrix substrate, rigidity is reduced, as when considering soft lithography, for example polyacrilamide gels. When considering the nanopillared topography described herein, with pillars etched in the surface oxide of quartz, rigidity of the substrate is increased. Previous proposals that surface rigidity affects cell behaviour (Lo et al, 2000) may account for the rear detachment of cells on a flexible substrate (Lee et al, 1999), and the lack of rear retraction on nanopillars etched into SiO_2 with a base substrate of quartz, Figure 4.8.

Stress across an entire cell, results in one major stress axis composed of many smaller stresses occurring in localised regions (Dembo and Wang, 1999). When considering cytoskeletal tensions occurring across this axis in relation to a more malleable substrate, movement of the adhesion site towards the stress gradient should result in relocation of the bulk of a plaque in the axis of tension induced by the cytoskeleton. This is especially true when considering the elastic properties of materials used as substrates altering their structure in relation to induced stress. A more rigid structure patterned with nanopillars may result in areas of adhesion plaques existing at a number of separate heights in the z-plane at early times, Figure 4.9a). Subsequently, at later times, Figure 4.9b), integrin complex maturation may result in plaques residing in the x- and y-planes, due to the 360° diameter of the pillar top as a result of the spherical colloidal etch mask. Calcium levels may act to alter integrin behaviour. Calcium is known to alter integrin function, where an in increase in Ca^{2+} results in increased clustering of integrins, specifically $\alpha L\beta 2$, where organised clusters occurring across the cell surface results in increased adhesion (Horton, 1996). The patterning of integrins in relation to nanopillars proposed, is thus further supported by the possible clustering behaviour of integrins occurring as a result of increased calcium levels suggested by observations of cell behaviour appearing related to calcium levels. This is especially true when considering calcium levels are believed to increase at early times during the establishment of cell-substrate contacts.

Integrin clustering at cell-substrate contacts would allow for the proposed clustering of focal contacts in relation to nanopillar dimensions as outlined in Figure 4.9b).

As cytoskeletal tension increases as a mechanism of adhesion detachment, stress will occur across an axis within the cell, with unified direction and tension. However, unified direction is unlikely to dislodge or disassemble integrin-substrate adhesions within a micrometric area due to the complexity of patterned adhesions at nanometric pillar sites, Figure 4.9b). A number of directions would be required to remove each individual cluster of integrins within a plaque, and this is not observed to occur due to the presence of elongated detachment sites of endothelial cells on nanopillars. Therefore, the physical mechanism of adhesion disassembly does not occur successfully, as integrin-substrate binding affinity is stronger than, or equal to cytoskeleton-integrin binding. When considering less rigid, planar structures, for example ECM or polyacrylamide gels, manipulation of the integrin-substrate adhesion may result in a more uniform positioning, due to a lack of spatial surface patterning and elastomeric properties, of integrins and substrates relative to one another in the z-plane. Furthermore, the lack of physical detachment mechanisms observed in relation to endothelial cells on nanopillared topography suggests a lack of strong adhesions at the leading edge, resulting in an imbalance of spatial adhesion strength across the cell. This suggests transient focal adhesions occurring at the leading edge, and also a lack of mature focal adhesion development throughout the cell, with the possible exception of the rear detachment site.

In summary, the physical mechanism of rear detachment is not observed in the time-lapse video microscopy images of endothelial cells on 50nm-diameter, 200nm high pillars, Figure 4.8. Mechanochemical regulation, with respect to intracellular calcium transients, is thus proposed as the mechanism of slow reeling of the rear detachment site towards the bulk of the cell. Endothelial cells contacting the surface immediately after seeding form nascent focal adhesion complexes where integrins locate at the upper z-plane area where flat pillar tops are presented. The area where leading lamella formation occurs is believed to be the first region to produce sensing mechanisms, for example lamellipodia and filopodia. The interaction of these features with the nanotopography results in the activation of stretch-activated calcium channels resulting in increased intracellular calcium transients within this area, Figure 4.10a). Activation and upregulation of calcium-dependent molecules results. As the cell continues to

follow its initiated migratory pathway established by the leading edge, the cell elongates and stretches, Figure 4.10b). This is believed to result in further activation of the transmembrane calcium channels resulting in increased intracellular calcium levels, in turn, fuelling phosphatase and/or protease function. A further final stretch is seen to occur, Figure 4.10c), and during this event, the stretch-activated calcium channels are believed to adapt to the continual membrane stress and stretching. Thus, the channels adapt to repeated stimulation and do not respond to further stretch activation, intracellular calcium is reduced, as is resultant calcium-dependent biochemical activity. Furthermore, endogenous inhibitors of these molecules are believed to be abundant within the cytoplasm of the cell, a direct result of the regulatory relationship believed to occur between these molecules (Menard and El-Amine, 1996). Phosphatase and/or protease activity is likely to be reduced by both a reduction in intracellular calcium transients and also an increased presence of their inhibitors.

Endothelial cell morphology becomes rounded, possibly following altered calcium levels as hypothesised, with a lack of retraction of the rear detachment site, Figure 4.10d). Previous work by Kulkarni and colleagues (1999) reports the lack of spreading in calpain-inhibited endothelial cells. This further supports the possibility that calpain inactivation is not present in endothelial cells when initially contacting the nanotopography as spreading and leading edge development is observed. Furthermore, calpain inhibition in all cell types reduces migration rate and invasiveness of cells (Perrin and Huttenlocher, 2002), and this is observed in the video footage following the first 12 hours in contact with the nanopillared substrate, once again suggesting that calpain inhibition only occurs following this period. Alterations in rear detachment retraction, as observed following the stretching and subsequent rounding of the cells, is more readily associated with calpain deficiency in fibroblasts (Palecek et al, 1998). However, as proposed, calpain was not deficient in these cells at early times and, in fact, appears to have been increased, and thus the lack of spreading of cells was not observed as previously reported for calpain deficient endothelial cells (Kulkarni et al, 1999). Thus the presence of rear detachment alterations are likely to be a direct result of previous cell spreading and motility across the nanopillared topography followed by reduced calpain activity, resulting in lack of disassembly of the focal adhesions. The physical arrangement of the integrin-substrate complexes throughout the cell, Figure 4.9, including the rear detachment site is believed to result in the lack of physical cytoskeletal-induced rear detachment, resulting in the role of mechanochemical

regulation of rear detachment adhesion disassembly. The physical arrangement of the integrin-substrate regions further implicates calpain as a contributory factor in the lack of detachment (Bhatt et al, 2002), as experiments on T-cells suggest that calpain may form part of a greater complex including β-1 integrin, talin and other membrane-associated proteins (Calderwood et al, 1999). Furthermore, it should be noted that vascular development defects are recorded in calpain-deficient transgenic mice (Arthur et al, 2000), suggesting that endothelial cells may be susceptible to alterations in calpain function.

Unfortunately, due to time constraints, intracellular calcium levels were not investigated. However, this would appear to be a relatively standard process, where a fluorescent calcium indicator can be added to the media on the topography following cell seeding. A single-wavelength intensity-modulating dye ((SW) indicator), for example Fluo-3, would allow for changes in intracellular calcium to be reflected in the intensity of fluorescence excitation (Kao, 1994). This would appear most beneficial in relation to endothelial cells on the 20nm-diameter, 200nm high nanopillars, indicating whether intracellular calcium alters over time as hypothesised within this chapter.

Similarly, calpain expression, the protease believed to be altered in relation to cytoskeletal remodelling and lack of FAC-associated rear detachment was not investigated. A number of techniques are available to determine calpain levels in cells and thus indicate the role of this protease in the observed behaviour of cells seeded on colloidal-based nanotopographies. These include transfection and selection of calpastatin-overexpressing clonal cell lines where calpain activity would be limited, and also immunoblot analysis of cytoplasmic extracts where primary anti-calpain and anti-calpastatin antibodies are used to probe antigens (Potter et al, 1998). Calpain mRNA levels can also be calculated by isolating total mRNA from cells on the nanotopography using the Trizol method, using electrophoresis on formaldehyde gels and transferring to a nylon membrane. ^{32}P-labeled DNA hybridisation probes generated from excised cDNA of calpain by the random primer method can then be incubated with the membrane, resulting in interaction and attachment to the protease of interest. However, the most accessible and possibly the best indicator of calpain expression in endothelial cells on the nanopillared topography would be to inhibit calpain utilising pharmacological techniques. Reversible calpain inhibitors, for example calpeptin and MDL (Potter et al, 1998), calpain inhibitor I (Palecek et al, 1996) or N-acetyl-leucinyl-

leucinyl-norleucinal (ALLN) (Bhatt et al, 2002) could be incubated with cells prior to seeding on the nanopillared substrate. Reduced calpain activity could then be calculated using a caseinolysis assay of cytoplasmic extracts from calpain-inhibited cells and controls cultured on the experimental topography. Furthermore, a "suicide" substrate inhibitor of calpain, benzyloxycarbonyl-(leucyl)$_2$-tyrosyl-diazomethane (ZLLYCHN$_2$) could be incubated with cells prior to seeding on the nanopillared topography. When compared to controls free from the calpain inhibitor, the effects of this protease could be examined.

4.4 hTERT Fibroblast Behaviour in Relation to Nanopillared Topography

hTERT fibroblasts were monitored for alterations in adhesion, morphology and cytoskeletal arrangements in relation to the experimental pillared nanotopography with various lateral and vertical dimensions. An adhesion assay was conducted to investigate the similarities between fibroblast adhesion in relation to a planar control, 200nm-etched planar control and 20nm-diameter, 200nm high pillared topography, Section 4.4.1. Cells were fixed at 20 minutes, 1 hour and 3 hours, and nuclei over a specific, constant area were counted and believed to indicate cells adhered to the substrates.

Fluorescent investigation of the actin and tubulin cytoskeleton arrangements and morphology of the same cell population investigated for adhesion alterations followed. Further fibroblast cytoskeletal investigation was performed by seeding cells on pillared substrates of various dimensions, with either 20nm or 50nm-diameter colloidal mask undergoing reactive ion etching resulting in a vertical height of either 80nm or 200nm, Section 4.4.2. The same hTERT cell population was used in all these experiments allowing for a more constant insight into behavioural alterations of fibroblasts in relation to the pillared nanotopography.

4.4.1 Cell-substrate adhesion assay

hTERT fibroblasts were plated at a seeding density of 50,000 cells per ml, in 3ml of media, on 20nm-diameter, 200nm high pillared structures, a planar quartz control and a planar quartz control etched to 200nm in the same dry etch run as the nanopillared substrates. All three substrates underwent reflux treatment to remove residual wax prior to acid cleaning and processing and were immersed in Hepes prior to seeding cells. The planar etched surface was included to discriminate between cell adhesion as a result of nanotopography and etch chemistry in relation to nanopillared surfaces. The planar

surface, etched to 200nm, underwent all chemical processes used to create the nanopillared structure, Section 4.2, with the exception of colloid addition. Cells were incubated on all three surfaces and were fixed on their structures at 20 minutes, 1 hour and 3 hours. These time periods were chosen as cell-substrate adhesion occurs within minutes of plating cells, becoming more established in the hours to follow.

Cell media was carefully pipetted from the samples at each time period, and PBS heated to 37°C was gently added to wash fibroblasts lacking cell-substrate adhesions from the surface using gentle agitation (in this instance, a slight rocking motion from side-to-side of the samples was conducted by hand). The PBS was then removed from the samples and 4% Formaldehyde, heated to 37°C was added as a fixative, with samples being incubated in this solution for 15 minutes in the hot room at 37°C. The Formaldehyde solution was removed and samples were rinsed in PBS prior to staining with Coomassie Blue. Cells fixed on the experimental surfaces were covered with dye for approximately 5 minutes, and this was poured from the surface and samples were rinsed with tap water, in which they were also stored.

Fibroblast adhesion on each experimental surface was calculated by firstly counting 30 non-specifically chosen fields of view using a Vickers light microscope with 10X Phaco 1 objective lens (170/-, 10/0.25). Cells lying within an area of the experimental surface contained within the 10 x 10 square graticule present in the eyepiece of the microscope were counted. A square graticule, placed in the eyepiece, was used to highlight an area of the surfaces at this magnification measuring 0.93mm^2. This was calculated by placing a 1mm graticule scale on the microscope stage, and measuring the length of the square graticule observed through the eyepiece. The data accumulated in this manner was then entered into Statview, where descriptive statistics and distribution histograms were calculated, Appendix V.

As previously discussed, Section 3.3.3.2, parametric statistical tests assume that data is drawn from normally populations which have homogenous variance, allowing for means and variances to be compared. Data describing the number of fibroblasts adhering to planar, planar etched and nanopillared topographies was entered into a contingency table, Appendix VI. Homogeneity of variance (F_{max}) was calculated as 308.71, however the critical value for F_{max}=0.05 level of significance, 3.21, was not met, indicating sample variance was not homogenous. Parametric tests tend to be

preferential to their non-parametric counterparts, as they are believed to be more powerful. This is due to the fact that non-parametric tests may be used with smaller samples and thus do not use all the data collected, where ranks are used rather than actual observations. It was therefore better if the data collected for this adhesion experiment could be used in a parametric test, for instance ANOVA.

One method of using data that does not have homogenous distribution is to transform the original data collected. Data normalised by transformation allows a parametric test such as ANOVA to be applied without risk of error. The original data was thus transformed by either taking the square root of the original data or calculating its LOG10, Appendix VII. Following transformation in this manner, further contingency tables were drawn and F_{max} was calculated. However, even following transformation of the data, the variance between samples, where F_{max} was calculated as 13.66 and 6.24 for square root and LOG10 transformed data respectively, did not meet the critical value of F_{max} for 0.05 level of significance, 3.21. Thus the variance between samples was too great to continue with a parametric test. As a result, a non-parametric statistical test was sought to analyse the data comparing fibroblast adhesion on different topographies at different time points.

Non-parametric tests compare the median of samples and do not require data to be normally distributed or have homogenous variance. The median is the middle observation in a set of data which have been ranked in magnitude, rather than the sum of observations divided by the number of observations as observed when calculating the mean. Thus, the median is resistant to extreme observation typically found in data that do not have homogenous variance and are not normally distributed. Thus the original data collected with respect to cell adhesion on the three different surfaces at the three different time points were ranked. As non-parametric tests compare medians, a residual plot of sample medians was made to indicate possible interactions between the two variables, namely topography and time, Graph 4.1.

Possible interactions are indicated in the residual plot between the number of fibroblasts adhering to the planar etched and nanopillared topography between 1 and 3 hours. As the plot of the medians for the number of cells adhering to the planar control topography does not parallel the other plots, interactions between the planar observations and other surfaces investigated in relation to time are suggested.

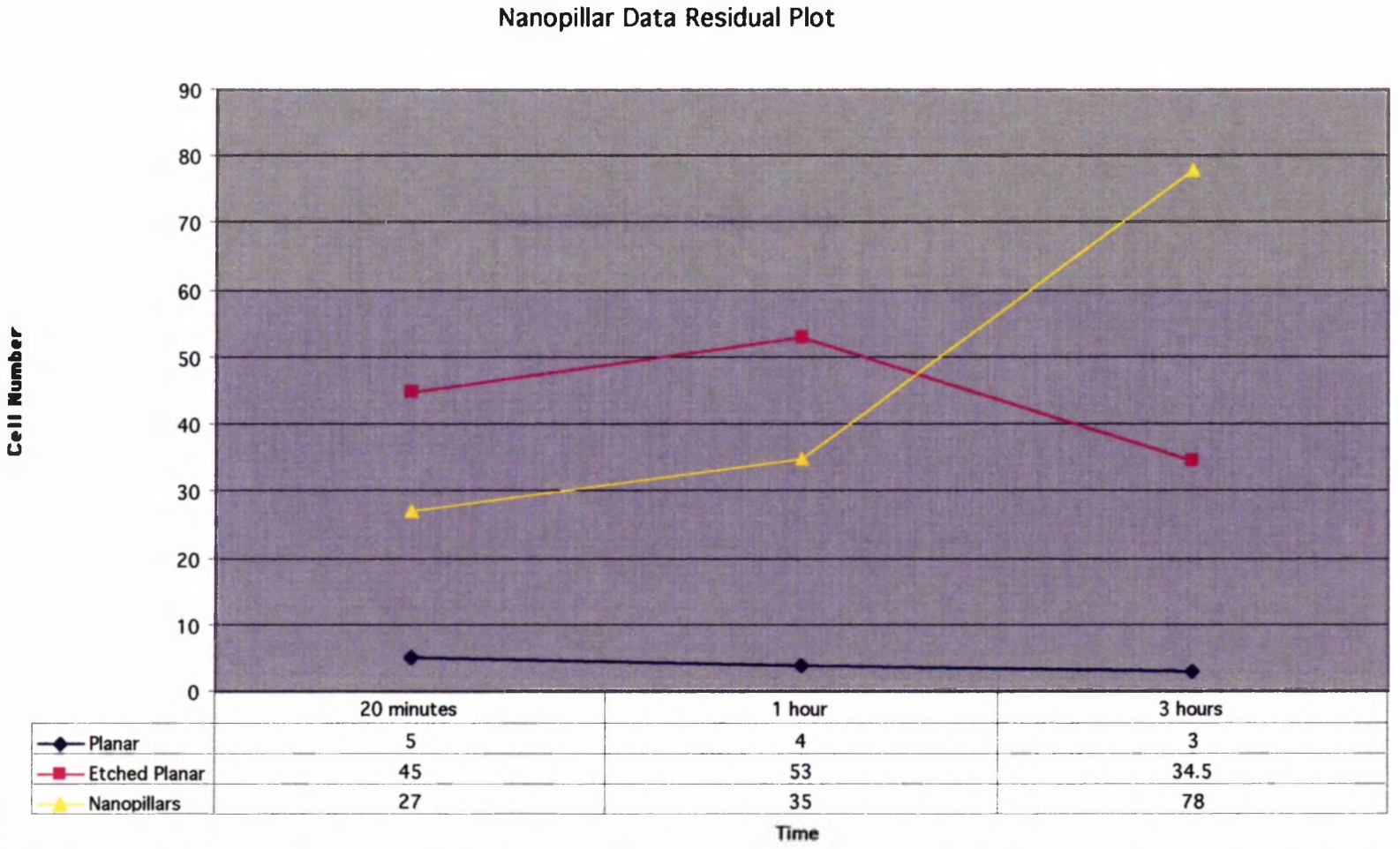

	20 minutes	1 hour	3 hours
Planar	5	4	3
Etched Planar	45	53	34.5
Nanopillars	27	35	78

Graph 4.1: Residual plot of the medians (highlighted in table at bottom of graph) calculated for the data collected from fibroblast counts on each individual topography at each individual time point. Fibroblast adhesion at 20 minutes and 1 hour on the planar etched and nanopillared substrates result in the production of parallel lines indicating no interactions between these variables at these time points. However, between 1 hour and 3 hours, interaction is observed between the number of fibroblasts adhering to the planar etched and nanopillared substrates. Similarly, the line connecting the medians calculated for the number of cells adhering to the planar control does not parallel the other plots indicating interaction may occur.

As previously discussed in relation to the number of fibroblasts adhering to the colloidal substrates, Section 3.3.3.2, two independent variables, topography and time, are being investigated for their effects on a dependent variable, fibroblast adhesion, in relation to this experiment, Section 4.4.1. Furthermore, a non-parametric test must be utilised as the data is not normally distributed and does not have homogenous variance, Appendix VI and VII. However, there is no non-parametric test available to analyse the effects of two independent variables on a dependent variable (personal communication with Dr M. Jones, Senior Lecturer, Medical Statistics, Keele University).

The Kruskal-Wallis test, a simple non-parametric test that compares the medians of three or more samples, allows for multiple comparisons to be made between an independent variable and a dependent variable. As such, the risk of committing a type 1 error, where the Null Hypothesis is rejected when it is actually true at P=0.05 level of significance, is limited. However, to compare the two independent variables, and thus test two independent Null Hypotheses, as observed within this data, at P=0.05 level of significance, the probability that neither test will be significant is 0.95 x 0.95 = 0.90, in comparison to 0.95 for a single test (Bland and Altman, 1995). The risk of committing a type 1 error can thus be overcome by setting the level of acceptance, the P-value, at a more stringent standard of P=0.01 (personal communication with Dr M. Jones). Thus, the Kruskal-Wallis non-parametric test was used at a significance level of P=0.01 to calculate comparisons between the two independent variables, topography and time, and their effects on fibroblast adhesion. The number of fibroblasts adhering to the three topographies, planar, planar etched and nanopillared, were compared at each time point, Table 4.1, and the number of fibroblasts adhering to each individual surface were compared at all time points, Table 4.2.

For the Kurskal-Wallis test, original data was ranked in relation to the samples being compared. For example, the number of fibroblasts adhering to planar, planar etched and nanopillared topographies were compared at 20 minutes, 1 hour and 3 hours, and were ranked within these groups. Similarly, comparisons were made in relation to the number of fibroblasts adhering to each individual substrate at each of the three time points, 20 minutes, 1 hour and 3 hour, where the original data was once again ranked within these groups. Following ranking of the data within each group, a number of calculations were required to allow the Kruskal-Wallis test statistic, K, to be calculated. Each group and the calculated values required for the test statistic are outlined in Tables 4.1 and 4.2.

	Planar	*Etched Planar*	*Nanopillared*	
n	30	30	30	***N = 90***
R	522.5	1951.5	1617.0	
R^2	273006.25	3808352.2	2614689.0	
R^2/n	9100.21	126945.07	87156.30	$\sum(R^2/n) = 223201.57$
a) *20 minutes*				$K = 54.03^{**}$
	Planar	*Etched Planar*	*Nanopillared*	
n	30	30	30	***N = 90***
R	543.0	1971.5	1580.5	
R^2	294849.0	3886812.2	2497980.2	
R^2/n	9828.30	129560.4	83266.01	$\sum(R^2/n) = 222654.7$
b) *1 hour*				$K = 53.23^{**}$
	Planar	*Etched Planar*	*Nanopillared*	
n	30	30	30	***N = 90***
R	675.5	1686.0	1733.5	
R^2	456300.25	2842596.0	3005022.2	
R^2/n	15210.01	94753.2	100167.4	$\sum(R^2/n) = 210130.6$
c) *3 hours*				$K = 34.88^{**}$

Table 4.1: The number of fibroblast adhesion on planar, etched planar and nanopillared topography were ranked according to the group they were in for example in this instance time intervals of 20 minutes a), 1 hour b) or 3 hours, c). Thus the rank of fibroblasts adhering on planar topography at 20 minutes may not be the same as the given ranks at 1 hour or 3 hours. The number of observations, n, the total number of observations, N, the sum of ranks, R, the square of the sum of ranks, R^2, the square of the sum of ranks divided by the number of observations, R^2/n and the sum of R^2/n, $\sum R^2/n$ were calculated and tabulated. From this, the Kruskal-Wallis test statistic, K, was calculated and compared with the distribution of chi-squared. Comparisons between the different topographies at each time interval indicate that fibroblast adhesion is significantly different between the substrates investigated, where ** indicates K is significant at $P<0.01$.

	20 minutes	*1 hour*	*3 hours*	
n	30	30	30	***N = 90***
R	1588.0	1305.0	1202.0	
R^2	2521744.0	1703025.0	1444804.0	
R^2/n	84058.13	56767.5	48160.13	$\sum(R^2/n) = 188985.76$
a) *Planar only*				$K = 3.90$
	20 minutes	*1 hour*	*3 hours*	
n	*30*	*30*	*30*	***N = 90***
R	*1292.0*	*1457.0*	*1346.0*	
R^2	*1669264.0*	*2122849.0*	*1811716.0*	
R^2/n	*55642.13*	*70761.63*	*60390.53*	$\sum(R^2/n) = 186794.29$
b) *Etched Planar*				$K = 0.69$
	20 minutes	*1 hour*	*3 hours*	
n	30	30	30	***N = 90***
R	1164.5	1216.0	1714.5	
R^2	1356060.2	1478656.0	2939510.2	
R^2/n	45202.01	49288.53	97983.67	$\sum(R^2/n) = 192474.2$
c) *Nanopillars*				$K = 9.01$

Table 4.2: The number of fibroblasts adhering to a specific surface at three time points was ranked according to their group. Calculations were performed as previously described above, Table 4.1, for each set of data, namely planar, a), etched planar, b) or nanopillared, c), at all three time intervals investigated. The Kruskal-Wallis test statistic, K, was calculated. No significant difference ($P<0.01$) was found within the data for the number of fibroblasts adhering to each individual surface, a)-c), at all three time points.

The Kruskal-Wallis test statistic, K, is calculated as:

$$K = \left[\sum(R^2/n) \times \frac{12}{N(N+1)} \right] - 3(N+1)$$

The data entered in Tables 4.1 and 4.2 contain the calculations required to complete the test statistic, K, which is also included in these tables. The resultant test statistic, K, is compared with the distribution of χ^2 (chi-squared), where the level of significance is 0.01 (Fowler et al, 1998, Appendix 3).

The Kruskal-Wallis test compares the averages of three or more samples. When the number of fibroblasts adhering to all three surfaces, planar, etched planar and nanopillared topographies, were compared at 20 minutes, K was calculated as 54.03, when df = 2, Table 4.1a). The value of K calculated exceeds the χ^2 value, indicating the Null Hypothesis, H_0, is rejected thus there's a highly significant difference between the number of cells adhering to these substrates at 20 minutes. As the highest and lowest sum of ranks is observed in the number of cells adhering to the etched planar and planar topographies respectively at 20 minutes, a significant difference between the effects of these two substrates on fibroblast adhesion can be specified. Similarly when comparing cell adhesion on the three different surfaces at 1 hour, Table 4.1b), and also at 3 hours, Table 4.1c), K-values, 53.23 and 34.88 respectively, indicate rejection of the Null Hypothesis. It may thus be concluded that there is a highly significant difference between the number of cells adhering to the three substrates at these times, where P=0.01. At 1 hour, specific differences can be drawn between cells adhering to planar and etched planar topographies, as previously observed at 20 minutes. However, at 3 hours, the significant difference of cell adhesion occurs specifically between planar and nanopillared topographies.

Significant differences were calculated between the number of fibroblasts adhering to the three different substrates at each time point using the Kruskal-Wallis test, Table 4.1. No significant difference was found when comparing the effects of time on cell adhesion to an individual substrate, Table 4.2. It is thus concluded that fibroblast adhesion is dependent upon which substrate topography, planar, planar etched or nanopillared, cells are seeded and cell adhesion is independent of time in these instances. Specific differences were calculated between cell adhesion on planar and planar etched surfaces at 20 minutes and 1 hour, while, at 3 hours, specific differences

were found between cell adhesion on planar and nanopillared topographies. Many possibilities exist to explain these differences including protein conformation alterations in relation to substrate topography and alterations in surface chemistry following dry etching, which may affect cell adhesion. With respect to the significant difference calculated at 3 hours, specifically between the planar and nanopillared substrates, the median of the number of cells adhering to the nanopillars, 78, is much greater than those for the other two substrates, Graph 4.1. Cell-substrate interactions are believed to have an important role in this observation, as filopodia are prevalent at three hours on the nanotopography in comparison to planar controls, Section 4.4.2. Intricate, specific interactions between filopodia and nanofeatures may account for the increase in the number of fibroblasts adhering to the nanotopography. This is further described in a proposed model of integrin-substrate interactions, Figure 4.9, and is discussed in Section 4.3.2.

When the number of fibroblasts adhering to each individual substrate at all three intervals was examined, Table 4.2, the test statistic, K, was less than the χ^2-value in all instances. Thus, the Null Hypothesis stands indicating there are no significant differences between cell adhesion on any of the substrates over time, when P=0.01. It may thus be concluded that fibroblast adhesion is dependent upon topography and independent of time when comparing planar, planar etched and nanopillared surfaces.

4.4.2 hTERT Fibroblast Morphology on Nanopillared Topography - Fluorescence microscopy

hTERT fibroblast cells from the same population seeded on the experimental surfaces during the adhesion assay, Section 4.4.1, were examined using antibody staining, Section 2.7.2, and fluorescent microscopy to ascertain cytoskeleton composition in relation to nanopillared topographies. A Vickers microscope was utilised in oil immersion mode using the 50x oil immersion objective lens. Fibroblasts were seeded at a density of 10,000 per ml in 3mls media on control planar, 200nm-etched planar and 20nm-diameter, 200nm high pillared substrates and were fixed and stained at 20 minutes, 1 hour and 3 hours, Section 4.2.2.1.

hTERT fibroblasts were also seeded on 80nm and 200nm etched planar substrates, 20nm-diameter, 80nm high pillars, 50nm-diameter, 80nm high pillars, 20nm-diameter, 200nm high and 50nm-diameter, 200nm high pillared substrates, Section 4.2.2.2. Cells

were fixed and stained at 8 hours and 24 hours using the same techniques utilised at earlier time periods. These surfaces and time periods were chosen in the belief that alterations in cytoskeleton distribution with respect to the fibroblasts on each surface could be related to either surface chemistry occurring due to the etching and chemical processing, pillar diameter and/or pillar height.

4.4.2.1 Cytoskeletal Morphology of Fibroblasts at 20 minutes

At 20 minutes, fibroblasts on the planar control surface exhibit typical early responses to the planar substrate, with actin distribution indicating circumferential lamella formation with centrally located nucleus and tubulin surrounding the nuclear area, Figure 4.11ai). Tubulin appears unpolymerised, with little sign of microtubules occurring throughout the cell, Figure 4.11aii). Fibroblasts on the planar control have a rounded morphology with no definitive leading edge, display signs of actin remodelling and polymerisation and limited tubulin polymerisation. These observations substantiate previous fluorescent results, where hTERT fibroblasts exhibited this type of morphology at this time period on planar controls, Section 3.3.3.4.1.

Cells seeded on the planar etched control share similarities with the cytoskeletal observations made in relation to the planar control cells. Fibroblasts appear rounded in morphology, with actin-rich ruffling lamella development, Figure 4.11bi). Tubulin, however, appears at a more progressed stage in cells on the etched surface, with evidence of microtubule processes extending into actin-established lamellapodia or filopodia, Figure 4.11bii). Although not many of these sensing features are observed, their spiky appearance suggests that focal adhesion sites may already be developing at 20 minutes, resulting in localisation of cytoskeletal structures to these areas. When comparing fibroblast morphology on the planar etched sample to both the planar and pillared surfaces, cells are observed to share similar properties with both groups. This suggests that the substrate surface will also share similar properties, namely planar topography and dry etch chemistry.

Fibroblast morphology on the 20nm-diameter, 200nm high pillars however, have a greatly altered morphology in comparison to the planar controls. Cells appear to be interacting with the experimental surface through the development of lamellapodia and filopodia. The most unusual observation is the presence of microtubules extending towards the furthest most areas of these features, Figure 4.11ci-ii). Previous work

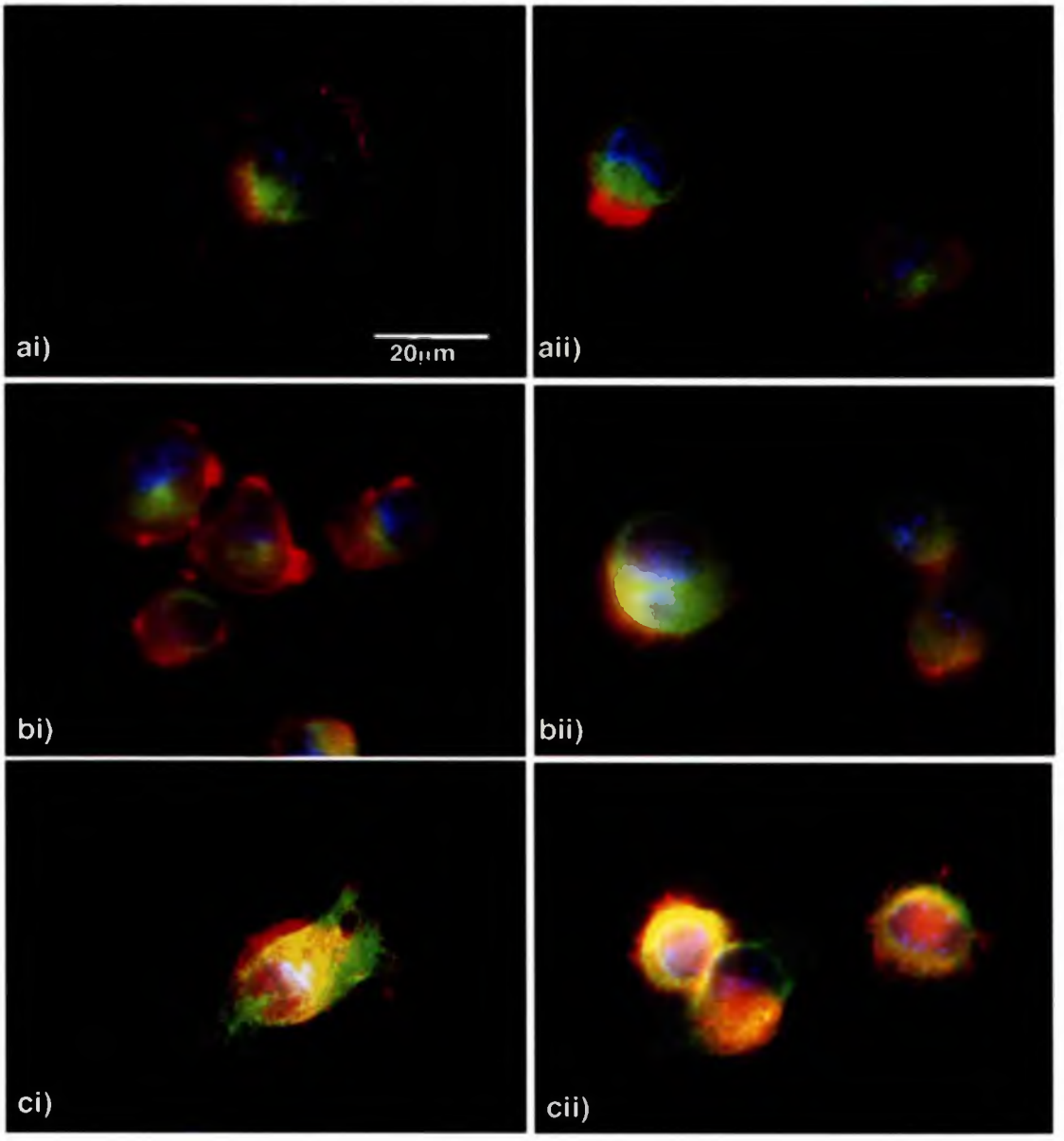

Figure 4.11: Fluorescent imaging of the actin and tubulin cytoskeleton of hTERT fibroblasts seeded on planar control, a), planar etched control, b), and 20nm-diameter, 200nm high nanopillars, c). Cells were fixed and stained following 20 minutes of contact with the substrates. A 50X oil immersion objective lens on the Vickers microscope was used to image cells. Actin is red, tubulin green and nuclei blue. Fibroblasts on the control planar surface appear rounded, with developing peripheral membrane ruffling occurring in a circumferential manner, ai), or extremely rounded as they settle on the substrate, aii). Fibroblasts on the planar etched control display a rounded morphology similar to the control cells, bi), and also appear to be developing a leading edge, visualised as actin ruffling, bii). Ruffling behaviour appears more similar to fibroblasts on the nanopillared substrate in comparison to the circumferential manner seen in relation to control cells, suggesting polarised development in the proximal-distal field. Fibroblasts in contact with the 20nm-diameter, 200nm high pillared surface display morphologies greatly altered in comparison to the other cell populations. Spiky peripheral extensions resembling actin-rich filopodia, ci), suggests sensing of the surrounding nanofeatures by the cell. Furthermore, microtubules appear to be contained within these elongations. Cells which do not display well-spread morphologies still appear to have spiky actin and tubulin containing peripheral extensions, cii), and appear capable of spatial discrimination in a lateral manner.

suggests f-actin as the main component of filopodia. The presence of microtubules extending throughout these protrusions suggests very localised focal adhesions, where cytoskeletal recruitment is occurring. Cell morphology on the nanotopography deviates from the rounded forms seen on the planar control, and to a lesser extent, on the planar etched surface. Fibroblast morphology and rectangular shape on the pillared surfaces suggests cells are in the early stages of elongation as opposed to more general cell spreading. Cell elongation is heavily reliant on focal adhesion establishments, which act as anchorage sites allowing the stress occurring in this phenomenon to be transmitted throughout the cell. The presence of elongated microtubules in lamellapodia and filopodia protrusions further supports the possibility of elongation, as these tubules act as scaffolds, maintaining cell shape. The fact that cell morphology suggests elongation, or more basically, detraction from the rounded morphologies of cells on the control surfaces, suggests fibroblast polarisation, with spatial and temporal distribution of intracellular factors within the cell.

4.4.2.2 Cytoskeletal Morphology of Fibroblasts at 1 hour

hTERT fibroblasts on the planar control following one hour of culturing exhibit a more developed morphology compared to 20 minutes, yet still appear rounded with circumferential actin lamella formation, Figure 4.12ai-ii). The actin-rich ruffling periphery of cells suggests spreading of the fibroblasts on the planar surface. The most notable alteration in cytoskeleton arrangement compared to 20 minutes is the more developed microtubule network. This suggests the development of spatial arrangements of intracellular components, with microtubules acting as a communicative system throughout the cytoplasm. Fibroblasts on the planar control at 1 hour also display tubulin arrangements and morphology more generally associated with telophase, Figure 4.12ai).

Fibroblasts on the planar etched surface appear rounded with peripheral actin radiating from the main bulk. , Figure 4.12bi-ii). The actin-rich lamella ruffling suggests cells are spreading on the surface as observed in the control population at this time. A spiky appearance at the peripheral edge of cells is observed in some instances, where actin protrusions occur, Figure 4.12bii), highlighting the interaction between cells and the surrounding planar-etched surface at specific, localised sites.

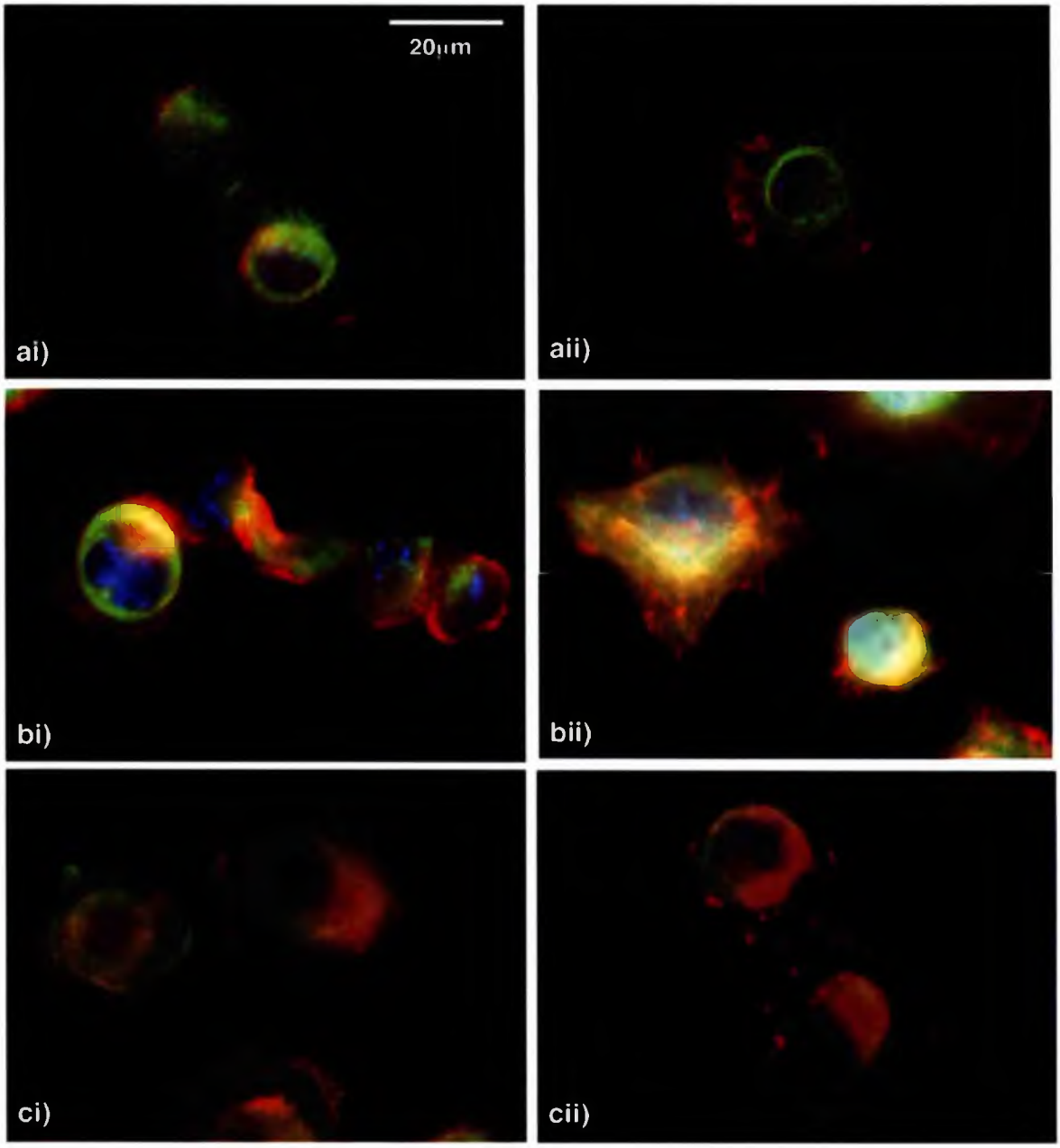

Figure 4.12: Fluorescent imaging of hTERt fibroblasts following 1 hour of contact with planar control, a), planar etched control, b), and 20nm-diameter, 200nm high nanopillared topography, c). A Vickers microscope was used to image cells using a 50X oil immersion objective. Actin is coloured red, tubulin green and nucleus blue. Fibroblasts on the control planar surface appear to be spreading at 1 hour, with active membrane ruffling, ai) and ii) as seen at 20 minutes, and development of microtubule networks, ai). On the planar 200nm-etched surface, fibroblasts appear to be spreading, again displaying actin-rich peripheral membrane ruffles, bi), occurring in a circumferential manner. Less rounded cells are also observed at 1 hour, bii), with slightly spiky peripheral regions of actin and more developed microtubule networks. hTERT fibroblasts on the nanopillared control at 1 hour appear well spread, yet differ in cytoskeletal morphology, where tubulin appears to compose the majority of the cell, with little peripheral actin observed, c). Although rounded, microtubules appear to protrude from cells rather than microfilaments, resulting in very localised microtubule spikes, ci). When cells appear to contact one another on the 20nm-diameter, 200nm high pillared surface, differentiation between cyoskeletal components is difficult, cii).

The most striking observation in relation to hTERT fibroblasts on the nanopillared topography at one hour is the presence of highly developed microtubule networks, Figure 4.12ci-ii). Developed networks of microtubules within cells suggest rigidity in structure resulting in greater possibility of cell contractility required in movement and translocation. As microtubule formation is believed to function in determining cell polarity (Alberts et al, 1994), contributing in spatial organisation of cellular components, polarity of cells on the nanotopography would appear to be highly developed following one hour. The spiky appearance of the peripheral membrane is once again observed on the nanopillars, with tubulin appearing almost as far, or in some cases further from the cell body than microfilaments in these areas. As previously described at 20 minutes, microtubules appear to elongate along membrane protrusions, suggesting very localised interactions with the surrounding surface due to the thinness of these protrusions terminating in a bead-like site.

4.4.2.3 Cytoskeletal Morphology of Fibroblasts at 3 hours

Following three hours, fibroblasts on the planar control appear well spread, Figure 4.13ai), with suggestions of directed motility in some individual cells, Figure 4.13aii). In spread cells, the periphery continues to exhibit circumferential actin-rich lamella ruffles. However, by three hours, in comparison to previous periods, microtubule networks appear to radiate from the nuclear area of cells exhibiting a rounded, spread morphology. hTERT fibroblasts on the planar control, in some instances, display cytoskeletal morphology associated with cell motility, Figure 413aii). Actin is seen to be localised both at the proximal and distal regions of the cell, with a rear detachment area visualised as a small actin aggregation (the left of the cell in this image), with membrane ruffling (right of cell) suggesting direction of movement (from left to right). Microtubules within this fibroblast are less distinct than in the spread cell due to the continual dynamic alterations undertaken by cells during movement and translocation.

Fibroblasts on the planar etched control appear, in general, most similar when considering cell cytoskeleton, to the planar control cells rather than the fibroblasts on the nanopillared topography, Figure 4.13bi-ii). However, in contrast, some cell-cell contacts do appear within this population. In general, most cells are observed to spread across the planar etched surface. Actin continues to radiate at the peripheral sites, suggesting continued spreading and sensing of a smooth, planar substrate as observed in fibroblasts on the control planar substrate, Figure 4.13ai). Alterations in this spreading

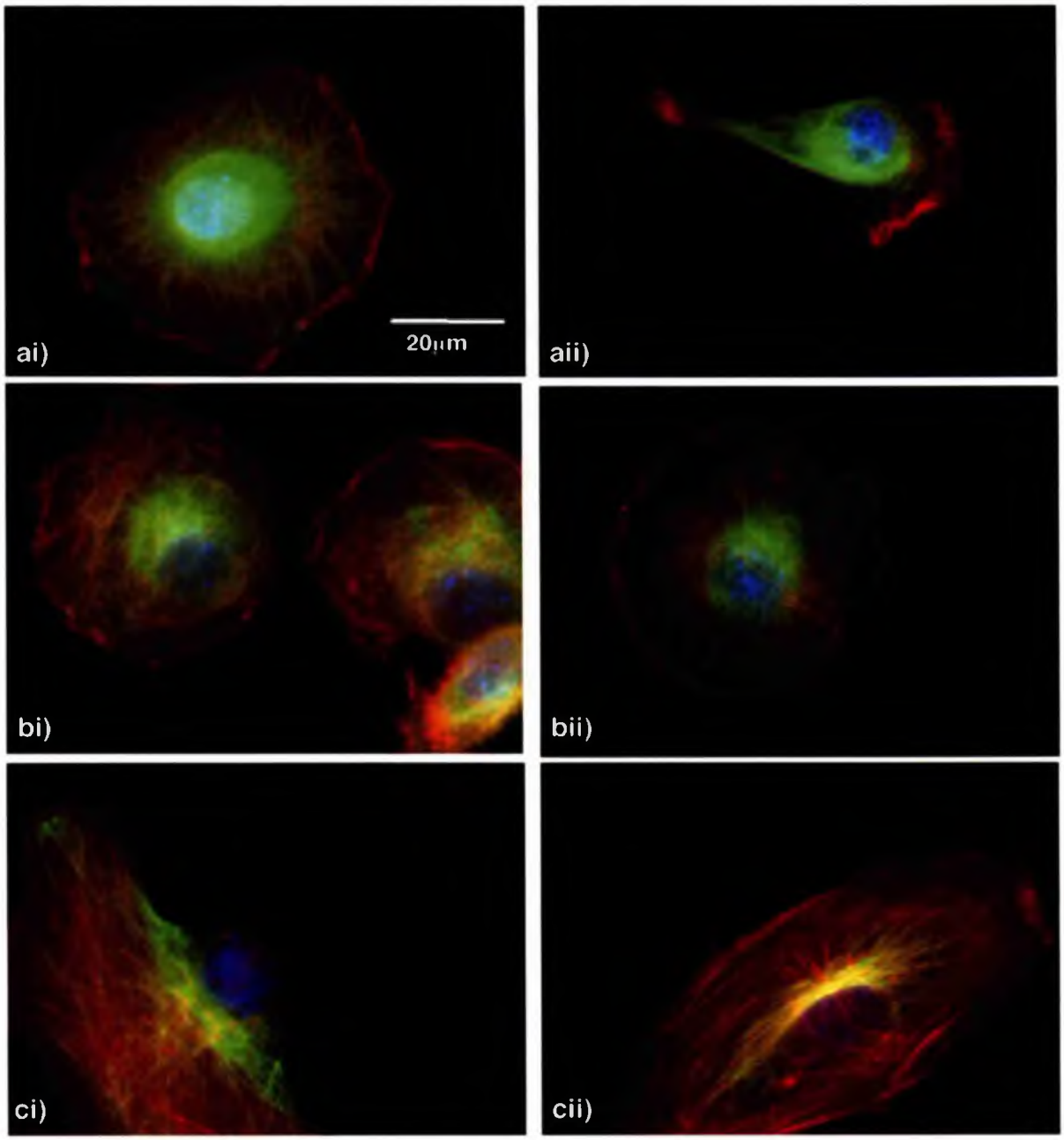

Figure 4.13: hTERT fibroblast cytoskeletal morphology following 3 hours of seeding on a) planar control, b) planar 200nm-etched surface, c) 20nm-diameter, 200nm high pillared topography. Images captured using a Vickers microscope in oil immersion mode (50X objective lens). Fibroblasts on the planar control substrate appear rounded, as previously seen at 20 minutes and 1 hour, and well spread with peipheral actin ruffling and developing microtubule network, ai). Cells are also beginning to display signs of motile behaviour on the planar control at 3 hours, aii). Similar rounded, spread morphologies are observed in fibroblasts on the etched control, b), with rich-actin preipheries and tubulin networks. Most fibroblasts observed on the nanopillared topography at 3 hours appear to have developed a leading edge containing actin at its immediate periphery, and microtubule networks, ci). The most unusual features in these cells are the non-central location of the nucleus, ci). Fibroblasts on the nanopillars are also seen to have an elongated, oval shape, where actin stress fibres stretch round the periphery of the cell, appearing to contain the tubulin network and nucleus, cii).

behaviour previously displayed by cells at 1 hour on the planar etched surface, Figure 4.12bii), is no longer present.

Fibroblast morphology on the 20nm-diameter, 200nm high pillared topography at 3 hours is markedly altered in comparison to both controls, Figure 4.13ci-ii). Although cells appear to be spreading on the experimental topography, this does not appear to occur as previously seen in relation to cells on both control surfaces. Actin ruffling per se does not occur in the conventional sense as described for fibroblasts on the planar and planar etched surfaces; notably, spreading is independent of circumference-localised actin activity. The most obvious alteration is the position of the nucleus. In the control cells, nuclei appear central to the main body of the cells. However, at 3 hours, the position of the nucleus in some cells on the nanotopography lies at a peripheral site, Figure 4.13ci). This suggests polarisation development, especially when considering the bulk of the microtubule network extending away from the nucleus in a general unidirectional appearance. Nucleus location is unusual in cells expressing this morphology, due to its peripheral positioning, with little support or protection occurring via the cytoskeleton or cytoplasm, where the most peripheral region of the nucleus appears to compose part of the peripheral circumference of the cell. The location of the microtubule network may account for the peripheral localisation of the nucleus, as motor proteins are believed to have a potential role in positioning the nucleus relative to the cell cortex by astral microtubules (Salmon and Way, 1999). As the microtubule network appears to extend away from the nucleus, motor proteins are unlikely to be abundant in the vicinity of the nucleus, resulting in its peripheral position.

Fibroblasts on the nanotopography are also seen to form morphology previously expressed by cells on the colloidal topography, Section 3.3.3.4. Cells appear well spread with a belt of actin running the entire length of the cell periphery, Figure 4.13ci). In relation to the colloidal topography, it was previously proposed that this feature might share similarities with adherens belts, more generally recorded in epithelial cells. Furthermore, actin appears very well developed in fibroblasts on the nanopillared substrate, with microfilament stress fibres occurring throughout cells, Figure 4.13ci-ii).

In summary, hTERT fibroblasts on the 20nm-diameter, 200nm high pillared topography exhibited altered cytoskeletal morphology in comparison to both planar and planar etched controls. At 20 minutes, cells on the nanopillars displayed spiky peripheral

membrane protrusions, highly developed microtubule networks and are well spread in contrast to their smoother, rounded control counterparts which exhibit smooth actin-rich peripheral membrane ruffling, Figure 4.11. This observation is extremely interesting when considering the observations by Wojciak-Stodhard et al that microtubules formed following 30 minutes of contact with micro-grooved topography (Wojciak-Stodhard et al, 1995), and that Oakley and Brunnette found that microtubules were the first element to align to grooves (Oakley and Brunnette, 1993). At 1 hour, cells on the nanopatterned substrate appear to be mainly composed of very well defined microtubule networks, parts of which often extend and terminate in peripheral spikes in the well spread fibroblasts, Figure 4.12c). Microtubules also appear to replace microfilaments in areas of the cell with similar shape to membrane ruffles. Control cells appear more rounded and less spread in comparison, and display actin-rich membrane ruffles and less developed microtubule networks. By 3 hours, Figure 4.13, fibroblasts on the nanotopography are very well spread, with very spiky filopodia-like peripheral protrusions containing mainly actin microfilaments. Microtubule networks are still prevalent throughout the cell body, and defined actin stress fibres are also observed in abundance, indicating strong cell-substrate adhesive interactions. In comparison to planar controls, fibroblasts on the nanopillars are highly altered in shape, deviating from the more generally observed rounded or triangular fibroblast forms.

4.4.2.4 Cytoskeletal Morphology of Fibroblasts at 8 hours

In contrast to the previous experimental arrangement, where hTERT fibroblasts were seeded on the experimental substrates and fixed in accordance with experiments conducted for the adhesion assay, Sections 4.4.2.1 to 4.4.2.3, fibroblasts fixed at 8 and 24 hours were seeded on a variety of pillared substrata. 20nm-diameter, 80nm high pillars, 50nm-diameter, 80nm high pillars, 20nm-diameter, 200nm high pillars and 50nm-diameter, 200nm high pillars were etched in SiO_2, and cells were fixed and labelled allowing for their tubulin and actin cytoskeleton to be observed. Two controls were used to monitor cell reactions to the nanopillared topographies, both of which were planar and underwent dry etching to a depth of either 80nm or 200nm prior to seeding cells. These surfaces were selected for use in monitoring cell reactions to nanotopography at these times, in an attempt to elucidate the importance of pillar diameter, height and the effects of dry etching in elicited cell response.

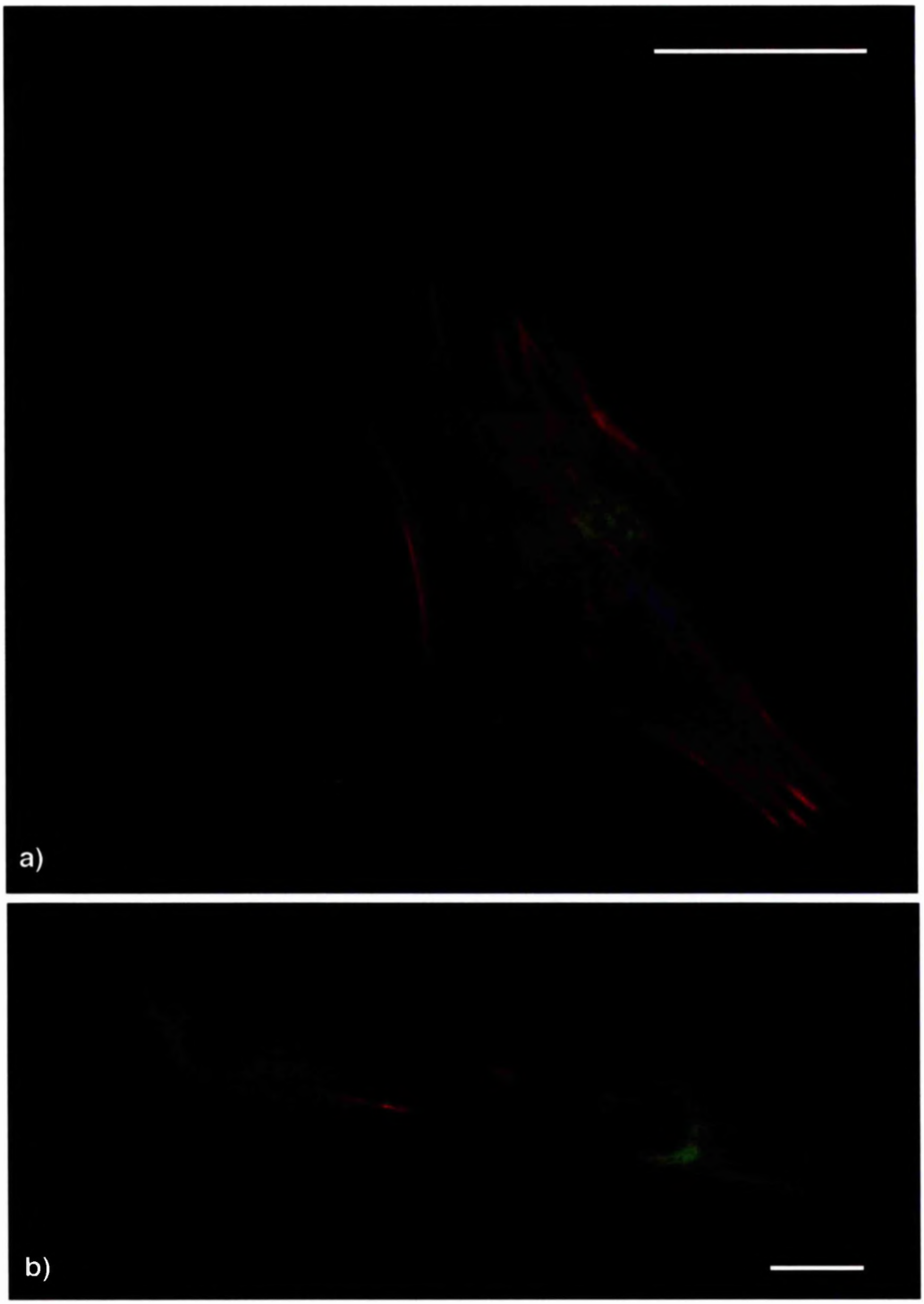

Figure 4.14: hTERT fibroblasts on 80nm-etched planar control at 8 hours. Images captured using Vickers microscope with 50X oil immersion objective. Actin is depicted as red, tubulin as green and nuclei are blue. Spread fibroblasts are observed on the 80nm-etched planar control at 8 hours, displaying microtubule networks, radiating from the nuclear regions towards the membrane periphery, and actin stress fibres specifically observed at the peripheral regions of the cell membrane, and underlying the nucleus, as the fibres run throughout the cell a) and b). Although in close proximity, b) cell-cell contacts are not observed on the 80nm-etched planar substrate, with individual fibroblasts, b) seen throughout this population. (Scale bars: 20μm).

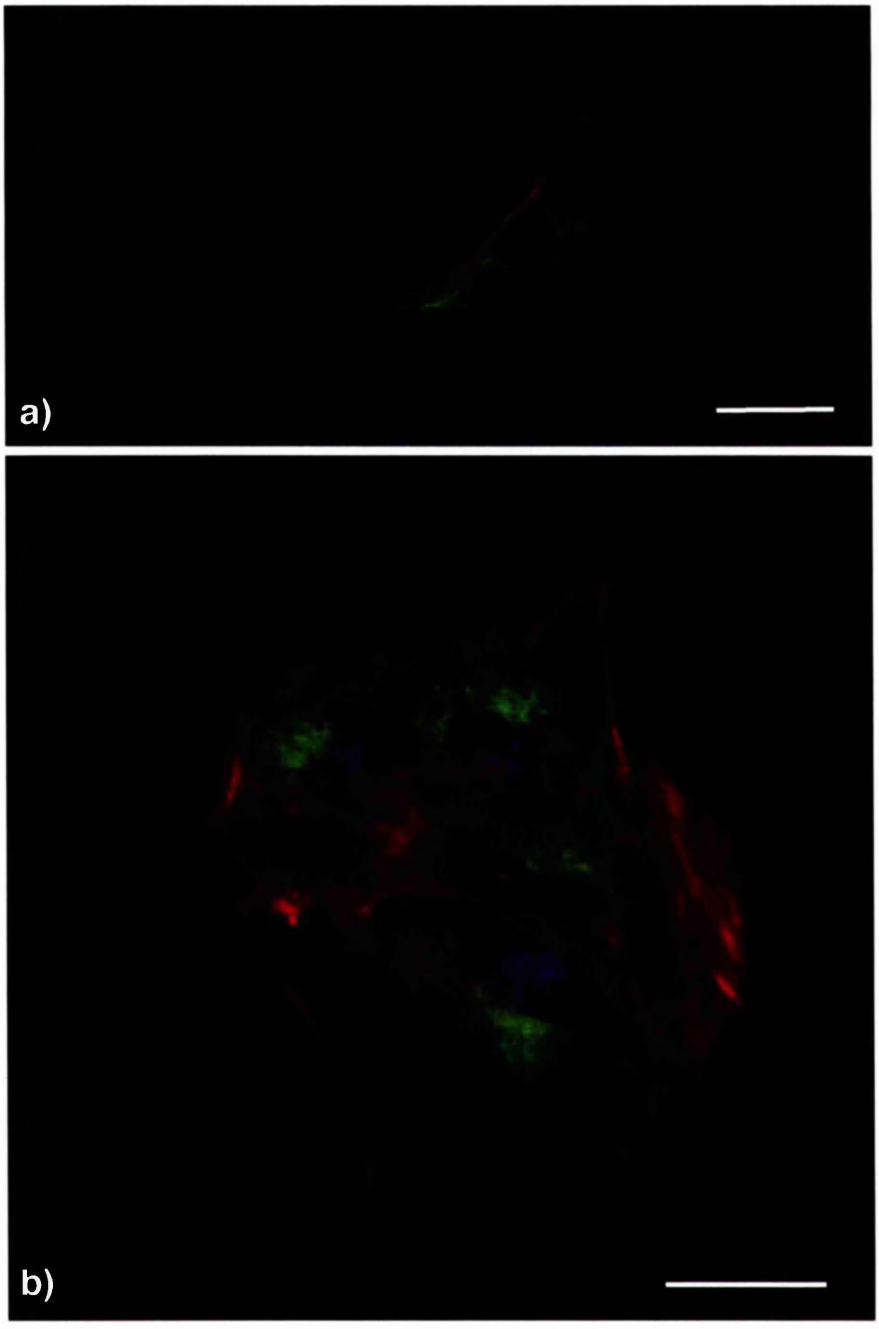

Figure 4.15: hTERT fibroblasts on 20nm-diamter, 80nm high pillars at 8 hours. Imaging conducted using Vickers microscope and 50X oil immersion objective. Atin is highlighted in red, tubulin as green and nuclei are blue. Cell-cell contact and contact inhibition appear altered on the experimental nanopillared substrate, where fibroblasts are observed to traverse neighbouring cells, a), or form multi-cellular aggregates, b). Individual fibroblasts often appear elongated on the nanopillared substrate, a). Cellular overlapping, a) suggests a lack of discrimination between cell surfaces and the nanopillared substrate by cells. Multi-cellular aggregates are observed on the 20nm-diameter, 80nm high pillared topography, b), suggesting increased cell-cell contacts. The distribution of the stress fibres within this aggregate, specifically located at the periphery of the group, b), is more representative of an individual cell with mature, stable focal adhesions. (Scale bars: 20μm).

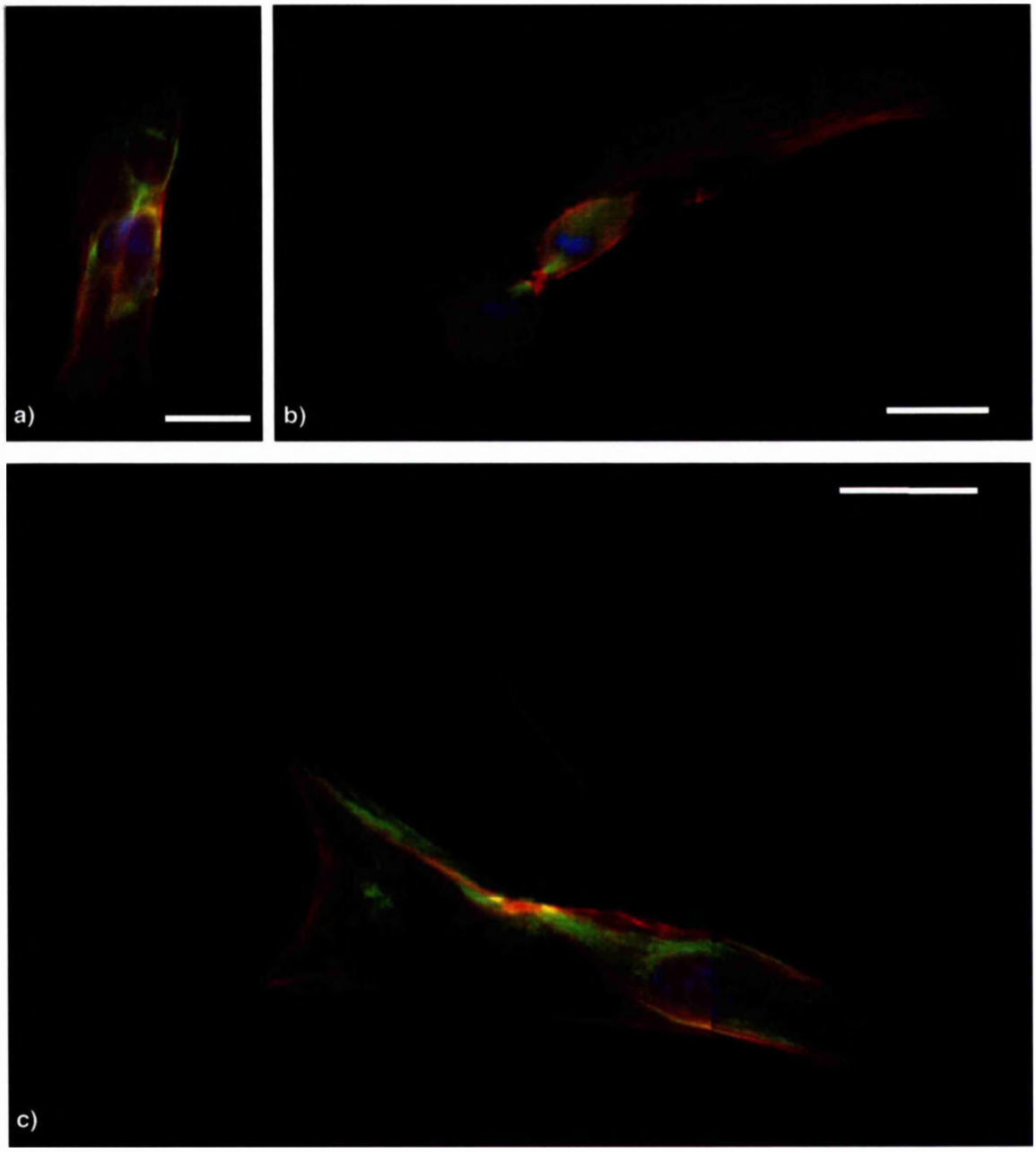

Figure 4.16: hTERT fibroblasts on 50nm-diameter, 80nm-high pillared topography at 8 hours, imaged using Vickers microscope with 50X oil immersion objective. Actin is coloured red in images, tubulin green and nuclei blue. Cellular aggregates are observed, where 3 cells group to form a multi-nuclear aggregate, a) and c). Aggregates appear elongated, with actin stress fibres surrounding the main body of the cells, a) and c). Three nuclei are observed within each aggregate, a) and c). Dividing cells are observed attaching to a neighbouring spread cell, b). The tension occurring across the spread cell (suggested in the observed parallel stress fibres), may act as a more preferable substrate for generating the tension required by the dividing cells to separate, b). This would account for the three nuclei observed in each aggregate, a) and c). (Scale bars: 20μm).

hTERT fibroblasts on the 80nm-etched planar control substrate appear spread, in a proximal-distal manner suggestive of elongation and movement across the surface at 8 hours, Figure 4.14. Actin stress fibres, located in the main at the periphery of the fibroblast, Figure 4.14a), suggest stable focal adhesion cell-substrate contacts, with a certain amount of stress occurring across the cell, indicated by actin stress fibres located within the nuclear region of the fibroblast. Microtubules appear to mirror stress fibre location, aligning to stresses occurring at the cell periphery. The bulk of the tubulin network is found within the nuclear region, radiating towards these microtubule-actin stress fibre regions. Stress fibres radiate outwards from the main cell body, culminating in proximal-distal positioning, suggestive of cell movement across the 80nm-etched planar surface, Figure 4.14a). Two fibroblasts within close proximity, Figure 4.14b), appear aligned, suggestive of a shared stress axis, possibly as a result of preceding division. Similarly, fibroblasts in this instance do not exhibit definite cell-cell contacts, although passive contacts appear via tubulin-containing membrane extensions, and do not display long elongations occurring in a distal manner, which would indicate a lack of rear detachment.

In comparison, hTERT fibroblasts on the 20nm-diameter, 80nm high pillared topography display cell-cell specific contacts, Figure 4.15, and also thin elongated proximal and distal trails, Figure 4.15a). Due to the exposed areas of the nanopillared substrate surrounding these cellular entities, it is unlikely this morphology is a result of proliferation, especially as an odd number of nuclei, 3 in this instance, are present. The morphology of these aggregates appears more as a miniaturised sample of tissue.

An elongated fibroblast, with fine protrusions containing both microfilaments and microtubules, appears to act as a substrate for the neighbouring, over-lapping cell, Figure 4.15a). The over-lapping cell appears to be in the process of moving across the substrate (and underlying cell), suggested in the actin protrusions accumulating in a leading, ruffling edge. Microtubules in both these cells appear to form a network radiating from the nuclear region, with very specific microtubule formations observed at the proximal and distal peripheries of cells, in alignment with actin stress fibres. Stress-fibres are also only observed at the proximal and distal regions, or along the length of the cell periphery linking these areas of fibroblasts, Figure 4.15a). Furthermore, at 8 hours, fibroblasts on the 20nm-diameter, 80nm high pillared topography also occur as multi-cellular units across the surface, Figure 4.15b). This behaviour is highly unusual,

especially when considering the effects of contact inhibition in hTERT cells *in vitro*. As fibroblasts are spread across the substrate, with stress fibres present, cell-substrate adhesion appears to occur. However, differentiation between cells and the 20nm-diameter, 80nm high pillared substrate appears altered, especially when considering one cell traversing its neighbour, Figure 4.15a). In the case of multicellular aggregates, where upwards of two cells form as a rounded individual entity, cell-cell contact would appear to be increased. One possibility, with respect to this cell-cell interactive behaviour, is the expression of cell-surface factors emulating underlying nanopillared topography resulting in similar topographic features occurring on the apical and aspect membrane of cells as observed on the nanopillared substrate. This type of altered membrane topography may be described in actin protrusion processes, for example filopodia extension, occurring across the cell membrane as it extends these fine processes in an attempt to negotiate the pillared substrate. As lamellapodia develop during cell movement, new actin processes pervade the developing area, resulting in the backward "not drowning, but waving" motion across the cell membrane surface (REF). Filopodia are capable of direct interactions with individual colloidal features (Wood et al, 2002), suggesting some similarity between the interacting protrusion and the feature of interest, for example the dimensions included in the interaction. Overlapping of cells, Figure 4.15a), with no distinct interaction, for example cell-cell alignment, with the upper-most cell possibly sensing only the filopodia, reminiscent of the underlying nanopillars. Furthermore, cellular aggregates may occur as a result of a "stickle-brick" effect, where cell-cell contact results in the tangling of opposing membrane, or filopodia, protrusions, Figure 4.15b).

hTERT fibroblasts on the 50nm-diameter, 80nm high pillared topography at 8 hours, Figure 4.16, display very similar morphology when compared to those cells observed on the 20nm-diameter, 80nm high nanopillars, as previously described, Figure 4.15. Cell-cell contacts are observed in all images, and are similar to those observed on the 20nm-diameter, 80nm high pillared topography, Figure 4.14b), where cells appear to form a continuous unit, Figure 4.16a) and c). However, cellular aggregates on the 50nm-diameter, 80nm high pillared topography, containing three nuclei, appear more elongated and less rounded in comparison to those on the 20nm-diameter, 80nm high pillared topography. Alterations in adhesion are most likely to underlie the discrimination between rounded and more elongated aggregates as a response to nanopillar diameter. Cell-cell aggregates appear more elongated on the 50nm-diameter,

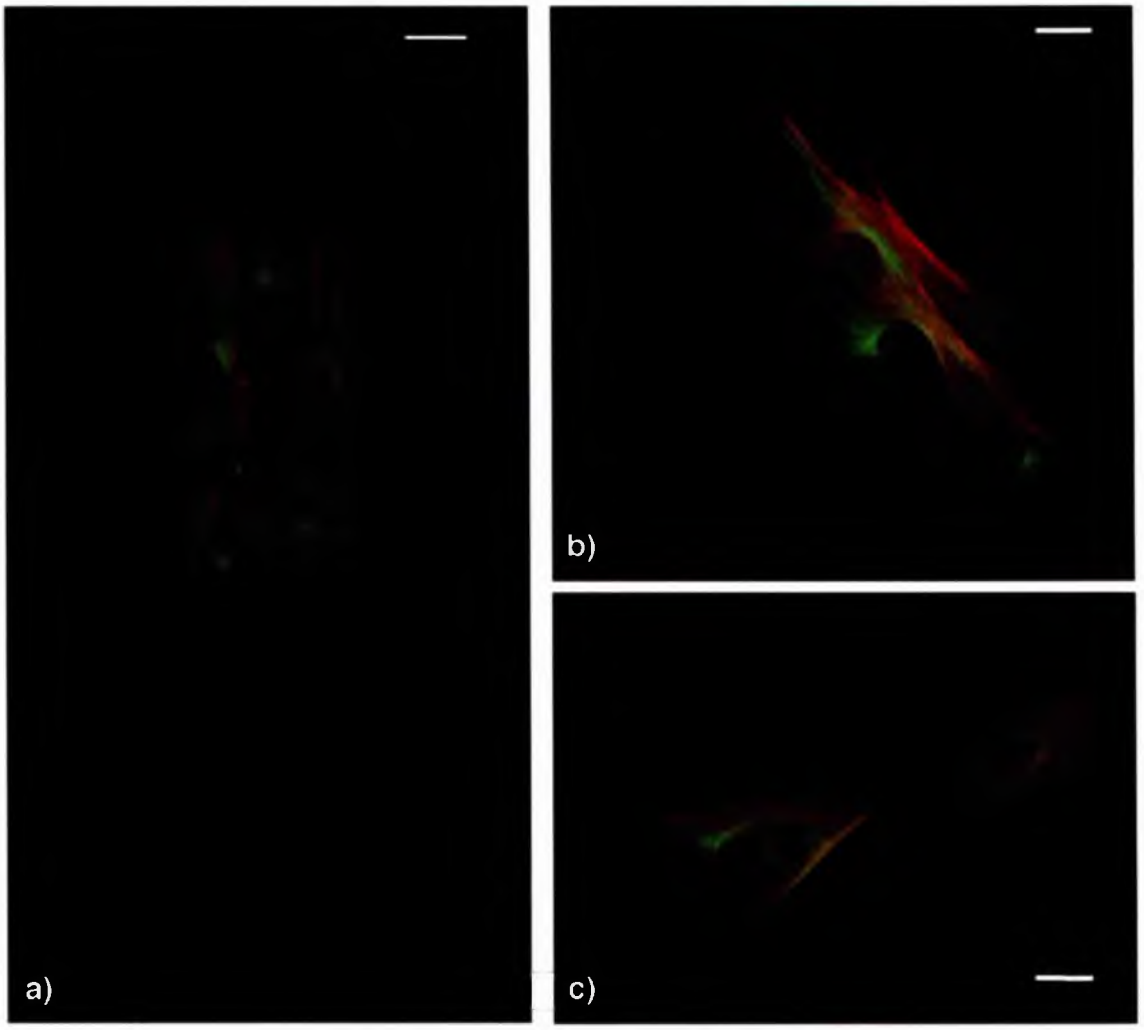

Figure 4.17: hTERT fibroblasts on 200nm-etched planar control at 8 hours. A Vickers microscope with 50X oil immersion objective was used to examine actin (red) and tubulin (green) within cells on the experimental substrate. Nuclei are blue. Cell-cell aggregates occur across the 200nm-planar etched substrate at 8 hours, with groups containing up to 6 cells, a). Smaller groups containing 2, c) or 3, b), cells are more readily observed. Actin stress fibres are seen in the majority of cells on the planar etched substrate, regardless of whether cells occur as individuals or groups, suggesting mature cell-substrate adhesions. Within an aggregate, individual cells often express specific boundaries, a) allowing for differentiation between each cell. Boundaries are mainly determined by actin peripheries. An actin and microtubule containing protrusion is also observed, a), extending from the main bulk of the aggregate from a single cell. In other instances, b) and c), it is difficult to discriminate between individual cells, with microfilaments and microtubules appearing to interconnect. (Scale bars: 20μm).

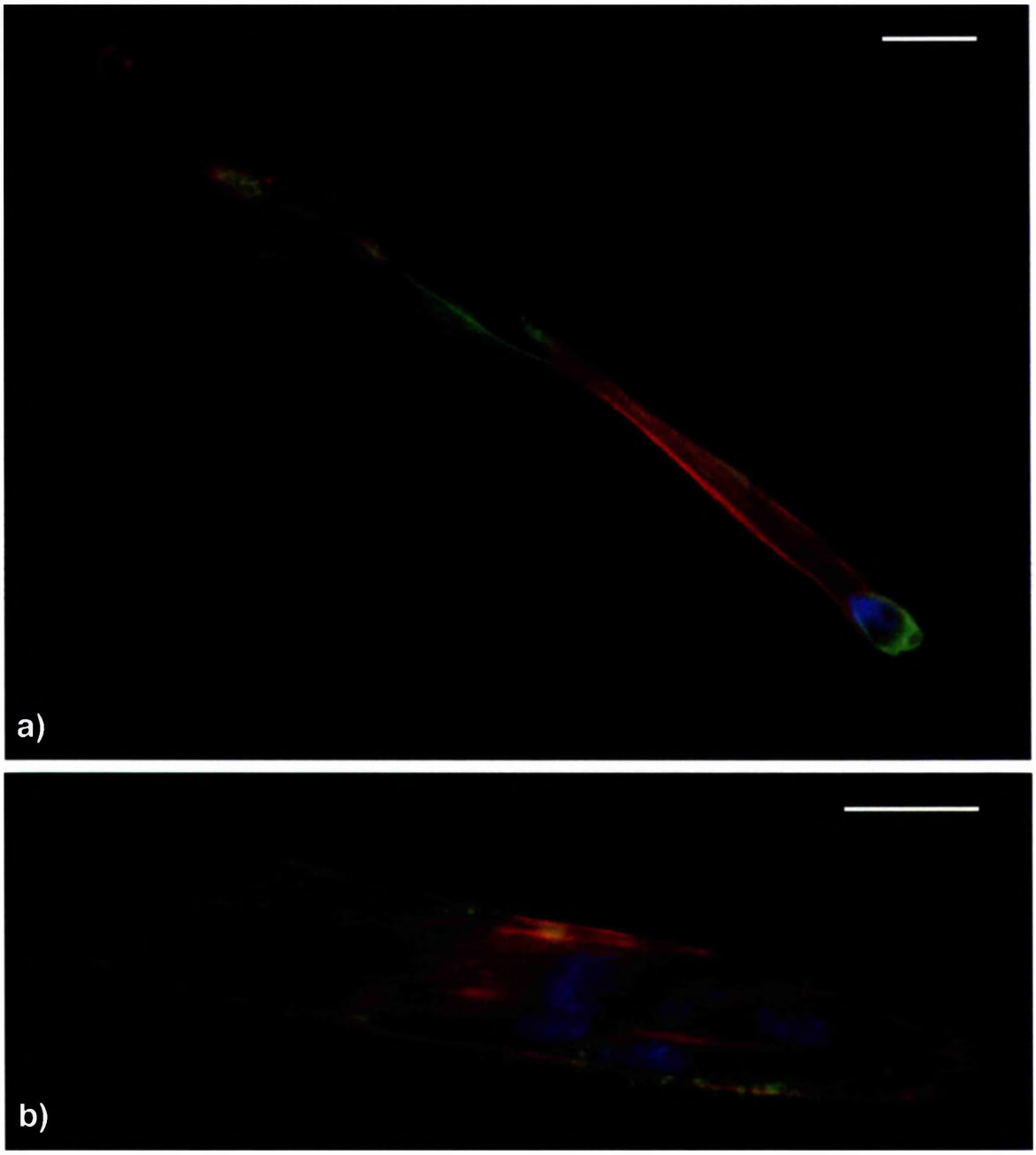

Figure 4.18: hTERT fibroblasts on 20nm-diameter, 200nm high pillared topography at 8 hours. Actin is depicted as red, tubulin green and nuclei blue. Cell-substrate adhesions appear to result in elongated tails in some instances, a). As a result, cells exhibit an elongated morphology, where tubulin islands compose the bulk of the detachment site, b). These "islands", which also contain actin, appear as a cytoskeletal temporal map, suggesting the path traversed by the cell. Cell-cell interactions appear increased, and, as a result, multi-cellular aggregates are observed on the 20nm-diameter, 200nm high pillared topography, b). Actin stress fibres within this aggregate are situated centrally within the cellular bulk, extending outwards towards the peripheral regions. The most distinguishable of features is the globular localisation of tubulin occurring at the periphery of the aggregate. Imaging conducted using Vickers microscope with 50X oil immersion objective. (Scale bar: 20μm).

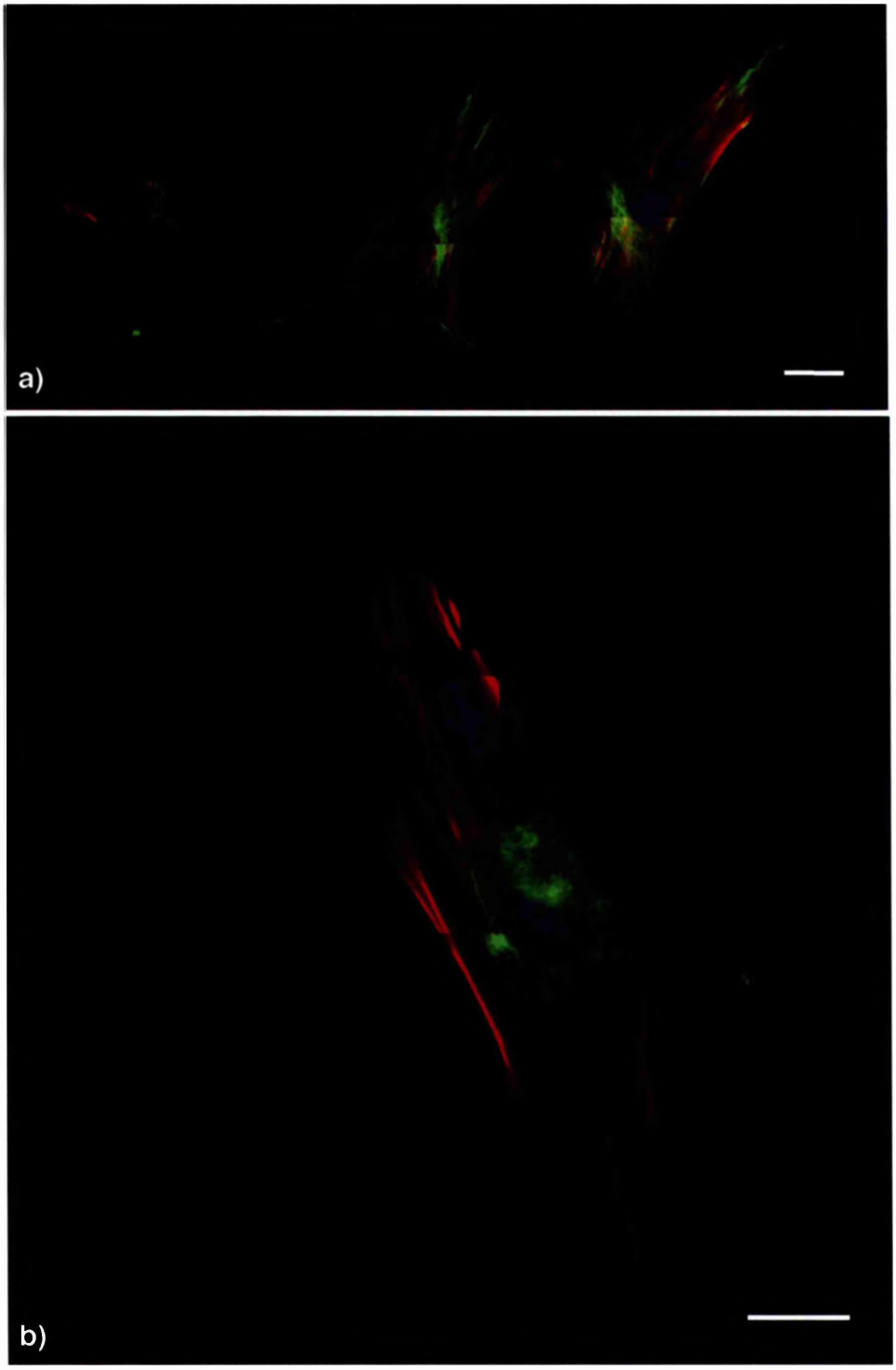

Figure 4.19: hTERT fibroblasts on 50nm-diameter, 200nm high pillars in silica at 8 hours. A Vickers microscope with 50X oil immersion objective lens was used to observed actin (red), tubulin (green) and cell nuclei (blue) arrangements within fibroblasts on experimental surfaces. Long, thin, twisting trails of cell, containing both actin and tubulin are observed, where rear detachment sites appear to lack focal adhesion disassembly required for motile behaviour, a). Cellular aggregates displaying spatial actin stress fibres more readily associated with an individual spread cell, b) are also observed. (Scale bars: 20μm).

80nm high pillared topography, and, in accordance with motile behaviour resulting in elongation, display microfilament- and microtubule-containing protrusions.

Figure 4.16b) suggests possible initiation of such aggregates, where dividing cells attach to a more stable, spread cell, suggested by developed actin stress fibres. As cells divide and attempt to undergo the final stages of cytokinesis, cell-cell contacts established with the non-dividing cell may provide more agreeable stress than the underlying nanopatterned substrate, and, as a result, dividing cells may attach to the "substrate" cell. This would account for the three nuclei observed in Figures 4.16a) and c).

Fibroblasts on the 200nm-etched planar control at 8 hours, Figure 4.17, share cytoskeletal morphology most similar to cells on the nanopillared topography, as previously discussed, in comparison to fibroblasts on the 80nm-etched planar control. This may occur as a result of dry etch chemistry or unintentional nanopatterning of theplanar topography during the dry etch process, where substrates patterned with colloids and planar substrates were etched in the same run.

Cell-cell contacts appear to occur between fibroblasts across the 200nm-etched surface at 8 hours, similar to the cell-cell aggregates observed in relation to the 80nm high pillared topographies. However, cell-cell contacts on the 200nm-etched planar substrate appear less compact, especially in relation to aggregates observed on the 20nm-diameter, 80nm high pillars, Figure 4.15b), with individual cells more distinct within a group, Figure 4.17a). Microtubule distribution appears to extend in a radial manner from the nuclear region of cells, towards the membrane periphery. Actin stress fibres occur mainly at peripheral regions, and also connecting these regions via the nuclear area, especially at the proximal and distal sites, where stress occurring during movement is at its greatest (Dembo and Wang, 1999).

20nm-diameter, 200nm high pillared topography appears to alter fibroblast morphology greatly at 8 hours, Figure 4.18. Extremely elongated cells, measuring upwards of 1mm in length, Figure 4.18a), resembling a comet, are observed. Actin and tubulin distribution occurs throughout the fibroblast, with tubulin islands, containing a lesser amount of actin, appearing almost separate from the main body. Stress across the cell appears to continue, resulting in the highly elongated shape of the cell body. This is suggested in the long actin stress fibres running the length of the cell body, Figure

4.18a). Tubulin also appears located around the cell nucleus, suggesting a possible supportive role of microtubule networks, buffering the nucleus from the tension occurring across the cells length.

Cell-cell aggregates are also observed on the 20nm-diameter, 200nm high pillared topography at 8 hours, Figure 4.18b). As observed in relation to the 20nm-diameter, 80nm high pillared topography, this aggregate, containing seven nuclei, exhibits a morphology more readily attributed to an individual cell. Actin stress fibres occur throughout the multi-cellular cluster, located, in the main, in the central region of the group and, to a lesser extent, at the periphery of the aggregate, suggestive of high cell-substrate adhesions within this area. The elongated shape of the cellular group suggests tension occurring across the aggregate. Tubulin distribution within the multi-cellular entity is particularly interesting, where globular tubulin appears localised at the peripheral regions of the aggregate, Figure 4.18b). The spherical shape of the localised tubulin is suggestive of the underlying nanopillared topography. Regardless of the cause, these tubulin accumulations are likely to arise due to some limit imposed upon polymerisation. This would result in a lack of continued microtubule formation throughout the aggregate.

Fibroblasts on the 50nm-diameter, 200nm high pillared topography at 8 hours, Figure 4.19, do not exhibit the drastic morphological alterations seen in cells on the 20nm-diameter, 200nm high nanopillars. However, cytoplasmic trails, containing both actin and tubulin, appear to occur across the nanotopography at 8 hours, Figure 4.19a). As previously described in relation to the HGTFN endothelial cell time-lapse video microscopy footage, Section 4.3.2, alterations occurring in focal adhesion disassembly, whether via extra- or intracellular components, is highly likely to account for lack of elongated rear detachment sites. Microtubules appear to extend outwards from the nuclear area of cells, protruding further than other cytoskeletal extensions, Figure 4.19a). This observation appears to relate to the previously observed elongated rear detachment sites, suggesting altered depolymerisation properties of microtubules in fibroblasts on this experimental substrate. Actin stress fibres are also observed, Figure 4.19a), implicating mature cell-substrate focal adhesions which would account for the spatial distribution of both actin and tubulin.

Cell aggregates containing 2 nuclei, Figure 4.19a), and 3 nuclei, Figure 4.19b), are also present on this substrate. Actin stress fibres surrounding the 3 nuclei aggregate, Figure 4.19b), are located at the periphery, more readily associated with well-spread single cells displaying stable focal adhesions. The cytoskeleton of individual cells within this group are difficult to analyse, suggesting intermingling of intercellular microfilaments and microtubules. Furthermore, fine elongated microtubule-containing protrusions are seen to extend from this cellular aggregate, Figure 4.19b), suggesting similar behaviour with respect to rear detachment disassembly in single cells, Figure 4.19a).

4.4.2.5 Cytoskeletal Morphology of Fibroblasts at 24 hours

As at 8 hours, fibroblasts seeded on 80nm-etched planar, 20nm-diameter, 80nm high pillars, 50nm-diameter, 80nm high pillars, 200nm-etched planar control, 20nm-diameter, 200nm high pillars and 50nm-diameter, 200nm high pillared substrates were fixed at 24 hours and processed to allow actin and tubulin to be visualised. Actin is depicted in all images as red, tubulin as green and nuclei are blue.

Figure 4.20 highlights three different states observed in hTERT fibroblasts on the 80nm-etched planar control substrate at 24 hours. Cell division is observed, where an elongated protrusion containing both actin filaments and tubulin extends from one cell across the substrate, Figure 4.20a), possibly in an attempt to produce the required migration axis believed to be involved in the completion of cytokinesis (Burton and Taylor, 1997). Fibroblasts are also observed in motility phases, Figure 4.20b), where a leading edge appears as actin protrusions, with microfilaments extending away from the main cell body, suggestive of detachment sites. Actin stress fibres appear located at the periphery of cells, and are also observed immediately behind the leading edge, suggesting dynamic focal adhesion behaviour within the distal portion of the cell, Figure 4.20b). An elongation, Figure 4.20c), measuring more than 100μm in length is also observed. Actin stress fibres are positioned at the peripheral regions of this cell, with a rear detachment protrusion containing both microfilaments and tubulin, positioned in the distal region (right), and an extended fan-shaped developing leading edge proximal (left), Figure 4.20c).

hTERT fibroblasts on the 20nm-diameter, 80nm high pillared topography at 24 hours appear primarily in multi-cellular aggregates, Figure 4.21a) and c), with intercellular connections established across many microns, often more than 1mm in length, Figure

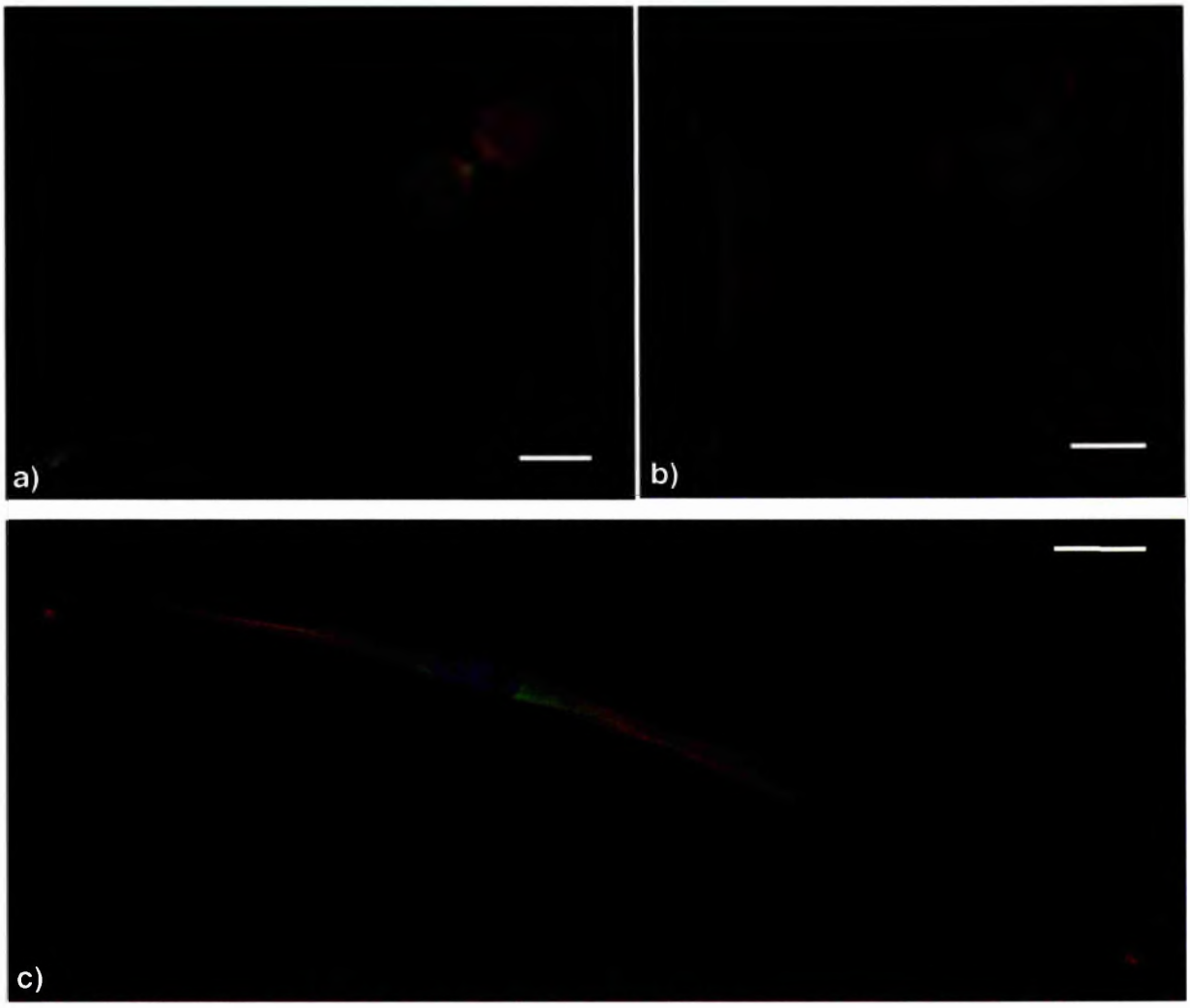

Figure 4.20: hTERT fibroblasts on 80nm-etched planar control at 24 hours. Imaging was conducted using a Vickers microscope with 50X oil immersion objective, allowing actin (red), tubulin (green) and nuclei (blue) to be visualised. Cells are seen to undergo a number of processes on the 80nm-planar etched surface including cell division, a), motility, b) and elongation and translocation, c). An elongated protrusion containing actin and tubulin is observed in one of the dividing cells, resulting in an migrational axis being established, a). Tension across both cells is further suggested by the actin stress fibres aligned in the same direction as the opposing protrusion, a). Cell migration is suggested in some of the fibroblast population, where a leading edge containing actin stress fibres and microtubule protrusion precedes a rear detachment site, primarily composed, in one instance, of microfilaments (right) and two protruding microtubule-containing sites in another (left). Elongated cells are also observed, c), where cell shape appears very linear, with a trailing detachment containing actin filaments, aligned to the length of the cell, and small microtubule containing island immediately at the distal site of the elongation. The soon-to-be leading edge of the cell (right) contains microtubules, and the beginnings of actin-rich membrane ruffles. (Scale bars: 20μm).

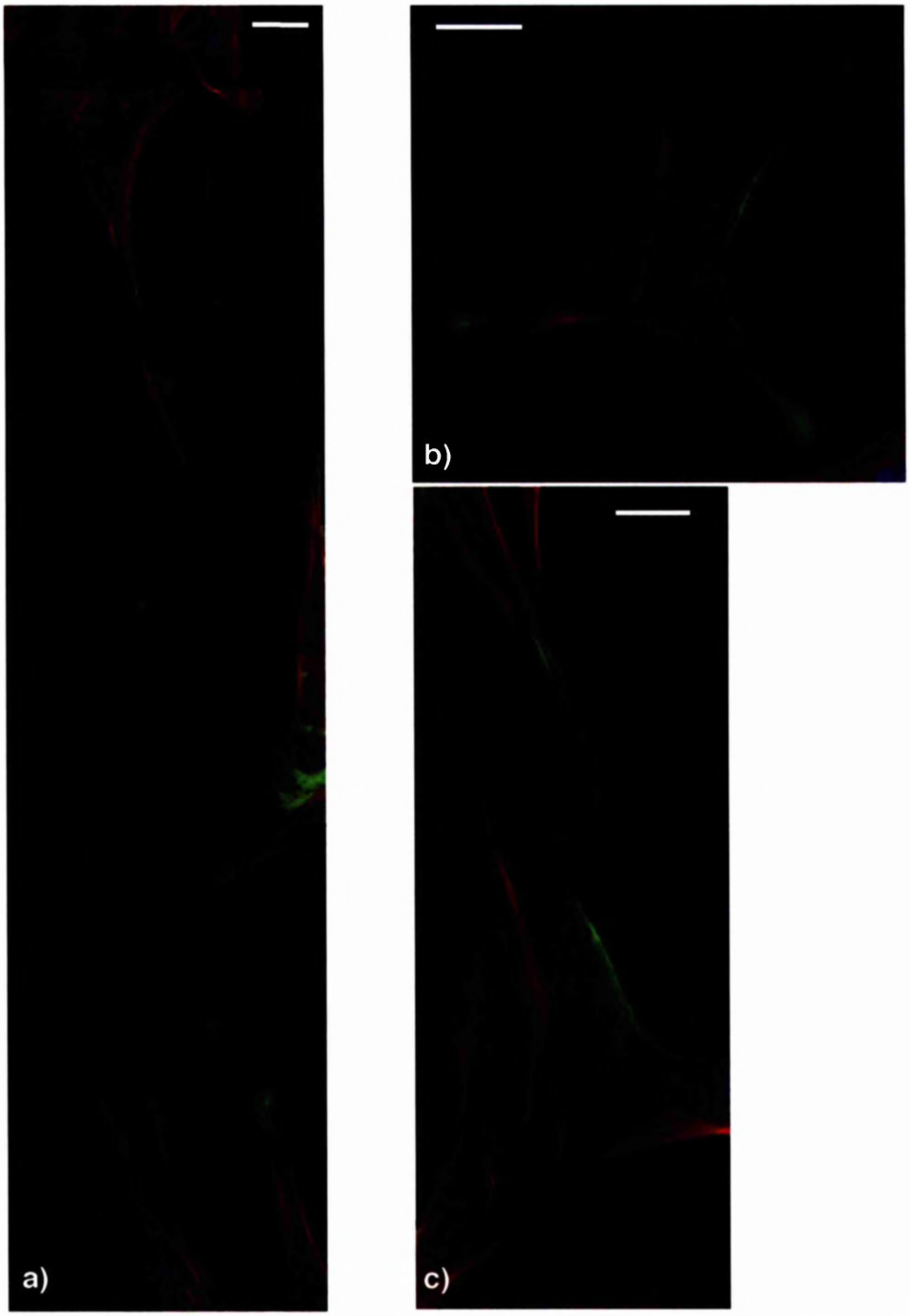

Figure 4.21: hTERT fibroblasts on 20nm-diameter, 80nm high nanopillars in SiO_2 at 24 hours. A Vickers microscope with 50X oil immersion objective was used to image actin (red), tubulin (green) and nuclei (blue) in fibroblasts on the experimental substrate. Cell-cell contacts are observed frequently within this fibroblast population, a) and c), and single cells are also seen, b). Although appearing in aggregates, actin and tubulin of individual cells appear distinct from neighbouring cells, a) and c), suggesting contact inhibition has occurred resulting in cell alignment to one another across the substrate. The presence of elongated protrusions containing both microfilaments and microtubules, appears to bridge gaps between neighbouring aggregates, a), and may arise due to disassembly problems associated with rear detachment. Stress fibres occur throughout the population, and the star-like shape of the individual cell imaged, b), suggests stress occurring between peripheral adhesions. (Scale bars: 20μm).

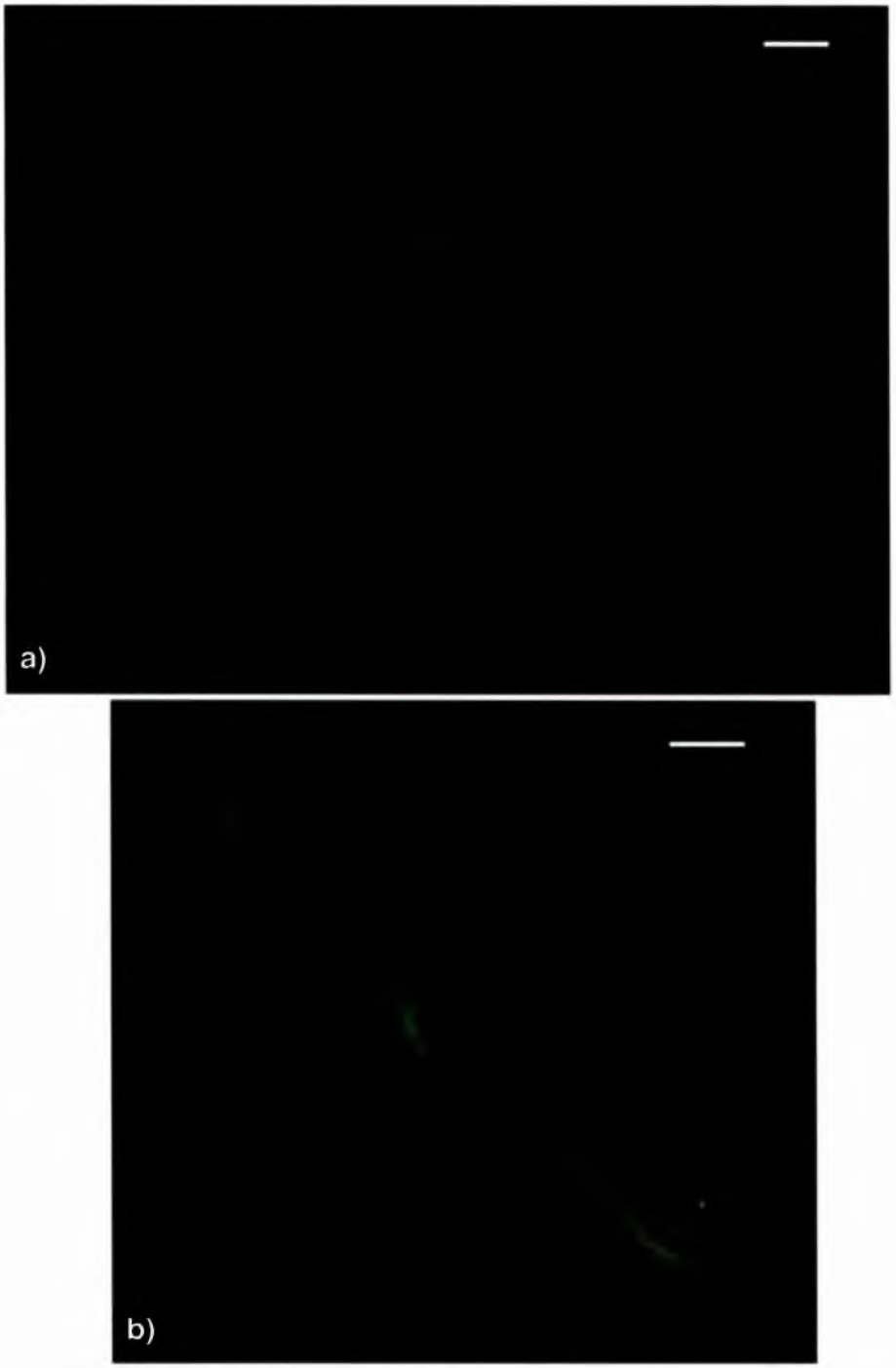

Figure 4.22: hTERT fibroblasts on 50nm-diameter, 80nm high pillared topography at 24 hours. A Vickers microscope with 50X oil immersion objective was used to image actin (red), tubulin (green) and cell nuclei (blue) on the experimental substrate. Elongated protrusion containing microtubules, and, to a lesser degree, microfilaments are observed on the 50nm-diameter, 80nm high pillared topography at 24 hours, a). This appears as a result of unsuccessful rear detachment. Microtubule networks within cells on the experimental topography appear well organised, providing a system for spatial organisation of intracellular organelles, and also communication and support throughout the cells, a) and b). The microtubules are often observed to radiate from the nuclear region to most extreme peripheral regions of the cell, a) Cell overlaps are also observed, b), suggesting a lack of discrimination between the nanopillared substrate and cell membranes. The presence of well-defined actin stress fibres indicates established, mature cell-substrate focal adhesion complexes on the 50nm-diameter, 80nm high pillared topography. (Scale bars: 20μm).

4.21a), which contain microfilaments and microtubules. These thin, elongated protrusions appear, at times, to be sacrificed by the cell, where rather than retract these features into the main cell body, severing of the protrusion is favoured. Very small clumps of actin and tubulin containing features left strewn across the nanopillared topography results. This is highlighted in the apparent lack of connection between one such elongation and the main cell body it protrudes from, Figure 4.21a). Possible retraction, as observed in relation to the HGTFN time-lapse video footage, Section 4.3.2, may occur in a reeling process, where the width of the process is gradually reduced. If the width of the elongation is drastically reduced close to the cell body, in comparison to the most distal region of the process, stress occurring across the cell and the attached protrusion may result in severing of the process.

Although fibroblasts on this surface appear to aggregate, some single cells are observed, Figure 4.21b). The star-like shape of this individual fibroblast suggests a great amount of stress occurring in a number of directions, further implied by the positioning of actinstress fibres at the peripheral, curved membrane regions occurring between adhesion sites positioned at the corner of the cell, Figure 4.21b). Once again, elongated protrusions are present, representing detachment sites, which contain both actin filaments and microtubules, which appear aligned, suggesting the spatial distribution of tension across this area.

Elongated detachment sites are also present in the hTERT population seeded on the 50nm-diameter, 80nm high pillared topography at 24 hours, Figure 4.22a). One of the cells in this image displays microtubule- and actin-containing detachment sites at two corners of the typically triangular appearance of fibroblasts, where thin protrusions suggest the previous location of the cell. As the cell has retracted, the original adhesions established during elongation have remained, Figure 4.22a). This suggests that cell-substrate adhesions are strong, and intracellular focal contact disassembly is absent or reduced. Cell-cell contacts are also observed, Figure 4.22b), but microtubules and microfilaments appear more distinct within this group than previously noted at 8 hours. Actin stress fibres are observed in fibroblasts involved in cell-cell contacts, again indicative of well-developed cell-substrate focal adhesions. The multi-cellular aggregates of fibroblasts, where approximately 3 nuclei are present within the cytoplasmic bulk of the group, previously observed on 50nm-diameter, 80nm high

pillars at 8 hours is no longer seen in relation to this topography at 24 hours. This suggests alterations with respect to temporal processes.

hTERT fibroblasts appear to form aggregates across the 200nm-etched planar control at 24 hours, Figure 4.23. Yet, in comparison to the aggregates previously observed on the nanopillared topography, especially where pillars have a diameter of 20nm, each individual cell is distinguishable from its adjoining neighbour. Furthermore, cell protrusions do not exhibit globular patterning associated with limited rear detachment of cellular processes as observed in relation to the nanopillared topographies. Very few elongated detachment sites are observed in relation to cells on the 200nm-etched planar substrate at 24 hours. One or two of these processes are present, however, they appear thicker and less elongated in relation to those observed on the pillared topography and also lack the spiky, localised beading attributed to these features on the nanopillars.

Cell-cell aggregates are also observed in the fibroblast population on the 20nm-diameter, 200nm high pillared topography at 24 hours, Figure 4.24. Individuals contained within multi-cellular aggregates, Figure 4.24c), appear to exert (or are affected by) tension occurring between neighbouring cells. As a result, cell alignment is apparent, Figure 4.24c). Furthermore, neighbouring cells often bridge aligned cells, perpendicular to established stress gradients, Figure 4.24c), suggesting some form of cell sensing with regard to the surrounding cellular environment. Stress axes and mature cell-substrate focal adhesions, are indicated by stress fibres occurring parallel to one another within aligned groups, Figure 4.24c).

Cell groups containing 2 or 3 nuclei are observed, Figure 4.24a) and b), however, cell overlapping at peripheral edges occurs, rather than aggregates appearing as multi-nucleated cells. Two cells, forming cell-cell contact, Figure 4.24a), are seen to overlap, where one cell (left) displays typically fibroblast morphology, with triangular shape. A microtubule network radiates from the nuclear region towards the peripheral membrane. The neighbouring cell appears in the process of dividing, as indicated by separating chromosomes, visualised in the nucleus, Figure 4.24a). Long actin-rich processes, displaying fine filopodia, stretch across the pillared substrate, allowing a migrational axis to be established. Cell-cell contacts are also observed in Figure 4.24b), where connections occur via an intercellular bridge containing both microfilaments and microtubules. This bridge appears to occur due to previous contact established between

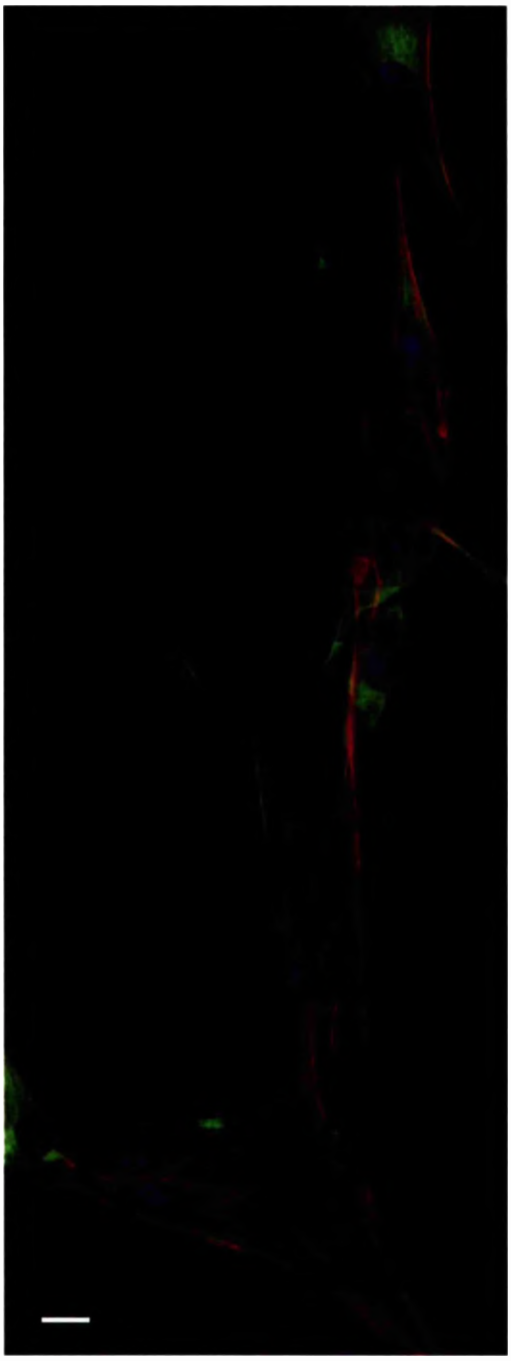

Figure 4.23: hTERT fibroblasts on 200nm-etched planar substrate at 24 hours. Actin (red), tubulin (green) and nuclei (blue) were imaged using a 50x oil immersion objective on the Vickers microscope. Cell-cell contacts appear to occur on the 200nm-ecthed, planar substrate. However, in contrast to hTERT fibroblasts on the nanopillared topographies, a lack of rear detachment features occur within the cell population on the planar, etched substrate. Furthermore, when elongated protrusions are observed, this feature lacks the localised tubulin and actin globules present in cell detachment sites on the nanopillared topographies. Microfilaments and microtubules of cells within the aggregate seen on the 200nm-etched, planar substrate can be allocated to each individual cell, also in contrast with the mutli-cellular aggregates observed on the 20nm-diameter pillared topographies, where aggregates appear more as multi-nuclear cells. (Scale Bar = 20μm).

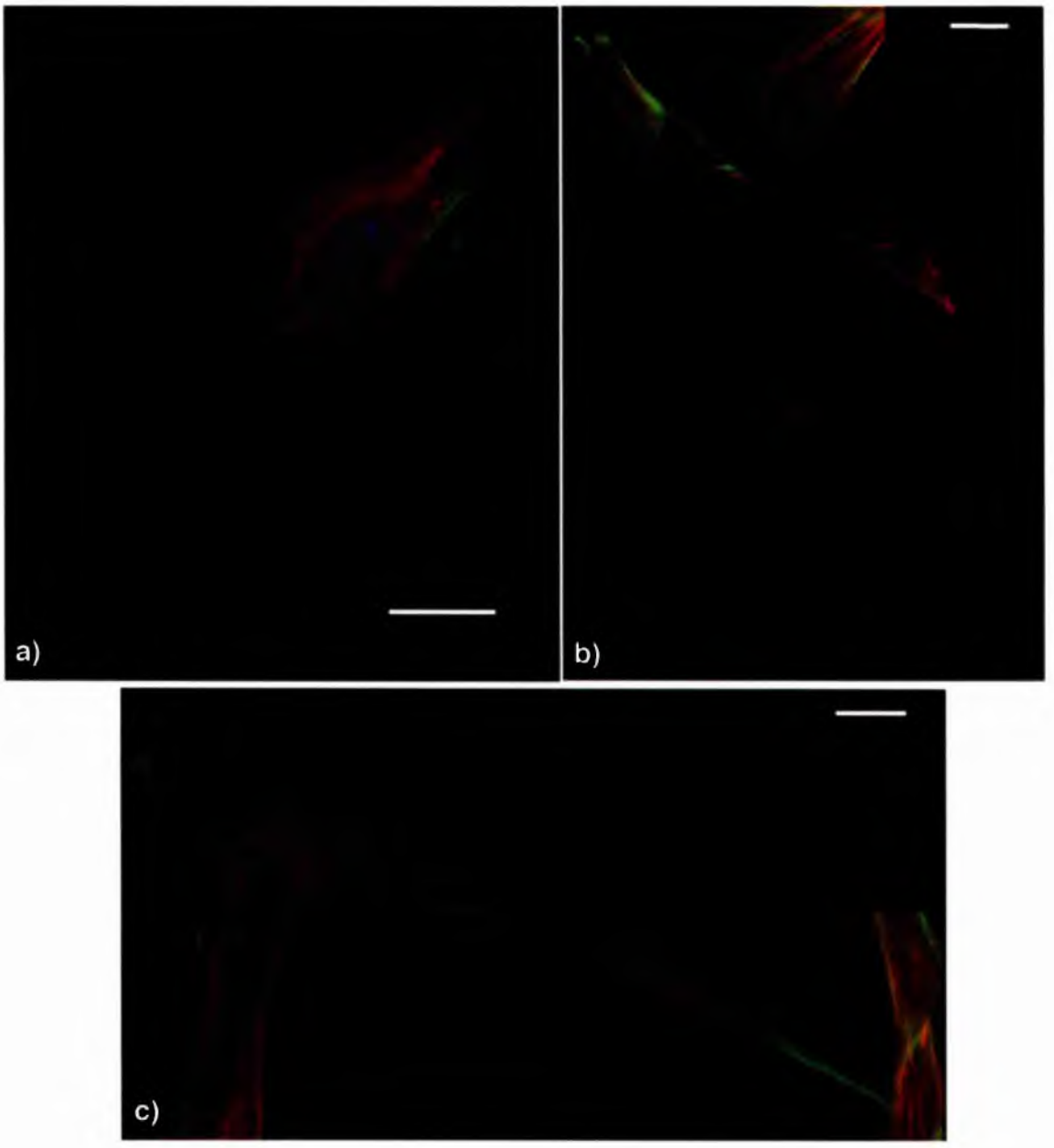

Figure 4.24: hTERT fibroblasts on 20nm-diameter, 200nm high pillars in SiO_2 at 24 hours. Actin (red), tubulin (green) and nuclei (blue) were imaged using a Vickers microscope in fluorescent mode with a 50X oil immersion objective. Cell-cell aggregates appear across the nanopillared substrate, c). In this instance, two cells appear to bridge two parallel cell aggregates. The presence of defined actin stress fibres suggests strong cell-substrate adhesions occurring at 24 hours. Cell overlaps are also noted between two neighbouring cells, a). Thin, elongated protrusions containing microfilaments and microtubules appear to bridge gaps occurring between cell, b), and are suggestive of previous elongation by cells occurring across the 20nm-diameter, 200nm high pillared substrate. This is further supported by the stretched shape of a fibroblast exhibiting two such features, b). Furthermore, these features may originate from cell-cell separation, where breakage of intercellular bridges are not complete, b). (Scale bars: 20μm).

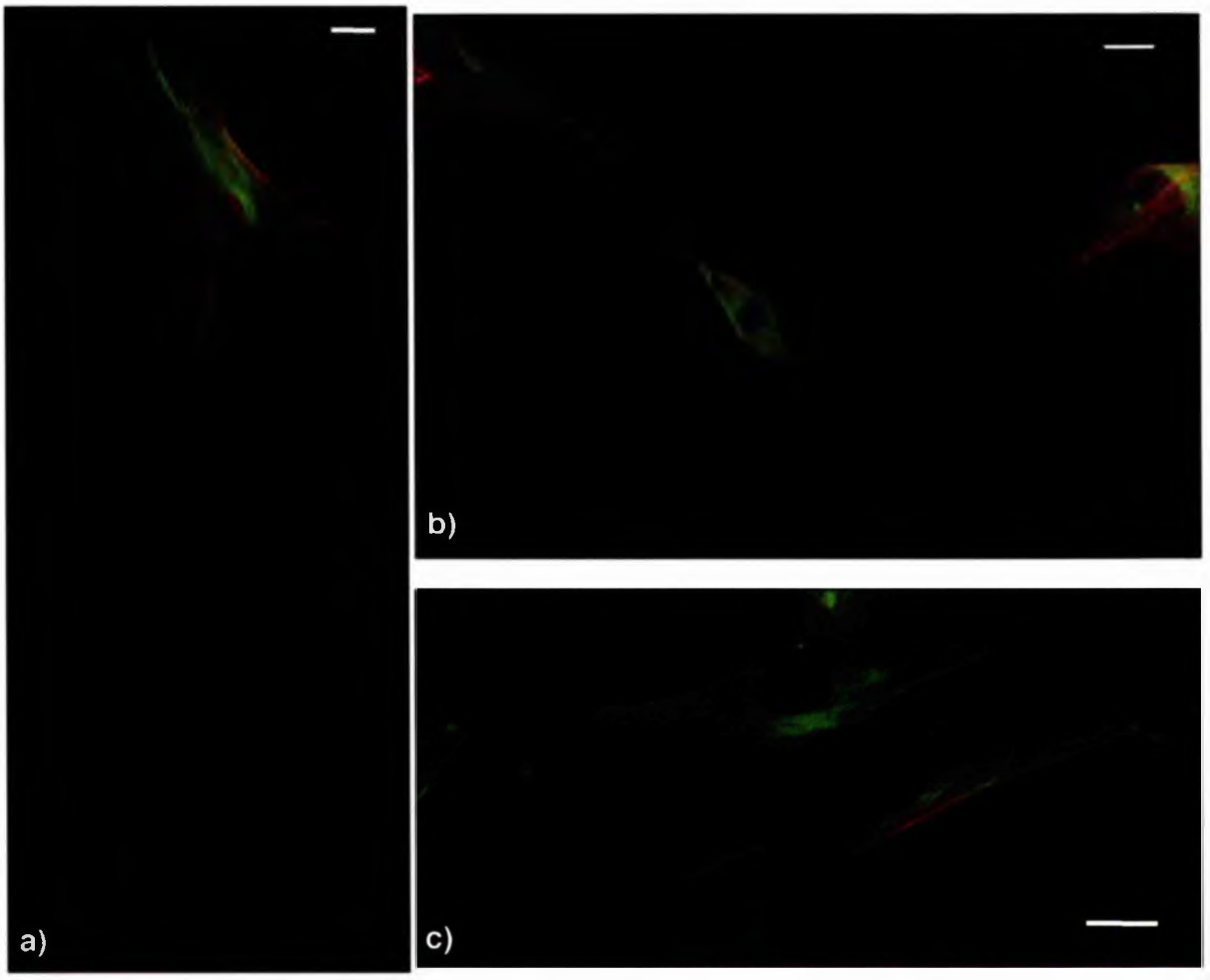

Figure 4.25: hTERT fibroblasts on 50nm-diameter, 200nm high pillars etched in silica at 24 hours. A Vickers microscope was used with 50X oil immersion objective to visualise actin (red), tubulin (green) and nuclei (blue). Elongated detachment sites, with globular actin- and tubulin-containing regions, a), are observed. Lack of rear detachment would appear to occur as a result of cell-substrate focal adhesions due to the positioning of the area across the 50nm-diameter, 200nm high pillared substrate, a). In one instance, b), two cells exhibiting elongated detachment sites share a connection of this feature. This suggests the possibility that rear detachment may initially be influenced by cell-cell contacts, or possibly, this area of the substrate is highly adhesive. Furthermore, cells lacking this elongated protrusion, c), do exhibit a large island containing microtubules encapsulated within an actin perimeter. This feature may act as a precursor to the more elongated structures observed in the other fibroblasts on the 50nm-diameter, 200nm high pillared topography at 24 hours. The presence of actin stress fibres throughout all the cells, occurring across the length of the cell, in a similar direction to the detachment sites, suggests an increase in stress or tension across this axis. (Scale bars: 20μm).

the two cell, and problems associated with severing the connection. A fine, globular connection, composed mainly of tubulin, is reminiscent of rear detachments observed in time-lapse video of HGTFN endothelial cells on nanopillars, Section 4.3.2. The presence of actin stress fibres indicates the presence of developed focal contacts, and suggests that the thin protrusions, although primarily established between cells, may contact the nanopillared topography, resulting in strong cell-substrate adhesions, accounting for the non-detached rear site.

hTERT fibroblasts seeded on the 50nm-diameter, 200nm high pillared topography exhibit elongated, globular detachment sites at 24 hours, Figure 4.25a) and b) previously discussed in relation to the 20nm-diameter, 200nm high pillared topography, Figure 4.24a) and b). These elongated detachment sites measure upwards of 2mm in some instances, Figure 4.25a). The globular patterning of the detachment site, containing localised tubulin, microfilaments and microtubules appear to occur due to direct cell-substrate adhesive interactions. The presence of stress fibres in cells displaying these elongations suggests that the detachment site may act to create a tension axis, Figure 4.25a). In some instances, Figure 4.25b), very fine detachment sites originating from two individual cells share a connection. This may occur due to a highly adhesive area of nanopillared substrate present at the adjoining connection site, or could possibly occur due to cell-cell contacts becoming entangled at this point. As one of the cells is elongated along the axis established by the most proximal area of detachment site (left in image), and stress fibres occurring in the neighbouring cells, again along the stress axis in-line with the proximal detachment site (right in image), Figure 4.25b), elongated rear detachments appear to effect cell directional alignment.

In summary, hTERT fibroblasts seeded on nanopillared topographies at 8 and 24 hours display certain distinct morphological features not observed in populations seeded on the control, planar-etched substrates. The most distinct alterations are the presence of highly elongated detachment sites, specifically containing globular regions of actin and tubulin, and the presence of developed actin stress fibres. Elongated detachment sites appear most frequently on the 200nm high pillared topographies, regardless of pillar diameter, Figures 4.18a), 4.19a), 4.24b), 4.25a) and b). Although possibly originating from cell-cell contacts, Figure 4.25b), the presence of long, fine detachment sites appear to occur due to reduced detachment functions, possibly as a result of altered cell-substrate adhesions in relation to the 200nm high pillared topographies.

Cell-cell adhesions occur throughout all the experimental samples, resulting in alignment of fibroblasts relative to one another, and may occur due to a lack of distinctive alignment patterns in relation to the topography, seen on grooves for example. Fibroblasts seeded on 20nm diameter pillared topography with both 80nm and 200nm height, form cell aggregates which appear highly polarised with respect to internal and external environments. These aggregates, although containing approximately 7 nuclei in each instance, Figures 4.15b) and 4.18b), display morphology more readily associated with a single, spread cell, and there is a distinct lack of differentiation between each individual cells cytoplasm and cytoskeleton. As the number of cells composing each group is approximately seven, this morphology may result due to the number of fibroblasts contained within the aggregates.

4.5 Summary

Nanopillared patterns can be fabricated in SiO_2 with a base substrate of either silicon or fused silica utilising a colloidal mask and reactive ion etching, Section 4.2. Pillar width is determined by the dimensions of the colloids used as a mask, and pillar height is determined by etch time. Colloids can be removed from the etched nanopillared topography, Section 4.2, resulting in an even surface chemistry across the device surface. Consistent chemistry across substrates, with nanotopography and planar surfaces, allows for behavioural alterations observed in cells to be more accurately attributed to specific experimental topography and conditions. Caro's Acid was found to have an etching effect on micrometric surface defects, Figure 4.2, rendering this acid wash unsuitable for use with nanopatterned structures due to the damage caused to patterns distracting from the structure believed to be in place.

Scanning electron microscopy (SEM) and atomic force microscopy (AFM) was successfully used to image nanopillared structures, Sections 4.2.1.1 and 4.2.1.2, respectively. SEM and AFM images indicate that nanopillared features are similarly distributed in relation to the original colloidal etch mask, Section 3.2.1. SEM highlighted the planar tops of pillars resulting during dry etching of the colloidal mask, Figure 4.3c), and also the occurrence of lateral etching immediately below the pillar apex, Figure 4.3b). Furthermore, pillars with larger diameter were seen to occur in EM images (termed "nanomountains"), Figure 4.3b), suggesting that colloids in contact with each other within the mask were not etched as individual pillars. Nanopillars of various

heights were also observed using SEM, as a direct result of altering the time samples were subjected to the etching process, Figure 4.3. Accurate heights, Figure 4.4, and spatial distribution, Figure 4.4 and 4.5, of nanopillars were once again observed to be in accordance with the original colloidal patterning of the etch mask using AFM, Section 3.2.1. However, nanopillars appeared to have a peak in the AFM images, rather than a flat top, as indicated in the EM images. This alteration can be accounted for by the known interactions between the AFM cantilever and substrate, especially as samples were imaged using contact mode.

Interference reflection microscopy (IRM) was also employed as a means of nanopattern imaging, Section 4.2.1.3. The increased dimensions of pillar bases in contrast to the original dimensions of the masking colloids resulted in an increased lateral dimension of features. These lateral dimensions were within the boundaries required for IRM imaging, resulting in the scattering of light in relation to the nanopillared topography, Figure 4.6 and Figure4.6IRM on the accompanying CD. However, individual nanopillars cannot be distinguished using this method, which serves only to suggest spatial patterning of the substrate with a nanotexture, rather than individual nano-features.

Rat epitenon cells are observed to adhere and spread on 20nm-diameter, 200nm high pillared topography at 1 hour, Figure 4.7. Lamellipodia and filopodia extend away from the cell, and interact with the surrounding nanopillars. Areas encapsulated by nanopillars are often seen to contain protein debris, Figure 4.7b) and c).

Behavioural alterations exhibited by HGTFN endothelial cells seeded on 50nm-diameter, 200nm high pillars was indicated during time-lapse video microscopy over a period of 36 hours. Endothelial cells on the nanopillared topography appear to undergo four main stages, completing one cycle of the observed behaviour. Firstly, cells develop a leading edge at the proximal region, resulting in elongation. Subsequently, endothelial cells undergo further stretching, which results, with time, in rounding of the main cell bulk and the development of a highly elongated and thin detachment site, Figure 4.10. It is hypothesised that this behaviour may occur as a result of altered phosphatase and/or protease activity, specifically calpain, due to the involvement of this molecule in actin remodelling, FAC stability and its role as a signalling intermediate. Altered intracellular calcium has been proposed as the main factor acting to alter phosphatase and/or

protease activity. Due to the stretching of cells observed on the nanopillared substrate, and also the relationship between calcium and calpain and similar bio-molecules, stretch-activated calcium channels are proposed as the underlying mechanism of this behaviour, Figure 4.10.

As elongated distal detachment sites emerge during this observed behaviour, focal adhesion distribution throughout cells required to be addressed. Nanopillar tops have a flat, planar top, Figure 4.3, thus cells are believed to initially interact with the uppermost planar region in the z-plane, namely the pillar tops. The stress occurring across endothelial cells on the nanopillared topography during elongation suggests highly adhesive cell-substrate interactions occur, Figure 4.8. This may be explained by integrin clustering, occurring around the immediate area underlying the nanopillar tops. Furthermore, integrin clustering, specifically $\alpha L\beta 2$, has been related to increases in intracellular calcium levels (Horton, 1996). Physical detachment of integrins binding to the nanotopography in this manner, Figure 4.9b), would require cytoskeletal tension occurring in a number of direction due to the 360° radius of the pillar tops. However, this does not appear to happen, resulting in the establishment of thin, elongated rear detachment sites. Intracellular molecular events could also act to sever localised FACs, yet, the only possible reaction to this type of event is observed in the very slow reeling of detachment sites, suggesting limited success of molecular focal adhesion disassembly. It is possible that protein conformation, with respect to proteins present within integrin-cytoskeleton connections, Figure 4.9, may be altered, resulting in the limited success of integrin-cytoskeleton disassembly of FACs. This hypothesis is further supported by the reduced tension observed at the proximal area of endothelial cells at later times, where the cell has rounded, and the distal detachment site is slowly reduced in breadth and length, Figure 4.8c)-n).

Fibroblast adhesion assays were conducted to establish the adhesive effects of 20nm-diameter, 200nm high pillared topography in comparison to planar controls. hTERT fibroblasts were seeded on a planar control, 200nm-etched planar control and 20nm-diameter, 200nm high pillared topography and counted over thirty $0.93mm^2$ areas of the substrates at 20 minutes, 1 hour and 3 hours. The data collected in this manner was then used to calculate sample variance, allowing for the correct test statistic to be selected. As previously discussed in Section 4.4.1, sample variance was not homogenous for the number of fibroblasts adhering to the substrates at these time points, even when the data

was normalised. Thus a non-parametric statistical test comparing sample medians was selected, as data is not required to be normally distributed or have homogenous variance.

A residual plot was made using sample medians, Graph 4.1, and indicated possible interactions between cells adhering to the planar etched and nanopillared substrates between 1 and 3 hours, and also between the planar control and these two substrates at all time points. Interactions suggested in a residual plot indicate the requirement to employ a statistical test to further our understanding of these relationships. However, no non-parametric test exists to analyse the effects of 2 independent variables, in this instance time and topography, on a dependent variable, for instance fibroblast adhesion. The Kruskal-Wallis test does allow multiple comparisons to be made between an independent and a dependent variable. To allow comparisons of 2 independent variables and limit the risk of committing a type 1 error (where the Null hypothesis is rejected when it is true), a level of acceptance can be set where $p=0.01$. Utilising this technique, the effects of time and nanopillared topography on fibroblast adhesion was investigated, Tables 4.1 and 4.2, for level of significance $p=0.01$. When comparing cell adhesion on all 3 substrates (planar, planar etched and nanopillared) at 20 minutes, a highly significant difference was calculated, where $K=54.03$ which is greater that the calculated chi-squared value, Table 4.1. Similarly, significant difference were calculated between the number of cells adhering to the three different substrates at 1 hour, where $K=53.23$, and at 3 hours, where $K=34.88$, Table 4.1. These results indicate fibroblast adhesion is dependent upon substrate topography. However, fibroblast adhesion was found to be independent of time, Table 4.2.

Fluorescent staining and imaging of hTERT fibroblasts, where actin and tubulin distribution within cells was observed, suggests a number of behavioural traits emerging as fibroblasts interact with the nanopillared topography. At 20 minutes, microtubule networks are highly developed in fibroblasts on the 20nm-diameter, 200nm high pillars, extending and terminating in spiky peripheral protrusions, Figure 4.11c). Cells are well spread in comparison to their smoother, rounded control counterparts on planar and 200nm-etched planar substrates. This observation is extremely interesting when considering Wojciak-Stodhard et al observed microtubule alignment to grooves as early as 30 minutes (Wojciak-Stodhard et al, 1995) and Oakley and Brunnette noted microtubules were the first intracellular element to align to grooves, followed by actin

(Oakley and Brunnette, 1993). Microtubule observations in fibroblasts on the nanopillared topography suggest quicker response in comparison to grooved microtopography. Furthermore, as microtubules are the first elements to respond to microtopography, the implications of the microtubule networks on nanopillars suggests similar mechanisms are involved during cell sensing and response to both nano- and micro-topography.

Similar observations are made at 1 hour, Figure 4.12c), although fibroblasts appear more spread on the nanopillars. However, by 3 hours, cell shape and morphology drastically differs from those on control surfaces in that they do not resemble typical fibroblast morphology, for example rounded, well-spread or triangular shape. Furthermore, peripheral spikes are observed, containing microfilaments, and actin stress fibres occur throughout the cell as do well defined microtubule networks. Cytoskeletal arrangements at 3 hours in fibroblasts on the nanopillars indicate cell-substrate adhesive interaction and great stress occurring across cells.

At later times, 8 and 24 hours, hTERT fibroblasts display distinct morphologies in relation to cells on the planar etched substrates. Extremely elongated detachment sites, where cell length can often measure up to 1mm, composed of globular actin and tubulin regions in trails at the distal sites of cells are present. Highly defined actin stress fibres are also observed. Elongated rear detachments are observed on 200nm high pillars regardless of pillar diameter. These features suggest increased cell-substrate adhesions, resulting in inhibition of FAC detachment function, also observed in the time-lapse video images of endothelial cells on 50nm-diameter, 200nm high pillared topography. Cell-cell adhesions occur across the nanopillared substrates also. However, fibroblasts in contact with 20nm diameter pillars, regardless of the 80nm or 200nm height, form cellular aggregates that appear highly polarised with respect to internal and external environments. The aggregates observed contain approximately 7 nuclei in each instance and more readily reflect tissue morphology, where individual cells share boundaries with neighbours resulting in closure of denuded substrate areas and well spread morphology, in comparison to individual cell morphologies.

In conclusion, diameter and height of pillars appear important when considering cell reaction to nanopillared topography, eliciting alternate cell responses when comparing fibroblasts from the same population.

The Application of Colloidal Nanofabrication to the Study of Biological Systems

VOLUME II

Mairead Anne Wood

For the Degree of PhD

Centre for Cell Engineering,
Division of Infection and Immunity,
University of Glasgow

September 2003

Chapter 5: Planar-nanopillared Topography and Fibroblast Behaviour

5.1 Introduction

When considering cell reactions in relation to an experimental surface, a control, planar surface is generally used as a comparison. It is therefore preferable to have both the experimental and control surface on the same substrate allowing for comparable culture conditions, for example temperature, pH concentrations, and nutrients available to cells on both surfaces. Cell preference for either surface can also be investigated on such a substrate, and cell reactions to nanotopography and the control surface can be viewed concurrently. Populations of cells can also be examined for their interactions along the nanopillared-planar boundary.

Attempts to create a structure where both the experimental nanotopography and planar control surface lie concurrently on the same substrate were made using a variety of methods; namely micro-contact printing and also a combination of photolithography and colloidal lithography techniques. The success of each method is discussed in this chapter. hTERT fibroblast reactions were then monitored on both the control, planar and nanopillared grating topography on the final substrate. 3T3 fibroblasts were also investigated in relation to a planar-nanopillared grating structure. These cells were chosen as fibroblasts had previously been used in relation to grating patterned surfaces, and as some of the experiments were conducted at the AO Research Institute, Davos, availability of fibroblasts was limited to mouse 3T3 cells.

hTERT fibroblast reactions to the planar-nanopillared topography was investigated using time-lapse video microscopy, and immunohistochemistry was used to identify actin and tubulin polymerisation and configuration within the cells on the planar and nanopatterned gratings. Investigations of 3T3 mouse fibroblasts were conducted using an Hitachi S-4700 Field Emission Scanning Electron Microscope (FESEM) while in Davos, Switzerland. 3T3 fibroblasts were investigated for vinculin arrangement within focal adhesion complexes on the planar-nanopillared surfaces using a gold immunolabelling technique (Richards et al, 2001). However, due to

problems with the gold enhancement, and as time was limited, the samples prepared in this manner represent morphological and cytoskeletal information with respect to the nanotopography and planar surface.

5.2 Fabricating a Planar-nanopillared Topography

The structure required must consist of the nanopillars and planar regions accurately within their allotted domains on the surface of the base substrate, with the two surfaces lying collaterally on the same device. The final structure must be created in an optically transparent medium so that high-resolution transmission optical microscopy can be utilised, allowing for time-lapse video microscopy. This base-substrate must also be a material that can be dry etched easily so that nanopillared topography may be fabricated. Final structures were therefore created in silicon dioxide present on the quartz surface, with initial patterning investigations conducted on silica surfaces of both borosilicate glass coverslips and silicon.

Two main approaches were taken to pattern surfaces in this manner. One method was based on a modified version of conventional micro-contact printing, while the other utilised a combination of both conventional photolithography and colloidal lithography.

5.2.1 Micro-contact Printing to Create a Planar-nanopillared Surface

Micro-contact printing has been used for chemical and protein modification of surfaces with respect to cell investigations (Craighead et al , 2001, James et al, 1998, Kane et al, 1999, Yang, 1997). One specific experiment has demonstrated the ability to pattern hydrophobic and hydrophilic aminosilanes using this technique (Lercel, 1995). Due to the fast, reproducible, accurate and simple approach that micro-contact printing presents, this appeared as an ideal method for creating planar-nanopillared topographies on the same substrate.

5.2.1.1Making a Sylgard Stamp from a Master Die

Firstly a stamp had to made reflecting the anticipated pattern under development. The method of creating this stamp is outlined in Figure 5.1. A master die, a), with the inverse of the pattern under development was created in a quartz microscope slide

using photolithography. The pattern present on the master die was a 100μm repeated grating (courtesy of Mary Robertson and Bill Monaghan, Electronics and Electrical Engineering, University of Glasgow). The image in Figure 5.1a) shows a schematic representation of one of these gratings.

The mixture used to create the sylgard stamp was composed by firstly depositing 10mls of Silicone Elastomer in a plastic universal (as this container is later to be placed under vacuum), with 1ml Silicone Elastomer curing agent added. This blend must be thoroughly mixed, and was done so with the syringe used to transport the liquids to the universal. The universal (minus lid) containing the Silicone Elastomer blend was then placed under vacuum to draw all the air bubbles and gas from the mixture. If this step is excluded the final sylgard stamp would contain micro-bubbled patterns within it, preventing the true replication of the master die thus distracting from the desired pattern.

The master die was encased in a slide holder and heated on a hotplate at 70°C for approximately 30 minutes prior to the following addition of the mixture. This is required in the curing of the sylgard. The mixture, having all gas removed during vacuum, is collected slowly in a plastic syringe (minimising the introduction of further gas bubbles) and transferred to the master die contained within the slide holder on the hot plate, Figure 5.1b). Only 3mls of the mixture are required for this set up. Spacers (in the form of broken microscope slides) are placed at either end, away from the pattern, and a clean glass microscope slide is placed on top of these. This ensures the back of the stamp is flat and therefore easier to use, with pressure applied when micro-contact printing being distributed evenly. The sylgard mix, sandwiched between the master die and plain microscope slide, is left to dry by setting on the hotplate at 70°C for approximately 2 hours.

Once the stamp has set, the master die and microscope slide are prised apart, with the top slide remaining fixed to the Silicone Elastase stamp. A scalpel is used to trim the stamp, so that any areas originally in contact with the spacers, and therefore are not flat, do not interfere with the resulting print. The top and bottom of the stamp are also

trimmed for the same reason, as they have been in contact with the edges of the slide holder, and require to be removed.

Three rinses of the resulting stamp, alternating between n-Heptane and 100% Ethanol follows. This process rids the stamp of uncured polymer, where the n-Heptane causes the structure to swell while the Ethanol has a de-swelling effect. The Silicone Elastomer stamp, backed with the planar glass microscope slide is put into a Coplin jar. Using a funnel, n-Heptane is transferred into a bottle, and then poured into the Coplin jar. The lid is put onto the jar and the stamp and solution are left for 1 minute. The n-Heptane is then poured back into its former bottle (to be re-used), and 100% Ethanol in applied to the stamp in the same manner, with the lid being replaced, and the stamp is immersed in Ethanol for 1 minute. The Ethanol is then discarded and the process is repeated twice more. The sylgard stamp can be stored in the Coplin jar in 100% Ethanol for as long as required.

Prior to printing, both the sylgard stamp and the base substrate being printed must be completely dried so as to optimise the effect of the aminosilane being printed. Base substrates of borosilicate glass coverslips ($25mm^2$) and glass microscope slides were cleaned using a Caro's Acid wash (1 part >30% (100 volume) Hydrogen Peroxide: 3 parts concentrated (96%) Sulphuric Acid) as previously described, Section 3.2. Glass substrates were immersed in the acid, as previously detailed, for 20 minutes, following which they were reacted with 0.5M Sodium hydroxide for 20 minutes. The glass was then rinsed in Reverse Osmosis (RO) water under sonication to ensure cleanliness of the surfaces and removal of excess chemicals. Structures were then dried, firstly with a nitrogen gun and then at approximately 70°C for 1 to 2 hours in an oven. Surfaces must be free from any residual water so that the hydroxyl layer may be presented to the aminosilane allowing it to bond correctly (Sato, 1997).

When micro-contact printing, the stamp is usually printed into the "ink", or chemical, and then printed onto the substrate in question. However, due to the polymeric and adhesive properties of the aminosilane being used in this instance, it was felt that the silane would adhere across the entire structure and not be limited to the areas selected for printing. Thus, a different approach was taken which, instead of reflecting the inverse of the master die, actually reproduces the exact pattern of the master, Figure 5.1.

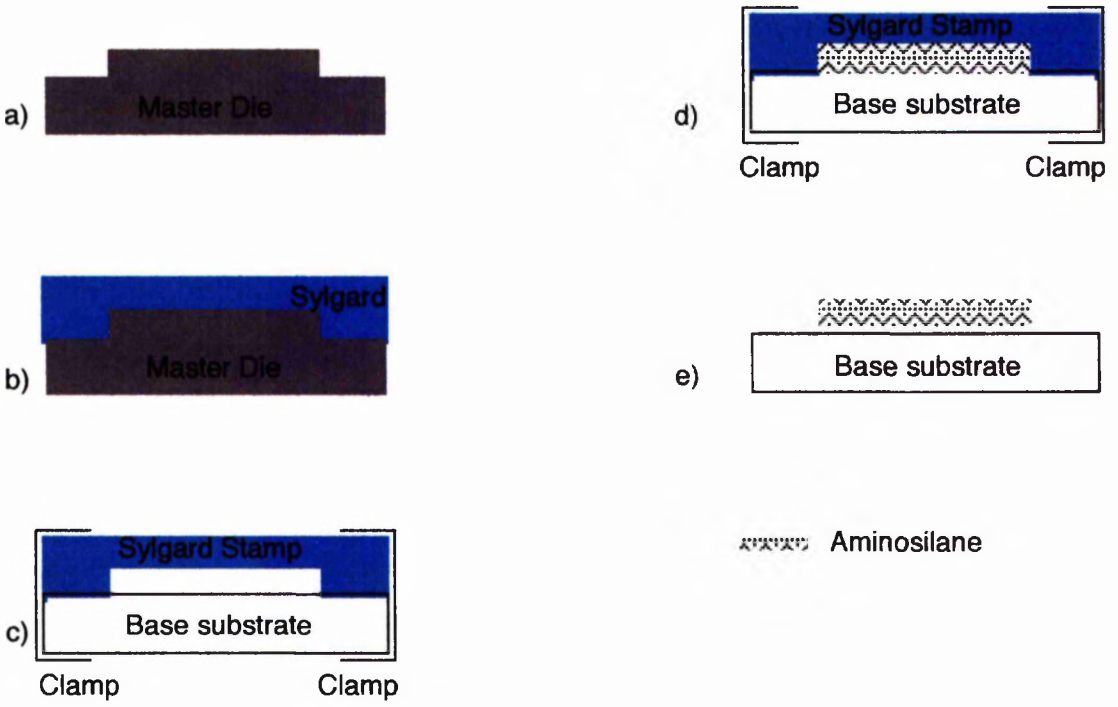

Figure 5.1: Modified approach to Micro-contact printing an aminosilane. A master die, a), is firstly fabricated in a quartz base substrate (SiO_2 surface) using conventional photolithography. Prepared sylgard is then added to the die, b). Following curing of sylgard, the stamp is removed from the master die and placed in contact with a clean base substrate prior to being clamped together, c). This results in protection of the base substrate in contact with stamp from the aminosilane, d). The aminosilane is added to the base substrate through the gap in the stamp, treated as described, and removed. This results in the patterning of the aminosilane structure, e).

Having dried the ethanol from the stamp with a nitrogen gun, and the base substrates (having undergone the Caro's Acid clean and Sodium hydroxide treatment) with nitrogen, followed by oven drying, the stamp and substrate were clamped together, Figure 5.1c). The clamped stamp and substrate were then dried once more in the oven at 70°C for 1 hour to ensure all surfaces were thoroughly dried.

An active aminosilane was made (as outlined in Section 3.2), consisting of 200µl of 0.1% APTS dissolved in 9.8mls of Acetic Ethanol (1ml glacial Acetic Acid per 100mls of ethanol, pH 5). Upon removal of the clamped structures from the oven, the aminosilane was added to the areas of the substrate not in contact with the sylgard stamp, Figure 5.1d). This was applied using a syringe with a 2µm dosing filter attached (to ensure purity of the silane) and syringe needle (to allow for directed addition of the aminosilane to areas of the substrate free from contact with the stamp). The aminosilane was left to react with the substrate for 20 minutes.

Following this time, the aminosilane was extracted (again using a syringe and needle) from the areas it had been in contact with the glass substrate. 100% Ethanol was added to the areas which had contacted the APTS, and removed in the same manner of extraction using a syringe and needle. This process was repeated 3 times, following which, a further 3 rinses of 100% Ethanol were applied. These subsequent rinses, however, did not undergo extraction with a syringe and needle as previously explained but were blow-dried using filtered air. This step of ethanol rinsing and blow-drying was included to ensure ethanol rinsing of the silanised surface was not limited to the edges of the pattern closest to the external environment, but also the silanised areas in the middle of the gratings.

RO water was used to rinse the ethanol from the surface, and was added using the syringe and needle, following which, it was removed using filtered air. This was repeated 3 times, to ensure residual material either from the ethanol or the silane was removed.

The clamped structures were oven dried at 70°C for 1 hour to ensure that, upon removal of the stamp from the substrate, the aminosilane would be positioned in the desired pattern, with no movement into areas previously masked by the stamp. The stamp and substrate were then unclamped and removed from one another, Figure 5.1e).

5.2.1.2 Patterning of 1μm Polystyrene Dyna Beads using Micro-contact Printing

1μm polystyrene Dyna beads (Sigma, UK) were initially used to test the effectiveness of the modified method of micro-contact printing outlined in Section 5.2.1. The 1μm-diameter beads could be examined using light microscopy, in this instance an Astrocam, with the requirement for high resolution imagining being kept within light microscopy capabilities.

Following the printing of the silane, 1μm fluorescent Dyna beads were added to the modified surface for approximately 2 hours. As the Dyna beads were suspended in an aqueous solution, enough of the solution was added to cover the primed surface. The structure was then immersed in water in an attempt to remove beads on the non-silanised areas, with the resultant structure reflecting the planar-nanopatterned substrate being developed.

When the final structure with attached Dyna beads was viewed using the Astrocam, the accuracy of the colloidal patterning was relatively successful, although not as specific as was being sought, Figure 5.2. The area highlighted by the super-imposed parallel lines would have been in contact with the stamp as outlined in the modified micro-contact printing technique, Figure 5.1. The surface of the base substrate in contact with the sylgard stamp should result in planar, bead-free areas in the final structure. As can be seen, Figures 5.2a) and b), this method appears to have been quite successful, with little or no Dyna beads present on the protected areas. However, when investigating cell response to a planar-beaded or nanopillared surface as in this instant, the accuracy must be ultimate so as to limit the possibility of cells on a planar area having some contact with nanometric surface features. Figure 5.2b) also indicates the possibility of aggregates of beads occurring at the planar-patterned interface when using this method.

5.2.1.3 Patterning 50nm-diameter Colloidal Gold Particles using Micro-contact Printing

The success of the modified micro-contact printing method when considering the 1μm Polystyrene Dyna bead distribution is not reflected in the captured images when

using 50nm-diameter colloidal gold particles. When investigating the images of the Dyna beads adhered to the patterned aminosilane, the method had appeared promising. However, when the experiment was repeated using 50nm-diameter colloidal gold particles, Figure 5.3, the patterning appeared unsuccessful with colloids present in both the specifically silanised and untreated regions of the substrate, Figure 5.3a). Colloidal gold aggregates were also observed to occur across the surface, Figure 5.3b).

When considering the relative success using Dyna beads, and the unsuccessful results when utilising the gold colloids, there are two possible reasons for the alterations seen in the patterning. Firstly, the Dyna beads have a diameter of 1μm, whereas the gold colloids used measure 50nm in diameter, so alterations could be attributed to the dimensions of the beads used. Secondly, and most likely, the Dyna beads are made from Polystyrene while the 50nm-diameter colloids are composed of gold. The high affinity the amino groups present on the silica surface following silanisation for gold results in colloidal immobilisation (Sato et al, 1997). The modified micro-contact printing method, Figure 5.1, requires the aminosilane to enter a tunnel between the sylgard stamp and base substrate. This may result in uneven patterning of the silane, and, as a polymer, may result in altered branching and configuration of the aminosilane, which will have a knock-on effect on the binding of the gold colloids. Due to the affinity of the amino groups in relation to the gold colloids being applied, the colloidal particles will have no alternative but to bind to the amino groups in their presented state on the base substrate. This modified approach to micro-contact printing is therefore unsuccessful as a means to pattering a planar-colloidal or planar-nanopatterned topography when utilising gold colloidal particles due to the occurrence of colloidal aggregates within the aminosilanised areas.

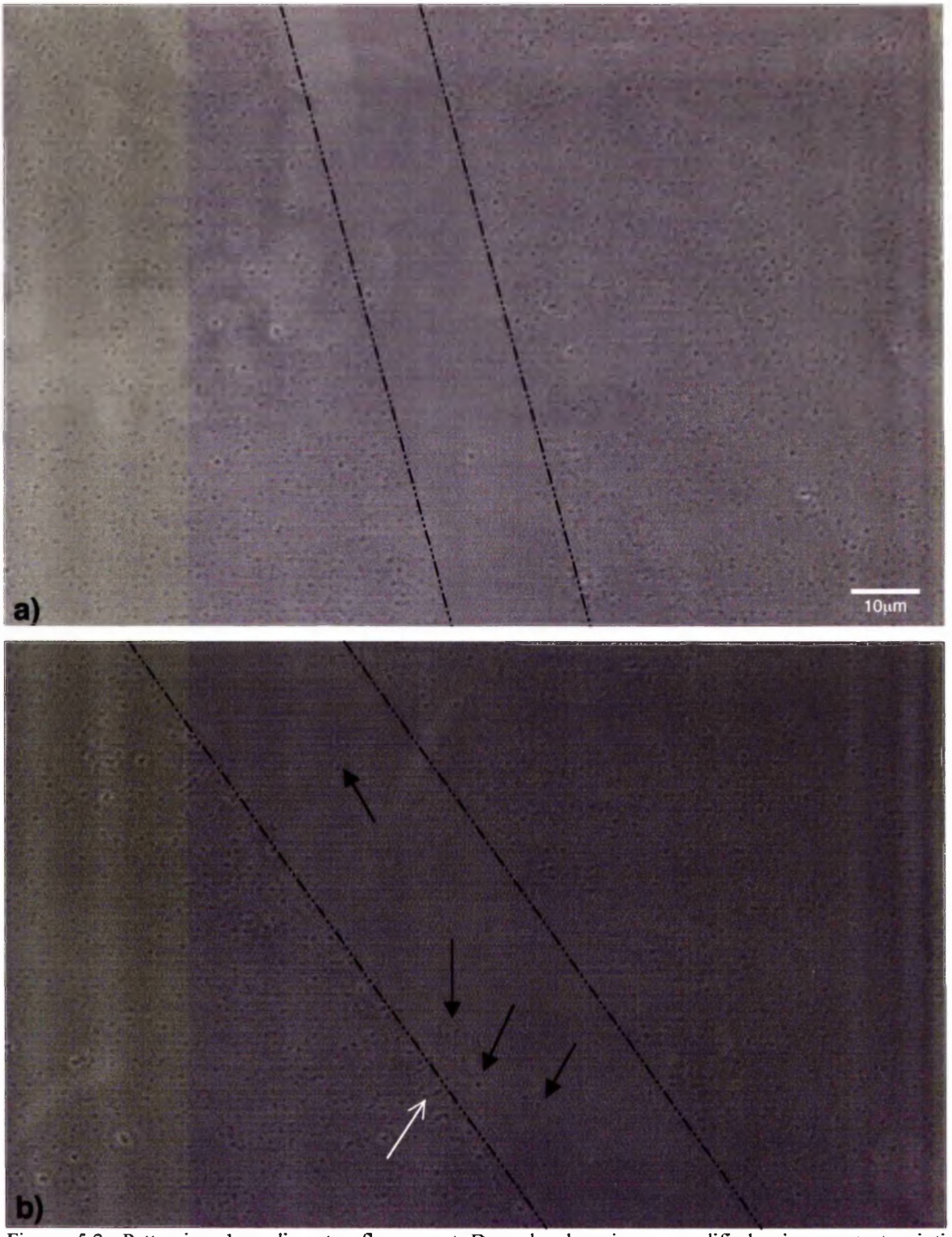

Figure 5.2: Patterning 1μm-diameter fluorescent Dyna beads using a modified micro-contact printing technique. The original grating pattern used consisted of 100μm repeats, patterned with the beads, inter-spaced with 20μm planar regions. Images were captured using an Astrocam with 40X objective lens. Superimposed lines in the image highlight boundaries of the grating. This modified approach to micro-contact printing appears relatively successful, however, some Dyna beads are located on the predicted planar region, closed black arrows in b), with aggregates occurring at the planar-patterned interface, white open arrow, b).

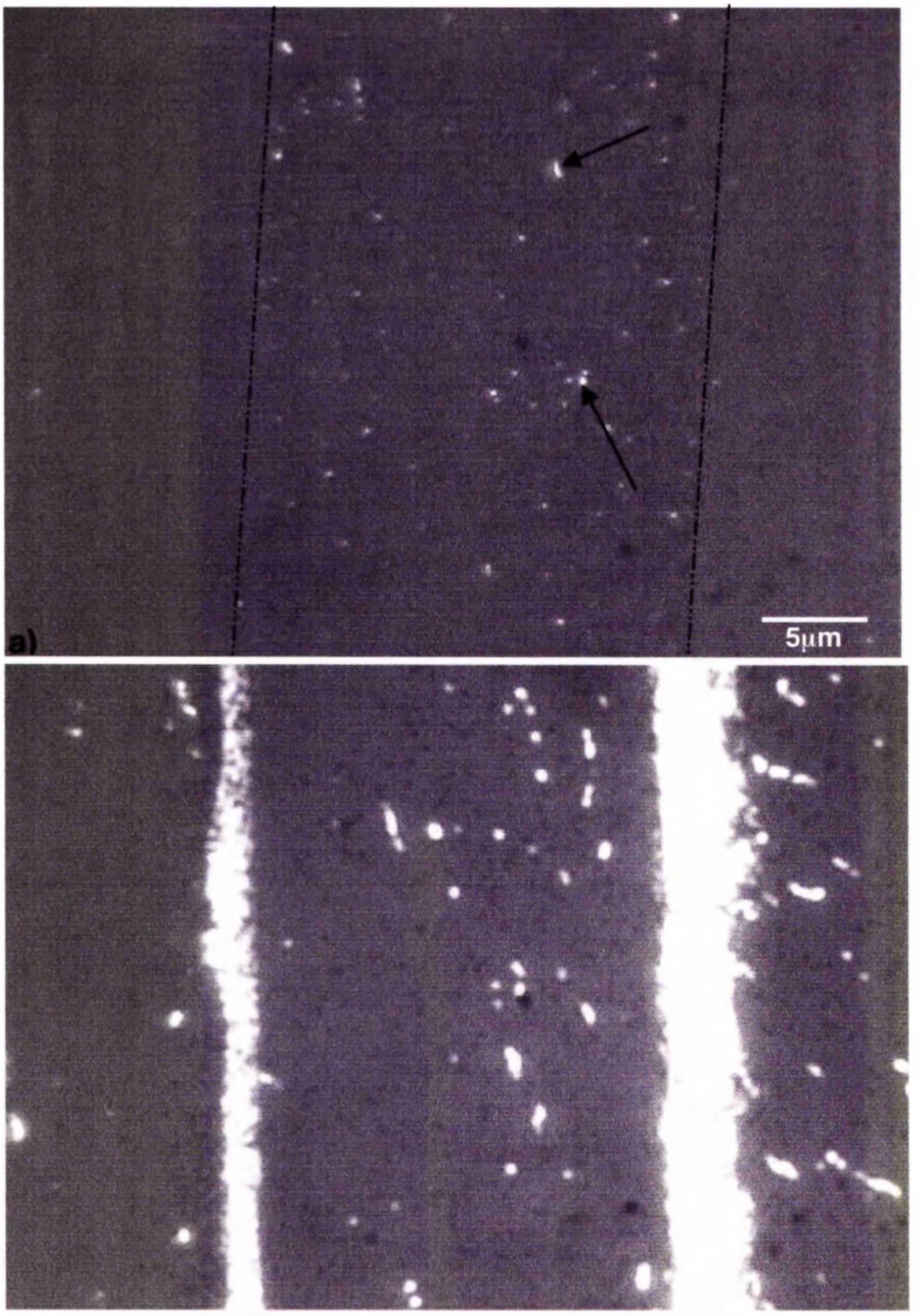

Figure 5.3: 50nm-diameter colloidal gold on the micro-patterned aminosilane. Images were captured using an Asrocam with 40X objective. Aggregates of gold colloids can be seen on the aminosilanised areas, indicated by arrows in a), where the speckling on the planar regions suggests the adhesion of colloids to this area also. Greater aggregations of colloids were also found to occur, b), suggesting problems associated with this method, rendering the technique ineffective with respect to colloidal gold patterning.

5.2.2 Photolithography and Colloidal Lithography to Create Planar-nanopillared Surfaces

Three approaches were taken to pattern a substrate with planar and nanopillared features running collaterally across the surface using conventional photolithography and colloidal lithography. All base substrates were either quartz or silicon (with SiO_2 surface) as all end products depend on being successfully dry etched using either the RIE 80 or the BP80 plasma etch machines. Sylgard™ was used as a paint to differentiate between areas of a substrate to be patterned with the nanotopography, using colloidal lithography, and those to remain planar. This approach was unsuccessful due to the unreliable patterning of the Sylard™ due to its movement during curing and also due to the difficulty of removing the silicone from the base substrate. Rubylith™ was used as a quick guide to indicate the possible success of the method outlined below, where a photoresist was patterned using a Rubylith™ mask. The photoresist was subsequently developed and the substrate was then treated with an aminosilane, described in Section 3.2., followed by immersion in a colloidal sol. This method was also unsuccessful due to the aminosilane carrier fluid (Acetic ethanol) removing the remaining photoresist protecting the planar region of the surface pattern. A successful method was however developed using conventional photolithography and colloidal lithography, where, following development of the desired pattern in a resist, Poly-L-lysine was applied to the entire surface, acting as a binding agent between the colloids and the substrate surface where the resist had been removed. This method, although outlined in brief below, Section 5.2.2.3, is discussed in greater detail elsewhere (Wood et al, 2002[b]).

5.2.2.1 Sylgard Painting as a Means to Patterning Colloids

A base substrate of quartz was treated using a Caro's Acid wash, discussed in Section 3.2, following which the surface underwent hydroxylisation by 0.5M Sodium hydroxide immersion. Aminosilane was then added to the structures as previously described in the basic adhesion of colloids to a surface, Section 3.2. Sylgard was prepared as previously described in Section 5.2.1.1 for stamp preparation in micro-contact printing. Subsequently, a nylon paintbrush was dipped into the Sylgard, and the mixture was painted onto the base substrate in the desired pattern; in this instance,

a square, free of Sylgard, was left in the middle of the coverslip. The substrate with painted Sylgard was then left on a hotplate at 70°C for 2 hours to cure.

The resultant structure was immersed in a colloidal sol and, following viewing under a light microscope, colloids were observed to adhere only to the free surface unprotected by the Sylgard mask. Sylgard is believed to etch at a rate of 6:1 in comparison to quartz (personal communication with Dr Riehle), and therefore should not be removed following the etching process, as structures undergo etching for approximately 2 minutes, resulting in a 200nm relief profile and the Sylgard appears some microns thick. Prior to etching, attempts to remove the Sylgard from a quartz surface were made, as the final structure design must include a planar region of the base substrate and the nano-pattern. Sylgard structures were immersed in Opticlear and sonicated for approximately 30 minutes. This process appeared to reduce the amount of Sylgard present at the upper-most surface, but did not remove the silicone completely. As this method did not remove the Sylgard, and no previous record of methods of removal existed, another approach was attempted, and is described in Section 5.2.2.2. Although hand-painting resulted in inaccurate mask features, the Sylgard also appeared to move when painting, due to the viscosity of the mixture, and following drying of the structure, had appeared to swell. These alterations would distract from the initial pattern and therefore added to the inappropriateness of this technique.

5.2.2.2 Patterning Colloids using a Rubylith™ mask, 1818 Photoresist and an aminosilane

A second attempt was made to create a planar-nanopillared substrate where a Rubylith™ mask, 1818 positive resist and Ultra Violet light as seen in conventional photolithography was utilised. A base substrate of quartz (with SiO_2 surface) was firstly cleaned using a Piranha Bath (7 parts Sulphuric acid: 1 part Hydrogen Peroxide at 80°C). Structures were then removed from the acid and immersed under a continuous flow of RO water for a minimum of 2 minutes. A primer was spun onto the surface to ensure that the following resist process would result in an even thickness adhered across the surface. An 1818 positive resist (Chestec, UK, catalogue

number 3454211) was spun onto the primed surface at 4000rpm for 30 seconds. Substrates were then baked at 90°C for 30 minutes to harden the resist.

A mask created using Rubylith™, similar to red "sellotape" which acts to block UV light was patterned by cutting a square area from the centre of the paper with a scalpel. The Rubylith™ was then backed on a 1-inch^2 wafer of glass, and positioned under a UV light source. The quartz sample prepared with the 1818 photoactive resist was then placed directly under the mask created, allowing light to selectively pass through the areas where Rubylith™ had been removed, thereby contacting specific regions of the resist. Following the 12 second exposure to UV light, the resist was developed in Microposit Concentrated Developer (Chestec, UK, catalogue number 3073113) and RO water (1:1(v/v)) for approximately 75 seconds. The developer was then removed from the structure, which was placed under a continuous flow of RO water for 2 minutes. The structure was dried with a nitrogen gun, and the accuracy of the pattern examined under a light microscope. The pattern appeared to directly reflect the primary Rubylith™ mask pattern.

The quartz structure, now patterned with 1818 photoresist was taken through the series of steps to create an active aminosilane across the surface as previously utilised during colloidal adhesion to a base substrate, Section 3.2. However, upon applying the aminosilane which is suspended in Acetic ethanol, the remaining, masking resist was washed from the surface. This resulted in the loss of the pattern, and the technique was deemed ineffective.

5.2.2.3 Patterning Colloids using 1818 Photoresist and Poly-L-lysine

The third, and only successful method of creating a truly planar-nanopillared surface was developed using conventional photolithography and colloidal lithography, which altered from previous work through the use of Poly-L-lysine, rather than the aminosilane, as an adhesive agent for colloids. This method was based on the previous attempt to pattern the nanotopography, where the application of the aminosilane to the resist resulted in its removal, Section 5.2.2.2. By choosing an alternative adhesive agent that did not require suspension in alcohol, a process based on the same principles could be utilised without the unwanted removal of the

photoresist occurring. The method is discussed elsewhere (Wood et al, 2002[b]), and shall therefore only be briefly discussed within this section.

A grating pattern was chosen to create this surface, allowing for cell reactions to be investigated concurrently, and comparisons to be drawn on both the nanotopography and the planar surface, and also at the boundary of these areas. However, it should be noted that this method allows for any photolithography pattern for which a mask has been produced and which a mask aligner is capable of reproducing.

As previously discussed in Chapter 4, a light transmitting material is required for use with light microscopes, and therefore time-lapse video microscopy, allowing for cells to be monitored on the experimental topography over time. Once again (as previously used for the nanopillared structures), quartz (with SiO_2 surface) was chosen as not only did it fit this criterion, it is also known and was previously shown to etch well in CHF_3, Section 4.2. As in the previous chapter, quartz used underwent a reflux treatment, Section 4.2, to remove residual wax present due to the manufacturing of the material, followed by a Caro's acid wash, Section 3.2. As with surface treatments prior to colloidal immersion in all earlier samples, a 0.5M Sodium hydroxide immersion ensued, followed by aminosilinisation, Section 3.2, of the surface, Figure 5.4a). An 1818 positive resist (Chestec, UK, catalogue number: 3454211) was spun at 4000rpm for 30 seconds onto the quartz sample surface, and baked at 90°C for 30 minutes. An aminosilane was used as in previous experiments to act as a primer for the resist, so conventional primer used in conventional photolithography was not required.

A mask with the desired pattern was selected, in this instance a 50μm or 100μm grating mask. Grating size is discussed in relation to the experiments in which they are used. A mask aligner was used to align the mask with the prepared surface coated with the photoresist. The resist coating the surface was subjected to 12 seconds of Ultra Violet (UV) light through the mask, with clear areas in the mask allowing the UV to expose the resist in these regions only, Figure 5.4b). The resist was then developed in Microposit Concentrated Developer and RO water (1:1(v/v)) for

approximately 75 seconds. Areas which had been subjected to the UV light were removed from the surface, while areas of resist protected from the UV by the mask remained, Figure 5.4c). Samples were rinsed under a continuous flow of RO water for 2 minutes to ensure removal of the developed resist. Substrates were dried with a nitrogen gun, and the accuracy of the patterning was viewed using a light microscope in the clean room.

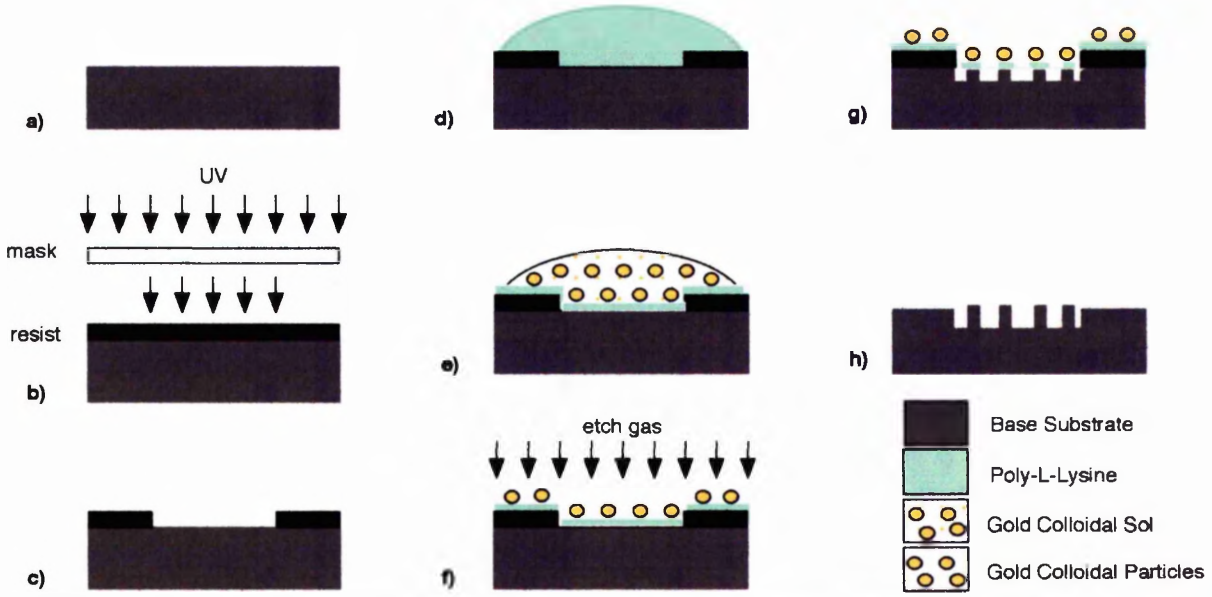

Figure 5.4: A diagrammatic overview of the planar-nanopillar patterning process: (a) the base substrate with AAPS-functionalised surface; (b) the 1818 resist spun onto the primed substrate and subjected to the UV light through the mask; (c) the developed resist; (d) poly-L-lysine is added to the structure for 1 hour; (e) poly-L-lysine is washed from the surface and the colloidal sol in question is applied (either 20nm or 50nm-diameter gold colloidal particles); (f) the mask comprising the resist and gold colloids are dry-etched to form pillars; (g) the etched structure prior to removal of the gold colloids and resist; (h) the final structure with patterned nanometric pillars and planar surface.

Poly-L-lysine solution (0.1% w/v aqueous solution, P8920, Sigma, UK) was applied to the patterned resist surface, Figure 5.4d), resulting in an adhesive surface where the resist had been removed, and also on the remaining resist. 100µl cm^{-2} was left to react for 1 hour with the prepared surface, following which RO water was pipetted directly onto the surface in question as a means of rinsing it. Having undergone this treatment, the structures were immersed in either the 20nm- or 50nm-diameter colloidal gold sol, and colloids were left to adhere to the poly-L-lysine primed surface for 24 hours, Figure 5.4e).

Following 24 hours immersion in the sol, structures were dried with a nitrogen gun perpendicularly to the surface in an attempt to limit capillary effects and movement of the colloids from their established position, which would result in altered colloidal distribution. Structures were held on a clean mat with forceps to allow direct perpendicular drying to be established. Images captured using the S-900 Scanning Electron Microscope indicated that problems in this drying process resulted in movement of both the colloids and the poly-L-lysine, with the final etched structure differing from the actual theoretical lithography design. Fabrication problems, particularly associated with drying techniques, are discussed later in this section.

The gold colloids and 1818 resist on the dried surface acted as a mask for reactive ion etching. An Oxford Plasma Technology BP80 dry etching machine was used for etching quartz samples (with SiO_2 surface) with CHF_3 with a flow rate of 20sccm, power 100W and chamber pressure of 16mTorr. Areas where the resist remained were protected from CHF_3, and thus remained as planar control regions, whereas areas coated with the colloids resulted in the formation of nanopillared regions following etching, reflecting the original mask design, Figure 5.4g).

The resist from the etched surface was removed by placing samples in a beaker of Acetone under sonication for 5 minutes. Subsequently, the Acetone was poured from the beaker which, still containing the structures, was then placed under a continual flow of RO water for 3 minutes. Samples were removed from the water, placed on a mat and dried using a nitrogen gun perpendicular to the substrate surface. The gold colloids were then removed using a gold etch so that the planar-nanopillared surface would reflect similar surface chemistry of the quartz (silica) base substrate. This should eliminate the possibility of cell reactions in relation to the structure being attributed to surface chemistry, resulting in behavioural alterations of cells being directly linked to surface topography.

Potassium iodide and iodine (32g potassium iodide, 200ml water, 8g iodine, Merck, UK) was used as the gold etch. Structures were constantly agitated in this mixture for approximately 20 seconds, prior to being immersed in RO water to remove the etchant and dried with a nitrogen gun. Patterning of the surface is now completed,

Figure 5.4h). Prior to the seeding of cells, substrates, as previously described for experimental structures, are immersed in Hepes solution for approximately 10 minutes.

The success of this method is observed in Figure 5.5. This method of planar-nanopillar patterning is believed to be reproducible when alterations deviating from the outlined drying technique do not occur. The existence of surface drying problems arising during fabrication processes has been referred to throughout this work and is mainly associated with nitrogen or air drying of the colloidal sol on the poly-L-lysine-coated substrate. It was during the development of this structure that the crucial nature of sol drying, where the water suspension is removed and colloids remain as nano-features on the SiO_2 surface, was realised. When characterising the planar-nanopillared surface using Scanning Electron Microscopy, the boundary between the planar and nano-featured areas were often indistinct, Figure 5.6. An avalanche or landslide morphology was observed at the planar-nanopillared boundary, Figure 5.6a) and b) replacing the vertical step that should have been reflected in the final pattern. These observations suggest an accumulation of poly-L-lysine occurring at the planar-nanopillared boundary due to the drying of the surface, may have acted as a resist resulting in this type of topographical patterning. As the success of the photolithography process was viewed using light microscopy and appeared extremely accurate, and, apart from the colloidal sol, the poly-L-lysine was the only other factor present on the surface, this further contributes to the proposed theory of polymer build-up in these regions. To further support this hypothesis, colloidal distribution appeared highly altered, with some areas of the surface lacking nano-pillars (as a result of absence of the initial colloidal lithography), while other regions indicated areas of densely packed colloidal arrangements resulting in the formation of nano-mountains, post-etch, Figure 5.7a) and b).

The formation of micrometric mountain ranges, a result of etching nanometric colloidal aggregations, suggests that etching densely packed colloidal arrangements,

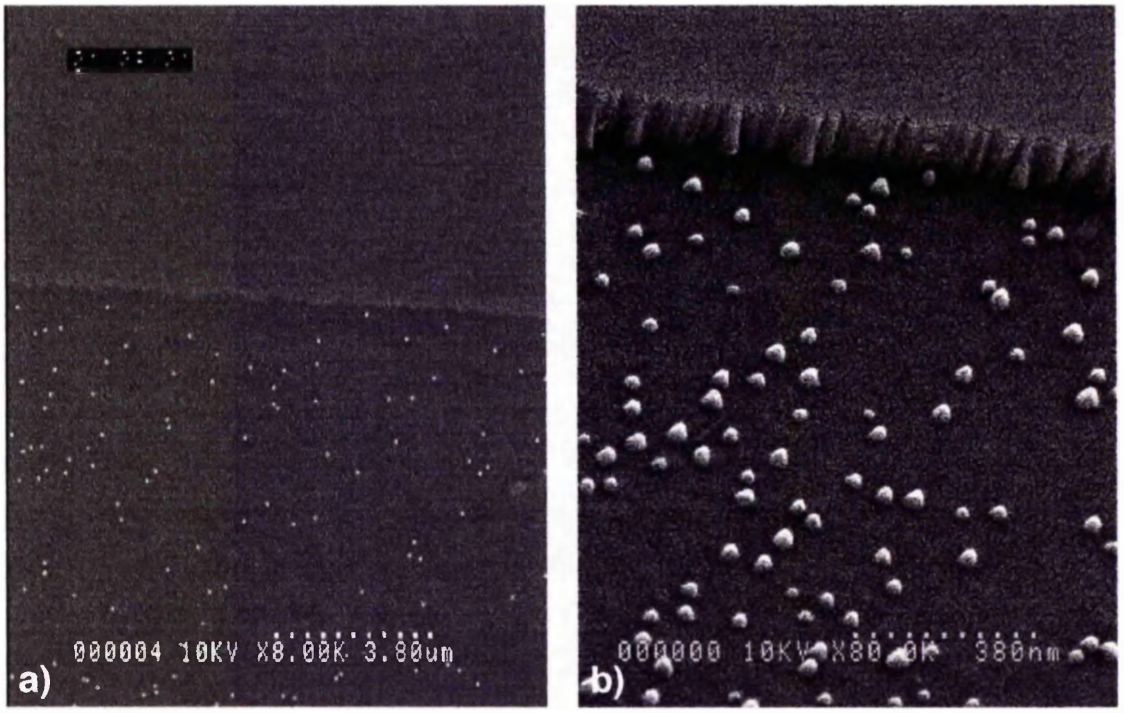

Figure 5.5: Scanning electron micrographs of planar-nanopillared topography established in quartz (SiO_2) captured using Hitachi S-900. 50nm-diameter pillars, a), viewed from above reflect the original colloidal lithography used as an etch mask. Pillar height is observed by tilting the sample, b), to 40° in the positive direction. These pillars were etched to 80nm in silca using 50nm-diameter colloids and 1818 photoresist as a mask to fabricate planar regions of the grating pattern.

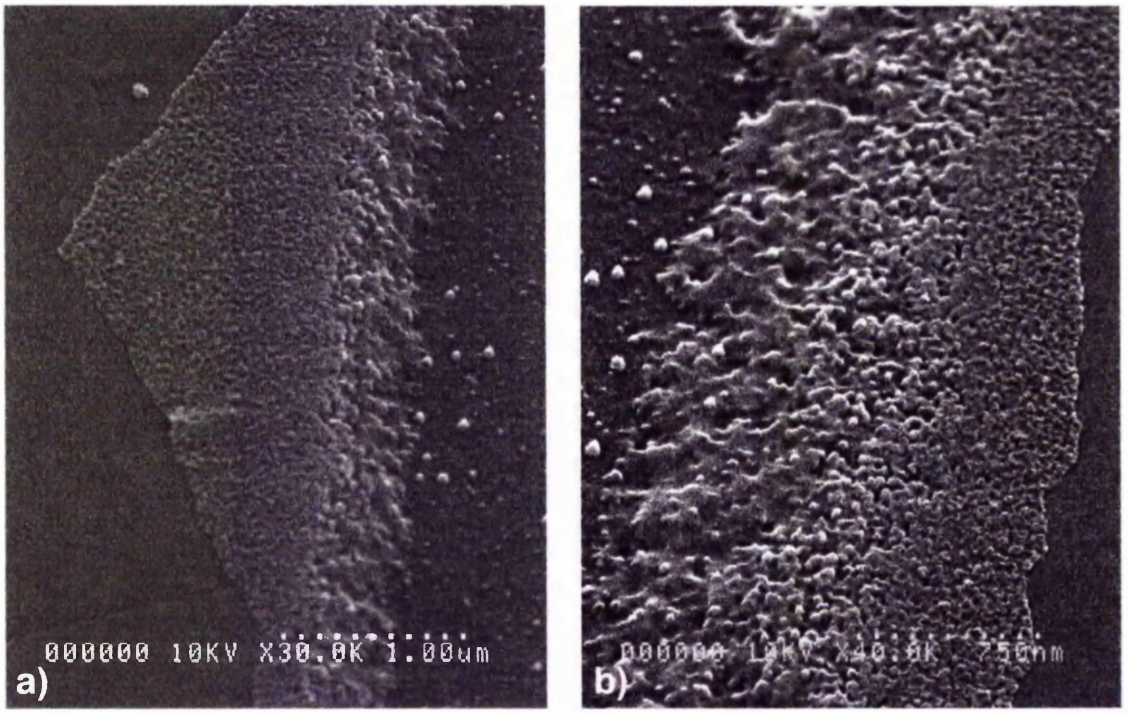

Figure 5.6: Scanning electron micrograph of the "landslide" morphology observed at the interface of the planar and nanopillared patterns. This feature appears to occur as a result of poly-L-lysine movement following colloidal sol application associated with nitrogen gun drying. Nanofeatures on the patterned areas appear sparse, a), due to aggregations of colloids appearing elsewhere on the surface, particularly in the accumulated mass at this interface, b).

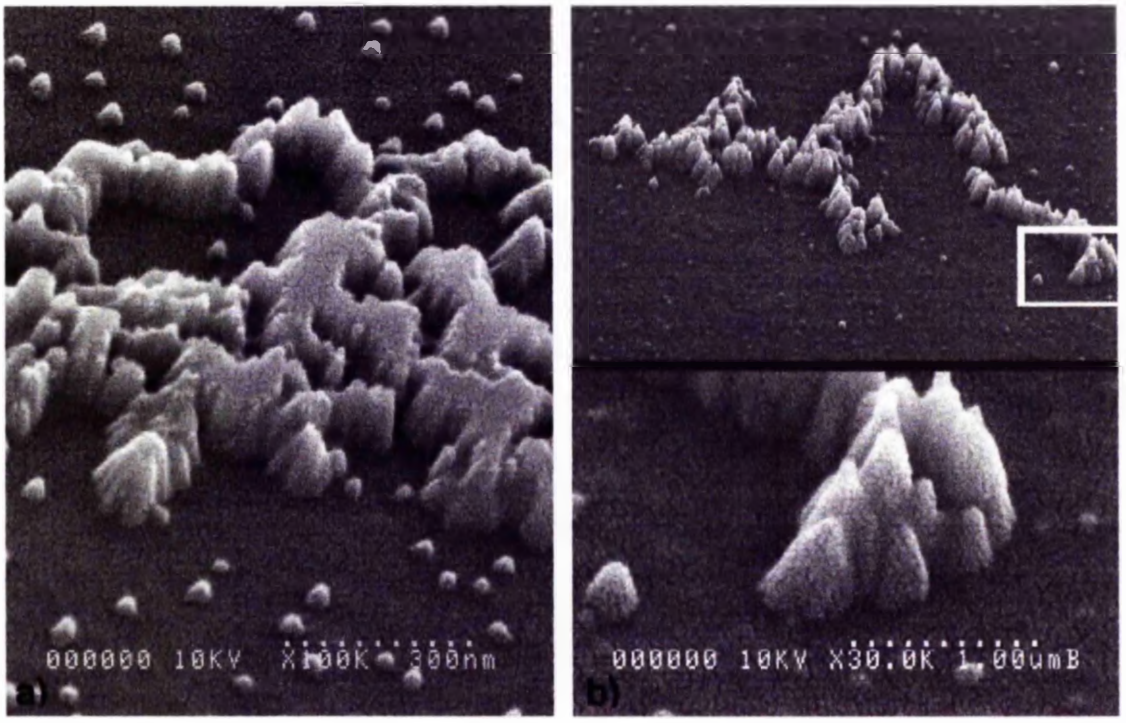

Figure 5.7: Scanning electron micrograph (Hitachi S-900) of nanomountains as a result of colloidal aggregations occurring during etch mask fabrication. Colloidal clumping in this manner occurs as a result of drying problems associated with reduction in the Debye length, where colloids spontaneously form groups. Flat tops of mountainous ridges, a), suggest aggregates surpassed monolayer formation, with multi-layers of colloids forming in clumps. The presence of very small, spherical features on the surrounding substrate, b), suggests sputtering of colloids from their original position towards the end of the etching process.

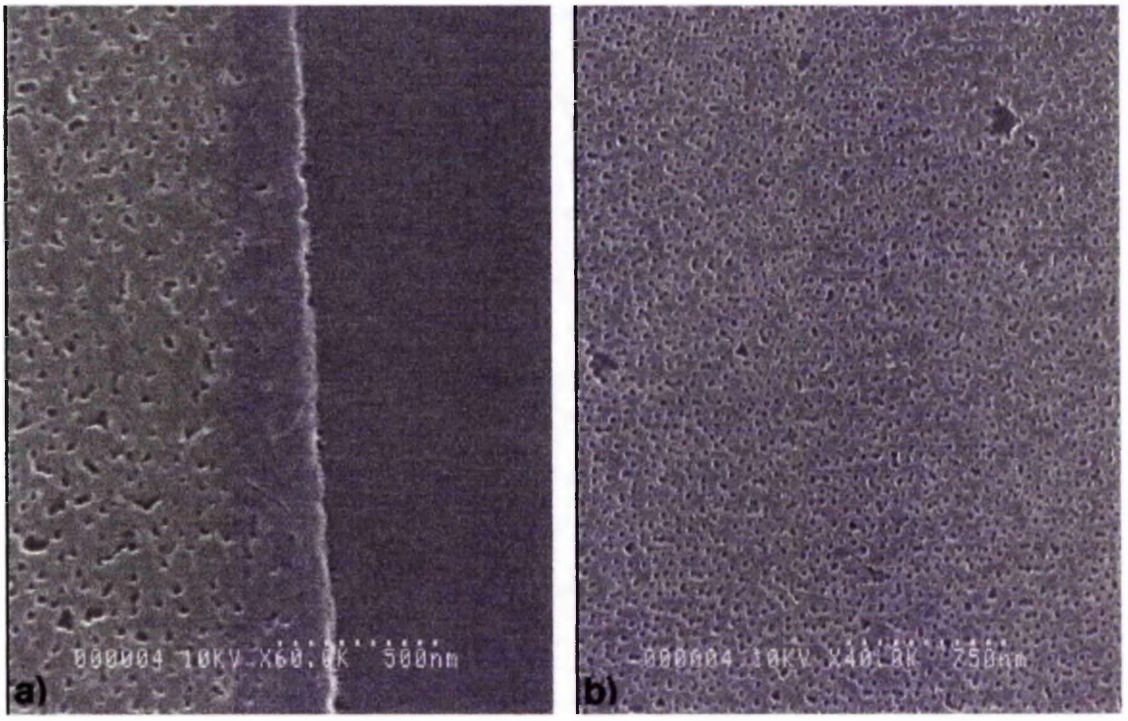

Figure 5.9: Scanning Electron Photomicrograph of polystyrene surfaces fabricated using a casting technique in relation to the planar-nanopillared quartz topography. Images, captured using a Hitachi S-900 FESEM, highlight the reproduced patterns, both at a planar-nanopillared interface, a), and on the nanopillared area only, b).

as was attempted in Section 3.2.2, would not result in dense pillar formation as previously believed. Instead, as the Debye length was reduced, clump formation of colloids would have formed, and following etching, would have resulted in the mountainous topography seen in these images, Figure 5.7a) and b). The flat tops of ridge formation indicate protection of this area from etching. This in turn suggests that multi-layers of colloids, deviating from the monolayer density, would have existed, thus planar tips are seen with no etching occurring. The presence of dwarfed spherical etched features on the surface surrounding these ridges indicate the occurrence of colloidal particle sputtering from their original position sometime after etching started. This is due to the very small size of features in the z-plane, where colloids would have landed following sputtering from their original position towards the end of the etching process. Through the use of Atomic Force Microscopy, these features could be measured in this plane, and the time they established their new positions could be calculated when considering the etch rate of the run in question.

The only possible solution to these lithography problems, which appear to occur as a result of drying procedures, is to ensure that surfaces, especially when the colloidal sol is being removed from the poly-L-lysine treated surface, are dried with an even pressure of nitrogen aimed perpendicularly to the surface.

The discovery of this drying issue appears to shed light on the uneven distribution of colloids on surfaces, highlighted, in particular, when attempting to alter colloidal density using Sodium salts, Section 3.2.2.1, Sodium citrate, Section 3.2.2.2 and alkanethiols, Section 3.2.2.3. Although constantly appearing as a problem, not only throughout this work, but also in published material describing "cracks" in dense colloidal monolayers or "grains" (Sato et al, 1997), no definitive answer has yet been proposed. It should be noted however, that the uneven nature of drying processes using, for example a nitrogen gun, may result in the removal of sol from one region prior to another, appears as the most probable origin of alterations in monolayer colloidal topographies. Thus a method resulting in the even drying of a surface is likely to yield better results. The use of temperature-controlled self-assembly techniques has been proposed (Ng, et al, 2002), where the accuracy of the results within this paper appear directly comparable to e-bean nanopatterning.

5.2.3 Casting Polymers to Create an Inverse Representation of the Planar-nanopillared Surface

Investigation into the effects of regularly patterned nano-pits in Poly-Caprolactone (PCL), fabricated by embossing the polymer on a previously established master die created using e-beam lithography, on cell behaviour, suggested the development of a surface non-adhesive to cells (Gallagher et al, 2002). A proposal outlined the possible role of nano-feature symmetry in the adhesive or non-adhesive behaviour of cells in relation to nanotopography (Curtis et al, 2002). As the colloidal lithography techniques detailed throughout this thesis resulted in irregular nano-featured arrays, an attempt to compare regular nano-pits with irregular nano-pits of similar dimensions was sought. A polymer, for example Polystyrene (PS) or PCL, was embossed or cast from the patterned planar-nanopillared structure developed using conventional photolithography and colloidal lithography, Section 5.2.2.3, to allow comparison with the previously developed regular nano-pits.

The production of an inverse pattern of nano-pits was attempted following the patterning of nanopillars as discussed in Chapter 4, where colloids masked areas of the SiO_2 base substrate resulting in nanopillared topography. However, polymers could not be cast successfully on these nanopillared surfaces, due to the difficulty of detaching the set polymer. Polymer detachment problems may occur as a result of alterations in surface energy (Kasemo et al, 1999). Following the development of the planar-nanopillared pattern, as described in Section 5.2.2.3 (Wood et al, 2002[b]), problems of polymer detachment from the surface were no longer present. This suggested the planar area surrounding the nanopillared pattern encouraged the initial detachment of the polymer from the experimental surface and ultimately its removal. An inverse pattern of the nanopillars in the polymer, resulting in an irregular array of nanopits, was thus achieved, Figure 5.9.

Although the original regularly patterned nano-pits were fabricated by embossing Poly-Caprolatone (PCL) onto the original e-beam fabricated master die, Polystyrene was used to indicate the success of the method using the irregularly patterned structure described herein, due to its light transmitting properties. PS is also inexpensive and successful replicas have previously been created by other members in the Centre for Cell Engineering, notably Dr Riehle.

Polystyrene (PS) solution (5% PS w/v in Chloroform) was poured onto the patterned structure; a method referred to as polymer casting, Figure 5.8. The structure with the PS coating was left in a fume cupboard for approximately 24 hours, allowing for solvent evaporation, resulting in a PS cast of the original structure. A scalpel was then used to make incisions around the cured Polystyrene on the master die, and these structures while still in contact, were placed in Ethanol in a sonicator for approximately 20 minutes. The incisions made at the edges of the PS and master die were enough for the cast to dissociate from the quartz-patterned structure. However, in some instances, following scalpel incisions, the polymer detached directly. Gentle agitation caused by sonication of the adhered structures aided in this separation.

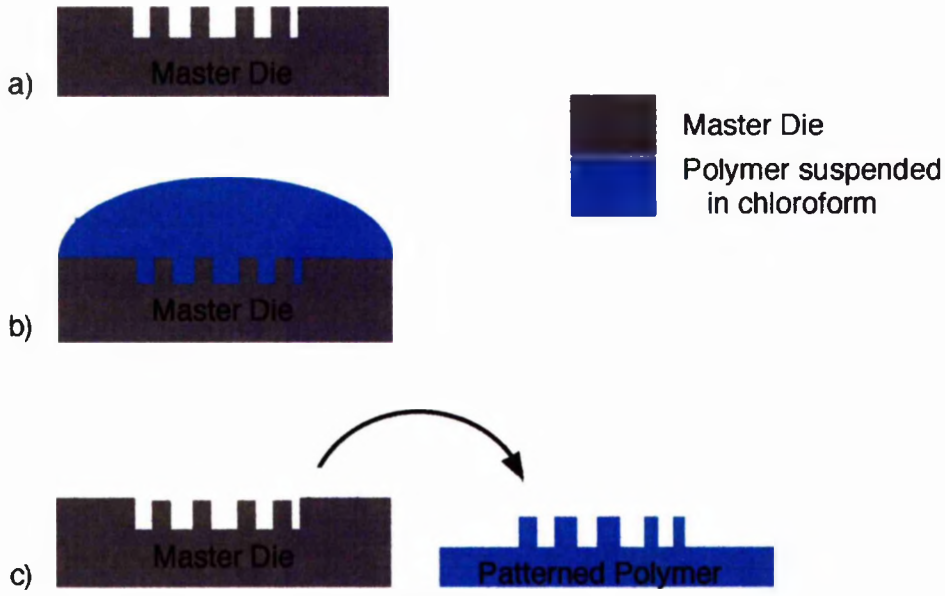

Figure 5.8: Casting polymer replicas from a master die, a). A polymer solution is added to the master die, b) and the carrier solution is left to evaporate resulting in a solid form of the polymer in question. The polymer is then removed from the master die, c). It would appear that a planar area must be present on the master die if the polymer is to be detached and retain the inverse irregularly patterned nanopillars of the master die.

The fabrication of a planar-nanopillared structure allowed for polystyrene replicas to be made. The accuracy of the patterning appears good and reflects the master from which the structure was developed, Figure 5.9. Unfortunately, due to time constraints, cells were not grown on irregular nano-pitted polymer structures as was intended, and therefore the effects of similarly nano-patterned features and symmetry have still to be elaborated upon.

5.3 hTERT Fibroblast Behaviour in Relation to Planar-nanopilllared Topography

Following the successful design of a grating patterned planar-nanopillared topography, Section 5.2.2.3 (Wood et al, 2002[b]), where both surfaces run concurrently across a substrate, the reactions of fibroblasts to the structure were investigated. Firstly, hTERT fibroblasts were monitored for behavioural alterations on 20nm diameter, 200nm high nanopillars and planar topography lying collaterally at 50μm width gratings using time-lapse video microscopy over two and a half days (66 hours), Section 5.3.1. Subsequently, the fibroblasts viewed using this method were fixed and fluorescently stained to allow the actin and tubulin cytoskeletal morphology in relation to the planar-nanopillared topography to be distinguished, Section 5.3.2.

While at the AO Research Institute, Davos examining the possibility of colloidal uptake by epitenon cells, Section 3.3.1.1, the opportunity to use a variety of Field Emission Scanning Electron Microscopes arose. These FESEMs were capable of investigating samples of a size greater than $5mm^2$; the required sample size when using the Hitachi S-900 in Glasgow. Unfortunately, hTERT cells were unavailable at this lab, so 3T3 Swiss Albino Mouse Fibroblasts were used. It was not until after this cell type was viewed on 20nm diameter, 80nm high pillared and planar structures using the Hitachi S-4100, that their loss of contact inhibition was identified. Therefore, the results of both the hTERT and 3T3 fibroblasts may reflect the alterations in contact inhibition between the two cell types. Thus, the presence of contact inhibition in hTERT cells, and loss of this phenomenon in the 3T3 fibroblasts should be noted when viewing the results of these experiments.

5.3.1 Video Microscopy Analysis of hTERT Fibroblasts on 50μm Grating Planar-(20nm diameter, 200nm high) nanopillared Topography

hTERT fibroblasts were seeded at a density of 10,000 cells per ml in 3mls of media on a 50μm grating planar-nanopillared topography, where nanopillars measured 200nm high with a diameter of approximately 20nm (the size of colloid used as a mask during the etching process). Surface patterns were made on a base substrate of quartz, although, as is case with all quartz and silicon base substrates, silica (SiO_2 oxide) was present and it is this surface oxide which will be contacted by cells and is thus important.

hTERT fibroblasts were recorded for 2 and a half days (66 hours) using time-lapse video microscopy in conjunction with a Zeiss Axiovert 25 Phase-contrast microscope,

Section 2.6. hTERT fibroblasts appeared to increase cell-cell contacts on the nanopillared areas of the surface resulting in aggregations occurring within these regions. In contrast, cells initially seen to adhere to the planar pattern were incorporated into aggregates on the nano-pillared regions, and thus, overall, cells, following initial contact with the substrate surface were primarily located on the nano-featured areas of the pattern.

Fibroblast behaviour on the nanopillared regions of the structure appears extremely similar to previous time-lapse work used to investigate hTERT fibroblasts on colloidal surfaces, Section 3.3.3.1. Upon the establishment of cell-cell contacts, occurring when fibroblasts interact with nanopillared regions of the structure, the catapult mechanism, previously described, occurs, as does the merging of cells to form united cellular entities. Thus, these phenomena will not be regurgitated herein, and the accompanying video footage on the CD regarding Chapter 3 should be referred to for further evidence of these phenomena. Instead, behaviour directly linked to the planar-nanopillared topography shall be discussed.

It should be noted that pillar tops are level with the planar region of the pattern upon which cells are seeded. Therefore, the nanopillar bases are lower in relation to the planar surface height, Figure 5.4h). This may be of importance when considering the dynamics of the surface, for example wettabiliy and convection currents occurring within the media. These features have, however, not been investigated during this work. When considering cell reactions at the planar-nanopillared boundary, the relation between the collateral surface designs should also be referred to, as the groove edge between the two surfaces is likely to be more accessible when considering cell interactions at this boundary.

Within the first 12 hours of contacting the planar-nanopillared surface, hTERT fibroblasts on the planar regions are observed to adhere, spread and move across the surface as individuals, with morphology reflecting cells on planar control samples previously investigated, Section 3.3. Cells in contact with the 20nm-diameter, 200nm high nanopillared structure behave very differently in comparison, with increased movement at quicker rates, catapulting from the surface and increased cell-cell contacts. This behaviour is discussed in Section 3.3.3.1 where cells are in contact with colloidal topography, and can be viewed on the accompanying CD. Upon contact with the

nanopatterned regions of the substrate, fibroblasts appear to suddenly relocate to this area, suggesting that, upon contact with the nanopillars, adhesions between the cells and the planar region decrease, or adhesions between the cell and the nanopillared area are greater in comparison. Regardless of this, an imbalance in adhesive qualities across the fibroblast appears to occur. This behaviour is extremely similar to the catapulting of the cells previously described on the colloidal topographies in Sections 3.3. Similarly, cell-cell contacts appear on the nanopillared regions of the surface as previously viewed on all other irregularly nanopatterned substrates with 20nm-diameter. As cell density increases on the surface over time, cell-cell contacts appear to increase across the surface as a whole. Cells on the planar regions, which come into contact with cells on a nanopillared area are recruited to the pillared region via cell-cell contacts. This suggests a number of possible factors instigating this behaviour. Firstly, fibroblasts may be expressing surface receptors, or expressing highly adhesive regions via, for instance cytoskeletal arrangement and mechanisms, where the cell on a planar region has no control with regard to joining the fibroblast reacting to the nanotopography. Similarly, due to the sudden departure of the cell from the planar region into the cellular aggregate on the nanotopography, the cell on the nanometric features may have problems establishing mature focal adhesions on the substrate, and may physically attach to the cell on the control surface. Evidence, previously discussed in Section 3.3, where cells on the colloidal substrate establish lamella extensions attached to its neighbours surface, exist to substantiate this theory.

The video stills discussed within this section, are aimed at giving an overall view of cell behaviour in relation to the planar-nanopillared substrate design. As described above, fibroblasts in contact with the nanopillars behave similarly to cells viewed on the colloidal, Chapter 3, and nanopillared, Chapter 4, structures with 20nm-diameter and 200nm height. This suggests that a similarity between all these surfaces exists, either in the diameter of the features, either 20nm or 50nm for the colloidal and nanopillared structures, or the irregular density reflected in all the surfaces. Pillar height would appear to have an influence, with more obvious cell-cell contacts and increased membranous extensions observed in relation to the 200nm high pillars. This is discussed further in Section 4.4.2.

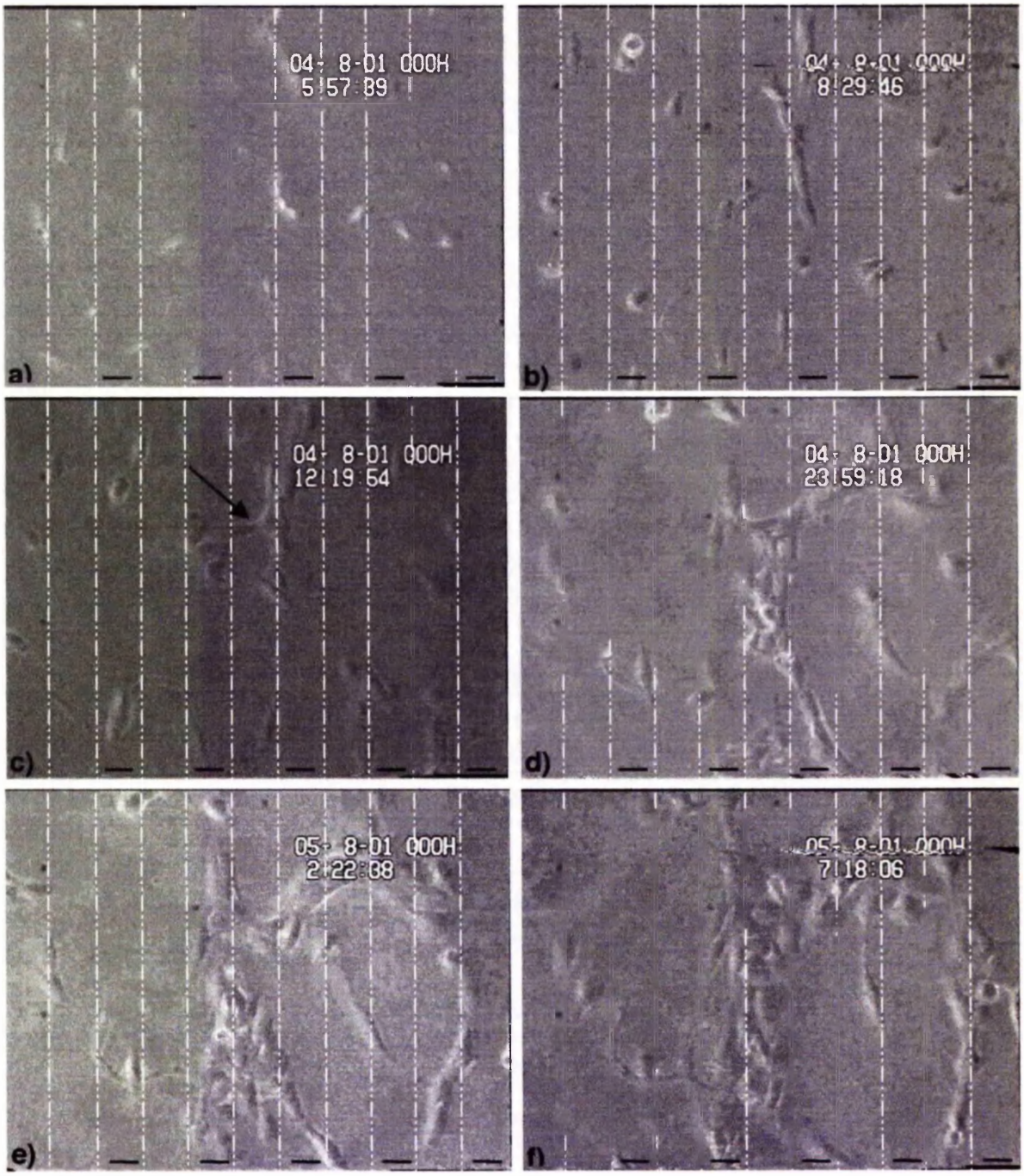

Figure 5.10: Time-lapse video microscopy of hTERT fibroblasts on 50μm planar-nanopillared gratings captured over a 2 and a half day period (starting image catured on 03/08/01 at 1728hrs, and final frame date and time read 06/08/01, 1105hrs) using a Zeiss microscope with 10X objective lens. Images g)-j) are continued overleaf (pp 300). White superimposed lines in all images represent the 50μm gratings on the silica surface of the quartz substrate, and can thus be used as a relative scale. Black dashes towards the bottom of the image indicate planar regions in the grating pattern, where unmarked gratings contain 20nm-diameter, 200nm high pillars. 12 hours after initial seeding of cells, a), indicates many of the fibroblasts, all of which are rounded and not well spread, interacting at the planar-nanopillared interface. Three hours later (15 hours after initial seeding), b), and cell-cell contacts have been established, with cell "trains" running the length of the grating border. Many of the fibroblasts still appear rounded, although a number are elongated in parallel with the gratings. All cells in a cell-cell contact situation appear to have some contact with nanopillared regions of the substrate, c). The arrow in c) indicates cells traversing the planar surface between two nanopatterned regions. Fibroblasts also appear to use established cell-cell contacts as a mechanical means of rearranging cell aggregates upon the patterned structure, d). This suggests the possible dragging of the basement membrane in the direction of movement. (Legend continued overleaf, pp 300).

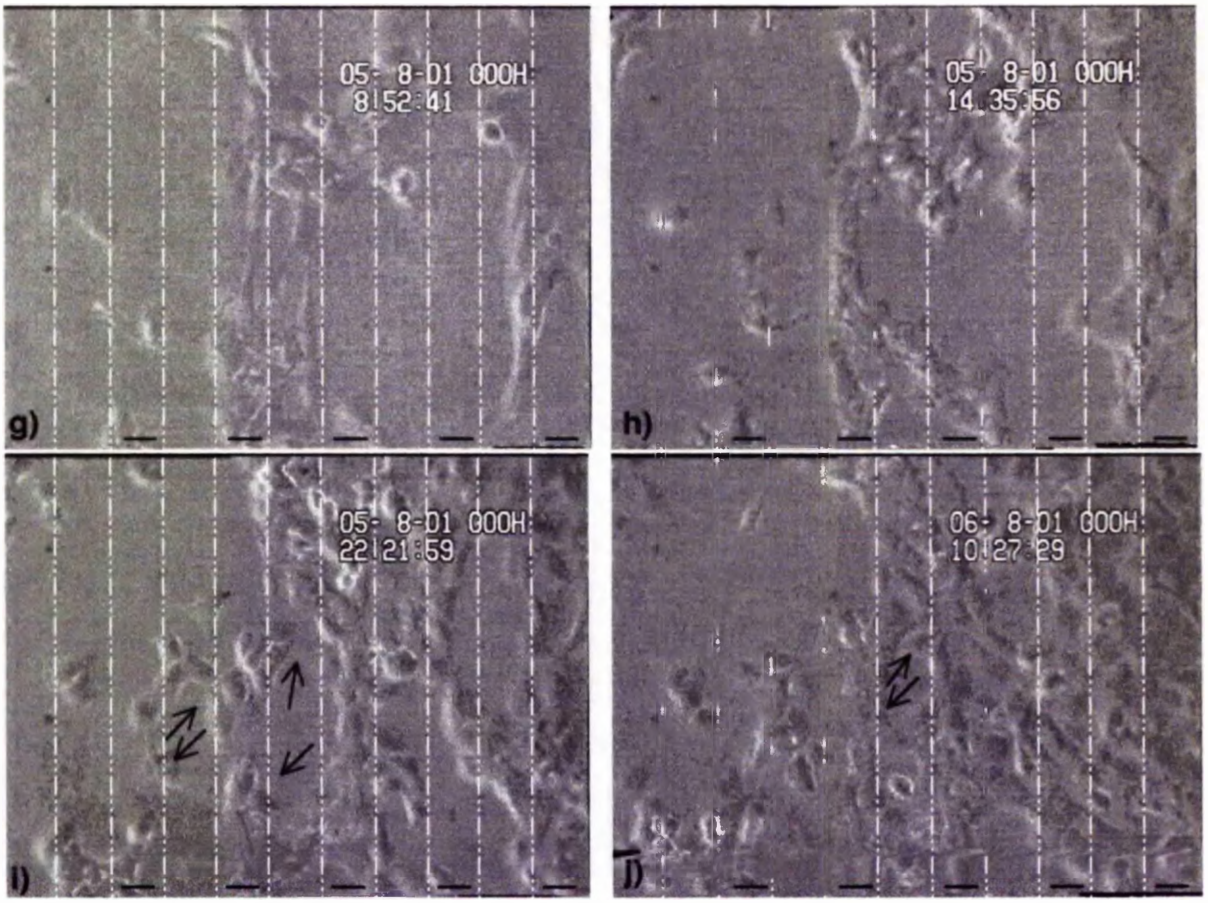

Figure 5.10 (continued): As previously described, fibroblasts traversing the planar regions of the substrate appear in contact with the nanopillars, or in contact with cells on the pillars, e). Alignment in relation to the grating pattern is observed, f) and g), however, fibroblast morphology and cell contact inhibition appear altered in comparison to previous work outlining cell reactions to micro-grooved substrata. Micropatterning of the surface appears to have a secondary influence with respect ot altered cell behaviour on the planar-nanopillared gratings, h), where fibroblasts alter alignment in favour of cell-cell contact influences. Areas of the substrate free from, but surrounded by multi-cellular aggregates, indicated by black arrows in i) and j), are eventually reduced. The possibility of a "purse-string" mechanism underlying this type of cell movement appears possible when investigating these video stills. However, upon closer examination of the video footage (Figure5.10Video on enclosed CD), lamellipodia appear as the primary agents of gap closure, with "purse-string" arrangements appearing as a supportive mechanisms in relation to these.

Following 12 hours in contact with either the planar or nanopillared regions of the experimental surface, where cell behaviour alters in relation to the substrate they are in contact with, fibroblasts begin to align to the micrometric dimensions of boundaries between each interface, Figure 5.10a). It would appear that the reactions at this scale are taking place on the nanopillared surface, with elongation of cells at the grating edge occurring in cellular aggregates as viewed on the nanofeatures. At this point, the majority of fibroblasts are observed to occupy nanopillared regions. When investigating the video footage, this would appear to be a result of both an increase in adhesion between cells, where a neighbouring cell on a planar region is recruited to an aggregate via cell-cell adhesion, or increased adhesion between the fibroblasts and the nanopillared features. The cell-substrate adhesion appears to manifest as cells contact the nanopillars, increase movement, membrane ruffling and extensions, and cannot dissociate from the underlying nanopillars. The alignment of cellular aggregates to the boundary of the nanopatterned substrate appears as a result of aggregate formation on the nanopillars, where groups of cells contact this interface. It may therefore be deduced that cells initially react to the nanometric surface features prior to the micrometric boundaries of the surface design. Super-imposed lines highlight boundaries in this image, Figure 5.10.

Within hours of fibroblast alignment to the planar-nanopillared interface, cells parallel to the boundaries establish a general order, Figure 5.10b). Most fibroblasts aligning to the micrometric grating pattern are seen to form long lines of cells in contact with one another, highlighted in Figure 5.10b). This further substantiates previous observations of alterations in cell contact inhibition and increased cell-cell contact establishment. At this point, almost all cells are in contact with the nanopillared gratings in comparison to the planar regions of the substrate. Previous work investigating cell reactions to micrometric grooved surface topography show that cells align to the boundaries of the grating pattern, with actin filament and microtubule arrangements lying parallel to the grating interface (Wojciak-Stodhard et al, 1995). These cells appear well spread parallel to the grooves. hTERT fibroblasts investigated in relation to the planar-nanopillared substrate discussed here, however, do not appear well spread, resulting in a relatively rounded morphology as observed in relation to both the colloidal and nanopillared substrates described in Chapter 3 and 4 respectively. This further indicates that cells are primarily reacting to the nanometric surface features present on the substrate surface. Although alignment to the grating

boundaries occurs, it would appear that the nanopillars have a greater influence on cell morphology and behaviour, thus cells do not exhibit alterations associated with micrometric features, except that as a cellular aggregate, they align to a limited degree with this interface. It would in fact appear that this boundary serves to confine cells to the nanopillared regions, with alterations in behaviour and morphology being primarily attributed to this nanopillared topography.

As cells begin to establish colonies on the nanopillared regions of the experimental structure, Figure 5.10c), aggregates lying parallel to other groups of fibroblasts on a separate grating of nanopillars attempt to bridge the gap between the two colonies (separated by a planar grating region) via single cell bridges. Again, this appears to occur as a result of increased cell-cell contact. Aggregates of cells occur on the nanopillared areas of the substrate, and by this point, approximately 20 hours of being in contact with the substrate, the planar regions of the surface are devoid of cells. This indicates that the nanopillared topography is more adhesive than the planar surface, and also, as most cells appear in aggregates, cell-cell contact is increased on the nanotopography. Fibroblasts which do appear to cross the planar region do so via adhesions established with cells on the nanopillars on either side of the control grating, indicated by the arrow in Figure 5.10c).

Twelve hours later (where cells have now been in contact with the experimental topography for approximately 30 hours), and differentiation between fibroblasts on the nanopillared and planar grating patterns becomes unclear, Figure 5.10d). Alignment to the grating patterns appears slightly less obvious in comparison to the previous image, however orientation of cells parallel to the boundaries is still observed, but to a lesser degree than previously seen, with only cells in direct contact with the grating edge aligning to the micrometric feature. Although not well demonstrated in this video still, Figure 5.10d), the video footage, Figure510Video on the accompanying CD, indicates that cells on the planar grating are in fact crossing the structure via cell-cell contacts established with neighbours on the nanopillared regions of the surface. As contacts are established between cells on both nanopillared grating regions across a planar stripe, and with time, the cells in this type of aggregate appear to relocate onto a nanopillared area, indicating transient contact with the planar surface. This relocation of cellular aggregates can be viewed when comparing Figure 5.10d) and e), where cells bridging two nanopillared regions across the planar area

move back towards a nanopillared stripe. Once again, this appears to be a result of increased cell-cell contact on the nanopillared area of the substrate and is more readily seen in the video footage in comparison to the selected stills, Figure5.10Video. As cells attach to one another, and reassemble the aggregates on the nanopillared areas of the substrate, rather than the planar regions, the increase in cell-cell contact would appear to be strongest on the nanopillared area, over-riding cell-substrate adhesions on the planar surface. Thus, central to the aggregates are cells exhibiting highly adhesive behaviour resulting in a return of cells to a nanopillared region.

As fibroblasts increase in number on the experimental substrate due to proliferation, surface area on the nanopillars is reduced resulting in population of the planar areas. As a result, cells appear to pervade the planar regions of the substrate. However this does not appear to occur in the manner that would be expected. Fibroblasts, which appear to move into planar regions, do so as a result of cell-cell contact with cells on neighbouring nanopillared regions, Figure 5.10f). Again, this is more visible in the accompanying video. At this point, cell-cell contact, increased due to the nanopillars appears to over-ride all patterning. For example, cells exhibiting an increase in cell-cell contact, or possibly an alteration in cell contact inhibition, appear to recruit cells regardless of the area from which they originate. Thus, it is no longer the nanotopography which is important, but rather the induced reaction of increased cell-cell contact expression of fibroblasts established on the nanopillars, which, in turn, appears to induce similar reactions in cells which they recruit, Figure 5.10g). This phenomenon would account for the occurrence of cellular aggregates occurring around a pivotal point (or cell), and deviating from the cues provided by the micrometric boundaries of the grating pattern. This is further expanded upon in Figure 5.10h), where bridging cells occur as assembled aggregates, rather than individual cells, across the planar regions of the experimental substrate. Aggregates containing upwards of twenty cells on the nanopillared regions appear to align to the micrometric patterning of the grating design, yet, again, they appear more rounded and less well spread than documented when investigating cell behaviour in relation to grooved substrata (Wojciak-Stodhard et al, 1995, Oakley and Brunette, 1993). This type of alignment appears as an anchoring system for cells traversing the planar regions of the substrate, especially when considering the mechanical features of tissues displaying this type of morphology in situ, for example tendon and meniscal tissues.

The increase in cell-cell contact, and possible alterations in contact inhibition occurring across the nanopillared regions appears to alter with time, becoming more apparent the longer the cells are in contact with the experimental substrate, Figure 5.10i) and j). What initially appears to be a phenomenon related to the nanopillared topography is no longer confined to this area of the substrate, although the cellular aggregates react with the patterned topography as a central point. This would suggest that, what began life as a behavioural alteration in cells in reaction to the nanotopography is now communicated via cell-cell interaction. To elaborate, the alterations in contact inhibition do not appear transient. When fibroblasts traverse the planar regions of the surface, emerging from a nanopillared area, the increase in cell-cell contact in cells on the neighbouring pillared topography results in the traversing cell being "dragged" into one of these aggregates. With increasing time, cells continue to proliferate and divide resulting in an increased number on the structure. The area of the nanopillared regions of the surface is thus reduced, as more cells inhabit it. As a result, fibroblasts begin to move onto the planar regions. However, no alteration in the increased cell-cell contacts occurs. This would suggest that fibroblasts expressing this type of behaviour are influencing neighbouring cells now resident on the planar regions of the substrate. In turn, this would suggest cell-cell contact has a greater effect on the situation than cell-substrate contact, as fibroblasts on planar regions do not revert back to behaviour previously observed on flat surfaces. Another possibility is that all cells are still in contact with the nanopillared areas of the substrate. As the grating features separating patterned from planar areas measure only 50μm wide, cells can bridge (as previously observed) the 50μm planar area to continue established contact with the nanotopography. One further possibility is a more enduring alteration in the cell as a whole; namely an alteration in gene regulation and expression resulting in altered cell contact inhibition. This would account for cells within the planar regions of the substrate, having emerged from the nanopillared areas, exhibiting an alteration in cell-cell contacts. Due to the period of cell-substrate contact, approximately two and a half days, fibroblasts may be actively structuring proteins within the extracellular matrix, which, in turn may account for the influence of the nanotopography across the grating pattern as a whole.

One method to investigate whether cells continue to contact the nanotopography, the lasting alteration in gene expression, the distance required between the experimental

nanotopography and planar areas for the influence of cell-cell contact to continue, or alterations in ECM assembly and structure, is to increase the grating patterns to a minimum of 200μm grating width. This width should limit the amount of contact with the experimental nanopillars, allowing for direct cell contact with planar regions of the patterned substrate, via fibroblast tails seen throughout this work, especially with regard to fluorescent images of cells on nanotopography.

An extremely interesting reaction occurs across a planar region, Figure 5.10i) and j), as the fibroblast population increases, where two neighbouring aggregates of cells on the nanopillars enclose and advance upon the control grating. This behaviour appears very similar to the description of the "purse-string" hypothesis associated with embryonic epithelial cells during wound healing, also seen in adult cornea and gut wounds (Jacinto et al, 2001). It should be noted at this point that nanoscale topography has been found underlying the corneal epithelium in macaque monkeys (Abrams et al, 1999). The corneal basement membrane appears as a rough, fractal structure of regular pores and ultra-fine topography located within the cavern of pores. Cell reactions to artificial ultra-fine topography *in vitro* has also been documented (Clark et al, 1991). The AFM image of the basement membrane is limited in that information regarding feature elevation and frequency only are displayed. The similarity between the AFM image of the corneal basement membrane and the nanopillared topography, Figure 4.2.2.2, is striking. This similarity between basement membrane topography and nanotopography fabricated through the utilisation of a colloidal lithography, may account for the fractal, or branching appearance of the proximal and distal cytoskeleton arrangements seen on nanopillars using SEM, where fibroblasts traverse a planar region of the patterned substrate, Figure 5.12.

Abrams et al suggest that the increase in surface area of the corneal basement membrane topography may provide a biomechanical advantage for stronger cell attachment. When considering the behaviour of fibroblasts investigated in relation to nanotopography described herein, increased cell attachments would appear as a possibility when considering cell catapulting across surfaces patterned with nanofeatures. Through increased cell attachment, cell shape alterations may occur as seen in morphology investigations throughout this work, namely elongated detachment sites. This, in turn, may alter the

biomechanical transduction and gene expression in cells contacting these surfaces (Curtis et al, 1997, Flemming et al, 1999). Abrams et al also suggested that an increase in substrate surface area may provide diffusion and active transport of components, which play an especially important role when considering avascular tissue, for instance the cornea. This is an important concept when considering a dynamic *in vitro* system as is seen in relation to the nanotopography investigated herein.

The contractile "purse-string" mechanism occurs via actomyosin cables contracting in leading-edge cells linked by adherens junctions. The wound epithelium draws forwards dragging its own basal lamina underneath it, across the substratum. In adult tissue, lamellipodia are used to close the wound gap. Upon closer inspection of the time-lapse video (Figure510Video on accompanying CD), lamellipodia connections appear more prevalent in the images. Any "purse-string" mechanism present is likely to have a support role in connection with the lamella formations. Lamellipodia-based wound healing results in the cells dragging themselves across substrata (or wound matrix consisting of fibrin, fibronectin and vitronectin) via connections established with neighbouring cells. The presence of proteins found in wound matrix on the planar-nanopillared areas, or other nanotopography discussed, requires further investigation. The contraction of actin required in both the embryonic and adult modes of wound healing is mediated by different members of the Rho family of GTPase molecules, suggesting up-regulation of gene expression with respect to these molecules in fibroblasts on the planar-nanopillared topography. Rac is highly likely be up-regulated, due to its requirement in lamellipodia extension and cell migration as exhibited by cells in this video footage. Cdc42 is required in the establishment of cell polarity during migration, suggesting its expression in fibroblasts on the experimental topography also. Unfortunately, due to time constraints, these possibilities require to be investigated.

A further possibility when considering the behaviour of fibroblasts on the planar-nanopillared topography is transient intracellular free Ca^{2+} signalling across cells (Sammack et al, 1997). Mechanical cues or stress on cells in contact with neighbouring cells may release contacts resulting in release from the constraints of contact inhibition mediated by cell surface proteins. Cells will be mechanically stretched at the moment of wounding, and appear stretched in much of the images obtained during this research,

resulting in the occurrence of transient intracellular free Ca^{2+}. The Ca^{2+}, or similar extracellular molecules leaking from mechanically stressed cells (where actin re-alignment along the axis of stress is recorded (Kolega, 1986) may act as transcriptional activators in cells experiencing Ca^{2+} signals (Woolley and Martin, 2000). Transient intracellular free Ca^{2+} can be detected as many as 12 cell layers back from the initial site of trauma (Sammack et al, 1997), an important factor when considering the multi-cellular aggregates viewed across the planar-nanopillared substrates under investigation. As the fibroblasts, both in this section and in previous sections appear to extend cellular material across the surface, cells may leak Ca^{2+} molecules due to the occurrence of mechanical stresses resulting in stretched calcium channels, or more dramatically, membrane rupture.

Both lamellipodia and "purse-string" mechanisms appear to occur on the planar-nanopillared substrate suggesting the occurrence of similar mechanisms found in both wound healing and similar processes seen during gastrulation. During gastrulation, activin is believed to have a role associated with the weakening of cadherin-based adhesions between epithelial cells. Reduction of adhesion between neighbouring cells is required to allow cell shuffling of convergent extension, and ultimately, gastrulation, to occur (Brieher and Gumbiner, 1994). If this is, in fact, seen to be the case in relation to planar-nanopillared topography, a possible inductive topography may exist to encourage this type of cellular binding during wound healing, or to further understanding of developmental processes, for example gastrulation.

5.3.2 hTERT Cell Morphology in Relation to Planar-nanopillared Topography-Fluorescence Microscopy of the Actin and Tubulin Cytoskeleton

hTERT fibroblasts were monitored using time-lapse video microscopy over 2 and a half days (66 hours), with stills taken using this method discussed above, Section 5.3.1. Following video monitoring, hTERT cells on the experimental substrate underwent fixation and the immunohistochemistry technique described in Section 2.7.3.1, to investigate alterations between the actin and tubulin cytoskeleton of fibroblasts on the planar and nanopillared topography. The grating pattern, where planar and nano-pillared features lie collaterally across the surface are 50μm wide, with nano-pillars measuring 200nm high and approximately 20nm in diameter.

Fibroblasts located on the planar region of the substrate, Figure 5.11a), reflect morphology previously observed in cells grown on the planar controls, Section 3.3. The fibroblast on the planar region appears well spread, with a generally smooth peripheral lamella, and the development of a leading edge indicating possible movement of the cell. No spiky features, for example filopodia are present as previously displayed by fibroblasts on nanotopography. In comparison, the most extreme case of cellular multi-layering, Figure 5.11b), is observed on the nanopillars. This can be related to the video microscopy stills, Section 5.3.1, where aggregates of fibroblasts occur. These groupings of cells appear to be related to the nanotopography, where an increase in cell-cell contact results in cellular aggregates.

Oriented microtubules appear from left to right in this image, Figure 5.11b), with actin stress fibres visible in the same plane. Fibroblasts are seen to overlap underlying cells, once again suggesting alterations in cell contact inhibition. This type of overlapping appears similar to primary tissue, with multi-layering of cells yet to occur. This is especially significant when considering the lack of cell aggregates on planar regions of the surface and that cells, seeded at 10,000 per ml in 3 ml media, have only been in contact with the surface for two and a half days. Actin appears throughout cells, but is predominantly located at peripheries, defining boundaries between neighbouring cells. However, where overlapping occurs, actin location at these sites appears diminished.

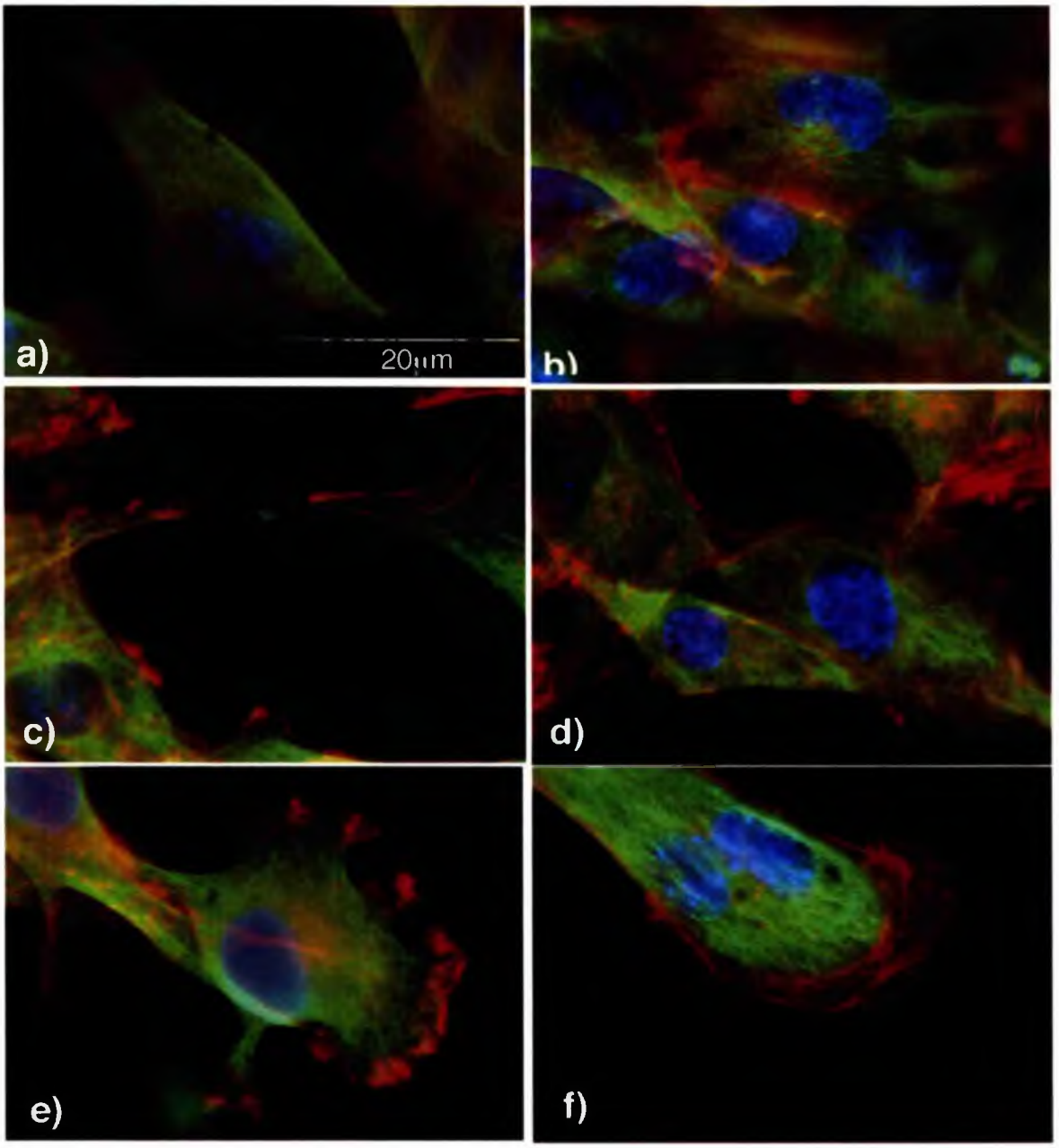

Figure 5.11: hTERT fibroblasts fluorescently stained for tubulin (green), actin (red) and DNA (blue) following 66 hours of culturing on the planar-nanopillared substrate. Images were taken on Vickers Microscope in fluorescent mode, using 50x oil immersion objection lens. Scale bar can be seen in (a), and is equal for all images. (a) shows the morphology of fibroblast on a planar area of the patterned surface, while in (b), multi-layer formation of cells on 20nm diameter, 200nm diameter nanopillars indicates the extreme differences between cells on planar and nanotopography. Images (c) - (f) exhibit the more subtle behaviour of fibroblasts on the patterned surface. Cell-cell contacts, (c), appear as fine fibrils extending between cells containing actin filaments and microtubules. Increased cell-cell contacts and possible alterations in contact inhibition, (d), results in aggregations of cells on the experimental nanotopography. Mechanical stresses occurring between cells appear to result in orientation of cells. Little evidence of cell-substrate contacts exist in relation to the two central cells (d)suggesting cell-cell contact may be greater than cell-substrate adhesions. Boundaries between cells are difficult to deduce, (e), where possible alterations in cell contact inhibition appear to occur, resulting in the overlapping of cells. A multi-nucleated cell, (f), appears with banding of actin microfilaments occurring around the peripheral edge of the fibroblasts as may be expected in adherens belts in epithelial cells. However, when relating these images to the video stills of these fibroblasts on this surface, this cell (f) is likely to be two cells in transient contact with one another, possibly merging to form a multi-nucleated fibroblast.

Figure 5.11c)-f) represent less obvious behavioural alterations, however when discussing the actin and tubulin cytoskeleton arrangements seen in these images, the video analysis must be referred to, to enlighten the filamentous structures imaged in these cells. Cell-cell contacts occurring on the nanopillars contain both actin filaments and microtubules, Figure 5..11c). The bridging effects of these contacts appear to result in directional stresses across the cells establishing the contacts. These stresses are indicated by actin filament alignment in the plane of the established cell-cell contact, Figure 5.11c). Similarly, Figure 5.11d), actin alignment in fibroblasts contacting neighbouring cells appears continuous, with little or no differentiation between the cytoskeleton of cells in contact with one another. Overlapping of fibroblasts in this image is also observed, with the cell on top of the underlying smaller cell exhibiting actin stress fibres generally associated with cell-substrate contact. This type of actin alignment suggests that the uppermost cell may be establishing adhesions with the underlying fibroblast. All cells in this image, Figure 5.11d), show actin arrangements at their peripheral edge, substantiating the previous hypothesis that adherens junctions are acting as the cell-cell adhesive contacts. Furthermore, the two central cells in this image display few filopodia, with general morphology similar to cells on control, planar surfaces. However, these cells have established cell-cell contacts. The lack of spiky peripheral membrane features suggests cell-substrate contacts are reduced in comparison to cell-cell contacts resulting in fewer interactions with the experimental nanofeatures. This in turn suggests that mechanical stress occurring across the cell may be a result of cell-cell interactions rather than cell-substrate contacts. This type of morphology and cell-cell interaction has been discussed previously, Section 4.4.2, where fibroblasts on nanopillared surfaces are slightly elevated from the nanotopography via cell-cell contacts. This results in cytoskeletal morphology of fibroblasts with established cell-cell contacts reflecting cells on planar surfaces.

Figure 5.11e) indicates the use of previously established cytoskeletal arrangements of neighbouring cells as a guide for directional alignment of subsequent cells in contact with the underlying stress fibres. Again, differentiation between the two cells in this image is difficult, with proximal and distal areas of the cells in contact appearing as a large cellular mass. The amount of tubulin in areas free of cells should be noted as, previously described, Sections 3.3.3.4 and 4.4.2, these may occur as a result of cellular debris from previously established focal adhesion complexes. The establishment of a leading edge viewed in the

principal cell in this image, indicated by actin aggregations at the peripheral sites, is in the opposite direction of the neighbouring cell it is in contact with. This suggests that cell contact promotion is not occurring, as the fibroblast is moving in the opposite direction from the neighbouring cell.

The appearance of multi-nucleated fibroblasts, Figure 5.11f), once again occurs on the experimental nanotopography. The appearance of these cells has been consistent throughout this work, Chapter 3 and 4. However, when referring to the time-lapse video images, the occurrence of cell-cell contacts throughout the sequence results in what originally appears to be a single cell actually being an aggregate containing a number of cells, Section 5.3.1. The actin arrangement, running the full length of the cellular periphery, appears similar to an adherens belt, as previously suggested in relation to actin arrangement in fibroblasts on nanotopography, Section 3.3.3.4. This type of actin filament arrangement supports the possibility of adherens junctions occurring at cell-cell contacts in fibroblasts on nanotopography. This brings into question a number of issues with respect to this type of cytoskeletal arrangement. Firstly, two cells are surrounded by this belt, and appear as a single organism. This two-cell entity appears as one through the establishment of a single leading lamella, suggesting that the cells are capable of acting in a unified manner, or, perhaps, one cell is acting as a control centre, incorporating the other cell whose functions would appear to be obsolete. As the microtubule arrangement in the unified cell appears indistinct with regard to two individual cells, communication throughout the cell would also appear unified, as would adhesions and cell-surface signalling. The possibility of this unified cell undergoing division is unlikely, due to the established nuclei, and unified direction of movement indicated by the leading edge. This type of morphology, where more than one cell appears as a unified cellular body, is seen to occur on all the experimental nanotopographies, investigated throughout this work, especially when features have a 20nm-diameter. United cells which appear and behave truly as one cell as is the case in Figure 5(f) are relatively unusual, although not unusual enough not to be brought into question and discussed. It still occurs regardless of cell passage and is never seen on planar control surfaces.

5.4 Swiss Albino Mouse 3T3 Fibroblasts on Planar-nanopillared Topography

Planar-nanopillared substrates were taken across to Davos when investigating colloidal uptake by epitenon cells, discussed in the Chapter 3. It was hoped that Stereo Electron Microscopy imaging of these surfaces could be achieved. However the surface features, whether expressing colloidal or nanopillared topography were deemed too small to obtain successful stereo imaging.

As the planar-nanopillared surfaces were greater than $5mm^2$, the size required for samples to be used in conjunction with the S-900 FESEM in Glasgow, and both the S-4100 and S-4700 FESEM at the AO Research Institute were capable of loading larger samples, the opportunity to view 3T3 fibroblasts on the patterned surface arose. Swiss Albino Mouse 3T3 cells (European Cell Culture Collection, Section 2.3.4) were the only fibroblasts available at this time in this lab and were therefore chosen, as they were believed to be comparable with the hTERT fibroblasts previously used in Glasgow. However, it was later discovered from ECCC data sheet and information on their web site that these cells were in fact not contact inhibited, thus differing from the hTERT and altering from the behaviour attempted to be conserved *in vitro*.

3T3 fibroblasts were cultured on the experimental planar-nanopillared topography for 24 hours. 100μm repeats composed the grating aspect of the experimental structure, with nanopillars measuring 50nm in diameter and 80nm in height. Cells were fixed, following which they were immunolabelled for vinculin, using a technique outlined elsewhere (Richards et al, 2002). This would allow the occurrence of Focal Adhesion Complexes containing vinculin to be compared in relation to the control planar area and nanopillared regions of the surface. Unfortunately this technique did not work, however samples were imaged regardless. As the technique involved the application of a detergent, Triton X-100, to cells allowing permeabilisation of the membrane for the immunolabelling technique, the cytoskeleton can be seen, Figures 5.12-5.14, rather than the overlying membrane. All the images within this section were viewed using an Hitachi S-4100 FESEM with a Secondary Electron detector.

5.4.1 Scanning Electron Microscopy of Permeabilised 3T3 Fibroblasts on Planar-nanopillared Topography

At low magnification, as seen in Figure 5.12a), two main observations can be made. Firstly, a great amount of cellular debris appears scattered across the experimental topography. As fibroblasts on these surfaces have been permeabilised, it is possible the debris is testament to this process. However, numerous rinses using PIPES buffer were made suggesting removal of waste from the surface. It is therefore likely that the material is either due to cellular activity or is protein in origin.

When considering previous experiments, where actin and tubulin were fluorescently stained, and cellular structures separate from the cells were highlighted, as with the breaking of fibroblast appendages observed using time-lapse video microscopy, the debris here is likely to contain cellular material regardless of the presence of proteins composing the debris.

Secondly, 3T3 fibroblasts viewed at this low magnification appear to be either of two main distinct morphologies. Cells found completely on the planar regions (dark areas, Figure 5.12a)) with no contact established between neighbouring cells, appear well spread and spherical in appearance with a central nucleus. Cells exhibiting possible alterations in contact inhibition via the establishment of cell-cell contacts appear contracted or condensed within a more elongated body. Fibroblasts observed to be in contact with neighbouring cells appear either to be on the nanopillars, in contact with a cell on the nanopillars, or spanning the planar region so that both proximal and distal sites are in contact with the nanotopography, Figure 5.12b).

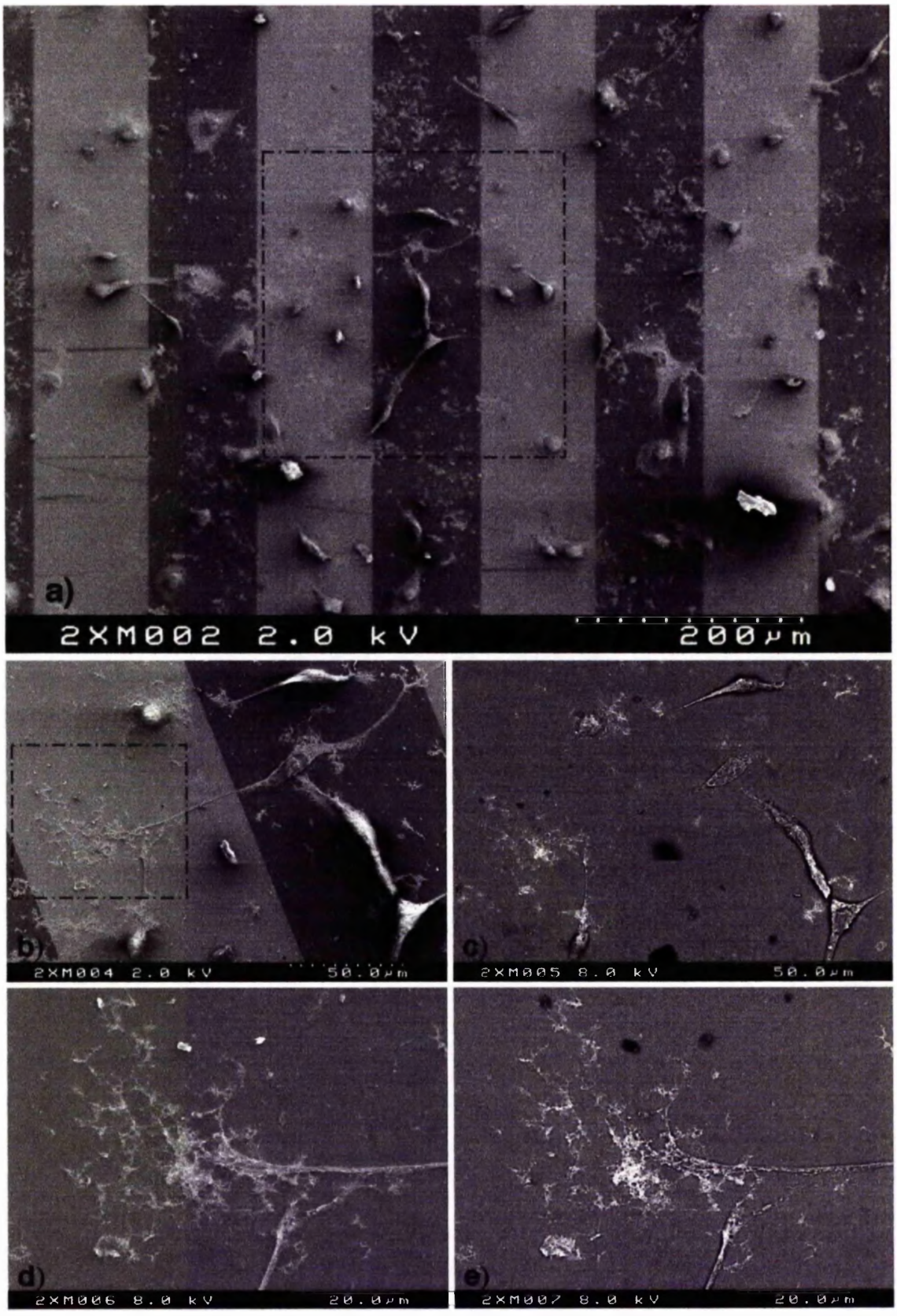

Figure 5.12: 3T3 Fibroblasts on 50nm-diameter, 80nm high nanopillars (light stripes in image) and planar (dark stripes) surface of 100µm grating after 48 hours. Images taken on Hitachi S-4100 FESEM. Boxed area in a) is seen at higher magnification in b), where secondary electrons are detected and c) where a backscattered electron detector is used. Similarly, d) and e) show higher magnification images of the cytoskeletal appendage highlighted in the previous image, b), in both SE, d), and BSE, e), modes.

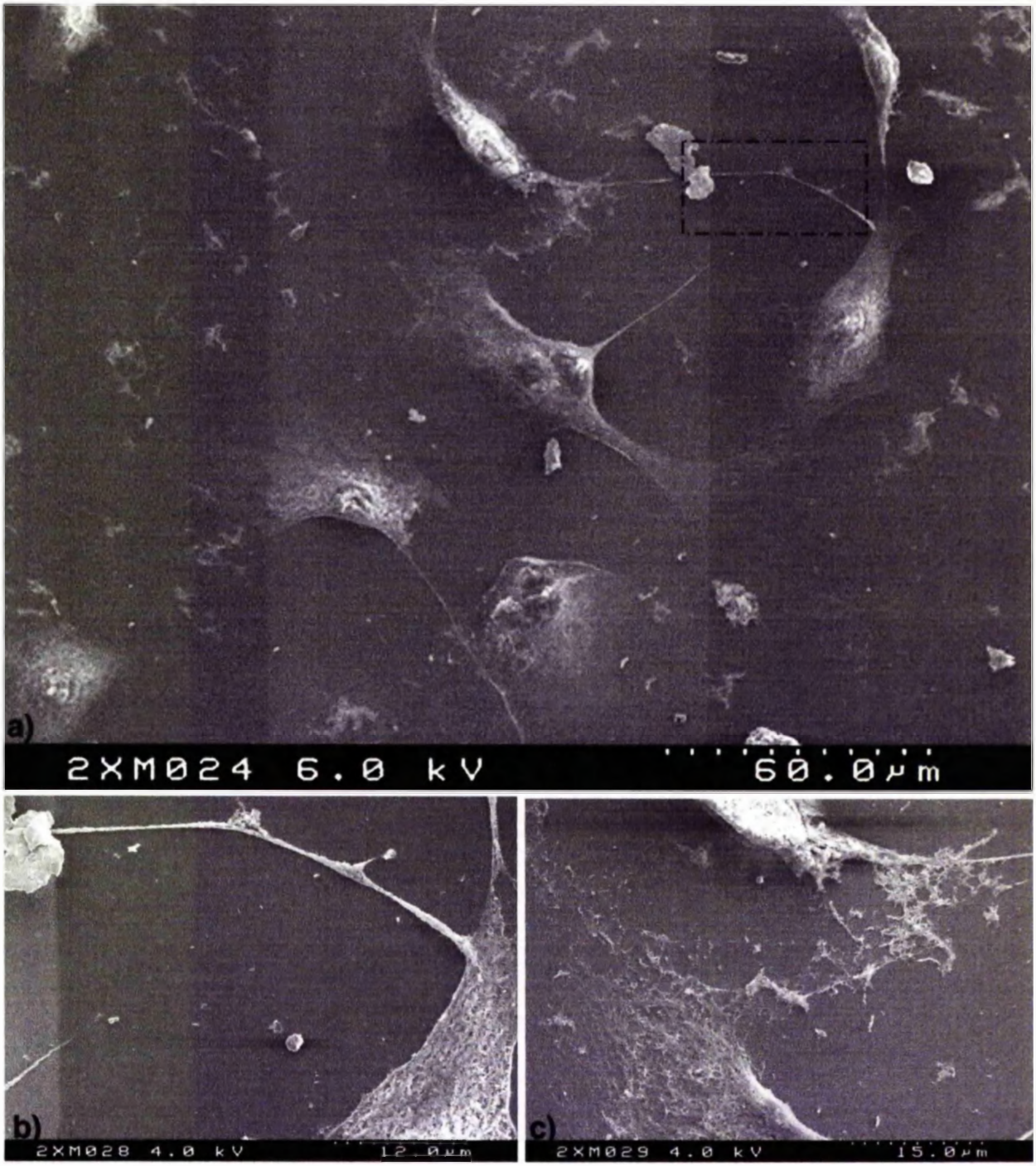

Figure 5.13: 3T3 fibroblasts in these images are located directly within a nanopillared grating, as opposed to interacting with the pillared-planar boundary. Images captured using Quartz PCI in conjunction with the Hitachi S-4100 FESEM. Fibroblasts on the 50nm-diameter, 80nm high pillars exhibit fibril extensions, a), previously viewed in relation to colloidal surfaces and nanopillars. These extensions appear to connect cells on the nanotopography, b). The behaviour described in Section 5.3.1, where fibroblasts react in the "purse-string" manner described in relation to wound healing appear to occur in 3T3 cells also. Differentiation between the cytoskeleton of cells in contact via these extensions is difficult, b), where the cytoskeleton appears continuous. Thin spreading of the cytoskeleton (and membrane) previously described in Figure 5 12, is observed on the nanotopography also, c). The cell in the lower region of this image appears connected to the previously peripheral membrane of the cell in the upper portion of the image. The cytoskeleton of the upper cell appears to have extended to this site of debris, and has some how retracted all cytoskeletal elements towards the cell body, leaving only the most extreme areas of adhesion behind on the nanotopography.

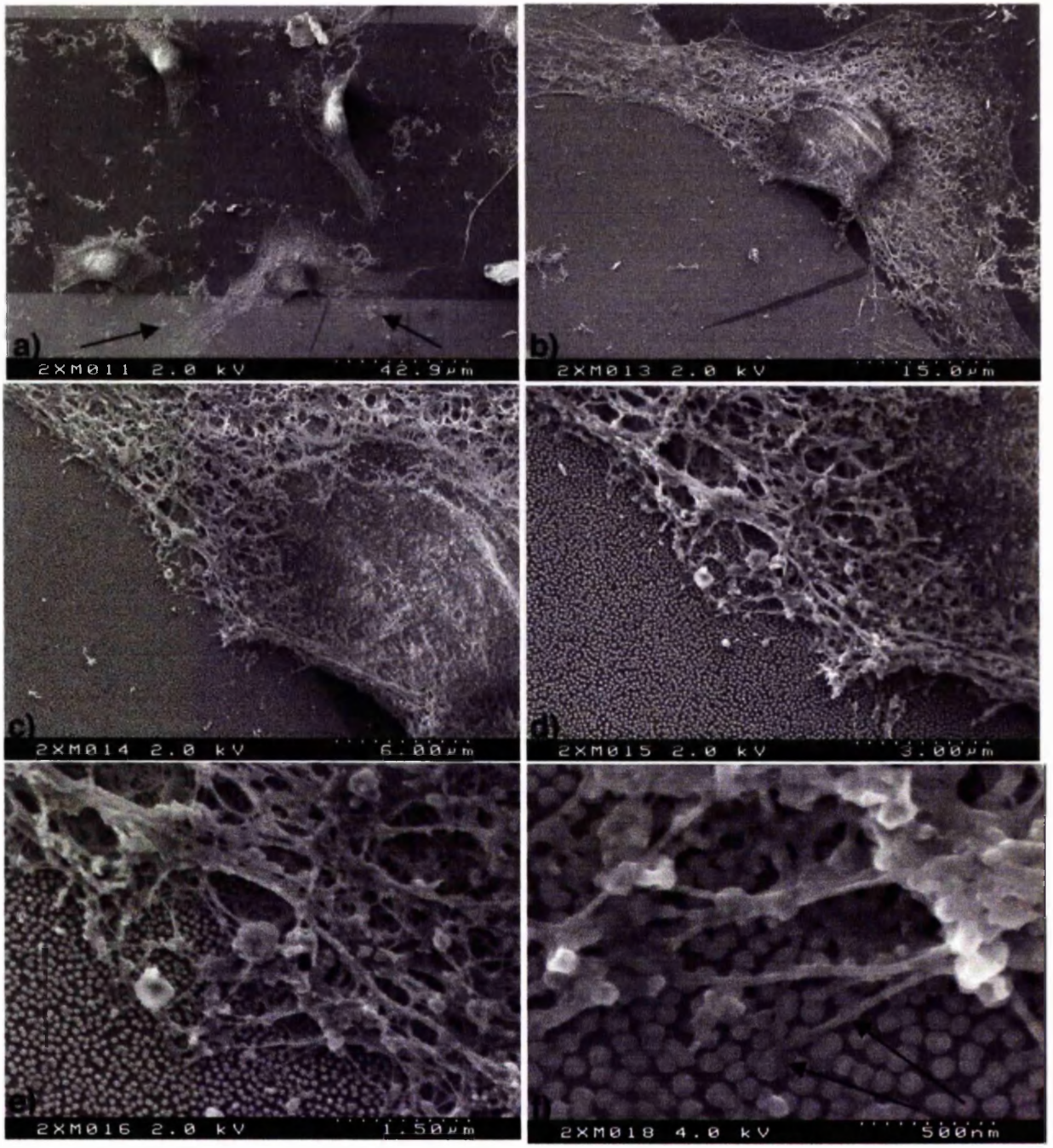

Figure 5.14: 3T3 fibroblasts on 50nm-diameter, 80nm high nanopillars (light stripes) and planar (dark areas) patterned 100µm grating surface. A low magnification scanning electron photomicrograph, a), of the cell under investigation within this figure. Black arrows indicate adhesion sites on the nanopillared area of the substrate, and can be seen more clearly in b), where membrane on the nanotopography appears extremely thinly spread in comparison to the planar region. The nuclear region of the cell, c), appears connected to the cell cytoskeleton, and is closely adhered to the nanopillared surface, d). Cytoskeletal structure appears very organised, e), with fibril elements extending towards the nanopillars. At the peripheral edge of this cell, f), cytoskeletal fibrils appear capable of direct interaction with the top of nanopillars.

Areas of cells in contact with the nanopillared regions of the grating pattern have extremely thinly spread cytoskeleton fibril arrangements, Figure 5.12b), with very intricate detailing resembling the branching seen in the lung. This suggests that a communication network established by the cytoskeleton extended to the furthest points from the cell body. This network may also have been involved in the positioning of focal adhesions and cell surface receptors. The rigidity and contractility of the fibroblast is likely to have been greatly influenced at these branching sites at both the proximal and distal regions of the cell as they account for the majority of the cytoskeleton arrangement. As the cytoskeleton is flat against the surface, it is likely that the membrane would also have been very thin in these areas. To have preserved this intricate arrangement during fixing, permeabilisation and dehydration of the samples suggests very strong adhesion of the cytoskeleton to the nanofeatured surface. This in turn indicates the presence of focal adhesion complexes, although, due to the intricacy of the spread features, the development of mature FACs in these areas is not obvious. Extending away from these remnants of cytoskeleton towards the nuclear area of the cell body is an elongated fibril extension previously observed when fluorescently staining hTERT fibroblasts on both the colloidal and nanopillared topographies, Sections 3.3.3.4 and 4.4.2 respectively. The narrow appearance of this area indicates very localised features, associated with the cell cytoskeleton, in these regions, for example focal adhesions and cell-surface receptors. It should be noted that these elongated regions do not share similar density with the branching areas when detecting Backscattered electrons, Figure 5.12c). In fact, they barely appear in this image, suggesting the material contained within these areas alters greatly in density compared to the material composing the branching on the nanopillars. The nucleus of this cell appears elongated and sunken, with little cytoskeleton support elevating it from the planar surface it traverses. When looking towards the opposing region of the cell to the right of Figure 5.12b), similar cytoskeleton structure is observed as described for the branching and fibril extension in relation to the opposite area. This results in the appearance of the cell body, containing the nucleus, being pulled apart. Again, this image suggests the nanopillared surface is highly adhesive in relation to the peripheral contact established by the fibroblast.

Figure 5.12b) was taken using a Secondary Electron detector, thus all information captured in the images provide morphological information with regard to cell and surface features. As previously mentioned, the amount of debris on the surface being viewed suggested

either cellular or protein debris. As the branching of the cell imaged in Figure 5.12b) shared similar characteristics with the general debris, a BSE detector was used to acquire information with regard to the density of the material within Figure 5.12b), to define whether the branching and fibril extensions were in fact cellular, Figure 5.12c). The resultant BSE image is extremely interesting. Firstly, indications that the branching areas are cellular can be ascertained due to the similarities in contrast between these and other more definite cellular areas (see small spread cell in upper portion of Figure 5.12b) in relation to d)) are striking. Furthermore, the contracted cells in the centre of the image appear to be slightly elevated from the surface due to the darker, shadowed areas observed in this image, Figure 5.12d). The fibroblast previously discussed traversing the planar region appears very flattened at the surface, accounting for the nuclear morphology previously described.

Connections between cells on both the colloidal and nanopillared topographies result in difficulty defining cell boundaries. This is seen in Figure 5.12d) and e). The two branching regions of separate cells on the nanopillared area of the substrate appear to merge, Figure 5.12d). The results of the BSE imaging once again give another view of the cellular material at this interface, Figure 5.12e). When viewing the secondary electron information, Figure 5.12d), little alteration between the branching sections and more fibril areas of both cells exists except when considering the distinct alterations in morphology. However, information regarding the density of these structures when detecting backscattered electrons emitted from deeper within the features highlight density alterations when comparing the branches and their associated trunks. The trunk regions would appear to be composed of more densely structured material, whereas the branching at the extreme periphery would appear less dense. This suggests contractility in the fibril area resulting in greater rigidity of this feature, which in turn indicates very localised expression of cell-surface receptors and possibly adhesion plaques. No evidence exists to suggest possible phagocytosis or endocytosis by the fibroblasts on this substrate.

3T3 fibroblasts in direct contact with the 20nm-diameter, 80nm high pillared area, Figure 5.13, appear to have a morphology more typically related to hTERT fibroblasts in relation to nanopillared surfaces as described in Section 4.4.2. Cells appear very well spread, with trailing tails suggestive of previous movements across the nanotopography, Figure 5.13a).

Such a trailing cytoskeletal appendage can be viewed in greater detail in Figure 5.13b). Again, it is difficult to deduce where the boundaries of cells in contact with each other in this manner lie. In the top right of this image, a similar extension appears interwoven with the main cellular area in Figure 5.13b) suggesting possible intertwining of fibroblast cytoskeletons when cell-cell contact occurs. Similarities between the fibroblast connecting via elongated fibrils and the "purse-string" effect, (Jacinto et al, 2001), can once again be visualised, Figure 5.12a) and b). This suggests that gaps between neighbouring cells in contact with the nanopillared topography may be closed through actin filament contraction.

The debris scattered across the planar-nanopillared surface as previously seen in Figure 5.12 is once again present. Figure 5.13c) highlights the possibility that debris may be cellular. Two peripheral membrane areas from two different fibroblasts appear to have come into contact, again with no distinguishable boundaries. Intertwining areas of cytoskeleton suggest an adhesive attachment established between the two cells. The cytoskeleton between the peripheral area and body of the fibroblast in the upper portion of the image appears to be lacking. This is suggestive of cytoskeletal retraction into the main body of the cell, with resultant peripheral adhesive sites remaining attached to the nanotopography and, thus, detaching from the cell, Figure 5.13c). This type of behaviour may be attributed to highly adhesive, and to a certain degree, static features within the focal adhesion complexes at these sites, (Palecek et al, 1998, Crowley et al, 1995) or in alterations in proteins associated with cellular detachment (Gopalakrishna et al, 1986, Huang et al, 1998, Sheilds et al, 1998).

3T3 mouse fibroblasts were also investigated for their interactions at the boundary of the planar and nanopillared gratings, Figure 5.14. The first striking feature with regard to cellular morphology is that cells appear typically fibroblast in appearance, exhibiting a triangular form, Figure 5.14a). Areas of cells seen in contact with the nanopillared regions of the surface display fragile cytoskeletal branching as previously described in Figure 5.12, where cells bridging a planar grating exhibit cytoskeleton branching of both proximal and distal regions on the nanopillars. Upon closer investigation, Figure 5.14b), the more intricate detailing in the branching cytoskeleton is observed. The nucleus of this cell in close proximity to or in contact with the nanopillared grating appears sunken, and very low in relation to the remainder of this feature on the planar region. At higher magnification,

Figure 5.14c), it would appear that adhesions occurring between the cytoskeleton and nanopillars have resulted in collapse of the cells nuclear region, possibly due to transmitted stress from substrate-cytoskeleton interactions. The cytoskeleton viewed in this image due to the permeabilisation of the cell membrane appears highly structured and connected to the nucleus. This would account for the shape of the cell nucleus in comparison to the area found on the planar grating. The nuclear morphology in relation to the cytoskeleton adhesions on the nanopillars suggests strong focal contacts are present resulting in the possibility of highly contractile fibres in the cytoskeleton on the pillared area, Figure 5.14d). Due to the contractility of these features, the nucleus whether moving to or from the nanotopography, is being pulled close to the pillared surface resulting in its deformed appearance.

The highly organised cytoskeleton of the fibroblast in contact with the 80nm high pillars, Figure 5.14e), suggests a number of factors with respect to the structure and function of the cell cytoskeleton and its appearance in this image. The cell exhibits a polarised state, as can be deduced by the tubulin and actin polymerised arrangement, believed to play a major role in the establishment of this state (Alberts et al, 1995). Spatial organisation of cellular components may occur in relation to the network established by the cytoskeleton due to its role in transporting organelles throughout the cell. Both cell-surface receptors and integrins involved in the formation of focal adhesions act as a foundation, allowing their establishment via binding to the cytoskeleton elements present, Section 1.1. Cell rigidity and also contractility appears great especially due to the arc-like structures highlighted by arrows in Figure 5.14e).

The ability of the fibroblast to interact with the individual pillars, Figure 5.14f), through both sensing features, for instance filopodia and lamellipodia, and also the cytoskeleton in general, is seen at high magnification, and are indicated by arrows in this image. The features indicated by arrows in Figure 5.14f) appear as precursors to both the overlying cytoskeleton of the cell and also the cytoskeleton appearing to pervade the area.

5.5 Summary

A planar-nanopillared surface can be fabricated through the utilisation of conventional photolithography and colloidal lithography techniques, Section 5.2.2.3 (Wood et al, 2002[b]).

The only problem when employing this method occurs when drying the poly-L-lysine-coated surface following the application of colloidal sol. By specifically drying the substrate with a nitrogen gun perpendicular to the surface, altered distributions in the colloidal monolayer are limited. A more promising approach to limiting altered colloidal distribution due to drying problems have been proposed by Ng et al (2002). Through temperature control with respect to colloidal sols, self-assembly of nanostructured arrays have resulted in accuracy previously limited to e-beam lithography. One problem when considering this approach in relation to the etching of colloidal lithography to form nanopillars in SiO_2 is, due to the density packing of colloids, nanomountain formations, Figure 5.7, are more likely to occur across the surface in comparison to individually etched nanopillars.

The application of aminosilane suspended in Acetic Ethanol (pH=5) to patterned 1818 resist resulted in the removal of the resist, Section 5.2.2.2, therefore an alternative non-alcohol based adhesive agent with respect to the colloids was sought and found in the form of a poly-L-lysine solution. Experiments utilising sylgard as an etch mask were also unsuccessful due to the mobility of the material prior to curing and also problems in the removal of cured sylgard from the experimental surface, Section 5.2.2.1.

Micro-contact printing appears as a promising method to fabricate a similar grating pattern, Section 5.2.1, expressing both planar and colloidal-based nanotopography on the same device. Modifications in the micro-contact printing processes discussed within Section 5.2.1 are required however, if a successful surface is to be fabricated in this manner. This method eliminates the requirement for Acid cleaning of structures, which has been shown to etch micrometric features, Section 4.2.1, deviating from both planar and nanometric patterning. One approach which may prove successful, where both a hydrophilic and hydrophobic pattern is firstly established on the surface has been developed (Yang et al, 1997). This would allow for the patterning of colloids via adhesive alterations, in relation to gold colloidal particles, occurring across the pattern.

Through the development of a planar-nanopillared topography, problems associated with polymer detachment from a nano-featured-only surface are overcome, Section 5.2.3. This allows for polymer surfaces, more readily applied to implant situations, especially

biodegradable or bioresorbable polymers, to be investigated for cellular reactions to nanotopography. The topographical features in the original design of the master, Figure 5.8, will be reflected inversely in the polymer substrate. By casting polymers, for example Polystyrene, which are readily available and inexpensive, the number of surfaces required in biological investigations, which is generally high due to repetitions of different experiments and cell populations, an overall inexpensive and high-throughput approach to surface patterning is established.

The development of a planar-nanopillared surface topography allows for cell investigations to be conducted where alterations in media pH concentrations, temperature, nutrients and proteins available to cells are reduced when compared to conventional planar control structures generally separate from the experimental substrate. When considering hTERT fibroblast reactions in relation to the 50μm-grating planar-nanopillared substrate, Section 5.3, comparisons between cells on the planar and nanofeatures are limited. This is due to cells either being in direct contact with the nanopillared surfaces, in contact with nanopillars via lamellipodia or filopodia extensions or interacting with other fibroblasts in contact with the nanotopography via cell-cell adhesions. hTERT fibroblast behaviour monitored by time-lapse video microscopy, Section 5.3.1, and immunohistochemistry used to highlight actin and tubulin assemblies, Section 5.3.2, suggest similarities between cells viewed on this topography and also colloidal, Chapter 3, and pillared, Chapter 4, topographies. Multi-nucleated cell aggregates occur on all of the experimental topographies discussed within this thesis, as does cell elongation, catapulting of fibroblasts in contact with irregular colloidal-based nanotopographies and lamellipodia and filopodia extension in relation to nanofeatures.

hTERT fibroblasts react to the micrometric interface separating planar and nanopillared regions of the substrate surface, as previously observed in relation to grooved substrata (Clark et al, 1987 and 1990, Oakley and Brunnette, 1993, Curtis et al, 1998, Wojciak-Stothard et al, 1995). The difference, however, between cells in contact with the micrometric grooves, and those in contact with micrometric gratings separating planar and nanopillared topography is the increased cell-cell contacts and lack of spreading observed in fibroblasts in relation to the patterned nanotopography described herein. This results in

cytoskeleton dissimilarities between fibroblasts on the grooved substrata's (Wojciak-Stodhard et al, 1995) and those visualised on the planar-nanopillared topography, Figure 5.11. hTERT fibroblasts, in reaction to the grating-patterned nanotopography, appear to primarily alter behaviour in relation to the nanotopography and, as a secondary response, interact with the grating interface . This would account for cell alignment being visualised on the patterned nanotopography after a significant amount of time has come to pass, upwards of 12 hours, and the alignment occurring in cell "trains" where cell-cell contacts are observed, as is non-spread and rounded morphology, Section 5.3.1.

Where two or more multi-cellular aggregates establish contacts via cell-cell adhesions where a central, exposed area of the substrate is present, the "purse-string" mechanism, observed during embryo wound healing, gastrulation and adult wound healing in the cornea and gut, and lamellipodia mechanisms, seen during adult wound healing (Jacinto et al, 2001), appear to occur during the closure of the denuded area of substrate. The "purse-string" closure mechanism appears in corneal wound healing in adults, where nanopatterns occurring in the corneal basement membrane *in situ* (Abrams et al, 2000), appear similar to the colloidal-based nanotopography, with respect to elevation and frequency, developed during this work with respect to 20nm-diameter features. Upon further viewing of the time-lapse video (Figure510Video on accompanying CD), lamellipodia involvement in gap closure appears prominent suggesting a supportive, mechanical role of actomyosin as viewed in "purse-string" closures. hTERT closure behaviour suggests possible dragging of basement membranes by cells, and may account for catapulting of cells seen on nanotopography throughout this work, where no stable or static topography exists to cells due to dragging of underlying established supports. The similarities visualised with respect to cell behaviour on the patterned planar-nanopillared topography and wound healing in the embryo and adult cornea and gut and also gastrulation suggests a possible role of nanotopography in these *in situ* events. Furthermore, the similarities between these phenomena suggest the possible development of colloidal-based topography capable of inciting wound healing behaviour.

Mechanical cues, where cells *in vitro* are simply pulled have been shown to result in actin filament realignment along the axis of stress (Kolega et al, 1986). Biomechanical stresses occurring across cells on the experimental planar-nanopillared topography, as indicated by

cytoskeleton arrangement, Figure 5.11, described in relation to actin realignment, may result in transient intracellular molecular signalling of, for instance, Ca^{2+} (Sammack et al, 1997). Intracellular calcium signalling may account for the cell-cell contact establishments observed in multi-cellular aggregates. Furthermore, cells experiencing an increase in intracellular Ca^{2+} may alter their transcriptional factors in accordance to the altered environment (Wooley et al, 2000).

Cell-cell contacts appear as one of the main behavioural alterations of cells in contact with colloidal-based nanotopography in contrast to their control counterparts. The type of contact has not been established at this time. However, when considering actin filament arrangement in fibroblasts, especially when appearing similar to adherens belt, Figure 5.11f), more generally associated with epithelial cells, adherens junctions would appear as a possible adhesion mechanism between cells. The possibility of adherens junctions occurring between fibroblasts is further supported in the role of this type of junction associated with wound healing and gastrulation (Jacinto et al, 2001), previously suggested with respect to behaviour of hTERT fibroblasts in the video still, Figure 5.10.

When considering 3T3 fibroblast reactions to 100μm-grating planar-nanopillared topography, cells in contact with the planar regions only are observed, although most are in contact with the nanopillars either physically or via cell-cell contact with fibroblasts on the pillared areas as similarly seen in hTERT on the 50μm-grating pattern. 3T3 fibroblasts appear in one of three states in relation to these grating patterns. Firstly, fibroblasts traversing the planar regions, with proximal and distal protrusions in contact with the nanopillars, Figure 5.12, display fractal patterning of the cytoskeleton in contact with the nanofeatures. This is important when considering the work by Abrams et al (2000) where fractal occurrences in the corneal basement membrane are incorporated into fractal patterns in the ECM. 3T3 fibroblasts in contact with the nanopillars only, Figure 5.13, have a different, more arc-like, well spread morphology, with cell-cell contacts established via lamellipodia extensions sharing similarities with cells undergoing "purse-string" behaviour (Jacinto et al, 2001). 3T3 fibroblast at the grating interface, Figure 5.14, display a cytoskeleton which appears to undergo fractal cytoskeleton patterning which can be directly related to the distribution of the nanopillars underlying these sites.

When considering the reaction of both hTERT and 3T3 fibroblasts in relation to the planar-nanopillared patterned structures, multi-cellular aggregates occur across the substrate as previously observed and discussed in relation to both the colloidal, Chapter 3, and nanopillared, Chapter 4, topographies. However, planar regions exist in the instances discussed within this chapter. When considering the occurrence of cellular aggregates, containing rounded, generally poorly spread fibroblasts at later times on all the nanotopographies investigated throughout this work, this would appear as a result of topographical influence on cell behaviour. It is possible that this phenomena is initiated via intercellular signalling, possibly in relation to cell cytoskeleton alterations due to biomechanical stress and adherens junctions, or other cell-cell specific junctions. Regulation of gene expression may also contribute to this activity. A further possibility is that intra- or extracellular signalling occurring as a direct result of pore stress in cell membranes, or in the most extreme of cases, possible membrane rupture, may play a role in cell-cell contacts. These types of alterations would account for the phenomena being visualised on planar regions of the patterned substrate, exhibited by cells with some contact with the nanopillars, either via lamellipodia or filopodia extension, or cell-cell adhesions with neighbours located on the nanopillared areas.

Chapter 6: Discussion

Epitenon, endothelial and fibroblast cell behaviour is altered as a result of contact with irregularly patterned colloidal-based nanotopographies. This conclusion has been reached through the analysis of adhesion assays, Section 3.3.3.2 and 4.4.1, time-lapse video microscopy examination, Sections 3.3.3.3.1, 4.3.2 and 5.3.1, scanning electron microscopy, Sections 3.3.1, 3.3.2, 3.3.3.3, 4.3.1 and 5.4, and fluorescence microscopy, Sections 3.3.3.4, 4.4.2 and 5.3.2, where comparisons between cell behaviour on control, planar substrates and experimental nanotopographies were made. Colloidal nanopatterns are presented to cells as a static topography, Section 3.3.1.1. As colloidal dimensions, chemistry and monolayer density and regularity, Section 3.2.2, can be altered and colloids remain as a stable substrate pattern following the addition of cells, this method of fabrication is proposed as a model nanotopography with respect to biological investigations (Wood et al, 2002[a]). Monolayer colloidal nanopatterns can be utilised as an etch mask in association with dry etching resulting in nanopillared topography, Section 4.2. Pillar diameter reflects colloidal diameter present in the original etch mask, and pillar height is controlled by etch time, Section 4.2. By removing the colloids post-etch, cells encounter a uniform surface chemistry. Furthermore, it is advantageous to seed cells on a device where control and experimental substrates lie collaterally across the surface. As a result, culture conditions remain constant with regard to both substrates. Patterning of colloidal nanotopographies in this manner can be achieved through the utilisation of both colloidal and conventional photolithography techniques, Section 5.2.2.3 (Wood et al, 2002[b]). Patterning of a substrate in this manner also allows for interactions between control, planar boundaries and the nanotopography to be examined and the preferential adhesion and behaviour of cells to be investigated in relation to two different surface topographies, Sections 5.3 and 5.4.

Colloidal topographies can be produced through the utilisation of an aminosilanised substrate, Section 3.2, for biological investigations. Colloidal density can be altered by charge screening of colloids and mobility restoration techniques, Section 3.2.2. Sub-monolayer colloidal patterning produced in the absence of these density-alteration techniques is dependent upon functionalised base substrate sol-immersion times, Section 3.2.1.1.1, Tables 3.2 - 3.4. Colloidal topography fabrication for biological investigations, where aminosilanised substrates were immersed in sols for 24 hours, resulted in colloidal surface coverage of approximately 5.1% for 20nm-diameter

colloids and 7% for 50nm-diameter colloids. Furthermore, 24-hour immersion in comparison to re-application of sols to the treated substrate surfaces resulted in the reduction of colloidal aggregates, Table 3.3, and thus a more regular distribution of colloids, where individual nanofeatures are present, was obtained.

20nm- and 50nm-diameter colloidal topographies are observed to elicit different cell responses. Two-way analysis of variance (ANOVA) was used to determine significant differences between the number of fibroblasts adhering to 20nm-diameter and 50nm-diameter colloidal topographies and a planar control, Section 3.3.3.2. hTERT fibroblast adhesion was found to be effected by surface topography and time, indicating an interactive affect between these variables on cell adhesion, Table 3.2. A Tukey test was utilised to identify specific differences between the mean number of fibroblasts adhering to the substrates at each time point, Table 3.3, the results of which further compounded the previous observations that an interactive effect between topography and time is present. The mean number of cells adhering to the three substrates is greatest on the 20nm-diameter colloids at 20 minutes and 50nm-diameter colloids at 1 hour, Graph 3.1, suggesting similar cellular adhesion mechanisms may act in relation to the nanotopographies. It is interesting to note at the final time point, 3 hours, the mean number of fibroblasts adhering to planar, 20nm- and 50nm-diameter colloids are very similar. This observation indicates colloidal topographies are highly adhesive at early times, becoming less adhesive over time so that the mean number of cells adhering to the nanotopographies is similar to those observed on the planar control surfaces suggesting adhesive adaptation of fibroblasts on the colloidal substrates.

Epitenon, Section 3.3.1, endothelial, Section 3.3.2, and hTERT fibroblasts, Section 3.3.3, cells are observed to form cell-cell contacts and protrude elongated membrane extensions regardless of colloidal diameter or cell type. However, when comparing hTERT fibroblast response to 20nm- and 50nm-diameter colloidal topographies, subtle differences in cellular activity as a result of colloidal dimensions, ultimately resulting in cell behavioural alterations, are observed. Temporal observations made using time-lapse video microscopy, Sections 3.3.3.1.1 and 3.3.3.1.2, indicate that fibroblasts seeded on 20nm-diameter colloidal topographies catapult across the substrate. Elongated rear detachment sites are observed in these cells, however, following stretching and elongation, rear adhesions appear to be overpowered by leading lamella interactions with the nanotopography. This behaviour is absent in fibroblasts on the 50nm-diameter

colloidal topography. Catapulting often occurs on the 20nm-diameter colloids following cell-cell contact, indicating the possibility that this behaviour may be due to changes in cell membrane receptors with respect to apical and basolateral polarisation alterations and cell-substrate versus cell-cell receptor expression. Cell-cell contact behaviour occurs on both colloidal nanotopographies investigated. Establishment of these contacts occurs as a result of protrusion and/or peripheral membrane connections. However, cellular aggregates observed on the 20nm-diameter colloidal topographies alter in comparison to those on the 50nm-diameter colloids, where fibroblasts within a group appear to actively recruit members via cell-cell contacts and resulting catapulting, and there is a lack of distinction between neighbouring cell membranes, Section 3.3.3.1.1. Cell-cell contacts occurring on the 50nm-diameter colloids appear to be established following unintentional contact between fibroblasts. Furthermore, following cell-cell contact on the 50nm-diameter colloidal substrates, alignment, where a common axis of stress is produced between neighbouring fibroblasts, is observed, Section 3.3.3.1.2. Alignment of cells on 50nm-diameter colloidal topography is also observed in epitenon cells at 24 hours, Section 3.3.1.2.

Tubulin and actin cytoskeletal morphology is altered in fibroblasts responding to colloidal topographies, Section 3.3.3.4. Developed microtubule networks are observed in spread fibroblasts on the nanotopographies, especially in relation to the 20nm-diameter colloids, while non-polarised tubulin is observed in cells on planar controls at 20 minutes. This is of particular interest when considering cell reactions to microtopography, Section 1.2, where Wojciak-Stothard and colleagues (1995) noted the development of microtubule networks at 30 minutes on grooved microtopography and Oakley and Brunnette (1993) noted that microtubules were the first cytoskeletal feature to align to the bottom of V-shaped grooves. These observations suggest similar microtubule behaviour on both microtopographies and nanotopographies at early times. Fibroblasts are observed to be more spread on colloidal topographies at 20 minutes in SEM micrographs, Section 3.3.3.3.1, where membranes are smoother at sites immediately preceding lamella ruffling, in comparison to control counterparts. Furthermore, fibroblasts seeded on 20nm-diameter colloidal topographies extend filopodia at basolateral sites and appear to elevate their main bulk above the nanopatterned surface. These protrusions appear to interact with the nanopatterned substrate, functioning as a means of cell-substrate connection. In some instances, fibroblasts on the 50nm-diameter colloidal topography are very rounded with smooth

membranes, suggesting highly polarised behaviour with respect to internal and external environments. In conclusion, fibroblasts on the colloidal topographies are more spread with more developed cytoskeletons at 20 minutes in comparison to their control counterparts and cells on the 20nm-diameter colloidal topographies are more spread with more developed microtubule networks in comparison to those observed on the 50nm-diameter colloidal topographies.

Actin stress fibres are observed on the colloidal topographies as early as 1 hour, which are absent in fibroblasts on the planar controls, and are particularly defined in cells on the 50nm-diameter colloidal substrates. Stress fibres indicate stable, mature focal adhesion complexes at the cell-substrate interface, and indicate stress occurring across the cell. Furthermore, when considering cell alignment to neighbouring fibroblasts on the 50nm-diameter colloids, stress fibres are likely to contribute to this behaviour, especially as observed cell-cell contacts display stress fibres parallel or perpendicular to each individual fibroblast in contact with a neighbouring cell. Elongated protrusions, observed in cells on the 20nm- and 50nm-diameter colloidal topographies, are composed of actin microfilaments at early times. SEM micrographs indicate the extent of membrane protrusions on colloidal topographies at 1 hour, Section 3.3.3.3.2, where elongations extend across and contact the nanopatterned surfaces. Cells are more spread on the colloidal structures in comparison to their control counterparts at this time, coinciding with fluorescence observations of defined stress fibres and microtubule networks. Furthermore, fibroblasts exhibit distinctive membrane features appearing as clusters, deviating from the generally spiky patterning of their surface, on the 20nm-diameter colloids, while instances of highly polarised, rounded cells are observed on the 50nm-diameter colloidal topographies at this time, Section 3.3.3.3.2.

The increase in defined actin stress fibres over time in hTERT fibroblasts coincides with the development of protrusions which are observed as an entangled accumulation of these membrane extensions on the 50nm-diameter colloidal topography at 3 hours, Figure 3.44. Fibroblasts on the colloidal topographies have also established cell-cell contacts at this time, Section 3.3.3.3.3. Stickle-bricking, where membrane protrusions become entangled at peripheral sites appears as one possible factor explaining the observed fibroblast behaviour. However, on the 20nm-diameter colloidal topography, cell-cell contacts arise in some instances from direct elongated protrusion contact with neighbouring cell membranes, where extensions terminate in prongs, Figure 3.43b),

which interact directly with other cell membranes. Alterations in cell contact inhibition are also brought into question, where fibroblasts are observed to locate directly upon other members of their population, Figure 3.43d). Fluorescent imaging of cell-cell contacts at 3 hours on the 20nm-diameter colloidal topography indicates a lack of distinction between actin and tubulin cytoskeletons of fibroblasts that have established contact, Figure 3.52. Endothelial cells also exhibit peripheral extensions, absent in controls, at early times on 50nm-diameter colloidal topographies. Endothelial protrusions appear to increase in length and quantity by 4 hours, where cell-cell contacts also occur, Section 3.3.2.

Fibroblasts on the 50nm-diameter colloidal topographies display beaded elongated detachment sites by 8 hours, again composed mainly of actin, absent in cells on the 20nm-diameter colloidal and planar substrates, Section 3.3.3.4.4. Furthermore, SEM observations indicate the production of globular protein-entities by fibroblasts at 8 hours on both colloidal topographies, absent in planar controls, Section 3.3.3.3.4. Protrusions continue to be observed, often acting to bridge cell-free areas of the colloidal substrates, acting as an intercellular connection. Differentiation between fibroblasts forming aggregates on the 20nm-diameter colloids is difficult, and cell membranes are very spiky and covered with globular material in these instances. Fibroblasts on the 50nm-diameter colloidal topographies establishing cell-cell contacts are more distinguishable from their neighbours, possibly due to their smoother membrane morphology. This behaviour is also observed in epitenon cells seeded on 50nm-diameter colloidal topographies at 24 hours, where cell-cell aggregates composed of well spread cells occur across the substrate, often via elongated protrusions, Section 3.3.1.2. In some instances, peripheral membranes are so finely spread that the underlying 50nm-diameter colloidal topography is visible. Extremely fine, elongated, string-like appendages appear to anchor cells to their neighbours membranes, where intercellular contacts are observed, Figures 3.22 and 3.23. In some cases, thicker protrusions bridge cells across denuded areas of the substrate surface, Figures 3.25 and 3.26, however in this instance, it is uncertain whether these features have contractile functions and are closing the gap between the cells involved, or if epitena are pulling apart from one another. Epitenon cells at this time are capable of direct interactions at their peripheral membrane with individual 50nm-diameter colloidal gold particles, Figure 3.18.

Cell contact inhibition is altered in fibroblasts seeded on the 20nm-diameter colloidal topography, where, at 24 hours, cells are often located on the apical membrane of their neighbours, Section 3.3.3.3.5. Protein entities are also entangled within string-like protrusions, and fibroblasts elevate their main bulk from the 20nm-diameter colloidal topography. By 48 hours, the actin-rich protrusions observed at early times on the 20nm-diameter colloids are observed to contain mainly tubulin on this substrate only, Section 3.3.3.4.6.

In conclusion, two-way ANOVA revealed that an interactive effect between time and topography influences cell adhesion, Table 3.2, which was further compounded by specific statistically significant differences identified using a Tukey test, Table 3.3. Furthermore, colloidal topographies are more adhesive at 20 minutes and 1 hour in comparison to planar surfaces, yet at 3 hours, mean fibroblast adhesion on all substrates is similar, Graph 3.1. Microtubule networks and actin stress fibres are also features of fibroblasts seeded on the colloidal topographies. Epitenon, endothelial and fibroblast cells are more spread, exhibit elongated membrane protrusions and form cell-cell contacts when seeded on colloidal topographies, in comparison to their control counterparts. However, alterations in cell behaviour are observed when fibroblasts are seeded on 20nm- and 50nm-diameter colloidal topographies. Cell motility is altered, where fibroblasts catapult across the 20nm-diameter colloids, and appear to actively engage in cell-cell aggregate formation. Individual cells are difficult to distinguish in these aggregates, yet on the 50nm-diameter colloids, fibroblasts forming cell-cell contacts are separate from their neighbours, and appear to utilise this behaviour as a means of alignment within their population. Furthermore, cell contact inhibition appears most compromised on the 20nm-diameter colloidal topography, where fibroblasts are observed to locate to the apical membrane of neighbouring cells. Microtubule networks are most developed in fibroblasts in contact with the 20nm-diameter colloidal substrates, while actin stress fibres are more readily associated with cells seeded on the 50nm-diameter colloids.

Colloids can be utilised as a mask for reactive ion etching, resulting in nanopillared patterning of silica Section 4.2. Pillar diameter and height can be controlled by selection of colloidal diameter and etching time respectively. Colloids can be removed from the nanopillared topography resulting in even surface chemistry across the device surface. SEM, Section 4.2.1.1, and AFM, Section 4.2.1.2, analysis of surfaces patterned in this

manner indicated that nanopillared topography reflects the original dimensions of the colloidal mask, and areas where colloids were in contact in the original mask are etched as "nanomountains", Figure 4.3b). Furthermore, nanopillars of different heights are often observed across surfaces, and are believed to occur as a result of colloidal sputtering due to lateral etching. Nanopillars fabricated in this manner have planar tops, as observed using SEM, due to the masking of the originally planar base substrate by colloids during etching. Interference reflection microscopy (IRM) is capable of imaging nanopillared topography with 50nm-diameter and 200nm height, where nanopillars act to scatter light suggesting a textured substrate, Section 4.2.2.3.

SEM imaging of epitenon cells seeded on 20nm-diameter, 200nm high pillars shows cells spread and exhibit lamellapodia and filopdia, which interact directly with the nanopillared topography at 1 hour. At this time, protein debris is observed to be encapsulated within areas of the substrate surrounded by nanopillars, Section 4.3.1. Filopodia and lamellipodia are located at the leading edge of epitenon cells on the nanopillared topography at 1 hour, Figure 4.7, although more general peripheral filopodia are also observed.

Time-lapse video microscopy of HGTFN endothelial cells on 50nm-diameter, 200nm high pillared topography indicates altered cell behaviour in relation to this nanotopography, Section 4.3.2. A cyclic series of events is observed, Figure 4.8 and 4.10, where immediately upon contact with the nanopillars, endothelial cells develop a leading edge and begin to elongate in this axis of stress. Further stretching ensues, following which the main cell body become rounded and elongated detachment sites emerge. In one instance of the video imaging, this cycle is repeated. It is proposed that this behaviour occurs as a result of strong cell-substrate interactions, where initial adhesions determine the degree of stretching and elongation. At this point, it is hypothesised that intracellular calcium is increased via stretch-activated calcium channels. Due to repeated stretch stimuli, endothelial cells are believed to become conditioned to this environment, resulting in lack of stretch response and a subsequent down-regulation of intracellular calcium, previously observed for keratocytes when repeatedly stimulated and stretched by an external force (Lee et al, 1999). This results in rounding of the main cell body, and preserved morphology of rear detachment sites. As cellular debris is lacking on this surface, intracellular molecular activities involved in focal adhesion disassembly are cited as the possible cause of preserved detachment

sites. Furthermore, increased intracellular calcium levels have been associated with integrin clustering (Horton, 1996), further compounding the proposed model of cell-substrate adhesive interactions.

hTERT fibroblast adhesion was assessed on 20nm-diameter, 200nm high-pillared topography, planar etched and planar controls at 20 minutes, 1 hour and 3 hours. Sample variance was not homogenous even following normalisation of the data, thus the Kruskal-Wallis test, a non-parametric test, was selected to analyse the data. A residual plot of sample medians indicated possible interactions between the number of cells adhering to the planar etched and nanopillared substrates at later times of 1 and 3 hours, and also between the planar control and the experimental substrates over time, Graph 4.1. The effects of time and substrate on fibroblast adhesion was investigated, Tables 4.1 and 4.2. A highly significant difference was found when comparing cell adhesion on all three substrates at 20 minutes, where $p=0.01$ level of significance. Similarly, significant differences were calculated between the number of fibroblasts adhering to the topographies at 1 hour and 3 hours, Table 4.1. It was thus concluded that fibroblast adhesion is topography-dependent when comparing planar, planar etched and 20nm-diameter, 200nm-high pillared substrates. The Kruskal-Wallis test was also utilised at level of significance $p=0.01$ to identify significant differences between cell adhesion and time, Table 4.2, however rejection of the Null hypothesis indicated that fibroblast adhesion in relation to these topographies was independent of time.

Actin and tubulin cytoskeletal arrangements are altered in fibroblasts on nanopillared topographies, Section 4.4.2. At early times of 20 minutes, microtubule networks are highly developed in well spread fibroblasts on the 20nm-diameter, 200nm high nanopillars, previously observed on the colloidal topographies at this time, where microtubules terminate in spiky peripheral protrusions, Section 4.4.2.1. Once again, the presence of microtubule networks as early as 20 minutes suggest similar sensing and response mechanisms occurring in cells seeded on micro- and nano-metric topographies (Wojciak-Stodhard et al, 1995, Oakley and Brunnette, 1993). Furthermore, Wojciak-Stodhard and colleagues reported microtubule development occurred as early as 30 minutes on grooved substrata, whereas this behaviour is observed on nanotopographies at 20 minutes, and possibly earlier suggesting a faster cellular response to nanopatterned surfaces, Section 4.4.2.1. Following 3 hours of seeding on the nanopillared substrates, Section 4.4.2.2, fibroblast shape and morphology differs considerably from control

cells. Cells appear to be under a greater amount of stress as a result of cell-substrate adhesive interactions, indicated by the presence of actin stress fibres, microfilament peripheral spikes and stretched, elongated shapes. Extremely elongated detachment sites, resulting in cell length measurements of up to 100μm, composed of globular actin and tubulin are observed at later times of 8 and 24 hours, Sections 4.4.2.4 and 4.4.2.5, respectively. Elongated detachment sites occur on 200nm high pillars regardless of pillar diameter. These detachment site features are reminiscent of those observed in HGTFN endothelial cells at similar times, Section 4.3.2. Highly defined actin stress fibres are also observed, indicating the amount of stress occurring across fibroblasts in one main axis on nanopillared topography due to adhesive cell-substrate interactions. The presence of elongated rear detachments indicate altered FAC disassembly, also suggested in relation to endothelial cells on 50nm-diameter, 200nm high pillared topography, Section 4.3.2.

Cell-cell adhesions occur throughout fibroblast populations on the nanopillared topography, where fibroblasts on the 20nm-diameter pillars, regardless of feature height, form polarised cellular aggregates, where internal, cellular and external environments are separated by cell grouping. Approximately seven nuclei are continuously observed within these aggregates which resemble tissue rather than individual cell morphology. Denuded areas of substrate, indicating this behaviour is not a result of over-population, surround these cellular entities. Cell-cell contacts occurring on the 50nm-diameter colloidal substrates do not result in miniaturised tissue formations, but in cell alignment with neighbours as previously observed on 50nm-diameter colloidal topographies, Section 3.3.3.4. In conclusion, pillar diameter and height are important factors of nanofeatures for biological cell investigations, where different dimensions elicit different cell behavioural responses.

A grating pattern where planar and nanopillared surfaces lie collaterally across the surface of a device can be fabricated by utilising natural, colloidal and conventional photolithography techniques, Section 5.2.2.3 (Wood et al, 2002[b]). Planar-nanopillared surfaces allow investigations of cell behaviour in relation to a planar control and nanopillared topography under constant culture conditions and interactions at the boundaries of these surfaces and preferential cell adhesion to be observed. Furthermore, possibly due to alterations in surface energy occurring at each alternate grating, polymers can be cast from these devices, Section 5.2.3.

hTERT fibroblast response to 20nm-diameter, 200nm high nanopillared regions of grating patterns is believed to emulate their reactions in relation to 20nm-diameter colloidal, Section 3.3.3, and 20nm-diameter, 200nm high nanopillared topographies, Section 4.4. Fibroblasts elongate and stretch, exhibit extended membrane protrusions, catapult across the nanotopography during motility and form multi-cellular aggregates, where definitive boundaries between neighbouring fibroblasts are absent, Section 5.3. Fibroblasts align to the micrometric planar-nanopillared grating interface, a secondary response following initial behaviour associated with nanotopography interactions, where trains of cells in contact with one another are observed, and cells appear very rounded, almost elevated from the nanotopography. This behaviour alters from previous reports of cell alignment on grooved substrata (Clark et al, 1987, 1990 and 1991, Wojciak-Stothard et al, 1995[a-c], Chou et al, 1995, Oakley and Brunnette, 1993), suggesting fibroblasts initially react to nanopillared topography and, as a secondary response, interact with the micrometric grating interfaces. "Purse-string" mechanisms are observed to occur, where denuded, planar areas of the grating pattern are closed via contraction of cell peripheries in fibroblasts forming a contractile ring around the exposed site. Contractile peripheries are believed to occur via actomyosin reactions, however this requires clarification. Lamellipodia and filopodia involvement in gap closure is prominent suggesting a supportive, mechanical role of actomyosin as described during "purse-string" closure in wound healing, and dragging of basement membranes (Jacinto et al, 2001). Actin stress fibres observed at cell peripheries further compound this behaviour, Section 5.3.2. Similar reactions to planar-nanopillared topography are observed in 3T3 fibroblasts. Furthermore, fractal features of corneal basement membrane are believed to be incorporated into ECM topography *in situ* (Abrams et al, 2000), and 3T3 fibroblasts display fractal cytoskeletal patterning on the nanopillared topography, directly related to the distribution and dimensions of the underlying surface features, Section 5.4.1. In conclusion, nanopillared gratings are more adhesive in comparison to planar areas of the substrate surface resulting in preferential location and adhesion of fibroblasts to these sites. Cell-cell contacts appear central to observed behaviour on 20nm-diameter, 200nm high pillars, resulting in fibroblast recruitment to nanopillared surface areas. Furthermore, fibroblasts on this device exhibit actomyosin , lamellipodia and filopodiabehaviour, where closure of denuded, planar areas results in cell adhesion across the substrate surface.

Observations made with respect to cell reactions to colloidal-based nanotopographies and cell reactions to microtopography, Section 1.2, and nanotopography, Section 1.4, are similar in many aspects. Firstly, although subtle, different responses are elicited in different cell types, in these instances, epitenon, endothelial and fibroblast cells. For example, rear detachment disassembly is altered in endothelial cells and fibroblasts in contact with 50nm-diameter, 200nm high pillared topography, Sections 4.3.2 and 4.4.2 respectively. Fibroblast morphology is elongated, where long, fine, string-like detachment sites are observed. These features do not appear to hamper cell motility and movement although these functions are altered, for example fibroblast morphology on nanotopographies are modified in comparison to control cells on planar surfaces. However endothelial cell morphology is drastically altered on the same nanopillared topography, with spiky peripheral membrane protrusions present and cells appear stuck on the surface and incapable of detaching rear sites resulting in inhibited motility. This can ultimately be attributed to the specific requirements of these cells *in situ*, and the topography presented within their natural environments. Furthermore, colloidal-based feature dimensions are paramount to elicited cellular response, where adjustments in a single plane are observed to have a different effect on cell behaviour, similarly recorded in previous biological investigations, Section 1.2 and 1.4.

Alterations in behavioural response of cells at different cell-cycle stages can ultimately be attributed to focal adhesion complex (FAC) morphology (Meredith et al, 2003). Rovensky and Samoilov (1994) observed that cells from the same population, but at different stages of the cell-cycle respond differently to cylindrical microtopography. Cells reactions to colloidal-based nanotopographies have not been distinguished in terms of cell-cycle status. The importance of focal adhesions and their bi-directional role in inter- and extra-cellular signalling, Section 1.1, dictates cell response to their surrounding environment. Furthermore, as the first means of established cell-substrate contact, FAC formation and morphology will determine final cell fate. Thus, although unsuccessfully attempted, Section 5.4, immunogold labelling of vinculin (Richards et al, 1995) is required to determine FAC morphology in relation to colloidal-based nanotopographies. In comparison to other methods of imaging focal adhesion morphology, namely fluorescent labelling, immunogold labelling offers a technique where high resolution SEM imaging of vinculin allows for direct comparisons to be drawn in relation to FAC localisation with respect to colloidal-based nanofeatures. Furthermore, vinculin morphology can be related to cell-cycle status (Meredith et al,

2003). This, in turn, can be utilised to chart the importance of each cell-cycle stage in relation to altered cell behaviour, initially attributed to cell morphology using EM and immunogold labelling techniques. These results can then be integrated with time-lapse video microscopy analysis to give an overall view of temporal behavioural alterations in relation to FAC morphology. Furthermore, vinculin distribution within cells will elucidate mechanisms underlying cell-cell contacts and serve to validate the proposed mechanism of endothelial FAC formation on nanopillared topography, Section 4.3.2.

Understanding FAC formation in relation to colloidal-based nanofeatures will allow insight into the possible underlying causes of observed alterations in cell behaviour on these nanotopographies. Furthermore, once vinculin distribution has been determined using high resolution microscopy, comparisons of temporal focal adhesion dynamics at lower resolutions in relation to planar and nanopillared substrates can be viewed utilising the planar-nanopillared fabrication technique developed during this work, Section 5.2.2.3 (Wood et al, 2002[b]). Green fluorescent protein (GFP)-vinculin-transfected cells (Kirchner et al, 2003, Small et al, 2002, Geiger et al, 2001) could be seeded on this surface, where planar and nanopillared structures lie collaterally. The planar and nanopillared gratings can be located on a light-transmitting surface, for example fused silica, where nanotopography appears darker when using light microscopy in comparison to the control surface. An image should be firstly captured of this area, where cell behaviour will be monitored. Fluorescence microscopy in combination with time-lapse video microscopy can then be used to monitor temporal alterations in vinculin dynamics in relation to both surfaces. The time-lapse images can then be referred to with respect to the immunogold labelling images, and should indicate the location and dynamics of focal adhesion complexes when comparing planar, control and colloidal-based nanopatterned surfaces. Furthermore, static, fixed samples imaged using the immunogold labelling technique in conjunction with high resolution SEM (Richards et al, 1995) will indicate the location of vinculin in relation to individual nanofeatures, where GFP-labelling will give insight into the distribution and dynamics of these proteins. Thus an overall view of FAC distribution on nanotopography in comparison to control, planar surfaces will be obtained. Focal adhesion disassembly is altered in endothelial cells seeded on nanopillared substrates, Section 4.3.2. GFP- and immunogold-labelling of vinculin would act to clarify the processes of assembly and disassembly of FACs in endothelial cells on the nanopillared topography. The involvement of intracellular calcium and its effects on molecular

mechanisms associated with focal adhesion dynamics has been hypothesised as a possible cause of the observed behaviour, and could be investigated further using the combination of immunogold- and fluorescent-labelling of vinculin proposed. Furthermore, cell-cell contacts are increased on colloidal-based nanotopographies. Labelling techniques would indicate vinculin distribution in relation to intercellular contacts and the association of this protein with cell-cell interactions, denoting whether adherens junctions are being established as previously hypothesised, Section 3.3.3.4.

Dunn and Heath (1976) proposed that mechanical restrictions on the locomotory apparatus of the cell might act to guide fibroblasts on patterned substrata. However, when investigating macrophage response to nanometric grating patterns, Wojciak-Stothard and colleagues (1996) noted that F-actin and vinculin were localised along groove-ridge boundaries and suggested that mechanical interactions between the cell membrane and groove-ridge sites leads to selective adhesion which determines cell morphology and orientation. Furthermore, Wojciak-Stothard et al believed these observations were unlikely to be caused by mechanical restrictions, as the surface features investigated were as small as 30nm. The proposed mechanism of focal adhesion complex interactions occurring in endothelial cells seeded on 50nm-diameter, 200nm high pillared topography, Section 4.3.2, leans towards the possibility that mechanical restrictions are imposed upon integrin clustering, and, ultimately, FAC assembly. However, following initial interactions occurring between the cell and nanotopography where FAC-associated proteins are effected, molecular mechanisms, for example the role of intracellular calcium in FAC-associated protein regulation, may have a greater bearing on expressed cell behaviour. When considering mechanical restrictions occurring on the locomotory apparatus of the cell, the possibility of nanotopography, or a derivative of these surface features, for example van der Waals' interactions (Curtis et al, 2002) acting in this manner appears plausible. The nanometric dimensions of cellular locomotory apparatus further indicate these features may be influenced by very fine nanofeatures. For example, intermediate filaments have a diameter of approximately 10nm, microtubules have an outer diameter of approximately 25nm (Alberts et al, 1995) and F-actin is believed to have a maximum width of 8nm and is composed of 2 helically wound strands which are axially staggered (Preston et al, 1990). The helically wound strands composing F-actin are staggered by approximately half a subunit, and cross over every 35nm along the right-handed double helix, with evidence existing to suggest microfilaments posses intrinsic disorder with random and

variable twists (Preston et al, 1990). Alterations in observed actin cytoskeletal morphology of cells seeded on irregularly patterned colloidal-based nanotopographies, Sections 3.3.3.4 and 4.4.2, may occur due to the influence of individual nanofeatures at specific cross over locations of F-actin. The frequency, distribution and interparticle spacing of colloids composing the experimental topographies, Section 3.2.1.1.1, further support this possibility. Investigation of this possibility would require high resolution EM imaging if alterations of the actin cytoskeleton were to be observed at the nanometric scale. Furthermore, the mechanical restrictions imposed at these sites would account for the catapulting of fibroblasts across the 20nm-diameter colloidal topography, Section 3.3.3.1.1, similarly observed in fibroblasts originating in the developing avian cornea (Bard and Hay, 1975).

Intracellular calcium levels effect many intracellular proteins associated with FAC assembly and disassembly. Stretch-activated calcium channels (Lee et al, 1999), have been hypothesised to alter rear detachment of endothelial cells on 50nm-diameter, 200nm-high pillared topography, Section 4.3.2. This requires further investigation, and, as previously described, Section 4.3.2, a fluorescent calcium indicator can be added to cells following seeding on the nanotopography under investigation, where alterations in fluorescent intensity would indicate alterations in intracellular calcium following stretching on the nanotopography (Kao, 1994). Calpain has been proposed as one molecule likely to be affected by alterations in intracellular calcium levels resulting in the observed lack of rear detachment of endothelial cells on the nanopillared substrates, also discussed in Section 4.3.2. Further investigations of alterations in calpain levels, utilising techniques described in Section 4.3.2, for example calculating calpain mRNA levels, are required to substantiate this theory.

To gain further insight into the effects of each colloidal-based nanotopography on each cell type investigated during this work, intra-molecular mechanisms underlying observed cell behaviour require to be understood. Cell and cytoskeletal morphological investigations are good indicators of altered cell behaviour in relation to nanopatterned topographies, and suggest alterations in gene and protein expression and regulation. As accessible techniques, for example 1.7K gene microarray (Dalby et al, 2002[d&e]), emerge, methods of determining alterations in gene and protein expression by cells in contact with nanotopography can be investigated. However, findings derived from microarray investigations act only as a rough guide to alterations in gene expression and

must be coupled with molecular biology techniques, for example Western blotting can be utilised to determine quantitative amounts of individual proteins, if these findings are to be validated.

Nanotopography can be utilised in the development of biomimetic devices where substrates are designed to reflect *in situ* environments. Imaging of nanopillared surface topographies using AFM techniques, Section 4.2.2.2, resulted in images with inadvertent qualities, irregularity and dimensions similar to those described by Abrams et al (2000) with respect to the basement membrane underlying the corneal epithelium in Macaque monkeys. Furthermore, fibroblasts from the developing avian cornea exhibit dramatic forward movement of the trailing process, on glass coverslips, artificial collagen lattices and isolated corneas, where adhesions are observed to break from the substratum (Bard and Hay, 1975). Similar movement and motile behaviour is observed using time-lapse video microscopy, where hTERT fibroblasts are in contact with 20nm-diameter colloidal topographies. Bard and Hay suggest this observation is a result of considerably stronger adhesions at the leading edge in comparison to the trailing edge, similar to that of ascidian tunic cells.

Colloidal-based nanopatterning of implant materials may offer methods of management with respect to host response and implant success. For example, bone tissue is observed to form close, but not direct contact with the implant surface of replacement teeth (O'Neal et al, 1992). The adhesive qualities of colloidal-based nanopatterns following immediate seeding of cells may encourage closure of this zone, resulting in better tissue-implant integration. The actomyosin contractile behaviour of fibroblasts on planar-nanopillared substrates, where nanopillars are fabricated with 20nm-diameter colloids and 200nm height, similar to "purse-string" mechanisms observed in adult wound healing (Jacinto et al, 2001), suggests this type of topography may be applied to defect sites, encouraging wound healing behaviour. As synergistic effects are often implicated in cell and tissue response to materials, colloidal-based fabrication techniques could be utilised in conjunction with hyalurona gels during wound healing, where topography, chemistry and mechanical implant properties could be designed to increase wound healing success. Furthermore, etching of colloidal masks appears to result in topography similar to the surface of the basement membrane underlying the corneal epithelium suggesting the application of nanopillared topographies in tissue engineering of corneas. Observations of cell behaviour in relation to colloidal-based

nanotopographies are also reflective of embryonic phenomena, for example parallels have been drawn between wound repair and morphogenetic movements (Jacinto et al, 2001), suggesting the utilisation of these surfaces in further investigation of fundamental cellular processes.

In summary, nanotopography can be utilised to manage or manipulate cellular response. As previously observed in relation to microtopography, Section 1.2, and nanotopography, Section 1.4, different cell types, namely epitenon, endothelial and fibroblast cells, exhibit altered behaviour in relation to the same colloidal-based nanotopography. The nature of physics shaping self-assembled nanopatterns, specifically colloidal monolayers, gives insight into the occurrence of forces, for example van der Waals' interactions, at the nanoscale. As a result, forces appearing at a nanometric level in relation to natural lithography techniques offer alternative perceptions with respect to mechanisms underlying the effects of nanotopography on cell behaviour.

Appendix I

Writing stages in the fabrication of nanolithography are generally serial techniques, thus are slow, for example using a focused beam of electrons as observed in e-beam lithography. In-plane nanostructure fabrication techniques excluding self-assembly techniques are described. A summary of nanofabrication techniques, limits and qualities is provided in Table 1.1, Section 1.3.

Conventional Lithography

Lithography techniques utilising photons, particles and scanning probes in combination with a resist-coated substrate have been categorised as conventional lithography techniques due to their successful employment within the microelectronics industry over the past decades. Methods fitting this criteria include photolithography (both contact and projection modes), particle writing using a scanned beam of electrons or ions or projected image and scanning probes where tips induce local changes in a resist or cause local deposition (Xia et al, 1999). Due to the serial process of scanning or writing, resultant structures are generally used as masters as cost and time prevent economical mass production, whereas replicas of the master using other process, for example soft lithography techniques (Section 1.3) are extremely effective and economical (Gadegaard et al, 2003).

Photolithography

There are two forms of photolithography, contact mode and projection printing, both of which share the same operational principles and generally undergo a sequential process, for example reactive ion etching (Chen and Ahmed, 1993), or wet etching (Ilic and Craighead, 2000). A photoresist coating the substrate to be patterned is exposed to electromagnetic radiation, for example ultraviolet (UV), deep ultraviolet (DUV), extreme ultraviolet (EUV) or X-ray, through a mask, in contact mode, or aperture, in projection mode photolithography. This results in the spatial distribution of radiation projected onto the photoresist-coated structure. Localisation of radiation in this manner induces a latent image, in this instance, an alteration in solubility, into the resist as a result of chemical changes in molecular structure, and thus induces localised photochemistry. The latent image is developed into a relief structure chemically utilising the altered solubility of the resist. The predominant use of photolithography techniques is to replicate a mask pattern into the photoresist. As one of the most highly developed of micro- and nano-fabrication technologies due to its employment in

integrated circuit manufacturing, photolithography is also the most widely used of all fabrication techniques now practised (Xia et al, 1999).

Contact mode photolithography employs a mask to distribute the desired radiation, and thus pattern, which is placed in direct, physical contact with the photoresist. As a result, damage to both the mask and sample can occur, especially when dealing with fragile nano-featured patterns. A gap often occurs between conventional rigid masters and rigid planar base substrates coated with the resist, even when taking into consideration the vacuum features allocated to the appropriate mask aligner machines. As the minimum feature size being produced is determined by the diffraction of light passing through the mask-resist gap, feature size present on masks is often amplified on the resist pattern, a major problem when considering the manufacture of nanopatterned features. When UV light (360-460nm) is utilised, feature resolution using contact mode photolithography has been recorded, at best, as 500nm (Xia et al, 1999). Sub 250nm UV light has been applied to fabricate trenches in plastic cellulose acetate using contact mode photolithography, following embossing of the material with a 60nm dot pattern from an e-beam fabricated quartz master die (Casey et al, 1997). The latent grating pattern measured 310nm in height, with dots presented at the bottom of trenches, suggesting a possible multi-layer application with respect to contact mode photolithography used in conjunction with other fabrication processes. This application highlights the reduction of radiation wavelength resulting in increased pattern resolution, however the gap between the mask and resist ultimately limits possible feature resolution.

With respect to projection mode photolithography, the mask image is reduced (usually by a factor of 4), and projected onto a photoresist using an optical system. This results in significantly smaller features occurring in the resist in comparison to those present on the original mask. As a projection method, problems associated with mask and sample damage occurring in contact mode photolithography due to physical contact between these features do not exist. The spatial depth of the mask is highly accurate and reproducible, and the theoretical resolution of features produced in this manner is limited by Rayleigh diffraction. As a result, reduction of wavelength in this instance will result in reduced feature size. 150nm features have been produced using projection writing in combination with 193nm light from an ArF excimer laser and synthetic fused silica or calcium fluoride lens (Levenson, 1995). However, at present, there is a lack of transparent optical materials suitable for use with wavelengths below 193nm.

Furthermore, damage and distortion of the mask upon exposure to high fluxes of energetic radiation poses a serious problem when using projection printing, as does repairing damaged masks and achieving registration required in multi-level fabrication. As a result, nano-featured pattern production in this manner continues to be expensive.

A further factor, which may be modified to allow for greater resolution of nanofeatures using photolithography, is the photoresist being patterned. Photoresist designs have been critical to the success of photolithography, often improving the speed of patterning and reproducibility of pattern transfer. Resists can be used to image distributions of radiation intensity and may thus offer an alternative, in comparison to conventional photolithography systems, revenue for the advancement of optical designs required in projection printing. Non-linear resists, where 2-photon adsorption is required for activation of a single area, can produce accurate three-dimensional nanofeatures, with spatial resolution of 120nm and fabrication accuracy of 150nm (Kawata, 2001). However, non-linear resists are not appropriate for nanopatterning due to their inability to produce densely packed features, and are believed more relevant in specialised applications, for example micromachining of functional microdevices.

E-beam Lithography

E-beam lithography utilises a focussed electron beam to induce local changes in the solubility of an electron-sensitive resist, for example poly(methyl methacrylate), generally referred to as PMMA, to fabricate nanopatterned surfaces. In the case of PMMA, the electrons effect local chain scissions and the formation of micropores causing material solubility in an appropriate developer (in this instance methyl-isobutyl ketone and 2- propanol). E-beam lithography has an extremely high-resolution capability. 0.5nm focused electron spots were possible in the early development of this technique over 20 years ago, and it is now possible to focus spots of 0.25nm diameter (REF). This due to spherical abberations (personal communication with Prof C. Wilkinson), rather than diffraction of electrons as suggested by some authors. By increasing electron voltage to the 100-300keV range, the range of electrons is also increased prior to backscattering in the substrate material or resist.

When considering the high-resolution aspect of e-beam, the lack of nanopatterns reflecting the aforementioned dimensions would appear as a result of the practical (or perhaps impractical) implications of subsequent fabrication steps, especially when

considering three dimensional in-plane patterns. For example, high aspect silicon pillars with diameters below 10nm have been unsuccessful as a result of metal, plated on e-beam patterned PMMA followed by lift-off, being etched away during reactive ion etching (Chen and Ahmed, 1993). However, the main concern when considering pattern resolution generated by e-beam lithography is the scattering of primary and secondary electrons from the source in the resist film and substrate resulting in lower resolution nanofeatures. Self-assembled monolayers (SAMs) have been utilised in relation to low energy electron-beam lithography due to the thin (1-3nm) layer of SAMs attainable. This method prevents forward scattering of primary electrons and decreased backscattering of electrons (Lercel et al, 1996). This has resulted in features below 10nm being patterned using low energy electron beams, and, due to the limited scattering of electrons in the SAM, resist sensitivity is found to be increased due to more efficient energy deposition occurring as a result. Patterning of SAM of aminosilanes, where amine groups are damaged or removed resulting in these regions of the monolayer being rendered inert, can be coupled with subsequent fabrication processes, for example immersion in a colloidal sol, resulting in further dimensional features of this patterning technique (Harnett et al, 2000).

As e-beam lithography employs a focussed electron beam to pattern substrates in a direct-write manner, this sequential process is deemed impractical for mass production due to lengthy writing times. Thus e-beam is more generally used in the fabrication of master dies (Gadegaard et al, 2003, Gallagher et al, 2002) or in the generations of a limited number of samples for research when considering biological research (Casey et al, 1997).

It is possible to pattern surfaces with nanofeatures using e-beam lithography at present, however this requires shifting of either sample or source beam, and again, due to the serial writing process, is time consuming. Stitching problems may occur, where patterns are unaligned and, due to the quantum mechanical effects dominating in nanosystems, stitching problems may cause great alterations in device function. This is especially troublesome when concerned with cell behaviour in relation to nanotopography if cellular reactions were to occur as a result of undefined stitching defects. Stencil masks and projection optics can be applied to allow exposure of large areas of a substrate to electrons, as previously applied in photolithography, and should reduce writing time. One method, SCALPEL (scattering with angular limitation projection electron

lithography), has demonstrated resolution approaching that of conventional direct-write systems, and is now being developed for mass production of patterned nanostructures. 80nm features have been fabricated using a 4x reduction projection system for electrons in this manner (Gibson, 1997). Large arrays of particle beams from single or multiple sources may also be one avenue of reducing writing time. Another approach has resulted in the fabrication of one nano-dot features on a single exposure by adjusting the focus of the beam on the substrate (Gadegaard et al, 2003) rather than conventional e-beam methods, where multiple beam exposures result in a number of dots composing one feature. Writing time can be reduced using this method, with large area (approximately $1cm^2$) patterning of features as small as 20nm-diameter possible. However, this method is sensitive to system abberations, for instance astigmatism and so the machine must be prepared carefully especially when writing dots of diameter less than 40nm.

Regardless of progress made in patterning nanofeatures over large areas, economically, electron-beam lithography continues to fill a niche within nanotechnology, as due to its as yet unparalleled resolution and reproducibility, e-beam lithography is often used where other methods simply fail.

X-ray Lithography (XLR)

X-ray lithography is often presented as a possible route to reducing wavelength limitations seen in photon-based lithography. Soft x-ray, also termed extreme ultraviolet (EUV), used in a projection manner with reflective optics appears as one method of nanofabrication (Dunn, 1994). Through the use of reflective optics, problems previously associated with the lack of suitable transmitting materials in photolithography is overcome. Yet reflective optics still require further development for the success of this method, as projection and reduction of mask image continues to cause problems. A further approach is proximity XLR using wavelengths of around 1nm, where a mask is placed in close proximity with a substrate without physical contact, which has proven difficult. 30nm structures have been produced using this second method (Cerrina and Marrian, 1996). However, as an emerging technique, much development is still required if XLR is to become a feasible means of producing nanostructured substrates.

Focused Ion Beam Lithography (FIB)

An additional serial technique, focussed ion beam lithography has two distinct advantages in comparison to e-beam lithography. Resist exposure sensitivity is increased in this instance, approximately 2-fold, with negligible ion scattering in resist and very low backscattering of ions from the substrate material. Nevertheless, high-energy ions cause sample damage, which is a distinct disadvantage and may detract from the nanopattern sought. Features measuring 6nm have been fabricated in this manner using 50kV Ga^+ 2-lens systems (Kubena et al, 1991), suggesting further development of this system would result in high resolution feature patterning, especially when considering resist films and repair of defects present in photo and x-ray masks.

Scanning Probes as a means of fabricating nanopatterns

More conventionally used as imaging systems, scanning probe microscopes are being utilised as surface modification instruments due to their atomic resolution capabilities. Most widely used in the fabrication of nanopatterns is the atomic force microscope (AFM). The tip of the AFM has been shown to be capable of scratching nanostructures in soft lithography, expose thin films of resist, induce or enhance oxidation of H-terminated Si(100), alter head-groups or density packing of monolayers and write 30nm patterns of alkanethiols on a gold substrate. Scanning Tunnelling Microscopy has been utilised similarly, altering the structure or order of organic monolayers, oxidizing H-terminated silicon, inducing phase-transition in solid materials and manipulating atoms or molecules. Near-field scanning optical microscope (NSOM) tips have accomplished photoresist film exposure in the nanometric range and Scanning electrochemical microscope (SECM) tips are capable of depositing metals on a substrate.

Scanning probe methods are capable of fabricating features with dimensions averaging a few tenths of a nanometer. However, as seen in techniques using focused beams to fabricate nanopatterns, scanning probe microscopy is a serial technique and is thus slow resulting in master writing rather than mass production of samples. As a physical method of modifying surfaces, projection approaches employed in particle-based nanofabrication are not possible. Yet a fundamentally similar route is being investigated, where parallel arrays of probes, containing thousands of STM tips have been fabricated (Minnie et al, 1996). Although increasing throughput of nanopatterned samples, the accuracy of this approach has yet to be clarified. When considering possible fluctuations in a planar substrate to be patterned, reproducibility of modified

structures is a primary concern. More realistically, single tip-induced alterations to a substrate have been accurate, with greater understanding of molecular interactions of molecules being developed. Thus scanning probe methods of fabricating nanotopographies are likely to be limited to master writing or very specific, small-scale applications.

Electrically Neutral Metastable Atoms

The most obvious advantage of this type of fabrication process is the lack electrostatic interactions occurring between atoms. As a result however, the neutrality of these particles requires the development of optics based on light forces if projection methods are to be used, resulting in the commercial appeal of this method. To-date, 50nm features have been fabricated in a single step, using stencil masks, over large areas and using a directed deposition technique with light-force lenses, 70nm features have been achieved. This suggests further development of nanopatterning using electrically neutral metastable atoms, with special consideration of optical requirements, will result in a successful, applicable method in the future.

Soft Lithography

Often referred to as replication technologies, soft lithography techniques, for example micro-contact printing (μCP), moulding, embossing and near-field confocal photolithography, employ patterned elastomer stamps or a master die, as a mask, mould or stamp to generate pattern transfer. As replication techniques, initial high cost master dies are reproducible in mass numbers using an array of materials, generally polymeric, over large areas. When considering for example micro-contact printing, where an elastomer stamp is utilised during pattern transfer, non-planar substrates can be patterned although alterations in stamp pattern dimensions must firstly be taken into consideration. Furthermore, for biological applications, many soft lithography techniques have been successfully applied in the patterning of proteins and cells (Kane et al, 1999).

Replica Moulding (REM)

An elastomeric stamp cast against a rigid master is firstly produced, against which new replicas are moulded. A single master can be used repeatedly, upwards of 100 times (personal communication with M. Riehle) to create replicas, with replicas also being used in this manner. When considering elastomeric materials in this type of

arrangement, problems regarding reproducibility are constantly brought into question due to the characteristic non-rigid properties of such material. The situation in which elastomeric stamps are placed has great bearing upon the pattern exhibited during replication and, thus, must be assessed *in situ*. However, the ability of elastomers to adapt to their environment results in small, fragile features being preserved from master die to stamp. PDMS is one material that is frequently used in stamp production. Low surface energy of organic polymers, especially PDMS, allows easy separation of the replica and mould, limiting deformation of the transferred pattern. Mechanical and thermal deformation of moulds is often applied to alter nanopattern dimensions intentionally, but can also result in unwanted alterations if unintentionally occurring.

Replication of moulds from the master is very accurate and reproducible. Problems mainly result when reproducing patterned substrates from the mould. However, if alterations are limited, multiple copies of indistinguishable nanostructures can be produced rapidly and economically from a single master (Xia et al, 1999). Further investigation is required with respect to control of pattern distortions and also development of registration if multi-level fabrication is to be practised.

Micro-contact Printing (μCP)

Micro-contact printing involves the production of an elastomeric stamp from a patterned master, which is subsequently inked with an appropriate solution, for example a protein or alkanethiol and brought into contact with a surface, transferring molecules to regions of the substrate in contact with the stamp in the desired pattern. Of fundamental importance during this procedure is the conformational contact between the stamp and base substrate surface due to the often rapid formation of highly ordered self-assembled monolayers, as is the case when utilising an alkanethiol. The autophobicity of the self-assembled monolayer is also critical, as it acts to block the reactive spreading of transferred molecules across the surface. With respect to SAMs, in particular aminosilanes, controlled coverage of functional groups can also be achieved in unison with pattern transfer (He et al, 2000).

Self-assembled monolayers can be transferred from stamp to substrate surface over large areas using micro-contact printing. Due to the elastomeric properties of the stamp, patterning can be applied to curved surfaces suggesting possible success of this technique with respect to 3-D fabrication. Similarly, the non-rigid properties of the

stamp allow patterning of inner surfaces unachievable with projection lithography methods.

Pattern resolution when using micro-contact printing is, however, limited. High resolution, in-plane patterning of "pancake" structures has been achieved to approximately 80nm, where octadecyltrichlorosilane (OTS), was used to ink an elastomer stamp, and the resultant pattern was subsequently wet etched (Wang et al, 1997). However, transfer of sub-100nm patterns using microcontact printing continues to be difficult. Edge roughness of hexadecanethiolate printed on gold, of less than 50nm, has been demonstrated using lateral force microscopy (LFM) by Xia and co-workers (1999). Micro-contact printing has the ability to produce patterns with lateral dimensions below 100nm, however this is likely to be based on the molecular weight and subsequent branching of applied molecules (He et al, 2000). When employed in the patterning of proteins, grating patterns in the micrometric scale (>10μm) have been fabricated, but have resulted in possible altered conformation of the applied molecules (Magnani et al, 2003). Protein layers have been successfully patterned using modified microcontact printing techniques. For example, a thin stamp of PDMS can firstly be treated in a low temperature plasma cleaner under oxygen to increase hydrophilicity of the stamp, and backed with a glass slide to increase rigidity of the stamp, preventing recessed areas from collapsing (James et al, 1997).

As with many of the fabrication techniques discussed within this section, further modification of patterned substrates can be applied to further develop the required nanopattern. In the case of alkanethiol patterning, self-assembled monolayers can be used as resists in selective wet etching (Wang et al, 1997) or as templates during selective deposition of colloids for instance (He et al, 2000), forming topographic structures composed of a variety of materials. Furthermore, μCP avoids the use of strong acids and bases required in other patterning techniques, for example photolithography, allowing a non-destructive method of patterning proteins and other biological materials (James et al, 1998).

Solvent-assisted Micro-moulding (SAMIM) and Casting

Once again, an elastomeric mould is cast from a master die, which is then used to create relief structures in polymeric materials when using solvent-assisted micro-moulding. A solvent is firstly added to the surface of the mould to "soften" the polymer being

applied, allowing for movement of the polymer to fit the pattern features of the mould during replication. It is important that solvent, which will dissolve the polymer and not the mould is selected, so that feature dimensions present on the mould are preserved and replicated accordingly. Casting is a term more generally used when applying a polymer/solvent suspension directly onto a master die. Both mould and polymer are left to set, where the solvent evaporates or dissipates, following which these structures are removed from one another, with the patterned, relief nanostructure on the polymeric material complementing the original design presented on the mould.

Many different types of polymers can be replicated in this manner, which are mixed with a relatively volatile solvent capable of dissolving the chosen substrate while only wetting, and not deforming, the patterned mould. Other materials may also be added to the solvent resulting in their incorporation in the final structure. SAMIM is also capable of creating 3-D structures over large areas in a single step. Parallel lines have been achieved through the utilisation of this technique, with dimensions approximating 60nm wide and 50nm high. Due to the nature of the process, where solvent-suspended polymers are added to the surface of a mould and left to set, both SAMIM and casting are "self-cleaning" techniques, where dust and other contaminating particles tend to by incorporated within the relief polymeric structure. This results in a clean mould being presented to each new polymer substrate, limiting the influence of particulates in each cycle. The main area of concern with SAMIM is the possible pattern alterations occurring at the surface of the mould due to wetting and physical damage, as is the case with respect to the master die used during casting.

Embossing with a rigid master

A master, for use with embossing techniques, is generally fabricated in silica or nickel by electroplating of a master die generally in quartz, and is referred to as a shim (Gadegaard et al, 2003). The shim is then used to imprint a relief pattern into a thermoplastic polymer, for example PMMA, polycarbonate or poly caprolactone (PCL), (Gallagher et al, 2002). Chou and co-workers have embossed silicon using a silicon shim with silica oxide layer, generating features with lateral dimensions measuring approximately 25nm over areas as large as $3cm^2$ (Chou et al, 1996). The possibility of generating pattern transfer between rigid structures, and the success of this demonstrated method implies that a great many materials can be used with embossing replication, especially when considering the problems associated with contact mode

photolithography. Hot embossing lithography (HEL) is also emerging as a promising technique with respect to in-plane nanopattern fabrication, with sub-100nm lateral resolution of features (Schift et al, 2001).

The success of nanopattern transfer utilising this method suggests existing microfabrication techniques offer transferable skills with respect to nanopatterning. As seen in solvent-assisted micro-moulding, casting and similar methods of replication from a master, issues regarding damage to mask, in this instance while under pressure, release of material being embossed and distortion in the final replicate, due to thermal cycling during embossing, remain to be defined. This method of relief nanopatterning is once again self-cleaning, simple, cost-effective, high throughput and accurate, and is currently applied in the manufacture of holograms, diffraction gratings and compact discs.

Near-field Phase-shift Photolithography (NSOM)

Narrow, subwavelength sources of light that can approach within 10nm of a resist surface as a scanned beam are applied in near-field phase-shift photolithography. Problems associated with conventional photolithography techniques are overcome through the employment of an organic elastomeric polymer mask, as opposed to a conventional rigid mask. These soft masks contact photoresist-coated substrates non-destructively, in a conformable, atomic-level manner over areas of many hundreds of cm^2. Thus, as previously seen when using conventional, rigid masks for photolithography, problems, for example mask and resist damage, are removed. Furthermore, the gap between the mask and resist is completely eliminated as is the previous issue of light diffraction occurring in the photoresist as a result of gaps using contact mode photolithography. The atomic-level contact established between the elastomeric mask and substrate allows for resist exposure to occur directly in the near-field of the mask, resulting in the possible fabrication of features measuring approximately 50nm. The flexible nature of the mask also allows for contact to be established, to a certain degree, over non-planar areas, suggesting the possible application of NSOM to curved substrates, for example implant surfaces.

Improvement of feature resolution generated using NSOM may be possible by reducing the wavelength of light, resist thickness, modulation component thickness and the

production of improved surface-sensitive resists (Xia et al, 1999). Patterns generated using this method are however limited. With simple binary phase masks, grating patterns are possible, with a more varied range of feature design described when using amplitude modulation components or altering feature sizes on mask which are less than or equal to the wavelength of exposure light (Schmidt et al). The two fundamental limitations of NSOM occur as lateral distortions of the elastomer when conformable contact is established, and vertical distortions resulting in slackening of recessed areas of the pattern present in the mask. However, near-field phase-shift photolithography continues to present a method of rapid, low-cost nanopatterning over large areas, which is of considerable use when considering biological experiments where a population of microscopic cells will cover a macrometric surface area of a substrate.

Size Reduction

The ability to reduce feature sizes created using conventional microlithography techniques is advantageous due to the success of these fabrication methods being implemented in the initial stages of nanopattern production. Through the production of accurate micrometric lithography across large areas, subsequent fabrication techniques can be applied to substrates, resulting in the final pattern reflecting nanometric features. A number of methods can be applied in size reduction, and are mainly associated with etching techniques, both isotropic, or dry etching, and anisotropic, or wet etching. This is a cost-effective strategy in relation to nanostructure manufacturing, as access to high-resolution techniques is not required.

Isotropic Deformation

Two main approaches exist when deforming microstructures resulting in nanometric pattern dimension. Physical isotropic deformation or shrinkage of amorphous substrate materials results in reduction of initial micrometric feature dimensions. For example, PDMS moulds can be compressed, effecting size reduction in one or two planes of the substrate features, resulting in an increase in dimension of the other two, or one, dimensions(s). If the substrate is constructed in an elastomeric material, this type of mechanical deformation is reversible thus feature size can continually be adjusted through controlling material deformation. However, uniformity of applied mechanical forces during this procedure are often difficult to control due to the three-dimensional nature of the substrate, and uniform feature size occurring across the surface relies upon

uniform distortion throughout the material. As a result, the level of uniformity of forces required when patterning sub-100nm features in this manner may prove difficult.

Anisotropic Etching

Lateral dimensions of a micropattern can be altered when utilising anisotropic etching methods, where features can be continuously reduced as etching time proceeds. Most fabricated surfaces produced in this manner are generally simple grooved patterns expressing initially linear micrometric topography. Furthermore, as with many of these fabrication techniques, anisotropic etching is generally combined with other techniques.

Appendix II

Percentage area coverage of both 20nm and 50nm diameter colloids calculated across $500nm^2$ and $1\mu m^2$ area respectively. Percentage area coverage over 12 randomly selected areas of the images was calculated utilising SEM micrographs, Figures 3.2 and 3.3 for 20nm- and 50nm-diamerter colloids respectively. Mean percentage area coverage and Standard Deviation were calculated using this data. The technique utilised and results are discussed in Section 3.2.1.1.1.

Frame Number	Number of beads per $500nm^2$	Area covered by colloids (nm^2) = Number of colloids(πr^2)	Area not covered by beads in $500nm^2$ test area (nm^2)	% Area coverage of colloids
1	40	12566.371	237433.629	5.027%
2	44	13823.008	236176.992	5.529%
3	47	14765.485	235234.515	5.906%
4	42	13194.689	236805.311	5.278%
5	42	13194.689	236805.311	5.278%
6	40	12566.371	237433.629	5.027%
7	37	11623.893	238376.107	4.650%
8	37	11623.893	238376.107	4.650%
9	38	11938.052	238061.948	4.775%
10	42	13194.689	236805.311	5.278%
11	38	11938.052	238061.948	4.775%
12	43	13508.848	236491.152	5.404%
			Mean	5.13%
			Standard Deviation	0.00385676

Data for 6* (15 minute) immersion of substrate in 20nm-diameter colloidal sol, Figure 3.2a).

Frame Number	Number of beads per $500nm^2$	Area covered by colloids (nm^2) = Number of colloids(πr^2)	Area not covered by beads in $500nm^2$ test area (nm^2)	% Area coverage of colloids
1	39	12252.212	237747.879	4.901%
2	40	12566.371	237433.629	5.027%
3	44	13823.008	236176.992	5.529%
4	41	12880.530	237119.470	5.152%
5	38	11938.052	238061.948	4.775%
6	36	11309.734	238690.266	4.524%
7	40	12566.371	237433.629	5.027%
8	44	13823.008	236176.992	5.529%
9	39	12252.212	237747.879	4.901%
10	42	13194.689	236805.311	5.278%
11	42	13194.689	236805.311	5.278%
12	39	12252.121	237747.879	4.901%
			Mean	5.07%
			Standard Deviation	0.00299865

Data for 24-hour immersion of substrate in 20nm-diameter colloidal sol, Figure 3.2b).

Frame Number	Number of beads per $1\mu m^2$	Area covered by colloids (nm^2) = Number of colloids(πr^2)	Area not covered by beads in $1\mu m^2$ test area (nm^2)	% Area coverage of colloids
1	33	64795.349	935204.652	6.48%
2	31	60868.358	939131.642	6.09%
3	30	58904.862	941095.138	5.89%
4	28	54977.871	945022.129	5.50%
5	28	54977.871	945022.129	5.50%
6	35	68722.339	931277.661	6.87%
7	33	64795.349	935204.652	6.48%
8	30	58904.862	941095.138	5.89%
9	38	74612.826	925387.174	7.46%
10	22	43196.900	956803.100	4.32%
11	31	60868.358	939131.642	6.09%
12	33	64795.349	935204.652	6.48%
			Mean	6.09%
			Standard Deviation	0.00789167

Data for 4* (15 minute) immersion of substrate in 50nm-diameter colloidal sol, Figure 3.3a).

Frame Number	Number of beads per $1\mu m^2$	Area covered by colloids (nm^2) = Number of colloids(πr^2)	Area not covered by beads in $1\mu m^2$ test area (nm^2)	% Area coverage of colloids
1	35	68722.339	931277.661	6.87%
2	34	66758.844	933241.156	6.68%
3	39	76576.321	923423.679	7.66%
4	41	80503.312	919496.688	8.05%
5	36	70685.835	929314.165	7.07%
6	37	72649.330	927350.670	7.26%
7	28	54997.871	945022.129	5.50%
8	33	64795.349	935204.652	6.48%
9	39	76576.321	923423.679	7.66%
10	36	70685.835	929314.165	7.07%
11	38	74612.826	925387.174	7.46%
12	40	78539.816	921460.184	7.85%
			Mean	7.13%
			Standard Deviation	0.00701226

Data for 6* (15 minute) immersion of substrate in 50nm-diameter colloidal sol, Figure 3.3b).

Appendix III

Original data collected with respect to the number of hTERT fibroblasts adhering to planar, 20nm-diameter and 50nm-diameter colloidal topographies at 20 minutes, 1 hour and 3 hours. Thirty non-specific fields of view of the cells on the substrate were used to calculate the number of cells within a $0.93mm^2$ area of the surface, and recorded as shown below. Data was used to identify statistical similarities between the number of fibroblasts adhering to the different substrates at the three time points using two-way ANOVA, Table 3.5. Time, topography and the interactions of time and topography and their effects on fibroblast adhesion were investigated, Section 3.3.3.2.

20 minutes			*1 hour*			*3 hours*		
Planar	20nm-diameter colloids	50nm-diameter colloids	Planar	20nm-diameter colloids	50nm-diameter colloids	Planar	20nm-diameter colloids	50nm-diameter colloids
24	92	77	33	69	134	50	78	34
23	45	41	57	48	60	42	38	34
24	33	37	55	44	43	51	38	29
34	24	47	54	93	51	18	55	28
47	43	53	28	29	35	56	37	37
17	87	120	47	47	60	38	36	32
22	43	49	34	54	62	38	28	36
29	72	32	26	36	31	38	43	32
41	22	68	76	39	35	38	39	36
24	45	35	36	40	90	36	38	46
34	53	83	61	77	36	49	49	26
69	49	83	59	65	34	38	28	41
35	112	31	37	53	40	46	26	27
33	49	39	37	47	57	43	30	34
32	26	22	36	40	76	44	36	52
23	75	28	29	45	39	40	41	48
22	57	20	51	39	38	38	38	33
40	51	50	37	37	33	32	18	35
68	38	52	30	42	92	41	33	31
25	32	66	24	53	53	38	42	34
36	30	61	23	57	36	38	37	39
25	34	35	64	44	38	37	47	52
25	62	39	49	52	56	35	46	36
27	37	33	31	41	30	31	23	36
22	109	50	41	42	114	44	32	36
25	48	46	38	96	26	36	41	32
40	38	55	47	71	123	38	31	36
39	99	27	50	46	33	46	44	31
56	23	46	76	52	48	36	59	46
29	50	96	37	88	24	31	36	48

Appendix IV

Descriptive statistics and distribution histogram of the original data collected with respect to the number of hTERT fibroblasts adhering to planar, 20nm-diameter and 50nm-diameter colloidal topographies at 20 minutes, 1 hour and 3 hours as listed in Appendix III. Note the standard deviation for the descriptive statistics varies from that calculated in the contingency table, Table 3.5, as discussed in Section 3.3.3.2.

Planar @ 20 minutes

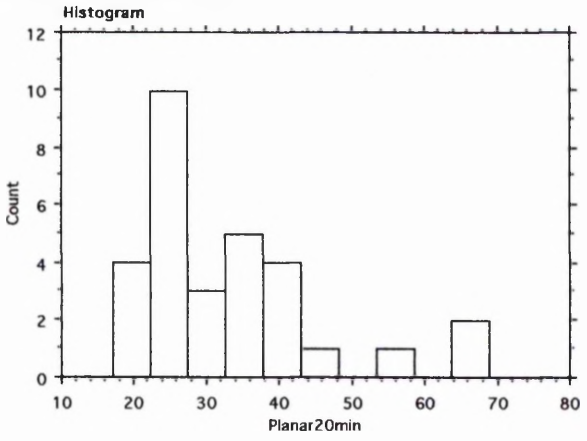

Descriptive Statistics

	Planar20min
Mean	33.000
Std. Dev.	12.927
Std. Error	2.360
Count	30
Minimum	17.000
Maximum	69.000
# Missing	0
Variance	167.103
Coef. Var.	.392
Range	52.000
Sum	990.000
Sum Squares	37516.000
Geom. Mean	31.037
Harm. Mean	29.463
Skewness	1.481
Kurtosis	1.696
Median	29.000
IQR	15.000
Mode	25.000
10% Tr. Mean	30.667
MAD	6.000

Planar @ 1 hour

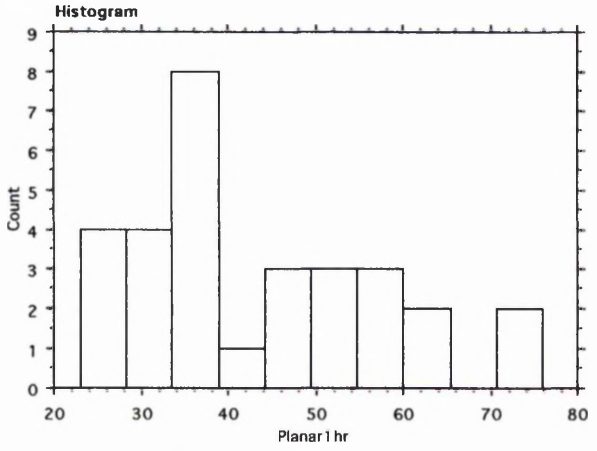

Descriptive Statistics

	Planar1hr
Mean	43.433
Std. Dev.	14.469
Std. Error	2.642
Count	30
Minimum	23.000
Maximum	76.000
# Missing	0
Variance	209.357
Coef. Var.	.333
Range	53.000
Sum	1303.000
Sum Squares	62665.000
Geom. Mean	41.230
Harm. Mean	39.186
Skewness	.659
Kurtosis	-.353
Median	37.500
IQR	21.000
Mode	37.000
10% Tr. Mean	42.250
MAD	9.500

Planar @ 3 hours

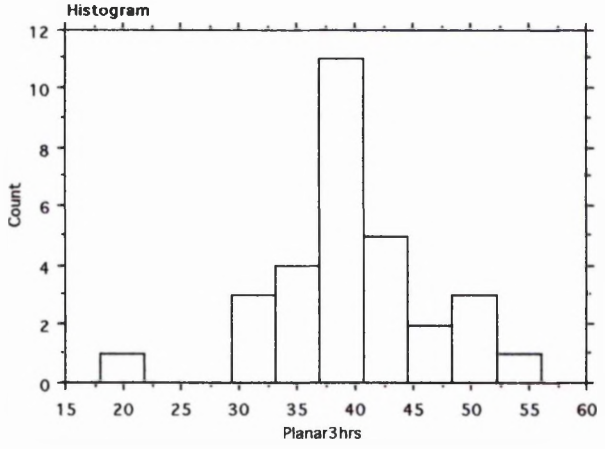

Descriptive Statistics

	Planar3hrs
Mean	39.533
Std. Dev.	7.186
Std. Error	1.312
Count	30
Minimum	18.000
Maximum	56.000
# Missing	0
Variance	51.637
Coef. Var.	.182
Range	38.000
Sum	1186.000
Sum Squares	48384.000
Geom. Mean	38.819
Harm. Mean	37.958
Skewness	-.301
Kurtosis	1.617
Median	38.000
IQR	8.000
Mode	38.000
10% Tr. Mean	39.542
MAD	3.000

20nm-diameter colloids @ 20 minutes

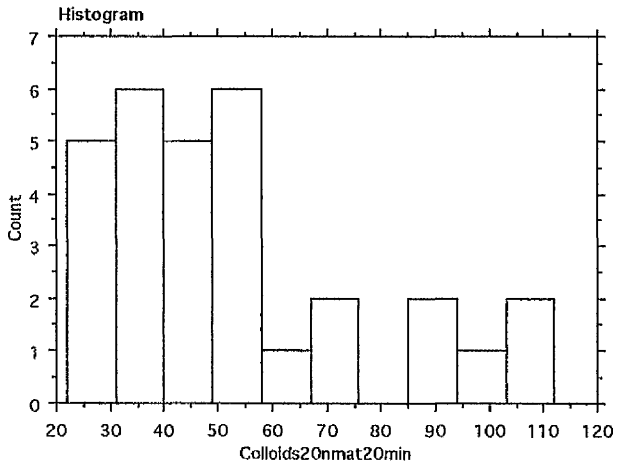

Descriptive Statistics

	Colloids20nmat20min
Mean	52.600
Std. Dev.	25.334
Std. Error	4.625
Count	30
Minimum	22.000
Maximum	112.000
# Missing	0
Variance	641.834
Coef. Var.	.482
Range	90.000
Sum	1578.000
Sum Squares	101616.000
Geom. Mean	47.466
Harm. Mean	43.131
Skewness	1.006
Kurtosis	.040
Median	46.500
IQR	28.000
Mode	.
10% Tr. Mean	49.542
MAD	13.000

20nm-diameter colloids @ 1 hour

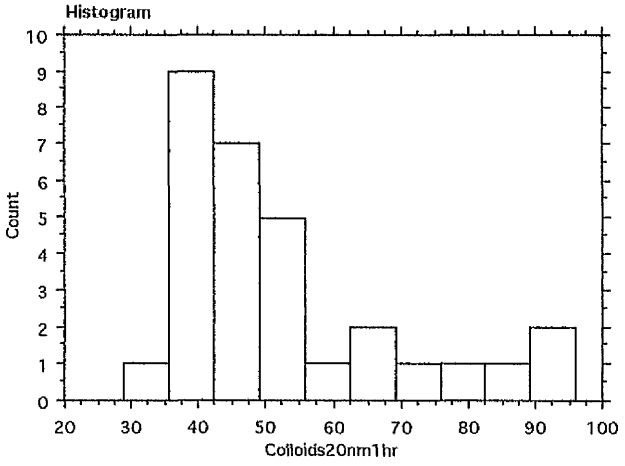

Descriptive Statistics

	Colloids20nm1hr
Mean	52.867
Std. Dev.	17.222
Std. Error	3.144
Count	30
Minimum	29.000
Maximum	96.000
# Missing	0
Variance	296.602
Coef. Var.	.326
Range	67.000
Sum	1586.000
Sum Squares	92448.000
Geom. Mean	50.560
Harm. Mean	48.613
Skewness	1.204
Kurtosis	.561
Median	47.000
IQR	16.000
Mode	.
10% Tr. Mean	50.292
MAD	7.000

20nm-diameter colloids @ 3 hours

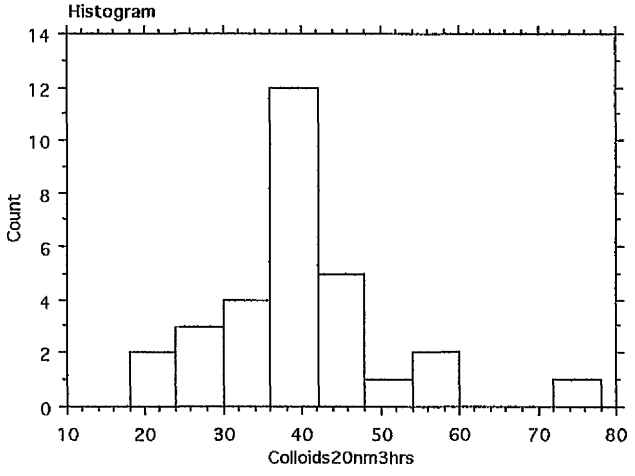

Descriptive Statistics

	Colloids20nm3hrs
Mean	38.900
Std. Dev.	11.484
Std. Error	2.097
Count	30
Minimum	18.000
Maximum	78.000
# Missing	0
Variance	131.886
Coef. Var.	.295
Range	60.000
Sum	1167.000
Sum Squares	49221.000
Geom. Mean	37.405
Harm. Mean	35.958
Skewness	1.263
Kurtosis	2.969
Median	38.000
IQR	11.000
Mode	38.000
10% Tr. Mean	37.833
MAD	5.500

50nm-diameter colloids @ 20 minutes

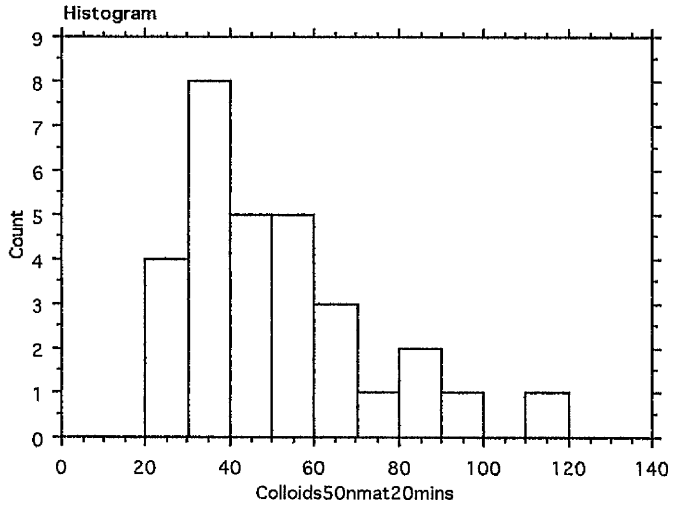

Descriptive Statistics

	Colloids50nmat20mins
Mean	50.700
Std. Dev.	22.971
Std. Error	4.194
Count	30
Minimum	20.000
Maximum	120.000
# Missing	0
Variance	527.666
Coef. Var.	.453
Range	100.000
Sum	1521.000
Sum Squares	92417.000
Geom. Mean	46.338
Harm. Mean	42.530
Skewness	1.184
Kurtosis	1.203
Median	46.500
IQR	26.000
Mode	.
10% Tr. Mean	48.042
MAD	12.500

50nm-diameter colloids @ 1 hour

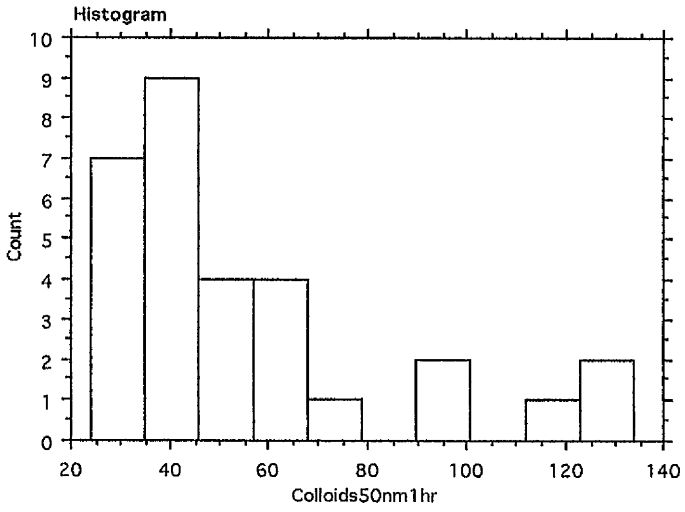

Descriptive Statistics

	Colloids50nm1hr
Mean	54.233
Std. Dev.	29.169
Std. Error	5.325
Count	30
Minimum	24.000
Maximum	134.000
# Missing	0
Variance	850.806
Coef. Var.	.538
Range	110.000
Sum	1627.000
Sum Squares	112911.000
Geom. Mean	48.446
Harm. Mean	44.206
Skewness	1.427
Kurtosis	1.087
Median	41.500
IQR	25.000
Mode	.
10% Tr. Mean	49.000
MAD	11.000

50nm-diameter colloids @ 3 hours

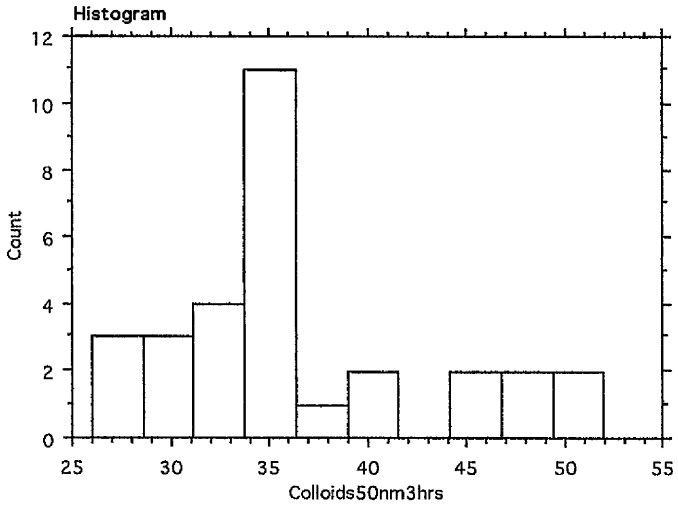

Descriptive Statistics

	Colloids50nm3hrs
Mean	36.567
Std. Dev.	7.055
Std. Error	1.288
Count	30
Minimum	26.000
Maximum	52.000
# Missing	0
Variance	49.771
Coef. Var.	.193
Range	26.000
Sum	1097.000
Sum Squares	41557.000
Geom. Mean	35.954
Harm. Mean	35.385
Skewness	.825
Kurtosis	-.164
Median	35.500
IQR	7.000
Mode	36.000
10% Tr. Mean	36.000
MAD	3.500

Appendix V

Descriptive statistics and distribution histogram of the original data collected with respect to the number of hTERT fibroblasts adhering to planar, 200nm planar etched and 20nm-diameter, 200nm-high pillared topographies at 20 minutes, 1 hour and 3 hours.

Planar @ 20 minutes

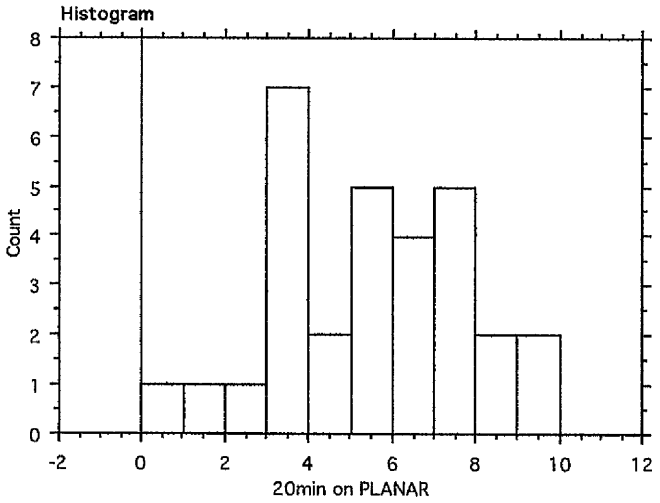

Descriptive Statistics

	20min on PLANAR
Mean	5.033
Std. Dev.	2.371
Std. Error	.433
Count	30
Minimum	0.000
Maximum	10.000
# Missing	0
Variance	5.620
Coef. Var.	.471
Range	10.000
Sum	151.000
Sum Squares	923.000
Geom. Mean	•
Harm. Mean	•
Skewness	-8.682E-3
Kurtosis	-.512
Median	5.000
IQR	4.000
Mode	3.000
10% Tr. Mean	5.042
MAD	2.000

Planar @ 1 hour

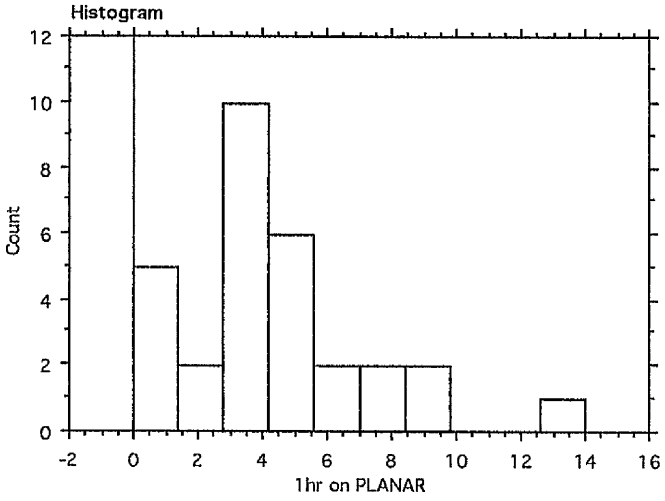

Descriptive Statistics

	1hr on PLANAR
Mean	4.367
Std. Dev.	2.988
Std. Error	.546
Count	30
Minimum	0.000
Maximum	14.000
# Missing	0
Variance	8.930
Coef. Var.	.684
Range	14.000
Sum	131.000
Sum Squares	831.000
Geom. Mean	•
Harm. Mean	•
Skewness	1.207
Kurtosis	1.859
Median	4.000
IQR	2.000
Mode	3.000
10% Tr. Mean	4.042
MAD	1.000

Planar @ 3 hours

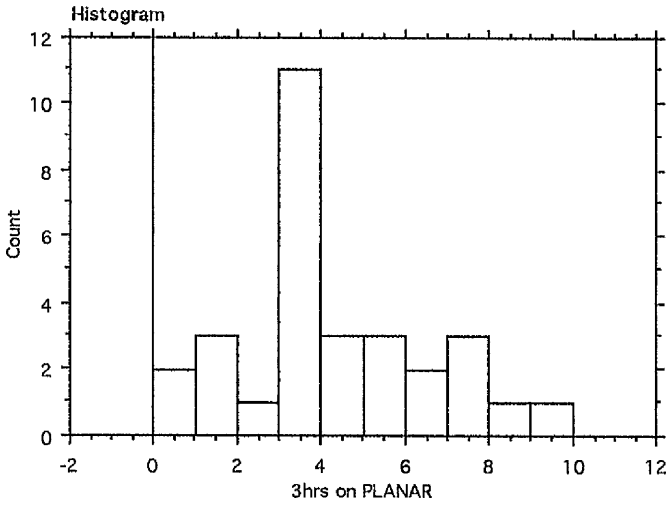

Descriptive Statistics

	3hrs on PLANAR
Mean	3.867
Std. Dev.	2.374
Std. Error	.433
Count	30
Minimum	0.000
Maximum	10.000
# Missing	0
Variance	5.637
Coef. Var.	.614
Range	10.000
Sum	116.000
Sum Squares	612.000
Geom. Mean	•
Harm. Mean	•
Skewness	.570
Kurtosis	.043
Median	3.000
IQR	2.000
Mode	3.000
10% Tr. Mean	3.750
MAD	1.500

Planar etched @ 20 minutes

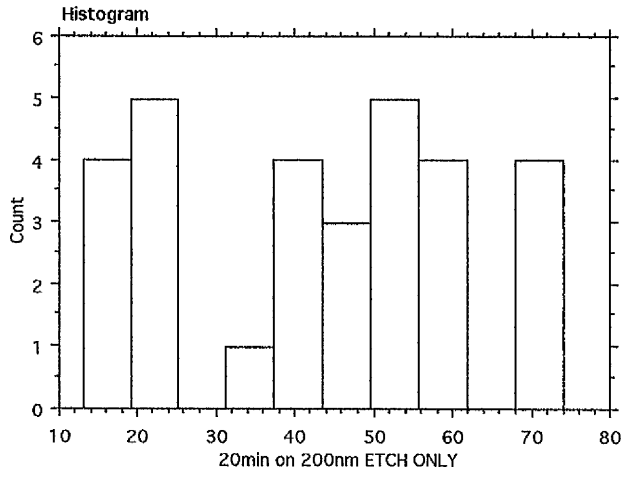

Descriptive Statistics

	20min on 200nm ETCH ONLY
Mean	42.767
Std. Dev.	18.504
Std. Error	3.378
Count	30
Minimum	13.000
Maximum	74.000
# Missing	0
Variance	342.392
Coef. Var.	.433
Range	61.000
Sum	1283.000
Sum Squares	64799.000
Geom. Mean	38.172
Harm. Mean	33.187
Skewness	-.071
Kurtosis	-1.066
Median	45.000
IQR	34.000
Mode	.
10% Tr. Mean	42.417
MAD	11.000

Planar etched @ 1 hour

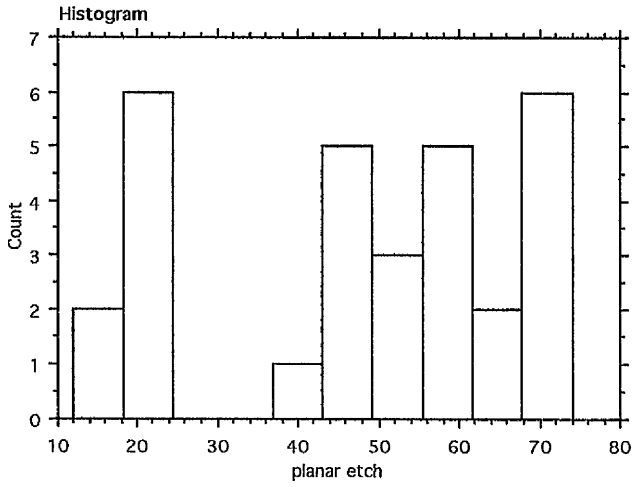

Descriptive Statistics

	planar etch
Mean	47.033
Std. Dev.	19.646
Std. Error	3.587
Count	30
Minimum	12.000
Maximum	74.000
# Missing	0
Variance	385.964
Coef. Var.	.418
Range	62.000
Sum	1411.000
Sum Squares	77557.000
Geom. Mean	41.880
Harm. Mean	35.869
Skewness	-.396
Kurtosis	-1.154
Median	53.000
IQR	41.000
Mode	58.000
10% Tr. Mean	47.667
MAD	13.000

Planar etched @ 3 hours

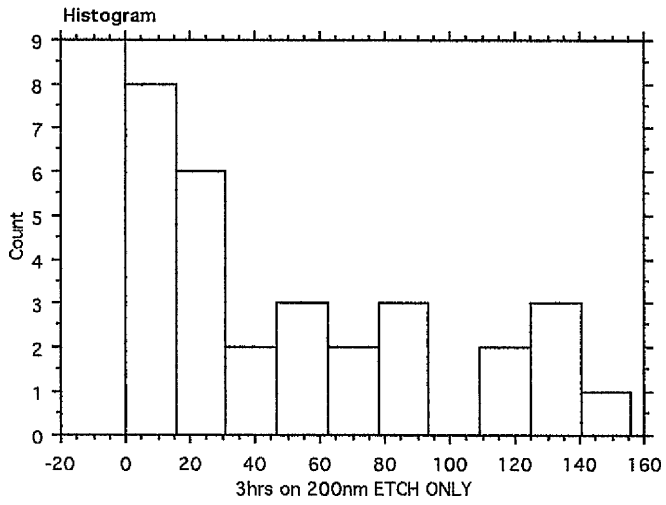

Descriptive Statistics

	3hrs on 200nm ETCH ONLY
Mean	53.133
Std. Dev.	46.585
Std. Error	8.505
Count	30
Minimum	0.000
Maximum	156.000
# Missing	0
Variance	2170.120
Coef. Var.	.877
Range	156.000
Sum	1594.000
Sum Squares	147628.000
Geom. Mean	.
Harm. Mean	.
Skewness	.707
Kurtosis	-.750
Median	34.500
IQR	69.000
Mode	.
10% Tr. Mean	48.542
MAD	29.000

20nm-diameter, 200nm-high nanopillars @ 20 minutes

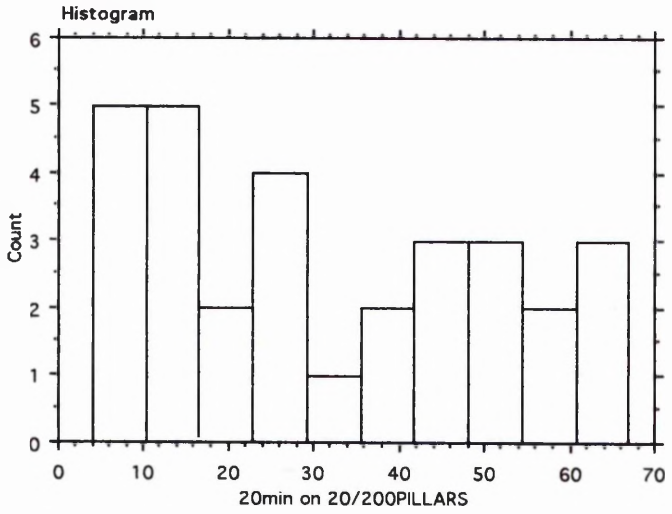

Descriptive Statistics

	20min on 20/200PILLARS
Mean	31.533
Std. Dev.	20.649
Std. Error	3.770
Count	30
Minimum	4.000
Maximum	67.000
# Missing	0
Variance	426.395
Coef. Var.	.655
Range	63.000
Sum	946.000
Sum Squares	42196.000
Geom. Mean	23.497
Harm. Mean	15.680
Skewness	.246
Kurtosis	-1.306
Median	27.000
IQR	40.000
Mode	11.000
10% Tr. Mean	30.750
MAD	16.000

20nm-diameter, 200nm-high nanopillars @ 1 hours

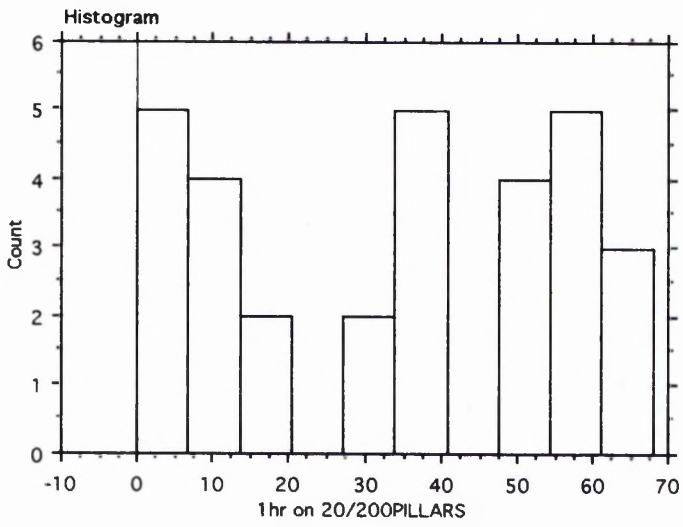

Descriptive Statistics

	1hr on 20/200PILLARS
Mean	34.167
Std. Dev.	22.102
Std. Error	4.035
Count	30
Minimum	0.000
Maximum	68.000
# Missing	0
Variance	488.489
Coef. Var.	.647
Range	68.000
Sum	1025.000
Sum Squares	49187.000
Geom. Mean	.
Harm. Mean	.
Skewness	-.117
Kurtosis	-1.439
Median	35.000
IQR	44.000
Mode	.
10% Tr. Mean	34.250
MAD	22.500

20nm-diameter, 200nm-high nanopillars @ 3 hours

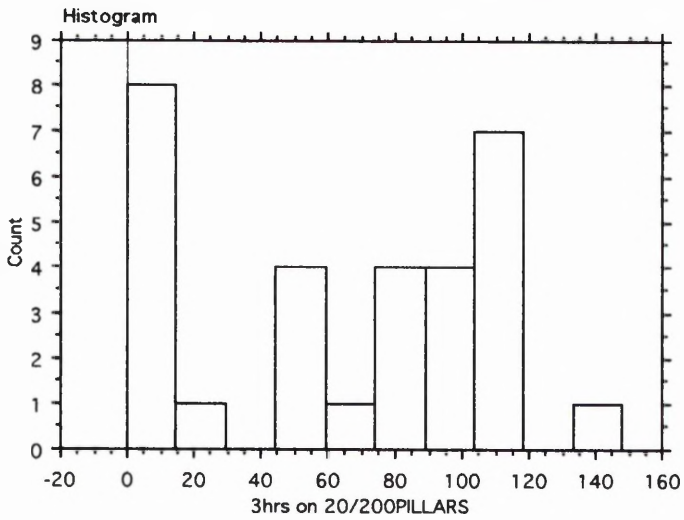

Descriptive Statistics

	3hrs on 20/200PILLARS
Mean	65.500
Std. Dev.	45.558
Std. Error	8.318
Count	30
Minimum	0.000
Maximum	148.000
# Missing	0
Variance	2075.569
Coef. Var.	.696
Range	148.000
Sum	1965.000
Sum Squares	188899.000
Geom. Mean	.
Harm. Mean	.
Skewness	.211
Kurtosis	-1.290
Median	78.000
IQR	96.000
Mode	114.000
10% Tr. Mean	66.125
MAD	34.000

Appendix VI

Data for the number of cells adhering to planar, planar etched and nanopillared topographies were used to construct a contingency table. Homogeneity of variance, F_{max}, must lie between 4.24 and 3.21 for 9 samples where degrees of freedom=29 if parametric tests are to be used. This is calculated by dividing the largest sample variance, outlined in red, by the smallest, outlined in blue. This value was 386.037 for original data, thus a parametric test can not be used on this data in its present state. Data can be transformed, Appendix VII, and homogeneity of variance calculated. If F_{max} lies within the required values, a parametric test can be used. However, even following transformation of the data, variance was not homogenous thus a non-parametric test, the Kruskal-Wallis test, was used to identify differences between the number of fibroblasts adhering to planar, planar etched and nanopillared substrates using sample medians. The contingency table below outlines the number of observations per sample, n, mean, X, standard deviation, s, sample variance, s^2, sum of variations, $\sum x$, the square of the sum, $(\sum x)^2$, and the sum of squares of the deviations, $\sum x^2$. Subtotals for each column and row are in bold, with the final totals in the bottom right cell.

Variable B: Surface Topography				
	Planar Situation 1 Column 1	*Etched Planar* Situation 2 Column 2	*Nanopillared* Situation 3 Column 3	**Total for Row**
20 minutes Row 1	n = 30 X= 5.033 s = 2.371 s^2= 5.62164 $\sum x$=151 $(\sum x)^2$=22801 $\sum x^2$=923	n = 30 X= 42.767 s = 18.504 s^2= 342.398 $\sum x$=1283 $(\sum x)^2$=1646089 $\sum x^2$=64799	n = 30 X= 31.533 s = 20.649 s^2= 426.3812 $\sum x$=946 $(\sum x)^2$=894916 $\sum x^2$=42196	**n_t = 90** **$\sum x_t$= 2380** **$\sum x^2_t$= 107918**
1 hour Row 2	n = 30 X= 4.367 s = 2.988 s^2= 8.92814 $\sum x$= 131 $(\sum x)^2$=17161 $\sum x^2$=831	n = 30 X= 47.033 s = 19.646 s^2= 385.9653 $\sum x$=1411 $(\sum x)^2$=1990921 $\sum x^2$=77557	n = 30 X= 34.167 s = 22.102 s^2= 488.4984 $\sum x$=1025 $(\sum x)^2$=1050625 $\sum x^2$=49187	**n_t = 90** **$\sum x_t$= 2567** **$\sum x^2_t$= 127575**
3 hours Row 3	n = 30 X= 3.867 s = 2.374 s^2= 5.63587 $\sum x$=116 $(\sum x)^2$=13456 $\sum x^2$=612	n = 30 X= 53.133 s = 46.585 s^2= 2170.16 $\sum x$= 1594 $(\sum x)^2$= 2540836 $\sum x^2$=147628	n = 30 X= 65.5 s = 45.558 s^2= 2075.531 $\sum x$= 1965 $(\sum x)^2$=3861225 $\sum x^2$=188899	**n_t = 90** **$\sum x_t$= 3675** **$\sum x^2_t$= 337139**
Total for Column	**n_t = 90** **$\sum x_t$= 398** **$\sum x^2_t$= 2366**	**n_t = 90** **$\sum x_t$= 4288** **$\sum x^2_t$= 289984**	**n_t = 90** **$\sum x_t$= 3936** **$\sum x^2_t$= 280282**	***n_T = 270*** ***$\sum x_T$= 8622*** ***$\sum x^2_T$= 572632***

Appendix VII

Original data collected with respect to the number of hTERT fibroblasts adhering to planar, planar etched and 20nm-diameter, 200nm-high nanopillared topographies at 20 minutes, 1 hour and 3 hours. Thirty non-specific fields of view of the cells on the substrate were used to calculate the number of cells within a $0.93mm^2$ area of the surface, and recorded as shown below. Sample variance was not homogenous when calculated using the original data (i), and even following square-root transformation (ii) and LOG10 transformation (iii) F_{max} exceeded the critical values. Original data was thus used in a non-parametric Kruskal-Wallis test, where time, topography and the interactions of time and topography and their effects on fibroblast adhesion were investigated, Section 4.4.1.

20 minutes			*1 hour*			*3 hours*		
Planar	Planar Etched	Nano-Pillared	Planar	Planar Etched	Nano-Pillared	Planar	Planar Etched	Nano-Pillared
5	43	43	14	44	6	3	0	101
6	45	65	2	45	33	0	5	105
3	56	60	2	58	58	4	84	114
0	46	63	5	46	8	7	156	62
6	13	47	4	17	15	3	17	0
8	38	11	5	38	20	6	127	114
3	22	4	3	22	39	5	15	112
10	45	9	5	45	5	2	53	113
9	56	5	1	56	51	3	16	112
3	39	11	4	12	36	1	2	148
3	56	22	5	56	6	3	6	2
3	74	21	6	74	68	8	62	22
7	19	16	3	19	59	7	26	49
5	68	29	4	68	40	0	56	3
4	20	67	3	20	49	3	26	93
7	23	23	6	64	34	3	5	7
5	53	12	8	63	7	3	69	9
6	53	51	1	53	55	1	34	101
7	74	54	5	74	58	5	23	79
7	54	53	0	54	50	4	10	114
8	71	40	3	71	13	5	79	81
7	14	57	3	21	64	7	68	48
3	51	42	9	69	4	10	86	77
5	21	7	1	21	11	3	112	0
1	58	4	3	58	62	6	132	2
3	36	25	5	70	34	3	35	96
2	19	39	1	19	32	4	27	57
4	20	11	8	58	60	3	115	57
5	53	25	3	53	0	3	14	7
6	43	30	9	43	48	1	134	80

(i) Original counts of the number of fibroblasts adhering to planar, planar etched and nanopillared topographies at 20 minutes, 1 hour and 3 hours.

20 minutes			*1 hour*			*3 hours*		
Planar	Planar Etched	Nano-Pillared	Planar	Planar Etched	Nano-Pillared	Planar	Planar Etched	Nano-Pillared
2.449	6.633	6.633	3.873	6.708	2.646	2.000	1.000	10.100
2.646	6.782	8.124	1.732	6.782	5.831	1.000	2.449	10.296

2.000	7.550	7.810	1.732	7.681	7.681	2.236	9.220	10.724
1.000	6.856	8.000	2.449	6.856	3.000	2.828	12.530	7.937
2.646	3.742	6.928	2.236	4.243	4.000	2.000	4.243	1.000
3.000	6.245	3.464	2.449	6.245	4.583	2.646	11.314	10.724
2.000	4.796	2.236	2.000	4.796	6.325	2.449	4.000	10.630
3.317	6.782	3.162	2.449	6.782	2.449	1.732	7.348	10.677
3.162	7.550	2.449	1.414	7.550	7.211	2.000	4.123	10.630
2.000	6.325	3.464	2.236	3.606	6.083	1.414	1.732	12.207
2.000	7.550	4.796	2.449	7.550	2.646	2.000	2.646	1.732
2.000	8.660	4.690	2.646	8.660	8.307	3.000	7.937	4.796
2.828	4.472	4.123	2.000	4.472	7.746	2.828	5.196	7.071
2.449	8.307	5.477	2.236	8.307	6.403	1.000	7.550	2.000
2.236	4.583	8.246	2.000	4.583	7.071	2.000	5.196	9.695
2.828	4.899	4.899	2.646	8.062	5.916	2.000	2.449	2.828
2.449	7.348	3.606	3.000	8.000	2.828	2.000	8.367	3.162
2.646	7.348	7.211	1.414	7.348	7.483	1.414	5.916	10.100
2.828	8.660	7.416	2.449	8.660	7.681	2.449	4.899	8.944
2.828	7.416	7.348	1.000	7.416	7.141	2.236	3.317	10.724
3.000	8.485	6.403	2.000	8.485	3.742	2.449	8.944	9.055
2.828	3.873	7.616	2.000	4.690	8.062	2.828	8.307	7.000
2.000	7.211	6.557	3.162	8.367	2.236	3.317	9.327	8.832
2.449	4.690	2.828	1.414	4.690	3.464	2.000	10.630	1.000
1.414	7.681	2.236	2.000	7.681	7.937	2.646	11.533	1.732
2.000	6.083	5.099	2.449	8.426	5.916	2.000	6.000	9.849
1.732	4.472	6.325	1.414	4.472	5.745	2.236	5.292	7.616
2.236	4.583	3.464	3.000	7.681	7.810	2.000	10.770	7.616
2.449	7.348	5.099	2.000	7.348	1.000	2.000	3.873	2.828
2.646	6.633	5.568	3.162	6.633	7.000	1.414	11.619	9.000

(ii) Square-root transformations of the original counts (i) of the number of fibroblasts adhering to planar, planar etched and nanopillared topographies at 20 minutes, 1 hour and 3 hours.

20 minutes			*1 hour*			*3 hours*		
Planar	Planar Etched	Nano-Pillared	Planar	Planar Etched	Nano-Pillared	Planar	Planar Etched	Nano-Pillared
.778	1.643	1.643	1.176	1.653	.845	.602	0.000	2.009
.845	1.663	1.820	.477	1.663	1.531	0	.778	2.025
.602	1.756	1.785	.477	1.771	1.771	.699	1.929	2.061
0	1.672	1.806	.778	1.672	.954	.903	2.196	1.799
.845	1.146	1.681	.699	1.255	1.204	.602	1.255	0
.954	1.591	1.079	.778	1.591	1.322	.845	2.107	2.061
.602	1.362	.699	.602	1.362	1.602	.778	1.204	2.053
1.041	1.663	1.000	.778	1.663	.778	.477	1.732	2.057
1.000	1.756	.778	.301	1.756	1.716	.602	1.230	2.053
.602	1.602	1.079	.699	1.114	1.568	.301	.477	2.173
.602	1.756	1.362	.778	1.756	.845	.602	.845	.477
.602	1.875	1.342	.845	1.875	1.839	.954	1.799	1.362
.903	1.301	1.230	.602	1.301	1.778	.903	1.431	1.699
.778	1.839	1.477	.699	1.839	1.613	0	1.756	.602
.699	1.322	1.833	.602	1.322	1.699	.602	1.431	1.973
.903	1.380	1.380	.845	1.813	1.544	.602	.778	.903
.778	1.732	1.114	.954	1.806	.903	.602	1.845	1.000
.845	1.732	1.716	.301	1.732	1.748	.301	1.544	2.009
.903	1.875	1.740	.778	1.875	1.771	.778	1.380	1.903
.903	1.740	1.732	0	1.740	1.708	.699	1.041	2.061
.954	1.857	1.613	.602	1.857	1.146	.778	1.903	1.914
.903	1.176	1.763	.602	1.342	1.813	.903	1.839	1.690
.602	1.716	1.633	1.000	1.845	.699	1.041	1.940	1.892
.778	1.342	.903	.301	1.342	1.079	.602	2.053	0
.301	1.771	.699	.602	1.771	1.799	.845	2.124	.477
.602	1.568	1.415	.778	1.851	1.544	.602	1.556	1.987
.477	1.301	1.602	.301	1.301	1.519	.699	1.447	1.763
.699	1.322	1.079	.954	1.771	1.785	.602	2.064	1.763
.778	1.732	1.415	.602	1.732	0	.602	1.176	.903
.845	1.643	1.491	1.000	1.643	1.690	.301	2.130	1.908

(iii) LOG10 transformations of the original counts (i) of the number of fibroblasts adhering to planar, planar etched and nanopillared topographies at 20 minutes, 1 hour and 3 hours.

References

Abercrombie, M., Heaysman, J. E. M., "Observations of the social behaviour of cells in tissue culture I: Speed of movement of chick fibroblasts in relation to their mutual contacts", Experimental Cell Research, 5, 1, pp111-131, 1952

Abercrombie, M., Heaysman, J. E. M., "Observations of the social behaviour of cells in tissue culture II: "Monolayering" of fibroblasts", Experimental Cell Research, 6, pp293-306, 1953

Abrahams, J. L., DeNee, P. B., "Scanning-electron-microscope histochemistry using backscattered electrons and metal stains", Lancet, 19, 1, pp1125, 1973

Abrams, G. A., Goodman, S. L., Nealey, P. F., Franco, M., Murphy, C. J., "Nanoscale topography of the basement membrane underlying the corneal epithelium of the rhesus macaque", Cell and Tissue Research, 299, 1, pp39-46, 1999

Adamczyk, Z., Zembala, M., Siwek, B., Warszynski, P., "Structure and ordering in localised adsorption of particles", Journal of Colloid and Interface Science, 140, 1, pp123-137, 1990

Ahmadi, T. S., Wang, Z. L., Green, T. C., Henglein, A., El-Sayed, M. A., "Shape-controlled synthesis of colloidal platinum nanoparticles", Science, 28, 272, pp1924-1926, 1996

Aizenberg, J., Black, A. J., Whitesides, G. M., "Controlling local disorder in self-assembled monolayers by patterning the topography of their metallic supports", Nature, 394, pp868-871, 1998

Alberts, B., Bray, D., Lewis, J., Raff, M., Roberts, K., Watson, J. D., "Molecular biology of the cell", 3rd Edition, New York: Garland Publishing Inc., 1994

Albrecht-Buehler, G., Goldman, R. D., "Microspike-mediated particle transport towards the cell body during early spreading of 3T3 cells", Experimental Cell Research, 97, pp329-339, 1976

[a]Albrecht-Buehler, G., "Phagokinetic tracks of 3T3 cells: Parallels between the orientation of track segments and of cellular structures which contain either actin or tubulin", Cell, 12, pp333-339, 1977

[b]Albrecht-Buehler, G., "Phagokinetic tracks of 3T3 cells", Cell, 11, pp395-404, 1977

Alpin, A. E., Howe, A. K., Juliano, R. L., "Cell adhesion molecules, signal transduction and cell growth", Current Opinions in Cell Biology, 11, pp737-744, 1999

Alivisatos, A. P., "Semiconductor clusters, nanocrystals and quantum dots", Science, 271, pp933-937, 1996

Andersson, A-S., Bäckhed, F., von Euler, A., Richter-Dahlfors, A., Sutherland, D., Kasemo, B., "Nanoscale features influence epithelial cell morphology and cytokine production", Biomaterials, 24, pp3427-3436, 2003

Balaban, N. Q., Schwartz, S. S., Riveline, D., Goichberg, P., "Force and focal adhesion assembly: a close relationship studied using elastic micropatterned substrates", Nature Cell Biology, 3, pp446-472, 2001

Bard, J. B. L., Hay, E. D., "The behaviour of fibroblasts from the developing avian cornea: Morphology in situ and in vitro", The Journal of Cell Biology, 67, pp400-418, 1975

Beningo, K. A., Dembo, M., Kaverina, I., Small, J. V., Wang, Y-I., "Nascent focal adhesions are responsible for the generation of strong propulsive forces on migrating fibroblasts", Journal of Cell Biology, 153, 4, pp881-887, 2001

Beningo, K. A., Wang, Y-I., "Flexible substrata for the detection of cellular traction forces", Trends in Cell Biology, 12, 2, pp79-84, 2002

Bershadsky, A. D., Tint, I. S., Neyfakh, A. A., Vasiliev, J. M., "Focal contacts of normal and RSV-transformed quail cells. Hypothesis of the transformation-induced

deficient maturation of focal contacts", Experimental Cell Research, 158, pp433-444, 1985

Bhatt, A., Kaverina, I., Otey, C., Huttenlocher, A., "Regulation of focal complex composition and disassembly by the calcium-dependent protease calpain", Journal of Cell Science, 115, pp3415-3425, 2002

Bland, J. M., Altman, D. G., "Multiple significance tests: the Bonferroni method", British Medical Journal, 310, pp170, 1995

Bodnar, A. G., Ouellette, M., Frolkis, M., Holt, S. E., Chiu, C. P., Morin, G. B., Harley, C. B., Shay, J. W., Lichtensteiner, S., Wright, W. E., "Extension of life-span by introduction of telomerase into normal human cells", Science, 16, 279, pp349-352, Science, 1998

Boeckl, M. S., Bass, T., Fujita, A., Hwang, K. O., Bramblett, A. L., Ratner, B. D., Rogers, J. W., Sasaki, T., "Template-assisted nano-patterning of solid surfaces", Biopolymers; Peptide Science, 47, pp185-193, 1998

Born, M., Wolf, E., "Principles of optics: Electromagnetic theory of propagation, interference and diffraction of light", 6th Edition, Cambridge, UK: Cambridge University Press, 1997

Bozzola, J. J., Russell, L. D., "Electron Microscopy: Principles and techniques for biologists", Jones and Bartlett Publishers, Boston, 1992

Brieher, W. M., Gumbiner, B. M., "Regulation of C-cadherin function during activin-induced morphogenesis of Xenopus animal caps", Journal of Cell Biology, 126, 2, pp519-527, 1994

Britland, S., Morgan, H., Wojiak-Stodhard, B., Riehle, M., Curtis, A., Wilkinson, C., "Synergistic and Hierarchical Adhesive and Topographic Guidance of BHK Cells", Experimental Cell Research, 228, pp313-325, 1996

Bucklew, J. A., Saleh, B. E. A., "Theorem for high-resolution high-contrast image synthesis", Journal of the Optical Society of America A, 2, 8, pp1233, 1985

Burnmeister, F., Schäfle, C., Mattes, T., Böhmisch, M., Boneberg, J., Leiderer, P., "Colloid monolayers as versatile lithographic masks", Langmuir, 13, pp2983-2987, 1997

Burton, K., Taylor, D. L., "Traction forces of cytokinesis measured with optically modified elastic substrata", Nature, 385, pp450-454, 1997

Calderwood, D. A., Zent, R., Grant, R., Rees, D. J. G., Hynes, R. O., Ginsberg, M. H., "The talin head domain binds to integrin β subunit cytoplasmic tails and regulates integrin activation", Journal of Biological Chemistry, 274, 40, pp28071-28074, 1999

Cannas, M., Denicolai, F., Webb, L. X., Gristina, A. G., "Bioimplant surfaces: Binding of fibronectin and fibroblast adhesion", Journal of Orthopaedic Research, 6, pp58-62, 1988

Carter, S. B., "Effects of Cytochalasins on mammalian cells", Nature, 213, pp261-264, 1967

Casey, B. G., Monaghan, W., Wilkinson, C. D. W., "Embossing of nanoscale features and environments", Microelectronic engineering, 35, pp393-396, 1997

Cass, T., Ligler, F. S., "Immobilised biomolecules in analysis: A practical approach", Oxford University Press, Oxford, 1998

Cerrina, F., Marrian, C., "A path to nanolithography", Materials Research Society Bulletin: "The Science of Art", pp56-62, December 1996

Chen, S., "Self-assembly of monlayer-protected gold nanoparticles", Journal of Physical Chemistry B, 104, 4, pp663-667, 2000

Chen, W., Ahmed, H., "Fabrication of high aspect ratio silicon pillars of <10nm diameter", Applied Physics Letters, 63, 8, pp1116-1118, 1993

Chiquet-Ehrismann, R., "Inhibition of cell adhesion by anti-adhesive molecules", Current Opinion in Cell Biology, 7, pp715-719, 1995

Choquet, D., Felsenfeld, D. P., Sheetz, M. P., "Extracellular matrix rigidity causes strengthening of integrin-cytoskeleton linkages", Cell, 88, pp39-48, 1997

Chou, L., Firth, J. D., Uitto, V-J., Brunette, D. M., "Substratum surface topography alters cell shape and regulates fibronectin mRNA level, mRNA stability, secretion and assembly in human fibroblasts", Journal of Cell Science, 108, pp1563-1573, 1995

Chou, S. Y., Krauss, P. R., Renstorm, P. J., "Imprint lithography with 25-nanometer resolution", Science, 272, pp85-87, 1996

Clark, P., Connolly, P., Curtis, A. S. G., Dow, J. A. T., Wilkinson, C. D. W., "Topographical control of cell behaviour: I. Simple step cues", Development, 99, pp439-448, 1987

Clark, P., Connolly, P., Curtis, A. S. G., Dow, J. A. T., Wilkinson, C. D. W., "Topographical control of cell behaviour: II. Multiple grooved substrata", Development, 108, pp635-644, 1990

Clark, P., Connolly, P., Curtis, A. S. G., Dow, J. A. T., Wilkinson, C. D. W., "Cell guidance by ultrafine topography *in vitro*", Journal of Cell Science, 99, pp73-77, 1991

Cooper, G. M., "The Cell: A Molecular Approach", 2nd Edition, 1999. Available online at Pubmed (www.ncbi.nlm.nih.gov)

Craighead, H. G., James, C. D., Turner, A. M. P., "Chemical and Topographical patterning for directed cell attachment", Current Opinions in Solid State and Materials Science, 5, pp177-184, 2001

Crowley, E., Horwitz, A. F., "Tyrosine phosphorylation and cytoskeleton tension regulate the release of fibroblast adhesions", Journal of Cell Biology, 131, pp525-537, 1995

Curtis, A. S. G., Wilkinson, C. D. W., "Review: Topographical control of cells", Biomaterials, 18, pp1573-1583, 1997

Curtis, A. S. G., Casey, B., Gallagher, J. O., Pasqui, D., Wood, M. A., Wilkinson, C. D. W., "Substratum nanotechnology and the adhesion of biological cells. Are symmetry or regularity of nanotopography important?", Biophysical Chemistry, 94, pp275-283, 2001

Curtis, A. S. G., Clark, P., "The effects of topographic and mechanical properties of materials on cell behaviour", Critical Reviews in Biocompatibility, 5, 4, pp343-362, 1990

Curtis, A. S. G., Wilkinson, C. D. W., "Nanotechniques and approaches in biotechnology", Trends in Biotechnology, 19, 3, pp97-101, 2001

Dalby, M. J., Di Silvio, L., Harper, E. J., Bonfield, W., "Initial interactions of osteoblasts with the surface of hydroxyapatite-poly(methylmethacrylate) cement, Biomaterials, 22, pp1739-1747, 2001

[a] Dalby, M., J., Marshall, G. E., Johnstone, H. J., Affrossman, S., Riehle, M. O., "Interactions of Human Blood and Tissue Cell Types with 95-nm-High Nanotpography", IEEE Transactions on Nanobioscience, 1, 1, pp18-23, 2002

[b] Dalby, M. J., Riehle, M. O., Johnstone, H. J. H., Affrossman, S. Curtis, A. S. G., "In vitro reaction of endothelial cells to polymer demixed nanotopography", Biomaterials, 23, pp2945-2954, 2002

[c] Dalby, M. J., Riehle, M. O., Johnstone, H. J. H., Affrossman, S. Curtis, A. S. G., "Polymer-demixed Nanotopography: Control of Fibroblast Spreading and Proliferation", Tissue Engineering, 8, 6, pp1099-1108, 2002

[d] Dalby, M. J., Yarwood, S. J., Johnstone, H. J. H., Affrossman, S., Riehle, M. O., "Fibroblast Signalling Events in Response to Nanotopography: A Gene Array Study", IEEE Transactions on Nanobioscience, 1, 1, pp12-17, 2002

[e] Dalby, M. J., Yarwood, S. J., Riehle, M. O., Johnstone, H. J. H., Affrossman, S., Curtis, A. S. G., "Increasing fibroblast response to materials using nanotopography: Morphological and genetic measurements of cell response to 13nm high polymer demixed islands", Experimental Cell research, 276, pp1-9, 2002

[a] Dalby, M. J., Childs, S., Riehle, M. O., Johnstone, H. J. H., Affrossman, S., Curtis, A. S. G., "Fibroblast reactions to island topography: Changes in cytoskeleton and morphology with time", Biomaterials, 24, pp927-935, 2003

[b] Dalby, M. J., Riehle, M. O., Sutherland, D. S., Agheli, H., Curtis, A. S. G., "Nanotopography produced by colloidal lithography reduces "self-induced" mechanotransduction in human fibroblasts", In Press, 2003

[c] Dalby, M. J., Riehle, M. O., Yarwood, S. J., Wilkinson, C. D. W., Curtis, A. S. G., "Nucleus alignment and cell signalling in fibroblasts: response to micro-grooved topography", Experimental Cell Research, 284, pp274-282, 2003

Davda, J., Labhasetwar, V., "Characterisation of nanoparticle uptake by endothelial cells", International Journal of Pharmacology, 233, pp51-59, 2002

Deckman, H. W., Dunsmuir, J. H., "Natural lithography", Applied Physics Letters, 41, 4, pp377-379, 1982

Deckman, H. W., Dunsmuir, J. H., "Applications of surface texture produced with natural lithography", Journal of Vacuum Science and Technology B, 1, 4, pp1109-1112, 1983

Dembo, M., Wang, Y., "Stresses at the cell-to-substrate interface during locomotion of fibroblasts", Biophys Journal, 76, pp2307-2316, 1999

Denasi, T. A., "Micro- and nanoscale structures for tissue engineering constructs", Medical Engineering and Physics, 22, pp595-606, 2000

Dunn, P. N., Solid State Technology, pp49-62, 1994

Dunn, G. A., Heath, J. P., "A new hypothesis of contact guidance", Experimental Cell Research, 101, 1, pp1-14, 1976

Eastham, D. A., Hamilton, B., Denby, P. M., "Formation of ordered assemblies from deposited gold clusters", Nanotechnology, 13, pp51-54, 2002

Fink, J., Kiely, C. J., Bethell, D., Schiffrin, D. J., "Self-assembly of nanosized gold clusters into regular arrays", International Physics Conference Series, 153, 13, IOP Publishing Limited, Cambridge, 1997

Fitch, R. M., Clarke, J., "Brownian deposition of latex particles onto glass and polystyrene", Colloids and Surfaces A: Physiochemical and Engineering Aspects, 153, pp525-535, 1999

Flemming, R. G., Murphy, C. J., Abrams, G. A., Goodman, S. L., Nealey, P. F., "The effects of synthetic micro- and nano-structured surfaces on cell behaviour", Biomaterials, 20, pp537-588, 1999

Fowler, J., Cohen, L., Jarvis, P, "Practical statistics for field biology", 2nd Edition, Wiley, Chichester, 1998

Fromherz, P., "Self-gating of ion channels in cell adhesion", Physical Review Letters, 78, 21, pp41314134, 1997

Gadegaard, N., Thoms, S., MacIntyre, D. S., McGhee, K., Gallagher, J., Casey, B., Wilkinson, C. D. W., "Arrays of nano-dots for cellular engineering", Microelectronic Engineering, 67-68, pp162-168, 2003

Galbraith, C. G., Sheetz, M. P., "Forces on adhesive contacts affect cell function", Current Opinions in Cell Biology, 10, pp566-571, 1998

Galding, A., Lauffenburger, D. A., Wells, A., "Cutting to the chase: calpain proteases in cell motility", Trends in Cell Biology, 12, 1, pp46-54, 2002

Gallagher, J. O., McGhee, K. F., Wilkinson, C. D. W., Riehle, M. O., "Interaction of animal cells with ordered nanotopography", IEEE Transactions in Nanobioscience, 1, pp24-26, 2002

Geiger, B., Bershadsky, A., "Assembly and mechanosensory function of focal contacts", Current Opinions in Cell Biology, 13, 5, pp584-592, 2001

Geiger, B., Bershadsky, A., "Exploring the neighbourhood: Adhesion-coupled cell mechanosensors", Cell, 110, pp139-142, 2002

Giersig, M., Mulvaney, P., "Formation of ordered two-dimensional colloidal lattices by electrophoretic deposition", Journal of Physical Chemistry, pp6334-6336, 1993

Gill, F. J., Padrós, A., Manero, J. M., Aparicio, C., Nilsson, M., Planell, J. A., "Growth of bioactive surfaces on titanium and its alloys for orthopaedic and dental implants", Materials Science and Engineering C, 22, 53-60, 2002

Gittin, D. I., Caruso, F. "Tailoring the polyelectrolyte coating of metal nanoparticles", Journal of Physical Chemistry B, 105, pp6846-6852, 2001

Gopalakrishna, R., Barsky, S. H., "Hydrophobic association of calpains with subcellular organelles", Journal of Biological Chemistry, 261, 30, pp13936-139342, 1986

Grabar, K. C., Smith, P. C., Musick, M. D., Davis, J. A., Walter, D. G., Jackson, M. A., Guthrie, A. P., Natan, M. J., "Kinetic Control of Interparticle Spacing in Au Colloid-Based Surfaces: Rational Nanometer-Scale Architecture", Journal of American Chemical Society, 118, pp1148-1153, 1996

Hanarp, P., Sutherland, D., Gold, J., Kasemo, B., "Nanostructured model biomaterial surfaces prepared by colloidal lithography", Nanostructured Materials, 12, pp429-432, 1999

Hanarp, P., Sutherland, D., Gold, J., Kasemo, B., "Control of nanoparticle film structure for colloidal lthography", Colloids and Surfaces A: Physicochemical Engineering Aspects, 214, pp23-36, 2003

Harley, C. B., Futcher, A. B., Greider, C. W., "Telomerase shorten during ageing of human fibroblasts", Nature, 345, pp458-460, 1990

Harnett, C. K., Satyalakshmi, K. M., Craighead, h. G., "Low-energy electron-beam patterning of amine-functionalized self-assembled monolayers", Applied Physics Letters, 76, 17, pp2466-2468, 2000

Harrison, R. G., "On the stereotropism of embryonic cells", Science, 34, pp279-381, 1911

He, H. X., Zhang, H., Li, Q. G., Zhu, T., Li, S. F. Y., Liu, Z. F., "Fabrication of designed archietectures of Au nanoparticles on solid substrate with printed self-assembled monolayers as templates", Langmuir, 16, pp3846-3851, 2000

Hidber, P. C., Helbig, W., Kim, E., Whitesides, G. M., "Microcontact Printing of Palladium Colloids: Micron-scale Patterning by Electroless Deposition of Copper", Langmuir, 12, pp1375-1380, 1996

Horton, M. A., "Molecular biology of cell adhesion molecules", Molecular Medical Science Series, Chichester, John Wiley and Sons, 1996

Horwitz, A. R., Parsons, J. T., "Cell Migration - Movin' On", Science, 286, 5442, pp1102-1103, 1999

Huang, J., Forsberg, N. E., "Role of calpain in skeletal muscle protein degradation", Proc. Natl. Acad. Sci. USA, 95, pp12100-12105, 1998

Hulteen, J. C., Van Duyne, R. P., "Nanosphere lithography: A materials general fabrication process for periodic particle array surfaces", Journal of Vacuum Science and Technology A, 13, 3, pp1553-1558, 1995

Hunter, R. J., "Foundations of Colloidal Science: Volume 1", Oxford Science Publications, Oxford University Press, Oxford, 1987

Huttenlocher, A., Ginsberg, M. H., Horwitz, A. F., "Modulation of cell migration by integrin-mediated cytoskeletal linkages and ligand-binding affinity", Journal of Cell Biology, 134, 6, pp1551-1562, 1996

Huttenlocher, A., Palecek, S. P., Lu, Q., Zhang, W., Mellgren, R. L., Lauffenburger, D. A., Ginsberg, M. H., Horwitz, A. F., "Regulation of cell migration by the calcium-dependent protease calpain", Journal of Biological Chemistry, 272, 52, pp 32719-32722, 1997

Ilic, B., Craighead, H. G., "Topographical patterning of chemically sensitive biological materials using a polymer-based dry lift off", Biomedical microdevices, 2:4, pp317-322, 2000

Ito, Y., "Surface micropatterning to regulate cell functions", Biomaterials, 20, pp2333-2342, 1999

Jacinto, A., Martinez-Arias, A., Martin, P., "Mechanisms of epithelial fusion and repair", Nature Cell Biology, 3, ppE117-E123, 2001

James, C. D., Davis, R. C., Kam, L., Craighead, H. G., Isaacson, M., Turner, J. N., Shain, W., "Patterned protein layers on solid substrates by thin stamp microcontact printing", Langmuir, 14, pp741-744, 1998

Jiang, X-R, Jimenez, G., Chang, E., Frolkis, M., Kusler, B., Sage, M., Beeche, M., Bodnar, A. G., Wahl, G. M., Tlsty, T. D., Chiu, C-P., "Telomerase expression in human somatic cells does not induce changes associated with a transformed phenotype", Nature Genetics, 21, pp111-114, 1999

Johnson, C. A., Lenhoff, A. M., "Adsorption of Charged Latex Particles on Mica Studied by Atomic Force Microscopy", Journal of Colloid and Interface Science, 179, pp587-599, 1996

Kane, R. S., Takayama, S., Ostuni, E., Ingber, D. E., Whitesides, G. M., "Patterning proteins and cells using soft lithography", Biomaterials, 20, pp2363-2376, 1999

Kannus, P., "Structure of the tendon connective tissue", Scandinavian Journal of Medical Science and Sports, 10, pp312-320, 2000

Kao, J. P. Y., "Methods in Cell Biology: Chapter 7: Practical Aspects of Measuring [Ca^{2+}] with Fluorescent Indicators", Academic Press Inc., 40, pp155-181, 1994

Kasemo, B., Gold, J., "Implant surfaces and interface processes", Advanced Dental Research, 13, pp8-20, 1999

Kasemo, B., Lausmaa, J., "Biomaterial and implant surfaces: A surface science approach", The International Journal of Oral and Maxillofacial implants", 3, pp247-259, 1988

Kasemo, B., Lausmaa, J., "Material-tissue interfaces: The role of surface properties and processes", Environmental Health Prospectives, 102, (5), pp41-45, 1994

Katz, B-N., Zamir, E., Bershadsky, A., Kam, Z., Yamada, K. M., Geiger, B., "Physical state of the extracellular matrix regulates the structure and molecular composition of the cell-matrix adhesions", Molecular Biology of the Cell, 11, pp1047-1060, 2000

Kawata, S., "Finer features for functional microdevices", Nature, 412, pp697-698, 2001

Kirchner, J., Karn, Z., Tzur, G., Bershadsky, A. D., Geiger, B., "Live-cell monitoring of tyrosine phosphorylation in focal adhesions following microtubule disruption", Journal of Cell Science, 116, 6, pp975-986, 2003

Kirkwood, T. B., "Human senescence", Bioessays, 18, 12, pp1009-1016, 1996

Kolega, J., "Effects of mechanical tension on protrusive activity and microfilament and intermediate filament organisation in an epidermal epithelium moving in culture", Journal of Cell Biology, 102, pp1400-1411, 1986

Kreis, T., Vale, R., "Guidebook to the extracellular matrix, anchor and adhesion proteins", Second Edition, Oxford: A Sambrook and Tooze Publication at Oxford University Press, 1999

Kubena, R. L., Ward, J. W., Stratton, F. P., Joyce, R. J., Atkinson, G. M., Journal of Vacuum Science and Technology B, 9, pp3079, 1991

Lackie, J. M., Dow, J. A. T., "The Dictionary of Cell and Molecular Biology", 3rd Edition, Academic Press, London, 1999

Laibinis, P. E., Nuzzo,R. G., Whitesides, G. M., "Structure of monolayers formed by coadsorption of two *n*-Alkanethiols of different chain lengths on gold and its relation to wetting", Journal of Physical Chemistry, 96, pp5097-5105, 1992

Lee, J., Ishihara, A., Oxford, G., Johnson, B., Jacobson, K., "Regulation of cell movement is mediated by stretch-activated calcium channels", Nature, 400, pp382-386, 1999

Lercel, M. J., Craighead, H. G., Parikh, A. N., Seshadri, K., Allara, D. L., "Sub-10nm lithography with self-assembled monolayers", Applied Physics Letters, 68, 11, pp1504-1506, 1996

Lercel, M. J., Redinbo, G. F., Rooks, M., Tiberio, R. C., Craighead, H.G., Sheen, C. W., Allara, D. L., "Electron Beam Nanofabrication with Self-Assembled Monolayers of Alkylthiols and Alkylsiloxanes", Microelectronic Engineering, 27, pp43-46, 1995

Levenson, M. D., Solid State Technology, pp57-66, 1995

Lewis, P. A., Ahmed, H., "Nanopillars formed with a colloidal gold etch mask", Journal of Vacuum Science and Technology B, 17, 6, pp3239-3234, 1999

Lewis, P. A., Ahmed, H., Sato, T., "Silicon nanopillars formed with colloidal particle masking", Journal of Vacuum Science and Technology B, 16, 6, pp2938-2941, 1998

Lo, C-M., Wang, H-B., Dembo, M., Wang, Y-L., "Cell movement is guided by the rigidity of the substrate", Biophysical Journal, 79, pp144-152, 2000

MacSween, R. N. M., Whaley, K., "Muir's Textbook of Pathology", 13th Edition, Edward Arnold, 1992

Magnani, A., Priamo, A., Pasqui, D., Barbucci, R., "Cell behaviour on chemically microstructured surfaces", Materials Science and Engineering C, 23, pp315-328, 2003

Maheshwari, G., Brown, G., Lauffenburger, D. A., Wells, A., Griffith, L. G., "Cell adhesion and motility depend on nanoscale RGD clustering", Journal of Cell Science, 113, pp1677-1686, 2000

Mayya, K. S., Gittins, D. I., Caruso, F., "Gold-titania core-shell nanoparticles by polyelectrolyte complexation with a titania precursor", Chemical Materials, 13, pp3833-3836, 2001

Menard, H-A., El-Amine, M., "The calpain-calpastatin system in rheumatoid arthritis", Trends in Immunology Today, 17, 12, pp545-547, 1996

Meredith, D. O., Owen, G. Rh., ap Gwyn, I, Richards, R. G., "Variation in cell-substratum adhesion in relation to cell-cycle phases", Experimental Cell Research, In Press, 2003

Minnie, S. C., Manalis, S. R., Atalar, A., Quate, C. F., "Independent parallel lithography using the atomic force microscope, Journal of Vacuum Science and Technology B, 14, 4, pp2456-2460, 1996

Miyaki, M., Fujimoto, K., Kawaguchi, H., "Cell response to micropatterned surfaces produced with polymeric microspheres", Colloids and Surfaces A: Physiochemical and Engineering Aspects, 153, pp603-608, 1999

Moczar, M., Lecerf, L., Ginat, M., Loisance, D., "Complement activation is involved in the structural deterioration of bovine pericardial bioprosthetic heart valves", American Society of Artificial Internal Organs Journal, 42, M375-M381, 1996

Mullins, J. M., Biesele, J. J., "Terminal phase of cytokinesis in D-98s cells", Journal of Cell Biology, 73, pp672-684, 1977

Munerva, S., Wang, Y-I., Dembo, M., "Distinct roles of frontal and rear cell-substrate adhesions in fibroblast migration", Molecular Biology of the Cell, 12, pp3947-3954, 2001

Murray, A., Hunt, T., "The cell cycle: An introduction", Oxford University Press, Oxford, 1993

Niemeyer, C. M., Ceyhan, B., Gao, S., Chi, L., Peschel, S., Simon, U., "Site-selective immobilisation of gold nanoparticles functionalised with DNA oligomers", Colloid and Polymer Science, 279, pp68-72, 2001

Ng, V., Lee, Y. V., Chen, B. T., Adeyeye, A. O., "Nanostructure array fabrication with temperature-controlled self-assembly techniques", Nanotechnology, 13, pp554-558, 2002

Oakley, C., Brunette, D. M., "The sequence and alignment of microtubules, focal contacts and actin filaments in fibroblasts spreading on smooth and grooved titanium substrata", Journal of Cell Science, 106, pp343-354, 1993

O'Neal, R. B., Sauk, J. J., Somerman, M. J., "Biological requirements for material integration", Journal of Oral Implantology, pp243-255, 1992

Palecek, S. P., Huttenlocher, A., Horwitz, A. F., Lauffenburger, D., A., "Physical and biochemical regulation of integrin release during rear detachment of migrating cells", Journal of Cell Science, 111, pp 929-940, 1998

Palecek, S. P., Schmidt, C. E., Lauffenburger, D. A., Horwitz, A. F., "Integrin dynamics on the tail region of migrating fibroblasts", Journal of Cell Science, 109, pp941-952, 1996

Park, K., Simmons, S. R., Albrecht, R. M., "Surface characterisation of biomaterials by immunogold staining - quantitative analysis", Scanning Microscopy, 1, pp339-350, 1987

Park, K., Park, H., Albreacht, R. M., Colloidal Gold: Principles, Methods and Applications, Hayat, M. A., Academic Press, San Diego, Volume 1, Chapter 18, 1989

Park, M., Harrison, C., Chaikin, P. M., Register, R. A., Adamson, D., "Block copolymer lithography: Periodic arrays of (approximately 10(to power of) 11 holes in 1 square centimeter", Science, 276, pp1401-1404, 1997

Park, M., Chaikin, P. M., Register, R. A., Adamson, D. H., "Large area dense nanoscale patterning of arbitrary surfaces", Applied Physics Letters, 79, 2, pp257-259, 2001

Perrin, B. J., Huttenlocher, A., "Molecules in focus: Calpain", The International Journal of Biochemistry and Cell Biology, 34, pp722-725, 2002

Peschel, S., Schmid, G., "First steps towards ordered monolayers of ligand-stabilised gold clusters", Angew Chem International Edition, Engl, 34, 13/14, pp1442-1443, 1995

Pohl, K., Bartelt, M. C., de la Figuera, J., Bartelt, N. C., Hrbek, J., Hwang, R. Q., "Identifying the forces responsible for self-organisation of nanostructures at crystal surfaces", Nature, 397, pp238-241, 1999

Potter, D. A., Tirnauer, J. S., Janssen, R., Croall, D. E., Hughes, C. N., Fiacco, K. A., Mier, J. W., Maki, M., Herman, I. M., "Calpain regulates actin remodelling during cell spreading", Journal of Cell Biology, 141, 3, pp 647-662, 1998

Preston, T. M., King, C. A., Hyams, J. S., "The cytoskeleton and cell motility", Tertiary Level Biology, Blackie and Son Ltd., Glasgow, 1990

Reetz, M. T., Winter, M., Tesche, B, "Self-assembly of tetraalkylammonium salt-stabilised giant palladium clusters on surfaces", Chemical Communications, pp147-148, 1997

Remacle, F., Collier, C. P., Markovich, G., Heath, J. R., Banin, U., Levine, R. D., "Networks of quantum dots: The role of disorder in modifying electronic and optical properties", Journal of Physical Chemistry B, 102, pp7727-7734, 1998

Richards, R. G., ap Gwynn, I., "Backscattered electron imaging of the undersurface of resin-embedded cells by field emission scanning electron microscopy, Journal of Microscopy, 177, 1, pp43-52, 1995

Riehle, M., Dalby, M., Johnstone, H., Gallagher, J. O., Wood, M. A., Casey, B., McGhee, K., "Nanometric surface patterns for tissue engineering: Fabrication and biocompatibility *in vitro*", Mat Res Soc Symp Proc, 705, pp Y5.1.1-Y5.1.11, 2002

Rohrer, H., "The nanometer age: Challenge and chance", Microelectronic engineering, 27, pp3-15, 1995

Rosenberg, M. D., "Long-range interactions between cells and substratum", Proceedings of the National Academy of Science, 48, pp1342-1349, 1962

Rosenberg, M. D., "Cell guidance by alterations in monomolecular films", Science, 139, pp411-412, 1963

Rovensky, Y. A., Samoilov, V. I., "Morphogenetic response of cultured normal and transformed fibroblasts, and epitheliocytes, to a cylindrical substratum surface", Journal of Cell Science, 107, pp1255-1263, 1994

Salmon, E. D., Way, M., "Cytoskeleton", Current Opinion in Cell Biology, 11, pp15-17, 1999

Sammack, P. J., Hinman, L. E., Tran, P. O. T, Sjaastad, M. D., Machen, T. E., "How do injured cells communicate with the surviving cell monolayer?", Journal of Cell Science, 110, pp465-475, 1997

Sato, T., Brown, D., Johnson, B. F. G., "Nucleation and growth of nano-gold colloidal lattices", Chem Comm, pp1007-1008, 1997

Sato, T., Hasko, Ahmed, H., "Nanoscale colloidal particles: Monolayer organisation and patterning", Journal of Vacuum Science and Technology B, 15, 1, pp, 1997

Schift, H., Gobrecht, J., Heyderman, L. J., Padeste, C., Vogelsang, K., "Chemical nanopatterning using hot embossing lithography", Paul Scherrer Institute Annual Report, 2001

Schmidt, G., Baumle, M., Beyer, N., "Ordered two-dimensional monolayers of Au55 clusters", Angew Chem International Edition, 39, 1, pp181-183, 2000

Schoenwaelder, S. M., Burridge, K, "Bidirectional signalling between the cytoskeleton and integrins", Current Opinions in Cell Biology, 11, pp274-286, 1999

Schwarz, U. S., Balaban, N. Q., Riveline, D., Bershadsky, A., Geiger, B., Safran, S. A., "Calculation of forces at focal adhesions from elastic substrate data: The effect of localised force and the need for regularisation", Biophysical Journal, 83, pp1380-1394, 2002

[a] Seeger, K., Palmer, R. E., "Fabrication of Ordered Arrays of Silicon Nanopillars", Journal of Physics D: Applied Physics, 32, ppL129-132, 1999

[b] Seeger, K., Palmer, R. E., "Fabrication of silicon cones and pillars using rough metal films as plasma etch masks", Applied Physics Letters, 74, 11, pp, 1999

Sheilds, D. C., Tyor, W. R., Deibler, G. E., Hogan, E. L., Banik, N. L., "Increased calpain expression in activated glial and inflammatory cells in experimental allergic encephalomyelitis", Neurobiology, 95, pp5768-5772, 1998

Small, J. V., Geiger, B., Kaverina, I., Bershadsky, A., "How do microtubules guide migrating cells?", Nature Reviews, Molecular Cell Biology, 3, pp957-964, 2002

Soll, D. R., Wessels, D., "Motion Analysis of Living Cells: Techniques in modern biomedical microscopy", Wiley-Liss, London, 1998

Tang, L., Liu, L., Elwing, H. B., "Complement activation and inflammation triggered by model biomaterial surfaces", pp333-340, 1998

Tuljapurkar, S., Li, N., Boe, C., "A universal pattern of mortality decline in the G7 countries", Nature, 405, pp789-92, 2000

Tsutsui, K., Hu, E. L., Wilkinson, C. D. W., "Controlling the profile of nanostructures", Journal of Vacuum Science and Technology B, 11, 6, pp2233-2236, 1993

Turner, S., Kam, L., Isaacson, M., Craighead, H. G., Shain, W., Turner, J., "Cell attachment to silicon nanostructures" J. Vac. Sci. Technol. B, 15(6), pp2848-2854, 1997

Van Mourik, J. A., de Wit, T. H., Voorberg, J., "Biogenesis and exocytosis of Weibel-Palade bodies", Histochem Cell Biol, 117, pp113-122, 2002

Voldman, Gray, Schmidt, "Microfabrication in Biology and Medicine", Annual Review of Biomedical Engineering, 01, pp401-425, 1999

Wang, D., Thomas, S. G., Wang, K. L., Xia, Y., Whitesides, G. M., "Nanometer scale patterning and pattern transfer on amorphous Si crystalline Si, and SiO_2 surfaces using self-assembled monolayers", Applied Physics Letters, 70, 12, pp1593-1595, 1997

Weiss, P., "In vitro experiments on the factors determining the course of the outgrowing nerve fibre" Journal of Experimental Zoology, 68, pp393-448, 1934

Wilkinson, C. D. W., "Nanostructures in Biology", Microelectronic Engineering, 27, pp61-65, 1995

Wilkinson, C. D. W., Curtis, A. S. G., Crossan, J., "Nanofabrication in cellular engineering", Journal of Vacuum Science and Technology B, 16, 6, pp3132-3136, 1998

Wilkinson, C. D. W., Riehle, M., Wood, M. A., Gallagher, J. O., Curtis, A. S. G., "The use of materials patterned on a nano- and micro-metric scale in cellular engineering", Materials Science and Engineering C, 19, pp 263-269, 2002

Willner, I., Katz, E., Shipway, A. N., "Nanoparticle arrays on surfaces for electronic, optical and sensor applications", Chemphyschem, 1, pp18-52, 2000

[a] Wojciak-Stodhard, B., Curtis, A. S. G., Monaghan, W., McGrath, M., Sommer, I., Wilkinson, C. D. W., "Role of the cytoskeleton in the reaction of fibroblasts to multiple grooved substrata", Cell Motility and the Cytoskeleton, 1995

[b] Wojciak-Stodhard, B., Madeja, Z., Korohoda, W., Curtis, A., Wilkinson, C., "Activation of macrophage-like cells by multiple grooved substrata. Topographical control of cell behaviour", Cell Biology International, 19, pp485-490, 1995

[c] Wojciak-Stodhard, B., Crossan, J., Curtis, A. S. G., Wilkinson, C. D. W., "Grooved substrata facilitate in vitro healing of completely divided flexor tendons", Journal of Materials Science: Materials in Medicine, 6, pp266-271, 1995

[a] Wood, M. A., Meredith, D. O., Owen, G. Rh., "Steps towards a model nanotopography", IEEE Transactions on Nanobioscience, 2002

[b] Wood, M. A., Riehle, M., Wilkinson, C. D. W. Wilkinson, "Patterning colloidal nanotopographies", Nanotechnology, 13, pp605-609, 2002

Woolley, K., Martin, P., "Conserved mechanisms of repair; from damaged single cells to wounds in multicellular tissues", BioEssays, 22, pp 911-919, 2000

Xia, Y., Rogers, J. A., Paul, K. E., Whitesides, G. M., "Unconventional methods for fabricating and patterning nanostructures", Chem Review, 99, pp1823-1848, 1999

Yang, D. Thomas, S. G., Wang, K. L., Xia, Y., Whitesides, G. M., "Nanometer scale patterning and pattern transfer on amorphous Si, crystalline Si, and SiO_2 surfaces using self-assembled monolayers", Applied Physics Letters, 70, 12, 1997

Zhdanov, V. P., Kasemo, B., "Ordering of adsorbed proteins", Proteins: Structure Function and Genetics, 40, pp539-542, 2000

Zhong, Z., Gates, B., Xia, Y, Qin, D., "Soft lithographic approach to the fabrication of highly ordered 2D arrays of magnetic nanoparticles on the surface of silicon substrates", Langmuir, 16, pp10369-10375, 2000

Zhou, H. S., Aoki, S., Honma, I., Hirasawa, M., Nagamune, T., Komiyama, H., "Conformational change of protein cytochrome b-562 adsorbed on colloidal gold particles; adsorption band shift", Chemical Communications, pp605-606, 1997

Website References

Chemical Education website: www.chem.sunysb.edu/courses/che133/beerslaw.html

Clonetech website: www.clontech.com/products/catalog02/HTML/1102.shtml

Blue Histology, Endothelial Cells, Professor John McGeachie, School of Anatomy and Human Biology, University of Western Australia website: www.lab.anhb.uwa.edu.au/mb140/MoreAbout/Endothel.htm